



*biomimetics*

Special Issue Reprint

---

# Advances in Biomimetics

The Power of Diversity

---

Edited by  
Stanislav N. Gorb, Giuseppe Carbone, Thomas Speck and Peter Fratzl

[mdpi.com/journal/biomimetics](https://mdpi.com/journal/biomimetics)



# **Advances in Biomimetics: The Power of Diversity**





# **Advances in Biomimetics: The Power of Diversity**

Guest Editors

**Stanislav N. Gorb**

**Giuseppe Carbone**

**Thomas Speck**

**Peter Fratzl**



Basel • Beijing • Wuhan • Barcelona • Belgrade • Novi Sad • Cluj • Manchester

*Guest Editors*

Stanislav N. Gorb

Department Functional  
Morphology and Biomechanics  
Zoological Institute of  
the University of Kiel  
Kiel  
Germany

Giuseppe Carbone

Department of Mechanics  
Mathematics and Management  
Polytechnic University of Bari  
Bari  
Italy

Thomas Speck

Botanic Garden  
University of Freiburg  
Freiburg  
Germany

Peter Fratzl

Max Planck Institute of  
Colloids and Interfaces  
Potsdam  
Germany

*Editorial Office*

MDPI AG

Grosspeteranlage 5  
4052 Basel, Switzerland

This is a reprint of the Special Issue, published open access by the journal *Biomimetics* (ISSN 2313-7673), freely accessible at: [www.mdpi.com/journal/biomimetics/special\\_issues/ZR93YZ9706](http://www.mdpi.com/journal/biomimetics/special_issues/ZR93YZ9706).

For citation purposes, cite each article independently as indicated on the article page online and using the guide below:

Lastname, A.A.; Lastname, B.B. Article Title. <i>Journal Name</i> <b>Year</b> , Volume Number, Page Range.
--

**ISBN 978-3-7258-3390-0 (Hbk)**

**ISBN 978-3-7258-3389-4 (PDF)**

**<https://doi.org/10.3390/books978-3-7258-3389-4>**

Cover image courtesy of Julian Winand

The TriTrap gripper inspired by tarsal chain of insects.

© 2025 by the authors. Articles in this book are Open Access and distributed under the Creative Commons Attribution (CC BY) license. The book as a whole is distributed by MDPI under the terms and conditions of the Creative Commons Attribution-NonCommercial-NoDerivs (CC BY-NC-ND) license (<https://creativecommons.org/licenses/by-nc-nd/4.0/>).

# Contents

About the Editors . . . . .	vii
-----------------------------	-----

**Stanislav N. Gorb, Giuseppe Carbone, Thomas Speck and Peter Fratzl**

Advances in Biomimetics: The Power of Diversity

Reprinted from: *Biomimetics* **2025**, *10*, 54, <https://doi.org/10.3390/biomimetics10010054> . . . . . 1

**Shengchang Fang, Guisong Chen, Tong Liu, Weimian Zhou, Yucheng Wang and Xiaojie Wang**

Role of Tail Dynamics on the Climbing Performance of Gecko-Inspired Robots: A Simulation and Experimental Study

Reprinted from: *Biomimetics* **2024**, *9*, 625, <https://doi.org/10.3390/biomimetics9100625> . . . . . 5

**Carolina Casagualda, Alba López-Moral, Paula Alfonso-Triguero, Julia Lorenzo, Ramon Alibés and Félix Busqué et al.**

Mussel-Inspired Multifunctional Polyethylene Glycol Nanoparticle Interfaces

Reprinted from: *Biomimetics* **2024**, *9*, 531, <https://doi.org/10.3390/biomimetics9090531> . . . . . 26

**Hermann Ehrlich, Alona Voronkina, Konstantin Tabachnik, Anita Kubiak, Alexander Ereskovsky and Teofil Jesionowski**

Silactins and Structural Diversity of Biosilica in Sponges

Reprinted from: *Biomimetics* **2024**, *9*, 393, <https://doi.org/10.3390/biomimetics9070393> . . . . . 42

**Elisabetta Rosellini, Cristiana Giordano, Lorenzo Guidi and Maria Grazia Cascone**

Biomimetic Approaches in Scaffold-Based Blood Vessel Tissue Engineering

Reprinted from: *Biomimetics* **2024**, *9*, 377, <https://doi.org/10.3390/biomimetics9070377> . . . . . 64

**Zhiwei Cui, Ye Wang and Jaap M. J. den Toonder**

Metachronal Motion of Biological and Artificial Cilia

Reprinted from: *Biomimetics* **2024**, *9*, 198, <https://doi.org/10.3390/biomimetics9040198> . . . . . 103

**Julian Winand, Thies H. Büscher and Stanislav N. Gorb**

TriTrap: A Robotic Gripper Inspired by Insect Tarsal Chains

Reprinted from: *Biomimetics* **2024**, *9*, 142, <https://doi.org/10.3390/biomimetics9030142> . . . . . 127

**Fenglin Chen, Ziyang Cheng, Lei Jiang and Zhichao Dong**

Capillary Wicking on *Heliamphora minor*-Mimicking Mesoscopic Trichomes Array

Reprinted from: *Biomimetics* **2024**, *9*, 102, <https://doi.org/10.3390/biomimetics9020102> . . . . . 141

**Adrien Saint-Sardos, Annabelle Aish, Nikolay Tchakarov, Thierry Bourgoïn, Luce-Marie Petit and Jian-Sheng Sun et al.**

Bioinspire-Explore: Taxonomy-Driven Exploration of Biodiversity Data for Bioinspired Innovation

Reprinted from: *Biomimetics* **2024**, *9*, 63, <https://doi.org/10.3390/biomimetics9020063> . . . . . 156

**Yu Wang, Jian Wang, Song Kang and Junzhi Yu**

Target-Following Control of a Biomimetic Autonomous System Based on Predictive Reinforcement Learning

Reprinted from: *Biomimetics* **2024**, *9*, 33, <https://doi.org/10.3390/biomimetics9010033> . . . . . 169

**Javad Meshkani, Hamed Rajabi, Alexander Kovalev and Stanislav N. Gorb**

Locomotory Behavior of Water Striders with Amputated Legs

Reprinted from: *Biomimetics* **2023**, *8*, 524, <https://doi.org/10.3390/biomimetics8070524> . . . . . 188



# About the Editors

## **Stanislav N. Gorb**

Prof. Dr. Stanislav N. Gorb is a full professor at Kiel University, Germany. His scientific interest is mainly on biological attachment, functional morphology, biomechanics, biotribology, and biomimetics. He now serves as the Editor-in-Chief of *Biomimetics*.

## **Giuseppe Carbone**

Prof. Dr. Giuseppe Carbone is currently a Full Professor of Applied Mechanics, Head of the Department of Mechanics Mathematics and Management at Politecnico di Bari, Italy and President of the Italian Association of Tribology. His scientific interests focus mainly on tribology, biomimetics, viscoelastic materials, contact mechanics, and adhesion.

## **Thomas Speck**

Prof. Dr. Thomas Speck is currently a Full Professor at the University of Freiburg, Germany. His scientific interest is mainly on the functional morphology of plants, plant biomechanics, plant–animal interactions, bioinspired materials/structures/surfaces, phylogeny of plants and paleobotany.




## **Peter Fratzl**

Prof. Dr. Peter Fratzl is currently a Full Professor at the Max Planck Institute of Colloids and Interfaces, Germany. His scientific interests focus mainly on biological and bio-inspired composite materials, osteoporosis and bone regeneration, biomaterials, mechanosensors and actuators.



Editorial

# Advances in Biomimetics: The Power of Diversity

Stanislav N. Gorb <sup>1,\*</sup> , Giuseppe Carbone <sup>2</sup> , Thomas Speck <sup>3,4</sup>  and Peter Fratzl <sup>5</sup>

<sup>1</sup> Department of Functional Morphology and Biomechanics, Zoological Institute, Kiel University, 24118 Kiel, Germany

<sup>2</sup> Dipartimento di Meccanica-Matematica-Management DMMM, Campus, Via Orabona 4, 70125 Bari, Italy; giuseppe.carbone@poliba.it

<sup>3</sup> Plant Biomechanics, Botanic Garden, Faculty of Biology, University of Freiburg, Schänzlestraße 1, D-79104 Freiburg, Germany; thomas.speck@biologie.uni-freiburg.de

<sup>4</sup> Cluster of Excellence livMatS @ FIT, Georges-Köhler-Allee 105, D-79110 Freiburg, Germany

<sup>5</sup> Max Planck Institute of Colloids and Interfaces, Department of Biomaterials, Research Campus Golm, Am Mühlenberg 1, 14476 Potsdam, Germany; peter.fratzl@mpikg.mpg.de

\* Correspondence: sgorb@zoologie.uni-kiel.de

Biomimetics research on living systems attempts to transfer their properties and functions to engineering applications. Biological materials, structures, and processes are predominantly based on the combination of various effects at different scales: from the nano- through to the micro-, meso-, and, finally, the macroscale. This Special Issue is devoted to the latest advances in biomimetics in all its subfields: (1) materials and structures; (2) designs, constructions, and devices; (3) surfaces and interfaces; (4) locomotion and bioinspired robotics; and (5) development of biomimetic methodology. The Special Issue contains papers from biological fields focusing on the proper identification of the underlying structure and functional principles in nature, which explains the observed properties of biological systems. Manuscripts that apply these to modern technologies have been included as well.

Two important review papers are included: the first is on scaffold-based blood vessel tissue engineering by Elisabetta Rosellini and coworkers (2024) [Contribution 1] and the second is on metachronal motion of biological and artificial cilia by Zhiwei Cui et al. (2024) [Contribution 2]. The first review provides the state of the art of vascular tissue engineering, specifically focusing on scaffolds designed by following a biomimetic approach. By mimicking native vessel properties, and particularly the complexly layered structure of the vascular wall, tissue-engineered scaffolds demonstrate improved long-term patency and promising clinical results. Moreover, modern biomimetic research is focused on enhancing the use of innovative scaffold materials, surface functionalization strategies, and the use of bioreactors mimicking the physiological microenvironment. Finally, this paper provides an overview of the latest advancements and future directions of vascular tissue engineering, with emphasis on the use of biomimetics to generate systems capable of reproducing the structure–function relationships present in the arterial wall (Rosellini et al., 2024) [Contribution 1]. The second review focuses on biological and artificial cilia. Biological cilia are slender, hair-like cell protrusions present in numerous organisms from protozoans to humans. They generate fluid flow, participate in locomotion, and support feeding. Their coordinated beating resulting in wavelike motions (so-called metachrony) supports flow generation and mucus transport. Researchers have meanwhile undertaken numerous attempts to fabricate artificial cilia and develop innovative approaches to mimic the metachronal motion observed in nature. In this review, different types of metachronal motion generated by both biological and artificial cilia are analyzed (pneumatically, photonically, electrically, and magnetically



Received: 8 January 2025

Accepted: 14 January 2025

Published: 15 January 2025

**Citation:** Gorb, S.N.; Carbone, G.; Speck, T.; Fratzl, P. Advances in Biomimetics: The Power of Diversity. *Biomimetics* **2025**, *10*, 54. <https://doi.org/10.3390/biomimetics10010054>

**Copyright:** © 2025 by the authors. Licensee MDPI, Basel, Switzerland. This article is an open access article distributed under the terms and conditions of the Creative Commons Attribution (CC BY) license (<https://creativecommons.org/licenses/by/4.0/>).



driven). Numerous possible applications of artificial cilia are proposed, and potential future directions within this field are suggested (Cui et al., 2024) [Contribution 2].

The simulation and experimental study by Fang et al. (2024) [Contribution 3] is focused on the role of tail dynamics on the climbing performance of gecko-inspired robots. They claim that the majority of research that has focused on the adhesion mechanisms of geckos has ignored that the tail plays a critical role in maintaining balance and stability during locomotion on the wall and ceiling. The authors systematically explore the role of tails on the climbing performance of gecko-inspired robots using both simulation and experimental approaches and developed a simulation system that predicts the robot's contact failures (Fang et al., 2024) [Contribution 3]. Their work provides an important step for further optimizing climbing robot performance.

The paper by Casagualda et al. (2024) [Contribution 4] reports on novel mussel-inspired multifunctional polyethylene glycol nanoparticle interfaces. The authors developed a bioinspired catechol-based strategy to obtain biocompatible and multifunctional coatings based on a previously developed polymerization methodology under mild oxidative conditions. Two types of nanoparticles were made: (1) mesoporous-silica-based nanoparticles and (2) magnetite-based nanoparticles. The authors have not only demonstrated the feasibility of their approach in obtaining coatings by using different types of nanoparticles but also incorporated fluorescein functionalities into their coatings that confer biocompatibility and excellent cell internalization and can be used for the imaging and tracking of nanoparticles in various biological and medical applications (Casagualda et al., 2024) [Contribution 4].

Sponges are well recognized as an archive of multi-scaled skeletal constructs with superficial micro-ornamentation patterned by biopolymers (Ehrlich et al., 2024) [Contribution 5]. In their study, Ehrlich et al. (2024) [Contribution 5] desilicified spicules and skeletal frameworks of some selected sponge species using 10% HF and obtained isolated axial filaments consisting of F-actins. These F-actins, called silactins, are presumably pattern drivers in skeletal constructs of sponges, and their understanding may open (1) the way to the fundamental understanding of the skeletogenesis of sponges and (2) the biomimetic potential towards the synthesis of poriferan biosilica patterned by silactins (Ehrlich et al., 2024) [Contribution 5].

Winand et al. (2024) [Contribution 6] have developed a robotic gripper (TriTrap gripping device) inspired by insect tarsal chains. In their paper, they highlight the potential of the tarsal chain principle. Just like its biological counterpart, the TriTrap utilizes strongly underactuated digits that function using morphological encoding and passive conformation. This results in a gripper that is versatile, robust, and low cost. The gripping performance of the TriTrap is demonstrated on a variety of 3D objects of different sizes, weights, and shapes (Winand et al., 2024) [Contribution 6]. The future potential of the insect tarsus principle in robotics in general is discussed.

The paper by Chen et al. (2024) [Contribution 7] is devoted to the liquid interaction with *Heliamphora minor* mimicking mesoscopic trichome arrays. It is well known that driven by the phenomenon of capillarity, a liquid can spread on rough lyophilic surfaces (capillary wicking). In this paper, the authors were inspired by the pitcher plant *H. minor*, which is capable of spreading water on its inside wall covered by anisotropically oriented trichomes. In the next step, the authors used a 3D printing technique to fabricate similar surface structures and investigated their capillary wicking capability. They also demonstrated the mass transportation on this biomimetic surface and suggested potential applications of their development in the design of low-cost, high-flux open fluidic devices (Chen et al., 2024) [Contribution 7].

The paper by Saint-Sardos et al. (2024) [Contribution 8] discusses the importance of the taxonomy-driven exploration of biodiversity for potential bioinspired innovations. The recent problem of searching for bioinspiration is due to the presentation of open-access biodiversity databases that are often adapted to life scientists rather than to bioinspired designers and engineers. In this paper, the authors suggested a new tool called “Bioinspire-Explore” capable of navigating biodiversity data to uncover biological systems of interest for different areas of bioinspired engineering. This tool allows for searching biological models using a taxonomy approach and provides information on the taxon’s position, its distribution, and its ecological niche (Saint-Sardos et al., 2024) [Contribution 8]. This novel tool has strong potential for biologists, but especially for bioinspired designers in gathering quick and reliable information about the organisms and their features that are potentially important for biomimetics.

Wang et al. (2024) [Contribution 9] reported on the target-following control of a biomimetic autonomous system inspired by the fish swimming in a group with improved hydrodynamic efficiency. In the established model, the follower robotic fish keeps a certain distance and orientation from the leader fish. Then a nonlinear predictive controller was designed that can be selected for the follower together with the predictive reinforcement learning (Wang et al., 2024) [Contribution 9]. After extensive simulations, the authors demonstrated the effectiveness of the cooperative control for underwater swarm locomotion.

The mechanisms that coordinate leg movement patterns are especially complex in organisms moving at the water–air interface. Meshkani et al. (2023) [Contribution 10] assumed the presence of compensatory factors, which are involved in the maintenance of the water strider posture after the amputation of individual legs. The authors studied load distribution among the legs and analyzed the effects of leg amputation on the locomotory behavior. A stable posture was quickly recovered by animals by using leg position modifications and load redistribution to the remaining legs. These experiments may assist the bioinspired design of robust aquatic robots (Meshkani et al., 2023) [Contribution 10].

Thanks to the theoretical, experimental, and review contributions provided by researchers in the fields of biology, physics, material science, engineering, this Special Issue of *Biomimetics* will certainly find its broad readership among all researchers who are engaged in this fast-growing field of science.

**Conflicts of Interest:** The authors declare no conflict of interest.

#### List of Contributions

1. Rosellini, E.; Giordano, C.; Guidi, L.; Cascone, M.G. Biomimetic Approaches in Scaffold-Based Blood Vessel Tissue Engineering *Biomimetics* **2024**, *9*, 377. <https://doi.org/10.3390/biomimetics9070377>.
2. Cui, Z.; Wang, Y.; den Toonder, J.M.J. Metachronal Motion of Biological and Artificial Cilia. *Biomimetics* **2024**, *9*, 198. <https://doi.org/10.3390/biomimetics9040198>.
3. Fang, S.; Chen, G.; Liu, T.; Zhou, W.; Wang, Y.; Wang, X. Role of Tail Dynamics on the Climbing Performance of Gecko-Inspired Robots: A Simulation and Experimental Study. *Biomimetics* **2024**, *9*, 625. <https://doi.org/10.3390/biomimetics9100625>.
4. Casagualda, C.; López-Moral, A.; Alfonso-Triguero, P.; Lorenzo, J.; Alibés, R.; Busqué, F.; Ruiz-Molina, D. Mussel-Inspired Multifunctional Polyethylene Glycol Nanoparticle Interfaces. *Biomimetics* **2024**, *9*, 531. <https://doi.org/10.3390/biomimetics9090531>.
5. Ehrlich, H.; Voronkina, A.; Tabachni, K.; Kubiak, A.; Ereskovsky, A.; Jesionowski, T. Silactins and Structural Diversity of Biosilica in Sponges. *Biomimetics* **2024**, *9*, 393. <https://doi.org/10.3390/biomimetics9070393>.
6. Winand, J.; Büscher, T.H.; Gorb, S.N. TriTrap: A Robotic Gripper Inspired by Insect Tarsal Chains. *Biomimetics* **2024**, *9*, 142. <https://doi.org/10.3390/biomimetics9030142>.

7. Chen, F.; Cheng, Z.; Jiang, L.; Dong, Z. Capillary Wicking on *Heliamphora minor*-Mimicking Mesoscopic Trichomes Array. *Biomimetics* **2024**, *9*, 102. <https://doi.org/10.3390/biomimetics9020102>.
8. Saint-Sardos, A.; Aish, A.; Tchakarov, N.; Bourgoïn, T.; Petit, L.-M.; Sun, J.-S.; Vignes-Lebbe, R. Bioinspire-Explore: Taxonomy-Driven Exploration of Biodiversity Data for Bioinspired Innovation. *Biomimetics* **2024**, *9*, 63. <https://doi.org/10.3390/biomimetics9020063>.
9. Wang, Y.; Wang, J.; Kang, S.; Yu, J. Target-Following Control of a Biomimetic Autonomous System Based on Predictive Reinforcement Learning. *Biomimetics* **2024**, *9*, 33. <https://doi.org/10.3390/biomimetics9010033>.
10. Meshkani, J.; Rajabi, H.; Kovalev, A.; Gorb, S.N. Locomotory Behavior of Water Striders with Amputated Legs. *Biomimetics* **2023**, *8*, 524. <https://doi.org/10.3390/biomimetics8070524>.

**Disclaimer/Publisher’s Note:** The statements, opinions and data contained in all publications are solely those of the individual author(s) and contributor(s) and not of MDPI and/or the editor(s). MDPI and/or the editor(s) disclaim responsibility for any injury to people or property resulting from any ideas, methods, instructions or products referred to in the content.



## Article

# Role of Tail Dynamics on the Climbing Performance of Gecko-Inspired Robots: A Simulation and Experimental Study

Shengchang Fang <sup>1,2</sup> , Guisong Chen <sup>1</sup>, Tong Liu <sup>1,2</sup> , Weimian Zhou <sup>1,2</sup>, Yucheng Wang <sup>1,\*</sup> and Xiaojie Wang <sup>1,\*</sup>

<sup>1</sup> Institute of Intelligent Machines, Hefei Institutes of Physical Science, Chinese Academy of Sciences, Hefei 230031, China; scfang@iamt.ac.cn (S.F.); chengs@iim.ac.cn (G.C.); lt1997@mail.ustc.edu.cn (T.L.); wzmzhou@mail.ustc.edu.cn (W.Z.)

<sup>2</sup> University of Science and Technology of China, Hefei 230026, China

\* Correspondence: ycwang@iamt.ac.cn (Y.W.); xjwang@iamt.ac.cn (X.W.)

**Abstract:** Geckos are renowned for their exceptional climbing abilities, enabled by their specialized feet with hairy toes that attach to surfaces using van der Waals forces. Inspired by these capabilities, various gecko-like robots have been developed for high-risk applications, such as search and rescue. While most research has focused on adhesion mechanisms, the gecko's tail also plays a critical role in maintaining balance and stability. In this study, we systematically explore the impact of tail dynamics on the climbing performance of gecko-inspired robots through both simulation and experimental analysis. We developed a dynamic climbing simulation system that models the robot's specialized attachment devices and predicts contact failures. Additionally, an adjustable-angle force measurement platform was constructed to validate the simulation results. Our findings reveal the significant influence of the tail on the robot's balance, stability, and maneuverability, providing insights for further optimizing climbing robot performance.

**Keywords:** gecko-inspired robots; tail dynamics; dynamic simulation; climbing performance



**Citation:** Fang, S.; Chen, G.; Liu, T.; Zhou, W.; Wang, Y.; Wang, X. Role of Tail Dynamics on the Climbing Performance of Gecko-Inspired Robots: A Simulation and Experimental Study. *Biomimetics* **2024**, *9*, 625. <https://doi.org/10.3390/biomimetics9100625>

Academic Editors: Stanislav N. Gorb, Giuseppe Carbone, Peter Fratzl and Thomas Speck

Received: 12 August 2024

Revised: 30 September 2024

Accepted: 10 October 2024

Published: 14 October 2024



**Copyright:** © 2024 by the authors. Licensee MDPI, Basel, Switzerland. This article is an open access article distributed under the terms and conditions of the Creative Commons Attribution (CC BY) license (<https://creativecommons.org/licenses/by/4.0/>).

## 1. Introduction

Geckos are natural climbing experts, capable of agile movement across various rugged environments. This ability is primarily due to their specialized feet, which feature hairy toes that can uncurl to attach to surfaces using van der Waals forces and peel off within milliseconds [1,2]. As a result, geckos have become a significant source of inspiration for the development of climbing robots, such as Geckobot [3] and Stickybot [4,5]. These bio-inspired robots have demonstrated immense potential and importance in a range of applications, particularly in high-risk tasks such as search and rescue, inspection and maintenance, and military reconnaissance.

Currently, most research has focused on developing adhesion mechanisms, including suction cups [6–8], magnets [9–11], micro-spines [12,13], and dry adhesive materials [14,15]. Based on these mechanisms, many climbing robots have demonstrated reliable climbing capabilities. However, the gecko's remarkable climbing ability is not solely due to the setae on its toe pads [16]; its tail also plays a crucial role. For instance, when a gecko slips during rapid climbing, it quickly presses its tail against the vertical surface to prevent its head from pitching backward. Even if the backward pitch cannot be fully prevented, the gecko positions its tail like a bicycle kickstand to avoid falling [17]. Additionally, some geckos use their tails to adjust their direction while gliding, allowing them to navigate through trees [18]. Geckos can also increase their speed by adjusting the amplitude and frequency of lateral undulations in their bodies and tails [19,20]. These biological phenomena suggest that the tail has significant potential for further enhancing the locomotion performance of climbing robots.

In this paper, our aim is to systematically explore the impact of the tail on the climbing performance of robots through experimental research. However, conducting experiments

on climbing robots designed for high-risk tasks is often challenging, as it typically requires large-scale equipment to ensure the safety of both the robot prototypes and the operators. To address this, we developed a climbing dynamics simulation system designed to replicate the robot's real climbing behavior in a simulated environment. Unlike existing dynamic climbing models that simplify the interaction between the robot's feet and the wall as stable contact [21–23], the core design of our simulation system focuses on dynamic contact modeling of the robot's specialized attachment devices. The model effectively predicts contact failures during the climbing process and outputs key parameters such as the robot's motion trajectory, contact forces, and joint torques.

Additionally, we developed an adjustable-angle force measurement platform to test the robot's climbing performance in real-world environments, further validating the effectiveness of the simulation model. By comparing the robot's performance with and without a tail, this paper explores the impact of the tail on the balance, stability, and maneuverability of climbing robots. The insights gained from the simulations and experimental results, along with the subsequent analysis, will contribute to the further optimization of the robot's climbing performance.

## 2. Construction of a Climbing Dynamics Simulation System

In our previous work, we designed a gecko-inspired climbing robot, WCQR-III [24], by mimicking the body structure of a gecko. Based on parameters such as the robot's dimensions, weight, and attachment mechanism, we constructed a climbing dynamics simulation system. This system was used to simulate the robot's climbing behavior in a virtual environment and to predict potential climbing failures in both tailed and tailless states.

### 2.1. Overall Structure of the WCQR-III Robot

Figure 1a shows the overall structure of a gecko, with its body connected to four legs and a tail. Each leg consists of three main parts: the thigh, crus, and claw, which are connected by various joints. The thigh is connected to the body via a hip joint, allowing for two degrees of freedom in spherical motion. The thigh and crus are connected by a knee joint, which provides one degree of freedom in rotational motion. The claw at the end is used for climbing surfaces. The tail is connected to the body through a tail joint. By abstracting the gecko's configuration, we designed the climbing robot WCQR-III, as shown in Figure 1b. The robot features four legs and a tail, with a flat body. The body is equipped with a circuit board, and the onboard battery is mounted at the bottom of the body to keep the center of gravity as close to the wall as possible, minimizing pitch moments caused by shifts in the center of gravity. Each leg of the robot has three active joints, each driven by an actuator (Model HV0916, Yobotics Co., Ltd., Jinan, China) with a rated output torque of 6.07 N·m. Unlike the gecko's hip joint, which has two degrees of freedom, we designed a combination of a lateral hip joint and a forward hip joint to achieve multi-degree-of-freedom control. The lateral hip joint controls the up-and-down movement of the crus, while the forward hip joint controls the forward and backward movement of the crus. The robot's tail is connected to the body via a torsion spring, and a roller is attached to the end of the tail to reduce friction with the wall. The tail can be manually removed to simulate the condition of "tail loss". The robot's body components are made of lightweight carbon fiber and nylon materials, keeping the total weight of the robot under 3 kg. Table 1 provides the parameters of key components.

In addition to the setae structures used for climbing on smooth surfaces, geckos possess sharp claws that provide adhesion on rough surfaces. To mimic this, we designed spiny claws as the robot's attachment devices, enabling it to climb rough surfaces, as shown in Figure 1c. An under-actuated compliance ankle connects the spiny toepad array to the crus, allowing the spiny claw to easily contact wall surfaces. Each spiny claw consists of an array of 50 spiny toepads, with each spiny toepad design adapted from reference [25], inspired primarily by the spines on insect legs (as shown in Figure 1d). The steel hooks at the top can engage with microscopic particles on rough surfaces, forming a mechanical

interlock that generates adhesion. The rigid linkage is made of nylon and is connected using flexible polyurethane material. This hybrid configuration of rigid and flexible components effectively enhances adhesion stability.

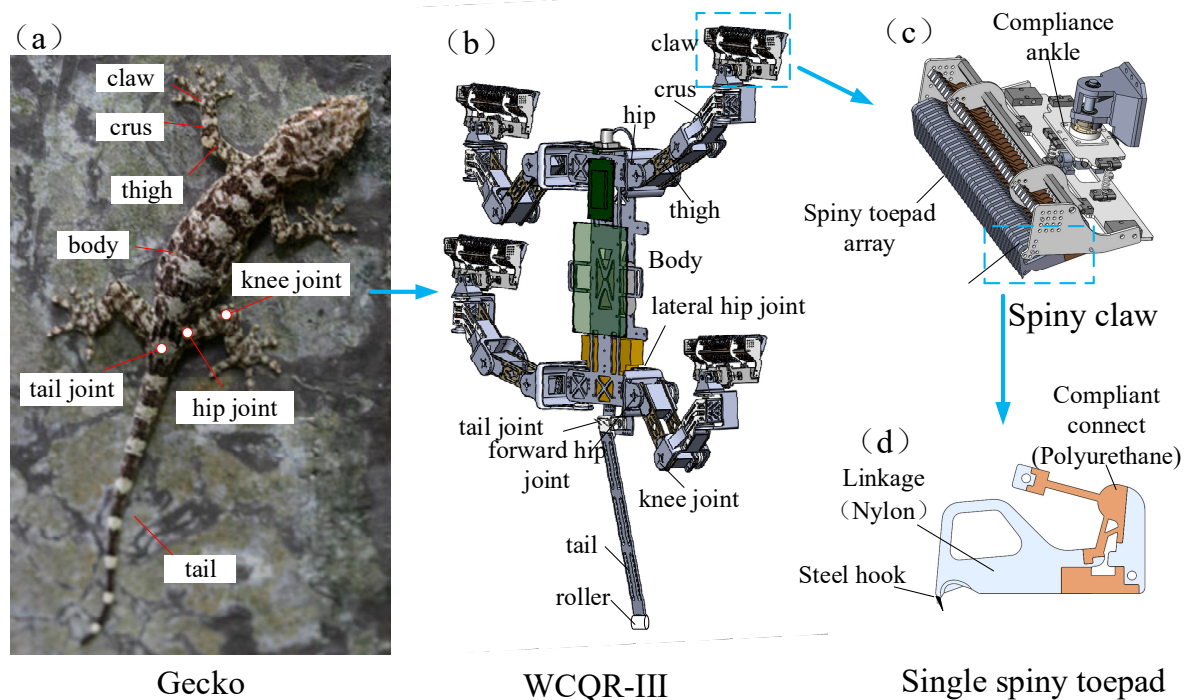


**Figure 1.** (a) Overall structure of the gecko, (b) Overall structure of the gecko-inspired robot WCQR-III, (c) The structure of the spiny claw, and (d) The structure of a single spiny toepad.

**Table 1.** Physical parameters of the robot.

Part	Mass (g)	Length (mm)
Body	2200	288 × 137
Hip	40.1	53
Thigh	203.5	100
Crus	72.9	100
Claw	231.1	100
Tail	20.3	300

After obtaining the overall structural parameters of the robot and the adhesion mechanism of the attachment devices, we will develop a multibody dynamics model of the robot's body structure and a dynamic contact model of the attachment devices. Finally, we will integrate these models to construct a comprehensive climbing dynamics simulation system.

## 2.2. Multibody Dynamics Modeling

Based on the parameters provided in Table 1, the overall structure of the robot can be simplified into links of different lengths with masses, connected by rotational joints, as shown in Figure 2. Considering that the robot is a complex multi-joint system, we use Kane's method for multibody dynamics modeling. Unlike the Newton-Euler and Lagrange's methods, Kane's method does not calculate constraint forces and energy, significantly reducing the computational load of the dynamics [26]. This makes it particularly suitable for systems with multiple degrees of freedom.

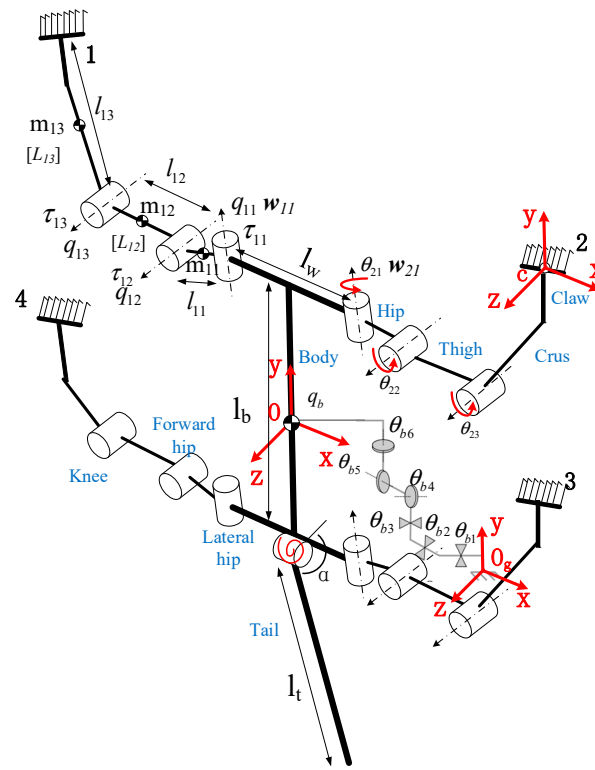


**Figure 2.** The topology of the WCQR-III robot.

For a complete system composed of  $n$  particles with  $m$  generalized degrees of freedom, the twist of the  $j$ -th degree of freedom in the body frame  $[L_{ij}]$  of the  $i$ -th particle is:

$$u_{ij} = \begin{bmatrix} q_{ij} \times \omega_{ij} \\ \omega_{ij} \end{bmatrix}, \quad i = 1, 2, \dots, n; j = 1, 2, \dots, m \quad (1)$$

where  $\omega_{ij}$  and  $q_{ij}$  respectively represent the unit vector in the positive direction and the generalized coordinate vector of the  $j$ -th degree of freedom in the body frame  $[L_{ij}]$  of the  $i$ th particle. The generalized active force  $F_j$  and the generalized inertia force  $F_j^*$  of the system on the  $j$ -th degree of freedom is

$$\begin{cases} F_j = \sum_{i=1}^n K_i \cdot u_{ij}, \\ F_j^* = \sum_{i=1}^n K_i^* \cdot u_{ij}, \end{cases} \quad i = 1, 2, \dots, n; j = 1, 2, \dots, m \quad (2)$$

Thus, we can obtain the Kane equation of the  $j$ -th degree of freedom of the system:

$$F_j + F_j^* = 0. \quad (3)$$

Next, we calculate the active wrenches for each link. Based on the different force conditions, the robot's links can be categorized into the body, links not in contact with the wall, and links in contact with the wall. First, we calculate the active wrenches  $K_{ij}$  for the links not in contact with the wall:

$$K_{ij} = \begin{pmatrix} M_{ij} \\ R_{ij} \end{pmatrix} = \begin{pmatrix} \tau_{ij} \omega_{ij} - \tau_{i(j+1)} \omega_{i(j+1)} \\ m_{ij} g \end{pmatrix}, \quad i = 1, 2, 3, 4; j = 1, 2. \quad (4)$$

where  $\tau_{ij}$  is the  $j$ -th joint torque of the  $i$ -th leg,  $\omega_{ij}$  is the unit vector in the positive direction of the  $j$ -th joint of the  $i$ -th leg, and  $m_{ij}$  is the mass of the  $j$ -th link of the  $i$ -th leg.

Considering the contact forces between the foot and the wall, the active wrenches  $K_{i3}$  for the links in contact with the wall are given by:

$$K_{i3} = \begin{pmatrix} M_{i3} \\ R_{i3} \end{pmatrix} = \begin{pmatrix} \tau_{i3}\omega_{i3} + F_{fi} \times (r_{fi} - r_{ci}) \\ m_{i3}g + F_{fi} \end{pmatrix}, \quad i = 1, 2, 3, 4. \quad (5)$$

where  $F_{fi}$  is the contact force between the foot on the  $i$ -th leg and the wall,  $r_{fi}$  is the position vector of the end-link on the  $i$ -th leg, and  $r_{ci}$  is the position vector of the center of mass of the end-link on the  $i$ -th leg.

Similarly, the active wrench  $K_b$  for the robot's body is calculated as follows:

$$K_b = \begin{pmatrix} M_b \\ R_b \end{pmatrix} = \begin{pmatrix} -\sum_{i=1}^4 \tau_{i1}\omega_{i1} - \tau_t\omega_t \\ m_bg \end{pmatrix} \quad (6)$$

where  $\tau_t = k_t\alpha$ ,  $k_t$  is the elastic coefficient of the tail joint torsion spring,  $\alpha$  is the rotational angle of the tail, and  $\omega_t$  is the unit directional vector of the tail joint.

In order to obtain the inertial wrench, the required angular velocity and the angular acceleration of each link via the following recursive formulas are given as:

$$\begin{cases} \omega_{L_{ij}}^b = R_{L_{ij}L_{i(j-1)}} \cdot \omega_{L_{i(j-1)}}^b + \dot{\theta}_{ij} \cdot \omega_{ij} \\ \dot{\omega}_{L_{ij}}^b = R_{L_{ij}L_{i(j-1)}} \cdot \dot{\omega}_{L_{i(j-1)}}^b + \ddot{\theta}_{ij} \cdot \omega_{L_{ij}} + \dot{\theta}_{ij} \cdot (\omega_{L_{i(j-1)}}^b \times \omega_{L_{ij}}) \\ \dot{v}_{L_{ij}}^b = R_{L_{ij}L_{i(j-1)}} \left\{ \dot{v}_{L_{i(j-1)}}^b + \dot{\omega}_{L_{i(j-1)}}^b \times (-l_{i(j-1)}^b) + \omega_{L_{i(j-1)}}^b \times [\omega_{L_{i(j-1)}}^b \times (-l_{i(j-1)}^b)] \right\} \\ \dot{v}_{C_{ij}}^b = \dot{v}_{L_{ij}}^b + \dot{\omega}_{L_{ij}}^b \times l_{ij}^b + \omega_{L_{ij}}^b \times (\omega_{L_{ij}}^b \times l_{ij}^b) \\ i = 1, 2, 3, 4; j = 1, 2, 3. \end{cases} \quad (7)$$

where  $\omega_{L_{ij}}^b$  and  $\dot{\omega}_{L_{ij}}^b$  are the angular velocity and the angular acceleration of the  $j$ -th link on the  $i$ -th leg in the body frame  $[L_{ij}]$ ,  $\dot{v}_{L_{ij}}^b$  is the acceleration in the body frame  $[L_{ij}]$ ,  $\dot{v}_{C_{ij}}^b$  is the acceleration of the CM in the body frame  $[L_{ij}]$ ,  $R_{L_{ij}L_{i(j-1)}}$  is the rotational transferring matrix of the frame  $[L_{ij}]$  relative to the frame  $[L_{i(j-1)}]$ , and  $l_{ij}^b$  is the distance from the CM to the joint of the  $j$ -th link on the  $i$ -th leg.

The inertial wrench of the body can be expressed as:

$$K_b^* = \begin{pmatrix} M_b^* \\ R_b^* \end{pmatrix} = \begin{pmatrix} -I_b\dot{\omega}_b - \omega_b \times I_b \cdot \omega_b \\ -m_b\dot{v}_b \end{pmatrix} = \begin{pmatrix} -I_b & \mathbf{0} \\ \mathbf{0} & -m_b \end{pmatrix} \ddot{q}_b + \begin{pmatrix} -\omega_b \times I_b \cdot \omega_b \\ \mathbf{0} \end{pmatrix} \quad (8)$$

The inertial wrench of the links can be expressed as:

$$K_{ij}^* = \begin{pmatrix} M_{ij}^* \\ R_{ij}^* \end{pmatrix} = \begin{pmatrix} -I_{ij}\dot{\omega}_{L_{ij}} - \omega_{L_{ij}} \times I_{ij} \cdot \omega_{L_{ij}} \\ -m_{ij}\dot{v}_{C_{ij}}^b \end{pmatrix} = \begin{pmatrix} -I_{ij} & \mathbf{0} \\ \mathbf{0} & -m_{ij} \end{pmatrix} \ddot{q}_{ij} + \begin{pmatrix} -\omega_{L_{ij}} \times I_{ij} \cdot \omega_{L_{ij}} \\ \mathbf{0} \end{pmatrix} \quad (9)$$

where  $I_{ij}$  is the inertia matrix of link  $j$  on the  $i$ -th leg with respect to the body frame  $[L_{ij}]$ ,  $I_b$  is the inertia matrix of the robot body in the global frame  $[O_g]$ , and  $\dot{\omega}_b\omega_b\dot{v}_b$  represents the angular acceleration, angular velocity, and linear acceleration of the robot body in the global frame  $[O_g]$ , respectively.



According to Equations (1)~(3), the Kane equations for the robot's body and the  $i$ -th leg can be obtained. By combining these equations, the complete set of dynamic equations for the robot is established:

$$\begin{cases} \sum_{i=1}^6 (F_{bi} + F_{bi}^*) = \sum_{i=1}^6 \left( \begin{bmatrix} M_b \\ R_b \end{bmatrix} \cdot u_{bi} + \begin{bmatrix} M_b^* \\ R_b^* \end{bmatrix} \cdot u_{bi} \right) = 0, \\ \sum_{i=1}^3 (F_{ni} + F_{ni}^*) = \sum_{i=1}^3 \left( \sum_{j=1}^3 \begin{bmatrix} M_{ni} \\ R_{ni} \end{bmatrix} \cdot u_{ij} + \sum_{j=1}^3 \begin{bmatrix} M_{ni}^* \\ R_{ni}^* \end{bmatrix} \cdot u_{ij} \right) = 0, (n = 1, 2, 3, 4) \end{cases} \quad (10)$$

### 2.3. Dynamic Contact Modeling

The Contact modeling is a critical aspect of dynamic analysis, especially in climbing dynamics, where the unique adhesion mechanisms of the foot attachment devices must be considered. For the spiny claw used by the WCQR-III, it can be simplified into a hybrid spring-damper linkage model, as shown in Figure 3b. This model represents the moment when the claw first makes contact with the wall. The model consists of two links, labeled as Link ① and Link ②, which are connected by a hinge joint. Link ① is directly connected to the robot's foot, and the end of Link ② is equipped with a steel hook designed to make contact with the wall. A torsion spring, with stiffness  $k_\beta$  and damping coefficient  $b_\beta$ , is installed between the two links. Additionally, a tension spring with stiffness  $k_a$  and damping coefficient  $b_a$  is used to allow for the extension and retraction of Link ②. In the initial state, Link ② has a length of  $a_0$  and forms an initial angle  $\beta_0$  with the  $y$ -axis. Table 2 presents the specific parameters of the model.

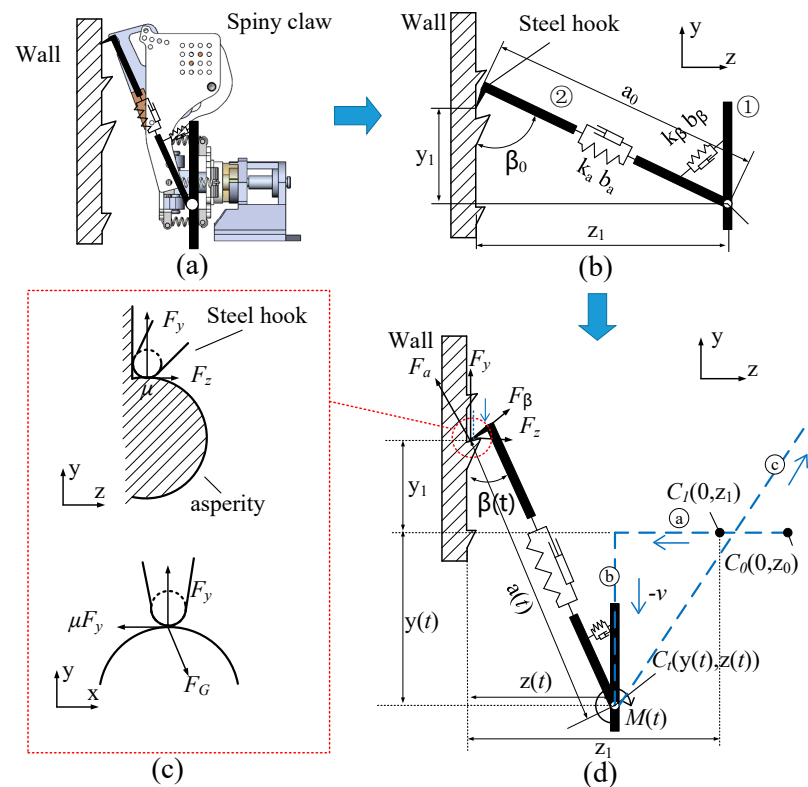


**Figure 3.** Dynamic contact model of spiny toepad: (a) the spiny claw; (b) hybrid spring-damper linkage model; (c) attachment process; (d) forces on the steel hook and rough surface.

**Table 2.** Parameters of spiny toepad.

Parameter	Value	Parameter	Value
$k_a$	191 N/m	$k_\beta$	0.0015 Nm/radian
$b_a$	0.42 Ns/m	$b_\beta$	0.02 Ns/m
$a_0$	30 mm	$\beta_0$	30°
$\mu$	0.25	$P$	20%
$\beta_{app}$	90°	$\beta_{detach}$	30°

During the robot's climbing process, the dynamic contact behavior of the spring-damper linkage model follows the foot trajectory shown by the blue dashed line in Figure 3c, progressing through three stages: (a) pressing, (b) dragging, and (c) detachment. In the pressing stage, the foot moves along the blue dashed line in the  $-z$  direction, starting from the initial point  $C_0(0, z_0)$ . When the foot reaches point  $C_1(0, z_1)$ , the steel hook at the tip of the spiny toepad first makes contact with the wall. The foot is then further pressed against the wall to ensure full contact between the spiny toepad and the wall surface. Once sufficient contact is achieved, the foot, under load, will move downward along the  $-y$  direction, entering the dragging phase. The steel hook at the end will mechanically interlock with the micro-particles on the rough wall surface, generating a contact force  $(F_a, F_\beta)$ . The components of this contact force along the  $y$ -axis and  $z$ -axis are denoted as  $(F_x, F_y)$ . Under the load, the tension spring stretches, causing the length of Link ② to change to  $a(t)$ , with an elongation of  $y(t)$  in the  $y$ -axis direction. The amount of elongation is determined by the load applied to the spiny toepad. However, if the load is too large, the tension spring may break. Therefore, we set a maximum elongation limit for the tension spring at 10 mm. Specifically, if  $y(t) < -10$  mm, the spring will be overstretched, leading to breakage and resulting in attachment failure. Due to the directional nature of the spiny toepad, it does not generate adhesion when moving in the direction opposite to the applied load [25]. Therefore, during the detachment phase, as the toepad moves upward in the reverse direction to  $y(t) > 0$ , the link returns to its initial length, completing the unloading process, and the contact force drops to zero.

By analyzing the dynamic contact process of the spiny toepad, the scenarios in which the contact force becomes zero at different stages can be inferred based on the relative position of the toepad to the wall. The following equations describe these conditions:

$$F = \begin{cases} 0 & \text{if } z(t) > z_1 \\ 0 & \text{if } y(t) > 0 \text{ or } y(t) < -10 \text{ and } z(t) \leq z_1 \\ \text{non-zero} & \text{if } -10 \leq y(t) \leq 0 \text{ and } z(t) \leq z_1 \end{cases} \quad (11)$$

Excluding cases where the contact force is zero, we calculate the changes in the foot's contact force at different moments when the spiny toepad forms effective adhesion. Subsequently, we establish the corresponding dynamic contact mathematical model.

Figure 3d illustrates the deformation of the spiny toepad after stable adhesion has been achieved. After undergoing the pressing and dragging actions, the length of Link ② and its angle with the wall can be expressed by the following equations:

$$a(t) = \sqrt{z(t)^2 + (y_1 + y(t))^2} \quad (12)$$

$$\beta(t) = \arctan \frac{z(t)}{y_1 + y(t)} \quad (13)$$

Furthermore, the elongation speed of Link ② and the angular velocity of its angle can be expressed as follows:

$$\dot{a}(t) = \frac{z(t) \cdot \dot{z}(t) + (y_1 + y(t)) \cdot \dot{y}(t)}{\sqrt{z(t)^2 + (y_1 + y(t))^2}} \quad (14)$$

$$\dot{\beta}(t) = \frac{\dot{z}(t) \cdot (y_1 + y(t)) - z(t) \cdot \dot{y}(t)}{(y_1 + y(t))^2 + z(t)^2} \quad (15)$$

The forces exerted by the steel hook on the rough wall surface are:

$$F_a = k_a \cdot (a(t) - a_0) + \dot{a}(t) \cdot b_a \quad (16)$$

$$F_\beta = \frac{k_\beta \cdot (\beta(t) - \beta_0) + \dot{\beta}(t) \cdot b_\beta}{a(t)} \quad (17)$$

After converting the calculation results to the y-z coordinate system, the tangential force  $F_y$  and the normal force  $F_z$  on the spiny toepads can be expressed as:

$$\begin{bmatrix} F_y \\ F_z \end{bmatrix} = \begin{bmatrix} -\sin \beta(t) & -\frac{1}{a(t)} \cos \beta(t) \\ \cos \beta(t) & -\frac{1}{a(t)} \sin \beta(t) \end{bmatrix} \cdot \left( \begin{bmatrix} k_a \cdot (a(t) - a_0) \\ k_\beta \cdot (\beta(t) - \beta_0) \end{bmatrix} - \begin{bmatrix} b_a \cdot \dot{a}(t) \\ b_\beta \cdot \dot{\beta}(t) \end{bmatrix} \right). \quad (18)$$

The lateral force of the spine in the x-direction can be calculated based on static equilibrium. Figure 3c illustrates the force situation of the spine in the x-y plane.  $F_G$  represents the load on the spiny toepad. The contact force of the spiny toepad in the x-axis direction is:

$$F_x = \mu F_y \quad (19)$$

where  $\mu$  is the friction coefficient between the metal and the rough rock.

Considering the adhesion probability of a spiny claw composed of n spiny toepads, the dynamic contact model equation for the spiny toepad can be expressed as:

$$F_f = n \cdot P \cdot [F_x, F_y, F_z]^T \quad (20)$$

Its inputs are the displacement and velocity of the spiny toepad relative to the wall, while its outputs are the adhesion forces generated by the spiny toepad in the tangential, normal, and lateral directions.

#### 2.4. Simulation Environment Setup

To visually demonstrate the robot's climbing process, a simulation environment was created using the multibody dynamics software RecurDyn (Student Version, FunctionBay), which can generate simulation animations. In this environment, contact constraints between the robot's body and the wall were established. The developed multibody dynamics and dynamic contact equations were input into MATLAB for mathematical computation. A co-simulation with RecurDyn was then conducted to calculate the changes in the robot's motion parameters during the climbing process.

The robot's climbing dynamics algorithm is shown as Algorithm 1. First, the desired motion trajectory is input, and the joint angle parameters of the robot are solved using inverse kinematics. Then, the center of mass trajectory of the robot is calculated using the dynamics Equation (10). After determining the current position of the foot through coordinate transformation, Equation (11) is used to assess whether effective contact has occurred. If effective contact is confirmed, the dynamic contact model is used to calculate the contact forces at the foot. Finally, the robot's foot contact forces, joint torques, and center of mass coordinates are output.

After constructing the simulation environment, the robot's climbing motion within the simulated environment can be observed by inputting the desired motion trajectory. We modeled the robot's desired motion trajectory after the movement pattern of a gecko. For quadrupedal climbing animals like geckos, the primary gait used is the diagonal gait, where two diagonal legs swing simultaneously in an alternating pattern [20], as shown in Figure 4a. Unlike the rapid alternating gait used for running on flat ground, during the climbing process, a gecko first ensures that the two diagonal legs in the air securely attach to the surface before detaching the legs that were previously in contact with the wall.

This approach ensures that at least two legs remain in contact with the wall at all times, providing stable adhesion throughout the climb.

#### Algorithm 1 Dynamic Climbing Algorithm

**Input:** desired motion trajectory coordinates  
**Output:** contact forces  $F_f$ ; joint torques  $\tau$ ; CM coordinates  $x_c(t), y_c(t), z_c(t)$

```

1  #Inverse Kinematics (IK) calculation to obtain joint angles
2  for t = 0; t ≤ T; t++ do
3       $\theta_{ij} \leftarrow IK(x(t), y(t), z(t))$ 
4      if  $-10 \leq y(t) \leq 0$  and  $z(t) \leq z_1$ 
5          CM coordinates  $x_c(t), y_c(t), z_c(t) \leftarrow$  use Equation (10)
6          Joint torques  $\tau \leftarrow$  use Equation (10)
7          Contact forces  $F_f \leftarrow$  use Equation (20)
8          break;
9      else:
10         Contact forces  $F_f \leftarrow 0$ 
11     continue

```

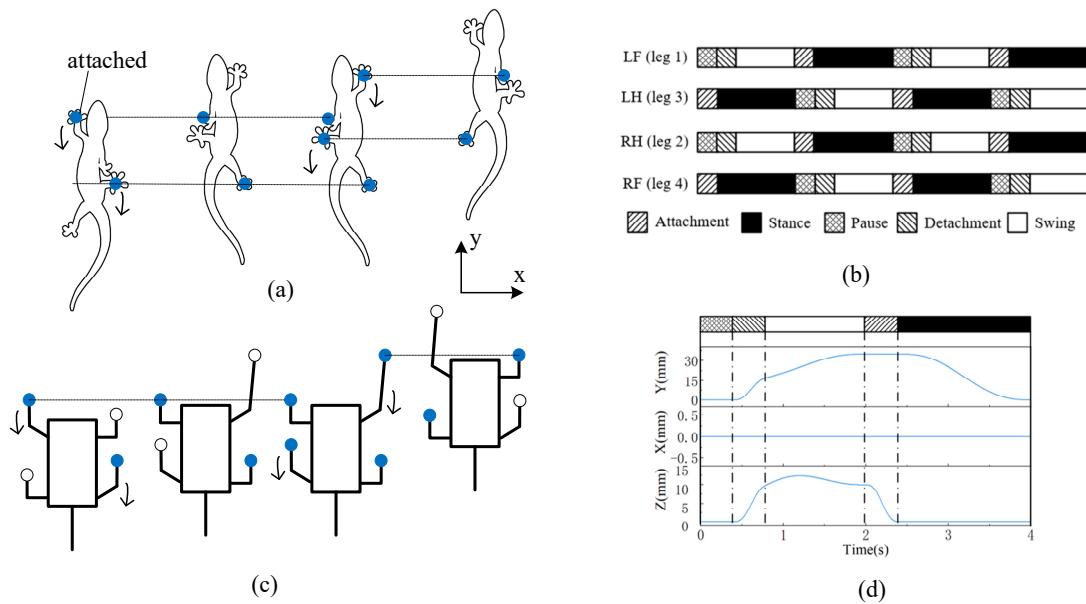


**Figure 4.** (a) Gecko's diagonal gait; (b) Duty cycle of each phase within a gait cycle; (c) Robot's climbing gait; (d) Foot coordinates during a gait cycle.

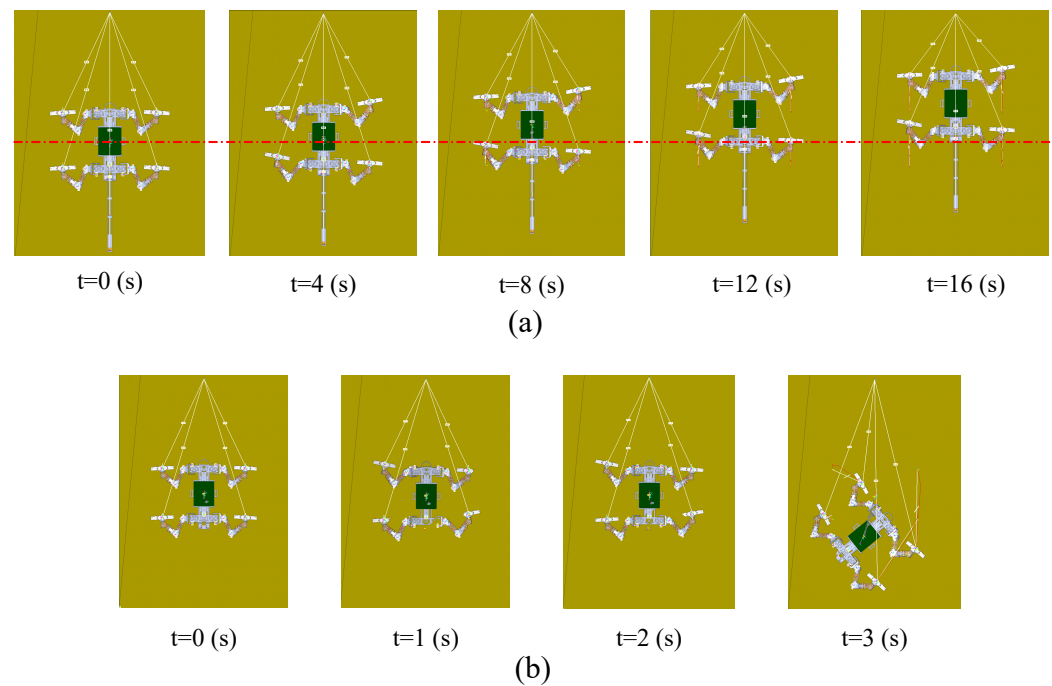
Similarly, we adopted this gait pattern for the robot and divided the foot movement into four phases: attachment, stance, detachment, and swing. To ensure that the robot always maintains contact with the wall with at least two legs, we introduced a Pause phase, as illustrated in Figure 4b,c. Figure 4d shows the predefined foot trajectory. We set the robot's gait cycle to 4 s. The horizontal displacement ( $x$ ) is set to zero to ensure that the robot climbs straight up; the vertical displacement ( $y$ ), representing the step length, is set to 35 mm; and the normal displacement ( $z$ ), representing the step height, is set to 15 mm.

### 3. Simulation Results

To assess the impact of the tail on climbing performance, we tested the robot's motion parameters under both tailed and tailless conditions at different inclines. The previously defined foot trajectory parameters were input into the developed climbing dynamics simulation system, with the simulation time set to 16 s to simulate the robot's climbing behavior over four cycles. The slope variations were simulated by modifying the direction of the gravitational acceleration parameter  $g$ .

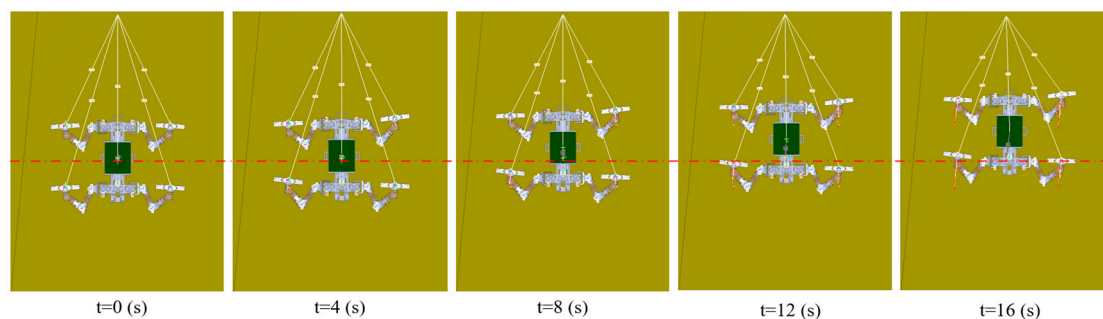
### 3.1. Maximum Climbing Angle Simulation

Figure 5 presents the time sequence diagrams of the robot climbing in a simulated vertical environment under both tailed and tailless conditions. In the tailed condition, the robot successfully climbs vertically along the predefined trajectory without falling. However, in the tailless condition, the robot begins to pitch backward after 2 s of upward movement, causing the front claws to gradually detach from the wall. Due to the constraints of the wall, the rear of the robot's body tilts to the right side after colliding with the wall, ultimately leading to a fall at the 3-s mark, preventing further upward climbing.



**Figure 5.** Simulation of the robot's climbing test on a  $90^\circ$  vertical surface: (a) With tail; (b) Without tail.

The robot is unable to climb vertical surfaces without its tail. To determine the maximum incline the robot can overcome in a tailless state, we gradually reduced the slope angle, starting from  $90^\circ$ , and simulated the climbing process at each angle. Only when the slope was reduced to  $86^\circ$  was the robot able to stably climb for four gait cycles without its tail, as shown in Figure 6.



**Figure 6.** The robot stably climbing an  $86^\circ$  slope in the simulation environment.

Figure 7 shows the variation in contact forces at each foot of the robot after four gait cycles of climbing on a  $90^\circ$  vertical surface with the tail. It also presents the contact force variation at each foot while climbing an  $86^\circ$  slope without the tail. Solid lines represent the contact forces in the tailed condition, while dashed lines represent the contact forces in the tailless condition. Through comparison, it can be observed that the robot generates

more stable adhesion forces in the tailed condition. In contrast, without the tail, the contact forces at the feet exhibit noticeable fluctuations, and the magnitudes of these forces in all directions are greater than those in the tailed condition. Further comparison of the forces in each direction reveals the following:

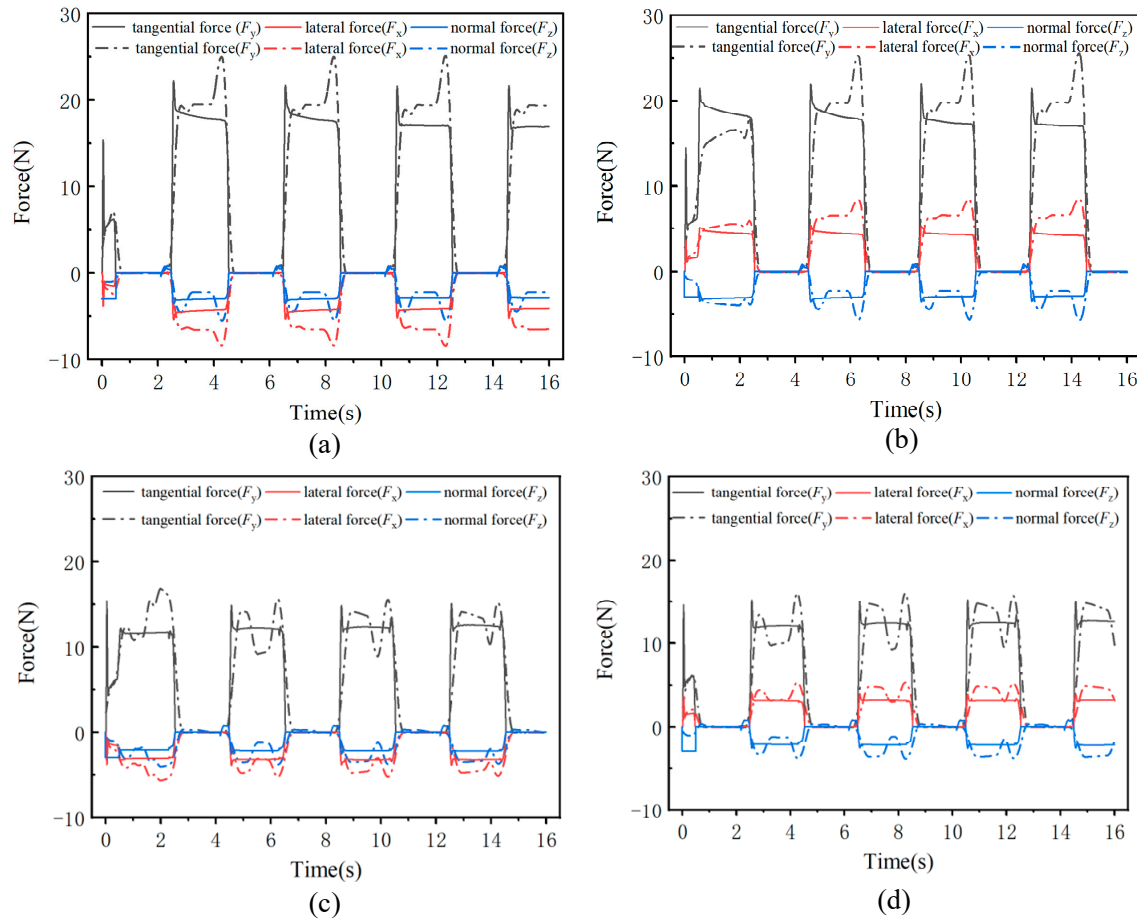


**Figure 7.** Comparison of foot-end contact forces during surface climbing with and without a tail: (a) Left front foot (b) Right front foot (c) Left hind foot (d) Right hind foot.

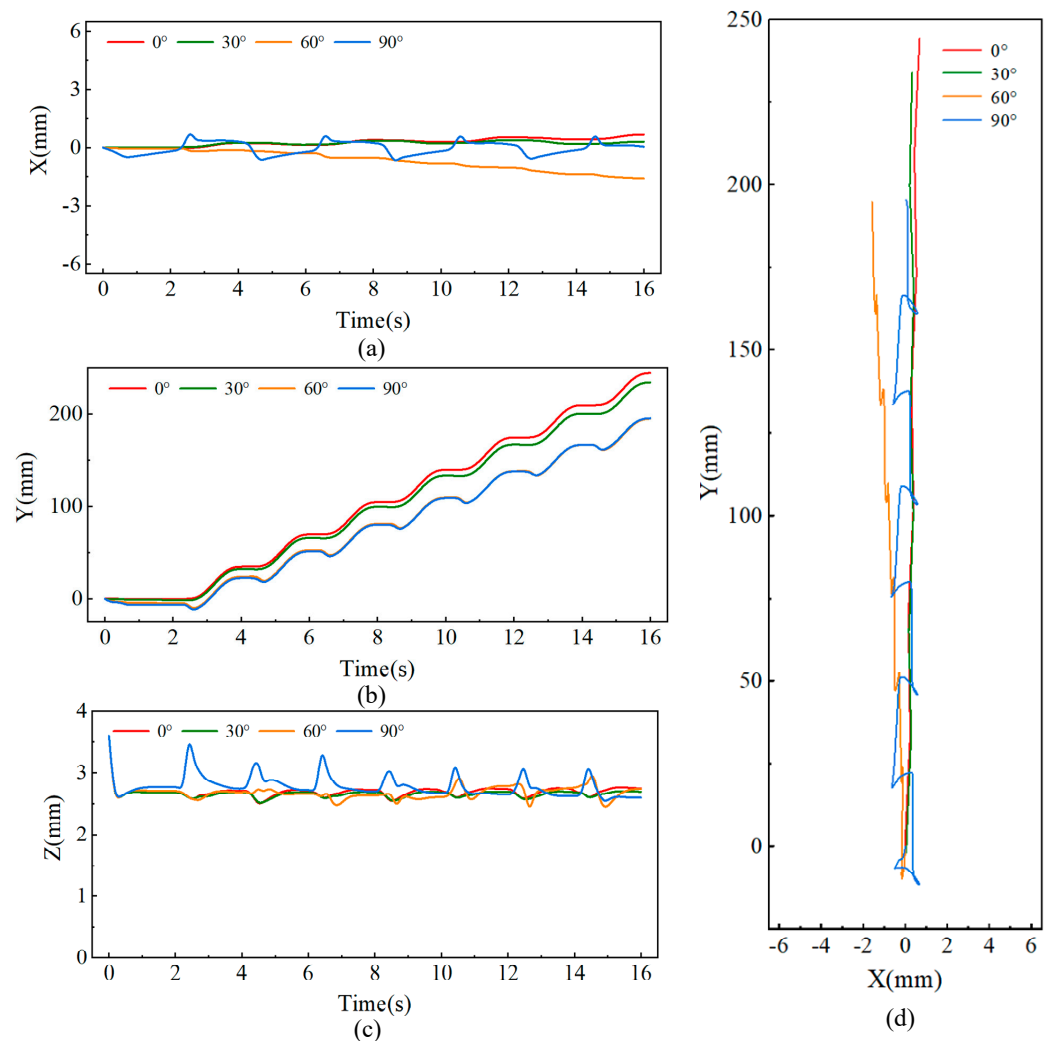
① For the lateral forces  $F_x$ , the left and right claws of the robot generate equal but opposite lateral forces, indicating that the limbs tend to converge toward the body's centerline during the climbing process. Additionally, the front claws generate greater forces than the rear claws. In the tailed condition, the lateral forces produced by the front and rear claws are 4.3 N and 3.2 N, respectively. In the tailless condition, the corresponding lateral forces increase to 5.1 N and 4.2 N.

② For the tangential forces  $F_y$ , regardless of whether the robot has a tail, the front claws generate greater contact forces than the rear claws. In the tailed condition, the tangential forces produced by the front and rear claws are 17.3 N and 12.8 N, respectively. In the tailless condition, these forces increase to 20.4 N for the front claws and 12.5 N for the rear claws.

③ For the normal forces  $F_z$ , the front claws generate greater adhesion forces than the rear claws. In the tailed condition, the robot's front and rear claws produce negative normal forces of  $-2.9$  N and  $-2.3$  N, respectively, indicating adhesion forces directed toward the wall. In the tailless condition, the robot requires greater normal adhesion forces to achieve stable climbing, with the front and rear claws generating contact forces of  $-3.24$  N and  $-2.5$  N, respectively.

### 3.2. Performance on Different Slopes

Figure 8 shows the changes in the center of mass (CoM) trajectory of the robot as it climbs slopes of  $0^\circ$ ,  $30^\circ$ ,  $60^\circ$ , and  $90^\circ$  in the tailed condition. For the lateral direction ( $x$ -direction), although the predefined foot trajectory has no lateral displacement, Figure 8a reveals that the robot's lateral deviation increases as the climbing angle increases. Notably, during vertical climbing at  $90^\circ$ , the robot exhibits periodic lateral oscillations of approximately 2 mm with each upward step.



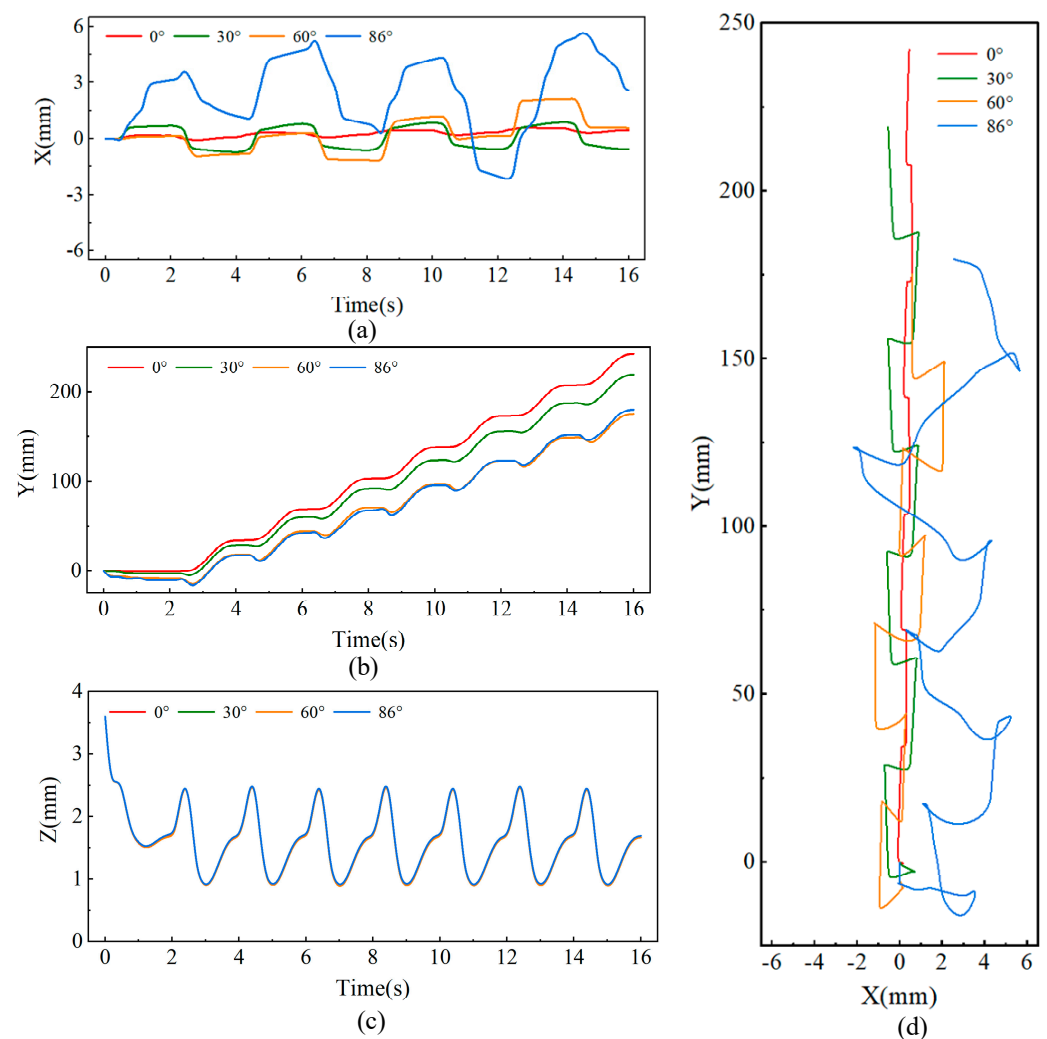
**Figure 8.** Center of mass displacement of the robot in the tailed condition while climbing at different angles: (a) Lateral displacement, (b) Vertical displacement, (c) Normal displacement, (d) CoM trajectory in the  $x$ - $y$  plane.

Figure 8b shows the variation in tangential displacement ( $y$ -direction) over time as the robot climbs different slopes. Throughout the entire motion, the robot takes a total of seven steps, with the displacement distance gradually decreasing as the slope increases. On a  $0^\circ$  surface, the robot moves a total distance of 244 mm, with an average step length of 34.8 mm. However, when the slope reaches  $90^\circ$ , the robot covers a distance of 196 mm, with an average step length of 28.0 mm, which is less than the planned step length of 35 mm. This reduction is due to increased slippage with each step as the slope increases.

Figure 8c shows the displacement of the robot in the normal direction ( $z$ -axis), where the robot's center of mass exhibits periodic oscillations during movement. As the slope increases, the amplitude of these oscillations also increases. When climbing a  $90^\circ$  surface,

the oscillation amplitude reaches approximately 1 mm. Figure 8d presents the robot's movement trajectory in the x-y plane.

Figure 9 shows the changes in the center of mass (CoM) trajectory of the robot as it climbs slopes of  $0^\circ$ ,  $30^\circ$ ,  $60^\circ$ , and  $86^\circ$  in the tailless condition. As shown in Figure 9a, compared to the tailed condition, the robot exhibits greater lateral oscillations in the tailless condition. When the slope reaches  $86^\circ$ , the maximum lateral amplitude is approximately 6 mm. Conversely, in the tangential direction, the robot's tangential displacement in the tailless condition is smaller than in the tailed condition, as shown in Figure 9b. On a  $0^\circ$  slope, the total displacement over 16 s is 242 mm, while on an  $86^\circ$  slope, it is 179 mm, corresponding to average step lengths of 34.6 mm and 25.6 mm, respectively. This indicates that the removal of the tail increases slippage with each step. Figure 9c shows the displacement in the normal direction under the tailless condition. Across different slopes, the robot's normal displacement remains consistent, exhibiting a normal oscillation of approximately 1.5 mm. The reason for this consistent normal trajectory is that the robot's rear leg foothold is positioned in the middle of the body rather than at the rear. Without a tail, the robot is unable to maintain balance in terms of pitch angle, leading to the maximum normal displacement during climbing on any slope. Figure 9d shows the robot's movement trajectory in the x-y plane. Compared to the tailed condition, the robot experiences greater displacement and lower stability during climbing in the tailless condition.



**Figure 9.** Center of mass displacement of the robot in the tailless condition while climbing at different angles: (a) Lateral displacement, (b) Vertical displacement, (c) Normal displacement, (d) CoM trajectory in the x-y plane.



#### 4. Experiments

In addition to the analysis conducted in the simulation environment, we further developed an experimental platform to test the physical prototype in a real-world setting. This allowed us to analyze the changes in the robot's performance with and without a tail under actual operating conditions.

##### 4.1. Experimental Platform

During movement, the ground reaction force (GRF) at the feet can reflect the dynamic characteristics of animals or robots [27,28]. To analyze the impact of tail removal on the robot's dynamic performance, we measured the GRF under both tailed and tailless conditions at different angles. Given the robot's large geometric size, a single force sensor is insufficient to fully capture the contact forces on each leg. Therefore, we employed an array of multiple force sensors to measure the contact forces at the feet during climbing. The overall structure of the measurement platform is shown in Figure 10.

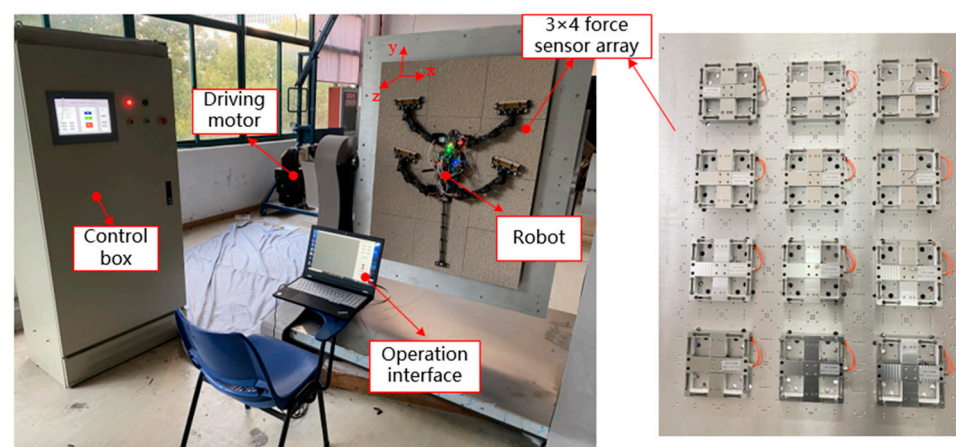


**Figure 10.** Adjustable angle contact force measurement platform.

The platform's rough surface is composed of  $3 \times 4$  metal plates coated with rough sand particles, with each plate mounted on a three-dimensional force sensor to measure the contact forces as the robot climbs on the rough surface. The parameters of these sensors are listed in Table 3. The measurement platform has a total length of 1200 mm and a width of 900 mm. The angle can be adjusted from  $0^\circ$  to  $180^\circ$  using a drive motor. A control cabinet is used to control the motor's rotation, while a computer connected to the sensor acquisition system reads and records the measurement data.

**Table 3.** Parameters of the measuring platform.

Number of Sensors	$3 \times 4$
Sensors Models	DYDW-005
Measurement Range	$\pm 100$ N
Individual Sensor Size	20 cm $\times$ 20 cm
Measurement Accuracy	0.2%FS
Sampling Frequency	90 Hz
Rotation Angle	$0\sim 90^\circ$

The WCQR-III physical prototype uses an open-loop control system and is equipped with a remote-control system. An STM32h7 chip was selected as the microcontroller. The servomotors on each joint of the robot are connected via the Controller Area Network (CAN) communication serial port. A wireless transmission module was designed for 4G mobile communication based on TDD-LTE, and the main board communicates with the remote controller through the RS232 protocol. The operator can remotely control the robot's direction and speed.

## 4.2. Experimental Results

### 4.2.1. Maximum Climbing Angle Test

To assess the impact of the tail on the robot's vertical climbing ability, we tested whether the physical prototype could achieve stable climbing on a  $90^\circ$  vertical surface under both tailed and tailless conditions. The robot prototype's motion parameters were based on the desired trajectory shown in Figure 4d, with a gait cycle of 4 s and a step length of 35 mm, matching the input trajectory used in the simulation.

Figure 11a shows the robot's climbing process on a  $90^\circ$  vertical rough surface with a tail. The results indicate that the robot stably climbed 178 mm in 16 s, which is very close to the simulation value of 196 mm. Figure 11b presents the climbing results without the tail. After removing the robot's tail, we used the same motion parameters to control the robot's climbing on the vertical wall. The results show that after 3 s of climbing, the robot's body began to pitch backward, and the front claws gradually detached from the wall. Subsequently, at the 4-s mark, the left front claw completely lost contact with the wall, failing to provide adhesion, which caused the robot to tilt to the left and fall from the wall. The experimental results are consistent with the simulation: without the tail, the robot is unable to achieve stable climbing on a  $90^\circ$  vertical surface.

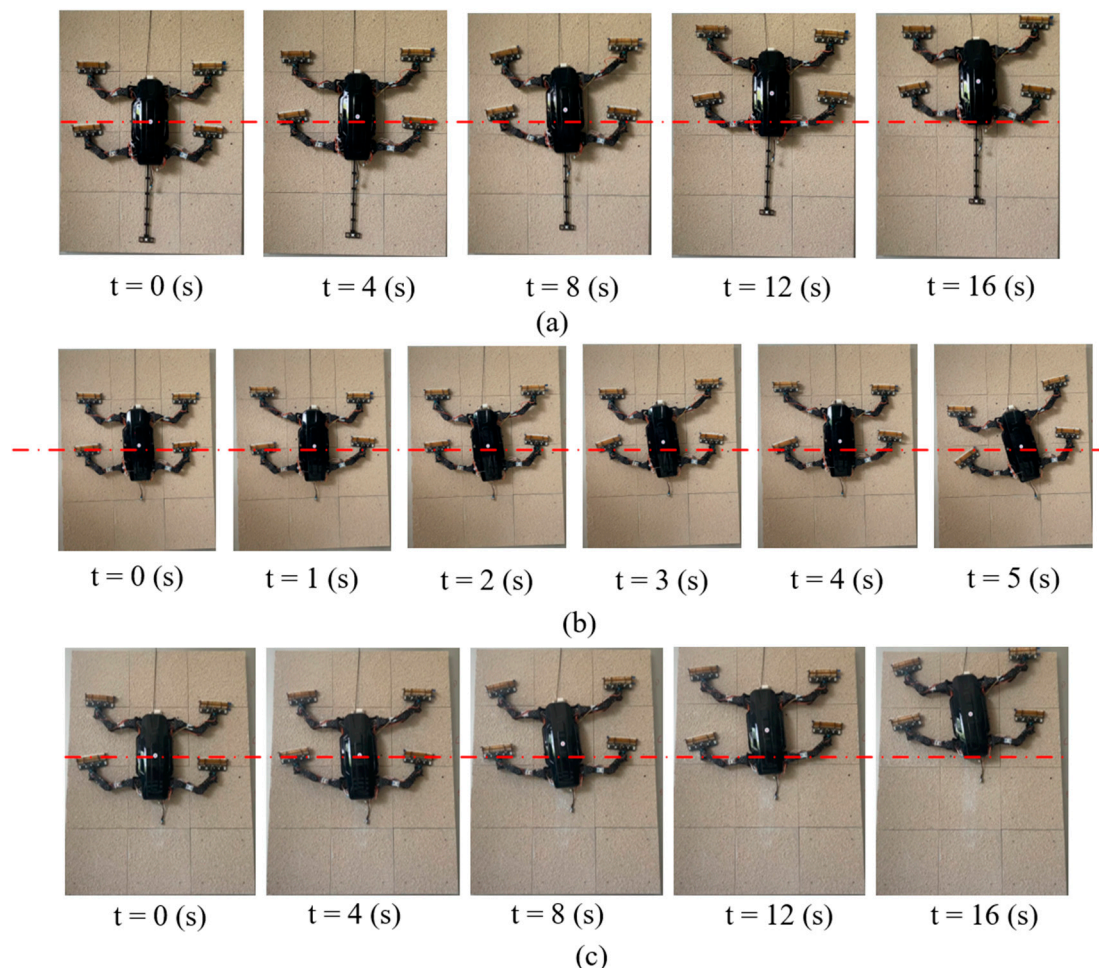


**Figure 11.** (a) Time sequence of the robot climbing a  $90^\circ$  surface with a tail; (b) Time sequence of the robot climbing a  $90^\circ$  surface without a tail; (c) Time sequence of the robot climbing a  $82^\circ$  surface without a tail.

To determine the maximum slope the robot can climb without a tail, we gradually reduced the platform's incline angle and tested the robot's ability to climb stably at different slopes. For each degree of reduction, three tests were conducted, and the slope angle at

which the robot did not fall or exhibit significant slippage in all three tests was considered the maximum climbable slope. The results, shown in Figure 11c, indicate that the robot was able to climb stably without a tail at an incline of  $82^\circ$ . Within 16 s, the robot successfully moved 174 mm along the surface.

#### 4.2.2. Motion Performance Testing on Different Slopes

As shown in Figure 12, we set the platform's incline angles to  $0^\circ$ ,  $30^\circ$ ,  $60^\circ$ , and  $90^\circ$ , and measured the robot's ground reaction forces (GRF) during climbing. Since the robot is unable to climb a  $90^\circ$  vertical surface without a tail, the corresponding platform angles for the tailless condition were set to  $0^\circ$ ,  $30^\circ$ ,  $60^\circ$ , and  $82^\circ$ . Considering the potential uneven distribution of surface roughness particles, which could affect the robot's foot forces during each climb, we conducted five climbing tests at each angle and collected the measurement data.

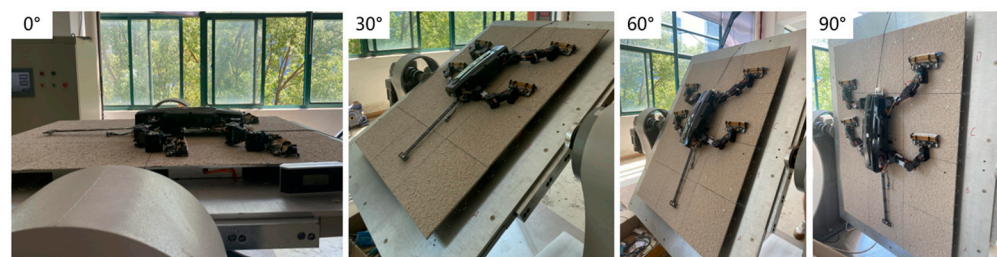


**Figure 12.** The robot climbing on rough surfaces with different incline angles.

Since the robot uses a diagonal gait, the contact forces on the left and right feet are the same in magnitude but offset by one cycle. After the robot achieved stable attachment, we measured the GRFs at different angles, conducting five measurements in total. All data are presented as average values with error bands. Figure 13 shows the ground reaction forces (GRF) at the robot's feet while climbing at different angles, both with and without a tail. The dashed lines represent the simulation values, while the solid lines represent the actual measured values.

For the lateral forces  $F_x$ , the simulation results show that as the incline angle increases, the lateral forces at the claws increase from 0.5 N to approximately 4 N. This indicates that as the climbing angle increases, the robot's limbs tend to draw closer to the body's centerline, creating a motion pattern similar to 'hugging'. In the experimental results, however, the lateral forces did not vary significantly with the increase in climbing angle, remaining around 4–5 N. We attribute the higher lateral forces observed in low-angle experiments compared to the simulation results to the system errors of the robot itself and the friction between the chassis and the surface, which causes lateral disturbances, requiring greater force to maintain lateral stability. Both the simulation and experimental results indicate that the tailless condition generates greater lateral forces compared to the tailed condition.

For the tangential forces  $F_y$ , the simulation results indicate that as the climbing angle increases, the tangential forces at the feet steadily rise. The tangential force at the front claws increases from 4–5 N to 17–20 N, while the rear claws see an increase from 4–5 N to 9–12 N. The difference between the front and rear claws widens as the angle increases, indicating that the front claws bear a greater dragging force. The experimental results follow the same trend as the simulation but are slightly higher than the simulation values. This discrepancy is likely due to the robot's chassis contacting the rough surface during actual tests, which requires the robot to overcome additional friction between the chassis and the surface. The tangential force component typically increases as the slope angle increases. However, the experimental results in Figure 13d show that the tangential force on the hind foot decreases between  $60^\circ$  and  $90^\circ$ . We believe this may be due to the moment generated by the shift in the robot's center of gravity on steeper slopes, which causes the

rear part of the robot's chassis to come into contact with the surface. This contact interferes with the hind foot's proper engagement with the wall, reducing the number of spines in contact and consequently decreasing the tangential force on the hind foot. Additionally, both the simulation and experimental results show that the robot's feet typically generate greater tangential forces in the tailless condition.

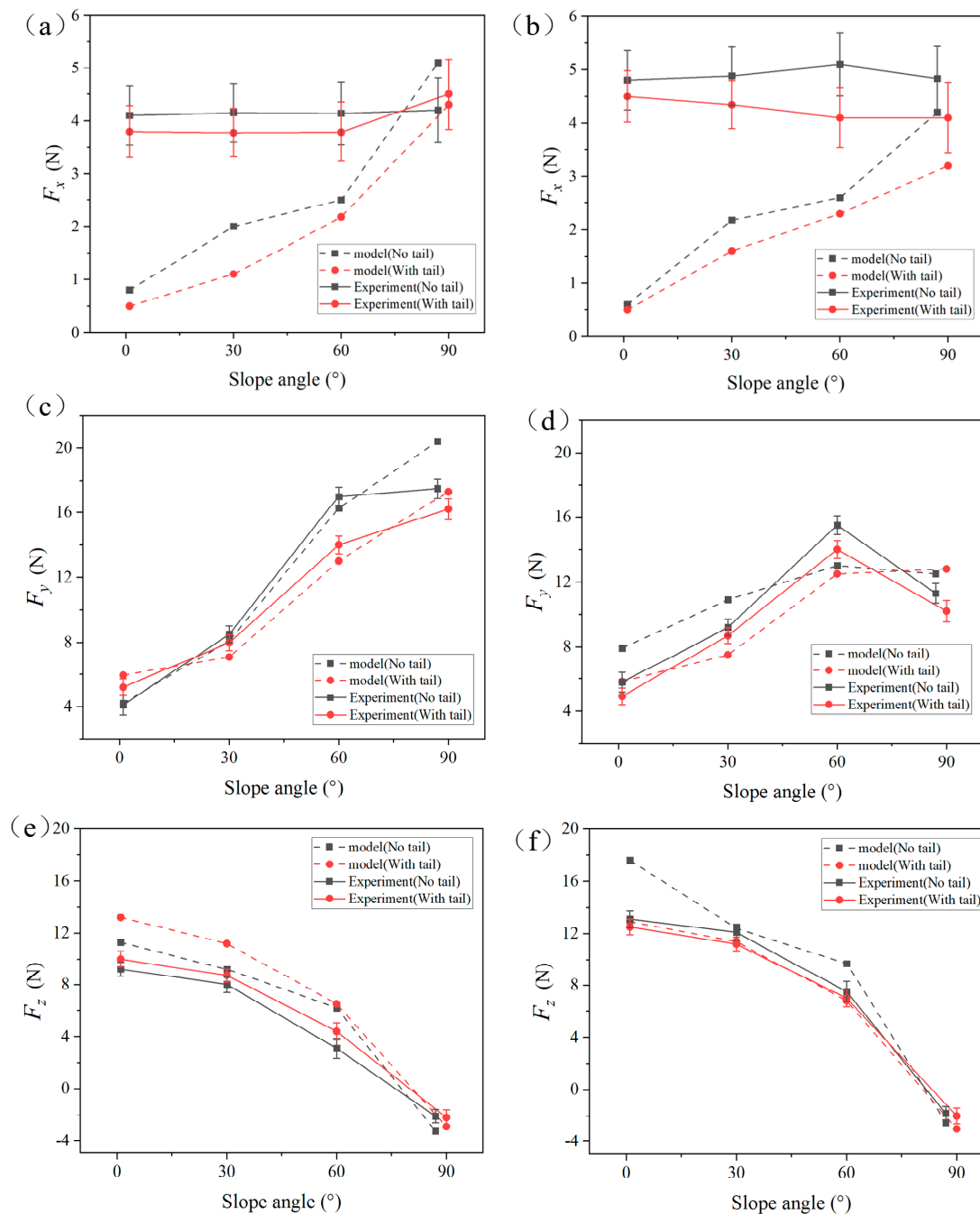


**Figure 13.** GRF generated by the robot at different angles with and without a tail: (a) Lateral force of the front claws, (b) Lateral force of the rear claws, (c) Tangential force of the front claws, (d) Tangential force of the rear claws, (e) Normal force of the front claws, (f) Normal force of the rear claws. Error bars show standard errors.

For the normal forces  $F_z$ , the simulation results show that as the climbing angle increases, the normal forces at the feet gradually decrease. When the climbing angles are 0°, 30°, and 60°, the normal forces are positive, indicating that the feet are supported



by the wall. However, at climbing angles of  $86^\circ$  and  $90^\circ$ , the normal forces become negative, indicating that the feet are relying on the adhesion of the spiny claws. In the tailless condition, the normal forces at the rear claws are greater than those at the front claws, due to the lack of tail support to distribute the load. The experimental results are similar to the simulation in both trend and magnitude, demonstrating the accuracy of the simulation results.

In addition to GRF testing, we also evaluated the impact of tail removal on the robot's climbing speed. We controlled the robot's speed by adjusting its step length using a remote controller and measured the time it took for the robot to cover a certain distance to calculate its actual speed. Five experiments were conducted at each slope, and the results are shown in Figure 14. With the tail, the robot achieved maximum speeds of 15.4 cm/s, 14.1 cm/s, 8.5 cm/s, and 2.12 cm/s on slopes of  $0^\circ$ ,  $30^\circ$ ,  $60^\circ$ , and  $90^\circ$ , respectively. After removing the tail, the robot's maximum speeds at  $0^\circ$ ,  $30^\circ$ , and  $60^\circ$  were 15.2 cm/s, 13.8 cm/s, and 7.9 cm/s, respectively, which are lower than the speeds with the tail. Additionally, the robot was unable to maintain stable climbing on a  $90^\circ$  vertical surface without the tail.

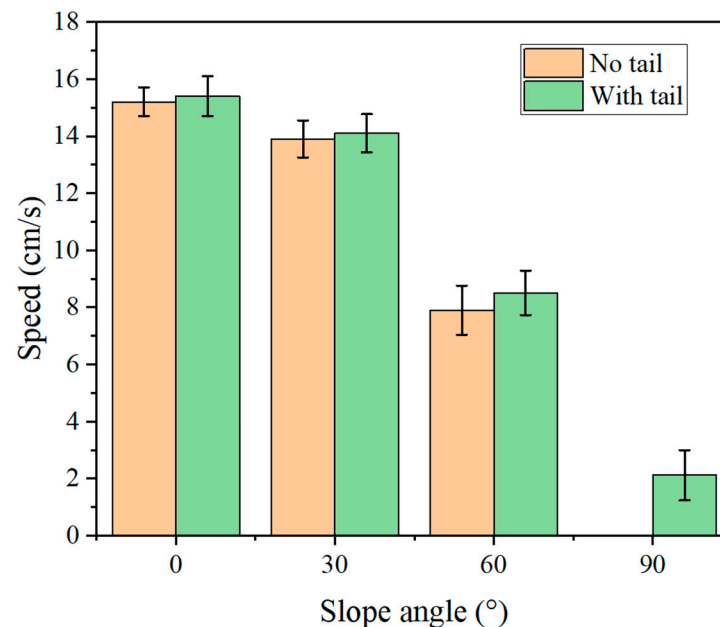


**Figure 14.** Maximum Speed of the Robot at Different Angles. Error bars show standard errors.

## 5. Discussion and Conclusions

Here we developed a gecko-inspired bionic climbing robot and constructed a corresponding climbing simulation system. This system allows us to set various motion parameters and inclination angles in a simulated environment, enabling the simulation of the robot's climbing behavior with and without a tail, as well as predicting potential climbing failures. Additionally, we built an adjustable-angle force measurement platform to test the contact forces and movement speed of the physical prototype on different slopes. Through simulations and experimental tests, we observed differences in the robot's performance with and without a tail. Based on the experimental results, we will discuss the impact of the tail on the robot's locomotion ability in terms of balance, stability, and maneuverability.

Extensive research on gecko tails has shown that the tail plays a crucial role in maintaining balance during locomotion. When a gecko's foot slips, its tail moves downward to maintain balance, preventing it from tipping backward and allowing it to continue climbing on vertical surfaces [17]. In our tests of the robot's vertical climbing performance, we also validated the balancing role of the tail. Both the simulation and experimental results indicate that after the robot's tail is removed, the body tends to pitch backward

during climbing, causing the front claws to slip, which further leads to a loss of adhesion in the front claws, ultimately resulting in the robot falling from the wall. Furthermore, from the movement trajectory of the robot's center of mass in the normal direction, it can be observed that after the tail is removed, the center of mass exhibits greater amplitude in the normal direction. During climbing, this normal displacement of the center of mass increases the pitch moment, significantly raising the risk of pitch failure. The forces experienced by the robot's feet during climbing reflect the tail's role in suppressing the pitch moment. Compared to the tailless condition, the robot with a tail exhibits a smaller difference in contact forces between the front and rear claws, meaning the front claws require less adhesive force to maintain the balance of the body.

Geckos can maintain their stability while moving quickly on horizontal and vertical surfaces by increasing the lateral undulation amplitude and frequency of their bodies and tails [19,20]. Although the climbing robot we designed does not have an active tail or flexible body, comparative experiments reveal that, after the tail is removed, the robot experiences greater slippage in the tangential direction and larger lateral oscillations during climbing. In the tailless condition, the robot's increased lateral oscillations are also reflected in the contact forces at its claws. Both simulation and experimental results indicate that, in the absence of a tail, the robot generates greater lateral forces at the claws to maintain stable climbing. These larger lateral forces also make the robot more prone to lateral disturbances. Since we measured the robot's average contact forces during stable attachment, and the robot uses the same gait with similar total displacement, larger GRFs at the foot-end throughout the climbing process result in greater work being done and, consequently, higher energy consumption. Compared to the tailless condition, the presence of a tail reduces the contact forces at the foot-end. Therefore, the tail can improve motion efficiency to some extent.

In nature, geckos sometimes detach their tails as a defense mechanism to distract predators [29,30]. However, studies on tailless geckos or lizards have found that losing the tail reduces their maneuverability and decreases their locomotion speed [31]. This aligns with our experimental findings. By comparing the climbing speed of the robot with and without a tail, we observed that the robot's climbing speed decreases on different slopes after the tail is removed.

In this study, we utilized a dynamic climbing model and experimental platform to compare the robot's performance with and without a tail through both simulations and experiments. The results indicate that the tail significantly enhances the robot's performance in three key areas: balance, stability, and maneuverability. Specifically, the tail helps maintain balance during climbing, improves the robot's stability on various slopes, and enhances its maneuverability. In future studies, we plan to further investigate the effects of tail length, mass distribution, and material composition on the climbing performance of the robot. This includes analyzing how different lengths and dimensions of the tail impact the robot's balance, stability, and energy consumption. Specifically, tail length may affect the position of the center of mass, the magnitude of pitch moments, and the distribution of contact forces, which will influence the robot's performance on various slopes and surface conditions. A soft tail material may effectively dissipate impact energy, reduce oscillations, and better adapt to irregular surfaces. By optimizing the geometric design of the tail, we aim to further enhance the climbing efficiency and adaptability of the robot.

**Author Contributions:** Conceptualization: S.F. and X.W.; Simulation: S.F.; Validation: T.L. and W.Z.; Data Curation: S.F.; Visualization: S.F. and G.C.; Writing—Original Draft Preparation: S.F.; Writing—Review and Editing: X.W.; Funding Acquisition: X.W. and Y.W. All authors have read and agreed to the published version of the manuscript.

**Funding:** This research was funded in part by the Nation Key R&D Program of China, grant number [2023YFB4704600], in part by special key project of technological innovation and application development in Chongqing, grant number [CSTB2022TIAD KPX0134].

**Institutional Review Board Statement:** Not applicable.

**Data Availability Statement:** The raw data supporting the conclusions of this article will be made available by the authors on request.

**Conflicts of Interest:** The authors declare no conflict of interest.

## References

1. Autumn, K.; Sitti, M.; Liang, Y.A.; Peattie, A.M.; Hansen, W.R.; Sponberg, S.; Kenny, T.W.; Fearing, R.; Israelachvili, J.N.; Full, R.J. Evidence for van der Waals adhesion in gecko setae. *Proc. Natl. Acad. Sci. USA* **2002**, *99*, 12252–12256. [CrossRef] [PubMed]
2. Autumn, K.; Liang, Y.A.; Hsieh, S.T.; Zesch, W.; Chan, W.P.; Kenny, T.W.; Fearing, R.; Full, R.J. Adhesive force of a single gecko foot-hair. *Nature* **2000**, *405*, 681–685. [CrossRef] [PubMed]
3. Unver, O.; Uneri, A.; Aydemir, A.; Sitti, M. Geckobot: A gecko inspired climbing robot using elastomer adhesives. In Proceedings of the 2006 IEEE International Conference on Robotics and Automation, ICRA 2006, Orlando, FL, USA, 15–19 May 2006; pp. 2329–2335.
4. Kim, S.; Spenko, M.; Trujillo, S.; Heyneman, B.; Mattoli, V.; Cutkosky, M.R. Whole body adhesion: Hierarchical, directional and distributed control of adhesive forces for a climbing robot. In Proceedings of the 2007 IEEE International Conference on Robotics and Automation, Roma, Italy, 10–14 April 2007; pp. 1268–1273.
5. Hawkes, E.W.; Ulmen, J.; Esparza, N.; Cutkosky, M.R. Scaling walls: Applying dry adhesives to the real world. In Proceedings of the 2011 IEEE/RSJ International Conference on Intelligent Robots and Systems, San Francisco, CA, USA, 25–30 September 2011; pp. 5100–5106.
6. Li, Z.; Li, Z.; Tam, L.M.; Xu, Q. Design and Development of a Versatile Quadruped Climbing Robot with Obstacle-Overcoming and Manipulation Capabilities. *IEEE/ASME Trans. Mechatron.* **2022**, *28*, 1649–1661. [CrossRef]
7. Hernando, M.; Gambao, E.; Prados, C.; Brito, D.; Brunete, A. ROMERIN: A new concept of a modular autonomous climbing robot. *Int. J. Adv. Robot. Syst.* **2022**, *19*, 17298806221123416. [CrossRef]
8. Zhu, H.; Lu, J.; Gu, S.; Wei, S.; Guan, Y. Planning three-dimensional collision-free optimized climbing path for biped wall-climbing robots. *IEEE/ASME Trans. Mechatron.* **2020**, *26*, 2712–2723. [CrossRef]
9. Zhao, D.; Luo, H.; Tu, Y.; Meng, C.; Lam, T.L. Snail-inspired robotic swarms: A hybrid connector drives collective adaptation in unstructured outdoor environments. *Nat. Commun.* **2024**, *15*, 3647. [CrossRef]
10. Hong, S.; Um, Y.; Park, J.; Park, H.-W. Agile and versatile climbing on ferromagnetic surfaces with a quadrupedal robot. *Sci. Robot.* **2022**, *7*, eadd1017. [CrossRef]
11. Zhang, W.; Zhang, W.; Sun, Z. A reconfigurable soft wall-climbing robot actuated by electromagnet. *Int. J. Adv. Robot. Syst.* **2021**, *18*, 1729881421992285. [CrossRef]
12. Zi, P.; Xu, K.; Chen, J.; Wang, C.; Zhang, T.; Luo, Y.; Tian, Y.; Wen, L.; Ding, X. Intelligent Rock-Climbing Robot Capable of Multimodal Locomotion and Hybrid Bioinspired Attachment. *Adv. Sci.* **2024**, *2024*, 2309058. [CrossRef]
13. Zi, P.; Xu, K.; Tian, Y.; Ding, X. A mechanical adhesive gripper inspired by beetle claw for a rock climbing robot. *Mech. Mach. Theory* **2023**, *181*, 105168. [CrossRef]
14. Xiao, J.; Hao, L.; Xu, H.; Zhang, X.; Li, X.; Li, Z. MST-Q: Micro Suction Tape Quadruped Robot with High Payload Capacity. *IEEE Robot. Autom. Lett.* **2023**, *8*, 7304–7311. [CrossRef]
15. Haomachai, W.; Shao, D.; Wang, W.; Ji, A.; Dai, Z.; Manoonpong, P. Lateral undulation of the bendable body of a gecko-inspired robot for energy-efficient inclined surface climbing. *IEEE Robot. Autom. Lett.* **2021**, *6*, 7917–7924. [CrossRef]
16. Autumn, K.; Dittmore, A.; Santos, D.; Spenko, M.; Cutkosky, M. Frictional adhesion: A new angle on gecko attachment. *J. Exp. Biol.* **2006**, *209*, 3569–3579. [CrossRef] [PubMed]
17. Jusufi, A.; Goldman, D.I.; Revzen, S.; Full, R.J. Active tails enhance arboreal acrobatics in geckos. *Proc. Natl. Acad. Sci. USA* **2008**, *105*, 4215–4219. [CrossRef] [PubMed]
18. Siddall, R.; Byrnes, G.; Full, R.J.; Jusufi, A. Tails stabilize landing of gliding geckos crashing head-first into tree trunks. *Commun. Biol.* **2021**, *4*, 1020. [CrossRef]
19. Schultz, J.T.; Cieri, R.L.; Proost, T.; Pilai, R.; Hodgson, M.; Plum, F.; Clemente, C.J. Tail base deflection but not tail curvature varies with speed in lizards: Results from an automated tracking analysis pipeline. *Integr. Comp. Biol.* **2021**, *61*, 1769–1782. [CrossRef]
20. Wang, W.; Ji, A.; Chen, G.; Ravi, S.; Shen, H.; Gorb, S.N.; Dai, Z. Kinematics of gecko climbing: The lateral undulation pattern. *Zoology* **2020**, *140*, 125768. [CrossRef]
21. Goldman, D.I.; Chen, T.S.; Dudek, D.M.; Full, R.J. Dynamics of rapid vertical climbing in cockroaches reveals a template. *J. Exp. Biol.* **2006**, *209*, 2990–3000. [CrossRef]
22. Ko, W.H.; Chiang, W.H.; Hsu, Y.H.; Yu, M.Y.; Lin, H.S.; Lin, P.C. A model-based two-arm robot with dynamic vertical and lateral climbing behaviors. *J. Mech. Robot.* **2016**, *8*, 044503. [CrossRef]
23. Wang, W.; Li, X.; Wu, S.; Zhu, P.; Zhao, F. Effects of pendular waist on gecko’s climbing: Dynamic gait, analytical model and bio-inspired robot. *J. Bionic Eng.* **2017**, *14*, 191–201. [CrossRef]
24. Fang, S.; Shi, S.; Wu, X.; Wang, X. A walking and climbing quadruped robot capable of ground-wall transition: Design, mobility analysis and gait planning. *Intell. Serv. Robot.* **2023**, *16*, 431–451. [CrossRef]
25. Asbeck, A.T. *Compliant Directional Suspensions for Climbing with Spines and Adhesives*; Stanford University: Stanford, CA, USA, 2010.
26. Kane, T.R.; Levinson, D.A. The use of Kane’s dynamical equations in robotics. *Int. J. Robot. Res.* **1983**, *2*, 3–21. [CrossRef]

27. Dickinson, M.H.; Farley, C.T.; Full, R.J.; Koehl, M.A.R.; Kram, R.; Lehman, S. How animals move: An integrative view. *Science* **2000**, *288*, 100–106. [CrossRef] [PubMed]
28. Miller, B.D.; Rivera, P.R.; Dickson, J.D.; Clark, J.E. Running up a wall: The role and challenges of dynamic climbing in enhancing multi-modal legged systems. *Bioinspiration Biomim.* **2015**, *10*, 025005. [CrossRef] [PubMed]
29. Chapple, D.G.; Swain, R. Effect of caudal autotomy on locomotor performance in a viviparous skink, *Niveoscincus metallicus*. *Funct. Ecol.* **2002**, *2002*, 817–825. [CrossRef]
30. Naya, D.E.; Veloso, C.; Muñoz, J.L.; Bozinovic, F. Some vaguely explored (but not trivial) costs of tail autotomy in lizards. *Comp. Biochem. Physiol. Part A Mol. Integr. Physiol.* **2007**, *146*, 189–193. [CrossRef]
31. Higham, T.E.; Russell, A.P.; Zani, P.A. Integrative biology of tail autotomy in lizards. *Physiol. Biochem. Zool.* **2013**, *86*, 603–610. [CrossRef]

**Disclaimer/Publisher’s Note:** The statements, opinions and data contained in all publications are solely those of the individual author(s) and contributor(s) and not of MDPI and/or the editor(s). MDPI and/or the editor(s) disclaim responsibility for any injury to people or property resulting from any ideas, methods, instructions or products referred to in the content.





## Article

# Mussel-Inspired Multifunctional Polyethylene Glycol Nanoparticle Interfaces

Carolina Casagualda <sup>1,2</sup>, Alba López-Moral <sup>1,2</sup> , Paula Alfonso-Triguero <sup>3</sup>, Julia Lorenzo <sup>3,4</sup> , Ramon Alibés <sup>2</sup> , Félix Busqué <sup>2,\*</sup> and Daniel Ruiz-Molina <sup>1,\*</sup>

<sup>1</sup> Catalan Institute of Nanoscience and Nanotechnology (ICN2), CSIC, and The Barcelona Institute of Science and Technology (BIST), Campus UAB, Bellaterra, 08193 Barcelona, Spain

<sup>2</sup> Departament de Química, Universitat Autònoma de Barcelona, Bellaterra, 08193 Barcelona, Spain

<sup>3</sup> Institut de Biotecnologia i de Biomedicina and Departament de Bioquímica i Biologia Molecular, Universitat Autònoma de Barcelona, Bellaterra, 08193 Barcelona, Spain; julia.lorenzo@uab.cat (J.L.)

<sup>4</sup> Centro de Investigación Biomédica en Red (CIBER), Bioingeniería, Biomateriales y Nanomedicina, 08193 Cerdanyola del Vallès, Spain

\* Correspondence: felix.busque@uab.cat (F.B.); dani.ruiz@icn2.cat (D.R.-M.)

**Abstract:** Nanoparticles (NPs) are receiving increasing interest in biomedical applications. However, due to their large surface area, in physiological environments, they tend to interact with plasma proteins, inducing their agglomeration and ultimately resulting in a substantial efficiency decrease in diagnostic and therapeutic applications. To overcome such problems, NPs are typically coated with a layer of hydrophilic and biocompatible polymers, such as PEG chains. However, few examples exist in which this property could be systematically fine-tuned and combined with added properties, such as emission. Herein, we report a novel mussel-inspired catechol-based strategy to obtain biocompatible and multifunctional coatings, using a previously developed polymerization methodology based on the formation of disulfide bridges under mild oxidative conditions. Two families of NPs were selected as the proof of concept: mesoporous silica NPs (MSNPs), due to their stability and known applications, and magnetite NPs (Fe<sub>3</sub>O<sub>4</sub> NPs), due to their small size (<10 nm) and magnetic properties. The PEG coating confers biocompatibility on the NPs and can be further functionalized with bioactive molecules, such as glucose units, through the end carboxylic acid moieties. Once we demonstrated the feasibility of our approach to obtaining PEG-based coatings on different families of NPs, we also obtained multifunctional coatings by incorporating fluorescein functionalities. The resulting coatings not only confer biocompatibility and excellent cell internalization, but also allow for the imaging and tracking of NPs within cells.

**Keywords:** catechol; functional coatings; bioinspired; functional nanoparticles; biocompatible; magnetite NPs; MSNPs



**Citation:** Casagualda, C.; López-Moral, A.; Alfonso-Triguero, P.; Lorenzo, J.; Alibés, R.; Busqué, F.; Ruiz-Molina, D. Mussel-Inspired Multifunctional Polyethylene Glycol Nanoparticle Interfaces. *Biomimetics* **2024**, *9*, 531. <https://doi.org/10.3390/biomimetics9090531>

Academic Editors: Stanislav N. Gorb, Giuseppe Carbone, Thomas Speck and Peter Fratzl

Received: 11 June 2024

Revised: 30 August 2024

Accepted: 31 August 2024

Published: 4 September 2024



**Copyright:** © 2024 by the authors. Licensee MDPI, Basel, Switzerland. This article is an open access article distributed under the terms and conditions of the Creative Commons Attribution (CC BY) license (<https://creativecommons.org/licenses/by/4.0/>).

## 1. Introduction

The substantial surface area of nanoparticles (NPs) makes them prone to interacting with plasma proteins in physiological environments, leading to agglomeration and precipitation. NPs are also considered intruders by the innate immunity system and engulfed by macrophage cells. In both scenarios, the particles are removed from the blood circulation system and lose their function quickly, leading to a dramatic diagnosis and therapy efficiency reduction. To address these issues, NPs are usually coated with a layer of hydrophilic and biocompatible polymers, such as dextran [1], dendrimers [2], or mainly PEG chains [3]. In this last case, several approaches have been followed to ensure proper surface functionalization. Undoubtedly, one of their most common uses is their covalent attachment to catechol units, drawing inspiration from numerous marine sandcastle worms, barnacles, or mussels. These organisms firmly attach to underwater surfaces, preventing displacement by currents and tides while carrying out essential life functions. Their remarkable adhesive

capabilities stem from catechol-based molecules, serving as a foundational element in the creation of innovative synthetic coatings in many different laboratories worldwide.

Indeed, so far, numerous research examples have showcased the use of catechol-based polyethylene glycol (cat-PEG) coatings to confer nanoparticles (NPs) with colloidal stability, antifouling and antimicrobial properties, as well as biocompatibility and biodegradability in physiological environments. For this purpose, one of the main approaches used is the polymerization of molecules covalently linking catechol and PEG chains, either with or without a short spacer in between. The polymerization occurs under oxidative conditions at basic pH, and surface coating is achieved through ex situ treatments (Figure 1a). Following this approach, numerous metallic, inorganic, and polymeric surfaces have been coated with polyethylene glycol dopamine (PEG-DA) polymers [4,5]. For instance, examples of coated  $\text{Fe}_3\text{O}_4$ ,  $\text{MnO}$ , and Au NPs dispersed in both aqueous and organic environments have been reported [6], with those with plasmon resonance responses (Au and Ag NPs) being suitable for diagnostic and therapy applications [7], or reduced graphene oxide (rGO) coated with cat-PEG polymers for the controlled release of doxorubicin (DOX) [8]. Overall, with this polymerization strategy, polymers [9–11], metals [12–14], metal oxides [15–18], and electrospun nanofiber meshes [19], reduced graphene oxide [20], and glass and polystyrene beads [21], ceria nanoparticles [22], or iron oxide nanocubes (IONCs) [23], have been effectively coated.

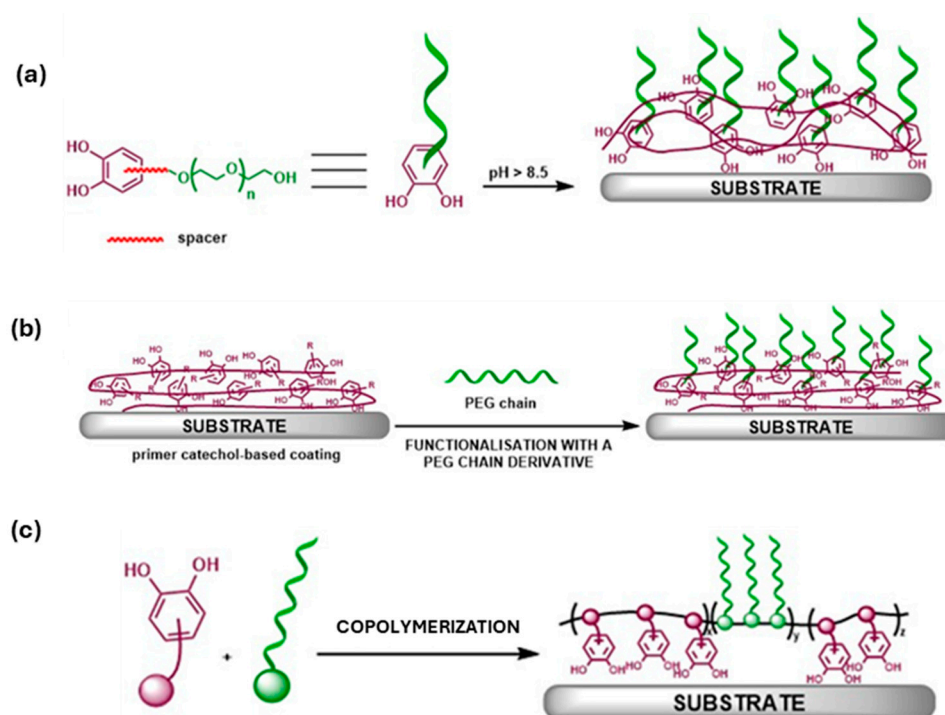
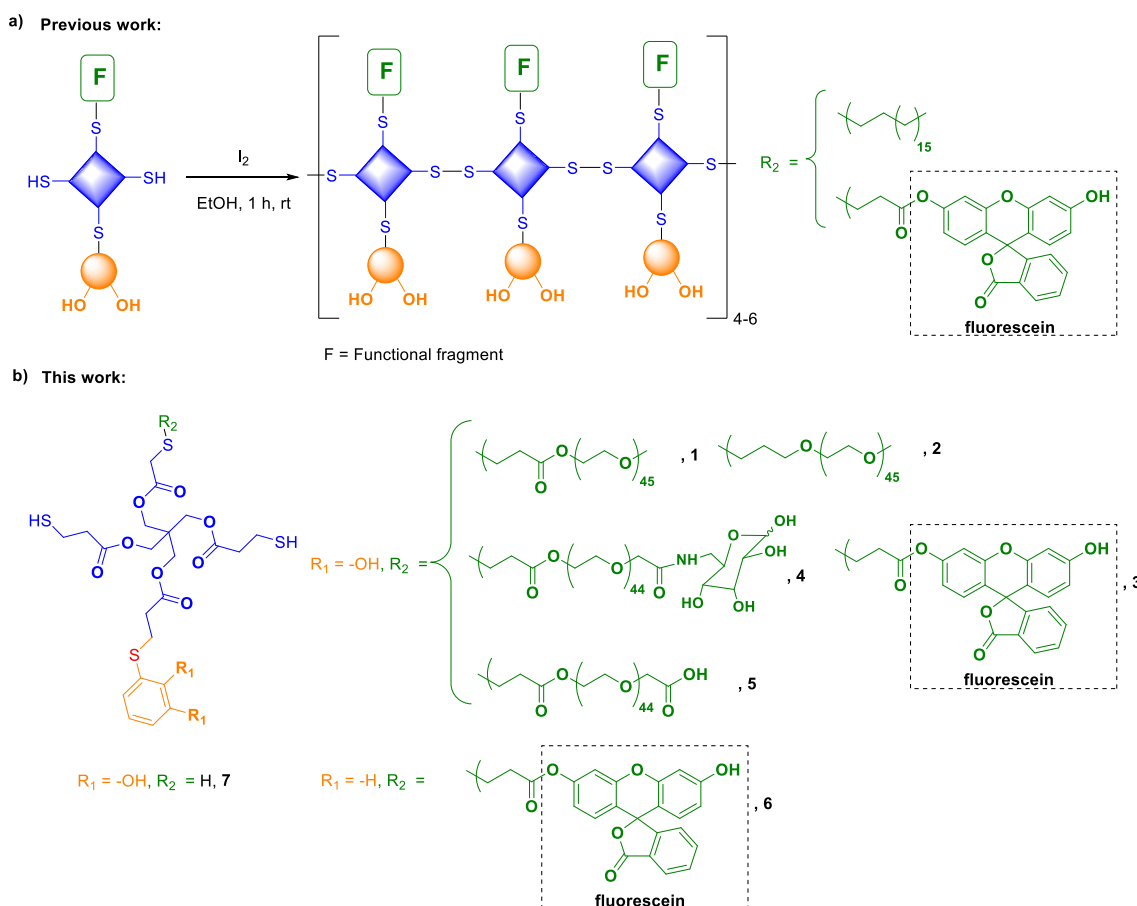


**Figure 1.** Overview of strategies followed in the literature using catechol-based polyethylene glycol (PEG) coatings to endow nanoparticles (NPs) with colloidal stability and biocompatible properties in physiological media. (a) Polymerization of cat-PEG-based molecules, where catechol and PEG chains are covalently bonded or with a short spacer in between. Surfaces are coated via ex-situ treatments. (b) Preliminary coating of the surface with catechol-based polymers, commonly PDA, and further functionalization with PEG derivatives through covalent bonds. (c) Copolymerization through reactive pendant groups between molecules containing catechol moieties and PEG chains.

A second alternative synthetic methodology involves first the formation of a catechol-based coating, typically polydopamine (PDA), followed by functionalization with PEG chain derivatives via covalent bonds (Figure 1b). Following this methodology, several representative examples have been reported, including, for instance, MoS<sub>2</sub> nanosheets for drug delivery and photothermal cancer treatment [24], PEGylated carbon nanotubes (CNTs) for the intracellular delivery of doxorubicin [25], multi-walled carbon nanotubes (MWCNT) [26], and Fe<sub>3</sub>O<sub>4</sub> NPs [27] or catechol-conjugated hydrogels produced by thiourea-quinone coupling [28].

All in all, numerous examples of cat-PEG coatings have already been described in the literature. However, the potential for obtaining multifunctional coatings is less frequently explored despite its interest, bringing the possibility of combining the advantages of PEG groups with, for instance, fluorescent tags for imaging. For this purpose, we hypothesize that the copolymerization of catechol moieties bearing PEG chains and other different functional groups represents one of the best scenarios (Figure 1c). With this third approach, the functionalization of polyether copolymers [29], coating Fe<sub>3</sub>O<sub>4</sub> NPs for bioimaging [30]/gene therapy [31]/contrast agents [32], SiO<sub>2</sub> NPs with cisplatin-controlled release kinetics [33], AuNPs as smart carriers for the doxorubicin drug [34], and polymeric micelles [35,36] or nanocarriers [37] as drug delivery systems have already been reported. Further examples involve multidentate cat-PEG-coated magnetic nanocrystals [38] or NPs [39], the surface modification of CNTs [40], metal-phenolic networks that reduce the cellular oxidative stress [41], or increasing the binding affinity of Au@PDA NPs [42]. Nevertheless, despite these numerous examples, no examples of fine-tuning added properties have been reported so far, as far as we know. Therefore, there is a strong need for the development of novel synthetic approaches to address this limitation.

We recently reported a novel family of colorless coatings that relies on a catechol-grafted polymeric architecture linked through disulfide bridges [43], being the basic framework for the modular design of all monomers, including the pentaerythritol tetrakis(3-mercaptopropionate). This scaffold is linked to the catechol unit through the addition of one of the thiol groups to the oxidized *o*-quinone form. A second thiol group allows for the simultaneous incorporation of a functional group bearing a terminal vinyl or acrylate group using a thiol-ene click reaction. Lastly, the remaining two accessible thiols undergo polymerization through the formation of disulfide bridges, under mild and selective conditions, using iodine (Figure 2a). Pursuing this approximation, herein, we report new multifunctional coatings combining methyl-, glucose- or carboxylic acid-capped polyethylene glycol chains (compounds 1 and 2, and 4 and 5, respectively) with fluorescein fragments (3) (see Figure 2b). As representative supports, two families of NPs were chosen: (I) mesoporous silica NPs (MSNPs), selected for their stability and ability to encapsulate and release drugs, and (II) small (<10 nm) magnetic NPs (MNPs, Fe<sub>3</sub>O<sub>4</sub> NPs), which are relevant in magnetic resonance imaging (MRI) [44], drug and gene delivery [45], magnetothermal therapy [46], biosensors and bioseparation [47]. Finally, and for comparison purposes, we also evaluated related model coatings bearing styrene moieties instead of catechols, to assess their role in the adhesion and coating capabilities.



## 2. Materials and Methods

### 2.1. General Procedures

The solvents, chemicals, and reagents were acquired with high quality without any need for further purification from various commercial chemical companies, such as Merck (Darmstadt, Germany), Scharlab (Sentmenat, Spain), Apollo Scientific (Cheshire, UK), Alfa Aesar (Kandel, Germany), and TCI (Zwijndrecht, Belgium). All reactions were monitored by analytical thin-layer chromatography (TLC) using silica gel 60 pre-coated aluminum plates (0.20 mm thickness). Flash column chromatography was performed using silica gel Geduran<sup>®</sup> SI 60 (40–63  $\mu\text{m}$ ).  $^1\text{H}$  NMR and  $^{13}\text{C}$  NMR spectra were recorded at 298 K at 250, 360, 400 MHz, and 90, 100 MHz, respectively. Proton chemical shifts are reported in ppm ( $\delta$ ) ( $\text{CDCl}_3$ ,  $\delta$  7.26 or  $\text{CD}_3\text{COCD}_3$ ,  $\delta$  2.06 or  $\text{CD}_2\text{Cl}_2$   $\delta$  5.32). Carbon chemical shifts are reported in ppm ( $\delta$ ) ( $\text{CDCl}_3$ ,  $\delta$  77.16 or  $\text{CD}_3\text{COCD}_3$ ,  $\delta$  29.8, and  $\text{CD}_2\text{Cl}_2$   $\delta$  53.5). Infrared spectra (IR) were recorded on a Bruker Tensor 27 Spectrophotometer equipped with a Golden Gate Single Refraction Diamond ATR (attenuated total reflectance) accessory. Peaks are reported in  $\text{cm}^{-1}$ . HRMS were recorded in an Agilent 6454 Q-TP spectrometer with an Agilent Jetstream Technology (AJT) source using electrospray ionization (ESI) or electronic impact (EI). The molecular weight distribution determined by gel permeation chromatography (GPC) was made using an Agilent Technologies 1260 Infinity chromatograph and THF as a solvent. The instrument is equipped with three gel columns: PLgel 5  $\mu\text{m}$  Guard/50  $\times$  7.5  $\text{mm}^2$ , PLgel 5  $\mu\text{m}$  10,000  $\text{\AA}$  MW 4 K–400 K, and PL Mixed gel C 5  $\mu\text{m}$  MW 200–3 M. Calibration was made by using polystyrene standards. In each experiment, the freshly prepared polymer sample of interest was dissolved in THF (1–2  $\text{mg/mL}$ ) and

immediately analyzed by GPC (1 mL/min flow; 30 °C column temperature). Transmission electron microscopy (TEM) analyses were performed with a JEOL JEM-1400 transmission microscope operating at 120 kV. TEM samples were prepared by dipping a carbon copper grid into a dilute suspension of the particles in freshly sonicated hexane. The average particle size and its standard deviation were estimated by measuring the edge length of at least 200 particles using the software ImageJ (Fiji). Data were fitted to a log-normal function and the polydispersity index (PDI) was calculated.

## 2.2. Synthesis of Monomers

The synthesis of all new monomers considered and their full chemical characterization are described in the literature [43] (compounds **3** and **6**) or in the supporting information (compounds **1**, **2**, **4**, and **5**).

## 2.3. Synthesis and Characterization of Oligomeric Materials **P1**, **P2**, **P5**, and **C2–3**

As a general procedure, a solution of 35 mM of resublimed iodine in EtOH 96% (1.1 equiv.) was added dropwise to a ~7 mM solution of CATPEG bis-thiol **1**, **2** or **5** (or a 4:1 mixture of **2** and **3**) in EtOH 96%, containing an additional 0.035 equivalents of related cat-Me-(SH)<sub>2</sub> **11** as doping reagent to improve crosslinking. The reaction mixture was stirred for 1 h at rt, after which a yellowish solid precipitated. The supernatant was decanted, and the solid was washed with fresh EtOH 96% three times and dried under vacuum, yielding 45%, 28%, 55%, and 48% of oligomeric material **P1**, **P2**, **P5**, and **C2–3**, respectively.

The products obtained from the polymerization reaction were characterized by different techniques, such as <sup>1</sup>H NMR and gel permeation chromatography (GPC). The <sup>1</sup>H NMR experiments were performed in THF-d<sub>8</sub>, whereas GPC analyses were performed in THF. In the <sup>1</sup>H NMR, the disappearance of the thiol's peak of monomers was observed around 1.6 ppm, thus indicating that the disulfide bonds had been formed. To prepare GPC samples, the derivatives obtained after polymerization were dissolved in THF (1 or 2 mg/mL) and filtered through 0.22 µm nylon filters.

## 2.4. Coating of Mesoporous Silica Nanoparticles

As a general procedure, 10 mg of NPs (synthesized as described in *Chemistry–A European Journal* 2014, 20 (47), 15443–15450) were dispersed in 1 mL HPLC-grade CH<sub>2</sub>Cl<sub>2</sub>, a solution of ~7 mM of the corresponding oligomer was added, and the mixture was left to stir at 500 rpm overnight at rt. The final dispersion was centrifuged at 14,000 rpm for 2 min, and the resulting MSNPs were washed with fresh CH<sub>2</sub>Cl<sub>2</sub> three times to remove the excess of mPEG derivatives.

## 2.5. Coating of Magnetite Nanoparticles

### 2.5.1. Preparation of Magnetite NPs (MNPs) [48]

Fe(acac)<sub>3</sub> (0.441 g, 1.24 mmol), sodium oleate (0.213 g, 0.68 mmol), and oleic acid (1.485 g, 5.26 mmol) in a mixture of solvents composed of dibenzyl ether (10 mL), 1-octadecene (10 mL), and 1-tetradecene (3 mL) were heated up to 110 °C and kept at this temperature during 1.5 h under vacuum. During this time, reactive intermediates were formed. The reaction mixture was then heated up to 290 °C with a heating rate of 3 °C/min, and kept at this temperature for 1 h under Ar flow. In this step, nucleation and the subsequent growth of the NPs took place. Finally, the reaction mixture was cooled down to 50 °C. To purify the MNPs, isopropanol (40 mL) and acetone (40 mL) were added to the reaction mixture, which was centrifuged (10,000 rpm, 12 min) to separate the MNPs from the supernatant. The MNPs were resuspended in a mixture of CHCl<sub>3</sub> (10 mL), acetone (40 mL), and isopropanol (40 mL), and the same centrifugation conditions were applied. Finally, the MNPs were redispersed in CHCl<sub>3</sub> (~6.5 mg/mL).

### 2.5.2. Coating of MNPs: Synthesis of Fe<sub>3</sub>O<sub>4</sub>@P5 NPs

To a suspension of MNPs (6.5 mg/mL, 2.6 mL, 17 mg), a solution of **P5** (10 mg, 0.004 mmol) in HPLC-grade CHCl<sub>3</sub> (1.1 mL) was added. The reaction mixture was left to stir at rt for 3–4 days. The final MNPs were transferred to the aqueous phase and washed with CHCl<sub>3</sub> once, and the water removed under vacuum.

### 2.5.3. Functionalization of Fe<sub>3</sub>O<sub>4</sub>@P5 NPs: Synthesis of Targeted Fe<sub>3</sub>O<sub>4</sub>@P5-Glucose NPs

To a suspension of Fe<sub>3</sub>O<sub>4</sub>@P5 NPs (12 mg) cooled down to 0 °C, a solution of aminoglucopyranose **15** (15.4 mg, 0.09 mmol) in diisopropylethyl amine (DIPEA) (314 mL, 1.8 mmol) was added. After 10 min of stirring at 0 °C, 1-ethyl-3-(3-dimethylaminopropyl) carbodiimide (EDCI) (0.12 mmol) was added and the reaction mixture was stirred at rt for 3–4 days under Ar atmosphere. The final MNPs were transferred to the aqueous phase and washed with CHCl<sub>3</sub> once, and the solvent was removed under vacuum. The resulting nanoparticles were treated with DCl 35% *w/w* in H<sub>2</sub>O and analyzed by <sup>1</sup>H NMR.

In the case of working with protected amino-glucofuranose derivative **8**, the procedure followed was the same, but sugar derivative **8** along with 4-(dimethylaminopropyl)pyridine (0.3 equivalents) was directly added into MNPs@P7 suspension.

In the case of the partial deprotection of Fe<sub>3</sub>O<sub>4</sub>@P5-ProtectAminoFuranose NPs, to a ~1.5 mg/mL suspension of Fe<sub>3</sub>O<sub>4</sub>@P5-ProtectAminoFuranose NPs, a mixture of AcOH/H<sub>2</sub>O with the corresponding ratio was added, and the reaction mixture was stirred. Subsequently, the aqueous phase was washed with CHCl<sub>3</sub> (x3) to remove non-polar impurities and evaporated under vacuum. The resulting NPs were treated with DCl 35% *w/w* in H<sub>2</sub>O and analyzed by <sup>1</sup>H NMR.

## 2.6. Cytotoxicity and Internalization Assays of C2–3 Coated MSNPs

### 2.6.1. Cytotoxicity Assay

Human SH-SY5Y cells were cultured in DMEM/F-12 culture medium supplemented with 10% FBS and 1% antibiotic-antimycotic solution (Gibco-BRL, Carlsbad, CA, USA) and incubated at 37 °C in a humidified atmosphere with 5% CO<sub>2</sub>. Cells were seeded into a 96-well plate at a cell density of  $3.0 \times 10^3$  cells per well and then incubated for 24 h. C2–3-coated MSNPs were resuspended in the medium discussed above to achieve the different concentrations used in this assay: 0, 1, 5, 10, 25, 50, 100, and 200 µg/mL. Next, the cells were incubated at 37 °C, in a humidified atmosphere with 5% CO<sub>2</sub> and 98% humidity for 24 h. The cytotoxicity effect was measured after 24 h treatment employing the PrestoBlue cell viability reagent (ThermoFisher, Waltham, MA, USA). PrestoBlue (10 µL; resazurin-based solution) was added to each well. After a two-hour incubation period (37 °C, 5% CO<sub>2</sub>, 98% humidity), the fluorescence was quantified using a fluorescent multilabel plate reader (Victor3, PerkinElmer, Waltham, MA, USA) with excitation at  $\lambda = 531$  nm and recorded at  $\lambda = 572$  nm. Cell cytotoxicity was evaluated in terms of cell viability and expressed as a percentage of the control conditions. Each experiment was repeated at least three times, and each concentration was tested in at least three replicates.

### 2.6.2. Internalization Assay

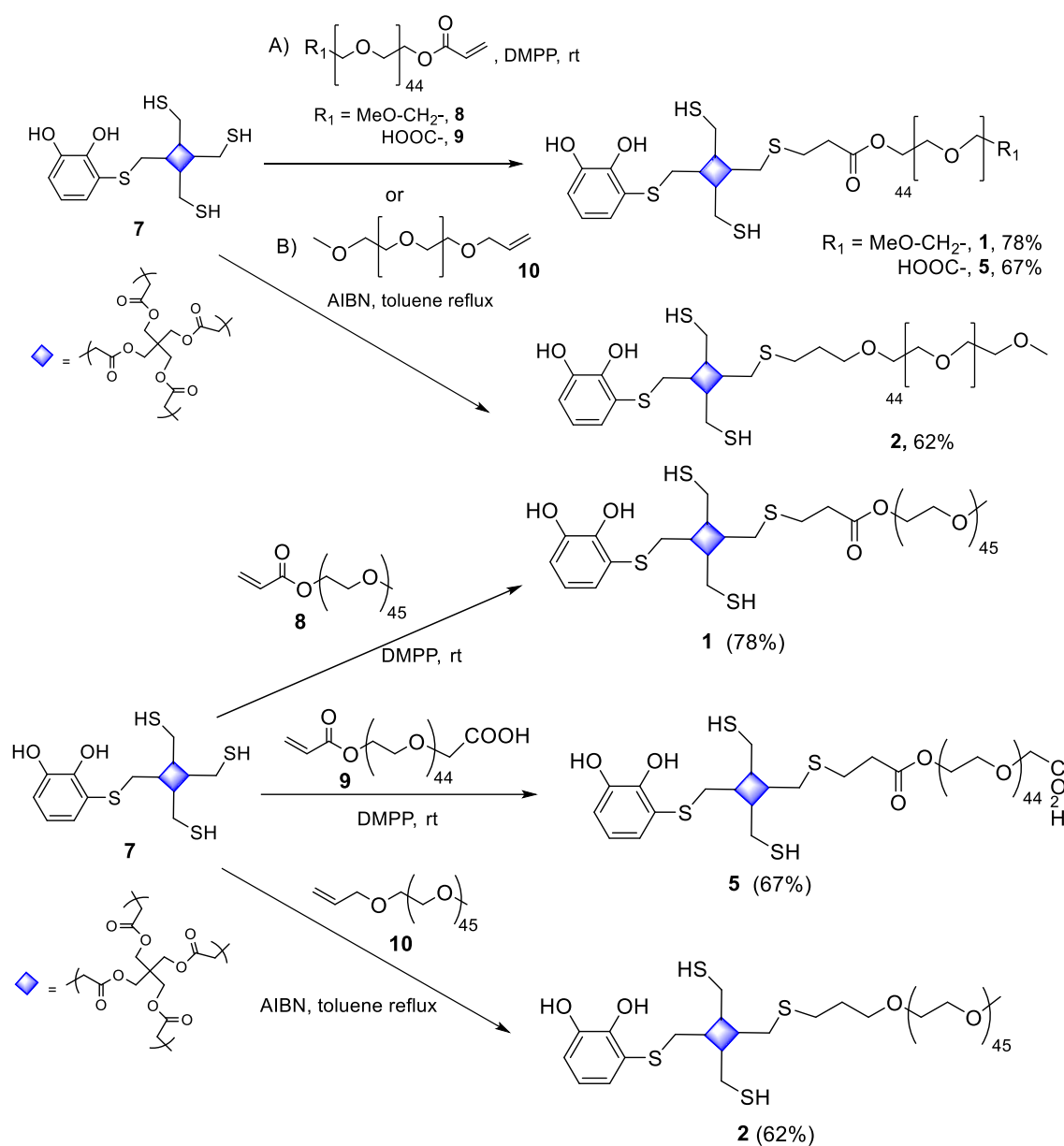
Human SH-SY5Y cells were cultured as in the previous assay for 24 h. C2–3-coated MSNPs (200 µg/mL) were added to four of the six wells (the other two were used as a negative control). One of the wells with C6–8-coated MSNPs was washed with PBS, and its cells were fixed with 4% paraformaldehyde (PFA) for 15 min at rt. The PFA was then removed, and PBS was added to the well. This procedure was repeated at 3, 6, and 24 h with one of the wells with C2–3-coated MSNPs. The same procedure was performed at 6 and 24 h for one of the wells without C2–3-coated MSNPs. Subsequently, the samples were blocked by adding a blocking buffer (5% bovine serum albumin solution in PBS buffer supplemented with 0.1% Triton X-100) (1 mL) and incubated for 1 h at rt. The blocking buffer was then removed, and the samples were washed with PBS for 5 min in agitation. Next, the samples were incubated with 4',6-diamidino-2-phenylindole (DAPI; 1/500) for

10 min at rt. After removing DAPI and washing the samples with PBS for 5 min in darkness, the samples were mounted on a drop of ProLong Gold.

### 3. Results and Discussion

### 3.1. Synthesis of Monomers **1–6** and the Corresponding Oligomeric Materials **P1–5**

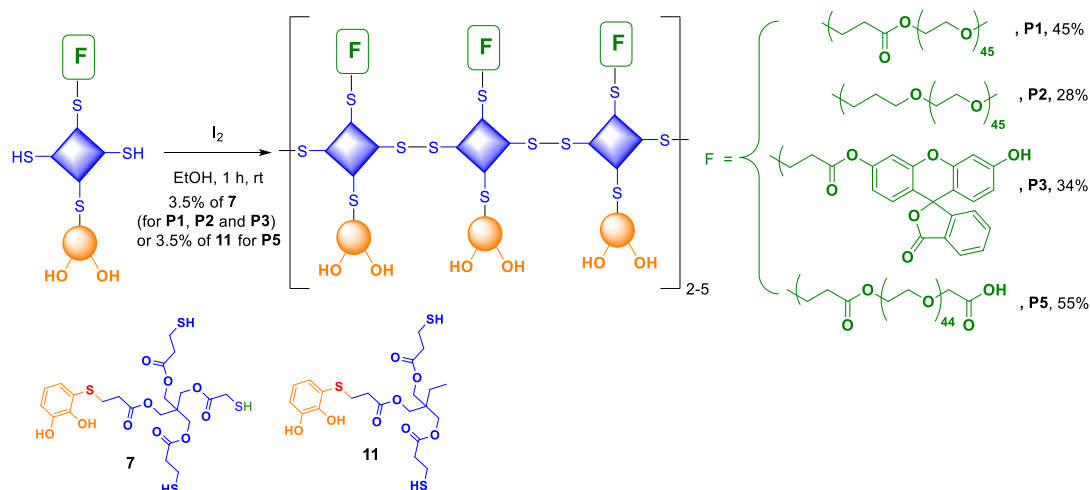
Compounds **3** and **6**, intermediate **7**, and the corresponding oligomers **P3** and **P6** were synthesized in our previous work [43]. Cat-PEG derivatives **1**, **2**, and **5** were obtained following the same synthetic methodology (Scheme 1). Thus, the intermediate *S*-catechol tris-thiol **7** was coupled with heterobifunctional PEG derivatives **8**, **9**, and **10**, to render the corresponding cat-PEG monomers **1**, **5**, and **2**, in 78%, 67%, and 62% yields, respectively. The obtention of **1** and **5** was based on a radical catalyzed thiol-ene reaction between **7** and **8** or **9**, and the synthesis of **2** consisted of a thia-Michael reaction between **7** and **10** using dimethylphenyl phosphine as the catalyst. Conversely, compound **4**, which contains a glucose unit, could not be isolated due to the instability of its immediate precursor (Scheme S1 in the Supplementary Material).



**Scheme 1.** Synthesis of cat-PEG monomers **1**, **5**, and **2**.



Next, we proceeded with the polymerization of the synthesized cat-PEG monomers **1**, **2**, and **5** under the same reaction conditions as in our previous work. Thus, oligomeric materials **P1**, **P2**, **P3**, and **P5** were obtained (Scheme 2) in 45%, 28%, 34%, and 55% yields, respectively, using iodine as an oxidant in EtOH. For **P1**, **P2**, and **P3**, 3.5% of the related cat-(SH)<sub>3</sub> **7** as the doping reagent was used to enhance crosslinking. These materials, insoluble in EtOH but soluble in CHCl<sub>3</sub>, exhibited <sup>1</sup>H NMR and IR spectra (see Supplementary Material) consistent with what was expected based on the precursors. In the <sup>1</sup>H NMR spectrum, a decrease in the intensity of the thiol proton around 1.6 ppm was observed, as expected after the formation of disulfide bonds. According to the diffusion-ordered-spectroscopy (DOSY) NMR experiments, all the materials resulted in oligomers between 2 and 3 units. In the case of material **P2**, characterization was additionally performed using the GPC technique with THF as the solvent, revealing that it consisted of an oligomer ranging between 2 and 5 units. For materials **P1** and **P3**, GPC analyses were not feasible due to their insolubility in THF. Regarding the oligomeric material **P5**, 3.5% of the related cat-Me-(SH)<sub>2</sub> **11** was used as the doping reagent to enhance crosslinking. The GPC analysis of the THF-soluble part of **P5** did not show any relevant peaks in the spectrum. Conversely, the corresponding precursor **5** displayed a distinct peak indicative of the monomeric compound, indirectly suggesting that monomer **5** was absent from the **P5** material.



**Scheme 2.** Synthesis of oligomeric materials **P1**, **P2**, **P3**, and **P5** from the corresponding monomers.

### 3.2. Coating of Mesoporous Silica Nanoparticles

Mesoporous SiO<sub>2</sub> NPs (MSNPs, Ø~200 nm) were dispersed in a ~7 mM CH<sub>2</sub>Cl<sub>2</sub> solution of oligomers **P1** and **P2** and the corresponding monomers **1** and **2**, for comparison (Figure 3a). The mixture was then stirred overnight at rt and subsequently centrifuged at 14,000 rpm. The resulting MSNPs were washed with fresh HPLC-grade CH<sub>2</sub>Cl<sub>2</sub> and characterized by different techniques, including scanning transmission electron microscopy (STEM), energy-dispersive X-ray spectroscopy (EDX), dynamic light scattering (DLS), and ζ-potential measurements. The results are shown in Figure 3.

From the STEM images, the PEGylated coating can be distinguished as thin lighter layers (ca. 20 nm) surrounding the NPs, whereas the untreated MSNPs did not exhibit any organic shells (Figure 3b). In the case of MSNPs@**P2**, the coating was confirmed in the EDX line scan (Figure 3c), with carbon (red line) across the whole diameter of the coated particles, while the oxygen signal (blue line) remained circumscribed to their inner sections, i.e., to the mineral core. Pristine and coated MSNPs (0.5–1 mg) were also dispersed in 1 mL of aqueous solution at different pHs and analyzed by DLS and ζ-potential measurements. While both families of NPs were stabilized with sizes around 200–250 nm within the pH range of 4–12, significant ζ-potential differences were found (Figure 3e), qualitatively evidencing the effectiveness of the coating. In any case, at pH 2, aggregates larger than 1 µm were formed, which was attributed to the worse electrostatic stabilization and the



gradual coating disaggregation from the NPs. The coating experiments were repeated under the same experimental conditions, now using **3** and **P3**. The STEM images showed a coating layer surrounding the NPs (Figure 4b, left) associated with bulk fluorescence under UV light (Figure 4a, left) or an optical microscope using the fluorescence mode and an Alexa Fluor 488 filter. Moreover, to prove the role of catechol units in the adhesive properties, the experiments were repeated using **6** and its corresponding oligomer, **P6**. The NPs treated with these derivatives did not exhibit any fluorescence (Figure 4a, right), and the STEM images revealed that MSNPs@**P6** resembled pristine MSNPs, devoid of any organic shells (Figure 4c). Thus, this simple example underscores the significant role of the catechol moiety as an anchor unit.

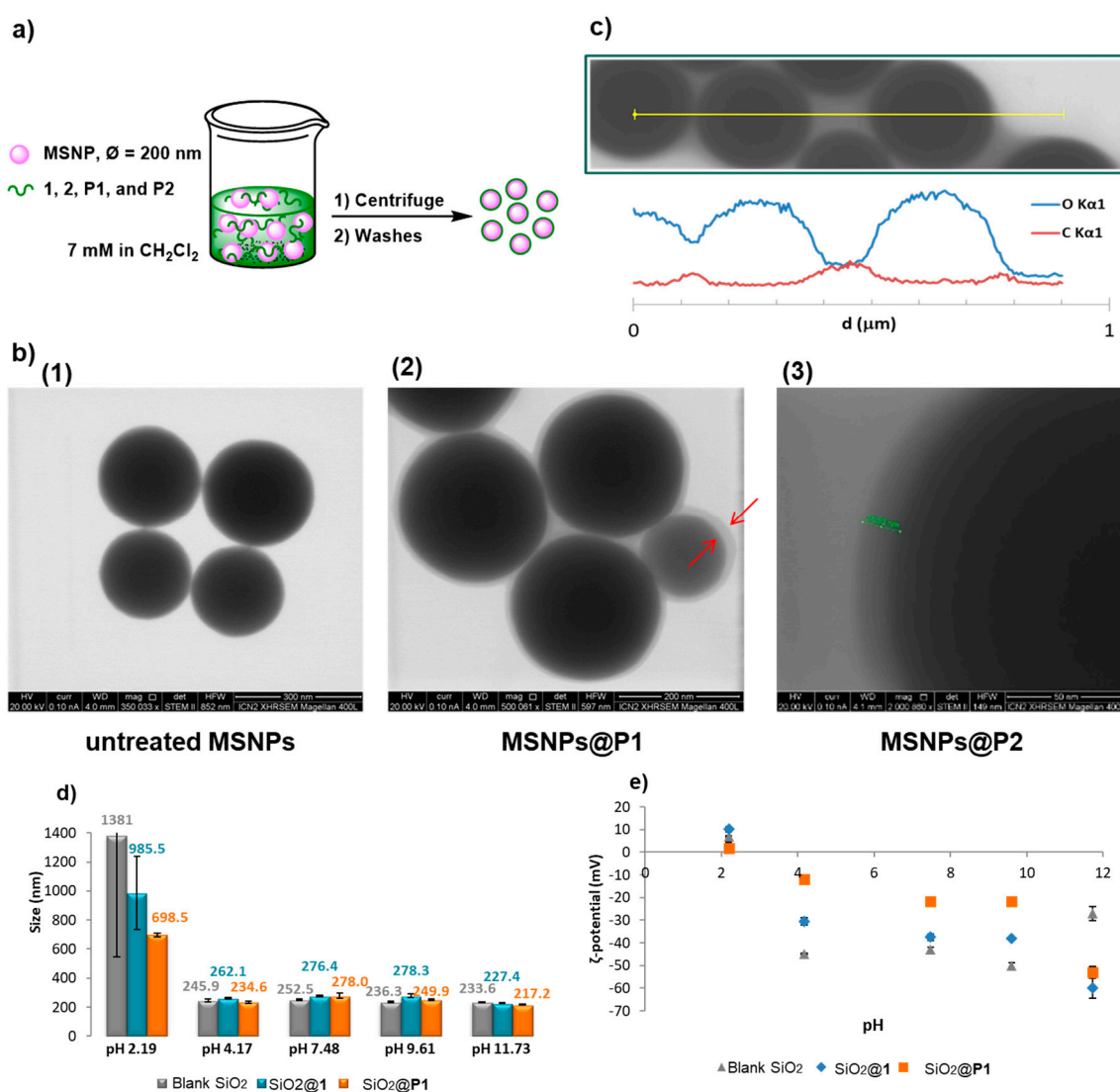


**Figure 3.** (a) Schematic representation of the procedure for coating onto MSNPs. (b) STEM images of untreated MSNPs (1), **P1**-coated MSNPs (2), and **P2**-coated MSNPs (3). (c) EDX line scan profile along the line drawn across the diameters of **P2**-coated MSNPs. (d) DLS analyses of untreated (gray) and treated (blue and orange) MSNPs at different pH. DLS values are the average of three measurements. (e)  $\zeta$ -potential values of untreated (gray) and treated (blue and orange) MSNPs at different pH.

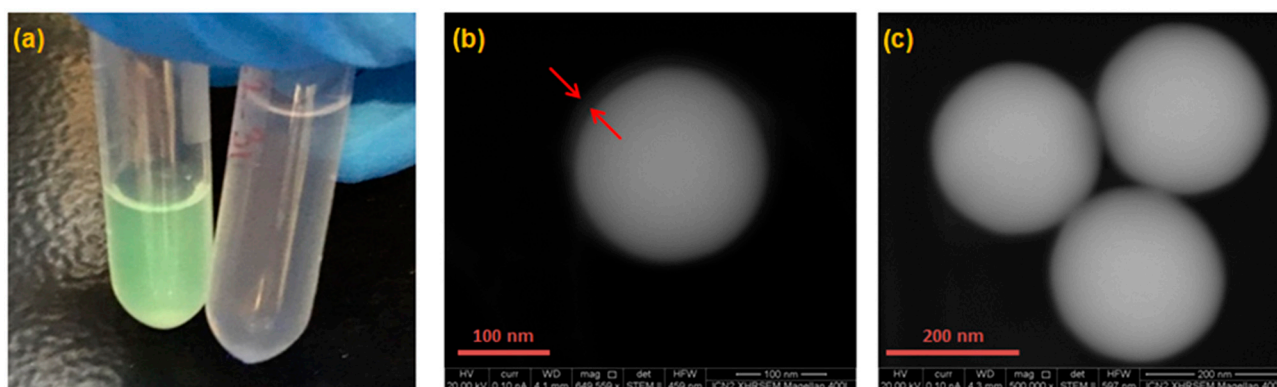


**Figure 4.** (a) P3-coated MSNPs (left) and P6-coated MSNPs (right) under UV lamp at 254 nm. STEM images of (b) MSNP@P3, where a coating layer can be identified and (c) MSNP@P6.

### 3.3. Coating of $Fe_3O_4$ NPs

To validate both our coating capabilities on different nanoparticle families and their subsequent use for additional biofunctionalization, we tackled the synthesis of  $Fe_3O_4$  NPs functionalized with P4; these are sugars recognized in Biology because of their barrier-crossing properties (Figure 5). Sadly, all the attempts to synthesize the precursor compound 4 failed (see Scheme S1 in the Supplementary Material). In the last synthetic stages, after incorporating the catechol and the protected sugar moieties, the resulting product proved to be unstable. Alternatively, we planned the first coating of the NPs with the oligomeric material P5, derived from cat-PEG-COOH bis thiol 5, to later couple the carboxylic acid residues with the suitable aminosugar derivative (Figure 5). Next, the first magnetic NPs stabilized with oleic acid ( $Fe_3O_4$ @OA NPs) were obtained through the thermal decomposition of  $Fe(acac)_3$  in the presence of oleic acid in a mixture of solvents. This procedure ensured a precise nanoparticle size (average 8 nm in diameter) and monodispersity, as confirmed by the electron microscopy (TEM) images [48]. Next, the  $Fe_3O_4$ @OA NPs were suspended in  $CHCl_3$  and coated with P5, previously dissolved in the same solvent. Despite many attempts, isolating the coated NPs through centrifugation proved unfeasible.

However, upon mixing the suspension with water, the NPs were transferred to the aqueous phase, unlike the uncoated NPs, which remained in the organic phase. This already represents a qualitative demonstration of the nanoparticle coating. The last step was the functionalization, performed by covalently attaching the carboxylic acid residues of the  $Fe_3O_4$ @P5 NPs with a suitable aminosugar derivative. Before this step, the reaction was optimized with a simple allylamine model, whose incorporation could be easily monitored by  $^1H$  NMR. Hence, a freshly prepared suspension of  $Fe_3O_4$ @P5 NPs in  $CHCl_3$  was treated with the coupling reagent EDCI and allylamine overnight. The resulting  $Fe_3O_4$ @P5-allylamide NPs were transferred to an aqueous phase and evaporated to dryness. The resulting solid was dispersed in deuterated methanol with some drops of DCl and left to stand overnight in this acidic medium to degrade the NPs. Finally, a  $^1H$ -NMR spectrum was recorded, revealing the presence of all the expected allyl signals coming from the linked allylamine, albeit slightly shifted to a lower field, according to the formation of the amide bond (see Supplementary Material, S7).

Finally, this synthetic procedure was successfully repeated with the protected aminosugar derivative 12, obtaining the  $Fe_3O_4$ @P5-ProtectFuranoseAmide NPs (as confirmed by the  $^1H$  NMR spectrum of the degraded NPs, see Supplementary Material, S7). However, the subsequent treatment of  $Fe_3O_4$ @P5-ProtectfuranoseAmide NPs in water with different acidic conditions to transform the attached sugar derivative fragments into the corresponding glucose units did not work. Under mildly acidic conditions, the protecting groups were not fully removed, while in stronger acidic media, an NP degradation was found. Therefore, the coupling was repeated using free amino-glucopyranose 13 (derived from the protected amino-glucofuranose 12, see Supplementary Material). In this way, the desired

$\text{Fe}_3\text{O}_4@\text{P5}$ -GlucoseAmide NPs (Figure 1) were directly obtained, as confirmed by the  $^1\text{H}$ - and  $^{13}\text{C}$  NMR spectra (see Supplementary Material, S7). The DLS and zeta  $\zeta$ -potential measurements at pH 7.4 (PBS buffer) showed aggregates around 360 nm and  $\alpha$   $\zeta$ -potential of  $-13.9$  mv, as well as 930 nm with a  $\zeta$ -potential value of  $3.3$  mv for the  $\text{Fe}_3\text{O}_4@\text{P5}$  NPs and  $\text{Fe}_3\text{O}_4@\text{P5}$ -Glucose NPs, respectively. These substantial  $\zeta$ -potential changes and the tendency to form larger aggregates for the  $\text{Fe}_3\text{O}_4@\text{P5}$ -Glucose NPs agree with the blocking of the carboxylic acid residues with the glucose units. Interestingly, the addition of the bovine serum albumin (BSA 10%) in the same PBS buffer to simulate physiological environments stabilized the monodispersed  $\text{Fe}_3\text{O}_4@\text{P5}$ -Glucose NPs on smaller aggregates around 100 nm, even though their  $\zeta$ -potential was close to 0 mv.

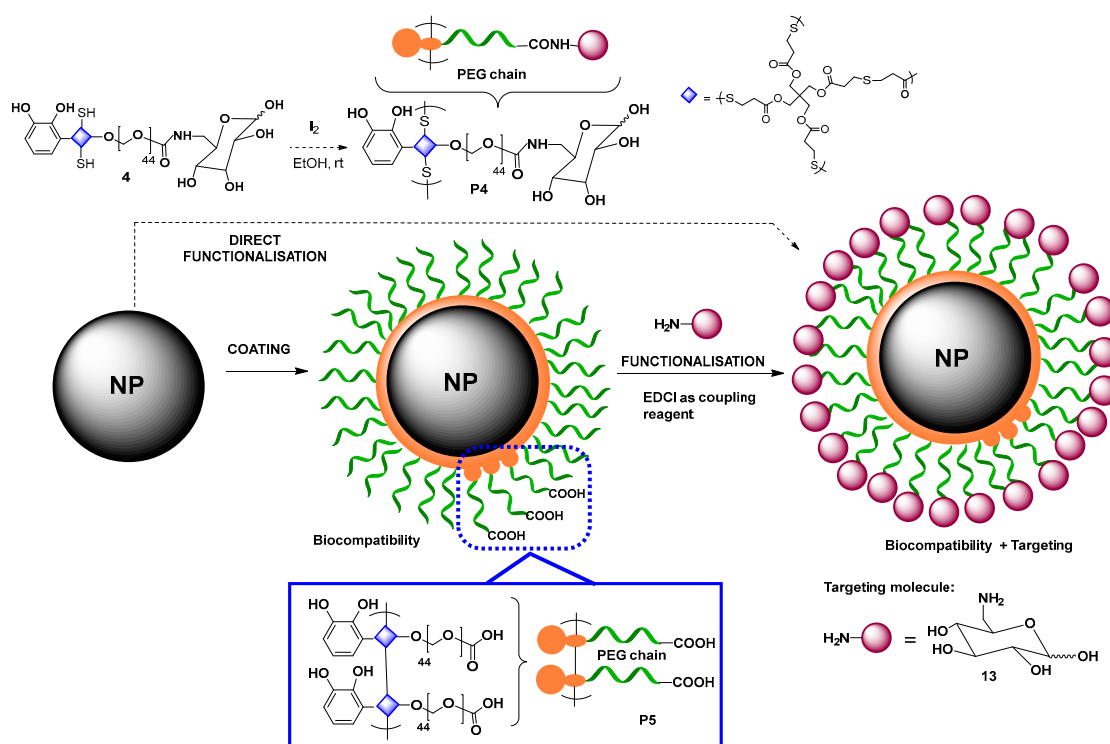


**Figure 5.** Strategies followed to obtain the functionalized coated  $\text{Fe}_3\text{O}_4@\text{P5}$ -glucose NPs with biocompatibility and possible targeting properties.

### 3.4. Multifunctional Coatings

Finally, a multifunctional coating (referred to, from now on, as **C2-3**) was obtained with a 48% yield by copolymerization of the cat-PEG **2** (80%) and the fluorescein-functionalized unit **3** (20%), using the polymerization protocol previously described (Figure 6a). The incorporation of both functionalities was confirmed by  $^1\text{H}$  NMR, with aromatic signals from the fluorescein in the 6.5–8.0 ppm range and the characteristic PEG signal at  $\sim 3.6$  ppm (see Supplementary Materials for full details). The posterior MSNP coating was confirmed by STEM analysis, which revealed a thin lighter layer around the surfaces (Figure 6b), and the fluorescence emission was detected by an optical fluorescent microscope equipped with an Alexa Fluor 488 filter (Figure 6c). The DLS measurements confirmed a colloidal stability increase at higher pHs, resulting in smaller sizes due to improved electrostatic stabilization (Figure 6d). The MSNP@**C2-3** formed larger aggregates than the non-treated MSNPs between pH 4 and pH 10.

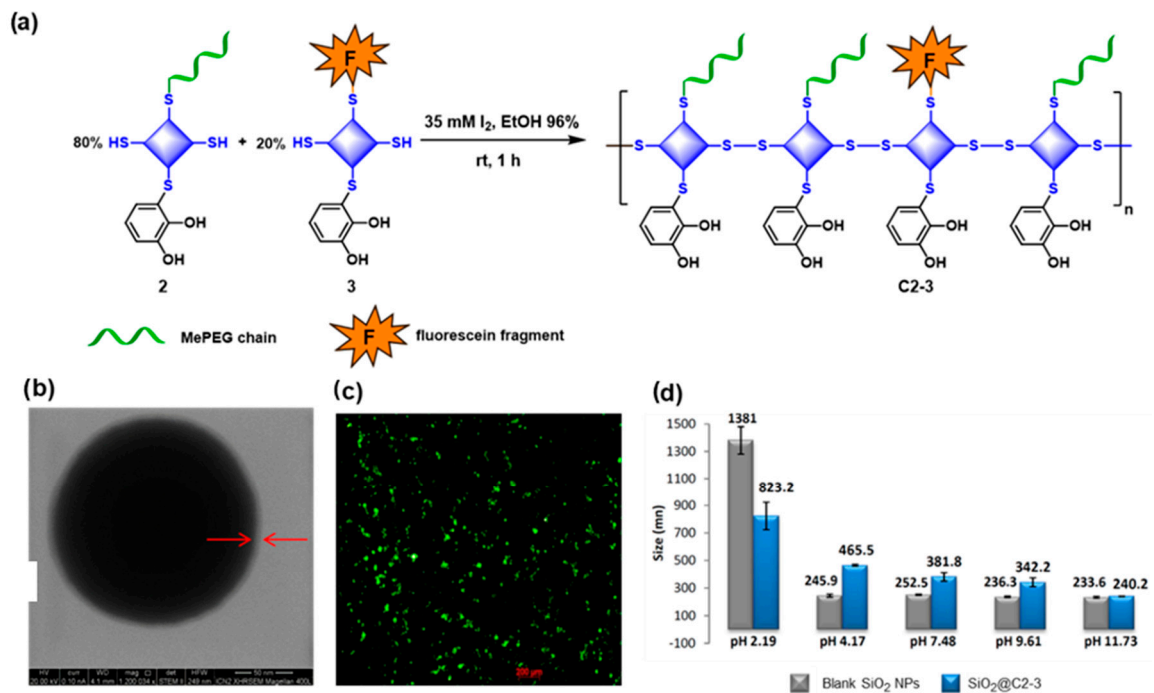


**Figure 6.** (a) Copolymerization of synthesized building blocks 2 and 3 to obtain a copolymer, C2-3, which is biocompatible, hydrophilic, and fluorescent, and is suitable for biomedical applications; (b) STEM image of coated MSNPs@C2-3 showing a lighter outer layer. (c) Image taken from an inverted optical/fluorescence microscope in fluorescence mode with an Alexa Fluor 488 filter of MSNPs@C2-3 showing fluorescence. (d) Representation of NPs' sizes at different pH taken from DLS analyses.

Finally, an internalization assay was conducted on SH-SY5Y cells. This involved adding MSNPs@C2-3 (200 µg/mL) to six-well plates containing 10<sup>5</sup> cells per well. At different time points (1, 3, 6, 24 h), the cells were fixed and stained (Figure 7b).

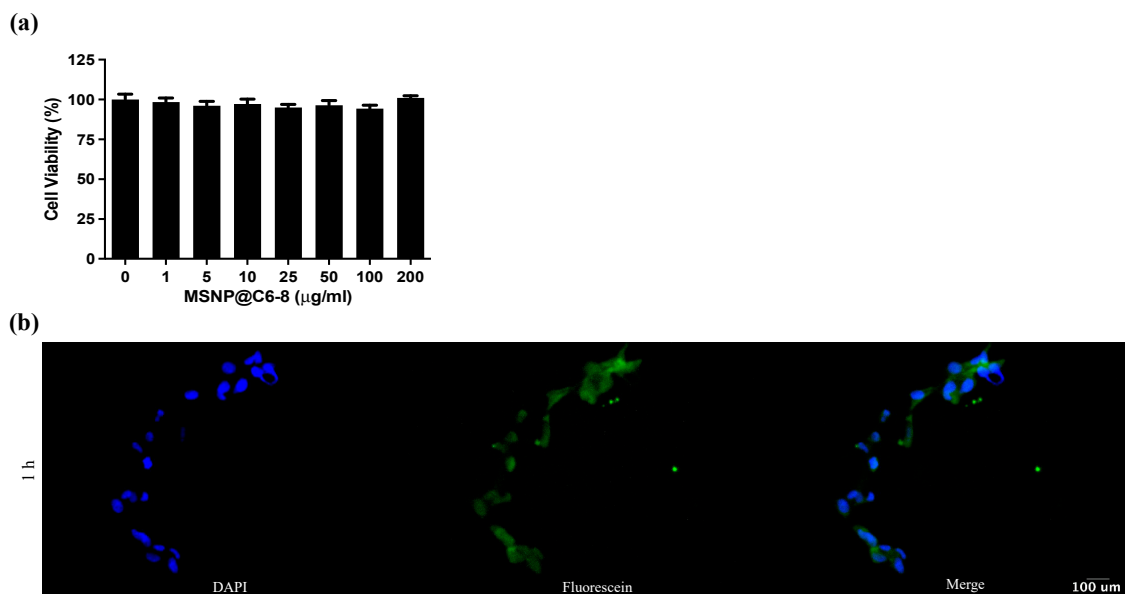


**Figure 7.** Cont.

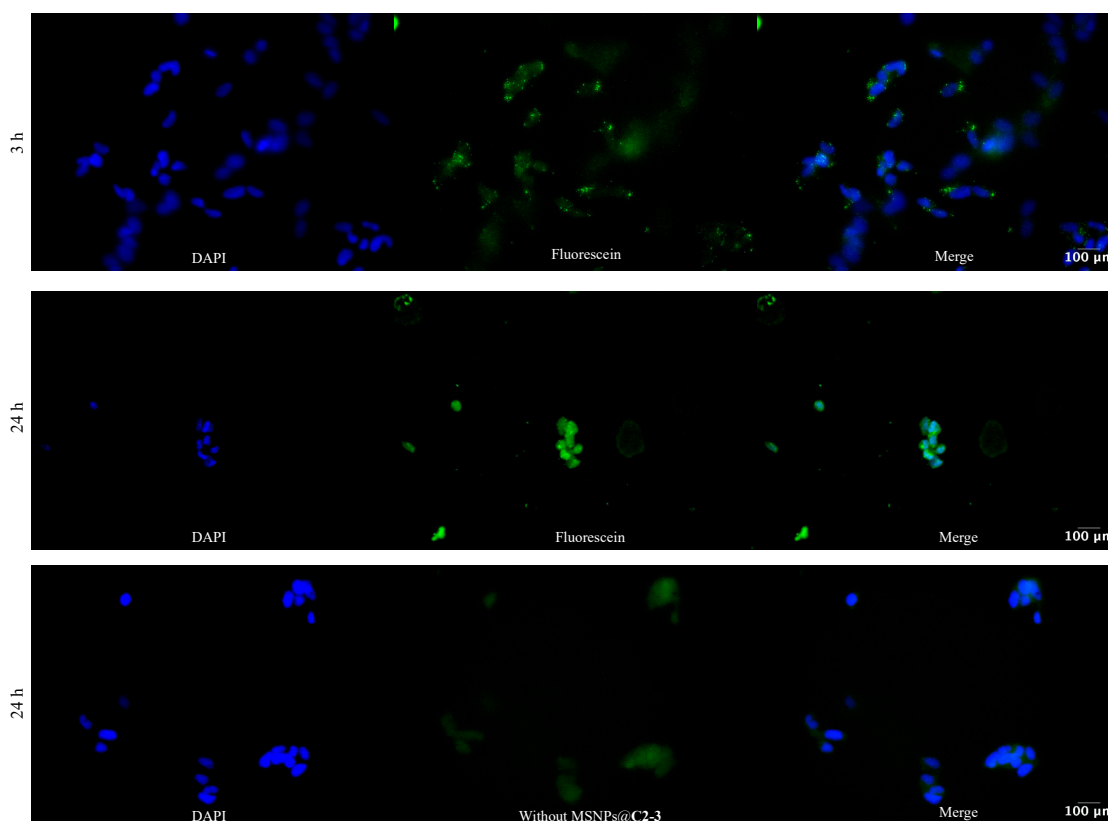


**Figure 7.** (a) Effect of MSNPs@C2–3 on the cell viability of SH-SY5Y cells (3000 cells per well). These cells were incubated for 24 h in the presence of indicated concentrations of MSNPs@C2–3. Cell viability is expressed as a percentage compared to an untreated control. Values are presented as mean  $\pm$  standard error of the mean ( $n = 3$ ). (b) Internalization assay on SH-SY5Y cells at 1 h, 3 h, 24 h, and 24 h without MSNPs@C2–3. Blue color shows 4',6-diamidino-2-phenylindole (DAPI) staining of cell nuclei. The green color shows fluorescein staining of MSNPs@C2–3. Scale: 100  $\mu$ m.

After 1 h, MSNPs@C2–3 were observed within the cells. At 3 h, these nanoparticles were not only internalized but also exhibited an organized distribution within the cellular compartments. By 24 h, nanoparticles were additionally detected in the nuclei of the cells, showing an organized arrangement. In contrast, cells without nanoparticles showed no fluorescence. Furthermore, the cytotoxic effect of the MSNPs@C2–3 on the SH-SY5Y cells was examined by treating them with varying concentrations of MSNPs@C2–3 for 24 h. These coated NPs did not exhibit a cytotoxic effect compared to the control at any of the concentrations tested (Figure 7a).

#### 4. Conclusions

We have developed a novel mussel-inspired strategy to obtain multifunctional PEG-based biocoatings by deploying the polymerization of catechol-based functionalized units using disulfide bridges under mild oxidative conditions. Thanks to its universal character, we successfully coated two families of NPs, mesoporous silica NPs (MSNPs) and magnetic NPs (MNPs,  $\text{Fe}_3\text{O}_4$  NPs), both of which are receiving increasing recognition for their biomedical uses. The PEG coating confers biocompatibility and colloidal stability to the NPs and is used as a primer for further functionalization through the carboxylic acid moieties with bioactive groups. In this case, and as a representative example, we introduced glucose units with potential barrier-crossing capabilities. Finally, and as a proof of concept, we have also shown the possibility of achieving multifunctional coatings combining PEG chains and fluorescein fragments, allowing for the optical tracking of additional cell internalization, with excellent biocompatibility.

**Supplementary Materials:** The following supporting information can be downloaded at: <https://www.mdpi.com/article/10.3390/biomimetics9090531/s1>: S1: experimental part of synthesis of monomers; S2: experimental part synthesis of amino glucopyranose; S3: experimental part of synthesis of intermediate **21**; S4:  $^1\text{H}$ ,  $^{13}\text{C}$  NMR and IR spectra of new compounds; S5:  $^1\text{H}$  NMR and IR spectra of oligomers and copolymers; S6: GPC spectra; S7: other  $^1\text{H}$ ,  $^{13}\text{C}$  NMR spectra.

**Author Contributions:** Conceptualization, D.R.-M., F.B., J.L. and R.A.; methodology, D.R.-M., F.B., J.L. and R.A.; formal analysis, R.A.; investigation, C.C., A.L.-M. and P.A.-T.; resources, D.R.-M., F.B., J.L. and R.A.; data curation, C.C. and A.L.-M.; writing—original draft preparation, C.C., D.R.-M. and F.B.; writing—review and editing, all the team; supervision, D.R.-M., F.B., J.L. and R.A.; project administration, D.R.-M., F.B. and R.A.; funding acquisition, D.R.-M., F.B., J.L. and R.A. All authors have read and agreed to the published version of the manuscript.

**Funding:** Funding support from the following grants: PID2019-106403RB-I00, PID2021-127983OB-C21, PID2021-127983OB-C22, and PID2022-139826OB-I00, funded by MCIN/AEI/10.13039/501100011033, co-financed with the European Fund for Regional Development (FEDER), and by ERDF's "A way of making Europe". The ICN2 is funded by the CERCA program/Generalitat de Catalunya. The ICN2 is supported by the Severo Ochoa Centers of Excellence program, and grant SEV-2017-0706 is funded by MCIN/AEI/10.13039/501100011033.

**Institutional Review Board Statement:** Not applicable.

**Data Availability Statement:** Data are contained within the article.

**Acknowledgments:** The authors would like to acknowledge the funding support previously defined.

**Conflicts of Interest:** The authors declare no conflict of interest.

## References

1. Lacava, L.M.; Lacava, Z.G.; Da Silva, M.F.; Silva, O.; Chaves, S.B.; Azevedo, R.B.; Pelegrini, F.; Gansau, C.; Buske, N.; Sabolovic, D.; et al. Magnetic resonance of a dextran-coated magnetic fluid intravenously administered in mice. *Biophys. J.* **2001**, *80*, 2483–2486. [CrossRef] [PubMed]
2. Strable, E.; Bulte, J.W.M.; Moskowitz, B.; Vivekanandan, K.; Allen, M.; Douglas, T. Synthesis and Characterization of Soluble Iron Oxide-Dendrimer Composites. *Chem. Mater.* **2001**, *13*, 2201–2209. [CrossRef]
3. Kohler, N.; Sun, C.; Fichtenholtz, A.; Gunn, J.; Fang, C.; Zhang, M. Methotrexate-immobilized poly(ethylene glycol) magnetic nanoparticles for MR imaging and drug delivery. *Small* **2006**, *2*, 785–792. [CrossRef] [PubMed]
4. Choi, C.K.K.; Zhuo, X.; Chiu, Y.T.E.; Yang, H.; Wang, J.; Choi, C.H.J. Polydopamine-based concentric nanoshells with programmable architectures and plasmonic properties. *Nanoscale* **2017**, *9*, 16968–16980. [CrossRef]
5. Wang, X.T.; Deng, X.; Zhang, T.D.; Zhang, J.; Chen, L.L.; Wang, Y.F.; Cao, X.; Zhang, Y.Z.; Zheng, X.; Yin, D.C. A Versatile Hydrophilic and Antifouling Coating Based on Dopamine Modified Four-Arm Polyethylene Glycol by One-Step Synthesis Method. *ACS Macro Lett.* **2022**, *11*, 805–812. [CrossRef]
6. Ling, D.; Park, W.; Park, Y.I.; Lee, N.; Li, F.; Song, C.; Yang, S.-G.; Choi, S.H.; Na, K.; Hyeon, T. Multiple-Interaction Ligands Inspired by Mussel Adhesive Protein: Synthesis of Highly Stable and Biocompatible Nanoparticles. *Angew. Chem. Int. Ed.* **2011**, *50*, 11360–11365. [CrossRef]
7. Black, K.C.L.; Liu, Z.; Messersmith, P.B. Catechol Redox Induced Formation of Metal Core-Polymer Shell Nanoparticles. *Chem. Mater.* **2011**, *23*, 1130–1135. [CrossRef]
8. Al-Nahain, A.; Lee, S.Y.; In, I.; Lee, K.D.; Park, S.Y. Triggered pH/redox responsive release of doxorubicin from prepared highly stable Graphene with thiol grafted Pluronic. *Int. J. Pharm.* **2013**, *450*, 208–217. [CrossRef]
9. Lee, H.; Lee, K.D.; Pyo, K.B.; Park, S.Y.; Lee, H. Catechol-Grafted Poly(ethylene glycol) for PEGylation on Versatile Substrates. *Langmuir* **2010**, *26*, 3790–3793. [CrossRef]
10. Zhang, F.; Liu, S.; Zhang, Y.; Chi, Z.; Xu, J.; Wei, Y. A facile approach to Surface modification on versatile substrates for biological applications. *J. Mater. Chem.* **2012**, *22*, 17159–17166. [CrossRef]
11. Wei, Q.; Becherer, T.; Mutihac, R.-C.; Noeske, P.-L.M.; Paulus, F.; Haag, R.; Grunwald, I. Multivalent Anchoring and Cross-Linking of Mussel-Inspired Antifouling Surface Coatings. *Biomacromolecules* **2014**, *15*, 3061–3071. [CrossRef] [PubMed]
12. Wilke, P.; Börner, H.G. Mussel-Glue Derived Peptide-Polymer Conjugates to Realize Enzyme-Activated Antifouling Coatings. *ACS Macro Lett.* **2012**, *1*, 871–875. [CrossRef]
13. Xu, L.Q.; Pranantyo, D.; Neoh, K.-G.; Kang, E.-T.; Teo, S.L.-M.; Fu, G.D. Synthesis of catechol and zwitterion-bifunctionalized poly(ethylene glycol) for the construction of antifouling surfaces. *Polym. Chem.* **2016**, *7*, 493–501. [CrossRef]
14. Dang, Y.; Quan, M.; Xing, C.-M.; Wang, Y.-B.; Gong, Y.-K. Biocompatible and antifouling coating of cell membrane phosphorylcholine and mussel catechol modified multi-arm PEGs. *J. Mater. Chem. B* **2015**, *3*, 2350–2361. [CrossRef] [PubMed]



15. Wilke, P.; Börne, H.G. Revealing the impact of poly(ethylene oxide) blocks on enzyme activable coatings from peptide-polymer conjugates. *Eur. Polym. J.* **2015**, *62*, 374–379. [CrossRef]
16. Dalsin, J.L.; Lin, L.; Tosatti, S.; Vörös, J.; Textor, M.; Messersmith, P.B. Protein Resistance of Titanium Oxide Surfaces Modified by Biologically Inspired mPEG-DOPA. *Langmuir* **2005**, *21*, 640–646. [CrossRef]
17. Ko, R.; Cadieux, P.A.; Dalsin, J.L.; Lee, B.P.; Elwood, C.N.; Razvi, H. First Prize: Novel Uropathogen-Resistant Coatings Inspired by Marine Mussels. *J. Endourol.* **2008**, *22*, 1153–1160. [CrossRef]
18. Gillich, T.; Benetti, E.M.; Rakhmatullina, E.; Konradi, R.; Li, W.; Zhang, A.; Schlüter, A.D.; Textor, M. Self-Assembly of Focal Point Oligo-catechol Ethylene Glycol Dendrons on Titanium Oxide Surfaces: Adsorption Kinetics, Surface Characterization, and Nonfouling Properties. *J. Am. Chem. Soc.* **2011**, *133*, 10940–10950. [CrossRef]
19. Kim, H.S.; Ham, H.O.; Son, Y.J.; Messersmith, P.B.; Yoo, H.S. Electrospun catechol-modified poly(ethylene glycol) nanofibrous mesh for anti-fouling properties. *J. Mater. Chem. B* **2013**, *1*, 3940–3949. [CrossRef]
20. Nam, J.A.; Nahain, A.-A.; Kim, S.M.; In, I.; Park, S.Y. Successful stabilization of functionalized hybrid Graphene for high-performance antimicrobial activity. *Acta Biomater.* **2013**, *9*, 7996–8003. [CrossRef]
21. Jeong, C.J.; Inb, I.; Park, S.Y. Facile preparation of metal nanoparticle-coated polystyrene beads by catechol conjugated polymer. *Surf. Interface Anal.* **2015**, *47*, 253–258. [CrossRef]
22. Hu, Y.; Zhang, Q.; Garcia-Rojas, D.; Ling, V.; Masterson, C.M.; Bi, Y.; Xiao, Z.; Guo, X.; Villanova, J.; Dunn, J.; et al. Increasing the Antioxidant Capacity of Ceria Nanoparticles with Catechol-Grafted Poly(Ethylene Glycol). *J. Mater. Chem. B* **2022**, *10*, 10042–10053. [CrossRef] [PubMed]
23. Mai, B.T.; Conteh, J.S.; Gavilán, H.; Di Girolamo, A.; Pellegrino, T. Clickable Polymer Ligand-Functionalized Iron Oxide Nanocubes: A Promising Nanoplatfrom for “Local Hot Spots” Magnetically Triggered Drug Release. *ACS Appl. Mater. Interfaces* **2022**, *14*, 48476–48488. [CrossRef]
24. Zeng, G.; Liu, M.; Liu, X.; Huang, Q.; Xu, D.; Mao, L.; Huang, H.; Deng, F.; Zhang, X.; Wei, Y. Mussel inspired preparation of MoS<sub>2</sub> based polymer nanocomposites: The case of polyPEGMA. *Appl. Surf. Sci.* **2016**, *387*, 399–405. [CrossRef]
25. Xu, H.; Liu, M.; Lan, M.; Yuan, H.; Yu, W.; Tian, J.; Wan, Q.; Zhang, X.; Wei, Y. Mussel-inspired PEGylated carbon nanotubes: Biocompatibility evaluation and drug delivery Applications. *Toxicol. Res.* **2016**, *5*, 1371–1379. [CrossRef] [PubMed]
26. Zhang, X.; Zeng, G.; Tian, J.; Wan, Q.; Huang, Q.; Wang, K.; Zhang, Q.; Liu, M.; Deng, F.; Wei, Y. PEGylation of carbon nanotubes via mussel inspired chemistry: Preparation, characterization and biocompatibility evaluation. *Appl. Surf. Sci.* **2015**, *351*, 425–432. [CrossRef]
27. Zhou, J.; Wang, C.; Wang, P.; Messersmith, P.B.; Duan, H. Multifunctional Magnetic Nanochains: Exploiting Self-Polymerization and Versatile Reactivity of Mussel-Inspired Polydopamine. *Chem. Mater.* **2015**, *27*, 3071–3076. [CrossRef]
28. Xu, Y.J.; Wei, K.; Zhao, P.; Feng, Q.; Choi, C.K.K.; Bian, L. Preserving the adhesion of catechol-conjugated hydrogels by thiourea–quinone coupling. *Biomater. Sci.* **2016**, *4*, 1726–1730. [CrossRef]
29. Mattson, K.M.; Latimer, A.A.; McGrath, A.J.; Lynd, N.A.; Lundberg, P.; Hudson, Z.M.; Hawker, C.J. A facile synthesis of catechol-functionalized poly(ethylene oxide) block and random copolymers. *J. Polym. Sci. Part A Polym. Chem.* **2015**, *53*, 2685–2692. [CrossRef]
30. Zhang, Q.; Nurumbetov, G.; Simula, A.; Zhu, C.; Li, M.; Wilson, P.; Kempe, K.; Yang, B.; Tao, L.; Haddleton, D.M. Synthesis of well-defined catechol polymers for surface functionalization of magnetic nanoparticles. *Polym. Chem.* **2016**, *7*, 7002–7010. [CrossRef]
31. Stephen, Z.R.; Dayringer, C.J.; Lim, J.J.; Revia, R.A.; Halbert, M.V.; Jeon, M.; Bakthavatsalam, A.; Ellenbogen, R.G.; Zhang, M. Approach to Rapid Synthesis and Functionalization of Iron Oxide Nanoparticles for High Gene Transfection. *ACS Appl. Mater. Interfaces* **2016**, *8*, 6320–6328. [CrossRef]
32. Lu, C.; Park, M.K.; Lu, C.; Lee, Y.H.; Chai, K.Y. A mussel-inspired chitooligosaccharide based multidentate ligand for highly stabilized nanoparticles. *J. Mater. Chem. B* **2015**, *18*, 3730–3737. [CrossRef] [PubMed]
33. Heng, C.; Liu, M.; Wang, P.; Wang, K.; Zheng, X.; Fan, D.; Hui, J.; Zhang, X.; Wei, Y. Preparation of silica nanoparticles based multifunctional therapeutic systems via one-step mussel inspired modification. *Chem. Eng. J.* **2016**, *296*, 268–276. [CrossRef]
34. Marcelo, G.; Kaplan, E.; Tarazona, M.P.; Mendicuti, F. Interaction of gold nanoparticles with Doxorubicin mediated by supramolecular chemistry. *Colloids Surf. B* **2015**, *128*, 237–244. [CrossRef]
35. Chan, J.M.W.; Tan, J.P.K.; Engler, A.C.; Ke, X.; Gao, S.; Yang, C.; Sardon, H.; Yang, Y.Y.; Hedrick, J.L. Organocatalytic Anticancer Drug Loading of Degradable Polymeric Mixed Micells via a Biomimetic Mechanism. *Macromolecules* **2016**, *49*, 2013–2021. [CrossRef]
36. Wu, S.; Kuang, H.; Meng, F.; Wu, Y.; Li, X.; Jing, X.; Huang, Y. Facile preparation of core cross-linked micells from catechol-containing amphiphilic triblock copolymer. *J. Mater. Chem.* **2012**, *22*, 15348–15356. [CrossRef]
37. Wu, S.; Qi, R.; Kuang, H.; Wei, Y.; Jing, X.; Meng, F.; Huang, Y. pH-Responsive Drug Delivery by Amphiphilic Copolymer through Boronate-Catechol Complexation. *ChemPlusChem* **2013**, *78*, 175–184. [CrossRef]
38. Na, H.B.; Palui, G.; Rosenberg, J.T.; Ji, X.; Grant, S.C.; Mattoussi, H. Multidentate Catechol-Based Polyethylene Glycol Oligomers Provide Enhanced Stability and Biocompatibility to Iron Oxide Nanoparticles. *ACS Nano* **2012**, *6*, 389–399. [CrossRef]
39. Wang, W.; Ji, X.; Na, H.B.; Safi, M.; Smith, A.; Palui, G.; Perez, J.M.; Mattoussi, H. Design of a Multi-Dopamine-Modified Polymer Ligand Optimally Suited for Interfacing Magnetic Nanoparticles with Biological Systems. *Langmuir* **2014**, *30*, 6197–6208. [CrossRef]

40. Wan, Q.; Tian, J.; Liu, M.; Zeng, G.; Li, Z.; Wang, K.; Zhang, Q.; Deng, F.; Zhang, X.; Wei, Y. Mussel inspired preparation of highly dispersible and biocompatible carbon nanotubes. *RSC Adv.* **2015**, *5*, 25329–25336. [CrossRef]
41. Liu, Y.; Choi, C.K.K.; Hong, H.; Xiao, Y.; Kwok, M.L.; Liu, H.; Tian, X.Y.; Choi, C.H.J. Dopamine Receptor-Mediated Binding and Cellular Uptake of Polydopamine-Coated Nanoparticles. *ACS Nano* **2021**, *15*, 13871–13890. [CrossRef] [PubMed]
42. Ercole, F.; Kim, C.J.; Dao, N.V.; Tse, W.K.L.; Whittaker, M.R.; Caruso, F.; Quinn, J.F. Synthesis of Thermoresponsive, Catechol-Rich Poly(Ethylene Glycol) Brush Polymers for Attenuating Cellular Oxidative Stress. *Biomacromolecules* **2023**, *24*, 387–399. [CrossRef] [PubMed]
43. Casagualda, C.; Mancebo-Aracil, J.; Moreno-Villaécija, M.A.; López-Moral, A.; Alibés, R.; Busqué, F.; Ruiz-Molina, D. Mussel-Inspired Lego Approach for Controlling the Wettability of Surfaces with Colorless Coatings. *Biomimetics* **2023**, *8*, 3. [CrossRef] [PubMed]
44. Smolensky, E.D.; Park, H.-Y.E.; Berquó, T.S.; Pierre, V.C. Surface functionalization of magnetic iron oxide nanoparticles for MRI applications-effect of anchoring group and ligand exchange protocol. *Contrast Media Mol. Imaging* **2011**, *6*, 189–199. [CrossRef] [PubMed]
45. Park, J.W.; Bae, K.H.; Kim, C.; Park, T.G. Clustered Magnetite Nanocrystals Cross-Linked with PEI for Efficient siRNA Delivery. *Biomacromolecules* **2011**, *12*, 457–465. [CrossRef] [PubMed]
46. Farokhi, M.; Mottaghiab, F.; Saeb, M.R.; Thomas, S. Functionalized theranostic nanocarriers with bio-inspired polydopamine for tumor imaging and chemo-photothermal therapy. *J. Control. Release* **2019**, *309*, 203–219. [CrossRef]
47. Xu, C.; Xu, K.; Gu, H.; Zheng, R.; Liu, H.; Zhang, X.; Guo, Z.; Xu, B. Dopamine as A Robust Anchor to Immobilize Functional Molecules on the Iron Oxide Shell of Magnetic Nanoparticles. *J. Am. Chem. Soc.* **2004**, *126*, 9938–9939. [CrossRef]
48. Muro-Cruces, J.; Roca, A.G.; López-Ortega, A.; Fantechi, E.; del-Pozo-Bueno, D.; Estrade, S.; Peiro, F.; Sepulveda, B.; Pineider, F.; Sangregorio, C. Precise Size Control of the Growth of Fe<sub>3</sub>O<sub>4</sub> Nanocubes over a Wide Size Range Using a Rationally Designed One-Pot Synthesis. *ACS Nano* **2019**, *13*, 7716–7728. [CrossRef]

**Disclaimer/Publisher’s Note:** The statements, opinions and data contained in all publications are solely those of the individual author(s) and contributor(s) and not of MDPI and/or the editor(s). MDPI and/or the editor(s) disclaim responsibility for any injury to people or property resulting from any ideas, methods, instructions or products referred to in the content.



## Article

# Silactins and Structural Diversity of Biosilica in Sponges

Hermann Ehrlich <sup>1,2,\*</sup> , Alona Voronkina <sup>3</sup> , Konstantin Tabachnik <sup>4</sup>, Anita Kubiak <sup>1,5</sup> ,  
Alexander Ereskovsky <sup>6</sup>  and Teofil Jesionowski <sup>2,\*</sup> 

<sup>1</sup> Center of Advanced Technology, Adam Mickiewicz University, Uniwersytetu Poznańskiego 10, 61-614 Poznań, Poland; anita.kubiak@amu.edu.pl

<sup>2</sup> Faculty of Chemical Technology, Institute of Chemical Technology and Engineering, Poznań University of Technology, Berdychowo 4, 60-965 Poznań, Poland

<sup>3</sup> Pharmacy Department, National Pirogov Memorial Medical University, Vinnytsya, Pirogov Street 56, 21018 Vinnytsya, Ukraine; voronkina@vnmu.edu.ua

<sup>4</sup> International Institute of Biomineralogy GmbH, Am St.-Niclas Schacht 13, 09599 Freiberg, Germany

<sup>5</sup> Faculty of Chemistry, Adam Mickiewicz University, Uniwersytetu Poznańskiego 8, 61-614 Poznań, Poland

<sup>6</sup> IMBE, CNRS, IRD, Aix Marseille University, Station Marine d'Endoume, Rue de la Batterie des Lions, 13007 Marseille, France; alexander.ereskovsky@imbe.fr

\* Correspondence: herehr@amu.edu.pl (H.E.); teofil.jesionowski@put.poznan.pl (T.J.)

**Abstract:** Sponges (phylum Porifera) were among the first metazoans on Earth, and represent a unique global source of highly structured and diverse biosilica that has been formed and tested over more than 800 million years of evolution. Poriferans are recognized as a unique archive of siliceous multiscaled skeletal constructs with superficial micro-ornamentation patterned by biopolymers. In the present study, spicules and skeletal frameworks of selected representatives of sponges in such classes as Demospongiae, Homoscleromorpha, and Hexactinellida were desilicified using 10% HF with the aim of isolating axial filaments, which resemble the shape and size of the original structures. These filaments were unambiguously identified in all specimens under study as F-actin, using the highly specific indicators iFluor™ 594-Phalloidin, iFluor™ 488-Phalloidin, and iFluor™ 350-Phalloidin. The identification of this kind of F-actins, termed for the first time as silactins, as specific pattern drivers in skeletal constructs of sponges opens the way to the fundamental understanding of their skeletogenesis. Examples illustrating the biomimetic potential of sophisticated poriferan biosilica patterned by silactins are presented and discussed.

**Keywords:** biosilica; sponges; actin; spicules; hierarchical biocomposites; biomimetics



**Citation:** Ehrlich, H.; Voronkina, A.; Tabachnik, K.; Kubiak, A.; Ereskovsky, A.; Jesionowski, T. Silactins and Structural Diversity of Biosilica in Sponges. *Biomimetics* **2024**, *9*, 393. <https://doi.org/10.3390/biomimetics9070393>

Academic Editors: Stanislav N. Gorb, Giuseppe Carbone, Peter Fratzl and Thomas Speck

Received: 29 May 2024

Revised: 23 June 2024

Accepted: 24 June 2024

Published: 27 June 2024



**Copyright:** © 2024 by the authors. Licensee MDPI, Basel, Switzerland. This article is an open access article distributed under the terms and conditions of the Creative Commons Attribution (CC BY) license (<https://creativecommons.org/licenses/by/4.0/>).

## 1. Introduction

Biosilica is one of the main globally distributed biominerals, present in a broad diversity of microorganisms, protists, diatoms, sponges, and plants (for overview see [1–5]). Sponges (phylum Porifera), with a more than 800 MYR-long history [6,7], represent an outstanding source of biosilica-based skeletal constructs, found in numerous representatives of such classes as Hexactinellida, Demospongiae, and Homoscleromorpha. The sizes of such biosilica formations in sponges range from several micrometers or millimeters up to 3 m in length [8]. At the same time, the sophisticated ornamentation features of their surface are striking in their structural diversity, especially in the case of spicules (microscleres) and reticulate skeletons with a complex geometry and ordered symmetry (for an overview, see [9–12]). The main functions of biosilicates of a poriferan origin are to create a microporous, mechanically stable skeleton for the optimal distribution of a number of special cells, and an aquiferous system responsible for the flow of water with the accompanying natural feed and oxygen [13]. Some, especially the hook-like microscleres, help retain the organic matrix of the sponge body, while others, with a ray-like morphology (i.e., anchoring spicules), specialize in retaining the entire sponge skeleton in muds and sandy bottoms [14–16]. The inorganic chemistry of such forms of poriferan biosilica is not so

complex as their structural diversity suggests. Most skeletal constructs of silica-producing sponges are made of pure, amorphous silica with inclusions of Na and K [17]; however, in the case of some deep-sea glass sponges, calcitic nanocrystals have also been found within highly specialized spicular formations (for details, see [18]). In contrast, the organic phases reported within sponges' glassy skeletons and spicules have been a hotly debated topic since 1888 [19,20] up to the present day [3,9,16,21–23]. According to the enzymatic view, such highly specialized biomolecules as silicateins, glassins, hexaxilins, and perisilins (for an overview, see [23]) are responsible for biosilicification as well as spicule formation in sponges. Alternatively, the view that the process is based on corresponding activities of such structural biopolymers as chitin, collagen, and actin is also represented in the literature [3,16,21,22,24,25].

Recently, it was shown with strong evidence (using special phalloidin staining, proteomics, immunostaining, inhibition tests, Western Blotting, Fast Fourier Transformation, HRTEM, and Raman spectroscopy) [24] that axial filaments within diverse skeletal constructs in numerous representatives of two sponge classes (Hexactinellida and Demospongiae) are made of F-actin. It is suggested that the epitaxy of uniquely structured biosilica in sponges is due to the presence, growth, and characteristic branching of actin filaments. Being immured in a glass frame, actin exhibits a patterning function in the sophisticated architecture of poriferan biosilica [22]. Similar results have been obtained previously for diatoms. For example, in large-sized species such as *Coscinodiscus granii* and *Cyclotella cryptica*, actin has been shown to control biosilica patterning in the frustule on the meso- and micro-scale [26,27].

As recently reported [22,24], actin has been identified within skeletal formations of 11 and 4 representatives of Hexactinellida and Demospongiae, respectively. However, despite the fact that actin was discovered in skeletons of these sponge species, the presence of various structural and molecular features of actin cannot be ruled out, causing this structural protein to be associated with a specific species or genus. To assign actins found in the biosilica skeletal structures of sponges to a special group and to avoid confusion with actins from other organisms, it is proposed here to call them silactins. A similar approach was taken previously with cathepsins: those identified as being involved in biosilicification in sponges were renamed silicateins (for overview see [28]).

The aim of this study is to identify silactins in the spicules and skeletal networks of selected representatives of freshwater and marine demosponges and in hexactinellids and homoscleromorphs. Hypotheses on the functioning of actin in poriferan biosilica and explanations for the formation of complex bioarchitectures and symmetries in sponges will be proposed and discussed. Also included is a discussion of the biomimetic potential of this kind of ancient biocomposites with their highly specific structural ornamentation.

## 2. Materials and Methods

### 2.1. Sample Origins

Freshwater sponges:

*Ephydatia muelleri* (Lieberkühn, 1856) (Demospongiae, Spongillida, Spongillidae) specimens were collected in the Moscow Channel (Moscow region, Russia) in July 2019.

*Lubomirskia baikalensis* (Pallas, 1776) and *Baikalospongia bacillifera* (Dybowsky, 1880) (Demospongiae, Spongillida, Lubomirskiidae) were collected during an expedition in June 2010 on the southeastern coast of Lake Baikal near the Bolshie Koty settlement (51°54'25" N–105°04'14" E) at a depth of 10–15 m, using SCUBA diving equipment. The apical parts of specimens over 30–40 cm tall were collected and immediately placed in containers with Baikal water and ice for transportation.

*Metania reticulata* (Bowerbank, 1863) (Demospongiae, Spongillida, Metaniidae) samples were collected in the Negro River (Amazon Central Basin region) during the dry season.

*Drulia uruguayensis* (Bonetto and Ezcurra de Drago, 1968) (Demospongiae, Spongillida, Metaniidae) samples were received from the scientific collection of Museu de Ciências Naturais, Fundação Zoobotânica do Rio Grande do Sul, Porto Alegre, RS, Brazil (MCN-POR1152).

*Ochridaspongia rotunda* (Arndt, 1937) (Demospongiae, Spongillida, Malawispongiidae) demosponges were collected from the locality of Velidab in the eastern part of Lake Ohrid (for details see [29]).

#### Marine sponges:

*Suberites domuncula* (Olivi, 1792) (Demospongiae, Suberitida, Suberitidae) sponges were collected from Roscoff region (Brittany, France) at a depth of 9–12 m using SCUBA diving equipment.

*Axinella damicornis* (Esper, 1794) (Demospongiae, Axinellida, Axinellidae) sponges were collected in July 2020, in the Gulf of Lion, Mediterranean Sea, at a depth of 14–18 m using SCUBA diving equipment.

*Petrosia ficiformis* (Poiret, 1789) (Demospongiae, Petrosiidae) sponges were collected in July 2020, in the Gulf of Lion, Mediterranean Sea, at a depth of 5–8 m using SCUBA diving equipment.

*Polymastia arctica* (Merejkowsky, 1878) (Demospongiae, Polymastiida, Polymastiidae) was collected in the White Sea, Onega Bay, 64°57'0–65°10'8 N, 35°29'4–35°51'6 E, 9–22 m, in summer 1877.

*Sphaerothylus borealis* (Swartschewsky, 1906) (Demospongiae, Polymastiida, Polymastiidae) was collected in the White Sea by Dr. A. Plotkin, Norway.

*Tethya norvegica* (Bowerbank, 1872) (Demospongiae, Tethyida, Tethyidae) was collected in coastal waters of northern Norway by Dr. A. Plotkin.

*Geodia cydonium* (Linnaeus, 1767) (Demospongia, Geodiida, Geodiidae) sponges were collected in Marseille, France, Cave Coral, Maire island, 43°12'37.60" N 5°20'24.86" E.

*Erylus granularis* Topsent, 1904 (Demospongia, Geodiida, Geodiidae) Topsent, 1904, UPSZMC 191573 (PC1384), and *Pachymatisma normani* Sollas, 1888 (Demospongia, Geodiida, Geodiidae) Sollas, 1888, UPSZMC 191572 (PC196) were received from the Museum of Evolution, Uppsala, Sweden (UPSZMC)

*Biemna* sp. (Demospongiae, Biemnida, Biemnidae)—dry-preserved freeze-dried sample was received from Western Australian Museum (WAM Z35650).

*Euplectella aspergillum* Owen, 1841 (Hexactinellida, Lyssacinosida, Euplectellidae)—collected in the Philippines, about 150 m depth, purchased from INTIB GmbH, Freiberg, Germany.

*Pheronema nasckaniense* (Tabachnick, 1990) (Hexactinellida, Amphidiscosida, Pheronematidae)—RV Ichthyander 25°46.5' W, 86°28.5' S, 395 v depth.

*Plakortis halichondroides* (Wilson, 1902) (Homoscleromorpha, Homosclerophorida, Plakinidae) specimens were collected in Jamaica in March 2005 from a coralligenous reef at depth of 15 m at Pear Tree Bottom using SCUBA equipment.

*Plakina jamaicensis* (Lehnert and van Soest, 1998) (Homoscleromorpha, Homosclerophorida, Plakinidae) specimens were collected in Jamaica from vertical walls of a coralligenous reef at depth of 28 m at Chalet Caribe, west of Montego using SCUBA equipment.

#### 2.2. Sample Preparation and Phalloidin Staining

The isolation of axial filaments from the investigated sponge spicules was performed using the “sliding drop technique” [24]. Selected spicules were first treated with 70% HNO<sub>3</sub> at room temperature for 72 h for removal of possible organic impurities. Then spicules were rinsed in distilled H<sub>2</sub>O up to pH 6.5, dried in air at room temperature, and placed on Nunc™ Permanox™ (Thermo Fisher Scientific, Rochester, NY, USA) plastic microscope slides (27/75 mm) in small drops of water. After water evaporation, one drop of 10% HF acid was added to each sample; the slide was placed in a Plexiglas Petri dish at an angle of about 10° and closed to prevent HF evaporation. Samples were left for 7–10 h to allow the silica to dissolve. The residual demineralized axial filaments of spicules were then rinsed with water and dried in air.

For larger amounts of demineralized spicules of *E. muelleri* and *S. domuncula*, dialysis through the membrane was used additionally for purification.

For fluorescence staining of demineralized spicules, Cell Navigator™ F-Actin labeling kits (AAT Bioquest, Pleasanton, CA, USA) were used: \*Red Fluorescence\* iFluor™ 594-Phalloidin (Cat#22664), \*Green Fluorescence\* iFluor™ 488-Phalloidin (Cat#22661), and \*Blue Fluorescence\* iFluor™ 350-Phalloidin (Cat#22660). To prepare a working solution, 10 µL of iFluor™ Phalloidin (Component A) was added to 10 mL of Labeling buffer (Component B). To the demineralized spicules fixed on Nunc™ Permax™ (Thermo Fisher Scientific) plastic microscope slides, iFluor™ Phalloidin working solution was added in a quantity of 100 µL per sample. Samples were stained for 60 min at room temperature in the dark. Afterwards the plates were carefully washed five times with distilled water to remove excess dye, dried, and observed using light and fluorescent microscopy. Unused iFluor™ Phalloidin stock solution was stored at −20 °C and protected from light.

### 2.3. Digital Microscopy

Organic-freed spicules of freshwater and marine sponges before and after demineralization were observed using a Keyence VHX-7000 digital optical microscope with the following zoom lenses: VHX E20 (magnification up to 100×) and VHX E100 (magnification up to 500×) (Keyence, Osaka, Japan).

### 2.4. Scanning Electron Microscopy (SEM)

Morphology of the spicules and asters isolated from *G. cydonium* as well as tylostyles of *S. domuncula* were analyzed using scanning electron microscope (XL 30 ESEM, Philips, Eindhoven, The Netherlands). Prior to scanning, the samples were coated with a gold layer using the Cressington Sputtercoater 108 auto, Crawley (GB) (sputtering time 45 s).

### 2.5. Fluorescence Microscopy

Fluorescent microscopy images were obtained using a Keyence BZ-9000 digital optical microscope (Keyence, Osaka, Japan) with the zoom lenses CFI Plan Apo 10× and CFI Plan Apo 40× using DAPI channel (Ex/Em = 360/460 nm) for blue-stained samples, GFP channel (Ex/Em = 470/525) for green-stained samples, TxRed channel (Ex/Em = 560/630) for red-stained samples, and the bright field for comparison and/or overlay.

### 2.6. SDS-PAGE

An amount of 300 µg of demineralized and dialyzed spicules of *E. muelleri* was dissolved in 37.5 µL 0.1 M Tris-HCl (pH 7.1) and 12.5 µL NuPAGE® LDS Sample Buffer (Thermo Fisher Scientific, Carlsbad, CA, USA). The sample was vortexed for 3 h, then placed at −20 °C overnight. The samples were heated at 70 °C for 10 min and then centrifuged (5 min, 10,000× g). After, 40 µL (for coomassie blue staining) and 10 µL (for silver staining) of the samples were electrophoresed in mPAGE™ 4–20% Bis-Tris Precast Gel (Merck, Germany). ROTI®Mark TRICOLOR (Carl Roth, Karlsruhe, Germany) was used as the marker and Actin from rabbit muscle (Sigma-Aldrich, Burlington, MA, USA) as the standard. The gel was run at 200 V and stained with ROTI®Blue Colloidal Coomassie Staining (Carl Roth, Karlsruhe, Germany) and ROTI®Black P Silver Staining kit for proteins (Carl Roth, Karlsruhe, Germany).

## 3. Results

### 3.1. Actin within Spicules of Freshwater Demosponges

Phalloidin is a bicyclic heptapeptide toxin isolated from the mushroom *Amanita phalloides* which, with high specificity, binds stoichiometrically to F-actin [30]. Already recognized as a “gold standard F-actin marker” [31], it is able to prevent the depolymerization of actin due to filament stabilization [32], even in paraffin-embedded or formaldehyde-fixed samples [33,34]. Also, proteins including actin which were isolated from the biosilica of diatoms’ cell walls [26,35] and spicules of sponges [22,24], after demineralization with

HF, have been shown to survive such harsh treatment and can be stained with diverse phalloidins. The preservation of the stability of actins of various origins after treatment with HF has been experimentally proven (for details, see [24]). To confirm the selectivity of phalloidins for actin identification after the HF treatment of poriferan biosilica, such recognized bioanalytical methods as immunostaining, Western blotting techniques, and Raman spectroscopy have been alternatively and successfully used [24]. Thus, the reliability of using phalloidins to identify actin is beyond doubt [36]. Consequently, in this study, we used three different phalloidin markers to confirm the presence of F-actin-based filaments within spicules of selected representatives of both freshwater and marine demosponges, as well as within hierarchically structured skeletal (dictyonal) frameworks of glass sponges.

The aforementioned freshwater sponges belong to eight families of the class Demospongiae (subclass Heteroscleromorpha, order Spongillida,) and include approximately 250 species [37]. For our investigation, we selected seven species from four different families, some of which, like Spongillidae, are cosmopolitan, while others such as Malawispongiidae and Lubomirskiidae are endemic to ancient lakes (Figure S1).

The demineralization of organic-freed spicules, called oxeas, isolated from the worldwide-distributed *Ephydatia muelleri* freshwater demosponge (Figure 1) as a typical representative of the Spongillidae family using both the “sliding drop technique” [22,24] and in bulk treatment with 10% HF, led to the obtaining of corresponding axial filaments (see Figures 2 and 3, respectively). These fibrillar structures were identified as F-actin filaments using characteristic phalloidin staining (Figures 2b,d,f and 3b). Moreover, the presence of actin together with silicateins within these formations was confirmed using SDS-PAGE (Figure 3c). Previously, only silicateins have been recognized as the main proteins localized in axial filaments of demosponges and being responsible for biosilicification (for a modern overview, see [23]). The data obtained are in good accordance with those reported for axial filaments of *Spongilla lacustris*, another broadly distributed representative of freshwater demosponges, where both proteins have also been identified using SDS-PAGE [24].



**Figure 1.** Digital microscopy imagery of *Ephydatia muelleri* freshwater demosponge oxeas with symmetrical tips after removal of organic material using  $\text{HNO}_3$  treatment. Desilicification of such spicules with HF led to isolation of organic axial filaments, which were identified as F-actin (see Figure 2).

For comparative purposes, with the aim of identifying F-actin, we also investigated axial filaments isolated from spicules of such freshwater Amazonian demosponges as *Metania reticulata* and *Drulia uruguayensis* (both of the Metaniidae family), two sponges of the Lubomirskiidae family (*L. baikalensis* and *B. bacilifera*), and the endemic *Ochridaspongia rotunda* (Malawispongiidae) demosponge inhabiting Ohrid lake in North Macedonia and Albania. The results are presented, respectively, in Figures 4, 5 and S2–S9.



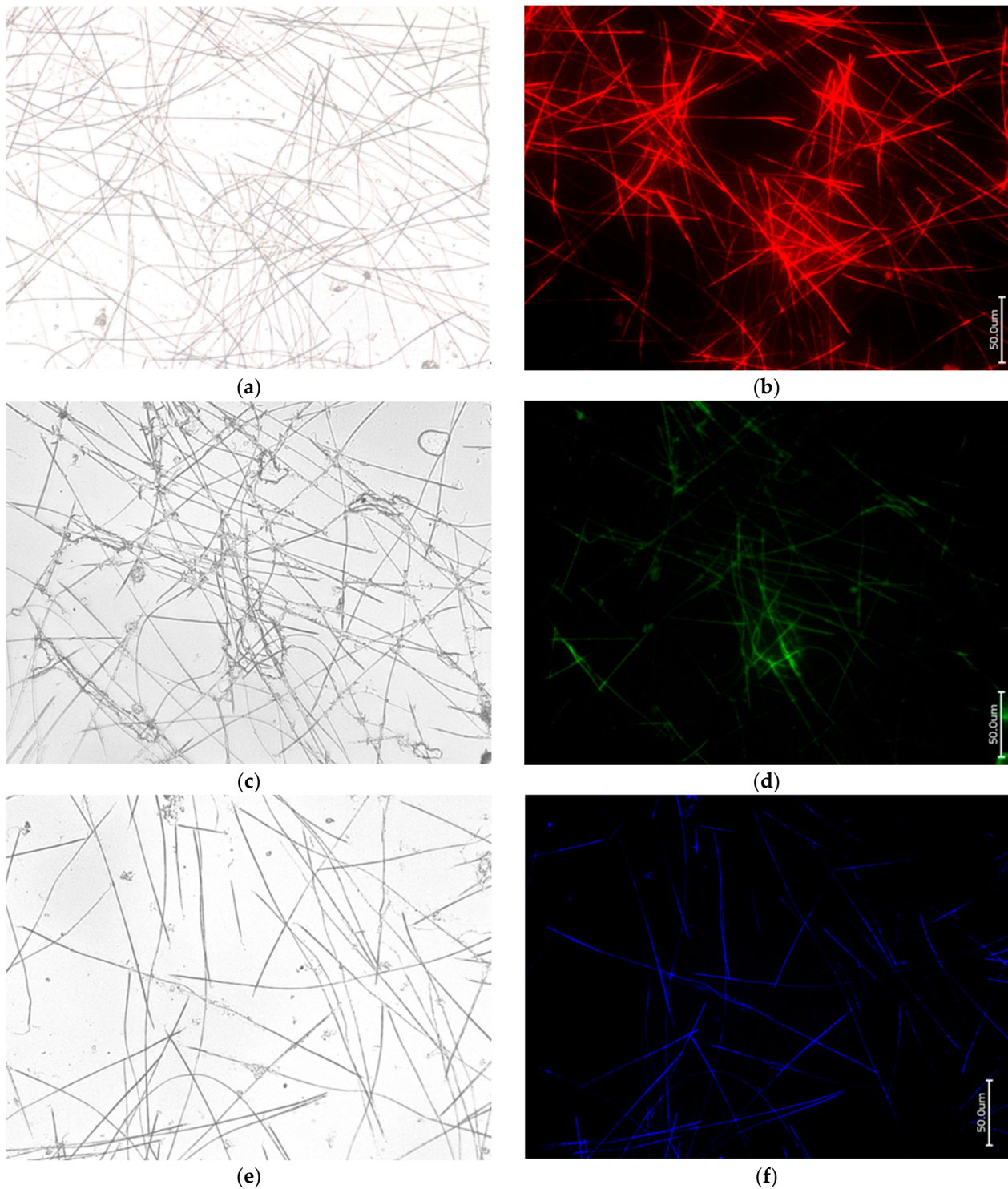


**Figure 2.** Bright field (a,c,e) and fluorescence microscopy imagery of the axial filaments obtained after demineralization of oxas of *E. muelleri* freshwater demosponge using HF under the conditions of the “sliding drop technique” [24] and stained with 594-Phalloidin (b); also with 488-Phalloidin (d) and 350-Phalloidin (f) for comparison.

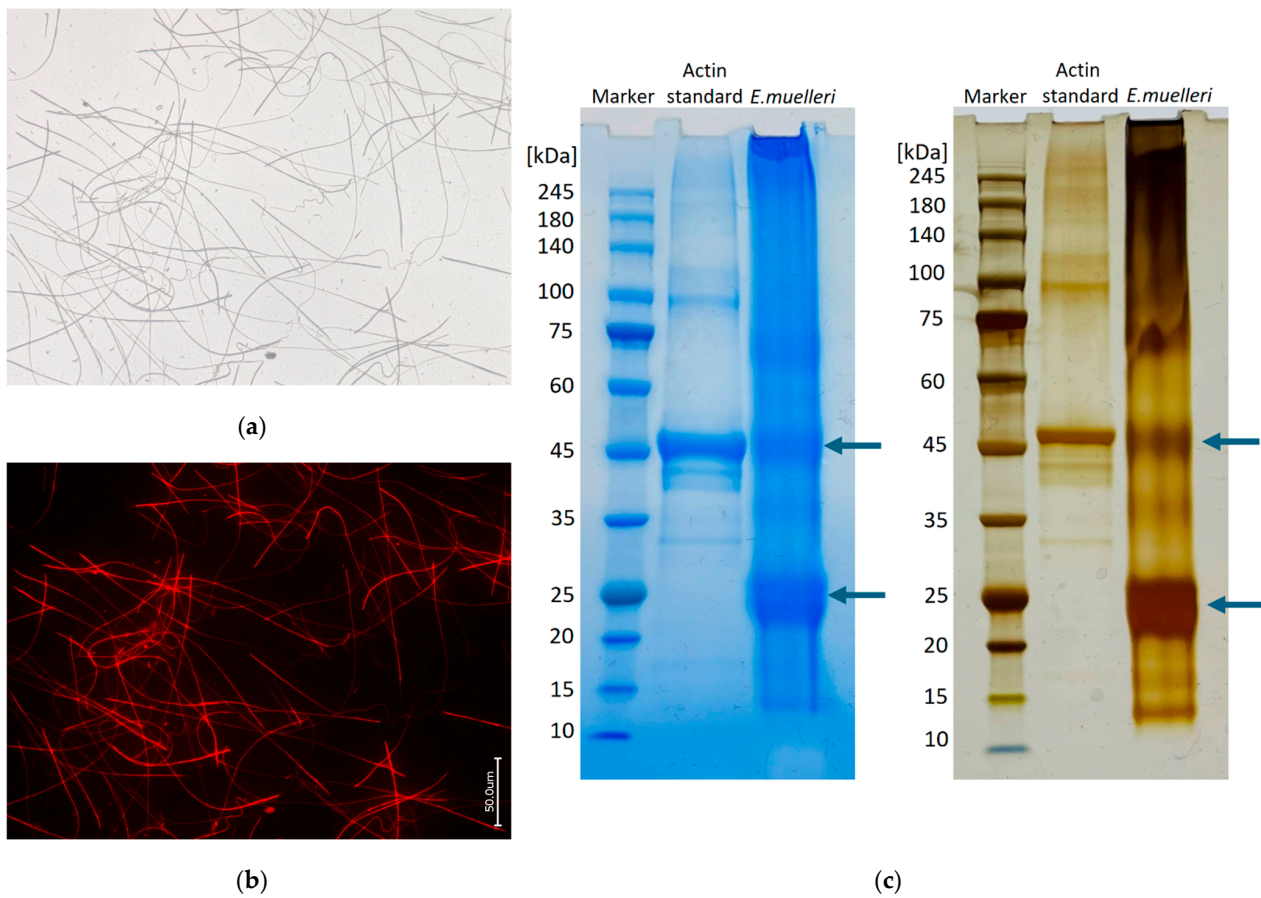


**Figure 3.** Bright field (a) and fluorescence microscopy (b) imagery of the axial filaments of *E. muelleri* demersal sponge oxeas isolated in bulk after HF treatment, dialyzed, and finally stained with 594-Phalloidin. (c) SDS-PAGE: arrows indicating the actin (45 kDa) and silicatein (25 kDa) bands well visible after both Coomassie blue (left gel) and silver reagent (right gel) staining of the axial filaments sample of *E. muelleri* under study.

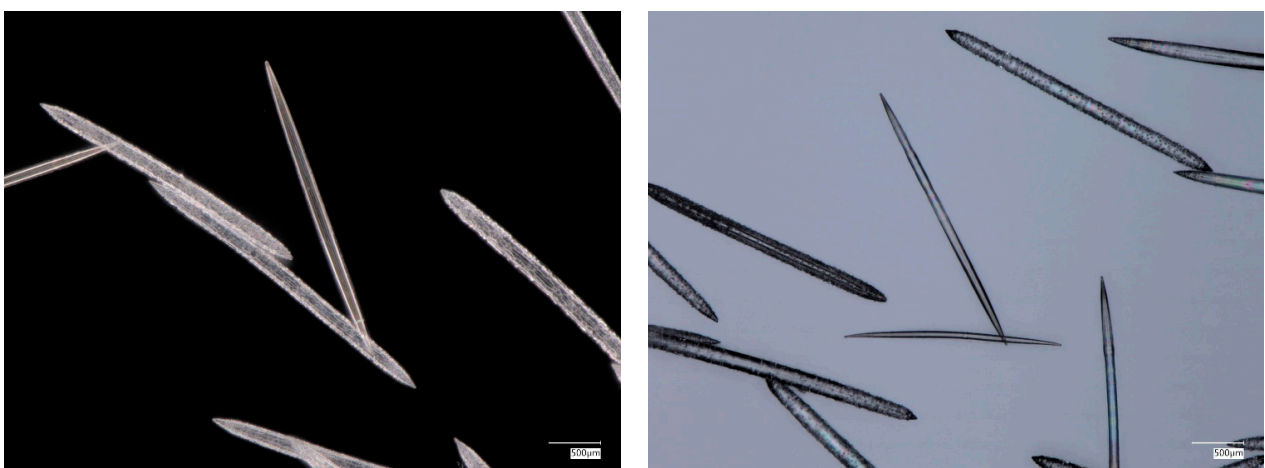


**Figure 4.** Digital microscopy images of organic-free acantoxeas and oxeas isolated from the endemic *O. rotunda* freshwater demersal sponge. Demineralization of such spicules with HF led to isolation of organic axial filaments, which were identified using such diverse phalloidin indicators as F-actin (see Figure 5).



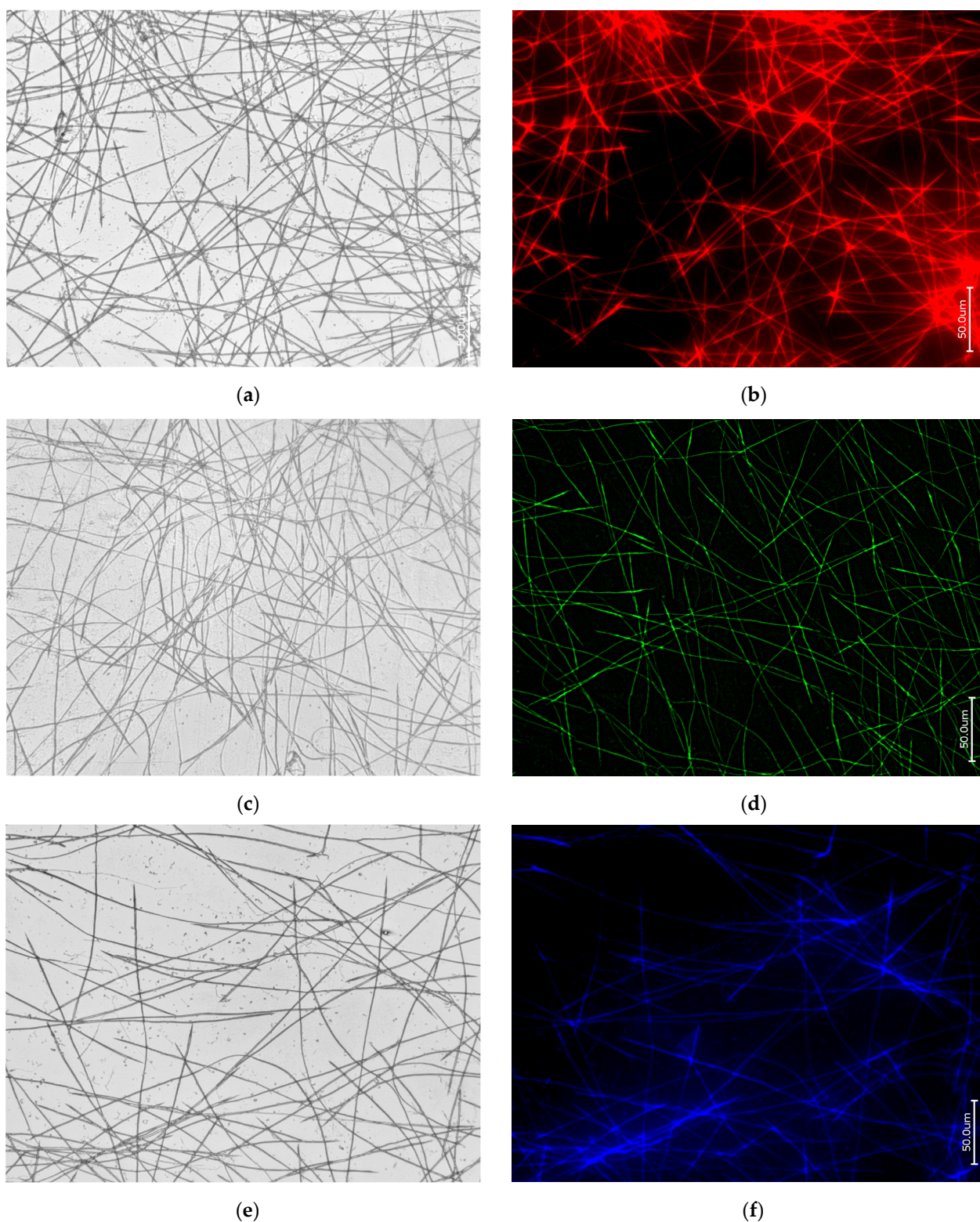


**Figure 5.** Bright field (a,c,e) and fluorescence microscopy imagery of the axial filaments obtained after demineralization of acantoxeas and oxeas of the *O. rotunda* freshwater demosponge with HF under the conditions of the “sliding drop technique” [24] and stained for comparative purposes with 594-Phalloidin (b), 488-Phalloidin (d), and 350-Phalloidin (f).

Thus, all representatives of the freshwater demossponges considered in this study, which belong to diverse families and inhabit different and distant geographical regions,



produce spicules with axial filaments which certainly contain F-actin. This does not exclude the presence of other proteins that are associated with actin or are simply present in the axial channels of spicules in order to perform their special functions, for example, to participate in biosilicification.

### 3.2. Actin within Spicules of Marine Demosponges

Among 30 orders of Heteroscleromorph marine demosponges [38], we selected representatives of seven families from seven orders for our study. The results are presented in Figures 6–8 and S10–S14.

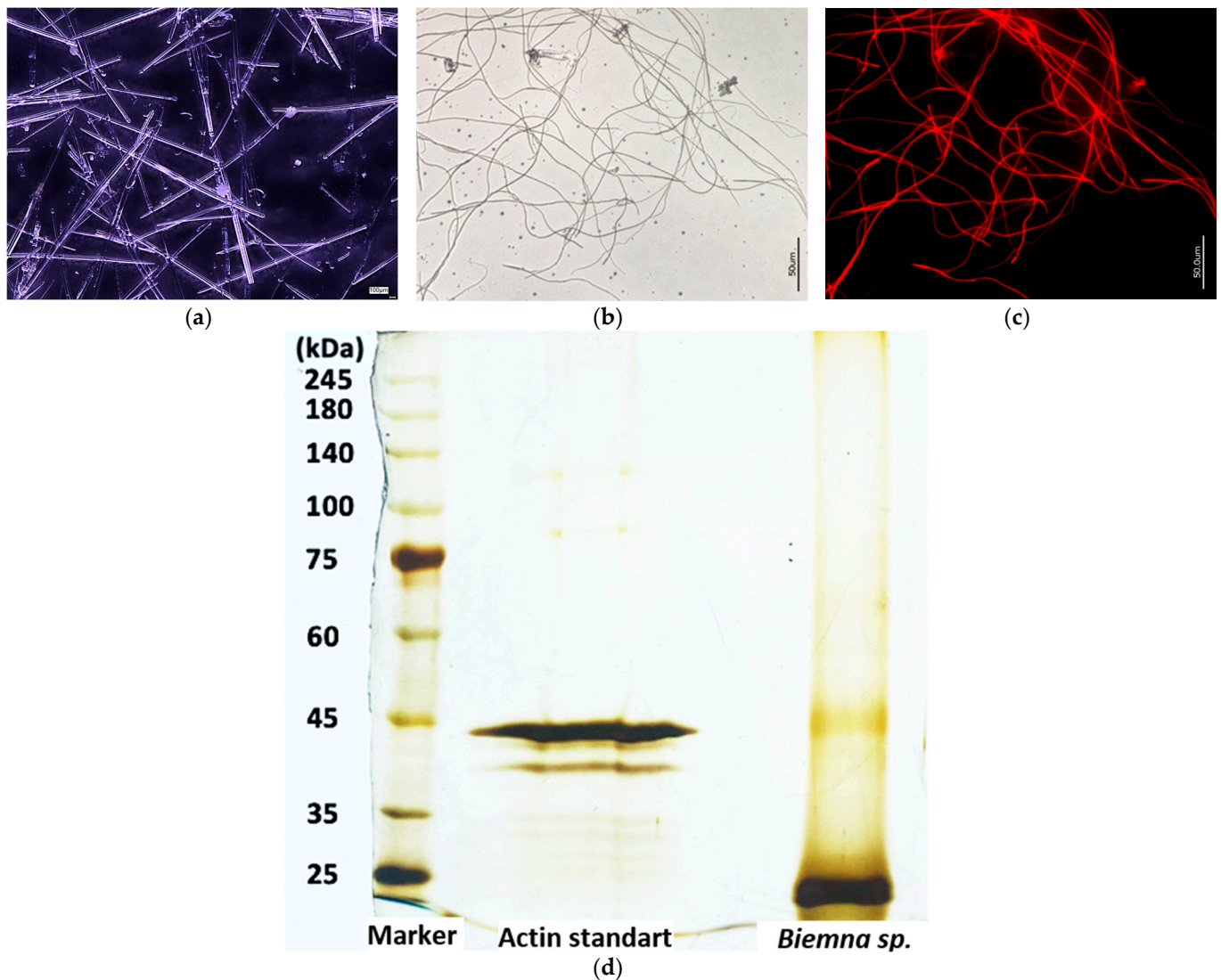


**Figure 6.** Bright field images of *Biemna* sp. marine demosponge spicules (a) and their axial filaments isolated in bulk after HF treatment (b). Fluorescence microscopy image (c) of dialyzed axial filaments stained with 594-Phalloidin showing the red color characteristic for phalloidin labeled F-actin. (d) SDS-PAGE: bands indicating the presence of both actin (45 kDa) and silicateins (25 kDa) in axial filaments extracted after HF-based desilicification of *Biemna* sp. remain well visible after silver reagent staining in two selected samples. For comparison, see Figure 3c.

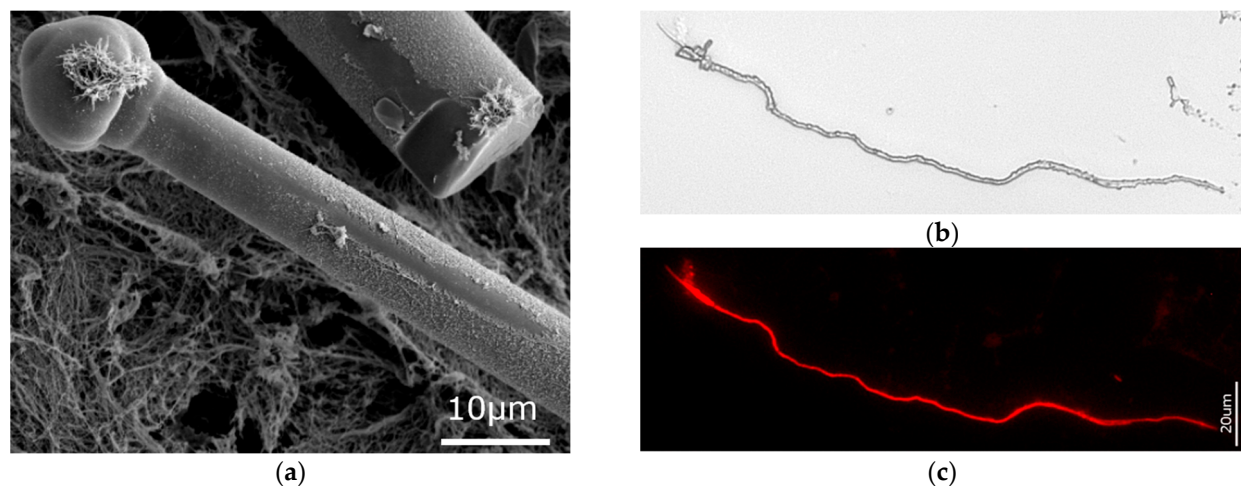


**Figure 7.** HF-based desilicification of the *S. domuncula* marine demosponge tylostyle (a) led to isolation of the axial filaments (b), which were identified as F-actin using 594-Phalloidin staining (fluorescence microscopy image (c)). F-actin branching of the axial filament fragment within the “club-like” structure is well visible. See also Figure S10.

Thus, axial filaments isolated from spicules of the marine demosponge *Biemna* sp. are also made of both actin and silicateins (Figure 6). The SDS-PAGE data obtained are similar to those presented above for the freshwater sponge *E. muelleri* (see Figure 3c).

Another focus of this research was the marine demosponge *Suberites domuncula*, which for many years served as a model organism for the study of silicateins. The discovery of these biosilica-related proteins has been repeatedly reported in the literature (for an overview, see [28,39,40]), but the existence of actin inside the spicules of this sponge as well as the potential involvement of actin was not appreciated or not observed by previous researchers. Figure 7 presents with strong evidence the actin-based nature of the axial filament isolated from this sponge species using the techniques described above. Even the branching—typical for F-actin [41]—of the axial filament fragment originally located within the spicule “club” became visible after corresponding staining with 594-phalloidin. It is suggested here that this kind of branching is responsible for the patterning of the biosilica with respect to the formation of the “club-like” structure.

Similar results (Figure 8) concerning the identification of such axial filaments of spicules as F-actin-based filaments have also been obtained in the case of such strongly psychrophilic Arctic marine demospoenges as *Polymastia arctica* (Polymastiidae), *Sphaerothylus borealis* (Polymastiidae), and *Tethya norvegica* (Tethyidae). Analogously to freshwater demospoenges, marine species contain F-actin in their spicules, regardless of their geographical habitat and the specific temperature regime of the corresponding marine environment.

In contrast to the simple structured spicules of the demospoenges described above, marine sponges belonging to the family Geodiidae can present even up to four types of mm-sized large spicules known as megascleres in combination with small µm-sized spicules (microscleres) [42]. Traditionally, the ball-shaped sterrasters with sizes of 30–560 µm, with their sophisticated surface micro-ornamentations (Figure 9), are the most striking, and thus researchers have been motivated to investigate the peculiarities of their structural organization. Despite the lack of experimental evidence for the presence of silicateins in these sterrasters, these proteins have previously been proposed as the only organic template [21].

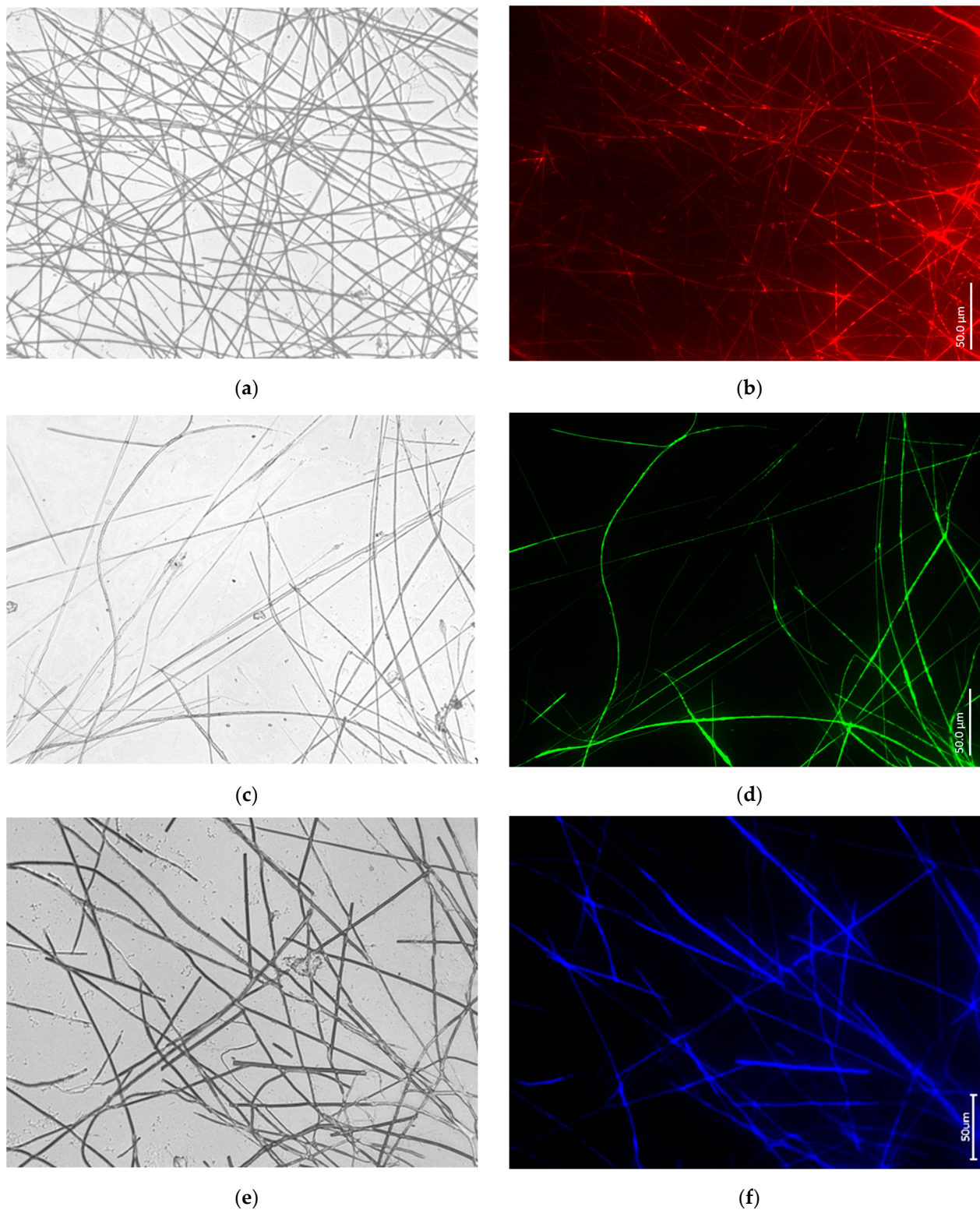


**Figure 8.** Bright field images of axial filaments isolated from spicules of marine demosponges *P. arctica* (a), *S. borealis* (c), and *T. norvegica* (e) using HF-based treatment as presented above (see Figure 5). Right: fluorescence microscopy images of respective species' axial filaments stained with 594-Phalloidin (b), 488-Phalloidin (d), and 350-Phalloidin (f).



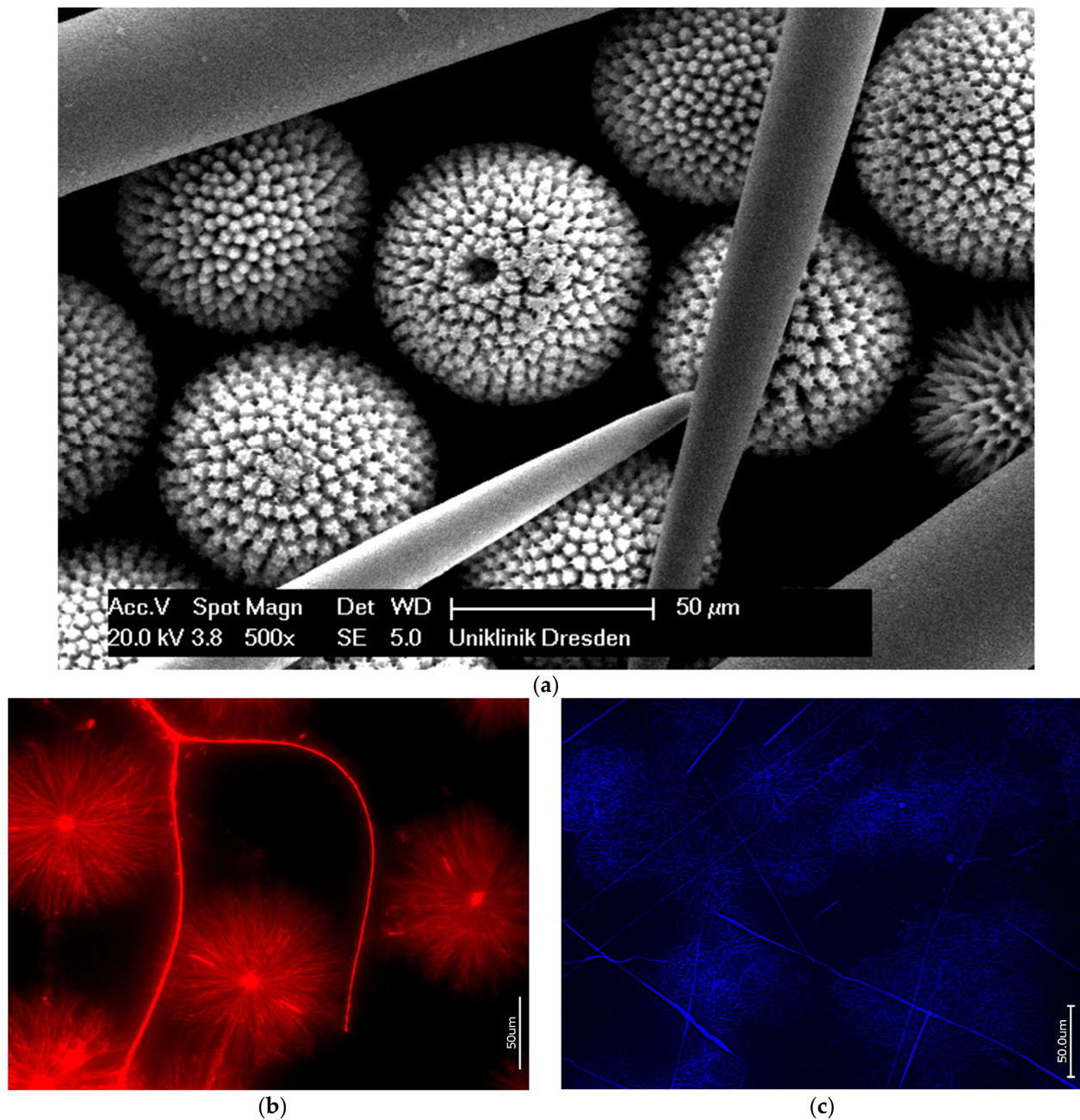


**Figure 9.** Polybranched microarchitecture of *Geodia cydonium* marine demosponge spicules are well visible, especially in SEM image (a). Both types of spicules, radially oriented sterrasters as well as linear megascleres after demineralization using HF, show the presence of correspondingly structured axial filaments, which have been identified as F-actin-based filaments through specific staining with 594-Phalloidin for *Erylus granularis* (Geodiidae) (b) and 350-Phalloidin for *G. cydonium* (c).

However, the results of our study on the desilicification of sterrasters and megascleres from the *Geodia cydonium*, *Erylus granularis*, and *Pachimatisma normani* demossponges, as typical representatives of the Geodiidae family, demonstrate that the organic phase within them belongs to F-actin (Figure 9b,c). These data echo previously reported findings concerning the presence of actin in *Geodia biosilica* [24]. The fact of the existence of this kind of radially oriented actin filaments is beyond doubt, and they will be discussed in detail below (see Section 4: Discussion).

### 3.3. Actin in the Skeleton of Glass Sponges

The basic triaxonic (six-rayed) symmetry of the skeletal formations found in a diverse range of more than 600 species of glass sponges (Hexactinellida) is one of the characteristic structural features [43,44]. It is well recognized that these sponges produce microporous biosilica-based 3D hierarchical constructs with highly sophisticated network-like geometries [3,15,45]; however, the identity of the biopolymer that may be responsible for the patterning of such structures is still under investigation [23].

Figure 11 presents the results of HF-based desilicification, using the “sliding drop technique” [24], of selected fragments isolated from the *Euplectella aspergillum* glass sponge. For demineralization, fragments of the square architecture were precisely selected and cut out from the glass skeleton with a scalpel. This architecture remained visible after demineralization (see Figure 11b,d,f). The corresponding square-formed elements were clearly stained with diverse phalloidins (Figure 11c,e,g), confirming the presence of F-actin.

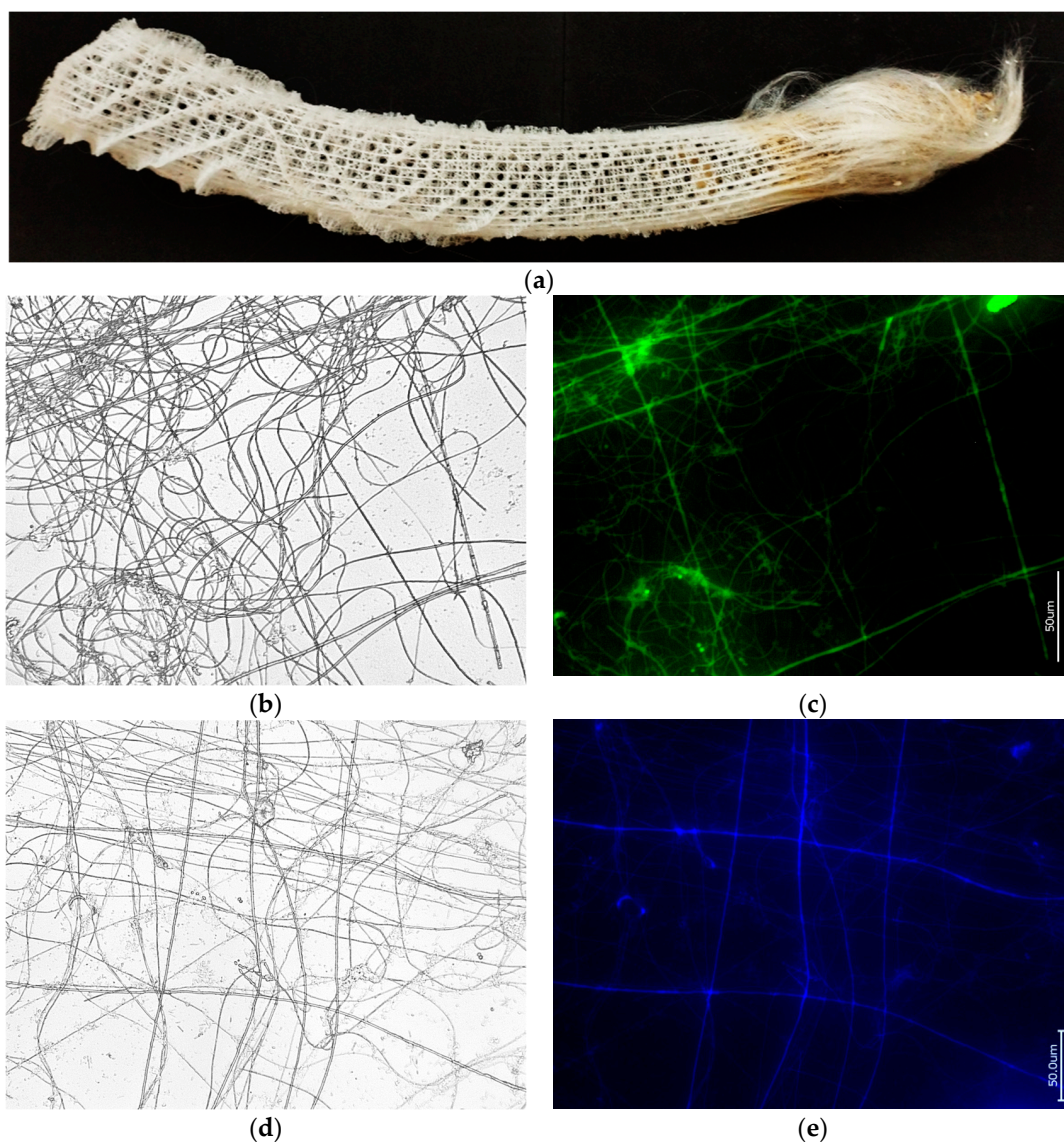
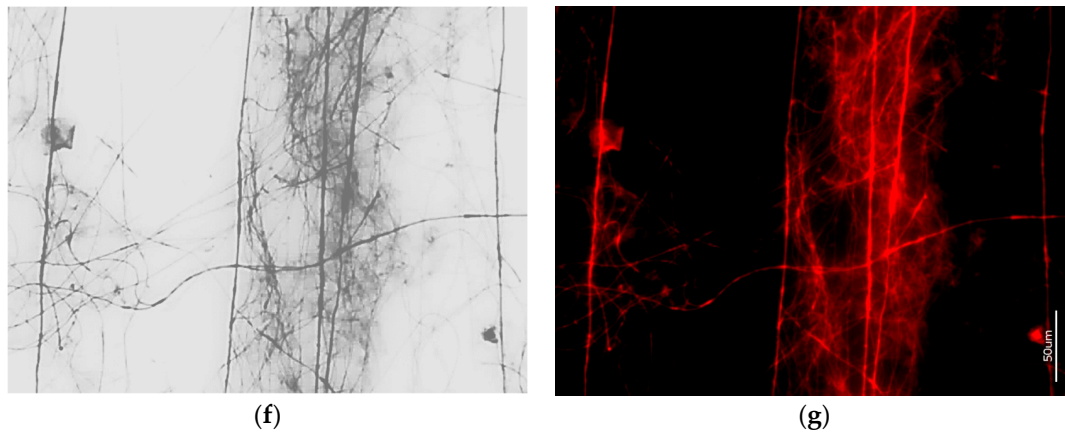


Figure 10. Cont.





**Figure 11.** Cell-free 18 cm-long skeleton of *E. aspergillum* glass sponge (a) used in the study. Bright field (b,d,f) images of selected skeletal fragments demineralized with HF, with characteristic square geometry of organic filaments. These filaments are identified as F-actin structures using fluorescence microscopy after staining with 488-Phalloidin (c), 350-Phalloidin (e), and 594-Phalloidin (g), corresponding to the bright field images.

At first glance, the discovery of this kind of square architecture of actin filaments in the skeleton of the glass sponge under study seems unexpected. However, actin structures of this type have been described previously, for example, in the endothelial actin cytoskeleton in mouse retinas [46] (Figure 12). The results obtained in our work confirm previously published data on the identification of actin filaments in various hexactinellid species [22,24], but differ from those recently published for the *Euplectella curvostellata* and *Vazella pourtalesii* glass sponges [23]. We do not exclude that the difference in the results obtained is due to different methods for isolating the corresponding proteins.

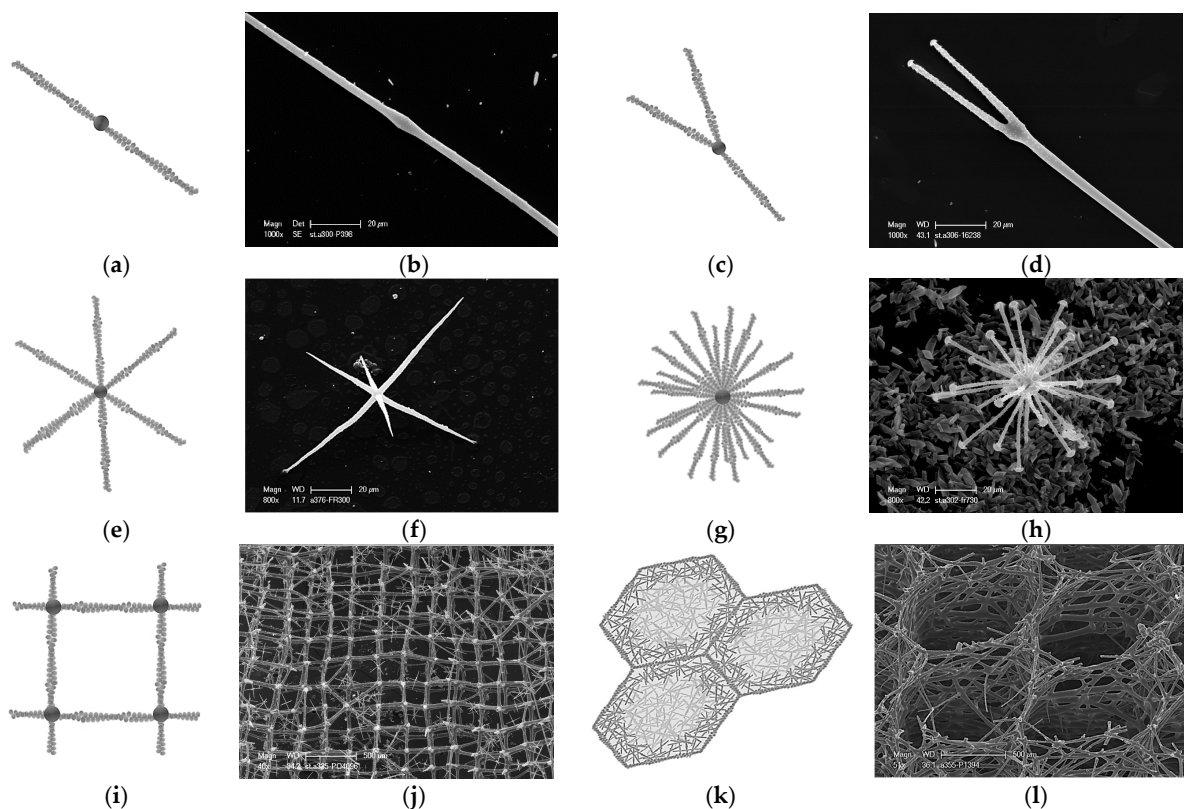


**Figure 12.** Schematic view of F-actin growth models previously described in the literature vs. siliceous structures observed in Hexactinellida sponges: (a) branching of bovine actin [41]; (b) uncinat spicule

of Tretodictyidae sponge; (c) cortical axon branching [47]; (d) discoscopule spicule (Hexactinellida, Tretodictyidae); (e) actin branching in lamellipodia of *Xenopus laevis* keratocytes [48]; (f) oxyhexactin spicule (Hexactinellida, Euretidae); (g) astrocytes actin branching in rat nervous system [49]; (h) discohexaster spicule (Hexactinellida, Tretodictyidae); (i) endothelial actine cytoskeleton in mouse retina [46]; (j) farreoid skeleton (Hexactinellida, Farreidae, *Farrea* sp.); (k) honeycomb actin structures in mouse lenses [50] and within diatom frustule [26]; (l) honeycomb skeleton of Aphrocallistidae glass sponge *Aphrocallistes* sp. (see also [22]).

As in the SDS-PAGE analysis of the axial filaments of a hexactinellid origin [16,24], in the case of the studied *E. aspergillum* glass sponge, no silicateins were found.

#### 4. Discussion

It has recently been shown [22,24,25] that actin as a unique pattern driver leads to the occurrence of superficial ornamentation and specific network connectivity (monaxons, triaxons, and tetraxons) in certain sponge species, which represent more than 46 and 80 morphotypes in Hexactinellida and Demospongiae, respectively. The experimental data presented here strongly confirm that F-actin is the main biosilica patterning biopolymer in a diverse range of simple structured spicules in freshwater and marine demosponges (Figures 1–8 and S2–S14) and in hierarchically structured skeletal networks of glass sponges (Figures 11 and S15) and spicules of Homoscleromorphs (Figures S16 and S17). The following are the arguments supporting this conclusion.

- (a) Genomic data. There is no evidence of silicatein genes, but those for glassin, as well as collagens and actins, have been reported in the genome of the reef-building psychrophilic glass sponge *Aphrocallistes vastus* (order Sceptrulophora) [51]. Also, in the genome of the Mediterranean *Oopsacas minuta* (order Lyssacinosida) glass sponge, there is no evidence of silicatein, silintaphin, or galectin genes, but actin and glassin genes have been recently reported [52].
- (b) Data on inhibition of actin polymerization. It is well recognized that latrunculin B binds to actin monomers and inhibits F-actin polymerization [53]. In recent experiments involving the cultivation of the *Spongilla lacustris* freshwater demosponge from its gemmules, it was shown with strong evidence that actin inhibition by latrunculin B prevents spicule formation [24]. In the samples of hatched gemmules, in the presence of latrunculin B, siliceous spicules never appeared; however, the young sponges grew. To our best knowledge, there are no data on the inhibitory effects of latrunculins against the biosynthesis or self-assembly of silicateins. Consequently, the occurrence of silicateins within sclerocytes of demosponges did not lead to the formation of spicules, but the absence of actin had a decisive impact on spiculogenesis. Put simply, the implication is no actin, no spicules!
- (c) Data on structural features characteristic only of actin. Such phenomena known from structural biology as bifurcation, dichotomic growth, and branching represent characteristic features only of actin [48,54]. They are also responsible for the formation of a broad range of higher-order 3D suprafilamentous structures of F-actin: bundles, aggregates, branched, cross-linked, and dendritic filamentous constructs [55–57] (see Figure 11). It should be noted that the micrometer size and the quantity of actin filaments that have been isolated from the skeletal formations of diverse demosponges (see Figure 9 as an example) and hexactinellids (see the corresponding images in [22,24]) are not surprising. For example, up to 500 actin filaments have been found in the actin bundles in bristle sprouts of *Drosophila* fruit flies [58]. Also, in the same organism, the bristle cell extension is supported by up to 400  $\mu\text{m}$ -long F-actin bundles assembled together [59,60]. The unique surface ornamentation and sophisticated microarchitecture of some star-like microscleres in demosponges (i.e., sterrasters of *Geodia* sponges) [11,21,24] may seem somewhat extraordinary, and the possible participation of radially oriented actin in this kind of spiculogenesis seems doubtful in principle. However, such a radial structural

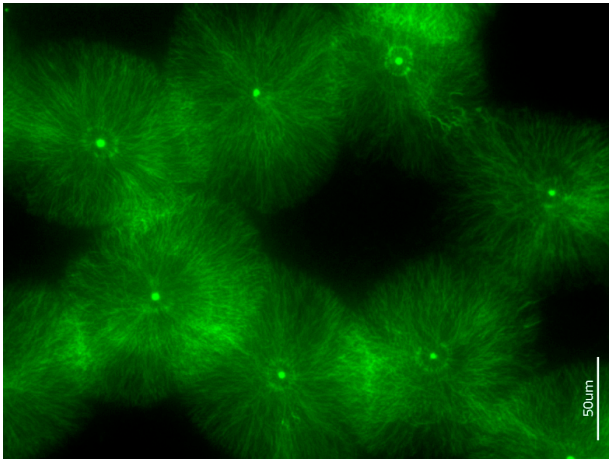
orientation has already been reported for intracellular actins in *Drosophila* S2 and in *Xenopus* XTC cells [61], as well as in filopodia [62] or lamellipodia of motile cells [63], in flagella [64], and in diverse neurons [65–67]. Regarding biosilica-producing organisms, the occurrence of radially oriented actin filaments has been reported within the frustules of such diatoms as *Coscinodiscus granii* and *Cyclotella cryptica* [26,27]. A fundamental remark should be made here: none of the above-mentioned proteins involved in biosilicification in sponges (i.e., silicateins, glassins, etc.) or in diatoms (i.e., silaffins, silacidins, etc.) possess structural features similar to those of actin.

A possible mechanism behind actin-driven pattern formation in poriferan biosilification has already been proposed as follows: “The sponge spicule is initially formed in the silicoblast in the form of a silica-free ‘proteic rodlet’, which is produced in a great vacuoles. This axial rodlet was electron-dense and of fibrillary nature, with spiral fibres 70–100 Å in diameter. The axial filament of F-actin does not mineralize itself but rather provides the base for the mineralization around it. Moreover, while the distal tip of the spicule is open F-actin can elongate, thus driving growth of the spicule. This may continue until the closure of the end of the spicule by mineralization, which stops spicule growth” [24]. If this is the case, the intriguing question of the influence of diverse ecological factors, including contamination with metals, on actin polymerization and spicule formation needs to be addressed. Recently, the number of structural anomalies of spicule-like T-shaped, bulbous enlargements, sharply bent, scissor- and cross-like, and bifurcated formations have been studied in *Eunapius fragilis* freshwater demosponges collected at Markovac (Velika Morava river) in Serbia in relation to water quality [68]. The identification of silactins within such spicule malformations may open the door to a better understanding of the principles of biosilica patterning by these actins under changing environmental conditions.

Our identification of F-actin-based axial filaments within spicules of *Plakortis halichondrioides* and *Plakina jamaicensis* (Figures S16 and S17), as typical representatives of more than 130 species [69] which belong to the class Homoscleromorpha [70], is also important. Despite advances in the molecular systematics and evolutionary biology of homoscleromorphs [71,72], the nature and origin of the organic phase within their mostly tetractinal spicules (calthrops) remain unknown. We are hopeful that our results will motivate homoscleromorph researchers to attempt to confirm the structural role of silactins in this class of biosilica-producing sponges as well.

An analysis of the literature regarding the role of actin in the biosilicification of various organisms reveals the existence of only six relevant publications. Moreover, only two of them are related to sponges [22,24]; the other four concern unicellular biosilicifying organisms. For example, in these studies, the central role of actin in regulating silica morphogenesis in the diatoms *Rhizosolenia setigera* [73] and *Coscinodiscus granii* [26] as well as in biosilica-producing haptophytes *Prymnesium neolepis* [74] was experimentally confirmed and described. It is hoped that actin will now become a focus of research, and that the sponge-derived silactins will receive particular attention. There are numerous open questions regarding the mechanisms of silactin patterning in diverse poriferan siliceous structures (Figure 12), and there are also plans to carry out in vitro experiments with actin molecules and filaments in the presence of silica sources to create artificial silica-based constructs with and without the addition of silicateins or other recognized substances [23] described previously as biosilicificators (Figure 13). Such studies remain challenging, but crucial for both structural and functional biomimetics. Without a doubt, the modern design strategies of a new generation of engineering materials related to poriferan multiscale hierarchical structures remain a significant trend (Table 1). It is well recognized that they are based on unifying naturally occurring design strategies in sustainable skeletal systems of demosponges, homoscleromorphs, and hexactinellids [45].





(a)

**Hexactinellida:** Silactins + Glassin, Hexaxilins, Perisilins

**Demospongiae:** Silactins + Silicateins

**Homoscleromorpha:** Silactins + ?

**Figure 13.** State-of-the-art overview on silactins’ distribution within skeletal structures of three poriferan classes. (a) Unique radial orientation of silactin microfilaments of *Pachymatisma normani* (Geodiidae) marine demosponge became well visible after HF-based desilicification of corresponding sterrasters and following staining with 488-phalloidin marker.

**Table 1.** Biomimetic potential of sophisticated poriferan biosilica.

Biomimetic Directions	References
Mimicking biosintering	[75]
Bioinspired selective laser melting	[76]
Bio-based generative honeycomb design	[22]
Multifunctional design	[77,78]
Bioinspired architecture:	[79,80]
next generation of high-performance buildings, skyscrapers, and bridges	
Biomimetics of lightweight structural biomaterials	[15,81–84]
Deep-sea sponge-inspired tubular metamaterials	[85]
Crashworthiness design of a sponge-inspired multicell tube	[86]
Architected ceramic fibers and damage evolution	[87,88]
Computational modeling of spicule-inspired nested structures	[89,90]
Artificial intelligence-enhanced bioinspiration	[91]
Analytic modeling, finite element modeling, and experimental validation	[92]
3D printing of sponge spicule-inspired flexible bioceramic-based scaffolds	[93,94]
Bioinspired stereolithography	[95]
Bioinspired models for tissue engineering scaffolding	[96]

5. Conclusions

The results of the experimental studies on the detection of actin filaments in biosilica-based formations of sponges representing three poriferan classes clearly show their involvement in spiculogenesis, regardless of the complexity of the glassy bioarchitecture. It was shown that the axial filaments within the spicules of five freshwater and ten marine demosponges contain F-actin as well as silicateins, but only F-actin was identified as a patterning driver of hierarchically structured biosilica in hexactinellids using the example of the *Euplectella aspergillum* glass sponge. For the first time, F-actin has been visualized using highly sensitive phalloidin markers in spicules of Homoscleromorpha, a still poorly investigated class of sponges. To avoid possible confusion and to draw attention to F-actins related to biosilica, it is proposed to call them silactins. The further study of silactins in the skeletal structures of modern as well as fossil sponges—representing the first multicellular organisms on the planet, with a long evolutionary history of more than 800 million years—appears to be an extremely relevant and promising direction of modern bioinspired material science and biomimetics.

**Supplementary Materials:** The following supporting information may be downloaded at <https://www.mdpi.com/article/10.3390/biomimetics9070393/s1>. Figure S1: Demosponge species selected for this study within the schematic tree of the systematic selection of freshwater sponges. Figure S2: Digital microscopy of *Drulia uruguayensis* (Metaniidae) freshwater demosponge fusiform oxeas after organic material removing using HNO<sub>3</sub>. Figure S3: Bright field (a,c) and fluorescence microscopy images of the axial filaments isolated from 10% HF-demineralized oxeas of *Drulia uruguayensis* (Metaniidae), which have been stained with 594-Phalloidin (b) and with 488-Phalloidin (d). Figure S4: Digital microscopy images of *Metania reticulata* (Metaniidae) freshwater demosponge strongly oxeas and birotulate gemmoscleres after organic material removing using HNO<sub>3</sub>. Figure S5: Bright field (a,c) and fluorescence microscopy images of the axial filaments isolated from 10% HF-demineralized spicules of *Metania reticulata* (Metaniidae) freshwater demosponge, which was stained with 594-Phalloidin (b) and with 350-Phalloidin (d). Figure S6: Digital microscopy of *Baikalospongia bacilifera* (Lubomirskiidae) freshwater demosponge monaxon megascleres (tilotes) with spiny tips after organic material removing using HNO<sub>3</sub>. Figure S7: Fluorescence microscopy imagery of the axial filaments isolated from 10% HF-demineralized spicules of *Baikalospongia bacilifera* (Lubomirskiidae) freshwater demosponge: (b) 594-Phalloidin stained; (d) 488-Phalloidin stained (f) 350-Phalloidin stained; (a,c,e)—bright field images for comparison. Figure S8: Digital microscopy images of *Lubomirskia baikalensis* (Lubomirskiidae) freshwater demosponge spiny megascleres (acanthoxeas) after organic material removing using HNO<sub>3</sub>. Figure S9: Fluorescence microscopy imagery of the axial filaments isolated from with 10% HF-demineralized spicules of *Lubomirskia baikalensis* (Lubomirskiidae) freshwater demosponge: (b) 594-Phalloidin stained; (d) 488-Phalloidin stained (f) 350-Phalloidin stained; (a,c,e)—bright field images for comparison. Figure S10: Fluorescence microscopy imagery of the axial filaments isolated from with 10% HF-demineralized spicules of *Suberites domuncula* (Suberitidae) marine demosponge: (b) 594-Phalloidin stained; (d) 488-Phalloidin stained; (a,c)—bright field images for comparison. Figure S11: Fluorescence microscopy image (b) of the axial filaments isolated from with 10% HF-demineralized spicules of *Axinella damicornis* (Axinellidae) marine demosponge after staining with 594-Phalloidin. (a)—bright field image for comparison. Figure S12: Fluorescence microscopy image (b) of the axial filaments isolated from with 10% HF-demineralized spicules of *Petrosia ficiformis* (Petrosiidae) marine demosponge after staining with 488-Phalloidin. (a)—bright field image for comparison. Figure S13: Fluorescence microscopy image (b) of the axial filaments isolated from with 10% HF-demineralized spicules of *Sphaerotylus borealis* (Polymastiidae) marine demosponge after staining with 594-Phalloidin. (a)—bright field image for comparison. Figure S14: Fluorescence microscopy imagery of the axial filaments isolated from with 10% HF-demineralized spicules of *Tethya norvegica* (Tethyidae) marine demosponge after staining with 594-Phalloidin (b) and 488-Phalloidin (d). (a)—bright field images for comparison. Figure S15: Fluorescence microscopy images of the axial filaments isolated from with 10% HF-demineralized spicules of *Pheronema* glass sponges (a) and stained with 488-Phalloidin (b) and 594-Phalloidin (c). Figure S16: Fluorescence microscopy imagery of the axial filaments isolated with 10% HF-demineralized spicules of Homoscleromorph sponge *Plakina jamaicensis* (Plakinidae) stained with (b) 594-Phalloidin and (d) with 350-Phalloidin. (a)—bright field image of the axial filaments for comparison. Figure S17: Fluorescence microscopy image (b) of the axial filament isolated from with 10% HF-partially demineralized spicules of Homoscleromorph sponge *Plakortis halichondroides* stained with 594-Phalloidin. (a) Image in bright field for comparison.

**Author Contributions:** Conceptualization, H.E. and K.T.; methodology, K.T.; investigation, A.E., A.V., A.K. and K.T.; resources, H.E. and T.J.; sponge collection, A.E.; writing—original draft preparation, A.V. and H.E.; writing—review and editing, K.T., A.E. and T.J.; visualization, A.V.; supervision, H.E.; project administration, H.E.; funding acquisition, H.E. and T.J. All authors have read and agreed to the published version of the manuscript.

**Funding:** The financial support provided by the National Science Center, Poland, under the MAE-STRO program (no. 2020/38/A/ST5/00151) and the OPUS program (no. 2020/37/B/ST5/01909) are gratefully acknowledged by H.E. and A.K.

**Institutional Review Board Statement:** Not applicable.

**Data Availability Statement:** Data are contained within the article and Supplementary Materials.

**Acknowledgments:** We express special gratitude to the International Institute of Biomineralogy (INTIB) GmbH, Freiberg, Germany, as well as to Jane Fromont, to Guilherme Muricy, to Alexander Plotkin, and to Paco Cárdenas for providing samples of sponges.

**Conflicts of Interest:** The authors declare no conflicts of interest.

## References

- Wang, X.; Schröder, H.C.; Wiens, M.; Schloßmacher, U.; Müller, W.E. Biosilica: Molecular Biology, Biochemistry and Function in Demosponges as well as its Applied Aspects for Tissue Engineering. *Adv. Mar. Biol.* **2012**, *62*, 231–271. [PubMed]
- Sahebi, M.; Hanafi, M.M.; Siti Nor Akmar, A.; Rafii, M.Y.; Azizi, P.; Tengoua, F.F.; Nurul Mayzaitul Azwa, J.; Shabanimofrad, M. Importance of silicon and mechanisms of biosilica formation in plants. *BioMed Res. Int.* **2015**, *2015*, 396010. [CrossRef] [PubMed]
- Wysokowski, M.; Jesionowski, T.; Ehrlich, H. Biosilica as a source for inspiration in biological materials science. *Am. Mineral.* **2018**, *103*, 665–691. [CrossRef]
- Ikeda, T. Bacterial biosilicification: A new insight into the global silicon cycle. *Biosci. Biotechnol. Biochem.* **2021**, *85*, 1324–1331. [CrossRef] [PubMed]
- Min, K.H.; Kim, D.H.; Youn, S.; Pack, S.P. Biomimetic Diatom Biosilica and Its Potential for Biomedical Applications and Prospects: A Review. *Int. J. Mol. Sci.* **2024**, *25*, 2023. [CrossRef] [PubMed]
- Tang, Q.; Wan, B.; Yuan, X.; Muscente, A.D.; Xiao, S. Spiculogenesis and biomineralization in early sponge animals. *Nat. Commun.* **2019**, *10*, 3348. [CrossRef] [PubMed]
- Turner, E.C. Possible poriferan body fossils in early Neoproterozoic microbial reefs. *Nature* **2021**, *596*, 87–91. [CrossRef] [PubMed]
- Pisera, A.; Łukowiak, M.; Masse, S.; Tabachnick, K.; Fromont, J.; Ehrlich, H.; Bertolino, M. Insights into the structure and morphogenesis of the giant basal spicule of the glass sponge *Monorhaphis chuni*. *Front. Zool.* **2021**, *18*, 58.
- Dendy, A. The tetraxonid sponge-spicule: A study in evolution. *Acta Zool.* **1921**, *2*, 95–152. [CrossRef]
- Uriz, M.J.; Turon, X.; Becerro, M.A.; Agell, G. Siliceous spicules and skeleton frameworks in sponges: Origin, diversity, ultrastructural patterns, and biological functions. *Microsc. Res. Tech.* **2003**, *62*, 279–299. [CrossRef]
- Cárdenas, P. Surface Microornamentation of Demosponge *Steraster* Spicules, Phylogenetic and Paleontological Implications. *Front. Mar. Sci.* **2020**, *7*, 613610. [CrossRef]
- Łukowiak, M.; Van Soest, R.; Klautau, M.; Pérez, T.; Pisera, A.; Tabachnick, K. The terminology of sponge spicules. *J. Morphol.* **2022**, *283*, 1517–1548. [CrossRef] [PubMed]
- Asadzadeh, S.S.; Kjørboe, T.; Larsen, P.S.; Leys, S.P.; Yahel, G.; Walther, J.H. Hydrodynamics of sponge pumps and evolution of the sponge body plan. *eLife* **2020**, *9*, e61012. [CrossRef]
- Tabachnick, K.R. Adaptation of the Hexactinellid Sponges to Deep-Sea Life. In *Fossil and Recent Sponges*; Reitner, J., Keupp, H., Eds.; Springer: Berlin/Heidelberg, Germany, 1997; pp. 378–386.
- Aizenberg, J.; Weaver, J.C.; Thanawala, M.S.; Sundar, V.C.; Morse, D.E.; Fratzl, P. Materials science: Skeleton of *Euplectella* sp.: Structural hierarchy from the nanoscale to the macroscale. *Science* **2005**, *309*, 275–278. [CrossRef] [PubMed]
- Ehrlich, H.; Deutzmann, R.; Brunner, E.; Cappellini, E.; Koon, H.; Solazzo, C.; Yang, Y.; Ashford, D.; Thomas-Oates, J.; Lubeck, M.; et al. Mineralization of the metre-long biosilica structures of glass sponges is templated on hydroxylated collagen. *Nat. Chem.* **2010**, *2*, 1084–1088. [CrossRef] [PubMed]
- Ehrlich, H. Silica biomineralization, Sponges. In *Encyclopedia of Geobiology. Encyclopedia of Earth Sciences Series*; Springer: Dordrecht, The Netherlands, 2011; pp. 796–808.
- Ehrlich, H.; Brunner, E.; Simon, P.; Bazhenov, V.V.; Botting, J.P.; Tabachnick, K.R.; Springer, A.; Kummer, K.; Vyalikh, D.V.; Molodtsov, S.L.; et al. Calcite reinforced silica-silica joints in the biocomposite skeleton of deep-sea glass sponges. *Adv. Funct. Mater.* **2011**, *21*, 3473–3481. [CrossRef]
- Dendy, A. *Studies on the Comparative Anatomy of Sponges*; Kessinger Publishing: Whitefish, MT, USA, 1888; p. 274.
- Bidder, G. The origin of sponge spicules. *Nature* **1925**, *115*, 298–299. [CrossRef]
- Schoeppler, V.; Reich, E.; Vacelet, J.; Rosenthal, M.; Pacureanu, A.; Rack, A.; Zaslansky, P.; Zolotoyabko, E.; Zlotnikov, I. Shaping highly regular glass architectures: A lesson from nature. *Sci. Adv.* **2017**, *3*, aao2047. [CrossRef]
- Voronkina, A.; Romanczuk-Ruszk, E.; Przekop, R.E.; Lipowicz, P.; Gabriel, E.; Heimler, K.; Rogoll, A.; Vogt, C.; Frydrych, M.; Wienclaw, P.; et al. Honeycomb Biosilica in Sponges: From Under-standing Principles of Unique Hierarchical Organization to Assessing Biomimetic Potential. *Biomimetics* **2023**, *8*, 234. [CrossRef]
- Shimizu, K.; Nishi, M.; Sakate, Y.; Kawanami, H.; Bito, T.; Arima, J.; Leria, L.; Maldonado, M. Silica-associated proteins from hexactinellid sponges support an alternative evolutionary scenario for biomineralization in Porifera. *Nat. Commun.* **2024**, *15*, 181. [CrossRef]
- Ehrlich, H.; Luczak, M.; Ziganshin, R.; Mikšík, I.; Wysokowski, M.; Simon, P.; Baranowska-Bosiacka, I.; Kupnicka, P.; Ereskovsky, A.; Galli, R.; et al. Arrested in Glass: Actin within Sophisticated Architectures of Biosilica in Sponges. *Adv. Sci.* **2022**, *9*, 2105059. [CrossRef] [PubMed]
- Ehrlich, H. Actin and the realization of unique biosilica-based architectures in sponges. In *11th World Sponge Conference. Book of Abstracts*; Naturalis Biodiversity Center: Leiden, The Netherlands, 10 October 2022.

26. Tesson, B.; Hildebrand, M. Extensive and intimate association of the cytoskeleton with forming silica in diatoms: Control over patterning on the meso- and micro-scale. *PLoS ONE* **2010**, *5*, 14300. [CrossRef] [PubMed]
27. Tesson, B.; Hildebrand, M. Dynamics of silica cell wall morphogenesis in the diatom *Cyclotella cryptica*: Substructure formation and the role of microfilaments. *J. Struct. Biol.* **2010**, *169*, 62–74. [CrossRef] [PubMed]
28. Povarova, N.V.; Barinov, N.A.; Baranov, M.S.; Markina, N.M.; Varizhuk, A.M.; Pozmogova, G.E.; Klinov, D.V.; Kozhemyako, V.B.; Lukyanov, K.A. Efficient silica synthesis from tetra(glycerol)orthosilicate with cathepsin- and silicatein-like proteins. *Sci. Rep.* **2018**, *8*, 16759. [CrossRef] [PubMed]
29. Talevski, T.; Talevska Leshoska, A.; Pejoshi, E.; Pejin, B.; Machalowski, T.; Wysokowski, M.; Tsurkan, M.V.; Petrova, O.; Sivkov, V.; Martinovic, R.; et al. Identification and first insights into the structure of chitin from the endemic freshwater demosponge *Ochridaspongia rotunda* (Arndt, 1937). *Int. J. Biol. Macromol.* **2020**, *162*, 1187–1194. [CrossRef] [PubMed]
30. Pospich, S.; Merino, F.; Raunser, S. Structural Effects and Functional Implications of Phalloidin and Jasplakinolide Binding to Actin Filaments. *Structure* **2020**, *28*, 437–449. [CrossRef] [PubMed]
31. Melak, M.; Plessner, M.; Grosse, R. Actin visualization at a glance. *J. Cell Sci.* **2017**, *130*, 525–530. [CrossRef] [PubMed]
32. Cano, M.L.; Cassimeris, L.; Fechheimer, M.; Zigmond, S.H. Mechanisms responsible for F-actin stabilization after lysis of polymorphonuclear leukocytes. *J. Cell Biol.* **1992**, *116*, 1123–1134. [CrossRef] [PubMed]
33. Dhakal, K.; Black, B.; Mohanty, S. Introduction of impermeable actin-staining molecules to mammalian cells by optoporation. *Sci. Rep.* **2014**, *4*, 6553. [CrossRef]
34. Romani, M.; Auwerx, J. Phalloidin staining of actin filaments for visualization of muscle fibers in *Caenorhabditis elegans*. *Bio-Protocol* **2021**, *11*, e4183.
35. Frigeri, L.G.; Radabaugh, T.R.; Haynes, P.A.; Hildebrand, M. Identification of proteins from a cell wall fraction of the diatom *Thalassiosira pseudonana*: Insights into silica structure formation. *Mol. Cell Proteom.* **2006**, *5*, 182–193. [CrossRef] [PubMed]
36. Han, Y.; Tu, S.; Gong, W.; Tao, W.; Tang, M.; Wei, Y.; Kuang, C.; Liu, X.; Zhang, Y.H.; Hao, X. Three-dimensional multi-color optical nanoscopy at sub-10-nm resolution based on small-molecule organic probes. *Cell Rep. Methods* **2023**, *3*, 100556. [CrossRef]
37. Manconi, R.; Pronzato, R. Suborder Spongillina subord. nov.: Freshwater Sponges. In *Systema Porifera*; Hooper, J.N.A., Van Soest, R.W.M., Willenz, P., Eds.; Springer: Boston, MA, USA, 2002.
38. Morrow, C.; Cárdenas, P. Proposal for a revised classification of the Demospongiae (Porifera). *Front. Zool.* **2015**, *12*, 7. [CrossRef] [PubMed]
39. Müller, W.E.G.; Krasko, A.; Le Pennec, G.; Steffen, R.; Wiens, M.; Ammar, M.S.A.; Müller, I.M.; Schröder, H.C. Molecular mechanism of spicule formation in the demosponge *Suberites domuncula*: Silicatein-collagen-myotrophin. *Regul. Altern. Splic.* **2003**, *33*, 195–221.
40. Müller, W.E.; Boreiko, A.; Wang, X.; Belikov, S.I.; Wiens, M.; Grebenjuk, V.A.; Schlossmacher, U.; Schröder, H.C. Silicateins, the major biosilica forming enzymes present in demsponges: Protein analysis and phylogenetic relationship. *Gene* **2007**, *395*, 62–71. [CrossRef] [PubMed]
41. Rouiller, I.; Xu, X.P.; Amann, K.J.; Egile, C.; Nickell, S.; Nicastro, D.; Li, R.; Pollard, T.D.; Volkmann, N.; Hanein, D. The structural basis of actin filament branching by the Arp2/3 complex. *J. Cell Biol.* **2008**, *180*, 887–895. [CrossRef] [PubMed]
42. Cárdenas, P.; Rapp, H.T.; Klitgaard, A.B.; Best, M.; Thollessen, M.; Tendal, O.S. Taxonomy, biogeography and DNA barcodes of *Geodia* species (Porifera, Demospongiae, Tetractinellida) in the Atlantic boreo-arctic region. *Zool. J. Linn. Soc.* **2013**, *169*, 251–311. [CrossRef]
43. Tabachnick, K.; Janussen, D.; Menshenina, L. Cold Biosilicification in Metazoan: Psychrophilic Glass Sponges. In *Extreme Biomimetics*; Ehrlich, H., Ed.; Springer International Publishing: Cham, Switzerland, 2016; pp. 53–80.
44. Dohrmann, M.; Kelley, C.; Kelly, M.; Pisera, A.; Hooper, J.N.A.; Reiswig, H.M. An integrative systematic framework helps to reconstruct skeletal evolution of glass sponges (Porifera, Hexactinellida). *Front. Zool.* **2017**, *14*, 18. [CrossRef] [PubMed]
45. Weaver, J.C.; Milliron, G.W.; Allen, P.; Miserez, A.; Rawal, A.; Garay, J.; Morse, D.E. Unifying Design Strategies in Demosponge and Hexactinellid Skeletal Systems. *J. Adhes.* **2010**, *86*, 72–95. [CrossRef]
46. Fraccaroli, A.; Franco, C.A.; Rognoni, E.; Neto, F.; Rehberg, M.; Aszodi, A.; Wedlich-Söldner, R.; Pohl, U.; Gerhardt, H.; Montanez, E. Visualization of endothelial actin cytoskeleton in the mouse retina. *PLoS ONE* **2012**, *7*, e47488. [CrossRef]
47. Kalil, K.; Li, L.; Hutchins, B.I. Signaling mechanisms in cortical axon growth, guidance, and branching. *Front. Neuroanat.* **2011**, *5*, 62. [CrossRef] [PubMed]
48. Svitkina, T.M.; Borisy, G.G. Arp2/3 complex and actin depolymerizing factor/cofilin in dendritic organization and treadmilling of actin filament array in lamellipodia. *J. Cell Biol.* **1999**, *145*, 1009–1026. [CrossRef] [PubMed]
49. Kalman, D.; Gomperts, S.N.; Hardy, S.; Kitamura, M.; Bishop, J.M. Ras family GTPases control growth of astrocyte processes. *Mol. Biol. Cell* **1999**, *10*, 1665–1683. [CrossRef] [PubMed]
50. Cheng, C.; Parreno, J.; Nowak, R.B.; Biswas, S.K.; Wang, K.; Hoshino, M.; Uesugi, K.; Yagi, N.; Moncaster, J.A.; Lo, W.K.; et al. Age-related changes in eye lens biomechanics, morphology, refractive index and transparency. *Aging* **2019**, *11*, 12497–12531. [CrossRef] [PubMed]
51. Francis, W.R.; Eitel, M.; Vargas, S.; Garcia-Escudero, C.A.; Conci, N.; Deister, F.; Mah, J.L.; Guiglielmoni, N.; Krebs, S.; Blum, H.; et al. The genome of the reef-building glass sponge *Aphrocallistes vastus* provides insights into silica biomineralization. *R. Soc. Open Sci.* **2023**, *10*, 230423. [CrossRef] [PubMed]

52. Santini, S.; Schenkelaars, Q.; Jourda, C.; Duchesne, M.; Belahbib, H.; Rocher, C.; Selva, M.; Riesgo, A.; Vervoort, M.; Leys, S.P.; et al. The compact genome of the sponge *Oopsacas minuta* (Hexactinellida) is lacking key metazoan core genes. *BMC Biol.* **2023**, *21*, 139. [CrossRef]
53. Moscatelli, A.; Idilli, A.I.; Rodighiero, S.; Caccianiga, M. Inhibition of actin polymerisation by low concentration Latrunculin B affects endocytosis and alters exocytosis in shank and tip of tobacco pollen tubes. *Plant Biol.* **2012**, *14*, 770–782. [CrossRef] [PubMed]
54. Pollard, T.D.; Blanchoin, L.; Mullins, R.D. Molecular mechanisms controlling actin filament dynamics in nonmuscle cells. *Annu. Rev. Biophys. Biomol. Struct.* **2000**, *29*, 545–576. [CrossRef] [PubMed]
55. Martiel, J.L.; Michelot, A.; Boujemaa-Paterski, R.; Blanchoin, L.; Berro, J. Force Production by a Bundle of Growing Actin Filaments Is Limited by Its Mechanical Properties. *Biophys. J.* **2020**, *118*, 39. [CrossRef]
56. Castaneda, N.; Park, J.; Kang, E.H. Regulation of Actin Bundle Mechanics and Structure by Intracellular Environmental Factors. *Front. Phys.* **2021**, *9*, 675885. [CrossRef]
57. Chen, X.; Roeters, S.J.; Cavanna, F.; Alvarado, J.; Baiz, C.R. Crowding alters F-actin secondary structure and hydration. *Commun. Biol.* **2023**, *6*, 900. [CrossRef] [PubMed]
58. Tilney, L.G.; Tilney, M.S.; Guild, G.M. F actin bundles in *Drosophila* bristles I. Two filament cross-links are involved in bundling. *J. Cell Biol.* **1995**, *130*, 629–638. [CrossRef] [PubMed]
59. Tilney, L.G.; Connelly, P.S.; Vranich, K.A.; Shaw, M.K.; Guild, G.M. Regulation of actin filament cross-linking and bundle shape in *Drosophila* bristles. *J. Cell Biol.* **2000**, *148*, 87–99. [CrossRef] [PubMed]
60. Guild, G.M.; Connelly, P.S.; Ruggiero, L.; Vranich, K.A.; Tilney, L.G. Actin filament bundles in *Drosophila* wing hairs: Hairs and bristles use different strategies for assembly. *Mol. Biol. Cell* **2005**, *16*, 3620–3631. [CrossRef] [PubMed]
61. Belin, B.J.; Goins, L.M.; Mullins, R.D. Comparative analysis of tools for live cell imaging of actin network architecture. *Bioarchitecture* **2014**, *4*, 189–202. [CrossRef]
62. Schaefer, A.W.; Kabir, N.; Forscher, P. Filopodia and actin arcs guide the assembly and transport of two populations of microtubules with unique dynamic parameters in neuronal growth cones. *J. Cell Biol.* **2002**, *158*, 139–152. [CrossRef]
63. Danuser, G.; Oldenbourg, R. Probing f-actin flow by tracking shape fluctuations of radial bundles in lamellipodia of motile cells. *Biophys. J.* **2000**, *79*, 191–201. [CrossRef]
64. Pochitaloff, M.; Miranda, M.; Richard, M.; Chaiyasitdhi, A.; Takagi, Y.; Cao, W.; De La Cruz, E.M.; Sellers, J.R.; Joanny, J.F.; Jülicher, F.; et al. Flagella-like beating of actin bundles driven by self-organized myosin waves. *Nat. Phys.* **2022**, *18*, 1240–1247. [CrossRef] [PubMed]
65. Katoh, K.; Hammar, K.; Smith, P.J.S.; Oldenbourg, R. Arrangement of radial actin bundles in the growth cone of *Aplysia* bag cell neurons shows the immediate past history of filopodial behavior. *Proc. Natl. Acad. Sci. USA* **1999**, *96*, 7928–7931. [CrossRef]
66. Katoh, K.; Hammar, K.; Smith, P.J.S.; Oldenbourg, R. Birefringence imaging directly reveals architectural dynamics of filamentous actin in living growth cones. *Mol. Biol. Cell* **1999**, *10*, 197–210. [CrossRef]
67. Oldenbourg, R.; Katoh, K.; Danuser, G. Mechanism of lateral movement of filopodia and radial actin bundles across neuronal growth cones. *Biophys. J.* **2000**, *78*, 1176–1182. [CrossRef] [PubMed]
68. Andjus, S.; Tubić, B.; Vasiljević, B.; Nikolić, V.; Paunović, M. Anomalies of Sponge Spicules: Exploring Links to Environmental Pollution. *Water* **2024**, *16*, 332. [CrossRef]
69. de Voogd, N.J.; Alvarez, B.; Boury-Esnault, N.; Cárdenas, P.; Díaz, M.-C.; Dohrmann, M.; Downey, R.; Goodwin, C.; Hajdu, E.; Hooper, J.N.A.; et al. World Porifera Database. Homoscleromorpha. 2024. Available online: <http://www.marinespecies.org/porifera/index.php> (accessed on 23 May 2024).
70. Gazave, E.; Lapébie, P.; Renard, E.; Vacelet, J.; Rocher, C.; Ereskovsky, A.V.; Cárdenas, P.; Borchellini, C. No longer Demospongiae: Homoscleromorpha formal nomination as a fourth class of Porifera. *Hydrobiologia* **2012**, *687*, 3–10. [CrossRef]
71. Ruiz, C.; Ereskovsky, A.; Pérez, T. New Skeleton-Less Homoscleromorphs (Porifera, Homoscleromorpha) from the Caribbean Sea: Exceptions to Rules Are Definitely Common in Sponge Taxonomy. *Zootaxa* **2022**, *5200*, 128–148. [CrossRef]
72. Stillitani, D.; Ereskovsky, A.V.; Pérez, T.; Ruiz, C.; Laport, M.S.; Puccinelli, G.; Hardoim, C.C.P.; Willenz, P.; Muricy, G. Solving a taxonomic puzzle: Integrative taxonomy reveals new cryptic and polymorphic species of *Oscarella* (Homoscleromorpha: Oscarellidae). *Invertebr. Syst.* **2022**, *36*, 714–750. [CrossRef]
73. Van de Meene, A.M.L.; Pickett-Heaps, J.D. Valve morphogenesis in the centric diatom *Rhizosolenia setigera* (Bacillariophyceae, Centrales) and its taxonomic implications. *Eur. J. Phycol.* **2004**, *39*, 93–104. [CrossRef]
74. Durak, G.M.; Brownlee, C.; Wheeler, G.L. The role of the cytoskeleton in biomineralisation in haptophyte algae. *Sci. Rep.* **2017**, *7*, 15409. [CrossRef]
75. Manning, L. Mimicking Biosintering: The Identification of Highly Condensed Surfaces in Bioinspired Silica Materials. *Langmuir* **2021**, *37*, 561–568. [CrossRef]
76. He, M.; Li, Y.; Yin, J.; Sun, Q.; Xiong, W.; Li, S.; Yang, L. Compressive performance and fracture mechanism of bio-inspired heterogeneous glass sponge lattice structures manufactured by selective laser melting. *Mater. Des.* **2022**, *214*, 110396. [CrossRef]
77. Chen, H.; Jia, Z.; Li, L. Lightweight lattice-based skeleton of the sponge *Euplectella aspergillum*: On the multifunctional design. *J. Mech. Behav. Biomed. Mater.* **2022**, *135*, 105448. [CrossRef]
78. Chen, H. Multiscale Structures and Mechanics of Biomineralized Lattices in Hexactinellid sponges and Echinoderms. Ph.D. Thesis, Virginia Polytechnic Institute and State University, Blacksburg, VA, USA, 2023.

79. Fernandes, M.C.; Aizenberg, J.; Weaver, J.C.; Bertoldi, K. Mechanically robust lattices inspired by deep-sea glass sponges. *Nat. Mater.* **2021**, *20*, 237–241. [CrossRef] [PubMed]
80. Heidarzadeh, S.; Mahdaviinejad, M.; Habib, F. Bio-inspiration from sponge for high-performance building. *Naqshejahan* **2023**, *13*, 86–101.
81. Sarikaya, M.; Fong, H.; Sunderland, N.; Flinn, B.D.; Mayer, G.; Mescher, A.; Gaiño, E. Biomimetic model of a sponge-spicular optical fiber—Mechanical properties and structure. *J. Mater. Res.* **2001**, *16*, 1420–1428. [CrossRef]
82. Aizenberg, J.; Sundar, V.C.; Yablon, A.D.; Weaver, J.C.; Chen, G. Biological glass fibers: Correlation between optical and structural properties. *Proc. Natl. Acad. Sci. USA* **2004**, *101*, 3358–3363. [CrossRef] [PubMed]
83. Ehrlich, H.; Maldonado, M.; Parker, A.R.; Kulchin, Y.N.; Schilling, J.; Köhler, B.; Skrzypczak, U.; Simon, P.; Reisswig, H.M.; Tsurkan, M.V.; et al. Supercontinuum Generation in Naturally Occurring Glass Sponges Spicules. *Adv. Opt. Mater.* **2016**, *4*, 1608–1613. [CrossRef]
84. Zhang, X.; Luan, Y.; Li, Y.; Wang, Z.; Li, Z.; Xu, F.; Guo, Z. Bioinspired design of lightweight laminated structural materials and the intralayer/interlayer strengthening and toughening mechanisms induced by the helical structure. *Compos. Struct.* **2021**, *276*, 114575. [CrossRef]
85. Zhang, X.; Luan, Y.; Li, Y.; Wang, Z.; Li, Z.; Xu, F.; Guo, Z.Z. Unveiling the mechanics of deep-sea sponge-inspired tubular metamaterials: Exploring bending, radial, and axial mechanical behavior. *Thin-Walled Struct.* **2024**, *196*, 111476. [CrossRef]
86. Li, Y.; Wang, Z.; Zhang, X.; Xu, F.; Guo, Z.Z. Crashworthiness design of a sponge-inspired multicell tube under axial crushing. *Int. J. Mech. Sci.* **2023**, *244*, 108070. [CrossRef]
87. Morankar, S.; Sundar Sundaram Singaravelu, A.; Niverty, S.; Mistry, Y.; Penick, C.A.; Bhate, D.; Chawla, N. Tensile and fracture behavior of silica fibers from the Venus flower basket (*Euplectella aspergillum*). *Int. J. Solids Struct.* **2022**, *253*, 111622. [CrossRef]
88. Morankar, S.K.; Mistry, Y.; Bhate, D.; Penick, C.A.; Chawla, N. In situ investigations of failure mechanisms of silica fibers from the venus flower basket (*Euplectella Aspergillum*). *Acta Biomater.* **2023**, *162*, 304–311. [CrossRef]
89. Tavangarian, F.; Sadeghzade, S.; Davami, K. A novel biomimetic design inspired by nested cylindrical structures of spicules. *J. Alloys Compd.* **2021**, *864*, 158197. [CrossRef]
90. Xiao, H. Nested structure role in the mechanical response of spicule inspired fibers. *Bioinspir. Biomim.* **2024**, *19*, 046008. [CrossRef] [PubMed]
91. Du, X.; Zhang, Y.; Li, J.; Chen, P.; Liu, Y. Artificial intelligence-enhanced bioinspiration: Design of optimized mechanical lattices beyond deep-sea sponges. *Extreme Mech. Lett.* **2023**, *62*, 102033. [CrossRef]
92. Sharma, D.; Hiremath, S.S. In-plane elastic properties of the *Euplectella aspergillum* inspired lattice structures: Analytic modelling, finite element modelling and experimental validation. *Structures* **2023**, *48*, 962–975. [CrossRef]
93. Yang, Z.; Xue, J.; Li, T.; Zhai, D.; Yu, X.; Huan, Z.; Wu, C. 3D printing of sponge spicules-inspired flexible bioceramic-based scaffolds. *Biofabrication* **2022**, *14*, 035009. [CrossRef] [PubMed]
94. Robson Brown, K.; Bacheva, D.; Trask, R.S. The structural efficiency of the sea sponge *Euplectella aspergillum* skeleton: Bio-inspiration for 3D printed architectures. *J. R. Soc. Interface* **2019**, *16*, 965. [CrossRef] [PubMed]
95. Tavangarian, F.; Sadeghzade, S.; Fani, N.; Khezrimotlagh, D.; Davami, K. 3D-printed bioinspired spicules: Strengthening and toughening via stereolithography. *J. Mech. Behav. Biomed. Mater.* **2024**, *136*, 105485. [CrossRef]
96. Martins, E.; Rapp, H.T.; Xavier, J.R.; Diogo, G.S.; Reis, R.L.; Silva, T.H. Macro and Microstructural Characteristics of North Atlantic Deep-Sea Sponges as Bioinspired Models for Tissue Engineering Scaffolding. *Front. Mar. Sci.* **2021**, *7*, 613647. [CrossRef]

**Disclaimer/Publisher’s Note:** The statements, opinions and data contained in all publications are solely those of the individual author(s) and contributor(s) and not of MDPI and/or the editor(s). MDPI and/or the editor(s) disclaim responsibility for any injury to people or property resulting from any ideas, methods, instructions or products referred to in the content.



## Review

# Biomimetic Approaches in Scaffold-Based Blood Vessel Tissue Engineering

Elisabetta Rosellini \*, Cristiana Giordano , Lorenzo Guidi and Maria Grazia Cascone \*

Department of Civil and Industrial Engineering, University of Pisa, Largo Lucio Lazzarino 1, 56122 Pisa, Italy; cristiana.giordano@phd.unipi.it (C.G.); lorenzo.guidi@phd.unipi.it (L.G.)

\* Correspondence: elisabetta.rosellini@unipi.it (E.R.); maria.grazia.cascone@unipi.it (M.G.C.)

**Abstract:** Cardiovascular diseases remain a leading cause of mortality globally, with atherosclerosis representing a significant pathological means, often leading to myocardial infarction. Coronary artery bypass surgery, a common procedure used to treat coronary artery disease, presents challenges due to the limited autologous tissue availability or the shortcomings of synthetic grafts. Consequently, there is a growing interest in tissue engineering approaches to develop vascular substitutes. This review offers an updated picture of the state of the art in vascular tissue engineering, emphasising the design of scaffolds and dynamic culture conditions following a biomimetic approach. By emulating native vessel properties and, in particular, by mimicking the three-layer structure of the vascular wall, tissue-engineered grafts can improve long-term patency and clinical outcomes. Furthermore, ongoing research focuses on enhancing biomimicry through innovative scaffold materials, surface functionalisation strategies, and the use of bioreactors mimicking the physiological microenvironment. Through a multidisciplinary lens, this review provides insight into the latest advancements and future directions of vascular tissue engineering, with particular reference to employing biomimicry to create systems capable of reproducing the structure–function relationships present in the arterial wall. Despite the existence of a gap between benchtop innovation and clinical translation, it appears that the biomimetic technologies developed to date demonstrate promising results in preventing vascular occlusion due to blood clotting under laboratory conditions and in preclinical studies. Therefore, a multifaceted biomimetic approach could represent a winning strategy to ensure the translation of vascular tissue engineering into clinical practice.



**Citation:** Rosellini, E.; Giordano, C.; Guidi, L.; Cascone, M.G. Biomimetic Approaches in Scaffold-Based Blood Vessel Tissue Engineering.

*Biomimetics* **2024**, *9*, 377.

[https://doi.org/](https://doi.org/10.3390/biomimetics9070377)

10.3390/biomimetics9070377

Academic Editor: Hermann Ehrlich

Received: 30 April 2024

Revised: 15 June 2024

Accepted: 19 June 2024

Published: 22 June 2024



**Copyright:** © 2024 by the authors. Licensee MDPI, Basel, Switzerland. This article is an open access article distributed under the terms and conditions of the Creative Commons Attribution (CC BY) license (<https://creativecommons.org/licenses/by/4.0/>).

**Keywords:** biomimicry; natural polymers; three-layered blood vessel; functionalisation; bioreactor; vascular tissue engineering

## 1. Introduction

Cardiovascular diseases remain the leading cause of death in industrialised countries, accounting for an estimated 17.8 million deaths in 2017, with projections indicating a rise to 23.3 million annually by the year 2030 [1]. One of the most severe cardiovascular pathologies is atherosclerosis, a process that leads to the narrowing of arteries. In the case of coronary arteries, this leads to the weakening of the myocardium, i.e., the heart wall, eventually leading to myocardial infarction. As the disease progresses, there is a reduction in coronary blood flow and an alteration of fluid-dynamic conditions.

Once the narrowing of the arteries has progressed to the point where myocardial infarction is imminent or has already occurred, surgical intervention of aorto-coronary bypass becomes necessary [2]. Approximately 500,000 aorto-coronary bypass surgeries are performed annually in the United States. Bypass surgery is also performed to treat aneurysms or trauma. Currently, surgeons use either autologous tissue or synthetic biomaterials as vascular prostheses.

The transplantation of natural tissue, mainly the saphenous vein or internal mammary artery, is the preferred choice for coronary artery replacement. Indeed, the results of this

procedure are quite favourable, with a success rate ranging from 50 to 70% [3]. Failures can be caused by various factors including intimal thickening (largely due to vessel adaptation in response to increased pressure and shear stress on the walls), vascular compression, inadequate vessel diameter, and disjunction near anastomoses [3]. However, many patients requiring aorto-coronary bypass surgery do not possess suitable autologous vessels, either due to illness or previous use during other procedures. Furthermore, even if available, the removal of autologous vessels from their native position in the vascular system is far from desirable. Given these considerations, it is clear how the need to construct alternative vascular substitutes for natural tissues arises.

The development of plastics and other polymers in the 1950s led to the use of the first synthetic materials to build vascular prostheses [4]. Such synthetic materials include polyesters, polyethylene terephthalate (PET, Dacron), and expanded polytetrafluoroethylene (ePTFE, Gore-Tex). However, the success rate of synthetic grafts was found to be substantially lower than that of natural vessels, particularly in small-diameter applications such as coronary arteries [5]. Issues associated with synthetic vessels include platelet adhesion, aggregation, and lower compliance compared to adjacent arterial tissues. The surface of synthetic materials is not as biocompatible as that of natural tissues, resulting in greater platelet activation and blood clotting. Despite their durability, synthetic materials can degrade over time, producing particles that may cause inflammation or other complications at the implant site. Unlike natural tissues, synthetic materials cannot integrate or reshape themselves within the body, potentially leading to long-term problems such as failure to adapt to changes in blood flow and pressure, and inability to grow with the patient, which is particularly relevant in pediatric cases. Additionally, synthetic materials cannot mimic the complexity of natural blood vessel functions, such as responses to vasodilation and vasoconstriction.

Conversely, allografts, although more biologically compatible than synthetic materials, can still trigger an immune response in the recipient, leading to transplant rejection. Even with immunosuppressive treatment, the risk of rejection cannot be completely eliminated. Allografts may lose their mechanical and functional properties over time, especially if not properly treated, and can undergo calcification, particularly if derived from animal tissues or inadequately processed. This calcification can result in loss of elasticity and vessel functionality. Although vessels treated with aldehydes to prevent reactivity have been used, they have exhibited thrombogenicity comparable to synthetic grafts. These challenges have driven the research and development of engineered vascular substitutes [6].

The fundamental concept of vascular tissue engineering involves designing a tubular scaffold using a biodegradable polymer which is then seeded with patient-specific cells. Following this, the graft matures within a dynamically simulated microenvironment before being implanted into the patient. Over time, the polymeric graft degrades with a precisely regulatable dynamic, allowing for the gradual replacement by a newly formed extracellular matrix (ECM). This process maintains the structural integrity of the graft while facilitating the development of native-like regenerated tissue. Compared with traditional prostheses, tissue-engineered vascular grafts (TEVGs) created in the laboratory can emulate the properties of autografts with remarkable accuracy.

Starting from the foundational work of Weinberg and Bell in 1986 [7], the field of vascular tissue engineering has demonstrated significant growth over the past few decades. Researchers have explored numerous approaches aimed at developing small-diameter blood vessels suitable for clinical applications, leading to substantial advancements in our comprehension of vascular biology and engineering principles.

Current research endeavours in this field are heavily focused on incorporating native-like features of autologous vessels into tissue-engineered grafts, to facilitate their clinical translation. As the development of biomimetic grafts requires a multifaceted approach, this review aims to provide an updated overview of the different biomimetic approaches investigated so far for vascular tissue engineering purposes, from scaffold material, architecture, and functionalisation cues, to bioreactor design. By these means, this review can



significantly contribute to the existing literature by introducing novel insights and perspectives on multidisciplinary technologies that could facilitate vascular tissue engineering transition from bench to bedside.

## 2. Anatomy and Functions of Healthy Blood Vessels

The engineering of biomimetic blood vessel substitutes should begin with a careful understanding of the anatomy and functions of the native tissue.

Blood vessels constitute closed circulatory systems that penetrate most of the body tissues. They are categorised into arteries, capillaries, and veins, based on their structure and function [8]. Large vessels, such as arteries and veins, primarily facilitate efficient transport to distant sites, while small vessels like capillaries and arterioles enable optimal exchange of nutrients, oxygen, and waste within organs and tissues. Consequently, engineering large vessels ( $>6$  mm) requires different design requirements and approaches when compared to manufacturing small vessels ( $<6$  mm).

The wall of natural arteries comprises three distinct layers of tissue: the intima, the media, and the adventitia (Figure 1). Each layer contributes significantly to the vessel's overall function, fulfilling essential roles in haemostasis, regulating vascular tone, and maintaining hemodynamic balance throughout the circulatory system. Collaboration between cells and ECM components is vital for preserving the dynamic environment of the artery wall.

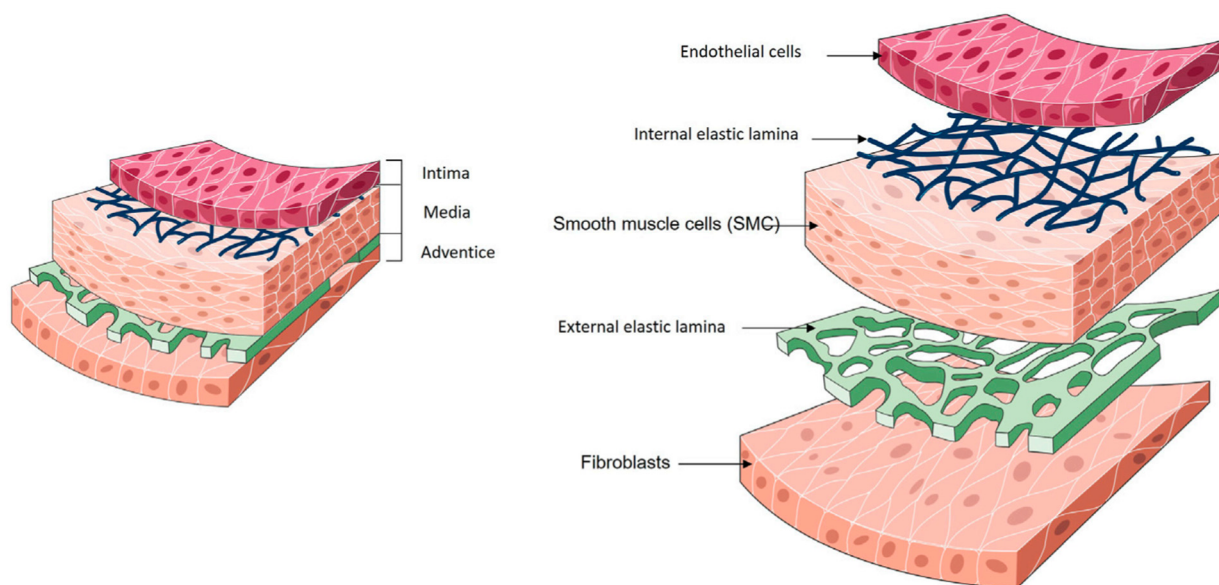


**Figure 1.** Anatomy of blood vessels. Reproduced from Devillard and Marquette [9], an open-access article distributed under the terms of the Creative Commons Attribution License (CC BY).

The intima, the inner layer, is in direct contact with the blood. It is lined with a single layer of endothelial cells (ECs), collectively referred to as the endothelium. The primary functions of the endothelium include providing an anti-thrombogenic layer, preventing platelet aggregation, and regulating vascular permeability and homeostasis. In vivo, the endothelium is subjected to constant shearing forces caused by blood flow. In response to these forces, ECs elongate in the direction of blood flow. ECs produce their ECM, called the basal lamina, during development and in response to injury. This basal lamina acts as a continuous boundary between the endothelium and underlying structures. The intima is separated from the media by a thin layer consisting of elastin and type IV collagen (COL), known as the internal elastic lamina [10]. This lamina is porous, facilitating the diffusion of nutrients from the vessel lumen to the underlying tissues. The primary function of the internal elastic lamina is associated with maintaining the elastic resilience of the vascular wall to sustain blood pressure [11,12].

The media represents the middle layer. Smooth muscle cells (SMCs) constitute the predominant cellular population within the medial layer of blood vessels. Their main role is to synthesise ECM components and regulate vascular tone throughout the cardiac cycle. SMCs are influenced by the secretion of small molecules and growth factors by ECs, establishing a paracrine signalling loop between ECs and SMCs. The ECM composition of the medial layer consists primarily of COL and elastin. In the medial layer, SMCs, COL and elastin fibres are concentrically organised along the axis of the vessel, thereby representing the main component of the vessel's mechanical strength [11,12].

The outer layer of the vessel is the adventitia, which is made of connective tissue and contains fibroblasts. Fibroblasts within the adventitia deposit an ECM that is rich in COL content, with collagenous fibres typically circumferentially arranged. Due to the high tensile strength of COL, its abundant presence, and its circumferential alignment, the adventitia emerges as the mechanically strongest layer in the vessel wall. Consequently, it plays a crucial role in preventing vessel rupture beyond physiological pressures. Additionally, the adventitia houses the vasa vasorum, a network of small blood vessels supplying nutrients and oxygen to all cells within the vessel wall [11,12]. In large-diameter arteries, an external elastic lamina is positioned between the media and the adventitia.

As it appears, vascular tissues represent intricate and constantly changing structures. In the vessel wall, the correct structure, composition, and function of each layer are vital for sustaining vascular homeostasis. The initiation and advancement of cardiovascular disease (CVD) disrupt the normal functioning of each layer, such as nutrient delivery and immune signalling, leading to severe clinical consequences. It is clear that the complexity of native blood vessels should be considered during vascular tissue engineering, as considering the recreation of all layers of the arterial wall, or at least the inner and middle layers, and their properties would be beneficial in obtaining a functional vascular substitute and achieving a good degree of success.

### 3. Challenges and Requirements of an Ideal Tissue-Engineered Blood Vessel

Although the engineering of blood vessels has significantly advanced since the first attempts, in the late 1980s, to produce the first in vitro TEVGs from vascular cells cultured on a COL matrix [7], several challenges still exist. Graft patency is still compromised due to thrombosis, most likely stemming from post-implantation endothelial cell retention or alteration of endothelial cell function following in vitro culture. Additionally, there is a possibility of graft failure due to post-implantation rupture in a physiological flow environment, which would lead to catastrophic consequences. Finally, it has been observed that the mechanical properties of engineered vascular grafts are inferior to those of natural arteries. Therefore, various approaches are being considered in terms of cell sourcing, scaffold materials, and culture conditions, to manufacture an optimal and clinically employable vascular substitute.

The ideal arterial substitute should fulfil the following criteria:

- Be biocompatible and non-immunogenic;
- Be resistant to infections and chronic inflammation;
- Offer an adequate microenvironment to support cell growth and ECM regeneration;
- Be able to acquire structural function immediately after implantation;
- Be devoid of cracks and thrombus-resistant, but with adequate porosity for effective metabolic exchange with the external environment, healing and angiogenesis. These attributes are generally provided by an artery possessing an intact endothelium, which also acts as a secretory tissue and barrier with selective permeability;
- Have appropriate mechanical properties (in terms of graft tensile strength, elastic modulus, burst pressure, compliance, and suture retention strength), in consideration of the high pressure to withstand after implantation [13]. Graft tensile strength is a crucial property in retaining graft integrity as it expresses the resistance of the graft to breakage caused by the mechanical forces, exerted on it during and after implantation. Elastic modulus is an equally critical parameter referring to the ability of the graft to

mimic the elastic properties of natural blood vessels, which is essential for long-term functioning and compatibility with the cardiovascular system. The balance of these parameters is essential to guarantee adequate resistance and flexibility of the graft. Suture retention strength is also essential to retain sutures during the surgical procedure for implantation. Graft compliance was demonstrated to be beneficial for long-term patency, as compliance mismatch at the anastomosis between the native vessel and the engineered substitute is associated with adverse biological responses and long-term graft failure. A high burst pressure is fundamental to sustain physiologic variations in pressure without rupture. There is still a lack of consensus regarding its ideal value, as it depends also on the implantation site. In general, a burst pressure value above 2000 mmHg is desirable [14];

- Possess appropriate vasoactive physiological properties, including the ability to contract or relax in response to neural and chemical stimuli;
- Be economically manufacturable within a short timeframe, meeting various patient-specific parameters, such as diameter and length;
- Be able to remodel in vivo.

In native blood vessels, all of these ideal requirements are provided by the composition and arrangement of cells and ECM across the different layers of the blood vessel wall [15]. This is the reason why a biomimetic approach in blood vessel tissue engineering is paramount to obtaining a functional replacement.

#### 4. Significance and Importance of Scaffold-Based Blood Vessel Tissue Engineering

A significant hurdle in vascular tissue engineering consists of identifying strategies for effectively distributing, arranging, and maturing different cell types within a tubular structure. One of the most significant challenges in creating blood vessels lies in effectively distributing cells within vascular tissue to mimic their natural arrangements [16]. Various techniques have been devised to tackle this challenge, for instance by employing cell sheet engineering techniques, or by exploiting the predefined ECM organisation by decellularising vascular tissue sourced from xenogeneic origins and using them as support for subsequent cell culture. Another investigated strategy is the creation of scaffolds using methods such as electrospinning or moulding, followed by cell seeding [9]. Scaffold-based tissue engineering strategies involve utilising a scaffold material to provide a structural framework for cell attachment, proliferation, and differentiation. Scaffolds can be fabricated using both natural and synthetic polymers. An important advantage of scaffold-based approaches is their ability to guide cell colonisation and proliferation along predefined pathways within the scaffold structure. This can help mimic the natural organisation of vascular tissues and promote the formation of functional blood vessels. [17]. Scaffold-based methods are therefore receiving significant attention due to their versatility, the wide availability of both synthetic and natural polymers, and the obtainable three-dimensional porous structures, which facilitate cell growth, nutrient diffusion, tissue regeneration, and scaffold biodegradation [18–25].

The report by Niklason et al. [26] marked a significant milestone in scaffold-based vessel tissue engineering, particularly in the field of small-diameter blood vessel regeneration. By seeding bovine aortic SMCs onto a polyglycolic acid (PGA) scaffold and culturing them dynamically in a bioreactor for 8 weeks, they were able to obtain an engineered tissue with mechanical properties comparable to native vessels. This interesting result has stimulated research on scaffold-guided vessel regeneration, especially for small-calibre vessels. However, to date, there are no clinically available scaffolds for tissue engineering of small-diameter blood vessels.

Certainly, significant progress has been made by moving on from monolayer scaffolds to multilayer scaffolds, given that the arterial wall is an intrinsically multilayered structure in which each layer performs specific functions. In recent years, there has been a shift towards accurately mimicking the native arterial geometry, as will be further discussed in Section 6. This approach aims to address the limitations of current scaffold-based

strategies by better replicating the complex structure and functionality of natural blood vessels. By developing multi-layer scaffolds that emulate the distinct properties of each layer in the arterial wall, scientists hope to improve the outcomes of tissue engineering for small-diameter blood vessels [27].

#### 4.1. Scaffold Cell Seeding

Once the scaffold for vessel regeneration has been produced, the next particularly critical step is correct cell seeding, to produce a system capable of reproducing vascular functionality.

Static seeding, a standard procedure, comes with drawbacks, including the uneven distribution of cells within the scaffold, a strong reliance on cell migration within the scaffold, and the porosity of the biomaterial utilised to construct the scaffold [28]. To address the shortcomings of static seeding, dynamic seeding techniques have been devised, notably through the implementation of rotational systems [29] in which centrifugal forces aid in the uniform transfer of cells into a porous scaffold. Researchers have observed improved seeding efficiency and homogeneity compared to static or spinner flask techniques. However, they also acknowledged a potential negative impact on cellular viability and morphology, although the extent of this impact was not quantified.

An alternative seeding method has been devised by utilising magnetic fields. This approach relies on directing magnetically labelled cells through a magnetic field gradient, facilitating their seeding into tubular structures [30]. The different vascular layers are created by repeating this procedure with various cell types.

As an alternative to *in vitro* cell seeding, *in vivo* scaffold cellularisation and tissue growth were investigated. In this approach, a scaffold without cells is implanted into the host, where it should promote cell colonisation [22,31–36]. Unfortunately, the major limitation of this method is that there is a lack of control over the interaction of the scaffold with the different types of host cells, therefore it is not possible to predict what may happen to the scaffold and processes like fibrosis, thrombosis, pore obstruction and slow degradation can occur [37–39].

#### 4.2. Moulding Cellularised Biomaterials

Several studies have demonstrated that moulding cellularised biomaterials can enable the manufacturing of custom-shaped structures [40–43]. This technique involves pouring a biomaterial solution into a mould with a custom external shape, allowing it to solidify or crosslink, and then removing the mould to obtain the desired structure. The versatility of this method lies in its ability to produce a wide range of shapes, simply by modifying the mould architecture.

A step-by-step casting technique was applied by Helms et al. to create a tri-layered blood vessel [44]. They first differentiated adipose-derived stem cells (ASCs) into SMCs, which were then embedded into a tubular fibrin matrix compacted in a mould to form the media layer. Then, a fibrin matrix was moulded around the media layer to mimic the adventitial layer. Finally, human umbilical vein endothelial cells (HUVECs) were seeded onto the luminal surface to cellularise the intimal layer. However, because of the static nature of the process, a non-uniform seeding of the cells was obtained, leading to an uneven cell distribution within the structure.

Another moulding technique was developed by Keita Kinoshita et al., who fabricated multilayered vascular tissue models by depositing cell layers in an agarose hydrogel mould [41]. SMCs were embedded into an agarose mould, and ECs were seeded on the lumen. This method allowed for the creation of complex-shaped constructs, but the problem of cell distribution inhomogeneity persisted.

Therefore, at the moment, it can be said that while moulding cellularised biomaterials allows for the fabrication of customised structures, challenges such as non-uniform cell distribution and gelation homogeneity need to be addressed to optimise the technique for tissue engineering applications.

### 4.3. 3D Bioprinting

The technique known as 3D bioprinting enables the fabrication of intricate and functional heterocellular structures, offering the potential for precise deposition of cells with anatomical morphology [45]. The bioink used in 3D bioprinting is represented by cell-laden hydrogels, where hydrogels serve as a scaffold to support cells. More recently, aggregates of thousands of individual cells called spheroids have emerged as a bioink for application in 3D bioprinting. Spheroids are deemed an optimal bioink since they enable cells to establish cell–cell junctions and construct their ECM [46].

In 2009, a study was conducted [47] in which an attempt was made to bioprint small-calibre vessels using spheroids of human skin fibroblasts bioprinted on agarose-based rods. The same researchers also demonstrated the construction of a vascular tube consisting of an internal layer generated from human umbilical vein SMC spheroids and an external layer obtained from human skin fibroblast spheroids.

Another research group created multicellular spheroids in 2015 [48] containing HU-VECs (40%), human aortic SMCs (10%), and human dermal fibroblasts (50%). These multicellular spheroids were inserted into a needle array where they formed tubular structures. After four days of incubation, the needle array was removed and the tubular structures were perfused within a bioreactor for another four days. These TEVGs were successfully implanted into the abdominal aorta of nude rats and remained patent until the study endpoint, postoperative day 5. Histological examination revealed post-implantation endothelialisation. Recently, the same research group introduced a method to cryopreserve spheroids using a 10% Me<sub>2</sub>SO<sub>4</sub> solution that would enable large-scale production of spheroids, increasing the potential feasibility of 3D bioprinted TEVGs for clinical use [49].

Today, various bioprinting techniques are available; however, not all of them are suitable for producing vascular tissues, comprising three different cell layers within tubular architectures. The most suitable technology is microextrusion-based bioprinting [50], a method in which a bioink containing an appropriate biomaterial and cells is loaded into a printing cartridge and extruded through a nozzle using a mechanical or pneumatic system. Microextrusion-based bioprinting offers the advantage of utilising a wide range of biomaterials and cells, which aids in replicating the complexity of vascular tissue structure.

Another technique facilitating the rapid and straightforward reconstruction of a multi-layered vascular tissue is the coaxial technique [51–53], which employs specialised coaxial nozzles. This method enables the encapsulation of one bioink within another and it is particularly useful in vascular tissue engineering for creating multiple concentric layers within a tubular structure.

A triple coaxial bioprinting technique was used to construct a biomimetic blood vessel using vascular tissue-derived extracellular matrix (VdECM) mixed with vascular smooth muscle cells (VSMCs) and alginate mixed with ECs as bioinks, to form the media and intima layers, respectively. After 3 days of static culture and 2 weeks of maturation under pulsatile stimulation, the constructs, cross-linked with a CaCl<sub>2</sub> solution, were fixed for histological analysis and good endothelialisation was demonstrated. The authors also evaluated the constructs *in vivo* using a rat model and observed that the implants remained patent for 3 weeks [52]. The triple coaxial bioprinting technique was further implemented by the same group, printing directly into a pre-gel bath containing fibroblasts [54]. In this way, the adventitia layer (which was missing in the previous system) was formed around the extruded tube.

While the coaxial extrusion technique currently stands as the most advanced method for generating vascular tissue with a three-layer structure, limitations persist concerning the dimensions and architecture of the produced vessels. These constraints primarily stem from the size of the coaxial nozzle.

## 5. Biomimicry in Scaffold Material

In recent years, research activity related to the design of scaffolds has moved in the direction of replicating the native characteristics of arteries. The development of a scaffold capable of mimicking the structure–function relationships present in the arterial wall offers significant advantages, particularly in addressing key limitations observed in current synthetic grafts, such as mechanical incompatibilities and thrombogenicity [27]. The biomimetic approach could be particularly advantageous in the engineering of small-diameter functional blood vessels. Although biomimicry is not a new concept, it has garnered considerable attention in tissue engineering in recent years. To date, synthetic and/or natural materials have been used in the literature to create double- and trilayer scaffolds [54]. However, to create a structure that closely mimics natural tissue, the use of natural materials (such as natural polymers and decellularised matrix) proves advantageous. Various multilayer approaches, which exclusively employ natural materials, and hybrid approaches that incorporate both synthetic and natural materials have been reported in the literature [27]. An overview will be provided in the next paragraphs.

### 5.1. Natural Polymers

Natural polymers, in particular ECM proteins, such as COL, fibrin, elastin, etc., have been widely investigated for the production of blood vessel scaffolds, thanks to their biocompatibility and numerous bioactive cues. These proteins offer a favourable 3D microenvironment with suitable binding sites for cellular populations, and various methods can be used for the proper production of tubular scaffolds by employing these proteins, such as electrospinning, freeze-drying, and mould casting [55–65].

Among these ECM proteins, COL has been used for decades to produce TEVGs [42,55,56,66,67]. COLs are a family of particularly abundant proteins that can be easily isolated, manipulated, and used for the production of scaffolds. COL I is the most abundant type in mammals and offers a great number of integrin-binding sites, which can control cell adhesion, differentiation, and overall cellular behaviour. Several studies have attempted to replicate the features of blood vessels through the production of scaffolds using COL, but the results were less than satisfactory due to the low mechanical properties of COL gels [55,66]. The mechanical properties of COL-based scaffolds can be improved by cross-linking. However, the use of chemical cross-linking agents, such as glutaraldehyde (GTA), while improving the mechanical properties, leads to severe cytotoxicity risks [55,66].

Alternative strategies to chemical cross-linking have been developed to enhance the poor mechanical properties of COL-based TEVGs, resulting in notable improvements in the integrity of the grafts [66–69]. Alternative methods of chemical cross-linking include physical and enzymatic approaches. UV or Gamma radiation can be used to induce cross-linking through the formation of free radicals that create covalent bonds between COL molecules. The thermal dehydration-based method involves heating COL under moisture-free conditions to promote cross-linking of the fibres. Freeze-drying followed by heating can also lead to the physical cross-linking of COL fibres, improving the mechanical stability of the material. Enzymatic methods instead involve the use of enzymes, such as transglutaminase, which catalyses the formation of covalent bonds between the amino groups and the carboxyl groups of COL molecules, creating a stable and biocompatible network, or such as Lysyl oxidase, which can be used to induce cross-linking, exploiting the natural stabilisation mechanisms of COL [66–69].

Strategies incorporating cells, matrix components, and intracellular biomolecules have also been employed to enhance the mechanical strength of COL-based constructs through the compacting and reorganisation of COL fibril architecture. Seliktar et al. [56] have shown that seeded cells and mechanical conditioning can rearrange COL fibrils circumferentially, resulting in increased strength. However, currently, the obtainable tensile strengths, burst pressures, and strength at the anastomosis of COL grafts remain much lower than those of native vessels.

Another natural polymer that has emerged as an interesting alternative to COL is fibrin, a protein produced through the cleavage of fibrinogen [70] and a rich source of growth factors, cytokines, and chemokines. Its natural role in wound healing, widespread clinical acceptance as a tissue sealant, and its potential to generate an autologous biomaterial from the patient's blood make it particularly appealing [71].

The first employments of fibrin involved the creation of coatings in COL-based vascular grafts [72]; subsequently, considerable efforts were made to develop vascular grafts based solely on fibrin [60,62]. It has been observed that these grafts require a pulsatile bioreactor system for correct maturation. Approaches involving the use of ECs and SMCs in fibrin-based vascular grafts have also been proposed [73]. Swartz et al. [61] analysed recellularised fibrin-based vascular grafts exhibiting compromised biomechanical properties, which possessed an average burst pressure of  $543 \pm 77$  mmHg, insufficient to withstand the physiological pressures of blood flow. A recent study by Yang et al. [74] demonstrated that the mechanical properties of these grafts can be improved by incorporating polycaprolactone (PCL). Electrospun hybrid PCL/fibrin vascular grafts were tested for mechanical properties, cytotoxic effects, and biocompatibility in vivo. The burst pressure of these hybrid vascular grafts was  $1811 \pm 101$  mmHg, similar to native blood vessels (2000 mmHg), and no cytotoxic effects or immune responses were reported in vivo. Furthermore, fibrin gels have been shown to stimulate SMCs to synthesise elastin, a vital component of the artery wall often overlooked in many COL-based tissue-engineered blood vessels [55].

Elastin is another interesting protein for vascular scaffold fabrication purposes, considering its role in native vessels. Elastin plays a crucial role in preserving the elasticity of blood vessels, preventing dynamic tissue creep by stretching under pressure and reverting to its original shape after the load is removed [75]. This property helps prevent permanent deformation under pulsatile flow and is advantageous for maintaining long-term compliance. Additionally, elastin exhibits anti-thrombogenic and anti-inflammatory properties, further contributing to the functionality of blood vessels. These properties are particularly essential for small-diameter TEVGs [63]. Similar to COL, elastin can enhance EC proliferation, viability, and endothelialisation of the lumen surface [76]. Besides providing cell-binding sites, elastin is also associated with activating pathways that regulate the proliferation and differentiation of vascular cells. Specifically, elastin has been shown to stimulate the gene expression of SMC markers in vitro [77,78] and it was found to modulate the phenotype of SMCs towards a contractile state [79].

The long-term failure of TEVGs is primarily linked to thrombosis, intimal hyperplasia, and aneurysm formation, which are often attributed to the scarcity of elastin.

To address the issue of constructive remodelling of implanted TEVGs, current approaches focus on incorporating elastin into the grafts before implantation. Therefore, one potential strategy is to cultivate SMCs in TEVGs to enable the synthesis of new elastin within the grafts. However, adult SMCs have limited capacity for elastin production, prompting researchers to turn to stem cell-derived SMCs which show promising improvements in tropoelastin production and assembly in response to biomechanical cues [80]. In an ideal scenario, a biodegradable TEVG would be seeded with patient-specific stem cells-derived SMCs and matured in a dynamic bioreactor environment alongside bioactive factors (transforming growth factor-beta 1 (TGF- $\beta$ 1), fibronectin, NO, miRNA-29A, and stromal vascular fraction (SVF) [65]), which stimulate the production of elastin by SMCs. This approach could produce an implantable graft with sufficient and well-organised elastin, thereby enhancing its functionality and durability in vivo. Alternative solutions involve integrating engineered elastin, such as recombinant tropoelastin and elastin-like recombinamers, into TEVGs. Another approach is to incorporate insoluble elastin extracted from native arteries into TEVGs. Utilising native decellularised vessels that maintain elastin organisation is another viable option. These strategies aim to enhance the elastin content and organisation within TEVGs, ultimately improving their performance and biocompatibility in vivo.

Natural polymers which are not derived from the ECM, such as chitosan (Ch) and silk fibroin (SF), have also found extensive use in the production of TEVGs. Systems based on

Ch and SF are characterised by easily controllable mechanical properties. Ch is a linear polysaccharide derived from the shells of shrimps and crabs and finds widespread application in tissue engineering. It has mild antibacterial properties, making it advantageous for in vivo use. In scaffold fabrication, Ch can be blended with degradable polymers like PCL and polylactic acid (PLA). In vascular graft development, electrospinning technology is used to create conduits with favourable properties for cell adhesion and proliferation. In a recent study [59], it was observed that by regulating the concentration of Ch it was possible to obtain a balance between adequate mechanical resistance to physiological stress and adequate compliance to prevent adverse hemodynamic conditions. Wang et al. realised a PCL/Ch hybrid vascular graft with anti-thrombogenic and antibacterial properties. Similarly, Yao et al. developed electrospun PCL/Ch grafts combined with heparin (Hep-PCL/Ch), enhancing patency and endothelialisation in vivo. These findings suggest the potential of Ch in crafting functional small-diameter vascular grafts (SDVGs) when combined with degradable polymers.

SF is also attractive because it is compatible with various manufacturing processes, including electrospinning, spinning and weaving techniques. Its thickness can vary greatly and it has customisable mechanical properties, a slow degradation rate, and good biocompatibility for cell infiltration. Fibroin has antithrombogenic properties and can degrade over time. Enomoto et al. [81] successfully developed fibroin-based SDVGs and compared their patency with ePTFE vascular conduits in vivo. They showed that, for over 64 weeks, fibroin-based SDVGs remained patent at a rate of 85%, while ePTFE grafts remained patent only 48% of the time. Furthermore, a greater number of SMCs and ECs were observed in fibroin-based SDVGs compared to ePTFE grafts, indicating better overall functionality of the former.

Blends of natural polymers, of both protein and polysaccharide type, can also be used to produce a scaffold more closely mimicking the composition of the natural vascular ECM, as proposed by Rosellini et al. [82]. Tubular scaffolds were produced using a specially designed mould, starting with a gelatin/gellan/elastin blend, selected to mimic the composition of the ECM of native blood vessels. Scaffolds were obtained through freeze-drying and subsequent cross-linking. Results of the in vitro characterisation showed good porosity, which could promote cell infiltration and proliferation, and a dense external surface, which could avoid bleeding. Moreover, the developed scaffolds showed good hydrophilicity, an elastic behaviour similar to natural vessels, suitability for sterilisation by an ISO-accepted treatment, and adequate suture retention strength. Additionally, the inclusion in the blend of a polysaccharide component increased the number of functional groups available for subsequent scaffold functionalisation.

## 5.2. Decellularised Tissues

Decellularisation is among the most used methods to produce vascular scaffolds. It consists of removing the totality of the cells from the tissue while maintaining its ECM intact by preserving its shape and characteristics [83]. The preservation of the natural components of vascular ECM confers a natural structure and native vessel-like mechanical properties to the resulting scaffold. Furthermore, proteins and glycosaminoglycans (GAGs) located in the natural vascular ECM provide various cell adhesion and development domains [73]. Decellularised scaffolds can be obtained from various sources, both allogeneic and xenogeneic, such as animals (e.g., porcine, sheep) or cadaver donors when effectively decellularised and used immediately. However, the use of animal-derived grafts poses challenges due to the potential immune response triggered by the presence of alpha-gal epitopes (Galalpha1-3Galbeta1-(3)4GlcNAc-R) in non-primate tissues. Efforts to mitigate this immune response include cleaving alpha-gal epitopes or using transgenic animals lacking these epitopes [84]. Cellular and antigenic material must be completely removed to avoid the risk of the immune and/or inflammatory response [27,85]. Vascular grafts have been obtained starting from various types of decellularised vessels such as carotid artery [86], aorta [87,88], internal mammary artery [89], umbilical artery [90], saphenous



vein [91], coronary artery [92], femoral vein [83], and vena cava [93]. Human-derived vascular grafts, obtained from cadaver femoral veins or umbilical vessels, have also been explored. While human umbilical arteries (hUAs) offer potential as SDVGs, challenges such as technical difficulties and lack of elasticity need to be addressed. Nonetheless, efforts to produce decellularised hUAs have shown promise, with studies demonstrating long-term patency and successful in vivo remodelling [94–96].

The protocols for vessel decellularisation include the use of chemical methods, physical methods, and enzymatic methods. For instance, surfactant detergents such as sodium dodecyl sulphate (SDS), TritonX-100 (TX) and tributylphosphate can be used, but also different types of enzymes such as DNase and trypsin. Detergents serve to remove cells from tissues through the solubilisation of the lipid bilayer of cell membranes and the dissociation of DNA from proteins [97]. On the other hand, enzymes are responsible for the proteolysis process. Trypsin acts on native COL and elastin, while nucleases, such as DNase, cleave nucleic acid sequences and can assist in the removal of nucleotides after cell lysis [97]. In addition to these agents, hypotonic and hypertonic solutions can also be utilised. Hypotonic solutions induce cell lysis through simple osmotic effects, while hypertonic saline solutions dissociate DNA from proteins [97]. For cell lysis, a freeze–thawing method can also be used, given its effectiveness in preserving the nature of ECM components (e.g., COL, elastin, and fibronectin) and the native mechanical strength when compared to detergent-based methods [98]. Nonetheless, it should be followed by further treatment since it does not allow the complete removal of all cellular components (e.g., 90% of DNA) [99]. The success of a protocol for vascular decellularisation stems from the use of adequate quantities of agents and treatment repetitions to allow the complete removal of cells without damaging or altering the ECM. The choice of the best method depends on various factors, such as original tissue thickness, cellularity, density and lipid content. Ineffective decellularisation may lead to inflammatory response and antigenicity, increasing the risk of graft failure [87]. Therefore, it is vital to adhere to specific criteria to ensure satisfactory tissue decellularisation. According to Crapo et al., decellularised tissues, including vessels, should exhibit < 50 ng dsDNA/mg ECM dry weight, <200 bp DNA fragment length, and a lack of visible nuclear material in stained tissue sections [97].

Some investigations employ physical methods alongside chemical or biological agents to enhance the penetration and efficacy of decellularisation in vascular tissue [100]. For instance, Simsa et al. examined the decellularisation of vena cava using TX-100, tri(n-butyl) phosphate (TnBP), and DNase under static, agitation, and perfusion conditions. They found that all three methods effectively reduced DNA content, with agitation and perfusion at velocities up to 100 mL/min proving optimal for promoting vessel decellularisation [93]. In their investigation, Omid et al. also combined chemical and physical decellularisation techniques on ovine coronary arteries. By inducing osmotic pressure with hypertonic/hypotonic solutions, cellular membranes were dissociated and removed effectively without the need for detergents or other chemical agents. A solution of 0.025% trypsin was then used to eliminate any remaining debris, followed by a final cleansing with 1% TX-100. Performing all decellularisation steps at 4 °C resulted in minimal damage to the ECM ultrastructure, as evidenced by similar mechanical strength and swelling ratio to native vessels, as well as robust cell attachment, migration, and proliferation observed via optical and scanning electron microscopy (SEM). Furthermore, cytotoxicity assessments via MTT assay confirmed the absence of cytotoxic effects, and the resulting biological scaffold proved to be storable at −20 °C. This decellularisation method yielded a biological scaffold with intact ultrastructure which meets both mechanical and cellular property requirements [101].

Evaluation of decellularised vascular scaffolds should also extend beyond cell removal and mechanical properties to include cytotoxicity and cytocompatibility assessment. For example, Campbell et al. decellularised porcine coronary arteries and seeded them with bovine aortic ECs and SMCs, resulting in successful cell adherence and endothelial layer formation [102]. Similarly, Lin et al. observed the adhesion and proliferation of rat ASCs

and HUVECs on decellularised arteries and demonstrated *in vivo* endothelialisation in a rat abdominal aorta repair model [92].

Lastly, to enhance scaffold success, researchers have modified decellularised vessel surfaces with biomolecules like heparin (Hep) to improve endothelialisation and prevent hyperplasia and thrombogenesis [85,88,103]. Dimitrievska et al. immobilised Hep on decellularised aorta arteries, reducing platelet adhesion and supporting HUVEC adhesion and proliferation [103].

Refinements in the decellularisation process have led to the near-complete removal of immunogenic components; however, achieving physiologically relevant mechanical properties without further processing, such as maturation through a bioreactor, remains a challenge [27]. Despite progress in decellularisation, several factors contribute to this difficulty. Firstly, there is no universal standardised protocol for decellularisation, and different methods can variably affect the structure and mechanical properties of the tissue. Additionally, cell repopulation and remodelling are complex processes that do not always succeed in fully restoring the physiological mechanical properties. Lastly, the intrinsic variability between tissue samples, due to genetic differences, age, and health status of donors, can influence the mechanical properties of decellularised tissues. Nonetheless, interesting approaches have been adopted. For instance, Gong et al. [104] adopted a unique approach by decellularising a rat aorta to preserve its histocompatibility and biomechanical properties, followed by electrospinning a circumferentially aligned layer of PCL to reinforce the decellularised vessel. The donor aortic vessels underwent decellularisation using a combination of detergents and were dehydrated through vacuum freeze-drying. PCL nanofibres were electrospun around the acellular aortic grafts to reinforce the decellularised matrix. Mechanical testing demonstrated that the addition of electrospun PCL significantly enhanced the biomechanics of the decellularised vessels. Vascular ultrasound and micro-CT angiography confirmed satisfactory patency of all grafts implanted in a rat model for up to 6 weeks. Furthermore, electrospun PCL effectively prevented vasodilation and aneurysm formation post-transplantation and reduced inflammatory cell infiltration. Building upon this work, other groups have reinforced decellularised vessels with electrospun layers, offering promising results by combining the biological advantages of natural materials with improved mechanical properties [104].

Another strategy to enhance the mechanical properties and patency of decellularised vessels involves re-cellularisation. A complete, continuous, and functional layer of ECs along the vessel wall is essential for the safe use of decellularised scaffolds in clinical applications. Thus, identifying the best cell source and the optimal recellularisation process is of great importance. The choice between *in vitro* pre-seeding and *in vivo* cell proliferation for decellularised engineered vascular grafts depends on various factors, including the efficacy of regeneration, the immune response, and the complexity of the process. *In vitro* pre-seeding offers several advantages: precise control of culture conditions, uniform distribution of cells, real-time monitoring and optimisation, and the ability to evaluate tissue functionality before implantation. However, it is a complex procedure involving a greater risk of contamination and longer preparation times. Conversely, *in vivo* cell proliferation is simpler and less expensive, with reduced risks of contamination and a natural regeneration response. Nevertheless, it offers less control over environmental conditions, potentially adverse immune responses, and longer, less predictable regeneration times [83,91]. *In vivo* performance studies have shown that, while decellularised vascular grafts lack proper function and are prone to thrombus formation and graft failure, cellularised engineered grafts exhibit improved properties, including a lower risk of thrombus formation and rejection. Recellularised TEVGs with uniform coverage of ECs and VSMCs offer superior outcomes compared to non-cellularised grafts [27,83,105]. Various cell types, including peripheral blood mononuclear cells, ECs, and endothelial progenitor cells (EPCs), have been used for reseeded to promote patency. In a particularly promising study, pre-seeding resulted in 100% patency after 30 days of implantation [105]. However, long-term patency studies exceeding one year are lacking.

Despite advances in decellularisation, mechanical reinforcement strategies, and cell reseeded, the clinical use of decellularised vessels remains limited by several factors. Batch-to-batch variability in mechanical, biochemical, and biological properties—influenced by donor age, health status, and manufacturing processes—poses a significant challenge [104–107]. One issue with using decellularised vessels is the potential for limited recellularisation in living organisms, possibly due to the vessel wall's dense ECM or chemical damage to the ECM during the decellularisation process. The limited success of currently available commercial decellularised grafts can be partly attributed to their lack of cellularity upon implantation. A functional endothelium, which is essential to prevent thrombosis in smaller calibre vessel grafts, is particularly important for decellularised grafts with their exposed COL luminal surface [83]. While studies have shown promising patency rates for implanted decellularised vessels, they have not demonstrated superiority over synthetic grafts [5,6,104,108]. Thus, further research is needed to address these limitations and optimise the clinical utility of decellularised vessels.

## 6. Biomimicry in Scaffold Architecture

An ideal TEVG is biocompatible, matches the mechanical properties of native vessels, and promotes endothelialisation and tissue integration. Mimicking the structure of native arteries, with layers such as tunica intima, tunica media, and adventitia, is crucial for functional replication. Various techniques, including electrospinning, self-assembly, and 3D bioprinting, have been explored for TEVG fabrication. However, the challenge remains in replicating the intricate structure of the native ECM, which is pivotal for functional tissue regeneration [100,109,110].

Electrospinning offers a method to fabricate fibrous scaffolds with controlled architecture and mechanical properties resembling the native ECM. These scaffolds provide a high surface-to-volume ratio and adjustable porosity, promoting cell adhesion and angiogenesis [111]. Multilayered scaffold designs aim to mimic the hierarchical organisation of blood vessel walls and incorporate various materials or functionalities to control cell behaviour and tissue development [27,110]. Additive manufacturing technologies such as 3D printing allow precise control over the geometry of the scaffold and the distribution of bioactive components, facilitating cellular organisation, vascular network formation, and tissue maturation [110]. Furthermore, the design of TEVGs must consider the microstructure of native arteries, incorporating suitable porosity and pore sizes to facilitate cell migration and metabolic exchange. Bioprinting technologies, including extrusion and light-based approaches, offer the possibility to fabricate complex, patient-specific tubular structures with high precision and reproducibility, enhancing the translatability of TEVGs to clinical settings [27,100,110].

In summary, the quest for small-calibre vascular grafts has spurred innovative methodologies in tissue engineering, driven by the need for alternatives to autologous grafts with improved patency rates and reduced complications. Mimicking the complex structure and function of native vessels remains a key challenge in TEVG development, emphasising the importance of biomimetic approaches and advanced scaffold design techniques.

### 6.1. Fibre-Based Scaffolds

Fibre-based scaffolds fabricated through electrospinning techniques have garnered significant attention in the field of vascular tissue engineering due to their ability to mimic the intricate structure of native ECM. It is important to evaluate the technical intricacies of controlling topological fibre arrangement in electrospun tubular scaffolds tailored for vascular applications. Processing parameters such as applied voltage, feed rate, needle-to-collector distance, and mandrel rotation speed affect the final properties of the scaffold [100]. In addition, it is important to consider not only the technical aspects of scaffold fabrication but also the functional requirements for the production of effective tissue-related constructs. The microstructural requirements, including porosity, pore size, and interconnectivity, are crucial in facilitating cell movement and metabolic sharing, which are critical for tissue

integration. Electrospinning emerges as a promising technique for precisely controlling the microstructure of scaffolds, particularly by regulating pore size and fibre alignment, which are critical for promoting tissue healing and integration after implantation. Electrospinning provides precise control over fibre diameters (50–500 nm) and mimics the ECM architecture of natural blood vessels. Challenges include poor cell penetration, surface properties that affect viability, and difficulties in regulating mechanical properties [100,109].

In recent years, significant progress has been made with electrospun vascular grafts (ESVGs). They have evolved from single-layer, single-component structures to multi-layer, multi-component designs. These grafts can be produced by spinning fibres onto a rotating mandrel or by forming a sheet that is subsequently rolled up. The production of tissue-engineered blood vessels by electrospinning may involve the use of a single polymer or a polymer mix, the use of two different polymers by a co-electrospinning process, or the use of two materials electrospun through coaxial systems [112]. Figure 2 illustrates the electrospinning technique and possible variations in the setup to fabricate tissue-engineered blood vessels.

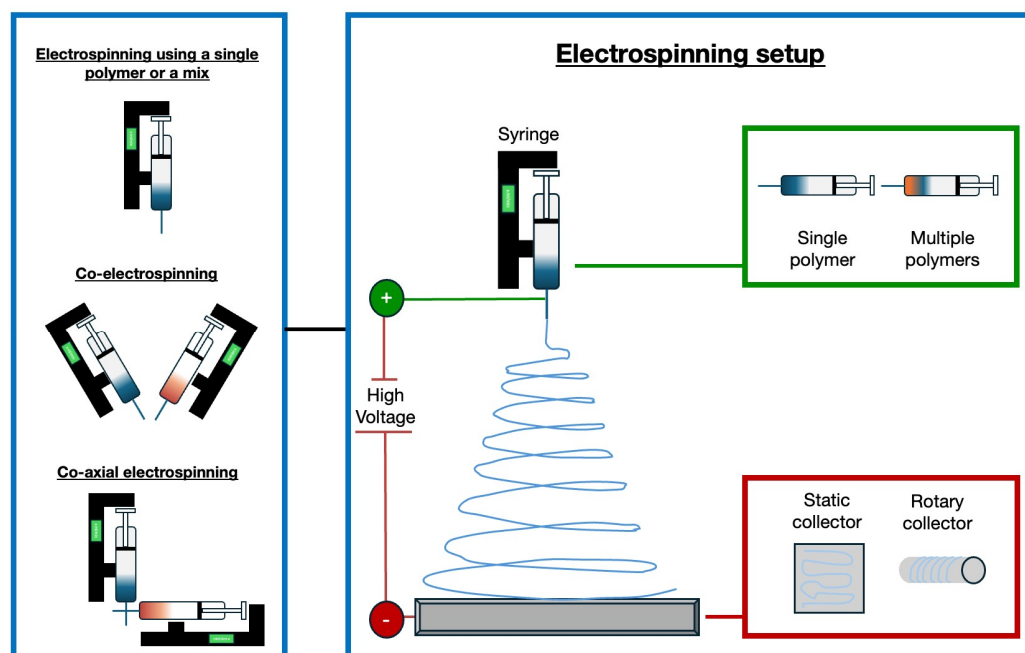


**Figure 2.** Experimental set-up for the production of tissue-engineered blood vessels using electrospinning. Various approaches are employed: a single polymer or a blend of polymers can be dispensed from a single syringe, or two distinct polymer filaments can be electrospun simultaneously using the co-electrospinning technique [113]. Coaxial needles are utilised to enable the electrospinning of two different materials via the co-axial electrospinning method, resulting in the formation of core-shell filaments. Different types of collectors can be used for the deposition of fibres, including static and rotating collectors [114].

The most investigated materials to produce vascular scaffolds by electrospinning include gelatin (Gt) [115] and PCL, among synthetic components [116].

For example, Kong et al. [113] developed biomimetic Gt/PCL composite nanofibres containing different amounts of chondroitin sulfate (CS) via electrospinning technology. All solutions were electrospun at room temperature and controlled humidity. The resulting nanofibres exhibited suitable porosity (~80%) and could absorb PBS solution up to 650%. Composite nanofibres of Gt/PCL with a specific proportion of CS demonstrated reduced thrombogenicity and enhanced EC response, suggesting their potential as a scaffold for tissue engineering in blood vessel repair and regeneration.

Elsayed et al. [114] developed a new approach for creating electrospun Gt fibre scaffolds, with a precisely controlled fibre orientation and optimised Gt cross-linking, to achieve

not only compliance equivalence with the coronary artery but also resistance equivalence of the wet tubular acellular scaffold (swollen with absorbed water) to that of the tunica media of coronary artery in both circumferential and axial directions. Solutions containing Gt type A in 2,2,2-Trifluoroethanol (TFE) were electrospun. To create scaffolds with multi-layer fibre alignment at  $\pm 45$  degrees, spinning occurred for 4 min before pausing to flip the collector by 180 degrees. Most importantly, this study represents the first case of high suture retention strength among natural scaffolds and, in particular, among Gt scaffolds. Suture retention strength in the range of 1.8–1.94 N was achieved for wet acellular scaffolds, which is equal to or better than that of a saphenous vein. The produced scaffolds showed exceptional efficacy in promoting human SMC proliferation. SMCs seeded onto the upper surface adhered, elongated, and aligned with nearby fibres, aiding their migration throughout the scaffold thickness.

Another interesting study in which, through the electrospinning technique, nanofibrous tubular scaffolds were obtained was presented by Zhu et al. [117]. They proposed a polyurethane/Gt nanofibrous tubular scaffold, obtained through electrospinning and Hep grafting, which demonstrated improved hydrophilicity, adequate mechanical properties, and enhanced blood compatibility. In vivo studies confirmed that the obtained nanofibrous tubular scaffolds effectively promoted vessel regeneration, closely mimicking natural vessels, thereby holding significant potential for the developed biodegradable composite vascular grafts to prevent intimal hyperplasia and acute thrombosis.

Various studies in the field of tissue engineering depict electrospinning as a powerful technique to produce tailored scaffolds for the tissue engineering of blood vessels, offering precise control over structure and alignment and enhancing their efficacy in promoting vascular regeneration. In particular, thanks to its versatility, electrospinning has also been largely investigated to produce two-layer and three-layer scaffolds, mimicking the multilayer architecture of native vessels, which will be further discussed in the next two sections.

## 6.2. Two-Layer Scaffolds

While various techniques, including cell sheets and synthetic or natural biomaterial platforms, have been explored, scaffold-based methods stand out due to their versatility and the abundance of usable synthetic and natural polymers. Biomimicry, and particularly structural biomimicry, plays a significant role in this domain, aiming to replicate the structure–function relationships of natural tissues. The multi-layered scaffold approach represents a solution to mitigate the primary shortcomings of existing synthetic grafts, namely, their mechanical incompatibility and propensity for thrombosis [100].

The first attempts in this direction are represented by the development of bi-layer scaffolds, obtained from both synthetic and natural materials [6,27,109–112].

While scaffolds made entirely of natural materials are rare due to their lack of mechanical strength, silk stands out as an exception. Liu et al. [118] demonstrated the potential of silk-based scaffolds, utilising heparinised braided silk tubes as a non-thrombogenic solid inner layer, complemented by an SF microporous sponge cast through lyophilisation as the outer layer. Compared with previously fabricated silk-based vascular scaffolds, the fibre reinforcement provided a comparable or higher mechanical strength, burst pressure, and suture retention strength, as well as mechanical compliance, to saphenous veins for vascular grafts. Additionally, the silk-based scaffold displayed promising hemocompatibility and biocompatibility in preliminary in vitro assessments [118].

Hybrid scaffolds, integrating ECM proteins with synthetic materials, have also been developed to enhance the biological activity of scaffolds for vascular tissue engineering. For instance, Goins et al. created non-thrombogenic inner lumens using a solid polymer film of poly(1,8 octanediol-co-citrate) (POC) and electrospun polymeric blends of POC, COL, and elastin as outer layers, aiming to leverage the inherent material properties for enhanced functionality [100,118].

In another work, Li et al. [119] proposed a dual-oriented/bilayered electrospun scaffold based on the use of a mixture of PCL, poly(D,L-lactide-co-glycolide) (PLGA), and Gt. An electrospinning system with a high-voltage power supply, a micropump, and a rotating stainless steel drum collector (diameter = 10 cm, speed 2500 r/m) was used to fabricate the scaffold. The resulting nanofibre sheet was then cut into a rectangle, with the fibres aligned along the longer side, and curled around a stainless-steel cylindrical roller (diameter = 5 mm). The junction was bonded with an aqueous solution of Gt. The outer layer was then electrospun onto the stainless-steel roller. This process resulted in a vascular scaffold with 7 cm length and 5 mm diameter. The morphology of all nanofibres obtained was fine and smooth and the diameter of the nanofibres in the inner and outer layers was  $609 \pm 251$  nm and  $657 \pm 220$  nm, respectively. In addition, the average pore sizes of the inner and outer layers were measured to be  $55.2 \pm 32.1 \mu\text{m}^2$  and  $52.9 \pm 35.3 \mu\text{m}^2$ , respectively. The ultimate tensile stress of the dual-oriented/bilayered scaffold was  $2.04 \pm 0.15$  MPa, while the elongation at break was  $342.48 \pm 4.13\%$ . These values were also higher than those obtained for pure PLGA and Gt scaffolds. All these results indicated that the dual-oriented and bilayered scaffold had excellent mechanical properties, and the bursting pressure in the dry state was consistent with the systolic and diastolic pressure of a natural blood vessel. The results of the biological characterisation showed that the mixed scaffold had excellent biocompatibility and could promote the proliferation of both SMCs and ECs.

In addition to material selection, scaffold design plays a crucial role [100]. Simultaneous seeding of ECs and SMCs can mitigate thrombogenicity issues and aid in tissue remodelling. Structurally, scaffolds with porous outer layers for cellular infiltration and solid inner layers for EC attachment have shown promise in creating non-thrombogenic barriers [109]. Alternatively, scaffolds with porous outer and inner layers, resembling the arterial wall's morphology and mechanics, have been fabricated to promote desirable EC and SMC functions, although these require additional steps to address thrombogenicity issues [110]. Fabrication techniques influence scaffold properties, with particulate leaching allowing for controlled pore size, while electrospinning produces nanosized pores resembling the arterial wall's fibrous layers. Porosity size considerations are vital, varying by layer to accommodate cell size differences and prevent leakage or pressure drops during remodelling [120].

In the quest for fabricating biomimetic bilayered vascular scaffolds, researchers have explored innovative methods. First, Zhou et al. [116] employed an advanced coaxial 3D-bioplotter platform to create tunable vessels for small-diameter blood vessel replacements. Their method involved the simultaneous deposition of two types of bioinks containing methacrylated gelatin (GelMA), poly(ethylene glycol) diacrylate (PEGDA), alginate, and alginate lyase, cross-linked under UV light. VSMCs and vascular endothelial cells (VECs) were precisely seeded in the outer layer and lumen, respectively. Post-printing, vessels were cross-linked and the sacrificial inner core material was leached out, resulting in a hollow core structure. These vessels exhibited robustness, perfusability, and porous structures conducive to nutrient exchange and cell proliferation. Notably, VSMCs demonstrated uniform distribution and proliferation, with vessels containing alginate lyase showing faster proliferation. Viability assays confirmed high VSMC viability over time.

Meanwhile, Nguyen et al. [64] pioneered an electrochemical fabrication method to develop biomimetic bi-layered COL scaffolds incorporating insoluble elastin. The process involved creating a COL lumen via self-assembly triggered by an electric field and synthesising COL-elastin fibres through isoelectric focusing. Optimisation of electrochemical parameters ensured the formation of a compact, smooth, and bubble-free COL lumen, which is crucial for scaffold integrity. Mechanical testing revealed that circumferentially oriented COL-elastin fibres significantly enhanced scaffold mechanics, indicating their robustness and ability to withstand physiological forces. Furthermore, the scaffolds supported the expression of functional markers by ECs on the luminal surface, which is crucial for preventing thrombosis and promoting vascularisation.



Recent examples of bi-layer design have led to some interesting results and significant advancements towards clinically relevant tissue-engineered vascular substitutes. Wang et al. [121] designed a bilayer vascular scaffold to facilitate in situ rapid endothelialisation and the alignment and infiltration of SMCs (Figure 3). The inner layer of the scaffold, made of electrospun poly(L-lactide-co-caprolactone) and COL (PLCL/COL) nanofibre, was loaded with Hep and vascular endothelial growth factors (VEGF), while the outer layer consisted of circumferentially aligned PLCL/COL nanofibre yarns loaded with platelet-derived growth factors (PDGFs) increasing in concentration from the outermost to the interior of the scaffold. The fabrication process involved coaxial electrospinning to create the inner layer and a modified setup integrating coaxial with conjugated electrospinning for the outer layer. The vascular scaffold was crosslinked using GTA vapours. The compliance of the vascular scaffold resulted comparable to that of a human saphenous vein (0.7–1.5%/100 mmHg) and superior to that of a commercial e-PTFE graft (0.1%/100 mmHg). The controlled release of VEGF and PDGF from the scaffold was investigated, with VEGF showing a continuous greater release percentage (ca. 15%) relative to PDGF over almost one month in vitro. The scaffold exhibited promising biological performance, with rapid endothelialisation observed at the luminal surface and oriented smooth muscles infiltrating inside the vascular wall at two months post-implantation in a rat abdominal aorta defect model. COL-rich connective tissues were produced at the outermost layer of the vascular scaffold, indicating its potential for in situ vascular repair or regeneration [121].

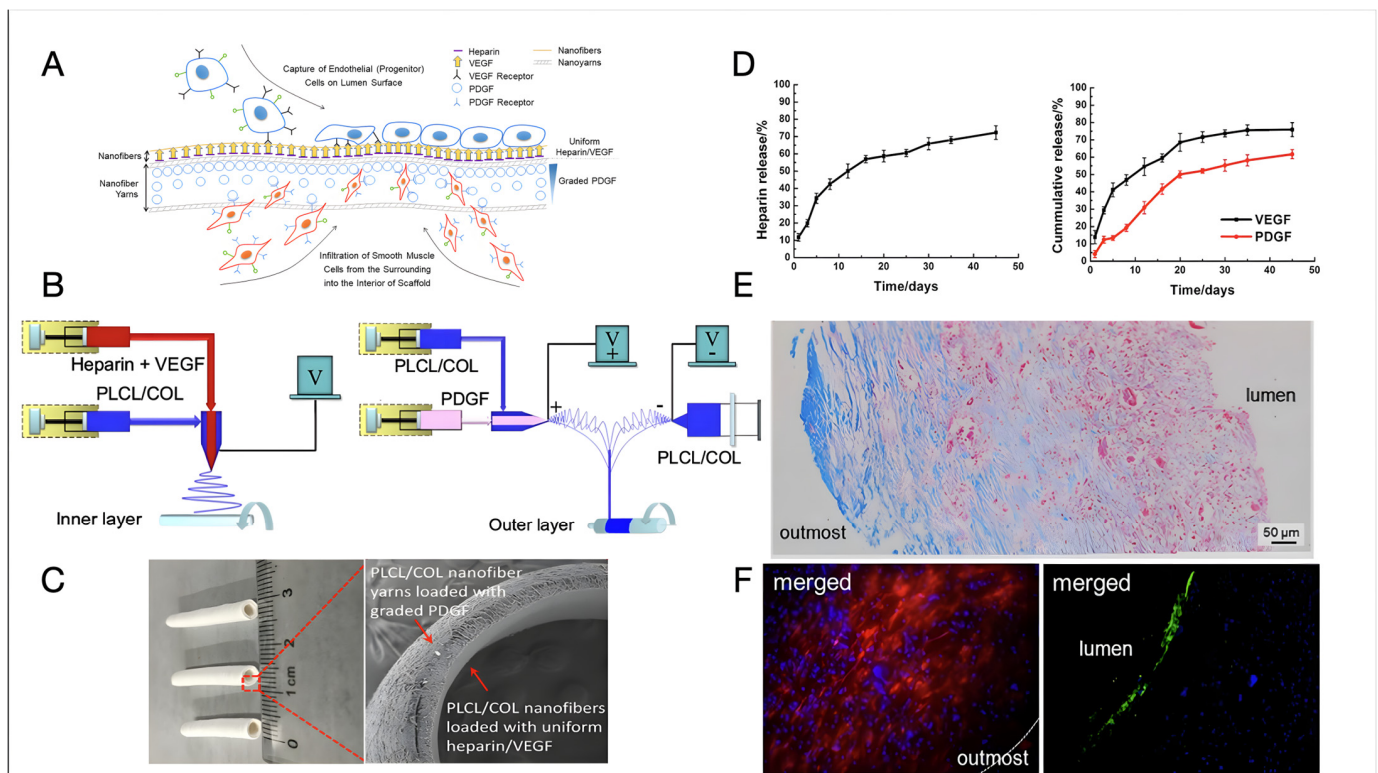


**Figure 3.** The design and fabrication of a bilayer vascular scaffold with spatially controlled release of growth factors from Wang et al. [121]. (A) A diagram depicting how the bilayer vascular scaffold should foster in situ tissue regeneration by capturing EPCs on the surface and allowing SMCs to infiltrate. Hep release is used to prevent early thrombus formation, while VEGF boosts endothelialisation and PDGF to facilitate SMC infiltration. (B) A schematic depiction of how the bilayer vascular scaffold was created using coaxial and conjugated electrospinning techniques. (C) A photograph displaying a sample of a vascular scaffold measuring 2 mm in inner diameter and 1 mm in thickness with SEM images illustrating its cross-section. (D) Graphs displaying the cumulative release of Hep (left), VEGF,

and PDGF (right) from the vascular scaffold after incubation in a PBS solution on a horizontal shaker at 37 °C and 120 rpm for 45 days. (E) Microscopic images illustrating cross-sections of the bilayer vascular scaffold stained with Masson's trichrome after being implanted in a rat abdominal aorta for two months. (F) Fluorescence micrographs depicting the vascular scaffold after immunohistochemical staining of DAPI and CD31 (lumen), and DAPI and  $\alpha$ -SMA (outmost) following 2-month implantation in a rat abdominal aortic defect model. Open access article distributed under the CC BY-NC-ND license.

More recently, a scaffold reproducing the endothelial and media layers of blood vessels was developed by Ding et al. [122], using a combination of beta-sheet-rich silk nanofibers (BSN) and poly(vinyl alcohol) (PVA). BSN and PVA were blended in an aqueous solution and processed using a tubular electrode to form tubular scaffolds composed of circumferentially and axially oriented BSN near the positive electrode and non-crosslinked PVA. This step was followed by the crystallisation of PVA obtained by freeze–thawing, with the aim of providing mechanical strength to the construct without altering the aligned morphology of BSN. The obtained scaffold morphology effectively replicated the structural characteristics of the vascular intima and media layers. The crystallised PVA provided the scaffolds with suitable mechanical properties, including adequate suture retention strength. Compared to homogeneous scaffolds, the preferential alignment of smooth muscle and ECs induced by the developed scaffolds led to improved cell adhesion and proliferation, along with enhanced expression of various cytokines. In vivo studies demonstrated that endothelial layers form within four weeks of implantation, ensuring sustained patency. Furthermore, after eight months post-implantation, both endothelial and smooth muscle layers were regenerated, creating hierarchical microstructures and compositions that closely resemble native vessels.

While the bilayer approach offers benefits in terms of tissue organisation, culture time can be inhibitory, and addressing concerns regarding cellular infiltration and nutrient delivery to the scaffold central portion is essential. Additionally, comprehensive studies assessing mechanical properties, degradation, and in vivo performance are imperative for the clinical translation of scaffold-based vascular tissue engineering [109].

### 6.3. Three-Layer Scaffolds

Three-layer scaffolds represent the most closely biomimetic approach in vascular tissue engineering. The simulation of three-layer structures enables the acquisition of grafts that closely mimic the anatomy and dynamics of blood vessels (Figure 4). Consequently, there is an escalating inclination towards the investigation of tissue engineering methodologies aimed at replicating the three distinct anatomical layers [123,124].

Natural trilayer scaffolds, such as those utilising GelMA and alginate, have been developed through layer-by-layer deposition techniques [125]. Incorporating ECs within the intimal layer was shown to enhance endothelialisation, a crucial aspect of scaffold success. Similarly, hybrid scaffolds combining synthetic and natural materials have capitalised on the mechanical and biological advantages of each component. For instance, blending COL and elastin with synthetic polymers like PCL yielded compositionally mimetic layers with improved mechanical properties [126]. Research efforts have also explored various combinations of synthetic and natural polymers to fabricate tri-layer scaffolds with desirable mechanical and biological properties. These efforts include electrospinning techniques and the incorporation of COL, SF, or Ch into different scaffold layers [127]. In vivo assessments have demonstrated promising outcomes, including neovascularisation and cellular remodelling, suggesting the efficacy of COL-containing scaffolds in promoting regeneration [27].

The versatility of synthetic and natural polymers offers numerous possibilities for fabricating complex scaffold morphologies that mimic native ECM structures. However, the successful engineering of multi-layer scaffolds for small-diameter vessel applications necessitates careful consideration of design parameters and fabrication techniques, to ensure optimal performance and functionality.

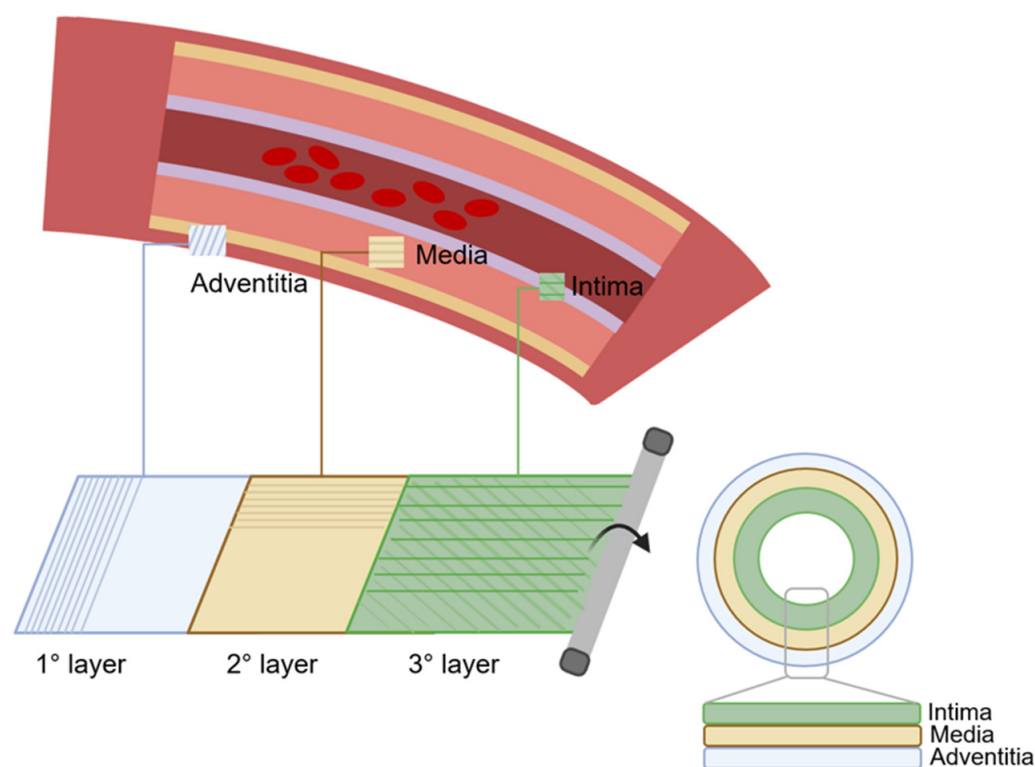


**Figure 4.** The preparation process of TEVGs using the three-layer technique. First, the outer layer is prepared, which corresponds to the tunica adventitia, then the second layer is prepared, which corresponds to the tunica media, and finally the third, which corresponds to the tunica intima. TEVG is obtained by rolling manipulation of the three layers.

Guo et al. proposed the construction of a biomimetic three-layer vascular scaffold with spatial alignment features, based on a blend of Gt, PCL, and PLGA [124]. A general strategy involving sequential electrospinning combined with folding and rolling manipulation was employed to achieve this. The resulting scaffold possessed three layers with inner and middle layers arranged perpendicular to each other, closely resembling the multi-layer structure of natural blood vessels. This architecture was branded essential to obtain integrated vascular remodelling and regeneration, facilitating spatial arrangement guidance for corresponding cells. Specifically, the inner layer promoted EC adhesion and proliferation, while the middle layer allowed for VSMC penetration. The outer layer provided mechanical support and biocompatibility. The sequential electrospinning process, combined with folding and rolling manipulations, ensured the formation of distinct layers with different fibrous arrangements and laminated structures.

Wu et al. [36] devised a novel tri-layer tubular graft composed of PLCL/COL fibres and PLGA/SF yarns using a three-step electrospinning approach. The graft had an inner layer of axially aligned PLCL/COL fibres, a middle layer of PLGA/SF yarns, and an outer layer of random PLCL/COL fibres. In the fabrication process, the axially aligned PLCL/COL fibres were first produced using a customised rotating collector under a magnetic field. Subsequently, PLGA/SF yarns were prepared via electrospinning with a double-nozzle system and twined onto the inner layer in a circumferential orientation. Finally, a layer of random PLCL/COL fibres was added on top to fix the entire structure in position. The obtained graft showed dense fibres on the inner and outer surfaces and a loose yarn structure in the middle layer. Mechanical testing revealed favourable tensile properties for each layer, with the inner layer providing structural support, the middle layer facilitating cell infiltration, and the outer layer fixing the yarns.

An important and often overlooked factor to consider when designing a blood vessel replacement is the discrepancy in compliance between the host vessel and the artificial

vascular graft at the site of anastomosis. Compliance, in the context of vascular structures, refers to the dimensional alteration of a tube in response to changes in intraluminal pressure. This misalignment of compliance induces haemodynamic flow disturbances within the vascular graft and concentrates stress on the anastomotic junction. As a result, pressure changes at the anastomosis can lead to intimal hyperplasia and thrombosis [128,129]. To obtain grafts with adequate compliance, it is necessary to replicate the biomechanical characteristics of native blood vessels, and, in their study, Zhang et al. worked on making grafts that could meet this need [123]. They developed a three-layered vascular graft utilising a combination of electrospinning and braiding techniques, mimicking the structure of human blood vessels. The scaffold consisted of three distinct layers: intima, media, and adventitia. The intima and media layers were formed by electrospinning SF and PLCL, with varying ratios to match native tissue properties. The outer adventitia layer was braided using SF yarns to enhance durability against high pressures. Mechanical properties, including Young's modulus and compliance, closely resembled those of natural blood vessels. Dynamic compliance values exhibited superior performance compared to synthetic Dacron grafts, with attained values indicating the compliance of the graft equivalent to that of the human saphenous vein. In vitro studies demonstrated cytocompatibility of the intima and media layers with ECs and SMCs, respectively.

The exploration of three-layered scaffolds for tissue engineering of blood vessels demonstrates significant promise in mimicking native vascular architecture; however, the current literature underscores not only the strengths but also the limitations. The versatility of these scaffolds allows for the replication of intricate vascular structures, fostering cellular infiltration and promoting tissue regeneration. However, challenges remain in achieving precise control over scaffold properties to replicate the dynamic mechanical behaviour and biochemical cues of natural vessels. Addressing these hurdles through continued research efforts holds the key to advancing the field of biomimetic scaffold architecture in vascular tissue engineering [9,27].

#### 6.4. 3D Printed Scaffolds

In recent years, 3D printing technology has revolutionised various fields, including tissue engineering. Specifically, 3D printing techniques enable the fabrication of complex structures using a range of polymers, including both synthetic and naturally derived materials. This technology has been instrumental in producing transplantable scaffolds and tissues, with inkjet, extrusion, and laser-assisted printing being the primary approaches used (Figure 5). Notably, 3D printing has facilitated the creation of SDVGs through innovative ink formulations and printing techniques [110].

Three-dimensional printing can produce two types of SDVGs: acellular or cellularised. Acellular SDVGs are vascular grafts that do not contain living cells, these grafts can serve as scaffolds for tissue regeneration, providing structural support and guiding the growth of new tissue. In contrast, cellularised SDVGs contain living cells within the scaffold structure and are produced by 3D bioprinting. Cellularised grafts have the potential to integrate seamlessly with patient tissues, promoting faster healing and potentially better long-term functionality [110]. Figure 5 shows the basic elements of the 3D printing technique for the fabrication of both acellular and cellularised SDVGs.

Using an advanced coaxial 3D bioplotter platform, Zhou et al. created biomimetic small-diameter blood vessels with two distinct cell layers [131]. A bioink made of VSMCs laden in GelMA/polyethylene(glycol)diacrylate and alginate lyase was used to fabricate the vessel wall, using a 3D extrusion-based bioprinter with a coaxial needle extrusion system. The presence of the coaxial needle enabled the simultaneous extrusion of two materials, one being the bioink and the other being Pluronic 127, which was used as a sacrificial material for supporting construction and then removed to generate a lumen structure. VECs were then seeded in the lumen, forming the inner layer of the vascular matrix. Since the space for the growth of the loaded cells was limited, lyase was introduced into the bioink to gradually degrade the alginate in the scaffold matrix. This special design favoured

nutrient exchange with the environment while leaving more space for cell proliferation in the matrix. The obtained vessel exhibited significant perfusable properties under different conditions of flow velocity, flow viscosity, and temperature. The loaded VSMCs grew faster in the lyase group than in the group without lyase. After seeding the VECs, both the VSMCs in the matrix and the VECs in the lumen continued to grow steadily over time. This novel bioprinted blood vessel with biomimetic EC and SMC layers represents a potential candidate for the future replacement of small-diameter blood vessels.

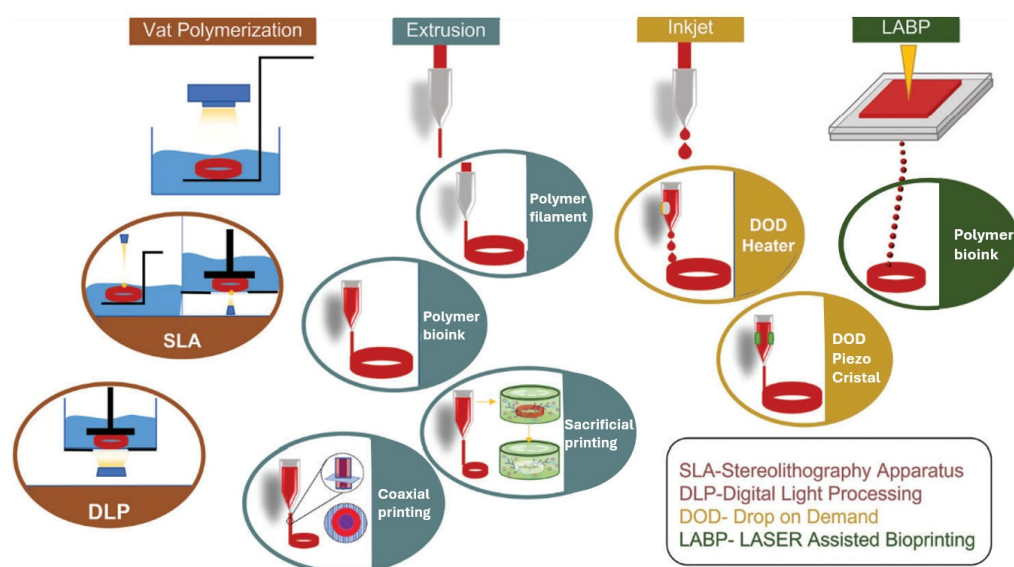


**Figure 5.** Different types of 3D bioprinting techniques employed for the generation of vascular grafts [130]. Open access article under the terms of the Creative Commons Attribution-NonCommercial License.

In addition to 3D printing, the emergence of 4D printing represents a significant advance in tissue engineering (Figure 6). In contrast to traditional 3D printing, a fourth dimension, time, is included, and it stems from materials that can transform in response to external stimuli such as pH, temperature, light, or humidity [110]. These “smart” materials dynamically change their shape and properties, enabling improved functionality in tissue engineering scaffolds [110]. Materials used in 4D printing include thermoresponsive polymers, pH-responsive polymers, and photoresponsive materials. Hydrogels are the predominant water-responsive material, while polyelectrolytes respond to electric fields, and magnetic nanoparticles respond to magnetic fields. Polymers such as COL and keratin respond to pH by changing the conformation of the polymer chain from a spherical to a coiled shape [130]. The potential applications of 4D printing are manifold. These include the development of vascular grafts that can adapt to changes in the body’s environment. A 4D-printed vascular graft could, for example, react to fluctuations in pH or temperature in the vascular system and possibly release therapeutic agents or adapt its shape accordingly. Although the field of “smart” materials in vascular engineering is still in its early stages, ongoing research ensures the development of advanced vascular grafts capable of recognising and responding to changes in the state of the human body [130].



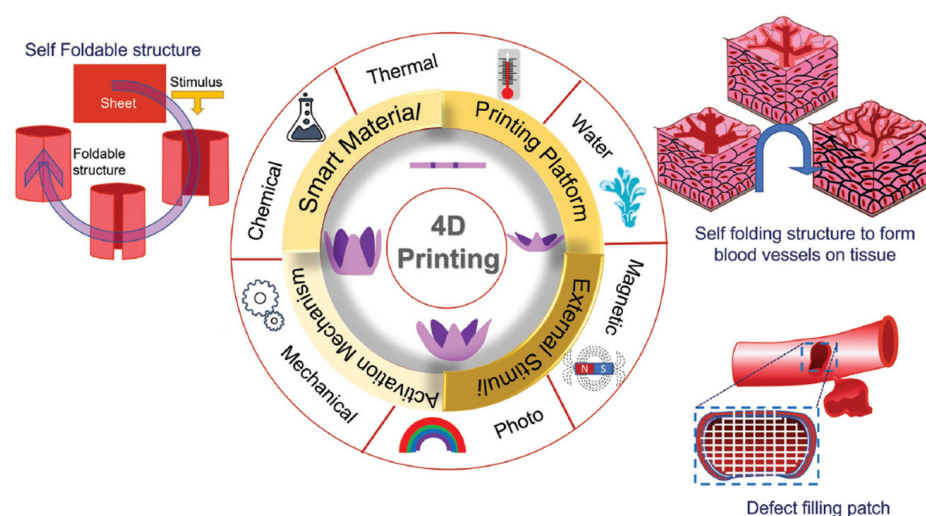


**Figure 6.** Main aspects of 4D printing and the application of 4D bioprinting in tissue engineering of blood vessels [130]. Open access article under the terms of the Creative Commons Attribution-NonCommercial License.

## 7. Biomimicry in Scaffold Functionalisation

### 7.1. Surface Modification for Antithrombogenicity

The continuous endothelium of native blood vessels, composed of a monolayer of ECs, serves to prevent blood coagulation and regulate vascular tone through the synthesis and regulation of various bioactive molecules. Damage to the endothelium exposes blood to underlying ECM proteins, facilitating platelet adhesion and initiating the blood coagulation cascade. Therefore, incorporating natural anticoagulant molecules into TEVGs represents a fundamental strategy to mitigate acute thrombosis.

Notably, Hep, a naturally occurring polysaccharide, has been extensively utilised in clinical settings as an anticoagulant molecule. For example, Zhang et al. developed a three-layered vascular graft by electrospinning and functionalised the inner layer by Hep immobilisation through EDC/NHS chemistry [123]. The successful immobilisation of Hep on the scaffold was verified by toluidine blue staining. The hemocompatibility of heparinised scaffolds was then investigated by measurement of blood coagulation time, in vitro blood coagulation tests, and quantification of platelet adhesion. Prothrombin time and activated partial thromboplastin activity time were measured after incubation of both heparinised and non-heparinised scaffolds in human plasma solution, and the results were significantly higher for the heparinised ones. Additionally, Hep functionalisation of the scaffolds demonstrated enhanced anticoagulant properties following incubation in whole blood. Moreover, both platelet adhesion and platelet activation were reduced on the Hep-functionalised scaffolds.

Hep was also used to develop a biomimetic surface with anticoagulant properties to mitigate thrombus formation in the work published by Zhu et al. [117]. Poly(ester-urethane)urea/Gt nanofibrous tubular scaffolds were fabricated by electrospinning and then modified by Hep grafting through EDC/NHS chemistry. The resulting tubular scaffold exhibited improved blood compatibility in terms of both low hemolysis and low platelet adhesion. Additionally, the presence of Hep on the fibre surface enhanced EC proliferation at 7 days after seeding. In vivo studies further confirmed that the Hep-modified nanofibrous tubular scaffolds favoured long-term patency.

In another study, Gong et al. developed hybrid TEVGs by combining synthetic polymers with naturally decellularised small-diameter vessels [104,132]. The intimal surfaces of the hybrid SDVGs were coated with Hep before allograft transplantation to resist platelet aggregation and inhibit thrombosis. The effects of Hep functionalisation on platelet adhesion were investigated first by a platelet adhesion test with microscope observation and then by quantification of lactate dehydrogenase activity. Both tests showed that Hep



modification significantly reduced the number of adhered platelets. Evaluation through vascular ultrasound and micro-CT angiography demonstrated satisfactory patency of all grafts implanted in a rat model for up to 6 weeks.

As Hep has a short *in vivo* half-life, researchers are looking into Hep-mimetic sulfated GAG and sulfonated polymers which are highly stable and possess Hep-like properties. In a work published by Kong et al. [113], nanofibres composed of a biomimetic blend of Gt and PCL incorporating varying amounts of CS were fabricated using electrospinning technology to examine their impact on antithrombogenicity and affinity towards ECs. In recent studies, CS was identified as a sulfated polysaccharide consisting of GAG and galactosamine. It was shown to exhibit strong adhesion to ECs while maintaining weak interactions with proteins and platelets, along with electrostatic repulsion of negatively charged blood components [133–135]. Moreover, CS was proven to inhibit cellular apoptosis and promote the healing process of vascular wounds [136,137]. The inclusion of different concentrations of CS in the nanofibres influenced their morphology and diameter. Moreover, the incorporation of CS into the nanofibres significantly improved their anticoagulant properties, extending their coagulation time, and promoting cell responses. Notably, nanofibres containing 10% CS demonstrated favourable outcomes in terms of cell attachment, elongation, and proliferation.

Alternatively, platelet adhesion can be avoided through the design of an anti-thrombogenic surface on the internal lumen of blood vessel scaffolds, replicating the continuous GAG layer present on ECs in native vessels. In this regard, a modification with hyaluronic acid on the internal surface of decellularised TEVGs has been investigated by Dimitrievska et al. to effectively shield blood platelets from activation triggered by COL [103]. By utilising the amine groups present on 4 mm diameter decellularised scaffolds a continuous hyaluronic acid hydrogel coating was constructed using a bifunctional thiol-reactive cross-linker, thus avoiding nonspecific COL matrix cross-linking. The hydrogel layer served to recreate a luminal wall, concealing exposed COL from direct contact with the bloodstream. *In vitro* blood tests demonstrated significantly lower levels of adhered platelets, fibrinogen absorption, and fibrin formation on the hyaluronic acid-coated decellularised scaffolds compared to the uncoated ones. Moreover, the hyaluronic acid surface exhibited inhibition of macrophage adhesion *in vitro*. Notably, *in vivo* experiments showed protection from aggressive thrombus formation, preservation of normal blood flow, and re-endothelialisation was also observed.

Another option to prevent acute thrombosis is represented by the immobilisation of NO. In native vessels, ECs are in contact with circulating blood and are subjected to continuous shear stress, which triggers the release of NO through the upregulation of endothelial NO synthase. This process results in vasodilation and suppresses platelet aggregation. To the best of our knowledge, however, this approach has so far been mainly investigated for vascular prostheses [138,139].

## 7.2. Surface Modification for Rapid Endothelialisation

The endothelium of native vessels plays a pivotal role in preventing thrombogenic complications and intimal hyperplasia, thus improving long-term patency. Therefore, although the incorporation of anti-thrombotic molecules onto vascular scaffolds plays a crucial role in preventing acute thrombosis, the sustained success of these grafts over the long term largely relies on the reconstruction of a continuous endothelium on the lumen surface.

Various methods have been investigated for *in vitro* endothelialisation, including the seeding with ECs on the inner surface of blood vessel scaffolds and subsequent *in vitro* maturation before implantation. These techniques have shown promise in enhancing graft patency; however, they also suffer from significant drawbacks. These include the need for supplementary procedures to harvest cells, particularly in the case of autologous cell use, risks of infections, prolonged culture times, and the associated high costs of the procedure [140].

Therefore, researchers' attention is now mainly focused on in situ endothelialisation. Following implantation, endothelialisation of the graft typically occurs through one of three mechanisms: (i) transanastomotic growth, which involves the migration of host intimal ECs from the anastomotic site toward the centre of the graft, in response to natural injury-induced mechanisms; (ii) transmural growth, which occurs when ECs reach the lumen by traversing newly formed capillaries through the graft wall; (iii) fallout process, which entails circulating progenitor cells populating the implanted TEVG. Considering that, in humans, transanastomotic growth is limited to 1–2 cm [141] and the mechanism of transmural growth is not clear, the latter process involving circulating progenitor cells seems to be the most promising. EPCs are circulating blood cells able to differentiate into ECs and secrete multiple bioactive molecules [142]. Other less well-defined CD133<sup>+</sup>, CD34<sup>+</sup>, and CD45<sup>−</sup> progenitor cells also hold the potential to be recruited onto a modified graft, facilitating in situ endothelialisation. Moreover, a specific subset of CD14<sup>+</sup> monocytic cells was demonstrated to possess the ability to differentiate into ECs. Intriguingly, these monocyte lineage cells derived from the bone marrow, which are capable of maturing into ECs, have been reported to exhibit a more pronounced inhibition of intimal hyperplasia compared to EPCs [143]. Therefore, various strategies have been developed to promote rapid in situ endothelialisation through the modification of the scaffold lumen with biomolecules promoting circulating progenitor cell migration, adhesion, proliferation, and differentiation.

Considering that EPCs express specific markers, such as CD133, CD34, and the kinase domain receptor, along with co-expressing markers indicative of their hematopoietic origin, specific antibodies targeting these markers have been used for scaffold surface functionalisation to facilitate the capture of EPCs [144]. For example, Wu et al. developed a bi-layer scaffold by electrospinning, which included the luminal and media layers. The luminal layer was loaded with Hep and anti-CD133 antibody [35]. The loaded bioactive components were gradually released over an approximately 40-day period, during which the structure of the nanofibres remained intact. Additionally, the released Hep initially provided anticoagulant functionality of the lumen, while the incorporated anti-CD133 antibody facilitated the formation of a neo-intima. In vivo tests revealed the regeneration of a monolayer of ECs (positive for CD31) on the inner layer, demonstrating the scaffold's capability to regenerate structures resembling native blood vessels. Nonetheless, despite demonstrating promising endothelialisation, grafts coated with antibodies led to excessive intimal hyperplasia at the anastomoses and markedly increased platelet adhesion [145,146].

Alternatively, VEGF and numerous other bioactive factors, such as interleukin-8, stromal cell-derived factor-1 (SDF-1), angiopoietin-1, and basic fibroblast growth factor, have been used to favour ECs proliferation and survival. In the work published by Hu et al., small-diameter tubular scaffolds were fabricated using the coaxial-electrospinning method and the fibre core was loaded with Hep and VEGF [147]. A gradual release of Hep and VEGF was registered over 28 days. In vitro and in vivo tests demonstrated an improvement in terms of EC proliferation and patency with respect to non-functionalised grafts. Similarly, Du et al. developed a gradient heparinised nanofibrous scaffold to support ECs lining on the inner surface [148]. To mimic the natural environment of blood vessels, Hep was covalently attached to the scaffold by EDC/NHS chemistry and VEGF was loaded in the nanofibres by adsorption. The amount of heparinised nanofibres gradually increased from the outer layer (tunica adventitia) to the inner surface (lumen) of the scaffold. Enhanced anti-thrombogenic properties of the heparinised scaffolds were demonstrated by activated partial thromboplastin time and platelet adhesion assays. Furthermore, the release of VEGF was stable and sustained, with a lower burst release within the initial 12 h. EC adhesion and proliferation were significantly improved, and the formation of a complete monolayer was observed.

Another strategy to promote rapid endothelialisation is represented by scaffold functionalisation with bioactive peptides derived from ECM components. It was demonstrated that several peptide sequences can be bound by receptors on cell membranes and consequently influence cell behaviour. The most investigated peptide sequence for scaffold

modification is Arg-Gly-Asp (RGD) from fibronectin. However, as the RGD sequence is recognised by receptors that are present in all cell types, it may induce not only EC adhesion but also adverse cell adhesion and platelet aggregation. It has been reported in the literature that ECs exhibit a higher affinity for immobilised cyclic RGD peptides compared to linear RGD peptides [149]. Remarkably, aside from promoting EC adhesion, certain cyclic RGD peptides have demonstrated potent and selective antagonistic effects on the platelet integrin  $\alpha 2\beta 3$ , effectively inhibiting platelet-mediated thrombus formation [150]. It is worth noting that ECs express a diverse range of integrins, with at least 13 variants identified thus far, depending on their developmental stage, differentiation state, and functional context. Notably,  $\alpha 4$  integrins, which are absent in platelets, represent an attractive target for ligands aimed at facilitating in situ endothelialisation of vascular grafts [151]. For example, the tetrapeptide REDV, derived from fibronectin, exhibits a specific binding affinity for the  $\alpha 4\beta 1$  integrin. As the  $\alpha 4\beta 1$  integrin is predominantly expressed in ECs and EPCs, REDV possesses the ability to selectively enhance the adhesion of ECs/EPCs [152,153].

In an interesting paper, published by Duan et al., a combinatorial approach was explored, involving the successful co-immobilisation of the REDV peptide, VEGF, and CD133 antibodies onto a blood vessel scaffold [154]. This modified surface exhibited favourable compatibility with blood and notably increased its capacity to capture CD133<sup>+</sup> EPCs. The co-immobilisation of REDV and VEGF significantly enhanced the proliferation of EPCs. Furthermore, it conspicuously elevated the expression of EC marker genes in EPCs, thereby promoting the differentiation of EPCs into ECs.

In the paper published by Rosellini et al., tubular scaffolds based on a protein/polysaccharide blend were functionalised using two different bioactive peptides, Gly-Arg-Gly-Asp-Ser-Pro (GRGDSP) and Arg-Glu-Asp-Val (REDV) [82]. In vitro cell culture tests showed that the functionalisation with the REDV peptide favoured the adhesion and growth of ECs, and therefore could be advantageous for the endothelialisation of the internal surface of an engineered vessel, while GRGDSP promoted the adhesion of fibroblasts, which are present in the external layer of the vessel wall. Therefore, a bi-functionalised tubular scaffold could be developed, with REDV grafted on the luminal side of the scaffold, to specifically promote EC adhesion, and GRGDSP immobilised on the external side, to promote fibroblasts and SMC adhesion. This bi-functionalised scaffold could be able to promote the regeneration of a layered tissue, resembling the native structure of small-calibre arteries.

Besides biochemical modifications of scaffolds for TEVGs, the geometrical configuration of the surface also plays a role in the in situ endothelialisation of grafts [155]. This is because the nanofibrous ECM found in native vessels provides numerous physical and biological cues that regulate homeostasis, morphogenesis, and endothelial cellular functions [156]. Therefore, in recent years there has been a growing interest in exploring the impact of interfacial properties, including surface micro/nano topography, on cell behaviour. For example, it was demonstrated that nano-scale fibres, replicating the dimensions of the natural ECM, are conducive to the adhesion and proliferation of ECs [157,158]. In another work, it was shown that EC coverage was promoted on nanometer-scale patterns, instead of micrometre-scale patterns [159]. Not only the presence of nanostructures on scaffold surfaces but also their orientation has an impact on cell response. In a concerted approach, reported by Wang et al., a biomimetic intima featuring an oriented nanotopographical structure and covalently immobilised anticoagulant molecules was investigated [160]. A blend of heparinised SF and PCL was utilised to create the oriented inner layer of the scaffold. The obtained results demonstrated that the immobilised Hep significantly influenced platelet adherence and activation, whereas the oriented nanotopography primarily influenced the elongation and alignment of ECs, as well as the hemodynamics of blood flow. Notably, the synergistic effects of the oriented structure and anticoagulation significantly promoted rapid endothelialisation, long-term patency, and neovessel remodelling. Consequently, this study successfully combined biochemical induction via Hep molecules with biophysical stimulation through oriented nanotopography to develop an off-the-shelf SVDG with

excellent early-stage antithrombotic properties and sustained patency in the long term. In another paper, the authors focused on the biomimetic design of an acellular SVDG, featuring a specific lamellar nanotopography on the luminal surface achieved through a modified freeze-cast technique. Experimental findings confirmed that the nanolamellar structure effectively impeded platelet adherence and activation, promoted the oriented growth of ECs, and ultimately facilitated the remodelling of neovessels to sustain long-term patency in vivo. Additionally, numerical simulations conducted under physically mimetic conditions demonstrated that the regular lamellar nanopattern could manipulate blood flow to decrease flow disturbance compared to random topography.

### 7.3. Scaffold Functionalisation for Preventing Intimal Hyperplasia

Intimal hyperplasia is a pathological condition characterised by the thickening of the vessel wall, stemming from the excessive growth and migration of SMCs from the medial layer into the intimal layer due to endothelial damage [161]. In a healthy blood vessel, the endothelium regulates the underlying SMCs by inhibiting their proliferation and promoting a quiescent, differentiated state characterised by a contractile phenotype [162]. Any unintended damage to the endothelium exposes the medial layer, leading to platelet activation. This triggers a transition in the phenotype of SMCs from a quiescent, contractile state to a highly proliferative one, ultimately resulting in intimal thickening. Surgical implantation of vascular grafts typically damages the endothelium, exposing the medial layer and thereby increasing the risk of developing intimal hyperplasia. Techniques aimed at inducing rapid endothelialisation may not suffice to prevent the thickening of the graft wall. The biological and mechanical properties of TEVGs serve as critical regulators of hyperplasia development.

The strategies employed to prevent intimal hyperplasia in bioengineered vascular grafts predominantly revolve around the incorporation of drug molecules aimed at reducing SMC proliferation and platelet adhesion. Potential drugs targeted for this purpose include sirolimus or rapamycin [163], aspirin [164], and paclitaxel [165]. However, the burst release of the drug, propelled by blood flow, minimises the interaction between cells and the drug, thereby challenging the overarching concept. Moreover, antiproliferative drugs may result in delayed endothelialisation and cellular ingrowth, leading to a reduction in neointima formation. The delayed endothelial coverage may pose an issue regarding early thrombogenicity.

Knowing these limitations, an alternative strategy was developed by Ding et al., who proposed an irregular mesh made of carbon nanotubes, and loaded with resveratrol, as a coating on the scaffold lumen [166]. The mesh aimed to slow down the drug release caused by blood flow, thanks to a high resistance against shear stress. Resveratrol was internalised by proinflammatory M1 macrophages and caused their conversion to the pro-healing M2 phenotype. The pro-healing M2 macrophages play a pivotal role in inhibiting chronic inflammation, thereby preserving the contractile phenotype of VSMCs, consequently mitigating intimal hyperplasia. Furthermore, the release of resveratrol from the mesh coating directly protected contractile VSMCs from transitioning to a secretory phenotype. By employing an anti-shear stress coating and macrophage-based intracellular drug delivery, the developed tissue-engineered blood vessel demonstrated sustained efficacy against intimal hyperplasia over the long term. Animal transplantation studies conducted on rat carotid arteries revealed a consistently high patency rate up to day 90 post-grafting.

A different biologically inspired approach was followed by Sugiura et al., who investigated the efficacy of tropoelastin seeding onto the luminal surface of the graft in preventing neointimal hyperplasia [167]. Tropoelastin was effective in reducing the thickness of the intimal layer, suppressing neointimal SMC proliferation.

Therapeutic strategies targeting both proliferation and inflammation have demonstrated efficacy in preventing intimal hyperplasia in both natural and synthetic blood vessel grafts. However, it is surprising that, despite being a fundamental factor in the development of intimal hyperplasia, the compliance mismatch between native vessels

and TEVGs is often overlooked, with hypo-compliant (stiffer) grafts commonly utilised. In a recent paper, the authors aimed to address this issue by producing a vascular substitute that matches the compliance of the abdominal rat aorta through computational optimisation [168]. One-month follow-up observations revealed consistent graft compliance and an increased expression of markers associated with contractile SMCs in the compliance-matched group.

#### 7.4. Strategies to Control Cell and ECM Arrangement

As depicted in Section 2, blood vessels possess a structural complexity that serves to maintain tissue balance by overseeing biological and physical attributes. Within the blood vessel, the luminal layer (intima) comprises a monolayer of ECs aligned with the blood flow direction, while the medial layer consists of radially aligned SMCs, and the adventitia contains randomly oriented fibroblasts. Moreover, COL and elastin fibres in the arterial wall are aligned at specific angles, influencing mechanical properties. Manipulating cell function through engineering at the cell-substrate interface presents promising avenues. A recent study demonstrated that surface properties, such as wettability, roughness, patterning, and stiffness, regulate the functionality of vascular cells [169].

The manipulation of nanoscale-oriented geometry of the intimal layer was demonstrated to have a regulatory effect on the hemocompatibility of grafts and to facilitate in situ endothelialisation [140,170]. Similarly, inducing unidirectional alignment of SMCs cultured on micro-patterned substrates has been observed to promote a transition from a proliferative to a contractile phenotype [171], potentially mitigating the risk of intimal hyperplasia. In another work, inspired by the radial arrangement of SMCs in native vessels, tubular scaffolds incorporating circumferentially oriented nanofibres were fabricated using electrospinning to facilitate the unidirectional alignment of SMCs via contact guidance [172]. In an analogous endeavour, a dual-layered tubular graft containing microfibers circumferentially aligned in the layer replacing the media attracted radially organised host SMCs after implantation into rat abdominal aortas. Histological examination indicated the absence of hyperplasia, with the regenerated neovessel demonstrating responsiveness to vasoactive agents [173]. Overall, these findings underscore the promise of engineering biomimetic grafts that mimic the native cellular organisation in blood vessel layers: the circumferential alignment of medial SMCs enhances mechanical properties and prevents hyperplasia by limiting cellular overgrowth and the nanolamellar luminal topography targets the orchestration of an anti-thrombotic surface, thereby inhibiting platelet adhesion.

While achieving native-like orientation of vascular cells has shown promising results, there is also significant research interest in exploring other structural aspects, as native tissues contain cells and an ECM. As mentioned above, one trending prospect in this field is the development of multilayered TEVGs. These systems aim to mimic the complex wall structure of natural vessels, which consist of multiple layers of different cell types and ECM components. By replicating this multilayered structure, researchers hope to enhance the performance and functionality of the grafts, potentially leading to improved outcomes in vascular tissue engineering, as described in Section 6. Moreover, the regeneration of ECM components is closely associated with the infiltration of fibroblasts and SMCs. Fibroblasts primarily contribute to the regeneration of COL but have a limited impact on other ECM components such as elastin and GAGs; on the other hand, SMCs play a crucial role in fostering the ECM [174,175]. Researchers have conducted numerous studies investigating the impact of graft microstructure on ECM regeneration. Initially, porosity and pore size were highlighted as critical factors influencing cell infiltration. Subsequent investigations revealed a strong correlation between the regeneration of SMCs and high porosity/pore size. Conversely, the structural requirements for endothelial cell adhesion and proliferation differed significantly. Consequently, developing multi-layered scaffolds, which can accommodate the distinct requirements of both ECs and SMCs, seems to be a promising strategy. Additionally, previous research has demonstrated that certain growth factors can facilitate ECM regeneration. Specifically, PDGF has been identified as capable

of attracting SMCs and pericytes, while transforming growth factor-beta is deemed crucial for ECM deposition. Furthermore, DKK-3 has been observed to play a role in enhancing the maturation of SMCs [174,176].

### 7.5. Tailoring Immune Response

Immunoengineering represents a recent advancement within the field of tissue engineering, focusing on directing the immune system towards facilitating tissue regeneration. Recognition of the pivotal role of the host immune response in guiding the remodelling of TEVGs emerged following notable research efforts of Roh et al., who demonstrated the involvement of inflammation in graft maturation [177]. Subsequent investigations also underscored the critical regulation of stenosis by the innate immune system [178]. The degree of inflammation governs the formation of new tissue, with excessive inflammation leading to graft stenosis. While ongoing research continues to identify key immune system components involved in vascular graft remodelling, macrophages have emerged as primary regulators [179]. These cells, along with fibroblasts, play a crucial role in determining biomaterial-induced fibrosis and the formation of new ECM [180]. The intricate balance between proinflammatory M1 and various anti-inflammatory M2 macrophage subtypes orchestrates the overall remodelling process. Macrophage plasticity offers a significant opportunity for tissue engineers to influence their function towards promoting favourable graft remodelling outcomes.

As recently reviewed by Zhang et al., numerous studies have highlighted the impact of biomaterial properties on macrophage response and, consequently, on vascular tissue regeneration [181].

Fiber size and pore size represent two physically controllable factors that significantly influence macrophage response. Wang et al. conducted a study where they fabricated electrospun PCL vascular grafts with varying fibre thickness and average pore size [182]. They found that grafts with thicker fibres and larger average pore sizes facilitated a moderate level of macrophage infiltration and induced a stronger M2 macrophage response. Conversely, substrates with thinner fibres and smaller average pore sizes limited macrophage infiltration and predominantly elicited an M1 macrophage response. Moreover, grafts with thick fibres and large average pore sizes exhibited superior patency in a rat abdominal aortic model for a duration of up to 100 days. In the study, the authors also noted the presence of M1 macrophages throughout the entire observation period, while M2 macrophages were observed as early as Day 7 post-implantation, and persisted for 100 days. In line with these findings, Liu et al. documented that nanofibre vascular grafts prompt a more intense inflammatory response and calcification in comparison to microfibre grafts. They observed that macrophage infiltration and polarisation towards a pro-regenerative phenotype were augmented by grafts with thicker fibres and larger pore sizes, particularly on the circumferential outer side of the graft [183]. Other studies investigated the effect of micro/nanotopography, mechanical properties (in terms of stiffness and radial compliance), and chemical composition on macrophages; however, the impact of these scaffold properties on macrophage phenotype polarisation was not completely clarified [181].

As an alternative to the customisation of scaffold properties, the immobilisation or encapsulation of signalling molecules on the surface or within the scaffold to achieve sustained release is now recognised as an additional strategy to modulate the immune response and enhance tissue regeneration. For example, acellular TEVGs functionalised with VEGF were found to have a greater abundance of M2 macrophages [184]. Conversely, grafts solely functionalised with Hep predominantly supported M1 macrophages and exhibited a limited development of vascular endothelium and medial layers. In another work, Bonito et al. designed a PCL scaffold conjugated with Hep and IL-4 which effectively stimulated a high ratio of M2 to M1 macrophages in vitro [185]. Recently, Wei et al. devised a method for releasing mesenchymal stem cell-derived small extracellular vesicles from a heparinised vascular graft to bolster vascular regeneration [186]. Their observations revealed that grafts loaded with sEVs exhibited fewer M1 macrophages and a higher



proportion of M2 macrophages. In a separate cell culture investigation, grafts laden with sEVs were capable of inducing macrophage polarisation towards the M2 phenotype at the gene expression level. The prevalence of the M2 macrophage phenotype was associated with superior vascular outcomes, such as enhanced patency rates and the regeneration of continuous endothelium and contractile SMCs within the neotissue.

## 8. Biomimicry in Bioreactor Design for Tissue Maturation

Notoriously, creating a three-layer vascular substitute—containing ECs, SMCs, and fibroblasts—is insufficient to generate a functional blood vessel. The subsequent phase, known as maturation, is complex, crucial, and time-consuming. During maturation, cells adapt to their 3D environment, produce an ECM, and establish cell–cell connections. Achieving tissue-like maturation requires an *in vivo*-like environment, making bioreactors crucial in vascular tissue engineering. Initially focused on endothelialising scaffold layers, bioreactors now play a vital role in controlling cell maturation and proliferation within constructs [9,187,188]. Bioreactors are essential tools in tissue engineering, designed to recreate a variable degree of the natural conditions for cell growth and tissue formation. Effective bioreactor design incorporates biomimetic principles to enhance tissue functionality by applying physiological conditions to stimulate cellular responses [189,190]. The tissue maturation process comprises an initial post-production stage, after which the tissue is generally fragile and unstable and necessitates measures to ensure cell survival and attachment to scaffolds or substrates. Over the subsequent weeks, tissue development and maturation occur. During this period, the bioreactor should offer dynamic conditions and customised stimulation to optimise tissue response while progressing its functionality and integration with host tissue. Gradually, the tissue may be exposed to challenging conditions in the bioreactor, including mechanical stimulation. Evaluation of tissue performance and quality remains critical throughout this phase [191,192].

In the field of blood vessel tissue engineering, bioreactors are categorised into three types: static, dynamic, and biomimetic. Static bioreactors passively mature constructs in standard vessels within controlled atmosphere incubators. Dynamic bioreactors consist of vessels with inlet and outlet, perfusing ECs for endothelialisation or inducing cell maturation through hydrodynamic stress. Biomimetic bioreactors aim to recreate *in vivo* tissue environments, controlling parameters like perfusion flows, pH, temperature, oxygen, and nutrient supply. Moreover, they aim to provide optimal conditions for cell proliferation and viability, mimicking physiological conditions, such as shear stress, to favour the development of vascular cell functions [9,188,193]. Researchers have utilised various commercially available bioreactor systems to replicate physiological vascular conditions, which implement pulsatile pumps, oscillators, culture medium reservoirs, and advanced scaffold chambers [194,195]. Nonetheless, homemade bioreactors are prevalent in vascular tissue engineering. Bono et al. developed a dual-mode bioreactor for construct fabrication and *in vitro* stimulation. At the same time, Iris Pennings et al. created a homemade perfused bioreactor for a bi-layered vascular graft, applying physiological shear rates to the luminal side for EC proliferation and exposing the outer layer to static culture conditions [196,197].

In vascular tissue engineering, the choice of a bioreactor system depends on the desired maturation conditions of the vascular construct. Various maturation strategies exist, including flow through the vessel, mechanical stimulation with a rotational bioreactor, or burst pressure. Studies have shown the crucial role of shear stress in cell migration and proliferation. Bioreactors can simulate shear stress through flow, pulses, or mimicking heartbeat [9]. For instance, a study by Chen Wang et al. demonstrated significant improvements in the biomechanical properties of vascular constructs under dynamic stimulation compared to static conditions. However, current bioreactors mostly focus on obtaining endothelialisation, leaving gaps in the maturation of other vascular layers [198,199].

Despite advancements like 3D bioprinting, newly created vascular tissues lack sufficient mechanical properties and require maturation in a bioreactor. This results in the

known paradox for which immature blood vessels need a bioreactor for functional maturation, but they are too fragile to be placed in one [9]. Nonetheless, there have been a consistent number of attempts at improving the quality of bioreactor-mediated tissue construct maturation by addressing the current limitations of this practice. Omid et al., for instance, addressed the limitations of traditional decellularisation methods, which often result in damage to ECM proteins and functional peptides, hindering the quality of biological scaffolds for vascular tissue engineering (Figure 7). By employing a combination of chemical and physical decellularisation methods and utilising a bioreactor for cyclic tensile and shear stresses, the researchers sought to enhance cell migration into the scaffold and improve the compactness of cells and scaffold, mimicking native tissue structure [101].

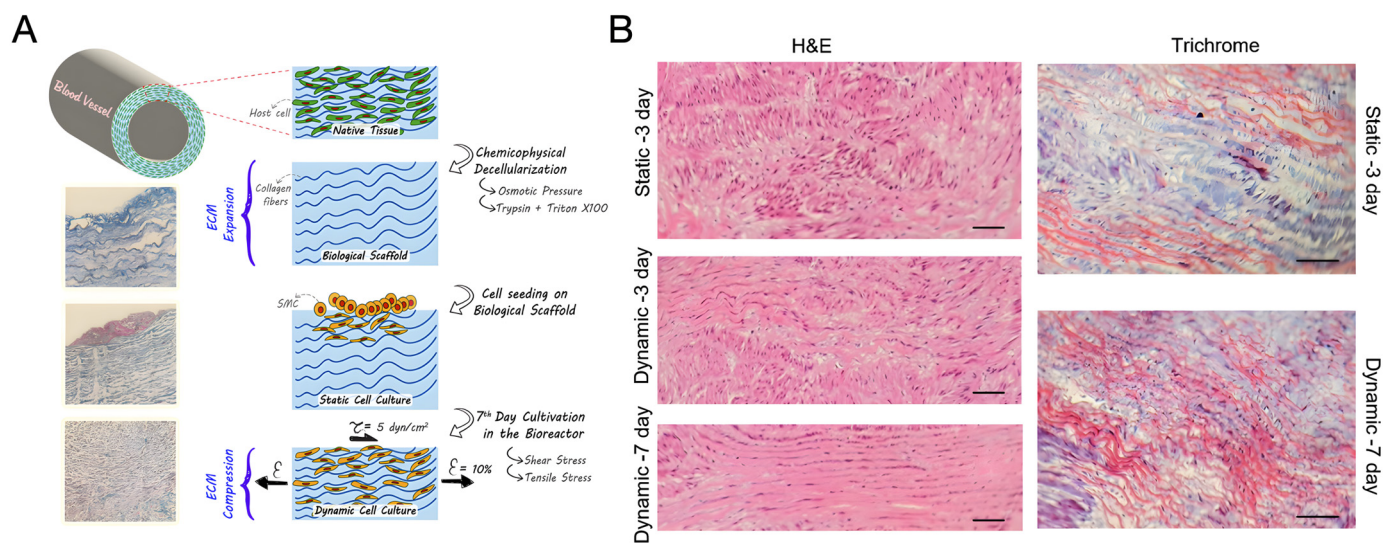


**Figure 7.** The attempt of Omid's group [101] the quality of bioreactor-mediated tissue construct maturation. (A) A graphical scheme illustrating their novel decellularisation method for biological scaffolds. Chemical and physical techniques, including hypertonic/hypotonic solutions and trypsin/Triton X-100 treatment, were employed to remove cellular components while preserving ECM integrity. Conducting decellularisation at 4 °C minimised damage, maintaining mechanical strength, and facilitating optimal cell attachment. Biocompatibility was confirmed via MTT assay, with storage viability at −20 °C. (B) Histological images of the biological scaffold following 3-day static, 3-day dynamic, and 7-day dynamic SMC cultivation, stained with H&E and Masson's trichrome, reveal distinct structural changes. Dynamic culture resulted in aligned and compressed COL filaments, facilitating cellular penetration (scale bar = 300  $\mu\text{m}$ ). The article is licensed under a Creative Commons Attribution 4.0 International License.

Derhambaksh et al. sought to tackle a key obstacle in vascular tissue engineering particularly concerning small-diameter vessels: the aberrant proliferation and migration of VSMCs from the media layer of the artery. By converting VSMCs from a synthetic to a contractile phenotype using electrical stimulation, the researchers aimed to prevent abnormal growth and migration, thus addressing a critical challenge in achieving successful vascular grafts [200]. On another note, Kojima et al. addressed the need for biologically compatible vascular grafts by exploring scaffoldless tissue engineering methods for fabricating functional vascular mimetics. By utilising hydrostatic pressurisation under hypoxia, the researchers aimed to promote the formation of multi-layered tunica media from human VSMCs, offering a potential solution for producing scaffoldless human vascular grafts [201].

## 9. Concluding Remarks and Future Directions

Blood vessel engineering represents a critical frontier in addressing the challenges posed by CVDs, notably atherosclerosis. The intricate nature of healthy arteries underscores the complexity inherent in replicating their functionality through tissue engineering. Although the fabrication of functional vascular substitutes is still a challenge, an incredible amount of research activity has been carried out in this field and significant advancements in scaffold-based methodologies offer promising avenues.

As illustrated in this review, the engineering of small-diameter blood vessels able to recapitulate all the biological and mechanical properties of native vessels requires the selection and combination of appropriate strategies for scaffold development. In particular, the need has arisen to follow a biomimetic approach on multiple fronts, including the choice of materials, the scaffold architecture, the functionalisation strategies to enrich the scaffold with signals, and the design of a dynamic culture environment (bioreactor).

The exploration of various scaffold materials and fabrication techniques reveals a concerted effort to mimic the native features of arteries. Natural polymers, such as COL, Gt, fibrin, and elastin, along with decellularised tissues, provide biocompatible substrates that closely resemble the composition of native ECM, offering superior cell response. Strategies to optimise scaffold architecture, mimicking the multi-layer structure of native vessels, are crucial for achieving long-term functionality and patency rates comparable to natural vessels. In this regard, electrospinning and, more recently, 3D printing, have emerged as the most promising techniques for this purpose, enabling precise control over scaffold morphology and bioactive component distribution, facilitating cellular organisation and tissue maturation.

Innovations in scaffold design extend beyond mimicking compositional and structural features to encompass functional aspects that are crucial for clinical success. Surface modification plays a pivotal role in enhancing hemocompatibility, promoting endothelialisation, and mitigating thrombosis risk. Functionalisation strategies can also enrich the scaffold with biochemical and topographical signals, which are useful to prevent intimal hyperplasia, guide cell and ECM organisation, and tailor the immune response. All of these aspects are crucial to obtain fully functional vascular grafts.

Moreover, the maturation of functional vascular tissue on the biomimetic scaffolds should be further promoted through the development of bioreactors for cell culture replicating the native biomechanical environment of small-diameter blood vessels.

Looking ahead, the field of vascular tissue engineering requires further advancements driven by ongoing research efforts and technological innovations. Currently, no biomimetic multi-layer vascular graft has reached clinical application. As outlined in this review, a multi-faceted biomimetic approach in scaffold design seems to be the right path towards clinical translation. At the same time, addressing challenges such as batch-to-batch variability, and the need to find a balance between scaffold complexity and scalability, will be paramount for translating experimental findings into clinically viable solutions. Ultimately, the convergence of interdisciplinary expertise and collaborative endeavours will be instrumental in realising the full potential of scaffold-based approaches for vascular repair and regeneration.

**Author Contributions:** Conceptualisation, E.R.; investigation, E.R.; writing—original draft preparation, E.R., C.G., L.G. and M.G.C.; writing—review and editing, E.R. and M.G.C.; visualisation, C.G. and L.G.; supervision, E.R. and M.G.C. All authors have read and agreed to the published version of the manuscript.

**Funding:** This research received no external funding.

**Data Availability Statement:** No new data were created or analysed in this study. Data sharing does not apply to this article.

**Conflicts of Interest:** The authors declare no conflicts of interest.

## References

1. Mensah, G.A.; Roth, G.A.; Fuster, V. The Global Burden of Cardiovascular Diseases and Risk Factors. *J. Am. Coll. Cardiol.* **2019**, *74*, 2529–2532. [CrossRef] [PubMed]
2. Niklason, L.E.; Lawson, J.H. Bioengineered Human Blood Vessels. *Science* **2020**, *370*, eaaw8682. [CrossRef] [PubMed]
3. Hall, A.B.; Brilakis, E.S. Saphenous Vein Graft Failure: Seeing the Bigger Picture. *J. Thorac. Dis.* **2019**, *11*, S1441–S1444. [CrossRef] [PubMed]
4. Veith, F.J.; Moss, C.M.; Sprayregen, S.; Montefusco, C. Preoperative Saphenous Venography in Arterial Reconstructive Surgery of the Lower-Extremity. *Surgery* **1979**, *85*, 253–256. [PubMed]
5. Stowell, C.E.T.; Wang, Y. Quickening: Translational Design of Resorbable Synthetic Vascular Grafts. *Biomaterials* **2018**, *173*, 71–86. [CrossRef] [PubMed]
6. Pashneh-Tala, S.; MacNeil, S.; Claeysens, F. The Tissue-Engineered Vascular Graft—Past, Present, and Future. *Tissue Eng. Part B Rev.* **2016**, *22*, 68–100. [CrossRef] [PubMed]
7. Weinberg, C.B.; Bell, E. A Blood Vessel Model Constructed from Collagen and Cultured Vascular Cells. *Science* **1986**, *231*, 397–400. [CrossRef] [PubMed]
8. Tennant, M.; McGeachie, J.K. Blood Vessel Structure And Function: A Brief Update on Recent Advances. *Aust. New Zealand J. Surg.* **1990**, *60*, 747–753. [CrossRef]
9. Devillard, C.D.; Marquette, C.A. Vascular Tissue Engineering: Challenges and Requirements for an Ideal Large Scale Blood Vessel. *Front. Bioeng. Biotechnol.* **2021**, *9*, 721843. [CrossRef] [PubMed]
10. Tucker, W.D.; Arora, Y.; Mahajan, K. Anatomy, Blood Vessels. In *StatPearls [Internet]*; StatPearls Publishing: Treasure Island, FL, USA, 2024. [PubMed]
11. Wagenseil, J.E.; Mecham, R.P. Vascular Extracellular Matrix and Arterial Mechanics. *Physiol. Rev.* **2009**, *89*, 957–989. [CrossRef] [PubMed]
12. Levy, B.I.; Tedgui, A. Morphologic Aspects of the Large Artery Vascular Wall. In *Biology of the Arterial Wall*; Springer: Boston, MA, USA, 1999; pp. 3–12.
13. Saito, J.; Kaneko, M.; Ishikawa, Y.; Yokoyama, U. Challenges and Possibilities of Cell-Based Tissue-Engineered Vascular Grafts. *Cyborg Bionic Syst.* **2021**, *2021*, 1532103. [CrossRef] [PubMed]
14. Peck, M.; Gebhart, D.; Dusserre, N.; McAllister, T.N.; L'Heureux, N. The Evolution of Vascular Tissue Engineering and Current State of the Art. *Cells Tissues Organs* **2012**, *195*, 144–158. [CrossRef] [PubMed]
15. Chan-Park, M.B.; Shen, J.Y.; Cao, Y.; Xiong, Y.; Liu, Y.; Rayatpisheh, S.; Kang, G.C.W.; Greisler, H.P. Biomimetic Control of Vascular Smooth Muscle Cell Morphology and Phenotype for Functional Tissue-Engineered Small-Diameter Blood Vessels. *J. Biomed. Mater. Res. A* **2009**, *88*, 1104–1121. [CrossRef] [PubMed]
16. Rouwkema, J.; Khademhosseini, A. Vascularization and Angiogenesis in Tissue Engineering: Beyond Creating Static Networks. *Trends Biotechnol.* **2016**, *34*, 733–745. [CrossRef]
17. Wang, P.; Sun, Y.; Shi, X.; Shen, H.; Ning, H.; Liu, H. 3D Printing of Tissue Engineering Scaffolds: A Focus on Vascular Regeneration. *Biores. Manuf.* **2021**, *4*, 344–378. [CrossRef] [PubMed]
18. Hutmacher, D.W. Scaffolds in Tissue Engineering Bone and Cartilage. *Biomaterials* **2000**, *21*, 2529–2543. [CrossRef] [PubMed]
19. Yang, S.; Leong, K.-F.; Du, Z.; Chua, C.-K. The Design of Scaffolds for Use in Tissue Engineering. Part I. Traditional Factors. *Tissue Eng.* **2001**, *7*, 679–689. [CrossRef] [PubMed]
20. Hollister, S.J. Porous Scaffold Design for Tissue Engineering. *Nat. Mater.* **2005**, *4*, 518–524. [CrossRef] [PubMed]
21. Rezwan, K.; Chen, Q.Z.; Blaker, J.J.; Boccaccini, A.R. Biodegradable and Bioactive Porous Polymer/Inorganic Composite Scaffolds for Bone Tissue Engineering. *Biomaterials* **2006**, *27*, 3413–3431. [CrossRef] [PubMed]
22. O'Brien, F.J. Biomaterials & Scaffolds for Tissue Engineering. *Mater. Today* **2011**, *14*, 88–95. [CrossRef]
23. Bose, S.; Roy, M.; Bandyopadhyay, A. Recent Advances in Bone Tissue Engineering Scaffolds. *Trends Biotechnol.* **2012**, *30*, 546–554. [CrossRef] [PubMed]
24. Wu, S.; Liu, X.; Yeung, K.W.K.; Liu, C.; Yang, X. Biomimetic Porous Scaffolds for Bone Tissue Engineering. *Mater. Sci. Eng. R Rep.* **2014**, *80*, 1–36. [CrossRef]
25. Ovsianikov, A.; Khademhosseini, A.; Mironov, V. The Synergy of Scaffold-Based and Scaffold-Free Tissue Engineering Strategies. *Trends Biotechnol.* **2018**, *36*, 348–357. [CrossRef]
26. Niklason, L.E.; Gao, J.; Abbott, W.M.; Hirschi, K.K.; Houser, S.; Marini, R.; Langer, R. Functional Arteries Grown in Vitro. *Science* **1999**, *284*, 489–493. [CrossRef] [PubMed]
27. Goins, A.; Webb, A.R.; Allen, J.B. Multi-Layer Approaches to Scaffold-Based Small Diameter Vessel Engineering: A Review. *Mater. Sci. Eng. C* **2019**, *97*, 896–912. [CrossRef]
28. Pawlowski, K.J. Endothelial Cell Seeding of Polymeric Vascular Grafts. *Front. Biosci.* **2004**, *9*, 1412. [CrossRef] [PubMed]
29. Godbey, W.T.; Stacey Hindy, B.S.; Sherman, M.E.; Atala, A. A Novel Use of Centrifugal Force for Cell Seeding into Porous Scaffolds. *Biomaterials* **2004**, *25*, 2799–2805. [CrossRef]
30. Perea, H.; Aigner, J.; Hopfner, U.; Wintermantel, E. Direct Magnetic Tubular Cell Seeding: A Novel Approach for Vascular Tissue Engineering. *Cells Tissues Organs* **2006**, *183*, 156–165. [CrossRef] [PubMed]
31. Zhang, L.; Zhou, J.; Lu, Q.; Wei, Y.; Hu, S. A Novel Small-diameter Vascular Graft: In Vivo Behavior of Biodegradable Three-layered Tubular Scaffolds. *Biotechnol. Bioeng.* **2008**, *99*, 1007–1015. [CrossRef] [PubMed]

32. Nieponice, A.; Soletti, L.; Guan, J.; Hong, Y.; Gharaibeh, B.; Maul, T.M.; Huard, J.; Wagner, W.R.; Vorp, D.A. In Vivo Assessment of a Tissue-Engineered Vascular Graft Combining a Biodegradable Elastomeric Scaffold and Muscle-Derived Stem Cells in a Rat Model. *Tissue Eng. Part A* **2010**, *16*, 1215–1223. [CrossRef] [PubMed]
33. Loh, Q.L.; Choong, C. Three-Dimensional Scaffolds for Tissue Engineering Applications: Role of Porosity and Pore Size. *Tissue Eng. Part B Rev.* **2013**, *19*, 485–502. [CrossRef]
34. Nair, P.; Thottappillil, N. Scaffolds in Vascular Regeneration: Current Status. *Vasc. Health Risk Manag.* **2015**, *11*, 79–91. [CrossRef] [PubMed]
35. Wu, T.; Zhang, J.; Wang, Y.; Sun, B.; Yin, M.; Bowlin, G.L.; Mo, X. Design and Fabrication of a Biomimetic Vascular Scaffold Promoting in Situ Endothelialization and Tunica Media Regeneration. *ACS Appl. Bio. Mater.* **2018**, *1*, 833–844. [CrossRef] [PubMed]
36. Wu, T.; Zhang, J.; Wang, Y.; Li, D.; Sun, B.; El-Hamshary, H.; Yin, M.; Mo, X. Fabrication and Preliminary Study of a Biomimetic Tri-Layer Tubular Graft Based on Fibers and Fiber Yarns for Vascular Tissue Engineering. *Mater. Sci. Eng. C* **2018**, *82*, 121–129. [CrossRef] [PubMed]
37. Tucker, E.I.; Marzec, U.M.; White, T.C.; Hurst, S.; Rugonyi, S.; McCarty, O.J.T.; Gailani, D.; Gruber, A.; Hanson, S.R. Prevention of Vascular Graft Occlusion and Thrombus-Associated Thrombin Generation by Inhibition of Factor XI. *Blood* **2009**, *113*, 936–944. [CrossRef] [PubMed]
38. Abbott, W.M.; Megerman, J.; Hasson, J.E.; L'Italien, G.; Warnock, D.F. Effect of Compliance Mismatch on Vascular Graft Patency. *J. Vasc. Surg.* **1987**, *5*, avs0050376. [CrossRef]
39. Tatterton, M.; Wilshaw, S.-P.; Ingham, E.; Homer-Vanniasinkam, S. The Use of Antithrombotic Therapies in Reducing Synthetic Small-Diameter Vascular Graft Thrombosis. *Vasc. Endovascular. Surg.* **2012**, *46*, 212–222. [CrossRef] [PubMed]
40. Hasan, A.; Paul, A.; Memic, A.; Khademhosseini, A. A Multilayered Microfluidic Blood Vessel-like Structure. *Biomed. Microdevices* **2015**, *17*, 88. [CrossRef] [PubMed]
41. Kinoshita, K.; Iwase, M.; Yamada, M.; Yajima, Y.; Seki, M. Fabrication of Multilayered Vascular Tissues Using Microfluidic Agarose Hydrogel Platforms. *Biotechnol. J.* **2016**, *11*, 1415–1423. [CrossRef] [PubMed]
42. Seifu, D.G.; Meghezi, S.; Unsworth, L.; Mequanint, K.; Mantovani, D. Viscoelastic Properties of Multi-Layered Cellularized Vascular Tissues Fabricated from Collagen Gel. *J. Mech. Behav. Biomed. Mater.* **2018**, *80*, 155–163. [CrossRef]
43. Santos-Rosales, V.; Iglesias-Mejuto, A.; García-González, C. Solvent-Free Approaches for the Processing of Scaffolds in Regenerative Medicine. *Polymers* **2020**, *12*, 533. [CrossRef] [PubMed]
44. Helms, F.; Lau, S.; Aper, T.; Zippusch, S.; Klingenberg, M.; Haverich, A.; Wilhelmi, M.; Böer, U. A 3-Layered Bioartificial Blood Vessel with Physiological Wall Architecture Generated by Mechanical Stimulation. *Ann. Biomed. Eng.* **2021**, *49*, 2066–2079. [CrossRef] [PubMed]
45. Datta, P.; Ayan, B.; Ozbolat, I.T. Bioprinting for Vascular and Vascularized Tissue Biofabrication. *Acta Biomater.* **2017**, *51*, 1–20. [CrossRef] [PubMed]
46. Borovjagin, A.V.; Ogle, B.M.; Berry, J.L.; Zhang, J. From Microscale Devices to 3D Printing: Advances in Fabrication of 3D Cardiovascular Tissues. *Circ. Res.* **2017**, *120*, 150–165. [CrossRef] [PubMed]
47. Norotte, C.; Marga, F.S.; Niklason, L.E.; Forgacs, G. Scaffold-Free Vascular Tissue Engineering Using Bioprinting. *Biomaterials* **2009**, *30*, 5910–5917. [CrossRef] [PubMed]
48. Itoh, M.; Nakayama, K.; Noguchi, R.; Kamohara, K.; Furukawa, K.; Uchihashi, K.; Toda, S.; Oyama, J.; Node, K.; Morita, S. Scaffold-Free Tubular Tissues Created by a Bio-3D Printer Undergo Remodeling and Endothelialization When Implanted in Rat Aortae. *PLoS ONE* **2015**, *10*, e0136681. [CrossRef]
49. Arai, K.; Murata, D.; Takao, S.; Verissimo, A.R.; Nakayama, K. Cryopreservation Method for Spheroids and Fabrication of Scaffold-Free Tubular Constructs. *PLoS ONE* **2020**, *15*, e0230428. [CrossRef]
50. Ozbolat, I.T.; Hospodiuk, M. Current Advances and Future Perspectives in Extrusion-Based Bioprinting. *Biomaterials* **2016**, *76*, 321–343. [CrossRef] [PubMed]
51. Pi, Q.; Maharjan, S.; Yan, X.; Liu, X.; Singh, B.; van Genderen, A.M.; Robledo-Padilla, F.; Parra-Saldivar, R.; Hu, N.; Jia, W.; et al. Digitally Tunable Microfluidic Bioprinting of Multilayered Cannular Tissues. *Adv. Mater.* **2018**, *30*, 1706913. [CrossRef]
52. Gao, G.; Kim, H.; Kim, B.S.; Kong, J.S.; Lee, J.Y.; Park, B.W.; Chae, S.; Kim, J.; Ban, K.; Jang, J.; et al. Tissue-Engineering of Vascular Grafts Containing Endothelium and Smooth-Muscle Using Triple-Coaxial Cell Printing. *Appl. Phys. Rev.* **2019**, *6*, 041402. [CrossRef]
53. Jia, W.; Gungor-Ozkerim, P.S.; Zhang, Y.S.; Yue, K.; Zhu, K.; Liu, W.; Pi, Q.; Byambaa, B.; Dokmeci, M.R.; Shin, S.R.; et al. Direct 3D Bioprinting of Perfusable Vascular Constructs Using a Blend Bioink. *Biomaterials* **2016**, *106*, 58–68. [CrossRef] [PubMed]
54. Gao, G.; Park, W.; Kim, B.S.; Ahn, M.; Chae, S.; Cho, W.; Kim, J.; Lee, J.Y.; Jang, J.; Cho, D. Construction of a Novel In Vitro Atherosclerotic Model from Geometry-Tunable Artery Equivalents Engineered via In-Bath Coaxial Cell Printing. *Adv. Funct. Mater.* **2021**, *31*, 2008878. [CrossRef]
55. Cummings, C.L.; Gawlitta, D.; Nerem, R.M.; Stegemann, J.P. Properties of Engineered Vascular Constructs Made from Collagen, Fibrin, and Collagen–Fibrin Mixtures. *Biomaterials* **2004**, *25*, 3699–3706. [CrossRef] [PubMed]
56. Seliktar, D.; Black, R.A.; Vito, R.P.; Nerem, R.M. Dynamic Mechanical Conditioning of Collagen-Gel Blood Vessel Constructs Induces Remodeling In Vitro. *Ann. Biomed. Eng.* **2000**, *28*, 351–362. [CrossRef] [PubMed]

57. Wang, S.; Zhang, Y.; Yin, G.; Wang, H.; Dong, Z. Electrospun Polylactide/Silk Fibroin-Gelatin Composite Tubular Scaffolds for Small-Diameter Tissue Engineering Blood Vessels. *J. Appl. Polym. Sci.* **2009**, *113*, 2675–2682. [CrossRef]
58. Badhe, R.V.; Bijukumar, D.; Chejara, D.R.; Mabrouk, M.; Choonara, Y.E.; Kumar, P.; du Toit, L.C.; Kondiah, P.P.D.; Pillay, V. A Composite Chitosan-Gelatin Bi-Layered, Biomimetic Macroporous Scaffold for Blood Vessel Tissue Engineering. *Carbohydr. Polym.* **2017**, *157*, 1215–1225. [CrossRef] [PubMed]
59. Aussel, A.; Montembault, A.; Malaise, S.; Foulc, M.P.; Faure, W.; Cornet, S.; Aid, R.; Chaouat, M.; Delair, T.; Letourneur, D.; et al. In Vitro Mechanical Property Evaluation of Chitosan-Based Hydrogels Intended for Vascular Graft Development. *J. Cardiovasc. Transl. Res.* **2017**, *10*, 480–488. [CrossRef] [PubMed]
60. Koch, S.; Flanagan, T.C.; Sachweh, J.S.; Tanios, F.; Schnoering, H.; Deichmann, T.; Ellä, V.; Kellomäki, M.; Gronloh, N.; Gries, T.; et al. Fibrin-Polylactide-Based Tissue-Engineered Vascular Graft in the Arterial Circulation. *Biomaterials* **2010**, *31*, 4731–4739. [CrossRef] [PubMed]
61. Swartz, D.D.; Russell, J.A.; Andreadis, S.T. Engineering of Fibrin-Based Functional and Implantable Small-Diameter Blood Vessels. *Am. J. Physiol. Heart Circ. Physiol.* **2005**, *288*, H1451–H1460. [CrossRef] [PubMed]
62. Koch, S.; Tschoeke, B.; Deichmann, T.; Ella, V.; Gronloh, N.; Gries, T.; Tolba, R.; Kellomäki, M.; Schmitz-Rode, T.; Jockenhoevel, S. Fibrin-Based Tissue Engineered Vascular Graft in Carotid Artery Position—The First in Vivo Experiences. *Thorac. Cardiovasc. Surg.* **2010**, *58*, MP25. [CrossRef]
63. Wise, S.G.; Byrom, M.J.; Waterhouse, A.; Bannon, P.G.; Ng, M.K.C.; Weiss, A.S. A Multilayered Synthetic Human Elastin/Polycaprolactone Hybrid Vascular Graft with Tailored Mechanical Properties. *Acta Biomater.* **2011**, *7*, 295–303. [CrossRef] [PubMed]
64. Nguyen, T.U.; Shojaaee, M.; Bashur, C.A.; Kishore, V. Electrochemical Fabrication of a Biomimetic Elastin-Containing Bi-Layered Scaffold for Vascular Tissue Engineering. *Biofabrication* **2019**, *11*, 015007. [CrossRef] [PubMed]
65. Fernández-Colino, A.; Wolf, F.; Rütten, S.; Schmitz-Rode, T.; Rodríguez-Cabello, J.C.; Jockenhoevel, S.; Mela, P. Small Caliber Compliant Vascular Grafts Based on Elastin-Like Recombinamers for in Situ Tissue Engineering. *Front. Bioeng. Biotechnol.* **2019**, *7*, 340. [CrossRef] [PubMed]
66. Achilli, M.; Lagueux, J.; Mantovani, D. On the Effects of UV-C and PH on the Mechanical Behavior, Molecular Conformation and Cell Viability of Collagen-Based Scaffold for Vascular Tissue Engineering. *Macromol. Biosci.* **2010**, *10*, 307–316. [CrossRef]
67. Li, X.; Xu, J.; Nicolescu, C.T.; Marinelli, J.T.; Tien, J. Generation, Endothelialization, and Microsurgical Suture Anastomosis of Strong 1-Mm-Diameter Collagen Tubes. *Tissue Eng. Part A* **2017**, *23*, 335–344. [CrossRef] [PubMed]
68. Liang, W.; Kienitz, B.L.; Penick, K.J.; Welter, J.F.; Zawodzinski, T.A.; Baskaran, H. Concentrated Collagen-chondroitin Sulfate Scaffolds for Tissue Engineering Applications. *J. Biomed. Mater. Res. A* **2010**, *94*, 1050–1060. [CrossRef] [PubMed]
69. Cheng, S.; Wang, W.; Li, Y.; Gao, G.; Zhang, K.; Zhou, J.; Wu, Z. Cross-Linking and Film-Forming Properties of Transglutaminase-Modified Collagen Fibers Tailored by Denaturation Temperature. *Food Chem.* **2019**, *271*, 527–535. [CrossRef] [PubMed]
70. Sarkar, S.; Hillery, C.; Seifalian, A.; Hamilton, G. Critical Parameter of Burst Pressure Measurement in Development of Bypass Grafts Is Highly Dependent on Methodology Used. *J. Vasc. Surg.* **2006**, *44*, 846–852. [CrossRef]
71. Grassl, E.D.; Oegema, T.R.; Tranquillo, R.T. Fibrin as an Alternative Biopolymer to Type-I Collagen for the Fabrication of a Media Equivalent. *J. Biomed. Mater. Res.* **2002**, *60*, 607–612. [CrossRef] [PubMed]
72. Singh, G.; Cordero, J.; Wiles, B.; Tembelis, M.N.; Liang, K.-L.; Rafailovich, M.; Simon, M.; Khan, S.U.; Bui, D.T.; Dagum, A.B. Development of In Vitro Bioengineered Vascular Grafts for Microsurgery and Vascular Surgery Applications. *Plast. Reconstr. Surg. Glob. Open* **2019**, *7*, e2264. [CrossRef]
73. Lin, C.-H.; Hsia, K.; Ma, H.; Lee, H.; Lu, J.-H. In Vivo Performance of Decellularized Vascular Grafts: A Review Article. *Int. J. Mol. Sci.* **2018**, *19*, 2101. [CrossRef] [PubMed]
74. Yang, L.; Li, X.; Wang, D.; Mu, S.; Lv, W.; Hao, Y.; Lu, X.; Zhang, G.; Nan, W.; Chen, H.; et al. Improved Mechanical Properties by Modifying Fibrin Scaffold with PCL and Its Biocompatibility Evaluation. *J. Biomater. Sci. Polym. Ed.* **2020**, *31*, 658–678. [CrossRef] [PubMed]
75. Wang, Z.; Liu, L.; Mithieux, S.M.; Weiss, A.S. Fabricating Organized Elastin in Vascular Grafts. *Trends Biotechnol.* **2021**, *39*, 505–518. [CrossRef]
76. Simionescu, D.T.; Lu, Q.; Song, Y.; Lee, J.; Rosenbalm, T.N.; Kelley, C.; Vyavahare, N.R. Biocompatibility and Remodeling Potential of Pure Arterial Elastin and Collagen Scaffolds. *Biomaterials* **2006**, *27*, 702–713. [CrossRef] [PubMed]
77. Park, J.S.; Chu, J.S.F.; Cheng, C.; Chen, F.; Chen, D.; Li, S. Differential Effects of Equiaxial and Uniaxial Strain on Mesenchymal Stem Cells. *Biotechnol. Bioeng.* **2004**, *88*, 359–368. [CrossRef] [PubMed]
78. Gong, Z.; Niklason, L.E. Small-diameter Human Vessel Wall Engineered from Bone Marrow-derived Mesenchymal Stem Cells (HMSCs). *FASEB J.* **2008**, *22*, 1635–1648. [CrossRef] [PubMed]
79. Ryan, A.J.; O'Brien, F.J. Insoluble Elastin Reduces Collagen Scaffold Stiffness, Improves Viscoelastic Properties, and Induces a Contractile Phenotype in Smooth Muscle Cells. *Biomaterials* **2015**, *73*, 296–307. [CrossRef] [PubMed]
80. Eoh, J.H.; Shen, N.; Burke, J.A.; Hinderer, S.; Xia, Z.; Schenke-Layland, K.; Gerecht, S. Enhanced Elastin Synthesis and Maturation in Human Vascular Smooth Muscle Tissue Derived from Induced-Pluripotent Stem Cells. *Acta Biomater.* **2017**, *52*, 49–59. [CrossRef]
81. Enomoto, S.; Sumi, M.; Kajimoto, K.; Nakazawa, Y.; Takahashi, R.; Takabayashi, C.; Asakura, T.; Sata, M. Long-Term Patency of Small-Diameter Vascular Graft Made from Fibroin, a Silk-Based Biodegradable Material. *J. Vasc. Surg.* **2010**, *51*, 155–164. [CrossRef]



82. Rosellini, E.; Barbani, N.; Lazzeri, L.; Cascone, M.G. Biomimetic and Bioactive Small Diameter Tubular Scaffolds for Vascular Tissue Engineering. *Biomimetics* **2022**, *7*, 199. [CrossRef] [PubMed]
83. Rambøl, M.H.; Hisdal, J.; Sundhagen, J.O.; Brinchmann, J.E.; Rosales, A. Recellularization of Decellularized Venous Grafts Using Peripheral Blood: A Critical Evaluation. *EBioMedicine* **2018**, *32*, 215–222. [CrossRef] [PubMed]
84. Huai, G.; Qi, P.; Yang, H.; Wang, Y. Characteristics of  $\alpha$ -Gal Epitope, Anti-Gal Antibody, A1,3 Galactosyltransferase and Its Clinical Exploitation (Review). *Int. J. Mol. Med.* **2016**, *37*, 11–20. [CrossRef] [PubMed]
85. Li, J.; Cai, Z.; Cheng, J.; Wang, C.; Fang, Z.; Xiao, Y.; Feng, Z.-G.; Gu, Y. Characterization of a Heparinized Decellularized Scaffold and Its Effects on Mechanical and Structural Properties. *J. Biomater. Sci. Polym. Ed.* **2020**, *31*, 999–1023. [CrossRef]
86. Eufrazio-da-Silva, T.; Ruiz-Hernandez, E.; O'Dwyer, J.; Picazo-Frutos, D.; Duffy, G.P.; Murphy, B.P. Enhancing Medial Layer Recellularization of Tissue-Engineered Blood Vessels Using Radial Microchannels. *Regen. Med.* **2019**, *14*, 1013–1028. [CrossRef] [PubMed]
87. Hazwani, A.; Sha'Ban, M.; Azhim, A. Characterization and in Vivo Study of Decellularized Aortic Scaffolds Using Closed Sonication System. *Organogenesis* **2019**, *15*, 120–136. [CrossRef] [PubMed]
88. Hsia, K.; Lin, C.-H.; Lee, H.-Y.; Chen, W.-M.; Yao, C.-L.; Chen, C.-C.; Ma, H.; Wang, S.-J.; Lu, J.-H. Sphingosine-1-Phosphate in Endothelial Cell Recellularization Improves Patency and Endothelialization of Decellularized Vascular Grafts In Vivo. *Int. J. Mol. Sci.* **2019**, *20*, 1641. [CrossRef] [PubMed]
89. Kajbafzadeh, A.-M.; Khorramirouz, R.; Kameli, S.M.; Fendereski, K.; Daryabari, S.S.; Tavangar, S.M.; Azizi Garajegayeh, B. Three-Year Efficacy and Patency Follow-up of Decellularized Human Internal Mammary Artery as a Novel Vascular Graft in Animal Models. *J. Thorac. Cardiovasc. Surg.* **2019**, *157*, 1494–1502. [CrossRef]
90. Mallis, P.; Michalopoulos, E.; Pantsios, P.; Kozaniti, F.; Deligianni, D.; Papapanagiotou, A.; Stavropoulos Giokas, C. Recellularization Potential of Small Diameter Vascular Grafts Derived from Human Umbilical Artery. *Biomed. Mater. Eng.* **2019**, *30*, 61–71. [CrossRef] [PubMed]
91. Kumar Kuna, V.; Xu, B.; Sumitran-Holgersson, S. Decellularization and Recellularization Methodology for Human Saphenous Veins. *J. Vis. Exp.* **2018**, *137*, e57803. [CrossRef]
92. Lin, C.-H.; Hsia, K.; Tsai, C.-H.; Ma, H.; Lu, J.-H.; Tsay, R.-Y. Decellularized Porcine Coronary Artery with Adipose Stem Cells for Vascular Tissue Engineering. *Biomed. Mater.* **2019**, *14*, 045014. [CrossRef]
93. Simsa, R.; Vila, X.M.; Salzer, E.; Teuschl, A.; Jenndahl, L.; Bergh, N.; Fogelstrand, P. Effect of Fluid Dynamics on Decellularization Efficacy and Mechanical Properties of Blood Vessels. *PLoS ONE* **2019**, *14*, e0220743. [CrossRef] [PubMed]
94. Asmussen, I.; Kjeldsen, K. Intimal Ultrastructure of Human Umbilical Arteries. Observations on Arteries from Newborn Children of Smoking and Nonsmoking Mothers. *Circ. Res.* **1975**, *36*, 579–589. [CrossRef] [PubMed]
95. Velarde, F.; Castañeda, V.; Morales, E.; Ortega, M.; Ocaña, E.; Álvarez-Barreto, J.; Grunauer, M.; Eguiguren, L.; Caicedo, A. Use of Human Umbilical Cord and Its Byproducts in Tissue Regeneration. *Front. Bioeng. Biotechnol.* **2020**, *8*, 117. [CrossRef] [PubMed]
96. Rodríguez-Rodríguez, V.E.; Martínez-González, B.; Quiroga-Garza, A.; Reyes-Hernández, C.G.; de la Fuente-Villarreal, D.; de la Garza-Castro, O.; Guzmán-López, S.; Elizondo-Omaña, R.E. Human Umbilical Vessels: Choosing the Optimal Decellularization Method. *ASAIO J.* **2018**, *64*, 575–580. [CrossRef] [PubMed]
97. Crapo, P.M.; Gilbert, T.W.; Badylak, S.F. An Overview of Tissue and Whole Organ Decellularization Processes. *Biomaterials* **2011**, *32*, 3233–3243. [CrossRef] [PubMed]
98. Xing, Q.; Yates, K.; Tahtinen, M.; Shearier, E.; Qian, Z.; Zhao, F. Decellularization of Fibroblast Cell Sheets for Natural Extracellular Matrix Scaffold Preparation. *Tissue Eng. Part C Methods* **2015**, *21*, 77–87. [CrossRef] [PubMed]
99. Gilbert, T.; Sellaro, T.; Badylak, S. Decellularization of Tissues and Organs. *Biomaterials* **2006**, *27*, 3675–3683. [CrossRef] [PubMed]
100. Leal, B.B.J.; Wakabayashi, N.; Oyama, K.; Kamiya, H.; Braghioroli, D.I.; Pranke, P. Vascular Tissue Engineering: Polymers and Methodologies for Small Caliber Vascular Grafts. *Front. Cardiovasc. Med.* **2021**, *7*, 592361. [CrossRef] [PubMed]
101. Omid, H.; Abdollahi, S.; Bonakdar, S.; Haghighipour, N.; Shokrgozar, M.A.; Mohammadi, J. Biomimetic Vascular Tissue Engineering by Decellularized Scaffold and Concurrent Cyclic Tensile and Shear Stresses. *J. Mater. Sci. Mater. Med.* **2023**, *34*, 12. [CrossRef] [PubMed]
102. Campbell, E.M.; Cahill, P.A.; Lally, C. Investigation of a Small-Diameter Decellularised Artery as a Potential Scaffold for Vascular Tissue Engineering; Biomechanical Evaluation and Preliminary Cell Seeding. *J. Mech. Behav. Biomed. Mater.* **2012**, *14*, 130–142. [CrossRef] [PubMed]
103. Dimitrievska, S.; Cai, C.; Weyers, A.; Balestrini, J.L.; Lin, T.; Sundaram, S.; Hatachi, G.; Spiegel, D.A.; Kyriakides, T.R.; Miao, J.; et al. Click-Coated, Heparinized, Decellularized Vascular Grafts. *Acta Biomater.* **2015**, *13*, 177–187. [CrossRef] [PubMed]
104. Gong, W.; Lei, D.; Li, S.; Huang, P.; Qi, Q.; Sun, Y.; Zhang, Y.; Wang, Z.; You, Z.; Ye, X.; et al. Hybrid Small-Diameter Vascular Grafts: Anti-Expansion Effect of Electrospun Poly  $\epsilon$ -Caprolactone on Heparin-Coated Decellularized Matrices. *Biomaterials* **2016**, *76*, 359–370. [CrossRef] [PubMed]
105. Quint, C.; Kondo, Y.; Manson, R.J.; Lawson, J.H.; Dardik, A.; Niklason, L.E. Decellularized Tissue-Engineered Blood Vessel as an Arterial Conduit. *Proc. Natl. Acad. Sci. USA* **2011**, *108*, 9214–9219. [CrossRef] [PubMed]
106. Catto, V.; Farè, S.; Freddi, G.; Tanzi, M.C. Vascular Tissue Engineering: Recent Advances in Small Diameter Blood Vessel Regeneration. *ISRN Vasc. Med.* **2014**, *2014*, 923030. [CrossRef]
107. Gui, L.; Muto, A.; Chan, S.A.; Breuer, C.K.; Niklason, L.E. Development of Decellularized Human Umbilical Arteries as Small-Diameter Vascular Grafts. *Tissue Eng. Part A* **2009**, *15*, 2665–2676. [CrossRef] [PubMed]

108. Dahl, S.L.M.; Rhim, C.; Song, Y.C.; Niklason, L.E. Mechanical Properties and Compositions of Tissue Engineered and Native Arteries. *Ann. Biomed. Eng.* **2007**, *35*, 348–355. [CrossRef] [PubMed]
109. Rickel, A.P.; Deng, X.; Engebretson, D.; Hong, Z. Electrospun Nanofiber Scaffold for Vascular Tissue Engineering. *Mater. Sci. Eng. C* **2021**, *129*, 112373. [CrossRef] [PubMed]
110. Mallis, P.; Kostakis, A.; Stavropoulos-Giokas, C.; Michalopoulos, E. Future Perspectives in Small-Diameter Vascular Graft Engineering. *Bioengineering* **2020**, *7*, 160. [CrossRef] [PubMed]
111. Suamte, L.; Tirkey, A.; Barman, J.; Jayasekhar Babu, P. Various Manufacturing Methods and Ideal Properties of Scaffolds for Tissue Engineering Applications. *Smart Mater. Manuf.* **2023**, *1*, 100011. [CrossRef]
112. Ramakrishna, S.; Fujihara, K.; Teo, W.-E.; Yong, T.; Ma, Z.; Ramaseshan, R. Electrospun Nanofibers: Solving Global Issues. *Mater. Today* **2006**, *9*, 40–50. [CrossRef]
113. Kong, X.; He, Y.; Zhou, H.; Gao, P.; Xu, L.; Han, Z.; Yang, L.; Wang, M. Chondroitin Sulfate/Polycaprolactone/Gelatin Electrospun Nanofibers with Antithrombogenicity and Enhanced Endothelial Cell Affinity as a Potential Scaffold for Blood Vessel Tissue Engineering. *Nanoscale Res. Lett.* **2021**, *16*, 62. [CrossRef] [PubMed]
114. Elsayed, Y.; Lekakou, C.; Labeed, F.; Tomlins, P. Fabrication and Characterisation of Biomimetic, Electrospun Gelatin Fibre Scaffolds for Tunica Media-Equivalent, Tissue Engineered Vascular Grafts. *Mater. Sci. Eng. C* **2016**, *61*, 473–483. [CrossRef] [PubMed]
115. Park, H.J.; Lee, J.S.; Lee, O.J.; Sheikh, F.A.; Moon, B.M.; Ju, H.W.; Kim, J.-H.; Kim, D.-K.; Park, C.H. Fabrication of Microporous Three-Dimensional Scaffolds from Silk Fibroin for Tissue Engineering. *Macromol. Res.* **2014**, *22*, 592–599. [CrossRef]
116. Dimopoulos, A.; Markatos, D.N.; Mitropoulou, A.; Panagiotopoulos, I.; Koletsis, E.; Mavrilas, D. A Novel Polymeric Fibrous Microstructured Biodegradable Small-Caliber Tubular Scaffold for Cardiovascular Tissue Engineering. *J. Mater. Sci. Mater. Med.* **2021**, *32*, 21. [CrossRef] [PubMed]
117. Zhu, J.; Chen, D.; Du, J.; Chen, X.; Wang, J.; Zhang, H.; Chen, S.; Wu, J.; Zhu, T.; Mo, X. Mechanical Matching Nanofibrous Vascular Scaffold with Effective Anticoagulation for Vascular Tissue Engineering. *Compos. B Eng.* **2020**, *186*, 107788. [CrossRef]
118. Rychter, M.; Baranowska-Korczyn, A.; Lulek, J. Progress and Perspectives in Bioactive Agent Delivery via Electrospun Vascular Grafts. *RSC Adv.* **2017**, *7*, 32164–32184. [CrossRef]
119. Li, X.; Huang, L.; Li, L.; Tang, Y.; Liu, Q.; Xie, H.; Tian, J.; Zhou, S.; Tang, G. Biomimetic Dual-Oriented/Bilayered Electrospun Scaffold for Vascular Tissue Engineering. *J. Biomater. Sci. Polym. Ed.* **2020**, *31*, 439–455. [CrossRef] [PubMed]
120. Fukunishi, T.; Best, C.A.; Sugiura, T.; Opfermann, J.; Ong, C.S.; Shinoka, T.; Breuer, C.K.; Krieger, A.; Johnson, J.; Hibino, N. Preclinical Study of Patient-Specific Cell-Free Nanofiber Tissue-Engineered Vascular Grafts Using 3-Dimensional Printing in a Sheep Model. *J. Thorac. Cardiovasc. Surg.* **2017**, *153*, 924–932. [CrossRef] [PubMed]
121. Wang, Y.; Wu, T.; Zhang, J.; Feng, Z.; Yin, M.; Mo, X. A Bilayer Vascular Scaffold with Spatially Controlled Release of Growth Factors to Enhance in Situ Rapid Endothelialization and Smooth Muscle Regeneration. *Mater. Des.* **2021**, *204*, 109649. [CrossRef]
122. Ding, Z.; Wang, Y.; Chen, F.; Hu, X.; Cheng, W.; Lu, Q.; Kaplan, D.L. Biomimetic Vascular Grafts with Circumferentially and Axially Oriented Microporous Structures for Native Blood Vessel Regeneration. *Adv. Funct. Mater.* **2024**, *34*, 2308888. [CrossRef]
123. Zhang, Y.; Li, X.S.; Guex, A.G.; Liu, S.S.; Müller, E.; Malini, R.I.; Zhao, H.J.; Rottmar, M.; Maniura-Weber, K.; Rossi, R.M.; et al. A Compliant and Biomimetic Three-Layered Vascular Graft for Small Blood Vessels. *Biofabrication* **2017**, *9*, 025010. [CrossRef] [PubMed]
124. Guo, S.; Jiang, Y.; Jiao, J.; Shi, Y.; Zhu, T.; Li, L. Electrospun Gelatin-Based Biomimetic Scaffold with Spatially Aligned and Three-Layer Architectures for Vascular Tissue Engineering. *Int. J. Biol. Macromol.* **2023**, *242*, 125039. [CrossRef] [PubMed]
125. Wilkens, C.A.; Rivet, C.J.; Akentjew, T.L.; Alverio, J.; Khoury, M.; Acevedo, J.P. Layer-by-Layer Approach for a Uniformed Fabrication of a Cell Patterned Vessel-like Construct. *Biofabrication* **2016**, *9*, 015001. [CrossRef] [PubMed]
126. Ju, Y.M.; Choi, J.S.; Atala, A.; Yoo, J.J.; Lee, S.J. Bilayered Scaffold for Engineering Cellularized Blood Vessels. *Biomaterials* **2010**, *31*, 4313–4321. [CrossRef] [PubMed]
127. Grus, T.; Lambert, L.; Mlcek, M.; Chlup, H.; Honsova, E.; Spacek, M.; Burgetova, A.; Lindner, J. In Vivo Evaluation of Short-Term Performance of New Three-Layer Collagen-Based Vascular Graft Designed for Low-Flow Peripheral Vascular Reconstructions. *Biomed. Res. Int.* **2018**, *2018*, 3519596. [CrossRef] [PubMed]
128. Konig, G.; McAllister, T.N.; Dusserre, N.; Garrido, S.A.; Iyican, C.; Marini, A.; Fiorillo, A.; Avila, H.; Wystrychowski, W.; Zagalski, K.; et al. Mechanical Properties of Completely Autologous Human Tissue Engineered Blood Vessels Compared to Human Saphenous Vein and Mammary Artery. *Biomaterials* **2009**, *30*, 1542–1550. [CrossRef]
129. El-Kurdi, M.S.; Hong, Y.; Stankus, J.J.; Soletti, L.; Wagner, W.R.; Vorp, D.A. Transient Elastic Support for Vein Grafts Using a Constricting Microfibrillar Polymer Wrap. *Biomaterials* **2008**, *29*, 3213–3220. [CrossRef] [PubMed]
130. Zeenat, L.; Zolfagharian, A.; Sriya, Y.; Sasikumar, S.; Bodaghi, M.; Pati, F. 4D Printing for Vascular Tissue Engineering: Progress and Challenges. *Adv. Mater. Technol.* **2023**, *8*, 2300200. [CrossRef]
131. Zhou, X.; Nowicki, M.; Sun, H.; Hann, S.Y.; Cui, H.; Esworthy, T.; Lee, J.D.; Plesniak, M.; Zhang, L.G. 3D Bioprinting-Tunable Small-Diameter Blood Vessels with Biomimetic Biphasic Cell Layers. *ACS Appl. Mater. Interfaces* **2020**, *12*, 45904–45915. [CrossRef] [PubMed]
132. Ran, X.; Ye, Z.; Fu, M.; Wang, Q.; Wu, H.; Lin, S.; Yin, T.; Hu, T.; Wang, G. Design, Preparation, and Performance of a Novel Bilayer Tissue-Engineered Small-Diameter Vascular Graft. *Macromol. Biosci.* **2019**, *19*, 1800189. [CrossRef] [PubMed]

133. Thalla, P.K.; Fadlallah, H.; Liberelle, B.; Lequoy, P.; De Crescenzo, G.; Merhi, Y.; Lerouge, S. Chondroitin Sulfate Coatings Display Low Platelet but High Endothelial Cell Adhesive Properties Favorable for Vascular Implants. *Biomacromolecules* **2014**, *15*, 2512–2520. [CrossRef] [PubMed]
134. Campelo, C.S.; Lima, L.D.; Rebêlo, L.M.; Mantovani, D.; Beppu, M.M.; Vieira, R.S. In Vitro Evaluation of Anti-Calcification and Anti-Coagulation on Sulfonated Chitosan and Carrageenan Surfaces. *Mater. Sci. Eng. C* **2016**, *59*, 241–248. [CrossRef] [PubMed]
135. Ma, L.; Li, X.; Guo, X.; Jiang, Y.; Li, X.; Guo, H.; Zhang, B.; Xu, Y.; Wang, X.; Li, Q. Promotion of Endothelial Cell Adhesion and Antithrombogenicity of Polytetrafluoroethylene by Chemical Grafting of Chondroitin Sulfate. *ACS Appl. Bio. Mater.* **2020**, *3*, 891–901. [CrossRef] [PubMed]
136. Charbonneau, C.; Ruiz, J.; Lequoy, P.; Hébert, M.; De Crescenzo, G.; Wertheimer, M.R.; Lerouge, S. Chondroitin Sulfate and Epidermal Growth Factor Immobilization after Plasma Polymerization: A Versatile Anti-Apoptotic Coating to Promote Healing Around Stent Grafts. *Macromol. Biosci.* **2012**, *12*, 812–821. [CrossRef] [PubMed]
137. Charbonneau, C.; Liberelle, B.; Hébert, M.-J.; De Crescenzo, G.; Lerouge, S. Stimulation of Cell Growth and Resistance to Apoptosis in Vascular Smooth Muscle Cells on a Chondroitin Sulfate/Epidermal Growth Factor Coating. *Biomaterials* **2011**, *32*, 1591–1600. [CrossRef] [PubMed]
138. Badv, M.; Bayat, F.; Weitz, J.I.; Didar, T.F. Single and Multi-Functional Coating Strategies for Enhancing the Biocompatibility and Tissue Integration of Blood-Contacting Medical Implants. *Biomaterials* **2020**, *258*, 120291. [CrossRef] [PubMed]
139. Devine, R.; Goudie, M.J.; Singha, P.; Schmiedt, C.; Douglass, M.; Brisbois, E.J.; Handa, H. Mimicking the Endothelium: Dual Action Heparinized Nitric Oxide Releasing Surface. *ACS Appl. Mater. Interfaces* **2020**, *12*, 20158–20171. [CrossRef] [PubMed]
140. Avci-Adali, M.; Ziemer, G.; Wendel, H.P. Induction of EPC Homing on Biofunctionalized Vascular Grafts for Rapid in Vivo Self-Endothelialization—A Review of Current Strategies. *Biotechnol. Adv.* **2010**, *28*, 119–129. [CrossRef] [PubMed]
141. Sánchez, P.F.; Brey, E.M.; Briceño, J.C. Endothelialization Mechanisms in Vascular Grafts. *J. Tissue Eng. Regen. Med.* **2018**, *12*, 2164–2178. [CrossRef] [PubMed]
142. Asahara, T.; Murohara, T.; Sullivan, A.; Silver, M.; van der Zee, R.; Li, T.; Witzendichler, B.; Schatteman, G.; Isner, J.M. Isolation of Putative Progenitor Endothelial Cells for Angiogenesis. *Science* **1997**, *275*, 964–966. [CrossRef]
143. Oh, J.-M.; Venters, C.C.; Di, C.; Pinto, A.M.; Wan, L.; Younis, I.; Cai, Z.; Arai, C.; So, B.R.; Duan, J.; et al. U1 SnRNP Regulates Cancer Cell Migration and Invasion in Vitro. *Nat. Commun.* **2020**, *11*, 1. [CrossRef] [PubMed]
144. Lin, Q.; Ding, X.; Qiu, F.; Song, X.; Fu, G.; Ji, J. In Situ Endothelialization of Intravascular Stents Coated with an Anti-CD34 Antibody Functionalized Heparin–Collagen Multilayer. *Biomaterials* **2010**, *31*, 4017–4025. [CrossRef] [PubMed]
145. Mrówczyński, W.; Rungtatscher, A.; Buchegger, F.; Tille, J.-C.; Namy, S.; Ratib, O.; Kutryk, M.; Walpoth, B.H. Experimental cardiovascular and lung research Biological Effects of Anti-CD34-Coated EPTFE Vascular Grafts. Early in Vivo Experimental Results. *Pol. J. Cardio-Thorac. Surg.* **2014**, *2*, 182–190. [CrossRef] [PubMed]
146. Rotmans, J.I.; Heyligers, J.M.M.; Verhagen, H.J.M.; Velema, E.; Nagtegaal, M.M.; de Kleijn, D.P.V.; de Groot, F.G.; Stroes, E.S.G.; Pasterkamp, G. In Vivo Cell Seeding with Anti-CD34 Antibodies Successfully Accelerates Endothelialization but Stimulates Intimal Hyperplasia in Porcine Arteriovenous Expanded Polytetrafluoroethylene Grafts. *Circulation* **2005**, *112*, 12–18. [CrossRef] [PubMed]
147. Hu, Y.T.; Pan, X.D.; Zheng, J.; Ma, W.G.; Sun, L.Z. In Vitro and in Vivo Evaluation of a Small-Caliber Coaxial Electrospun Vascular Graft Loaded with Heparin and VEGF. *Int. J. Surg.* **2017**, *44*, 244–249. [CrossRef]
148. Du, F.; Wang, H.; Zhao, W.; Li, D.; Kong, D.; Yang, J.; Zhang, Y. Gradient Nanofibrous Chitosan/Poly  $\epsilon$ -Caprolactone Scaffolds as Extracellular Microenvironments for Vascular Tissue Engineering. *Biomaterials* **2012**, *33*, 762–770. [CrossRef] [PubMed]
149. Xiao, Y.; Truskey, G.A. Effect of Receptor-Ligand Affinity on the Strength of Endothelial Cell Adhesion. *Biophys. J.* **1996**, *71*, 2869–2884. [CrossRef]
150. Cheng, S.; Craig, W.S.; Mullen, D.; Tschopp, J.F.; Dixon, D.; Pierschbacher, M.D. Design and Synthesis of Novel Cyclic RGD-Containing Peptides as Highly Potent and Selective Integrin.  $\alpha$ IIb.  $\beta$ 3 Antagonists. *J. Med. Chem.* **1994**, *37*, 1–8. [CrossRef]
151. Rodenberg, E.J.; Pavalko, F.M. Peptides Derived from Fibronectin Type III Connecting Segments Promote Endothelial Cell Adhesion but Not Platelet Adhesion: Implications in Tissue-Engineered Vascular Grafts. *Tissue Eng.* **2007**, *13*, 2653–2666. [CrossRef] [PubMed]
152. Devalliere, J.; Chen, Y.; Dooley, K.; Yarmush, M.L.; Uygun, B.E. Improving Functional Re-Endothelialization of Acellular Liver Scaffold Using REDV Cell-Binding Domain. *Acta Biomater.* **2018**, *78*, 151–164. [CrossRef]
153. Wei, Y.; Ji, Y.; Xiao, L.; Lin, Q.; Ji, J. Different Complex Surfaces of Polyethyleneglycol (PEG) and REDV Ligand to Enhance the Endothelial Cells Selectivity over Smooth Muscle Cells. *Colloids Surf. B Biointerfaces* **2011**, *84*, 369–378. [CrossRef] [PubMed]
154. Duan, Y.; Yu, S.; Xu, P.; Wang, X.; Feng, X.; Mao, Z.; Gao, C. Co-Immobilization of CD133 Antibodies, Vascular Endothelial Growth Factors, and REDV Peptide Promotes Capture, Proliferation, and Differentiation of Endothelial Progenitor Cells. *Acta Biomater.* **2019**, *96*, 137–148. [CrossRef] [PubMed]
155. Melchiorri, A.J.; Bracaglia, L.G.; Kimerer, L.K.; Hibino, N.; Fisher, J.P. In Vitro Endothelialization of Biodegradable Vascular Grafts via Endothelial Progenitor Cell Seeding and Maturation in a Tubular Perfusion System Bioreactor. *Tissue Eng. Part C Methods* **2016**, *22*, 663–670. [CrossRef] [PubMed]
156. Aird, W.C. Phenotypic Heterogeneity of the Endothelium. *Circ. Res.* **2007**, *100*, 158–173. [CrossRef] [PubMed]
157. Xu, C.; Inai, R.; Kotaki, M.; Ramakrishna, S. Electrospun Nanofiber Fabrication as Synthetic Extracellular Matrix and Its Potential for Vascular Tissue Engineering. *Tissue Eng.* **2004**, *10*, 1160–1168. [CrossRef] [PubMed]

158. Mo, X.M.; Xu, C.Y.; Kotaki, M.; Ramakrishna, S. Electrospun P(LLA-CL) Nanofiber: A Biomimetic Extracellular Matrix for Smooth Muscle Cell and Endothelial Cell Proliferation. *Biomaterials* **2004**, *25*, 1883–1890. [CrossRef] [PubMed]
159. Lu, J.; Rao, M.P.; MacDonald, N.C.; Khang, D.; Webster, T.J. Improved Endothelial Cell Adhesion and Proliferation on Patterned Titanium Surfaces with Rationally Designed, Micrometer to Nanometer Features. *Acta Biomater.* **2008**, *4*, 192–201. [CrossRef] [PubMed]
160. Wang, Z.; Liu, C.; Zhu, D.; Gu, X.; Xu, Y.; Qin, Q.; Dong, N.; Zhang, S.; Wang, J. Untangling the Co-Effects of Oriented Nanotopography and Sustained Anticoagulation in a Biomimetic Intima on Neovessel Remodeling. *Biomaterials* **2020**, *231*, 119654. [CrossRef] [PubMed]
161. Jeong, Y.; Yao, Y.; Yim, E.K.F. Current Understanding of Intimal Hyperplasia and Effect of Compliance in Synthetic Small Diameter Vascular Grafts. *Biomater. Sci.* **2020**, *8*, 4383–4395. [CrossRef] [PubMed]
162. Castellot, J.; Addonizio, M.; Rosenberg, R.; Karnovsky, M. Cultured Endothelial Cells Produce Heparinlike Inhibitor of Smooth Muscle Cell Growth. *J. Cell Biol.* **1981**, *90*, 372–379. [CrossRef] [PubMed]
163. Baek, I.; Bai, C.Z.; Hwang, J.; Park, J.; Park, J.-S.; Kim, D.J. Suppression of Neointimal Hyperplasia by Sirolimus-Eluting Expanded Polytetrafluoroethylene (EPTFE) Haemodialysis Grafts in Comparison with Paclitaxel-Coated Grafts. *Nephrol. Dial. Transplant.* **2012**, *27*, 1997–2004. [CrossRef] [PubMed]
164. Tara, S.; Kurobe, H.; de Dios Ruiz Rosado, J.; Best, C.A.; Shoji, T.; Mahler, N.; Yi, T.; Lee, Y.-U.; Sugiura, T.; Hibino, N.; et al. Cilostazol, Not Aspirin, Prevents Stenosis of Bioresorbable Vascular Grafts in a Venous Model. *Arterioscler. Thromb. Vasc. Biol.* **2015**, *35*, 2003–2010. [CrossRef] [PubMed]
165. Innocente, F.; Mandracchia, D.; Pektok, E.; Nottelet, B.; Tille, J.-C.; de Valence, S.; Faggian, G.; Mazzucco, A.; Kalangos, A.; Gurny, R.; et al. Paclitaxel-Eluting Biodegradable Synthetic Vascular Prostheses. *Circulation* **2009**, *120*, S37–S45. [CrossRef] [PubMed]
166. Ding, N.; Dou, C.; Wang, Y.; Liu, F.; Guan, G.; Huo, D.; Li, Y.; Yang, J.; Wei, K.; Yang, M.; et al. Antishear Stress Bionic Carbon Nanotube Mesh Coating with Intracellular Controlled Drug Delivery Constructing Small-Diameter Tissue-Engineered Vascular Grafts. *Adv. Healthc. Mater.* **2018**, *7*, 1800026. [CrossRef]
167. Sugiura, T.; Agarwal, R.; Tara, S.; Yi, T.; Lee, Y.-U.; Breuer, C.K.; Weiss, A.S.; Shinoka, T. Tropoelastin Inhibits Intimal Hyperplasia of Mouse Bioresorbable Arterial Vascular Grafts. *Acta Biomater.* **2017**, *52*, 74–80. [CrossRef]
168. Furdella, K.J.; Higuchi, S.; Behrangzade, A.; Kim, K.; Wagner, W.R.; Vande Geest, J.P. In-Vivo Assessment of a Tissue Engineered Vascular Graft Computationally Optimized for Target Vessel Compliance. *Acta Biomater.* **2021**, *123*, 298–311. [CrossRef] [PubMed]
169. Gupta, P.; Moses, J.C.; Mandal, B.B. Surface Patterning and Innate Physicochemical Attributes of Silk Films Concomitantly Govern Vascular Cell Dynamics. *ACS Biomater. Sci. Eng.* **2019**, *5*, 933–949. [CrossRef]
170. Nakayama, K.H.; Surya, V.N.; Gole, M.; Walker, T.W.; Yang, W.; Lai, E.S.; Ostrowski, M.A.; Fuller, G.G.; Dunn, A.R.; Huang, N.F. Nanoscale Patterning of Extracellular Matrix Alters Endothelial Function under Shear Stress. *Nano Lett.* **2016**, *16*, 410–419. [CrossRef] [PubMed]
171. Cao, Y.; Poon, Y.F.; Feng, J.; Rayatpisheh, S.; Chan, V.; Chan-Park, M.B. Regulating Orientation and Phenotype of Primary Vascular Smooth Muscle Cells by Biodegradable Films Patterned with Arrays of Microchannels and Discontinuous Microwalls. *Biomaterials* **2010**, *31*, 6228–6238. [CrossRef]
172. Wang, Y.; Shi, H.; Qiao, J.; Tian, Y.; Wu, M.; Zhang, W.; Lin, Y.; Niu, Z.; Huang, Y. Electrospun Tubular Scaffold with Circumferentially Aligned Nanofibers for Regulating Smooth Muscle Cell Growth. *ACS Appl. Mater. Interfaces* **2014**, *6*, 2958–2962. [CrossRef]
173. Zhu, M.; Wang, Z.; Zhang, J.; Wang, L.; Yang, X.; Chen, J.; Fan, G.; Ji, S.; Xing, C.; Wang, K.; et al. Circumferentially Aligned Fibers Guided Functional Neovessel Regeneration in Vivo. *Biomaterials* **2015**, *61*, 85–94. [CrossRef] [PubMed]
174. Moosmang, S. Dominant Role of Smooth Muscle L-Type Calcium Channel Cav1.2 for Blood Pressure Regulation. *EMBO J.* **2003**, *22*, 6027–6034. [CrossRef]
175. Sartore, S.; Chiavegato, A.; Faggian, E.; Franch, R.; Puato, M.; Ausoni, S.; Pauletto, P. Contribution of Adventitial Fibroblasts to Neointima Formation and Vascular Remodeling. *Circ. Res.* **2001**, *89*, 1111–1121. [CrossRef] [PubMed]
176. Issa Bhaloo, S.; Wu, Y.; Le Bras, A.; Yu, B.; Gu, W.; Xie, Y.; Deng, J.; Wang, Z.; Zhang, Z.; Kong, D.; et al. Binding of Dickkopf-3 to CXCR7 Enhances Vascular Progenitor Cell Migration and Degradable Graft Regeneration. *Circ. Res.* **2018**, *123*, 451–466. [CrossRef] [PubMed]
177. Roh, J.D.; Sawh-Martinez, R.; Brennan, M.P.; Jay, S.M.; Devine, L.; Rao, D.A.; Yi, T.; Mirensky, T.L.; Nalbandian, A.; Udelsman, B.; et al. Tissue-Engineered Vascular Grafts Transform into Mature Blood Vessels via an Inflammation-Mediated Process of Vascular Remodeling. *Proc. Natl. Acad. Sci. USA* **2010**, *107*, 4669–4674. [CrossRef] [PubMed]
178. Hibino, N.; Mejias, D.; Pietris, N.; Dean, E.; Yi, T.; Best, C.; Shinoka, T.; Breuer, C. The Innate Immune System Contributes to Tissue-engineered Vascular Graft Performance. *FASEB J.* **2015**, *29*, 2431–2438. [CrossRef] [PubMed]
179. Graney, P.L.; Ben-Shaul, S.; Landau, S.; Bajpai, A.; Singh, B.; Eager, J.; Cohen, A.; Levenberg, S.; Spiller, K.L. Macrophages of Diverse Phenotypes Drive Vascularization of Engineered Tissues. *Sci. Adv.* **2020**, *6*, eaay6391. [CrossRef] [PubMed]
180. Witherel, C.E.; Abeyayehu, D.; Barker, T.H.; Spiller, K.L. Macrophage and Fibroblast Interactions in Biomaterial-Mediated Fibrosis. *Adv. Healthc. Mater.* **2019**, *8*, 1801451. [CrossRef]
181. Zhang, F.; King, M.W. Immunomodulation Strategies for the Successful Regeneration of a Tissue-Engineered Vascular Graft. *Adv. Healthc. Mater.* **2022**, *11*, 2200045. [CrossRef] [PubMed]

182. Wang, Z.; Cui, Y.; Wang, J.; Yang, X.; Wu, Y.; Wang, K.; Gao, X.; Li, D.; Li, Y.; Zheng, X.-L.; et al. The Effect of Thick Fibers and Large Pores of Electrospun Poly( $\epsilon$ -Caprolactone) Vascular Grafts on Macrophage Polarization and Arterial Regeneration. *Biomaterials* **2014**, *35*, 5700–5710. [CrossRef] [PubMed]
183. Liu, J.; Qin, Y.; Wu, Y.; Sun, Z.; Li, B.; Jing, H.; Zhang, C.; Li, C.; Leng, X.; Wang, Z.; et al. The Surrounding Tissue Contributes to Smooth Muscle Cells' Regeneration and Vascularization of Small Diameter Vascular Grafts. *Biomater. Sci.* **2019**, *7*, 914–925. [CrossRef] [PubMed]
184. Smith, R.J.; Yi, T.; Nasiri, B.; Breuer, C.K.; Andreadis, S.T. Implantation of VEGF-functionalized Cell-free Vascular Grafts: Regenerative and Immunological Response. *FASEB J.* **2019**, *33*, 5089–5100. [CrossRef] [PubMed]
185. Bonito, V.; Smits, A.I.P.M.; Goor, O.J.G.M.; Ippel, B.D.; Driessen-Mol, A.; Munker, T.J.A.G.; Bosman, A.W.; Mes, T.; Dankers, P.Y.W.; Bouten, C.V.C. Modulation of Macrophage Phenotype and Protein Secretion via Heparin-IL-4 Functionalized Supramolecular Elastomers. *Acta Biomater.* **2018**, *71*, 247–260. [CrossRef] [PubMed]
186. Wei, Y.; Wu, Y.; Zhao, R.; Zhang, K.; Midgley, A.C.; Kong, D.; Li, Z.; Zhao, Q. MSC-Derived SEVs Enhance Patency and Inhibit Calcification of Synthetic Vascular Grafts by Immunomodulation in a Rat Model of Hyperlipidemia. *Biomaterials* **2019**, *204*, 13–24. [CrossRef]
187. Kobayashi, N.; Yasu, T.; Ueba, H.; Sata, M.; Hashimoto, S.; Kuroki, M.; Saito, M.; Kawakami, M. Mechanical Stress Promotes the Expression of Smooth Muscle-like Properties in Marrow Stromal Cells. *Exp. Hematol.* **2004**, *32*, 1238–1245. [CrossRef] [PubMed]
188. Çelebi-Saltik, B.; Öteyaka, M.Ö.; Gökçinar-Yagci, B. Stem Cell-Based Small-Diameter Vascular Grafts in Dynamic Culture. *Connect. Tissue Res.* **2021**, *62*, 151–163. [CrossRef]
189. Moheb Afzali, A.; Kheradmand, M.A.; Naghib, S.M. Bioreactor Design-Assisted Bioprinting of Stimuli-Responsive Materials for Tissue Engineering and Drug Delivery Applications. *Bioprinting* **2024**, *37*, e00325. [CrossRef]
190. Lim, D.; Renteria, E.S.; Sime, D.S.; Ju, Y.M.; Kim, J.H.; Criswell, T.; Shupe, T.D.; Atala, A.; Marini, F.C.; Gurcan, M.N.; et al. Bioreactor Design and Validation for Manufacturing Strategies in Tissue Engineering. *Biodes. Manuf.* **2022**, *5*, 43–63. [CrossRef] [PubMed]
191. Chen, H.-C.; Hu, Y.-C. Bioreactors for Tissue Engineering. *Biotechnol. Lett.* **2006**, *28*, 1415–1423. [CrossRef] [PubMed]
192. Voß, K.; Werner, M.P.; Gesenhues, J.; Kučikas, V.; van Zandvoort, M.; Jockenhoevel, S.; Schmitz-Rode, T.; Abel, D. Towards Technically Controlled Bioreactor Maturation of Tissue-Engineered Heart Valves. *Biomed. Eng./Biomed. Tech.* **2022**, *67*, 461–470. [CrossRef] [PubMed]
193. Lujan, T.J.; Wirtz, K.M.; Bahney, C.S.; Madey, S.M.; Johnstone, B.; Bottlang, M. A Novel Bioreactor for the Dynamic Stimulation and Mechanical Evaluation of Multiple Tissue-Engineered Constructs. *Tissue Eng. Part C Methods* **2011**, *17*, 367–374. [CrossRef] [PubMed]
194. Lin, S.; Mequanint, K. Bioreactor-Induced Mesenchymal Progenitor Cell Differentiation and Elastic Fiber Assembly in Engineered Vascular Tissues. *Acta Biomater.* **2017**, *59*, 200–209. [CrossRef] [PubMed]
195. Wang, J.; Liu, L.; Wu, Y.; Maitz, M.F.; Wang, Z.; Koo, Y.; Zhao, A.; Sankar, J.; Kong, D.; Huang, N.; et al. Ex Vivo Blood Vessel Bioreactor for Analysis of the Biodegradation of Magnesium Stent Models with and without Vessel Wall Integration. *Acta Biomater.* **2017**, *50*, 546–555. [CrossRef] [PubMed]
196. Bono, N.; Meghezi, S.; Soncini, M.; Piola, M.; Mantovani, D.; Fiore, G.B. A Dual-Mode Bioreactor System for Tissue Engineered Vascular Models. *Ann. Biomed. Eng.* **2017**, *45*, 1496–1510. [CrossRef] [PubMed]
197. Pennings, I.; van Haaften, E.E.; Jungst, T.; Bulsink, J.A.; Rosenberg, A.J.W.P.; Groll, J.; Bouten, C.V.C.; Kurniawan, N.A.; Smits, A.I.P.M.; Gawlitta, D. Layer-Specific Cell Differentiation in Bi-Layered Vascular Grafts under Flow Perfusion. *Biofabrication* **2019**, *12*, 015009. [CrossRef] [PubMed]
198. Wang, C.; Cen, L.; Yin, S.; Liu, Q.; Liu, W.; Cao, Y.; Cui, L. A Small Diameter Elastic Blood Vessel Wall Prepared under Pulsatile Conditions from Polyglycolic Acid Mesh and Smooth Muscle Cells Differentiated from Adipose-Derived Stem Cells. *Biomaterials* **2010**, *31*, 621–630. [CrossRef] [PubMed]
199. Bilodeau, K.; Couet, F.; Boccafroschi, F.; Mantovani, D. Design of a Perfusion Bioreactor Specific to the Regeneration of Vascular Tissues Under Mechanical Stresses. *Artif. Organs* **2005**, *29*, 906–912. [CrossRef] [PubMed]
200. Derhambakhsh, S.; Mohammadi, J.; Shokrgozar, M.A.; Rabbani, H.; Sadeghi, N.; Nekounam, H.; Mohammadi, S.; Lee, K.B.; Khakbiz, M. Investigation of Electrical Stimulation on Phenotypic Vascular Smooth Muscle Cells Differentiation in Tissue-Engineered Small-Diameter Vascular Graft. *Tissue Cell* **2023**, *81*, 101996. [CrossRef] [PubMed]
201. Kojima, T.; Nakamura, T.; Saito, J.; Hidaka, Y.; Akimoto, T.; Inoue, H.; Chick, C.N.; Usuki, T.; Kaneko, M.; Miyagi, E.; et al. Hydrostatic Pressure under Hypoxia Facilitates Fabrication of Tissue-Engineered Vascular Grafts Derived from Human Vascular Smooth Muscle Cells in Vitro. *Acta Biomater.* **2023**, *171*, 209–222. [CrossRef] [PubMed]

**Disclaimer/Publisher's Note:** The statements, opinions and data contained in all publications are solely those of the individual author(s) and contributor(s) and not of MDPI and/or the editor(s). MDPI and/or the editor(s) disclaim responsibility for any injury to people or property resulting from any ideas, methods, instructions or products referred to in the content.



## Review

# Metachronal Motion of Biological and Artificial Cilia

Zhiwei Cui <sup>1,2</sup>, Ye Wang <sup>1,2</sup> and Jaap M. J. den Toonder <sup>1,2,\*</sup>

<sup>1</sup> Department of Mechanical Engineering, Eindhoven University of Technology,  
P.O. Box 513, 5600 MB Eindhoven, The Netherlands; z.cui@tue.nl (Z.C.); y.wang2@tue.nl (Y.W.)

<sup>2</sup> Institute for Complex Molecular Systems, Eindhoven University of Technology,  
P.O. Box 513, 5600 MB Eindhoven, The Netherlands

\* Correspondence: j.m.j.d.toonder@tue.nl

**Abstract:** Cilia are slender, hair-like cell protrusions that are present ubiquitously in the natural world. They perform essential functions, such as generating fluid flow, propulsion, and feeding, in organisms ranging from protozoa to the human body. The coordinated beating of cilia, which results in wavelike motions known as metachrony, has fascinated researchers for decades for its role in functions such as flow generation and mucus transport. Inspired by nature, researchers have explored diverse materials for the fabrication of artificial cilia and developed several methods to mimic the metachronal motion observed in their biological counterparts. In this review, we will introduce the different types of metachronal motion generated by both biological and artificial cilia, the latter including pneumatically, photonically, electrically, and magnetically driven artificial cilia. Furthermore, we review the possible applications of metachronal motion by artificial cilia, focusing on flow generation, transport of mucus, particles, and droplets, and microrobotic locomotion. The overall aim of this review is to offer a comprehensive overview of the metachronal motions exhibited by diverse artificial cilia and the corresponding practical implementations. Additionally, we identify the potential future directions within this field. These insights present an exciting opportunity for further advancements in this domain.

**Keywords:** metachronal motion; cilia; flow generation; transportation; microrobot



**Citation:** Cui, Z.; Wang, Y.; den Toonder, J.M.J. Metachronal Motion of Biological and Artificial Cilia. *Biomimetics* **2024**, *9*, 198. <https://doi.org/10.3390/biomimetics9040198>

Academic Editors: Stanislav N. Gorb and Thomas Speck

Received: 24 January 2024

Revised: 22 March 2024

Accepted: 23 March 2024

Published: 27 March 2024



**Copyright:** © 2024 by the authors. Licensee MDPI, Basel, Switzerland. This article is an open access article distributed under the terms and conditions of the Creative Commons Attribution (CC BY) license (<https://creativecommons.org/licenses/by/4.0/>).

## 1. Introduction

Cilia are slender, hair-like microstructures projecting from cells that are present in numerous organisms ranging from unicellular entities to the human body; their typical length ranges from 1 to 30  $\mu\text{m}$  [1–3]. The individual cilium exhibits asymmetric beating at low Reynolds numbers, with viscous forces dominating inertial forces due to the small scale of the biological cilia. A single beating cycle of the cilium comprises two phases, namely the effective stroke and the recovery stroke [4–8]. During the effective stroke, the cilium undergoes linear, rod-like movement, whereas in the recovery stroke, it takes a more curved shape, moving often closer to the surface [9–11]. A phenomenon often observed in biological cilia is their collective wavelike motion, with adjacent cilia displaying a slight phase lag, which is known as metachronal motion. This coordinated asynchrony can result in various types of wave-like patterns of cilia movement. There are four types of metachronal motion, which can be distinguished by the direction of the wave propagation in relation to the beating motion of individual cilia (see Figure 1). For symplectic metachronal motion, the wave propagation direction is the same as that of the effective stroke; antiplectic metachronal motion is characterized by the wave propagation direction being opposite to the direction of the effective stroke; in dextroplectic metachronal motion, the wave propagates perpendicularly to the effective stroke and the beat is to the right of the wave; finally, laeoplectic metachronal motion involves wave propagation perpendicular to the effective stroke and the beat is to the left of the wave [4,5,8]. In nature, symplectic and antiplectic metachrony are predominant.

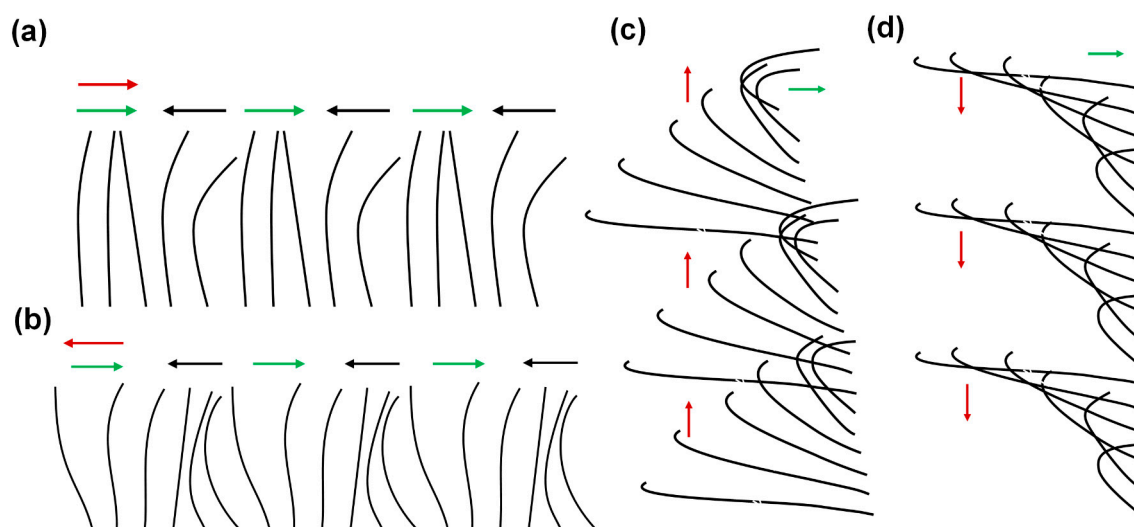


**Figure 1.** Schematics of the four types of metachronal motion exhibited by biological cilia. Each diagram represents a row of cilia. The red arrows indicate the direction of the metachronal wave, the green arrows represent the directions of the effective stroke, and the black arrows represent the recovery stroke. (a) Symplectic metachronal motion; (b) antiplectic metachronal motion; (c) dexioplectic metachronal motion; and (d) laeoplectic metachronal motion.

Research has indicated that the metachronal motion of the cilia plays an important role in many biological processes, such as mucociliary clearance [1,9,12–15], fluid transport [16–18], and sensory functions [3,19]. The malfunction of the cilia is associated with serious diseases such as cystic fibrosis (CF), primary ciliary dyskinesia (PCD), and chronic obstructive pulmonary disease (COPD) [1]. One of the most common instances of metachronal coordination is observed in the cilia found within the respiratory system of mammals, where the metachronal coordination facilitates the clearance of mucus and the removal of pathogens from the airways [20]. The disorder of the metachronal motion will result in the accumulation of mucus and bacteria in the airways and lead to infections. Furthermore, the metachronal motion of the cilia facilitates the transport of ovum and sperm within the female oviduct [9]. In the case of *Paramecium*, the metachronal motion of the cilia covering its outer surface can propel this microorganism at speeds equivalent to 10 times its own body length per second [17]. Also, numerical studies have shown that the metachronal motion of artificial cilia can enhance flow generation in lab-on-chip devices compared to synchronous cilia motion [17,21]. Inspired by the prominence of metachronal motion in various biological processes, researchers have endeavored to develop artificial cilia that can exhibit metachronal motion.

Research on the metachronal motion of artificial cilia started over a decade ago and is currently undergoing rapid development. Several research groups have developed different methods to fabricate artificial cilia while realizing metachronal motion through various approaches based on the properties of the artificial cilia patch/array. Artificial cilia, as micro-actuators, can be actuated in many ways, including but not limited to electric fields [22–25], pneumatic pumps [21,26,27], light [28–30], and magnetic fields [31–35]. In these systems, the prime goal is mostly to achieve asymmetric motion of the individual artificial cilia, and the metachronal motion must be realized by controlling the phase difference in motion of neighboring cilia. By mimicking the metachronal motion of biological cilia, researchers have been exploring the capabilities of the developed artificial cilia and the added value of metachronal motion in applications such as generating flow in microfluidic chips, transportation of particles, droplets, and mucus, as well as walking robots [3,19,35–38].

The current state of the topic of metachronal cilia motion presents an exciting stage of development, prompting a comprehensive review of its status and future potential, which is the aim of this paper. We collected all the relevant studies by searching the literature for the



keywords “metachronal motion” and “cilia”. Different from existing reviews about cilia, in this review, we focus specifically on the metachronal motion of cilia and its corresponding applications. We start with a brief overview of natural cilia and the metachronal motion shown by them. Then we describe how artificial cilia can mimic biological metachronal motion by reviewing the proposed methods to fabricate and actuate the artificial cilia to achieve metachronal motion for different actuation principles. Subsequently, we review the main applications of metachronal cilia motion that have been studied, including flow generation, particle/droplet transportation, and microrobot locomotion. We conclude the review with a general summary and a forward-looking perspective on the future development of the metachronal motion of artificial cilia.

## 2. Metachronal Motion of Biological Cilia

In this section, we present a comprehensive review of the metachronal motion exhibited by natural biological cilia.

Biological cilia were first observed in 1675 by Antonie van Leeuwenhoek, marking the discovery of these hair-like structures protruding from the surface of cells [39]. In the centuries after this, researchers extensively studied the structure, movement, and functions of the biological cilia in detail. Biological cilia, quite ubiquitous in nature, can be found in many different organisms, tissues, and small creatures. For instance, protozoa, zebrafish, rats, and almost all the tissues of the human body have cilia [11,40–42]. Cilia dimensions exhibit considerable variability, ranging from a few micrometers in length to several tens of micrometers, but typically within the range of 1 to 30  $\mu\text{m}$  [3]. Notably, certain cilia, for instance, the flagellum of sperm cells, attain lengths extending into the tens of micrometers [40]. Furthermore, it has been observed that the structures of cilia are different depending on their location, leading to distinct functions. Cilia are responsible for a wide range of physiological functions, including motility, sensing, and signaling [1,43–45]. A cilium is composed of two fundamental components: a basal body connecting it to the cell, and an axoneme forming the hairlike protrusion. There are two main categories: motile cilia, with an axoneme characterized by a  $9 + 2$  microtubular configuration featuring nine peripheral doublet microtubules enveloping two central singlet microtubules, and non-motile or primary cilia, defined by a  $9 + 0$  microtubular arrangement of the axoneme that lacks the central pair of microtubules [40,41,46,47].

A noteworthy observation in the domain of biological cilia is the prevalence of metachronal motion, a phenomenon of coordinated wavelike movement of arrays of cilia. As explained earlier, there are four basic types of metachronal motion in nature, as illustrated in Figure 1. Morphologically, in symplectic metachrony shown in Figure 1a, the cilia performing the effective stroke are spaced more closely together than the ones performing the recovery stroke, while this is the other way around for antiplectic metachromism in Figure 1b. In dexioplectic and laeoplectic metachronism, shown in Figure 1c,d, respectively, the individual cilia have more freedom of movement than in symplectic and antiplectic metachronism [5,8].

Symplectic metachronal motion has been observed in *Opalina*, a multinucleate protozoon inhabiting the rectal environment of frogs [5,11]. While *Opalina* is not classified as a true ciliate, it possesses numerous ciliary organelles, often referred to as flagella. This organism exhibits a distinctive morphology, taking the form of a slender, flat disk with average dimensions of approximately 200–300  $\mu\text{m}$  in length, 200  $\mu\text{m}$  in width, and a mere 20  $\mu\text{m}$  in thickness [5]. The ciliary organelles are arranged in parallel rows, separated by approximately 3  $\mu\text{m}$ , and the individual cilia within these rows are spaced at intervals of about 0.33  $\mu\text{m}$ . Typically, these cilia measure 10–15  $\mu\text{m}$  in length, although they may extend further towards the posterior end of the organism [5]. Figure 2a(i) illustrates that these rows generate metachronal waves; the individual cilia show a beat pattern that can be represented approximately by Figure 2a(ii), especially when disregarding minor lateral movements in their three-dimensional beats. The cilia lie close together throughout their beat, resulting in a continuous wave outline, as shown in Figure 2a(iii) [5].

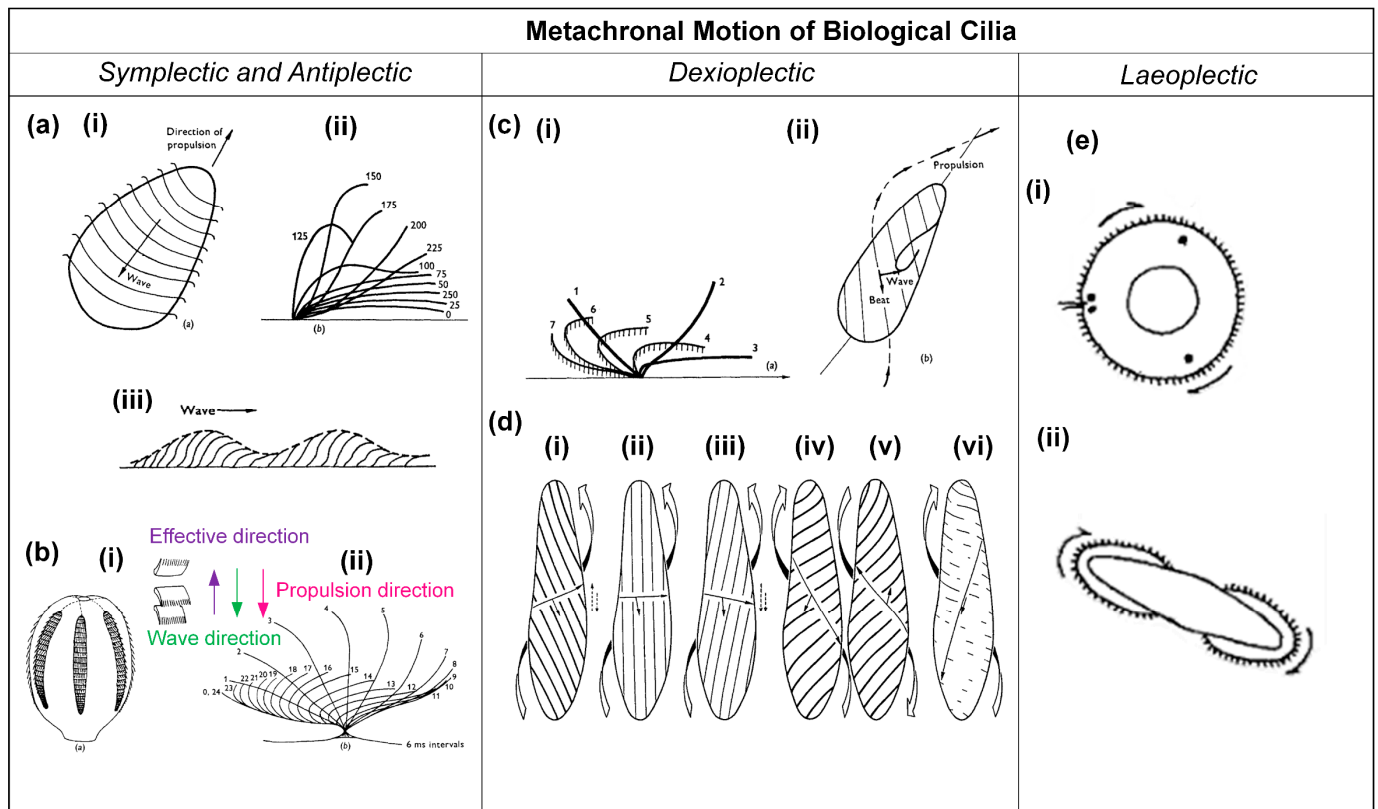


**Figure 2.** Schematics of examples for the four different types of metachronal motion found in nature. (a) (i) Metachronal wave patterns of rows of cilia on the protozoon *Opalina*, exhibiting symplectic metachrony; (ii) the beating of an individual cilium on *Opalina*, with the effective stroke to the right; (iii) the envelope over the metachronal wave of *Opalina*, where the arrow indicates the direction of the metachronal wave, coinciding with the effective stroke direction. Reproduced from ref. [5] with permission from John Wiley and Sons. (b) (i) Diagram showing the arrangement of combe-plates of *Pleurobrachia*, as well as the metachronal wave direction and the propulsion direction; (ii) the beat cycle of *Pleurobrachia*, with the effective stroke to the right; the wave propagation direction is against this, i.e., the metachrony is antiplectic. Reproduced from ref. [5] with permission from John Wiley and Sons. (c) Features of *Paramecium*. (i) Schematic of the cilia beating shape during one cycle, with the effective stroke to the right; (ii) schematic of the metachronal wave, which is dexioplectic, and the direction of propulsion. Reproduced from ref. [5] with permission from Wiley. (d) Metachronism and locomotion of *Paramecium* for different viscosities of the medium; (i) normal conditions, in medium with a viscosity of 1 cP, showing dexioplectic metachrony; (ii) in medium with a viscosity of 2.6 cP; (iii) in medium with a viscosity of 5.6 cP; (iv) in medium with a viscosity of 40 cP, forward swimming; (v) in medium with a viscosity of 40 cP, backward swimming; (vi) in medium with a viscosity of 135 cP, symplectic metachrony. Reproduced from ref. [4] with permission from The Company of Biologists. (e) (i) Larva of *Bugula*, viewed apically; (ii) *Cyphonautes* larva of bryozoan, viewed apically. The metachronal wave is indicated by the arrows; the effective stroke of the individual cilia is pointing into the plane of view; hence, the metachrony is laeoplectic. Reproduced from ref. [5] with permission from John Wiley and Sons.

The antiplectic metachronal motion has been observed in the marine organism *Pleurobrachia*, which possesses eight rows of comb plates, as schematically represented in Figure 2b(i) [5]. A typical comb plate is 800  $\mu\text{m}$  long and has a base measuring 30  $\mu\text{m}$  by 600  $\mu\text{m}$ . These plates are aligned in parallel planes and are arranged at intervals ranging from 300 to 400  $\mu\text{m}$  within their respective rows [5]. Each comb plate comprises approximately 105 cilia, which are interconnected within rows through lamellar connections, providing a degree of cohesion [5]. The whole comb plate functions as a unified entity,

and it exhibits a beat pattern when viewed in profile, as illustrated in Figure 2b(ii) [5]. The metachronal coordination is normally antiplectic, as indicated in Figure 2b(i) [5].

Dexioplectic metachronal motion has been found in the *Paramecium*, and the movement of this microorganism has been studied in detail [5]. *Paramecium* measures between 200 and 300  $\mu\text{m}$  in length, possesses cilia approximately 10–12  $\mu\text{m}$  in length, and is organized in longitudinal rows [5]. These rows are separated at a distance of approximately 1.5  $\mu\text{m}$ , while the individual cilia within these rows are spaced approximately 2.5  $\mu\text{m}$  apart [5]. During a complete beating cycle, each individual cilium undergoes a three-dimensional motion, as illustrated in Figure 2c(i) [5]. In positions one to three, the effective stroke, the cilium is more or less straight and undergoes a more rapid and nearly planar phase of movement; in positions four to seven, the recovery stroke, the cilium enters a slower phase in which it has a curved shape and performs a backward motion during which it bends away from the plane of observation [5]. From Figure 2c(ii), it can be seen that the orientation of the effective stroke is towards the right of, and perpendicular to, the direction of propagation of the metachronal wave, so that the metachronism is truly dexioplectic, although the organism as a whole exhibits an antiplectic metachronal pattern at first sight [5]. Interestingly, it was found that the metachronism of the *Paramecium* can be impacted by the viscosity of the surrounding fluid, as shown in Figure 2d [4]. As illustrated in Figure 2d(i), the *Paramecium* exhibits dexioplectic metachrony, a behavior consistent with its typical swimming pattern under normal conditions, characterized by a viscosity of 1 cP. Figure 2d(ii–vi) depict the behavior of *Paramecium* under varying viscosity conditions: 2.6 cP, 5.6 cP, 40 cP, 40 cP, and 135 cP, respectively [4]. It can be seen that there is a clockwise rotation of the power stroke and a transition from dexioplectic metachronism to symplectic metachronism as viscosity increases.

Laeoplectic metachronal motion has been identified in various organisms, including *Chaetopterus*, *Mollusca*, *Bryozoa*, and *Ploima*. Two examples are illustrated in Figure 2e [8]. Figure 2e(i) shows the larva of *Bugula*, while Figure 2e(ii) depicts the cyphonautes larva of a bryozoan [8]. Both figures show the apical view. The cilia are indicated at the circumference, and the arrows indicate the wave motion; the effective stroke of the cilia is directed into the plane of observation.

In conclusion, metachronal cilia motion is a prevalent phenomenon in nature, playing an important role in various organisms. In *Paramecium*, metachronal motion contributes significantly to locomotion, enabling efficient propulsion for swift swimming [11,48]. In mammalian respiratory systems, metachronal motion helps in expelling mucus and clearing debris and pathogens, thereby maintaining respiratory health [2,49]. Additionally, metachronal motion within the reproductive system assists in the transport of the ovum from the fallopian tube to the uterus [50,51]. Overall, metachronal ciliary motion is a remarkable and versatile biological phenomenon that contributes to various important functions in organisms across different ecosystems and life forms. Its coordinated and rhythmic nature is essential for the survival and ecological interactions of many species in the natural world.

### 3. Metachronal Motion of Artificial Cilia

In this section, we will provide an overview of the current state of the art of metachronal motion of artificial cilia based on the existing literature.

Inspired by nature, researchers have tried to mimic the metachronal motion of biological cilia by using artificial cilia, with the intention of applying this technology across diverse scientific domains, for instance, by integrating it into microfluidic chips and other specialized platforms. To date, researchers have developed various fabrication techniques to produce a range of artificial cilia configurations. It is important to clarify that the term “artificial cilia”, as discussed in this article, does not imply an exact replication of the size or structure observed in biological cilia. Artificial cilia can vary in length and need not adhere strictly to a hair-like morphology. Additionally, they can be actuated using diverse

stimuli, including pneumatic forces [26,27], light [28,30,51], electric fields [22–24], magnetic fields [31,52–54], pH variations [55,56], temperature changes [3], and more.

To the best of our knowledge, researchers have successfully realized metachronal motion in artificial cilia through pneumatic actuation [21], light-induced actuation [29], electric field-driven actuation [23], and magnetic field-driven actuation [18,35,36,50,57–59]. Consequently, our discussion will focus on these distinct actuation mechanisms and their respective achievements in realizing metachronal motion in artificial cilia.

### 3.1. Metachronal Motion of Pneumatically Driven Artificial Cilia

Pneumatic artificial cilia were first reported by Gorissen and coworkers [26]. These artificial cilia are flexible, hollow cylindrical tubes made of polydimethylsiloxane (PDMS) with an eccentric void, as shown in a cross-section in Figure 3a by the hatched area. If the void were concentric, as in the case of regular tubes, the flexible tube would solely expand in diameter when applying pressure [21,26,37,60]. However, the eccentricity of the void creates an asymmetric stiffness, which causes the cilia to bend when pressurized. Each cilium is connected to a pressure controller, meaning that every single cilium in a cilia array can be actuated independently [21]. The effective stroke of the cilia is defined as the movement from an upright to a bent state when being pressurized. The fabrication process of these cilia is shown in Figure 3b, where we can see that they can be produced by a high aspect ratio molding process. The cavity of the cilia is formed by a polished tungsten carbide microrod with a diameter of 0.61 mm placed in one half of the mold. The other half of the mold consists of a micro-drilled hole that defines the outer dimensions of the cilia (diameter of 1 mm and length of 8 mm). Alignment of both halves of the mold is achieved using locating pins, which are positioned accurately to define the eccentricity (0.14 mm) between the microrod and the drilled hole. After closing the mold, liquid PDMS is poured in and cured, and subsequent demolding finishes the production process. To achieve metachronal motion, the authors fabricated six pneumatic bending cilia positioned in line to form a ciliated surface and applied six fast switching solenoid valves to control the pressure applied to each cilium individually, allowing for imposing pressure waves with an arbitrary phase shift. The authors realized both antiplectic and symplectic metachronal motion by this method, as shown in Figure 3c, in which (i) shows the antiplectic metachronal motion with a phase difference of 45 degrees and (ii) shows the symplectic metachronal motion with a phase difference of 45 degrees as well.

Recently, the same research group enhanced the technique by introducing an additional degree of freedom to the cilia array. This was achieved through the fabrication of a shorter cilium with offsetting hollow structures [21]. Figure 3d illustrates the fabrication process, which closely resembles the first method but with the inclusion of a shorter cilium featuring an offset inner cavity. As these cilia possess a pair of inner cavities rather than a single one, an extra degree of freedom becomes available for the purpose of generating spatial asymmetry, thereby introducing a swept area. This is achieved by applying pressure to each cavity independently, using dedicated pressure sources. The phase difference between the applied trapezoidal pressure profiles serves as a method to finely control the extent of the area swept by the cilia tips, as illustrated in Figure 3e. By using this method, the researchers induced both symplectic and antiplectic metachronal motion as well as synchronous motion with a cilia array having six cilia, as shown in Figure 3f. The superimposed colored lines show the metachronal wave propagation. The continuous line corresponds to the initial metachronal wave formed by connecting the tips of the cilia, while the dashed line represents the wave in the subsequent frame. The effective stroke, determined by the cilia geometry, is to the right; in the case of symplectic metachronal motion, the wave propagates to the right (positive), whereas for antiplectic metachronal motion, it propagates to the left (negative).

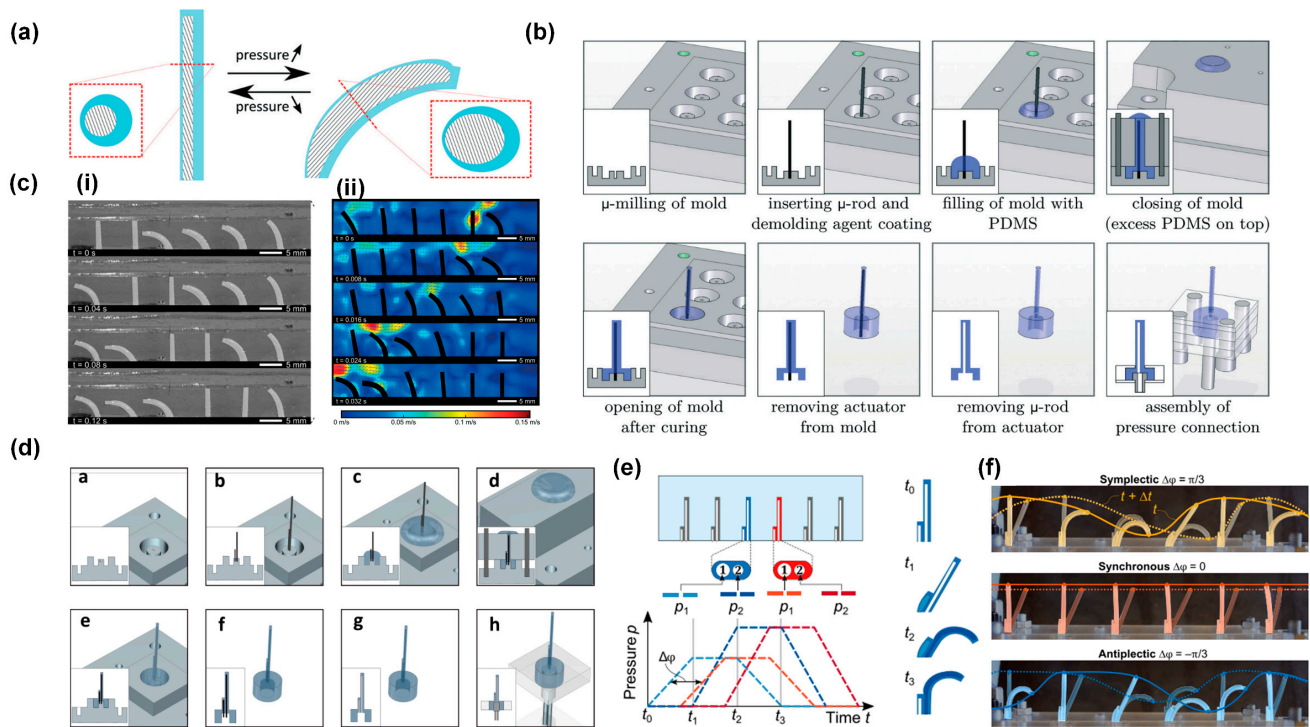


**Figure 3.** Metachronal motion by pneumatic cilia. (a) Schematic of the principle of a flexible bending actuator that consists of an asymmetric void (hatched) surrounded by a highly flexible material; the cross-section view is shown in the zoom-in figure. (b) The fabrication process of the pneumatic artificial cilia. (c) (i) Experimental results showing an antiplectic metachronal wave with a phase difference between adjacent cilia of 45 degrees; (ii) a symplectic metachronal wave with a phase difference between cilia of 45 degrees. Reproduced from ref. [26] with permission from the Royal Society of Chemistry. (d) Fabrication process of a pneumatic actuator with more degrees of freedom, enabling an asymmetric cilia stroke. (e) Pressure input functions: each cilium is actuated with two trapezoidal waves. A metachronal wave is applied by shifting the trapezoidal waves of the neighboring cilium by a constant phase angle. (f) An array of six artificial pneumatic cilia independently actuated by 12 fluid pressure inputs. Symplectic and antiplectic waves, as well as synchronous motion, can be applied to the array. Reproduced from ref. [21] with permission from the American Association for the Advancement of Science.

### 3.2. Metachronal Motion of Light-Driven Artificial Cilia

Light-driven microactuators offer distinct advantages, including wireless control, scalability, and spatiotemporally selective capabilities. Light-driven artificial cilia are mostly made from liquid crystal polymer networks that are light-responsive by incorporating photo-responsive elements like azobenzene, which undergo reversible molecular conformational changes upon exposure to UV-range light. These molecular changes are translated to a macroscopic level as the bending of artificial cilia, facilitated by the alignment of liquid crystal molecules within the actuator network.

Palagi et al. [29] reported the generation of wave-like motion using liquid crystal elastomers with incorporated azobenzene, through local time-dependent illumination, causing local expansion or contraction of these materials, as shown in Figure 4a. Complex wavelike motion could be induced by structured light fields generated by an optical system based on a digital micromirror device (DMD) with  $1024 \times 768$  mirrors, as shown in Figure 4b. The researchers realized swimmers could exhibit both symplectic and antiplectic metachronal motions by controlling illumination conditions to manipulate the relative amplitudes of longitudinal and axial deformations, as exemplified in Figure 4c. Figure 4d shows a result, showcasing the displacement of a microswimmer when subjected to light patterns of varying wavelengths (illustrated in green overlays, with corresponding directional indications

in green arrows). Although not strictly based on cilia-like structures, this example shows that microswimmers based on metachronal motions, reminiscent of the biological examples in Figure 2, can be realized using light-responsive materials.

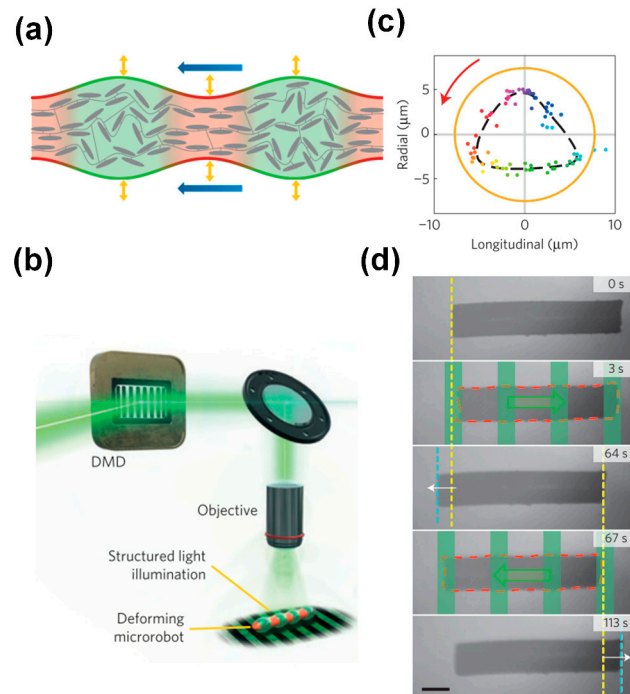


**Figure 4.** Light-driven metachronal motion. (a) Local illumination of a liquid crystal polymer that incorporates azobenzene can induce local contraction and expansion. (b) A Digital Micromirror Device (DMD) can generate structured light fields that can induce complex wavelike motion. (c) By controlling illumination conditions, the relative amplitudes of longitudinal and axial deformations can be manipulated. (d) Back and forth swimming of a cylindrical microrobot propelled by traveling-wave deformations (red dashed line: deformed profile). The green overlays and arrows represent the periodic light pattern and its traveling direction, respectively. Yellow and cyan dashed lines represent the initial and final positions of the leading edge of the robot, respectively. Reproduced from ref. [29] with permission from Nature Portfolio.

### 3.3. Metachronal Motion of Electrically Driven Artificial Cilia

There has been significant research into the development of artificial cilia that are responsive to electrical fields. Den Toonder et al. [22] first reported the successful creation of electrically driven artificial cilia, demonstrating their efficacy in enhancing microfluidic mixing and pumping.

Later, Wang et al. [23] successfully engineered voltage-actuated cilia capable of generating non-reciprocal motion individually and metachronal motion collectively. These cilia have the shape of strips, measuring approximately  $50\ \mu\text{m}$  in length,  $5\ \mu\text{m}$  in width, and having a thickness of about  $10\ \text{nm}$ . They consist of a platinum (Pt) thin film with a thickness of  $7\ \text{nm}$  and are sealed on one side by a passive titanium (Ti) layer anchored to the substrate at one end, as illustrated in Figure 5a. A scanning electron microscope (SEM) image of an assembled artificial cilia array is presented in Figure 5b. The inset in Figure 5b is a scanning transmission electron microscope (STEM) image of a cilium cross-section showing platinum (white) and titanium (black). The artificial cilia are actuated in phosphate-buffered saline (PBS;  $1\times$ , pH 7.45) by raising their potential to about  $1\ \text{V}$  relative to a  $\text{Ag}/\text{AgCl}$  reference electrode, triggering electrochemical oxidation of the exposed Pt surface and resulting in surface expansion and consequent bending of the actuator (Figure 5a, red reaction pathway, left to right). Applying a voltage of approximately  $-0.2\ \text{V}$  reduces the Pt film, which returns the actuator to its initial state (Figure 5a, blue reaction pathway, right to left). Furthermore,



the researchers seamlessly integrated the cilia array with complementary CMOS-based microcircuits, enabling untethered control. This integration involved the fabrication of a photovoltaic-powered CMOS clock circuit, as shown in Figure 5c. These integrated components worked together to produce a sequence of phase-shifted voltage signals at a user-defined frequency when exposed to light, as shown in Figure 5d. This approach facilitated the realization of a metachronal wave pattern across the cilia array.

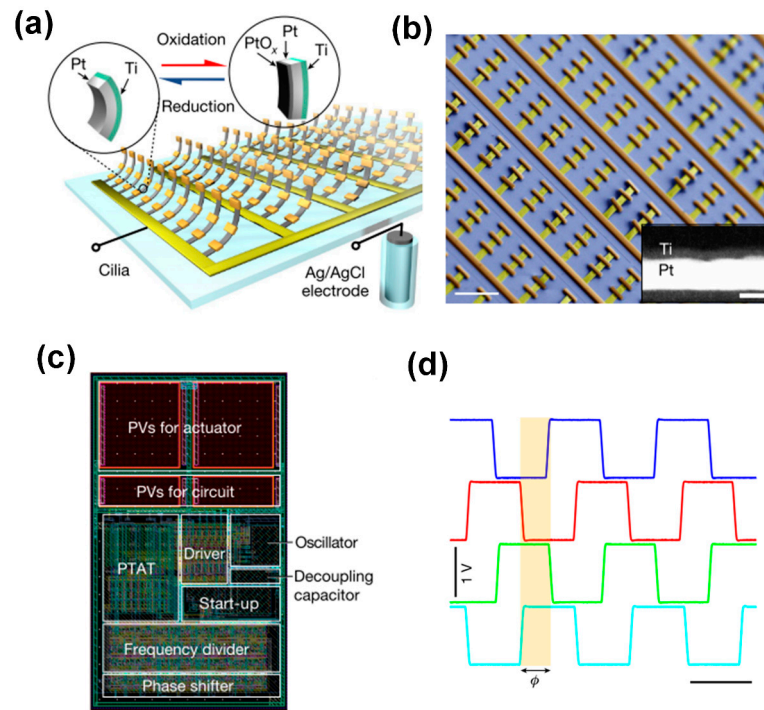


**Figure 5.** Metachronal motion of electrically driven artificial cilia. (a) Artificial cilia array based on surface electrochemical actuators; each cilium consists of a thin platinum strip capped on one side by a titanium film. (b) SEM image of a released artificial cilia array with each row connected by a single busbar; the inset is a STEM image of a cilium cross-section. (c) Remote control of the cilia is realized by a CMOS circuit, the layout of which is shown here. (d) Four voltage outputs from the CMOS circuit enable metachronal motion of the artificial cilia. Reproduced from ref. [23] with permission from Nature Portfolio.

### 3.4. Metachronal Motion of Magnetically Driven Artificial Cilia

Magnetic artificial cilia are the most widely and extensively investigated category within the artificial cilia field, primarily owing to their distinctive advantages, including that the external magnetic field does not require any complex external physical connections, and that the magnetic field does not interfere with (biological) processes within microfluidic chips. Recently, researchers have devised various methodologies to achieve the metachronal motion of magnetic artificial cilia. There are two main approaches to inducing phase differences in a beating magnetic artificial cilia array. One approach is having cilia with different responses to a uniform forcing applied to the entire cilia array, which can be realized by tuning the alignment of magnetic particles within the magnetic artificial cilia to different angles between consecutive cilia, or by varying the geometry of the cilia within an array; the cilia array is then actuated by a rotational uniform magnetic field. The other approach is applying different forcings to each cilium, which is realized by applying a complex external magnetic field to create different magnetic forces and/or torques on neighboring cilia [57]. In this section, we will describe the metachronal motion of magnetic artificial cilia arrays realized by the following three methods: by controlling the magnetic particle distribution in the cilia within the array; by changing the geometry of the cilia



within the array; and by controlling the local magnetic field experienced by the cilia within the array.

- Controlling the magnetic particle distribution within the artificial cilia.

Researchers have developed different methods to control the magnetic particle distribution of individual artificial cilia within the array. Tsumori et al. [59] reported the realization of the metachronal motion of magnetic artificial cilia by fabricating cilia arrays in which individual cilia have different particle distributions and actuating the cilia array with a rotating permanent magnet, as shown in Figure 6a. The fabrication process of this cilia array involved filling silanized PDMS molds with a composite of iron powder and PDMS in multiple sequential steps. Initially, specific cavities were manually filled, followed by the application of a magnetic flux to induce the formation of aligned iron particle chains and curing the PDMS to fix that alignment. This process was then repeated by filling the remaining cavities while altering the direction of the applied magnetic field, resulting in iron particles aligning in different directions. Lastly, clear PDMS was applied to the top surface of the mold and cured, serving as a substrate for the final fabricated structure. The result was an array of artificial cilia in which the magnetic particle alignment, and hence the magnetization direction, gradually varied across the array. These cilia exhibited distinct responses to the applied actuation magnetic field with metachronal motion, as shown in Figure 6a. A disadvantage of this approach is that the fabrication process is time consuming, and miniaturization is difficult. Gu et al. [58] developed a different method to control the “particle distribution” inside the cilia array. They presented a simple and scalable method to fabricate a stretchable magnetic cilia carpet, which was composed of cilia made of a magnetic composite material, specifically NdFeB particles and Ecoflex, and a non-magnetic stretchable substrate (pure Ecoflex). By stretching the carpet to conform to various three-dimensional geometries, they encoded complex magnetization patterns in the cilia arrays using a magnetizer. The magnetization profile on the cilia carpet will later translate to metachronal wave patterns under a dynamic magnetic field, as shown in Figure 6b. Recently, Zhang et al. [57] successfully controlled particle distribution inside the magnetic artificial cilia in a straightforward way. The metachronal magnetic cilia were fabricated using a micromolding process, during which the distribution of the paramagnetic particles in the cilia was controlled by placing a rod-shaped magnet array, arranged to have an alternating dipole orientation between consecutive magnets, underneath the mold. Because the paramagnetic particles tend to align with the applied magnetic field, neighboring cilia assume different paramagnetic particle alignments, and they will, therefore, have different magnetization directions. Consequently, the geometrically identical cilia exhibit nonidentical bending behaviors in a static uniform magnetic field and perform a metachronal motion in a 2D rotating uniform magnetic field, as shown in Figure 6c.

- Controlling the geometry of the artificial cilia.

Another way to realize the metachronal motion of magnetic artificial cilia is by designing the geometry of the individual cilia in the array to be different, which is shown in Figure 6d [50]. Hanasoge et al. [50] fabricated magnetic artificial cilia consisting of micromachined thin magnetic strips of varying length attached at one end to a substrate. They showed that the difference in cilium length controls the phase of the beating motion. Making use of this property, the researchers could realize metachronal waves within a ciliary array with cilia lengths ranging from 60  $\mu\text{m}$  to 600  $\mu\text{m}$ , and actuated by a permanent magnet, as shown in Figure 6d. The phase of a cilium beating is fully defined by the magnetic force acting on the cilium and its elasticity. For a given magnetic flux density, the effect scales with cilium length, enabling the use of cilium geometry to induce metachronal motion.

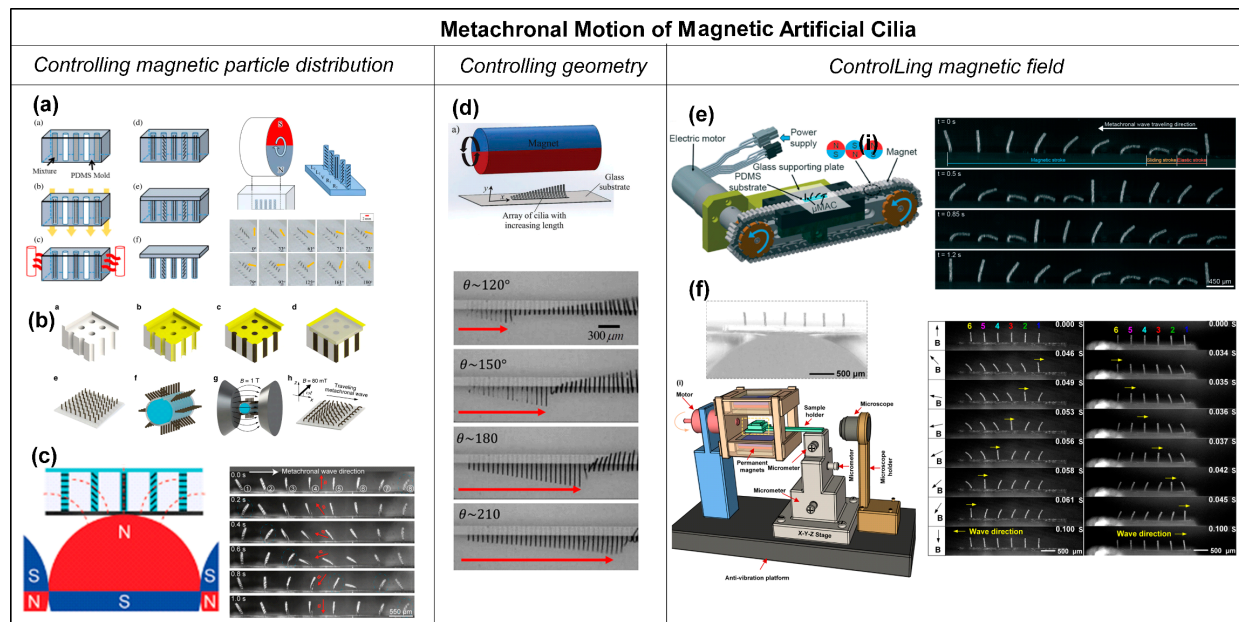


**Figure 6.** Metachronal motion of magnetic artificial cilia. (a) Fabrication process of a cilia array with magnetic particle alignment varying across the array, achieved by a step-by-step filling of the cilia mold and solidifying the material while applying a magnetic field with a changing field angle. Reproduced from ref. [59] with permission from the Japan Society of Applied Physics. (b) Fabrication and magnetization process of magnetic artificial cilia carpets with magnetization direction variation across the cilia array by stretching the array (made from NdFeB particles and Ecoflex) around a magnetizing structure. Reproduced from ref. [58] with permission from Nature Portfolio. (c) Curing the magnetic cilia array (PDMS and paramagnetic particles) on top of a rod-shaped magnet, leading to varying magnetic particle distribution over the cilia array, and the demonstration of metachronal motion generated by the magnetic cilia array when applying a rotating uniform magnetic field. Reproduced from ref. [57] with permission from the American Chemical Society. (d) Magnetic cilia having different lengths actuated with an external rotational magnetic field and the achieved metachronal motion. The arrow indicates the position of the wave front. Reproduced from ref. [50] with permission from the Royal Society of Chemistry. (e) Array with identical magnetic artificial cilia, actuated with a translating magnetic belt consisting of rod-shaped magnets arranged with opposite dipoles between adjacent magnets, and the metachronal motion demonstrated for this array. Reproduced from ref. [38] with permission from the Royal Society of Chemistry. (f) Array with identical magnetic artificial cilia having a rod-shaped magnetic substructure underneath and the symplectic and antiplectic metachronal motion realized by the method when actuated with a rotational uniform magnetic field. Reproduced from ref. [18] with permission from the National Academy of Sciences.

- Controlling the magnetic field.

Metachronal motion of the magnetic artificial cilia can also be realized by controlling the magnetic field applied to each cilium in an array. Zhang et al. [38] achieved antiplectic metachronal motion of a cilia array with identical magnetic artificial cilia by actuating them with a translating magnetic belt having rod-shaped magnets with alternating dipole orientation between consecutive magnets (shown in Figure 6e). The cilia were fabricated with a mixture of PDMS and iron particles using a micromolding method. The mold was fabricated by photolithography. After filling the mixture in the mold, the cilia structures were cured under a perpendicular magnetic field to align the magnetic particles along the cilia length, identically for all cilia. Since the actuation setup generates a non-uniform but periodic magnetic field, the magnetic field applied to each cilium is also different but also time-dependent due to the translation of the belt. This generated a metachronal wave. However, the action system is rather complex, and it is difficult to miniaturize the

metachronal motion due to the size constraints imposed by the actuation magnets. Most recently, our research group achieved a breakthrough in miniaturizing the metachronal motion of identical magnetic artificial cilia; see Cui et al. [18]. This advancement was accomplished through the integration of a paramagnetic substructure underneath the cilia array and actuating the array by a simple rotational, uniform magnetic field, as shown in Figure 6f. The underlying principle hinges on the response of the paramagnetic substructure to an external magnetic field, which induces perturbations in the spatial distribution of the field, generating a time-dependent local magnetic field. When appropriately dimensioned, neighboring identical cilia experience distinct magnetic fields at any given moment, thereby giving rise to metachrony in their motion. Notably, we realized both symplectic and antiplectic metachronal motion using this novel approach, as shown in Figure 6f. One of the key advantages of this method is that it enables further miniaturization of artificial cilia metachrony, in contrast to the earlier approaches.

In conclusion, there are four main types of artificial cilia: pneumatically controlled cilia, light-driven cilia, electrically driven cilia, and magnetically actuated cilia. Each method has its advantages and disadvantages.

The pneumatic control of the artificial cilia enables individual cilia triggering and precise control of the phase difference between each cilium. Hence, the nature of the metachrony (symplectic versus antiplectic) can be varied in a straightforward manner. This capability gives the possibility to study the effects of type of metachrony and phase differences on fluid flow generation by artificial cilia, which we will discuss below. The disadvantages of using pneumatic actuation for metachronal cilia motion are the need for many pressure connections and the difficulty of miniaturizing the cilia.

The metachronal motion achieved through light-driven cilia is noteworthy due to its potential for facilitating remote and precise actuation of arrays of artificial cilia. Importantly, this approach often obviates the need for external connections or complex mechanical linkages. The disadvantages are that the response times are often relatively slow (i.e., seconds or more), and light is not a suitable cue for some applications because of the lack of optical access.

Electrically driven artificial cilia can be actuated quickly and offer much flexibility in controlling the timing of actuation through the design of the electrical circuit, which enables metachrony. A disadvantage is that either high voltages are needed [22], or the actuation requires a specific fluidic environment [23]. Conventional electrical actuation requires electrical connections [22], but the solution introduced by Wang et al. [23] makes it possible to remotely control the cilia motion.

Magnetically driven artificial cilia exhibit rapid responsiveness and can penetrate biological tissues smoothly without causing damage. Although the actuation mechanism does not require complex external connections, the setup for actuation itself continues to be somewhat intricate.

#### 4. Applications of Metachronal Motion in Artificial Cilia

In this section, we will review the main applications of the metachronal motion created by artificial cilia, which include flow generation, transportation, and microrobot locomotion.

##### 4.1. Flow Generation

The generation of fluid flow holds important significance within the field of microfluidic applications. As mentioned before, a main function of biological cilia is to generate fluid flow or propulsion in liquids, in which metachrony often plays an important role, such as in the propulsion of *Paramecium*. Hence, extensive research has been conducted on the fluid flow generation of artificial cilia and on the role of metachronal motion on the induced flows, using both experimental and computational approaches [21,38,61–63]. The maximum flow velocities that have been achieved experimentally using metachronal artificial cilia actuation are 19,000  $\mu\text{m/s}$  for pneumatic and 3000  $\mu\text{m/s}$  for magnetic artificial cilia at high Reynolds number conditions (in water), and 500  $\mu\text{m/s}$  for pneumatic and

450  $\mu\text{m/s}$  for magnetic artificial cilia at low Reynolds number conditions (in glycerol) [3]. In this review, we will focus on the proposed mechanisms of flow generation by metachronal cilia motion rather than on comparing quantitative flow speed, which was covered in our previous review [3].

Khaderi et al. [64] studied fluid flow generation by the metachronal motion of symmetrically beating magnetic artificial cilia using numerical simulations. They found the ciliary motion to generate a unidirectional fluid flow in the direction opposite to the metachronal wave. In addition, they found that the flow reaches a maximum for a critical value of the wavelength of the metachronal wave, which depends on the competition between the elastic and viscous forces acting in the ciliary system. The authors explained the observed behavior from two different viewpoints: from a Eulerian point-of-view and a Lagrangian point-of-view, as illustrated in Figure 7a,b; the metachronal wave travels to the right. Figure 7a illustrates the Eulerian viewpoint, showing pressure contours with superimposed streamlines in (i) and the contours of the normalized absolute value of the horizontal component of the velocity in (ii). Due to the instantaneous velocity of the cilia, high-pressure and low-pressure regions develop (the red and blue regions in Figure 7a(i), respectively). Fluid is squeezed out of the high-pressure regions and drawn in by the low-pressure regions, resulting in a series of counter-rotating vortices in the channel. Since the distance between the high-pressure and low-pressure regions opposite to the wave direction is smaller, the pressure gradient is larger, so the counter-clockwise vortices are stronger (see Figure 7a(ii)). As a result, the velocity distribution has a dominant horizontal component to the left, against the metachronal wave. In addition, the authors analyzed the system from a Lagrangian perspective by tracing fluid particles within the fluid domain, as illustrated in Figure 7b. In this figure, the contours represent the normalized absolute velocity in the horizontal direction, while the streamlines indicate the direction of the fluid velocity. The analysis revealed that the out-of-phase motion of cilia generates a net tracer particle velocity towards the left, biggest for the particles closest to the cilia tips, which is opposite to the propagation direction of the metachronal wave.

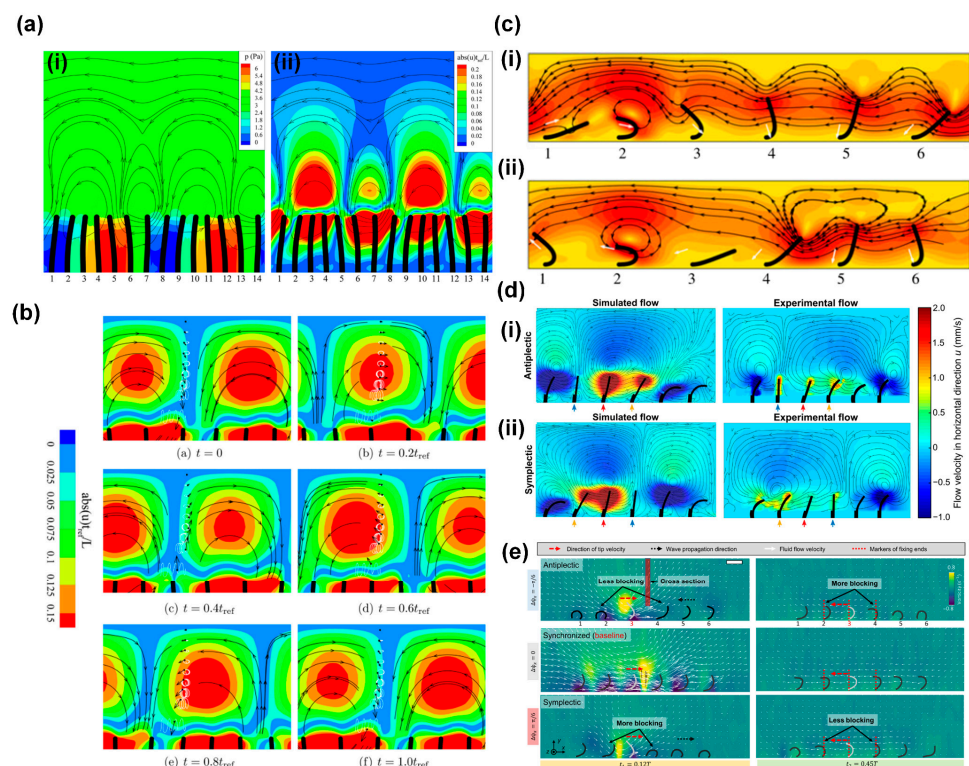


**Figure 7.** Mechanisms of flow generation by metachronal motion of artificial cilia. (a) Numerical simulations of flow generation by symmetrically beating cilia exhibiting metachronal motion, with

the metachronal wave traveling to the right, showing (i) pressure contours (red is high pressure and blue is low pressure) and (ii) contours of normalized absolute horizontal velocity; the streamlines represent the direction of velocity. Reproduced from ref. [64] with permission from the American Institute of Physics. (b) Numerical simulations of flow generation by symmetrically beating cilia exhibiting metachronal motion, with the metachronal wave traveling to the right, showing the motion of tracer particles with time; the white curves represent the trajectory of particles, and the black dots represent the particles. Reproduced from ref. [64] with permission from the American Institute of Physics. (c) Snapshots of antiplectic and symplectic metachronal motion of cilia from numerical simulations; the effective stroke of the non-reciprocally moving cilia is to the left; the contours represent the normalized absolute velocity; the streamlines represent the direction of the velocity; (i) antiplectic metachrony, in which waves travel to the right; and (ii) symplectic metachrony, in which waves travel to the left. Reproduced from ref. [63] with permission from Cambridge University Press. (d) Simulation and experimental results for pneumatically actuated artificial cilia for both (i) antiplectic and (ii) symplectic metachrony; the color represents the absolute value of generated flow velocity, and the streamlines indicate the direction of flow. Reproduced from ref. [21] with permission from the American Association for the Advancement of Science. (e) Experimentally observed fluid flow distribution generated by a magnetic artificial cilia array with antiplectic, synchronized, and symplectic metachrony. The cilia in the array undergoing antiplectic metachrony have less blocked local fluid flow from their neighbors during the power stroke than in the synchronous case and more blocked local fluid flow during the recovery stroke; this is the other way around for symplectic metachrony. Reproduced from ref. [35] with permission from the American Association for the Advancement of Science.

The analysis of Khaderi et al. [64] showed that metachrony alone can generate net flow, even in the absence of asymmetric motion of the cilia. However, most cilia in nature exhibit non-reciprocal motion. Therefore, researchers also investigated the effect of metachrony of non-reciprocally moving cilia on flow generation, both numerically and experimentally [16,21,63]. These studies found that antiplectic metachronal motion is more effective in enhancing flow generation by synchronous asymmetric cilia motion than symplectic metachronal motion. The common explanation for this effect given in most studies is based on the notion that cilia can have different shielding or obstruction effects on the fluid flow generated by adjacent cilia, depending on the type of metachrony. This can be illustrated by numerical simulation results from Khaderi et al. [63], who reported that antiplectic metachrony leads to a considerable enhancement in flow compared to symplectic metachrony, especially when the cilia spacing is small [62]. Figure 7c depicts the velocity field for both antiplectic (Figure 7c(i), wave traveling to the right) and symplectic (Figure 7c(ii), wave traveling to the left) metachrony at moments of maximum flux during simulations. In both images, the fifth cilium is at the peak of its effective stroke, towards the left. In the case of symplectic metachrony (ii), the flow created by the fifth cilium is obstructed by the close proximity of the fourth cilium, which has just initiated its effective stroke, resulting in the formation of a vortex. Conversely, in the case of antiplectic metachrony (i), the position of the fourth cilium allows unimpeded flow from the fifth cilium, resulting in a greater net fluid flow compared to its symplectic counterpart. Milana et al. [21] reported similar results based on experiments using pneumatically actuated artificial cilia and corresponding numerical simulations, shown in Figure 7d. For small-phase difference metachronal waves, they found that antiplectic coordination increases fluid flow velocity up to 50% compared to a synchronous beating mode, while symplectic metachrony decreases it. Like Khaderi et al. [63], Milana et al. [21] came to the conclusion that these effects are caused by an obstruction mechanism between cilia in the array that hinders effective flow generation in the case of symplectic waves. Also, Dong et al. [35] reported that only antiplectic metachronal waves with specific wave vectors could enhance fluid flows compared with the synchronized case, based both on experiments with magnetic artificial cilia and on simulations. Similar to the explanations given above, the authors proposed that the differences in fluid flow generation for the two metachrony types are

due to differences in obstruction effects of fluid flow between adjacent cilia, as illustrated in Figure 7e for antiplectic, synchronized, and symplectic metachrony. Compared to synchronous motion, the cilia in an array with antiplectic metachrony have less blocked local fluid flow from their neighbors during the effective stroke, but more blocked local fluid flow during the recovery stroke; for symplectic metachrony, this is the other way around.

These numerical and experimental studies show that metachrony has an important influence on the fluid generated by arrays of (artificial) cilia, and they give a common explanation for the observed effects. It is important to note that the metachronal motion of the cilia is just one of several influential factors impacting the induced flow rates. Parameters such as cilia geometry, cilia density, actuation frequency, and others can also have significant effects. However, for the sake of brevity and focus, we will not deeply go into this matter here but refer the reader to prior reviews in which these aspects are comprehensively reported [3].

#### 4.2. Transportation

Next to generating fluid flow, biological cilia transport matter like mucus, particles (in the airways), and cells (in the fallopian tube). Researchers have attempted to mimic these transportation functions in several studies using metachronal motion-driven artificial cilia for mucus, solid particles, and droplets, which we will review next.

- Mucus transportation.

Mucus transportation in the airways by metachronal coordination of natural cilia is essential for healthy respiration [1,15,46,65,66]. To mimic this process in vitro, researchers have carried out studies of mucus transportation by metachronal artificial cilia; the knowledge obtained in these studies could be relevant for understanding impaired mucus clearance and eventually can help in developing treatments.

Pedersoli et al. [66] conducted experiments on the transportation of artificial mucus by the metachronal motion of magnetic artificial cilia, as shown in Figure 8a. The metachronal motion of magnetic artificial cilia was realized by actuating identical cilia arrays using a magnetic belt, as shown in Figure 1e. The researchers studied the transportation properties of both physiological and pathological states of artificial mucus and the impact of the periciliary layer (PCL) on the transport; the PCL is a thin, low-viscosity fluid layer present just below the mucus layer, as indicated in Figure 8a. Figure 8a(ii) shows three situations of mucus transportation. In the first, mucus is in direct contact with the magnetic artificial cilia and with the underlying substrate, and the PCL is absent, as happens in some airway diseases; in this case, no mucus propulsion was observed. In the second and third situations, a PCL layer of different heights is present. The key to mucus transportation turned out to be a balance between the hydrodynamic resistance and the driving force exerted by the cilia.

This first study of mucus transportation by metachronal motion-driven artificial cilia indicates the potential of this approach; however, to reach a model that is physiologically relevant, many more steps need to be taken. In particular, artificial cilia must be miniaturized, and the cilia areal density must be substantially increased to approximate the in vivo situation more faithfully.

- Particle transportation.

The controlled and directed transport of particles (both synthetic and biological, e.g., cells) is desirable in both fundamental research and applications such as biomedical and biochemical research, disease diagnostic and therapeutics, drug discovery and delivery systems, and self-cleaning and anti-fouling technologies. Various principles have been developed to achieve controlled particle transportation, especially for microfluidic applications [67]. Recently, metachronal artificial cilia have been studied and investigated to achieve particle transportation.

Inspired by the ciliary structure and the asymmetric wave-form motion observed in the mammalian airway epithelial surface, Ben et al. [68] devised a novel method for



transporting polystyrene (PS) microparticles using magnetic artificial cilia. These artificial cilia were designed in both conical and columnar shapes and were actuated using a periodically moving external magnet, as depicted in Figure 8b. Consequently, the cilia array exhibited a periodic wave-like motion. Furthermore, their investigation revealed that the average transport speed of the conical cilia array exceeded that of the columnar arrays. This difference in transport efficiency was attributed to the reduced friction encountered by the conical cilia during the recovery stroke, resulting in a larger resultant force acting on the particles. Additionally, the bending of the conical cilia caused the center of gravity of the PS microsphere to shift forward, promoting transportation due to its inertia. However, the effectiveness of this transportation was also dependent on factors such as the elasticity, height, separation distance, and beating frequency of the cilia array. The highest achieved PS microsphere transportation speed reached approximately 0.09 mm/s at a cycle frequency of around 0.6 Hz for the flexible conical arrays.

Subsequently, within the same research group, Ben et al. [69] successfully demonstrated the underwater transport of silica microspheres using a magnetic artificial cilia array. This array was fabricated and actuated using a periodic external magnetic field as well, as depicted in Figure 8c. Silica particles could be transported by the wave-like motion exhibited by the artificial cilia. The transportation of these particles was found to depend on various factors, including gravity, buoyancy, supporting forces, fluid driving forces, and friction forces acting on the silica sphere. The study further explored the impact of cilia array beating frequency, inter-cilium spacing, cilia array height, microsphere mass, and solution density on transport performance. Notably, the investigation concluded that the peak speed for silica microsphere transportation, amounting to 0.07 mm/s, was attained at a cycling frequency of around 0.6 Hz underwater [69].

The particle transportation capabilities of metachronal artificial cilia have been studied both through numerical simulations and experimental investigations in recent years. Nevertheless, the investigation of the relationship between the metachronal motion of artificial cilia, the particle properties, and particle transportation still deserves further comprehensive exploration.

- Droplet transportation.

Droplet manipulation is a rich field in microfluidics, since droplets offer the possibility of manipulating, controlling, and analyzing small volumes of fluids, and droplet microfluidics can facilitate high-throughput experiments. Among many other approaches to transporting droplets, the use of artificial cilia has been studied increasingly in recent years [32,70–74]. Here, we focus on using metachronal cilia motion to achieve droplet transportation.

Song et al. [72] demonstrated the successful transportation of droplets through the utilization of unidirectional metachronal waves of magnetic artificial cilia. These waves were dynamically generated through the real-time response of the cilia array to the motion of a set of two permanent magnets with opposite dipoles, thereby enabling the transport of droplets ranging in volume from 1 to 6  $\mu\text{L}$  along a predefined trajectory, as illustrated in Figure 8d. The cilia were made of PDMS containing carbonyl iron powder. After their fabrication, the surface of the cilia was treated with a femtosecond laser to achieve a superhydrophobic, low-adhesion surface. Figure 8d(i,ii) illustrate the metachronal wave made by the cilia in response to the moving magnets. Figure 8d(iii) shows that droplets can be transported along straight or curved lines in the direction of the traveling wave and come to a stop as desired, and that droplets can be merged. Through a thorough analysis of the forces exerted on the droplet, the researchers determined that the droplet moves in the wave direction because the driving force applied to the droplet by the cilia exceeds the frictional forces.

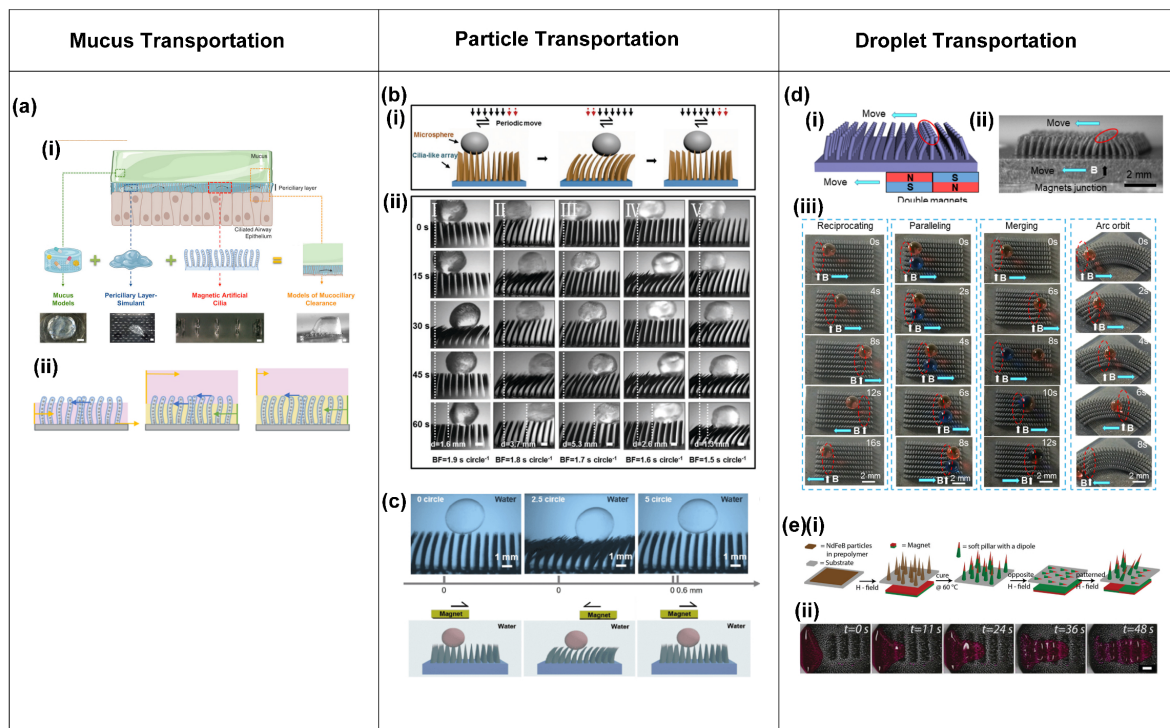


**Figure 8.** Transportation of mucus, particles, and droplets realized by the metachronal motion of artificial cilia. (a) (i) Artificial mucus transportation by metachronal motion of magnetic artificial cilia, illustrated by a schematic (top) and images of transportation results (bottom); (ii) a schematic of mucus transportation by cilia with different thicknesses of periciliary layer (PCL); mucus: pink, PCL: yellow. Reproduced from ref. [66] with permission from Wiley. (b) (i) Schematic of microparticle transportation by magnetic artificial cilia that are actuated by a periodic magnetic field; (ii) experimental results of a polystyrene (PS) particle transported by metachronal magnetic cilia at different actuation frequencies. Reproduced from ref. [68] with permission from Wiley. (c) Transportation of a silica microparticle in water by metachronal magnetic artificial cilia actuated by a periodic magnetic field. Reproduced from ref. [69] with permission from Science China Press. (d) (i) Schematic of the response of an array of magnetic artificial cilia to a moving set of permanent magnets; (ii) microscopy image of the response of an array of magnetic artificial cilia to a moving set of permanent magnets; (iii) droplet transportation by metachronal magnetic cilia. Reproduced from ref. [72] with permission from the American Chemical Society. (e) (i) Realization of a dynamic magnetic carpet from a soft silicone matrix with embedded NdFeB particles; (ii) transportation of glycerol droplets by the magnetic cilia carpet. Reproduced from ref. [25] with permission from John Wiley & Sons.

Demirörs et al. [25] achieved the versatile transportation of both fluids and solid materials using the wave-like motion of soft magnetic cilia carpets. The researchers fabricated the magnetic cilia carpet from a soft silicone matrix with embedded neodymium iron boron (NdFeB) particles. By employing varying external magnetic fields, cilia-like soft pillars emerged and exhibited distinct responses, as illustrated in Figure 8e(i). Using this property, the research team successfully demonstrated the transportation of glycerol droplets across the magnetic carpet, as depicted in Figure 8e(ii). The investigation revealed that the glycerol droplet moves in a direction opposite to the motion of the magnetic field wave. The droplet traverses a distance of over 23 mm in less than a minute, showcasing the capabilities of this system [25].

The investigation of droplet transportation by metachronal motion of artificial cilia shows that it has good potential. However, it is important to acknowledge that this research area is still in its early stages, highlighting the need for further in-depth investigations in the future.

- Microrobot locomotion.

In the developing field of robotics, scientists and engineers have constantly sought inspiration from the natural world to create machines that mimic the extraordinary capabilities of living creatures. This pursuit has led to the exploration of diverse microscale robotic systems, including those propelled by light-induced actuation, magnetic field manipulation, and other innovative mechanisms [75–83]. A noteworthy development in this exploration of biomimicry is the creation of walking robots propelled by metachronal motion, inspired by the locomotion of the millipede, where the legs of the robots are made from cilia-like actuators.

Zhang et al. [57] achieved metachronal motion of magnetic artificial cilia through the precise control of magnetic particle alignment in individual cilia within an array, driven by a uniform rotational magnetic field, as explained above and shown in Figure 6c. The same publication presents a walking microrobot with legs composed of magnetic cilia. The intricate interplay among frictional forces, adhesion forces, and magnetic forces, in combination with the resultant slight bending of the robot body, resulted in forward locomotion of the microrobot, as shown in Figure 9a(i). By simply reverting the rotation direction of the magnetic field, the robot could be made to walk in opposite directions, as shown in Figure 9a(ii). Furthermore, the researchers showcased the remarkable capability of robots to climb across hills, as depicted in Figure 9a(iii). The metachronal motion of the cilia turned out to be crucial for the locomotion: when the cilia moved synchronously, the microrobot did not show any net displacement. Gu et al. [58] also introduced a soft-walking robot with metachronal magnetic artificial cilia as legs, drawing inspiration from the locomotion patterns observed in the African millipede, as illustrated in Figure 9b(i–iii). Their investigation revealed a significant difference in locomotion speed between robots employing antiplectic wave patterns and those with symplectic waves, with the antiplectic wave being much more effective. The authors explained that this difference in speed could be attributed to the opposing curvatures of the substrate during the recovery stroke. As depicted in Figure 9b(iv), the robot body shows an indent at the location of the recovery stroke in the case of symplectic waves, impeding the movement of magnetic cilia due to increased surface friction; conversely, antiplectic soft robots experience bulging of the body at the recovery stroke location, facilitating unconstrained motion of the cilia. This observation sheds light on the mechanism underlying the locomotion of soft-walking robots, offering insights valuable for their design and optimization.

Several experimental studies have explored the capabilities of various soft-walking robots, yet simulation-based research has remained relatively limited. Recently, Jiang et al. [84] established a comprehensive numerical model aimed at investigating the metachronal wave-modulated locomotion of magnetic artificial cilia robots. The authors achieved an accurate replication of the deformation of individual cilia, the coordinated metachronal wave motion exhibited by multiple cilia, and the resulting crawling and rolling locomotion patterns observed in magnetic cilia soft robots. Additionally, they conducted an insightful comparative analysis of substrate deformation in both antiplectic and symplectic metachronal wave soft robots, as shown in Figure 9c. This model holds the potential to provide valuable insights that can guide the design, optimization, and customization of the microrobots.

Next to the magnetic actuation of artificial cilia, light has also been used to create metachronal motion using liquid crystal elastomers with light-responsive azobenzene, as explained before and shown in Figure 4a–d [29,83]. Based on this principle, Palagi et al. designed a microswimmer made from a strip of the light-responsive liquid crystal elastomer (LCE), which is dynamically illuminated with a light pattern, as shown in Figure 9d. Indeed, as shown in the figure, the microrobot exhibits swimming behavior in the direction determined by the anti- or symplectic metachronal wave. Remarkably, these two distinct swimming modes closely resemble the symplectic and antiplectic metachrony types observed in ciliates.

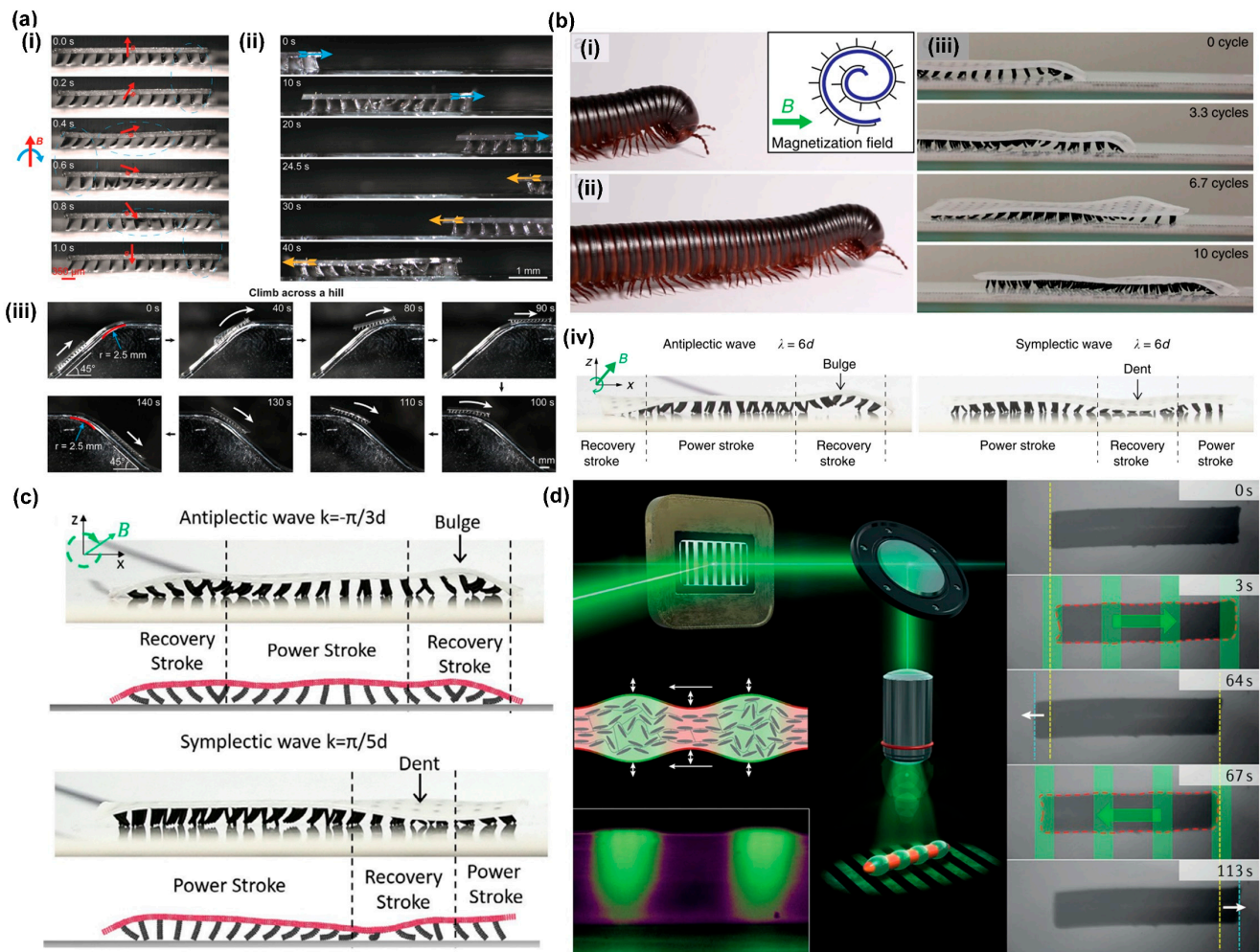


**Figure 9.** Microrobot locomotion realized by the metachronal motion of artificial cilia. (a) (i) A walking metachronal microrobot with metachronal magnetic artificial cilia as legs under a rotational uniform magnetic field in air during one beating cycle; (ii) demonstration of the bi-directional walking capability of the metachronal robot, achieved by reversing the rotating direction of the external magnetic field; (iii) demonstration of the climbing ability of the microrobot across a steep hill. Reproduced from ref. [57] with permission from the American Chemical Society (b) (i) and (ii) a crawling giant African millipede with legs moving in traveling metachronal waves; (iii) crawling magnetic soft microrobots inspired by the giant African millipede; (iv) a curved body of antiplectic and symplectic wave soft robots; the body of the antiplectic soft microrobot bulges at the location of the recovery stroke, helping the legs to freely move; the body of the symplectic soft microrobot dents and obstructs the recovery stroke, which slows down the robotic locomotion. Reproduced from ref. [58] with permission from Nature Portfolio. (c) Robot body deformation for antiplectic and symplectic wave soft robots, compared between experiments (photos) and simulations (drawings). Reproduced from ref. [84] with permission from John Wiley & Sons. (d) A soft microrobot based on a photoresponsive liquid-crystal elastomer swims by traveling-wave deformations, mimicking metachronal waves in ciliates. Reproduced from ref. [29] with permission from Nature Portfolio.

Walking and swimming robots driven by the metachronal motion of artificial cilia hold significant promise for a wide range of applications, including biomedical devices and microsystems. Nevertheless, the realization of their complete capabilities demands a more thorough and comprehensive exploration. Particularly interesting would be to investigate the possibility of creating amphibious microrobots to enhance their versatility and adaptability.

Taken together, metachronal motion offers a broad range of potential applications. While the mechanism of flow generation through metachronal motion has been extensively investigated, the underlying mechanisms linking metachronal motion to other applications, such as transportation and microrobot locomotion, are still in the early stages of understanding.

## 5. Conclusions and Perspectives

Over recent decades, notable advancements have been made in the field of artificial cilia research, including significant progress in both fabrication techniques and actuation strategies. In particular, the last decade has witnessed an increase in the exploration of the metachronal motion of artificial cilia, inspired by the coordinated, wave-like motion of natural cilia found in various organisms. Researchers and engineers have investigated the intricate mechanics governing metachronal motion and have used various actuation methods to achieve metachronal ciliary motion, including pneumatic, optical, electrical, and magnetic techniques. Magnetic artificial cilia have been studied the most since they can be actuated remotely and they provide versatility since metachrony can be realized in diverse ways by either shaping the magnetic actuation field or by controlling individual cilia properties. However, the complicated actuation setup and the shape-isotropic properties of the magnetic artificial cilia still limit the miniaturization of the metachronal motion [3]. Pneumatic artificial cilia offer the unique advantage of completely independent actuation of individual cilia, but their potential is hindered by challenges in miniaturization and the need for intricate connections to actuate the cilia. Overcoming these limitations would significantly broaden their applicability. Light-driven artificial cilia have the advantage of remote actuation of single or clusters of cilia. However, their reliance on a light-transparent environment and their relatively slow response restrict their practical application. Electrically driven artificial cilia face limitations in real-world applications due to their requirement for a high electric field or a specific conductive medium for operation [3]. It will be interesting to combine light and magnetic actuation to realize the metachronal motion of artificial cilia arrays. These two actuation mechanisms do not interfere with each other and may, when combined, provide the possibility to achieve complex shape and motion changes of individual cilia as well as cilia arrays.

In this review, we mainly focus on methods to create the metachronal motion of artificial cilia and the related applications. However, the artificial cilia we have shown in this review still present challenges and limitations. They are still larger than biological cilia, which limits their application to a relatively large scale. Therefore, it is worthwhile to explore the fabrication of artificial cilia arrays with dimensions and aspect ratios close to those of biological cilia. Achieving this goal will involve enhancements in both the materials used and the manufacturing techniques. Specifically, for template-based manufacturing methods, using materials with greater tear strength could significantly improve the demolding success rate for artificial cilia, marking an important step towards more scalable production. To ensure sufficient actuation response, further development towards materials that are both flexible and highly magnetic remains a goal. In terms of creating artificial cilia at the scale of biological ones, it is still a major challenge to increase the areal density of the artificial cilia. Finally, further miniaturizing and integrating the magnetic actuation means will continue to be a necessity for successful application in lab-on-a-chip or organ-on-a-chip systems.

Applications of the metachronal motion of artificial cilia include flow generation, transportation of substances such as mucus, particles, and droplets, and the locomotion of microrobots. Such functions are useful in microfluidic applications, for example, lab-on-a-chip and organ-on-a-chip. Of these functions, fluid flow generation has been investigated the most. Studies have pointed out the relevance of anti-versus symplectic metachrony, with the former leading to more effective fluid transport. The flow velocities that have been achieved using metachronal artificial cilia actuation, for example, 19,000  $\mu\text{m/s}$  for pneumatic and 3000  $\mu\text{m/s}$  for magnetic artificial cilia in water, are well suited to microflu-



idic applications. The utilization of metachronal motion of artificial cilia for investigating mucus transportation has provided interesting results towards understanding mucociliary clearing of the airways in both healthy and diseased states. However, further development is needed to reach more (patho)physiological relevance, towards miniaturization of the cilia and increasing their spatial density. The application of metachronal motion to particle and droplet transportation not only showcases its capabilities but also suggests promising medical applications, particularly in the domain of drug delivery. However, fundamental research to better understand the underlying transportation mechanisms and facilitate the development of more robust and efficient industrial implementations is necessary. The utilization of metachronal motion in the locomotion of robotic systems remains in its nascent stages of development. While some initial experimental investigations have been conducted, they have primarily focused on applications within controlled environments. Consequently, the broader potential of metachronal motion in versatile terrains, for example, towards amphibious microrobots being capable of both walking in air and swimming in liquid, remains largely unexplored. Moreover, the use of numerical simulations to advance our understanding of mechanisms of robotic locomotion and to enable the directed design of metachronal microrobots also requires efforts in the future.

In conclusion, the study of the metachronal motion of artificial cilia remains a vibrant and evolving research domain. The many emerging developments are catalyzing opportunities for scientific exploration as well as applications, thus shaping a dynamic landscape of innovation.

**Author Contributions:** Conceptualization, Z.C. and J.M.J.d.T.; investigation, Z.C.; writing—original draft preparation, Z.C.; writing—review and editing, Y.W. and J.M.J.d.T.; supervision, J.M.J.d.T.; project administration, J.M.J.d.T.; funding acquisition, J.M.J.d.T. All authors have read and agreed to the published version of the manuscript.

**Funding:** This research was funded by the European Research Council (ERC) Advanced Grant Bio-Plan project under grant agreement no. 833214.

**Institutional Review Board Statement:** Not applicable.

**Data Availability Statement:** There were no new data created in this article.

**Acknowledgments:** We thank the European Research Council (ERC) Advanced Grant Bio-Plan for its financial support.

**Conflicts of Interest:** The authors declare no conflicts of interest.

## References

1. Bustamante-Marin, X.M.; Ostrowski, L.E. Cilia and Mucociliary Clearance. *Cold Spring Harb. Perspect. Biol.* **2017**, *9*, a02824. [CrossRef]
2. Sanderson, M.J.; Sleight, M.A. Ciliary Activity of Cultured Rabbit Tracheal Epithelium: Beat Pattern and Metachrony. *J. Cell Sci.* **1981**, *47*, 331–347. [CrossRef]
3. ul Islam, T.; Wang, Y.; Aggarwal, I.; Cui, Z.; Eslami Amirabadi, H.; Garg, H.; Kooi, R.; Venkataramanachar, B.B.; Wang, T.; Zhang, S.; et al. Microscopic Artificial Cilia—A Review. *Lab Chip* **2022**, *22*, 1650–1679. [CrossRef]
4. Machemer, H. Ciliary Activity and the Origin of Metachrony in Paramecium: Effects of Increased Viscosity. *J. Exp. Biol.* **1972**, *57*, 239–259. [CrossRef]
5. Blake, J.R.; Sleight, M.A. Mechanics of Ciliary Locomotion. *Biol. Rev. Camb. Philos. Soc.* **1974**, *49*, 85–125. [CrossRef]
6. Mellor, J.S.; Hyams, J.S. Metachronism of Cilia of the Digestive Epithelium of Cirriformia Tentaculata. *Micron* **1978**, *9*, 91–94. [CrossRef]
7. Satir, P. The Fixation of the Metachronal Wave. *J. Cell Biol.* **1963**, *18*, 345–365. [CrossRef]
8. Knight-Jones, E.W. Relations between Metachronism and the Direction of Ciliary Beat in Metazoa. *J. Cell Sci.* **1954**, s3–s95, 503–521. [CrossRef]
9. Fulford, G.R.; Blake, J.R. Muco-Ciliary Transport in the Lung. *J. Theor. Biol.* **1986**, *121*, 381–402. [CrossRef]
10. Gueron, S.; Levit-Gurevich, K. Energetic Considerations of Ciliary Beating and the Advantage of Metachronal Coordination. *Proc. Natl. Acad. Sci. USA* **1999**, *96*, 12240–12245. [CrossRef]
11. Guirao, B.; Joanny, J.F. Spontaneous Creation of Macroscopic Flow and Metachronal Waves in an Array of Cilia. *Biophys. J.* **2007**, *92*, 1900–1917. [CrossRef]



12. Blake, J.R. Mechanics of Muco-Ciliary Transport. *IMA J. Appl. Math.* **1984**, *32*, 69–87. [CrossRef]
13. Mitran, S.M. Metachronal Wave Formation in a Model of Pulmonary Cilia. *Comput. Struct.* **2007**, *85*, 763–774. [CrossRef]
14. Norton, M.M.; Robinson, R.J.; Weinstein, S.J. Model of Ciliary Clearance and the Role of Mucus Rheology. *Phys. Rev. E-Stat. Nonlinear Soft Matter. Phys.* **2011**, *83*, 011921. [CrossRef]
15. Chateau, S.; Favier, J.; Poncet, S.; D'Ortona, U. Why Antiplectic Metachronal Cilia Waves Are Optimal to Transport Bronchial Mucus. *Phys. Rev. E* **2019**, *100*, 042405. [CrossRef]
16. Khaderi, S.N.; Craus, C.B.; Hussong, J.; Schorr, N.; Belardi, J.; Westerweel, J.; Prucker, O.; R  he, J.; Den Toonder, J.M.J.; Onck, P.R. Magnetically-Actuated Artificial Cilia for Microfluidic Propulsion. *Lab Chip* **2011**, *11*, 2002–2010. [CrossRef]
17. Elgeti, J.; G  mpper, G. Emergence of Metachronal Waves in Cilia Arrays. *Proc. Natl. Acad. Sci. USA* **2013**, *110*, 4470–4475. [CrossRef]
18. Cui, Z.; Wang, Y.; Zhang, S.; Wang, T.; den Toonder, J.M. Miniaturized Metachronal Magnetic Artificial Cilia. *Proc. Natl. Acad. Sci. USA* **2023**, *120*, e2304519120. [CrossRef]
19. Zhang, X.; Guo, J.; Fu, X.; Zhang, D.; Zhao, Y. Tailoring Flexible Arrays for Artificial Cilia Actuators. *Adv. Intell. Syst.* **2021**, *3*, 2000225. [CrossRef]
20. Burn, A.; Schneider, M.; Ryser, M.; Gehr, P.; Ri  ka, J.; Frenz, M. A Quantitative Interspecies Comparison of the Respiratory Mucociliary Clearance Mechanism. *Eur. Biophys. J.* **2022**, *51*, 51–65. [CrossRef]
21. Milana, E.; Zhang, R.; Vetrano, M.R.; Peerlinck, S.; de Volder, M.; Onck, P.R.; Reynaerts, D.; Gorissen, B. Metachronal Patterns in Artificial Cilia for Low Reynolds Number Fluid Propulsion. *Sci. Adv.* **2020**, *6*, eabd2508. [CrossRef]
22. Toonder, J.D.; Bos, F.; Broer, D.; Filippini, L.; Gillies, M.; De Goede, J.; Mol, T.; Reijme, M.; Talen, W.; Wilderbeek, H.; et al. Artificial Cilia for Active Micro-Fluidic Mixing. *Lab Chip* **2008**, *8*, 533–541. [CrossRef]
23. Wang, W.; Liu, Q.; Tanasijevic, I.; Reynolds, M.F.; Cortese, A.J.; Miskin, M.Z.; Cao, M.C.; Muller, D.A.; Molnar, A.C.; Lauga, E. Cilia Metasurfaces for Electronically Programmable Microfluidic Manipulation. *Nature* **2022**, *605*, 681–686. [CrossRef]
24. Dai, B.; Li, S.; Xu, T.; Wang, Y.; Zhang, F.; Gu, Z.; Wang, S. Arti Fi Cial Asymmetric Cilia Array of Dielectric Elastomer for Cargo Transportation. *ACS Appl. Mater. Interfaces* **2018**, *10*, 6–11. [CrossRef]
25. Demir  rs, A.F.; Aykut, S.; Ganzeboom, S.; Meier, Y.A.; Hardeman, R.; de Graaf, J.; Mathijssen, A.J.T.M.T.M.; Poloni, E.; Carpenter, J.A.;   nl  , C.; et al. Amphibious Transport of Fluids and Solids by Soft Magnetic Carpets. *Adv. Sci.* **2021**, *8*, 2102510. [CrossRef]
26. Gorissen, B.; De Volder, M.; Reynaerts, D. Pneumatically-Actuated Artificial Cilia Array for Biomimetic Fluid Propulsion. *Lab Chip* **2015**, *15*, 4348–4355. [CrossRef]
27. Zhang, R.; den Toonder, J.; Onck, P.R. Transport and Mixing by Metachronal Waves in Nonreciprocal Soft Robotic Pneumatic Artificial Cilia at Low Reynolds Numbers. *Phys. Fluids* **2021**, *33*, 092009. [CrossRef]
28. Van Oosten, C.L.; Bastiaansen, C.W.M.; Broer, D.J. Printed Artificial Cilia from Liquid-Crystal Network Actuators Modularly Driven by Light. *Nat. Mater.* **2009**, *8*, 677–682. [CrossRef]
29. Palagi, S.; Mark, A.G.; Reigh, S.Y.; Melde, K.; Qiu, T.; Zeng, H.; Parmeggiani, C.; Martella, D.; Sanchez-Castillo, A.; Kapernaum, N.; et al. Structured Light Enables Biomimetic Swimming and Versatile Locomotion of Photoresponsive Soft Microrobots. *Nat. Mater.* **2016**, *15*, 647–653. [CrossRef]
30. Li, S.; Lerch, M.M.; Waters, J.T.; Deng, B.; Martens, R.S.; Yao, Y.; Kim, D.Y.; Bertoldi, K.; Grinthal, A.; Balazs, A.C.; et al. Self-Regulated Non-Reciprocal Motions in Single-Material Microstructures. *Nature* **2022**, *605*, 76–83. [CrossRef]
31. Miao, J.; Zhang, T.; Li, G.; Shang, W.; Shen, Y. Magnetic Artificial Cilia Carpets for Transport, Mixing, and Directional Diffusion. *Adv. Eng. Mater.* **2021**, *24*, 2101399. [CrossRef]
32. Chen, G.; Dai, Z.; Li, S.; Huang, Y.; Xu, Y.; She, J.; Zhou, B. Magnetically Responsive Film Decorated with Microcilia for Robust and Controllable Manipulation of Droplets. *ACS Appl. Mater. Interfaces* **2021**, *13*, 1754–1765. [CrossRef]
33. Lin, Y.; Hu, Z.; Zhang, M.; Xu, T.; Feng, S.; Jiang, L.; Zheng, Y. Magnetically Induced Low Adhesive Direction of Nano/Micropillar Arrays for Microdroplet Transport. *Adv. Funct. Mater.* **2018**, *28*, 1800163. [CrossRef]
34. Zhou, Y.; Huang, S.; Tian, X. Magnetoresponse Surfaces for Manipulation of Nonmagnetic Liquids: Design and Applications. *Adv. Funct. Mater.* **2020**, *30*, 1906507. [CrossRef]
35. Dong, X.; Lum, G.Z.; Hu, W.; Zhang, R.; Ren, Z.; Onck, P.R.; Sitti, M. Bioinspired Cilia Arrays with Programmable Nonreciprocal Motion and Metachronal Coordination. *Sci. Adv.* **2020**, *6*, eabc9323. [CrossRef]
36. Hanasoge, S.; Hesketh, P.J.; Alexeev, A. Metachronal Motion of Artificial Magnetic Cilia. *Soft Matter.* **2018**, *14*, 3689–3693. [CrossRef]
37. Zhang, R.; den Toonder, J.; Onck, P.R. Metachronal Patterns by Magnetically-Programmable Artificial Cilia Surfaces for Low Reynolds Number Fluid Transport and Mixing. *Soft Matter.* **2022**, *18*, 3902–3909. [CrossRef]
38. Zhang, S.; Cui, Z.; Wang, Y.; Den Toonder, J.M.J.; Toonder, J. den Metachronal Actuation of Microscopic Magnetic Artificial Cilia Generates Strong Microfluidic Pumping. *Lab Chip* **2020**, *20*, 3569–3581. [CrossRef]
39. Choksi, S.P.; Lauter, G.; Swoboda, P.; Roy, S. Switching on Cilia: Transcriptional Networks Regulating Ciliogenesis. *Development* **2014**, *141*, 1427–1441. [CrossRef]
40. Gilpin, W.; Bull, M.S.; Prakash, M. The Multiscale Physics of Cilia and Flagella. *Nat. Rev. Phys.* **2020**, *2*, 74–88. [CrossRef]
41. Elgeti, J.; Winkler, R.G.; G  mpper, G. Physics of Microswimmers—Single Particle Motion and Collective Behavior: A Review. *Rep. Prog. Phys.* **2015**, *78*, 056601. [CrossRef]

42. Wang, C.; Tang, H.; Zhang, X. Fluid-Structure Interaction of Bio-Inspired Flexible Slender Structures: A Review of Selected Topics. *Bioinspir. Biomim.* **2022**, *17*, 041002. [CrossRef]
43. Pazour, G.J.; Quarmby, L.; Smith, A.O.; Desai, P.B.; Schmidts, M. Cilia in Cystic Kidney and Other Diseases. *Cell Signal.* **2019**, *69*, 109519. [CrossRef]
44. Hirokawa, N.; Okada, Y.; Tanaka, Y. Fluid Dynamic Mechanism Responsible for Breaking the Left-Right Symmetry of the Human Body: The Nodal Flow. *Annu. Rev. Fluid Mech.* **2009**, *41*, 53–72. [CrossRef]
45. Ul Islam, T.; Bellouard, Y.; Den Toonder, J.M.J. Highly Motile Nanoscale Magnetic Artificial Cilia. *Proc. Natl. Acad. Sci. USA* **2021**, *118*, e2104930118. [CrossRef]
46. Vanaki, S.M.; Holmes, D.; Saha, S.C.; Chen, J.; Brown, R.J.; Jayathilake, P.G. Muco-Ciliary Clearance: A Review of Modelling Techniques. *J. Biomech.* **2020**, *99*, 109578. [CrossRef]
47. Odor, D.L.; Blandau, R.J. Observations on the Solitary Cilium of Rabbit Oviductal Epithelium: Its Motility and Ultrastructure. *Am. J. Anat.* **1985**, *174*, 437–453. [CrossRef]
48. Osterman, N.; Vilfan, A. Finding the Ciliary Beating Pattern with Optimal Efficiency. *Proc. Natl. Acad. Sci. USA* **2011**, *108*, 15727–15732. [CrossRef]
49. Chateau, S.; Favier, J.; D’Ortona, U.; Poncet, S. Transport Efficiency of Metachronal Waves in 3D Cilium Arrays Immersed in a Two-Phase Flow. *J. Fluid Mech.* **2017**, *824*, 931–961. [CrossRef]
50. Hanasoge, S.; Hesketh, P.J.; Alexeev, A. Metachronal Actuation of Microscale Magnetic Artificial Cilia. *ACS Appl. Mater. Interfaces* **2020**, *12*, 46963–46971. [CrossRef]
51. Lyons, R.; Saridogan, E.; Djahanbakhch, O. The reproductive significance of human Fallopian tube cilia. *Hum. Reprod. Update* **2006**, *12*, 363–372. [CrossRef]
52. Sitti, M.; Wiersma, D.S. Pros and Cons: Magnetic versus Optical Microrobots. *Adv. Mater.* **2020**, *32*, 1906766. [CrossRef]
53. Liu, Z.; Li, M.; Dong, X.; Ren, Z.; Hu, W.; Sitti, M. Creating Three-Dimensional Magnetic Functional Microdevices via Molding-Integrated Direct Laser Writing. *Nat. Commun.* **2022**, *13*, 2016. [CrossRef]
54. Wang, Z.; Wang, K.; Liang, D.; Yan, L.; Ni, K.; Huang, H.; Li, B.; Guo, Z.; Wang, J.; Ma, X.; et al. Hybrid Magnetic Micropillar Arrays for Programmable Actuation. *Adv. Mater.* **2020**, *32*, 2001879. [CrossRef]
55. Kim, J.; Chung, S.E.; Choi, S.E.; Lee, H.; Kim, J.; Kwon, S. Programming Magnetic Anisotropy in Polymeric Microactuators. *Nat. Mater.* **2011**, *10*, 747–752. [CrossRef]
56. Zarzar, L.; Kim, P.; Aizenberg, J. Bio-inspired design of submerged hydrogel-actuated polymer microstructures operating in response to pH. *Adv. Mater.* **2011**, *23*, 1442–1446. [CrossRef]
57. Zhang, S.; Cui, Z.; Wang, Y.; Den Toonder, J. Metachronal  $\mu$ -Cilia for On-Chip Integrated Pumps and Climbing Robots. *ACS Appl. Mater. Interfaces* **2021**, *13*, 20845–20857. [CrossRef]
58. Gu, H.; Boehler, Q.; Cui, H.; Secchi, E.; Savorana, G.; De Marco, C.; Gervasoni, S.; Peyron, Q.; Huang, T.Y.; Pane, S.; et al. Magnetic Cilia Carpets with Programmable Metachronal Waves. *Nat. Commun.* **2020**, *11*, 2637. [CrossRef]
59. Tsumori, F.; Marume, R.; Saijou, A.; Kudo, K.; Osada, T.; Miura, H. Metachronal Wave of Artificial Cilia Array Actuated by Applied Magnetic Field. *JPN J. Appl. Phys.* **2016**, *55*, 06GP19. [CrossRef]
60. Milana, E.; Gorissen, B.; Peerlinck, S.; De Volder, M.; Reynaerts, D. Artificial Soft Cilia with Asymmetric Beating Patterns for Biomimetic Low-Reynolds-Number Fluid Propulsion. *Adv. Funct. Mater.* **2019**, *29*, 1900462. [CrossRef]
61. Hussong, J.; Breugem, W.P.; Westerweel, J. A Continuum Model for Flow Induced by Metachronal Coordination between Beating Cilia. *J. Fluid Mech.* **2011**, *684*, 137–162. [CrossRef]
62. Hall, J.; Clarke, N. The Mechanics of Cilium Beating: Quantifying the Relationship between Metachronal Wavelength and Fluid Flow Rate. *J. Fluid Mech.* **2020**, *891*, A20. [CrossRef]
63. Khaderi, S.N.; Den Toonder, J.M.J.; Onck, P.R. Microfluidic Propulsion by the Metachronal Beating of Magnetic Artificial Cilia: A Numerical Analysis. *J. Fluid Mech.* **2011**, *688*, 44–65. [CrossRef]
64. Khaderi, S.N.; den Toonder, J.M.J.; Onck, P.R. Fluid Flow Due to Collective Non-Reciprocal Motion of Symmetrically-Beating Artificial Cilia. *Biomicrofluidics* **2012**, *6*, 014106. [CrossRef]
65. Mesdjian, O.; Wang, C.; Gsell, S.; D’Ortona, U.; Favier, J.; Viallat, A.; Loiseau, E. Longitudinal to Transverse Metachronal Wave Transitions in an in Vitro Model of Ciliated Bronchial Epithelium. *Phys. Rev. Lett.* **2022**, *129*, 38101. [CrossRef]
66. Pedersoli, L.; Zhang, S.; Briatico-Vangosa, F.; Petrini, P.; Cardinaels, R.; den Toonder, J.; Peneda Pacheco, D. Engineered Modular Microphysiological Models of the Human Airway Clearance Phenomena. *Biotechnol. Bioeng.* **2021**, *118*, 3898–3913. [CrossRef]
67. Zhang, S.; Wang, Y.; Onck, P.; den Toonder, J. A Concise Review of Microfluidic Particle Manipulation Methods. *Microfluid. Nanofluidics* **2020**, *24*, 24. [CrossRef]
68. Ben, S.; Tai, J.; Ma, H.; Peng, Y.; Zhang, Y.; Tian, D.; Liu, K.; Jiang, L. Cilia-Inspired Flexible Arrays for Intelligent Transport of Viscoelastic Microspheres. *Adv. Funct. Mater.* **2018**, *28*, 1706666. [CrossRef]
69. Ben, S.; Yao, J.; Ning, Y.; Zhao, Z.; Zha, J.; Tian, D.; Liu, K.; Jiang, L. A Bioinspired Magnetic Responsive Cilia Array Surface for Microspheres Underwater Directional Transport. *Sci. China Chem.* **2020**, *63*, 347–353. [CrossRef]
70. Kim, J.H.; Kang, S.M.; Lee, B.J.; Ko, H.; Bae, W. Remote Manipulation of Droplets on a Flexible Magnetically Responsive Film. *Nat. Publ. Gr.* **2015**, *5*, 17843. [CrossRef]
71. Ben, S.; Zhou, T.; Ma, H.; Yao, J.; Ning, Y.; Tian, D.; Liu, K.; Jiang, L. Multifunctional Magnetocontrollable Superwetable-Microcilia Surface for Directional Droplet Manipulation. *Adv. Sci.* **2019**, *6*, 1900834. [CrossRef]

72. Song, Y.; Jiang, S.; Li, G.; Zhang, Y.; Wu, H.; Xue, C.; You, H.; Zhang, D.; Cai, Y.; Zhu, J.; et al. Cross-Species Bioinspired Anisotropic Surfaces for Active Droplet Transportation Driven by Unidirectional Microcolumn Waves. *ACS Appl. Mater. Interfaces* **2020**, *12*, 42264–42273. [CrossRef]
73. Wang, H.; Zhang, Z.; Wang, Z.; Liang, Y.; Cui, Z.; Zhao, J.; Li, X.; Ren, L. Multistimuli-Responsive Microstructured Superamphiphobic Surfaces with Large-Range, Reversible Switchable Wettability for Oil. *ACS Appl. Mater. Interfaces* **2019**, *11*, 28478–28486. [CrossRef]
74. Jiang, S.; Hu, Y.; Wu, H.; Li, R.; Zhang, Y.; Chen, C.; Xue, C.; Xu, B.; Zhu, W.; Li, J.; et al. Three-Dimensional Multifunctional Magnetically Responsive Liquid Manipulator Fabricated by Femtosecond Laser Writing and Soft Transfer. *Nano Lett.* **2020**, *20*, 7519–7529. [CrossRef]
75. Zeng, H.; Wasylczyk, P.; Parmeggiani, C.; Martella, D.; Burrelli, M.; Wiersma, D.S. Light-Fueled Microscopic Walkers. *Adv. Mater.* **2015**, *27*, 3883–3887. [CrossRef]
76. Zeng, H.; Wani, O.M.; Wasylczyk, P.; Priimagi, A. Light-Driven, Caterpillar-Inspired Miniature Inching Robot. *Macromol. Rapid Commun.* **2018**, *39*, 1700224. [CrossRef]
77. Zheng, Q.; Wu, Z.L. Light-Steered Locomotion of Muscle-like Hydrogel by Self-Coordinated Shape Change and Friction Modulation. *Nat. Commun.* **2020**, *11*, 5166. [CrossRef]
78. Joyee, E.B.; Pan, Y. A Fully Three-Dimensional Printed Inchworm-Inspired Soft Robot with Magnetic Actuation. *Soft Robot.* **2019**, *6*, 333–345. [CrossRef]
79. Alapan, Y.; Karacakol, A.C.; Guzelhan, S.N.; Isik, I.; Sitti, M. Reprogrammable Shape Morphing of Magnetic Soft Machines. *Sci. Adv.* **2020**, *6*, eabc6414. [CrossRef]
80. Venkiteswaran, V.K.; Samaniego, L.F.P.; Sikorski, J.; Misra, S. Bio-Inspired Terrestrial Motion of Magnetic Soft Millirobots. *IEEE Robot. Autom. Lett.* **2019**, *4*, 1753–1759. [CrossRef]
81. Xu, T.; Zhang, J.; Salehizadeh, M.; Onaizah, O.; Diller, E. Millimeter-Scale Flexible Robots with Programmable Three-Dimensional Magnetization and Motions. *Sci. Robot.* **2019**, *4*, eaav4494. [CrossRef]
82. Hu, W.; Lum, G.Z.; Mastrangeli, M.; Sitti, M. Small-Scale Soft-Bodied Robot with Multimodal Locomotion. *Nature* **2018**, *554*, 81–85. [CrossRef]
83. Palagi, S.; Fischer, P. Bioinspired Microrobots. *Nat. Rev. Mater.* **2018**, *3*, 113–124. [CrossRef]
84. Jiang, H.; Gu, H.; Nelson, B.J.; Zhang, T. Numerical Study of Metachronal Wave-Modulated Locomotion in Magnetic Cilia Carpets. *Adv. Intell. Syst.* **2023**, *5*, 2300212. [CrossRef]

**Disclaimer/Publisher’s Note:** The statements, opinions and data contained in all publications are solely those of the individual author(s) and contributor(s) and not of MDPI and/or the editor(s). MDPI and/or the editor(s) disclaim responsibility for any injury to people or property resulting from any ideas, methods, instructions or products referred to in the content.



## Article

# TriTrap: A Robotic Gripper Inspired by Insect Tarsal Chains

Julian Winand \*, Thies H. Büscher and Stanislav N. Gorb

Department of Functional Morphology and Biomechanics, Zoological Institute, University of Kiel,  
Am Botanischen Garten 1-9, 24118 Kiel, Germany; tbuescher@zoologie.uni-kiel.de (T.H.B.);  
sgorb@zoologie.uni-kiel.de (S.N.G.)

\* Correspondence: jwinand@zoologie.uni-kiel.de

**Abstract:** Gripping, holding, and moving objects are among the main functional purposes of robots. Ever since automation first took hold in society, optimizing these functions has been of high priority, and a multitude of approaches has been taken to enable cheaper, more reliable, and more versatile gripping. Attempts are ongoing to reduce grippers' weight, energy consumption, and production and maintenance costs while simultaneously improving their reliability, the range of eligible objects, working loads, and environmental independence. While the upper bounds of precision and flexibility have been pushed to an impressive level, the corresponding solutions are often dependent on support systems (e.g., sophisticated sensors and complex actuation machinery), advanced control paradigms (e.g., artificial intelligence and machine learning), and typically require more maintenance owed to their complexity, also increasing their cost. These factors make them unsuited for more modest applications, where moderate to semi-high performance is desired, but simplicity is required. In this paper, we attempt to highlight the potential of the tarsal chain principle on the example of a prototype biomimetic gripping device called the TriTrap gripper, inspired by the eponymous tarsal chain of insects. Insects possess a rigid exoskeleton that receives mobility due to several joints and internally attaching muscles. The tarsus (foot) itself does not contain any major intrinsic muscles but is moved by an extrinsically pulled tendon. Just like its biological counterpart, the TriTrap gripping device utilizes strongly underactuated digits that perform their function using morphological encoding and passive conformation, resulting in a gripper that is versatile, robust, and low cost. Its gripping performance was tested on a variety of everyday objects, each of which represented different size, weight, and shape categories. The TriTrap gripper was able to securely hold most of the tested objects in place while they were lifted, rotated, and transported without further optimization. These results show that the insect tarsus selected approach is viable and warrants further development, particularly in the direction of interface optimization. As such, the main goal of the TriTrap gripper, which was to showcase the tarsal chain principle as a viable approach to gripping in general, was achieved.

**Keywords:** morphology; tarsomeres; biomechanics; soft robot; bioinspired gripping; underactuation; biomimetics



**Citation:** Winand, J.; Büscher, T.H.; Gorb, S.N. TriTrap: A Robotic Gripper Inspired by Insect Tarsal Chains. *Biomimetics* **2024**, *9*, 142. <https://doi.org/10.3390/biomimetics9030142>

Academic Editor: Jinyou Shao

Received: 12 January 2024

Revised: 23 February 2024

Accepted: 24 February 2024

Published: 26 February 2024



**Copyright:** © 2024 by the authors. Licensee MDPI, Basel, Switzerland. This article is an open access article distributed under the terms and conditions of the Creative Commons Attribution (CC BY) license (<https://creativecommons.org/licenses/by/4.0/>).

## 1. Biological Inspiration

A wide variety of solutions has evolved for the locomotion and contacting/gripping of objects in living organisms [1]. Insects, in particular, show an interesting spectrum of such functions due to the presence of an exoskeleton, which provides strong variability and flexibility in evolving a multitude of various functional solutions [2,3]. The legs of some insect groups are modified to perform highly derived tasks. Some examples include praying mantises grasping prey with their forelegs [4], cicadas jumping with their hind legs [5], corbiculate bees collecting pollen with an elaborate collecting apparatus [6], webspinners using their forefeet to spin silk [7], mole crickets having shovels for digging [8], etc. As a result of evolution, a solution to a problem poses a sufficiently good compromise between energy/material investment and functional returns to be advantageous for survival [9]. Insects are often relatively short-living animals but also highly diverse in their environmental

adaptations and diversity of functional solutions. They, therefore, employ a digit paradigm that, on the one hand, is comparatively simple and, on the other hand, performs well under diverse conditions with little need for direct control [10]. These properties are mainly tied to the distal part of insect legs, a strongly underactuated system called the tarsal chain (Figure 1).

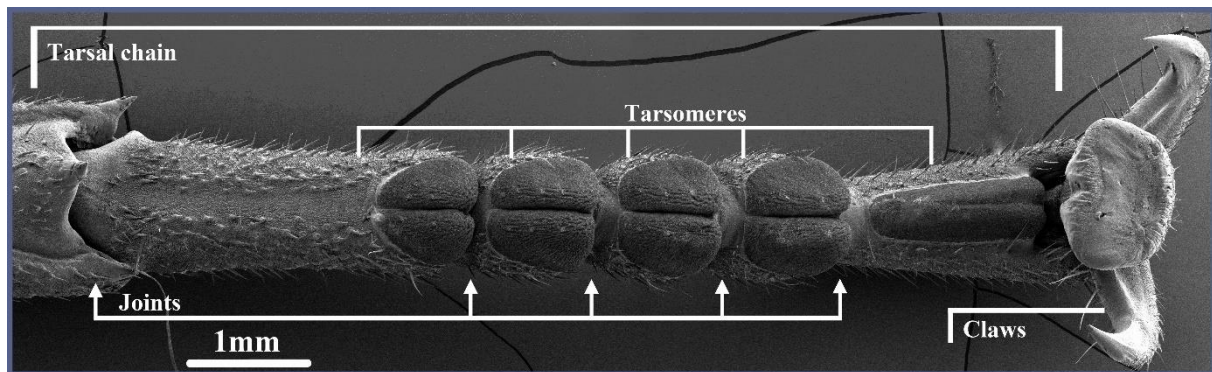


**Figure 1.** SEM micrograph of the ventral aspect of the tarsal chain in the stick insect *Sungaya inexpectata*. It consists of mobile-linked chain elements called tarsomeres and is strongly underactuated.

These systems consist of multiple, loosely linked chain elements (tarsomeres) whose active channel of actuation is flexion along the ground-facing side of the leg [11]. In some cases, the system can also be actively bent backward [11]. This movement is facilitated by two antagonistic muscles (protractor and retractor) in spiders, but in insects, the simplest case occurs—one tendon supplemented by a few muscles differently arranged depending on the species (altogether, they represent the *musculus retractor unguis*) [12]. Additionally, the chain possesses a large number of passive degrees of freedom along other directions due to the complementary shape of the tarsomeres and their loose connection [13]. This enables the tarsus to passively conform to a large number of shapes, directions, and conditions that simple flexion of a two-segmented system would be unable to manage on its own [14,15]. Exploratory sweeping of the leg over surfaces more or less automatically predetermines a shape suitable for the task at hand. This poses a highly economical approach to contacting and thus also gripping and manipulating various objects [16]. While the chain lacks the precision and high-performance nature of dedicated and highly advanced technical manipulation devices, its relative simplicity in structure and control makes for a very good compromise between investment and returns from a performance point of view.

This attractive cost–use relationship is promising for technical systems in the fields of robotic locomotion and gripping [3]. There are ongoing efforts to push the boundaries in the development of such gripping systems, and many inspiring as well as promising approaches exist [17]. However, almost all of them either require some form of additional advanced infrastructure to work (e.g., pumps, heating, magnetic field generation, etc.), sophisticated sensory equipment (e.g., spatial/optical/force sensor arrays working in concert), and/or highly complex control mechanisms (e.g., complex adaptive movement programs, machine learning, artificial intelligence, etc.) [17]. This applies to classical “hard” robotics, where all degrees of freedom are actively controlled, as well as to the emerging field of soft robotics that attempts to employ morphological computation or encoding [18]. While this is not necessarily problematic in most scenarios, as long as these requirements result in higher performance gripping, there are some cases where this poses a hindrance. Ambient conditions, such as high humidity, high/low temperature, chemical hazards, etc., might have a detractive effect on device components of highly complex systems. Additionally, a high degree of complexity inevitably results in a higher chance of malfunction and requires more maintenance and financial investment. The insect tarsal chain is a system with a relatively simple internal working principle and, thus, few requirements with respect to construction and maintenance if replicated in a

technical context [19]. Still, it provides a surprising range of possible usages, as it is seen in nature [1–8], and operates with only a few channels of direct control. In this work, an artificial gripper end effector utilizing the tarsal chain principle was designed and assembled to capitalize on these points and provide proof of concept for the tarsal chain principle.

## 2. Adopted Working Principles and Design Considerations

Tarsomeres and tarsal chains have already been used as inspiration for robotic applications, most prominently locomotion. Some recent examples include a mechanical adhesive gripper inspired by beetle claws and tarsi that was later employed in a climbing robot [20,21]; a complete walking and climbing robot called Drosiphobot modeled after the common fruit fly *Drosophila melanogaster*, which used passive tarsal chains as end effectors on its feet [22]; a spine-based wall climbing robot utilizing a tarsal chain inspired mount for its climbing spines [23]; a novel robotic gripper used in fruit harvesting that employs tarsal chain based end effectors to prevent fruit slipping after harvesting [24]; and another vertical climbing robot imitating the passive conformability of cockroach tarsal chains [25]. Another example would be the utilization of the tarsal chain structure and actuation principle in a very general sense in hyper-redundant manipulators for endoscopic surgery [26] or the creation of a tarsus-based robot leg for locomotion [27]. There have been efforts to utilize the tarsal chain principle to improve the performance of tree-climbing robots [28], to enhance the traversal of robots during the construction of orbital structures in space [29], to improve vertical traversal under outdoor conditions [30], to exploit characteristics of structures tied to tarsal chains, such as insect claws, to improve robotic gait on certain types of terrain [31], or in a climbing robot utilizing tracks inspired by tarsal chains [32]. The vast majority of work in this regard focuses on locomotion systems for robots, which is not surprising considering that tarsal chains are used for locomotion in nature as well. However, the tarsal chains' ability to passively conform to contacted objects should lend itself well to dedicated gripping tasks on the vast majority of objects if appropriately adjusted. Therefore, it was decided here to adopt this principle and create a prototype gripping device to evaluate the tarsal chain concept and its possible implications for universal grippers.

As shown in Figure 1, the biological tarsal chain on its basic level consists of several loosely linked elements, the tarsomeres [33]. The chain's actuation is facilitated by a tendon that runs through its whole length at a lateral offset to the pivot points between the tarsomeres. When it is pulled by its muscle, the transmitted force is exerted off-center from the joints' neutral positions, resulting in a torque towards the tendon side of the chain.

Figure 2 shows the generalized force interactions in such a case, using a representative, isolated element pair connected through a joint. It contains general relationships, which need to be considered in order to create an artificial, tarsal-chain-inspired folding structure. Schematically, the pulling force along the tendon  $F_t$  creates a force  $F_{Ax}$  at the tip of the upper element, which then results in a folding movement within the joint. Its magnitude can be derived from the overall reaction forces caused by the tendon pull. At the equilibrium, it holds that the sum of linearly dependent individual forces must be zero. It follows that in the case of the  $x$ -direction:

$$\begin{aligned}\sum F_x = 0 &= F_{Ax} + F_{Bx} \\ F_{Bx} &= -F_{Ax}\end{aligned}\quad (1)$$

Furthermore, the total equilibrium torque at point  $A$  must be zero:

$$\begin{aligned}\sum M(A) = 0 &= F_t \cdot a + F_{Bx} \cdot l \\ F_{Bx} &= -\frac{F_t \cdot a}{l}\end{aligned}\quad (2)$$



Combined with (1), it follows that the expected closing force at the tip of a given folding element can be given as

$$F_{Ax} = F_{closing} = \frac{F_t \cdot a}{l} \quad (3)$$

The tendon force  $F_t$  is likely limited by material and mechanical constraints in most cases [34]. Therefore, the main task for designing a biologically inspired tendon–tarsomere folding system of this kind is based on these considerations. Either the lateral offset  $a$  between the joint and the tendon guide needs to be sufficiently large, or the folding element length  $l$  needs to be small enough to permit flexion against the structure’s weight as well as expected workloads. With this criterion met, the principle can then be expanded to multiple folding elements chained together with a single tendon running through all of them along specific guides. If actuated and without further modification, the first element to fold is the topmost one because the tendon is attached there, but this order can be changed and/or reversed by introducing specifically tailored resistances to each link pair. Then, as soon as a link exhausts its angular movement space, the next one starts to fold, and so forth, until the last element has switched position, and no link is able to move anymore.

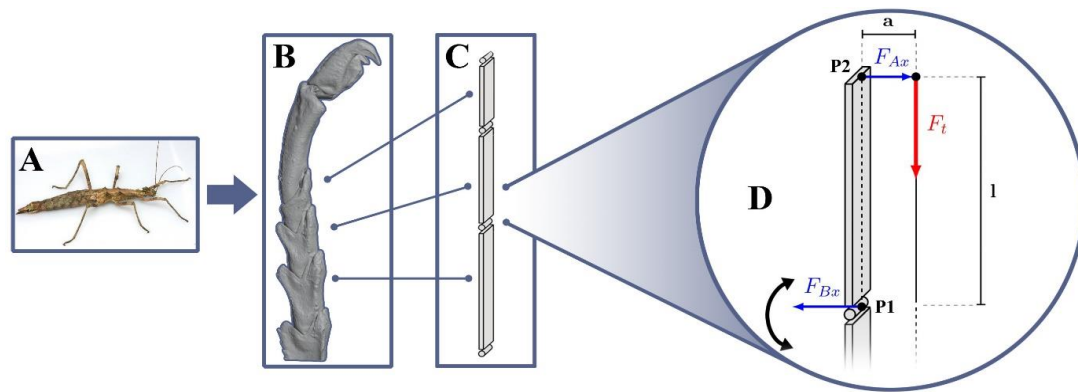


**Figure 2.** Generalized working principle of tarsal chain actuation. (A) Model insect species that was previously investigated, *Sungaya inexpectata* (distributed under the Creative Commons license (CC BY 4.0)). (B) A 3D model of its tarsus generated using  $\mu$ -computed tomography. (C) The underlying, simplified mechanical setup represented as beams connected by joints. (D) Schematic representation of the forces at work during the actuation of individual links on the example of one tarsomere–tarsomere joint.

This behavior constitutes a form of control by shape or morphological encoding [18]. Even though the only input the system receives is a linear pull at the tendon, the resulting movement is a specific sequence of different rotational and translative movements that result in a concerted, directed overall effect—it is encoded in the morphological relations of the participating elements, and not actively controlled. Furthermore, while any resistance the folding chain meets on its way to full flexion (such as an object to grip) will hinder the bending of one or more links because the tendon folds them based on the resistance force each individual link exhibits, the unobstructed links will still bend around the object that caused the obstruction. This results in good contact (conformation) between the tarsal-chain-based arm and the object without any form of active control.

This encoding can be changed by changing the structure of the device. For example, the chain tip trajectory or closing speed are functions of (a) the number of chain elements, (b) the length of chain elements, (c) the allowed maximum bending angles between elements, and (d) the order of both allowed angles and lengths along the chain (e.g., rising, falling, mixed, etc.). Additionally, as previously mentioned, the folding order could also be changed by introducing resistances of specific strengths between the chain elements, in the most basic case by mere rubber bands—which also mimics the original tarsal chain where, in many cases, relaxation is achieved by elastic reservoirs (resilin) instead of muscles [35].

Depending on how points (a) through (d) are handled, the resulting chain can potentially achieve many different actuation patterns, ranging from simple sequential folding to varying types of “embracing” movements: pulling, sideways shifting, and specific combinations of those. In this work, three identical chains of elements, called arms from now on, have been adjusted to perform embracing movements towards a common center, creating a gripping device. As described earlier in this section, these abilities of the tarsal chain are expected to lend themselves well to gripping, and the resultant gripper was supposed to prove this postulate.

### 3. Materials and Methods

The TriTrap gripper was constructed using mainly 3D-printed polylactic acid (PLA). For the computer-assisted design (CAD) process, Blender (Blender Foundation, open source) was used for all printed parts, and both the slicer programs PrusaSlicer (Prusa Research, Prague, Czech Republic) and Ultimaker Cura (Ultimaker B.V., Utrecht, The Netherlands) were used to prepare the G-code. The 3D printer was a Prusa Mk3S (Prusa Research, Prague, Czech Republic) with a 0.4 mm nozzle that used varying layer thicknesses, ranging from 0.1 to 0.3 mm, depending on the precision required for the respective parts.

Apart from 3D-printed PLA, some additional materials were used. For the tendons, a specialized fiber fishing line (Kogha Braid 12, Askari Sport GmbH, Lüdinghausen, Germany) was employed, as well as a 1.5 mm braided steel cable. The elastic returning mechanism was realized using rubber bands, which were also used to reverse the folding order of the arms to increase performance. For the assembly, 2-component epoxy glue (Plus Endfest, Uhu GmbH & Co. KG, Bühl, Germany) was used where it was not practical to print mechanical connections. In some instances, it was necessary to post-process some parts after printing for reasons of precision. For that, Proxxon (Proxxon S.A., Wecker, Germany) fine power tools were used.

For the qualitative evaluation of the concept’s viability, a range of everyday objects with different sizes, shapes, and weights were used, as shown in Figure 3: an electric water boiler device (weight: 600 g), a PC keyboard (400 g), a textile bag (40 g), a piece of polystyrene in the shape of a vase (20 g), an empty beverage bottle made of plastic (30 g), and a grill attachment made of steel (160 g). For all objects, multiple attempts were made to pick them off the ground from the top down for two different object orientations: standing upright (where applicable) and lying on the side. While heavier objects would not be a problem for a tarsal-chain-based gripper per se, the TriTrap gripper was mainly constructed using PLA, which results in very distinct limits as to its mechanical durability. Therefore, relatively light objects were used.

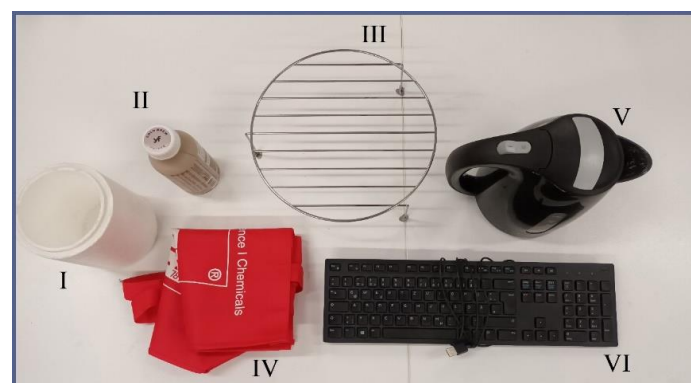


**Figure 3.** Test objects used for qualitative testing of the TriTrap gripper: I—polystyrene vase (20 g); II—empty beverage bottle made of plastic (30 g); III—steel grill attachment (160 g); IV—textile bag (40 g); V—electric water boiler (600 g); and VI—PC keyboard (400 g).

## 4. The TriTrap Gripper

### 4.1. Overview

The prototype gripper built in this work, called the TriTrap gripper, can be seen in Figure 4. It consists of three parts: (1) the gripper arms that perform the gripping; (2) the actuation cage, which houses the pulling handle and the force-distribution disc; and (3) the base plate, which acts as a foundation for both the arms and the cage. Each arm consists of seven linked segments, called links from now on, of which the topmost one terminates in a pointed wedge that imitates the claw found on insect legs. These wedges can be used for objects that, for reasons of shape or size, will not fit between the closed arms and provide additional support for the object inside the gripper when fully flexed. The links correspond to the tarsomeres of the biological tarsus, and rubber bands on their backsides correspond to the resilin patches found on the animal's legs, where they act as elastic energy storage units for unfolding them again [29]. The three arms' anchor joints are arranged in a triangle shape on the base plate, making them meet on top of it when completely flexed. The lengths of the links on each arm decrease from bottom to top the same way as in the biological model, and the allowed folding angles between the links are deliberately chosen via specifically designed angle adjusters that functionally mimic the tarsus–tarsus bending interaction in nature. This arrangement makes the arms move from their open to their closed state in an “embracing” way and causes them to meet over the center of the base plate with the faces of their wedges touching each other. In the current configuration, the TriTrap has a maximum opening angle of  $90^\circ$  and an open-state tip-to-tip width of 65 cm, although those specifications can be changed by changing the angle adjusters and link lengths. As for the closing speed, the arms can close as fast as actuation allows. However, the fact that there is no cushioning or braking mechanism to prevent the arms from crashing into one another with high impact necessitates caution when trying to quickly close the gripper. This issue gets compounded by the scale and, by extension, the length and mass of the arms, which naturally increases the system's inertia. The whole device is actuated by pulling a single handle, which is situated below the base plate. The handle is connected to the arms through a force-distribution disc, which splits up the actuation force along three individual tendons associated with the arms, effectively actuating them via a single tendon per arm, as in the biological example. In its closed state, the TriTrap encloses a certain volume of space, as seen in Figure 4C. While this means that objects of sizes smaller than that cannot be properly gripped by this version of the gripper, this constitutes a design choice and not a limitation intrinsic to grippers based on tarsal chains. In the case of the TriTrap gripper, the authors intended to preserve some space between the arms to be able to equip them with different interfacing modules to increase friction in a follow-up work, which would minimize that volume in any case.

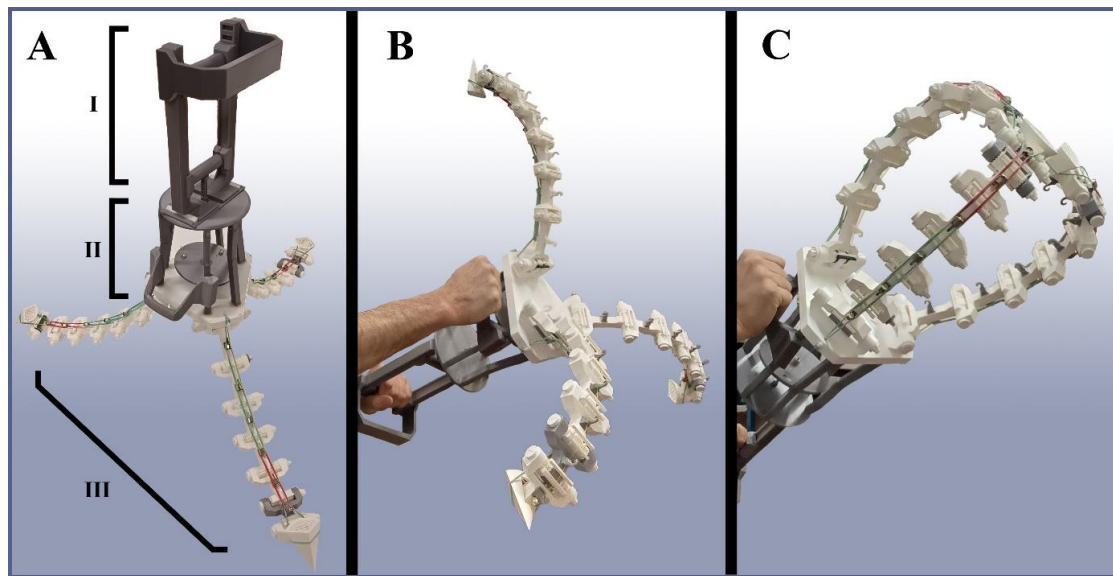


**Figure 4.** Overview of the TriTrap gripper: (A) open gripper, showcasing the handle (I), the actuation cage (II), and the arms (III); (B) gripper in hand while completely unflexed; and (C) gripper actuated to full flexion by hand.

#### 4.2. Arms

The arms' links are connected by monoaxial axle joints that have been designed for easy assembly and disassembly to facilitate quick replacements and part interchange, for example, to employ links of different lengths in the future. The axle runs through both connected links, as well as through an angle adjuster situated between them and terminating in a tapered head equipped with a snap-on stopper piece to hold it in place. The angle adjusters limit the maximum allowed folding angle between the links. They are designed in such a way that the angle can be changed by taking the adjuster out of the joint and rotating its cog elements relative to one another until the desired angle is locked in. Figure 5 shows an isolated link–link joint with its angle stopper and axle assembled.

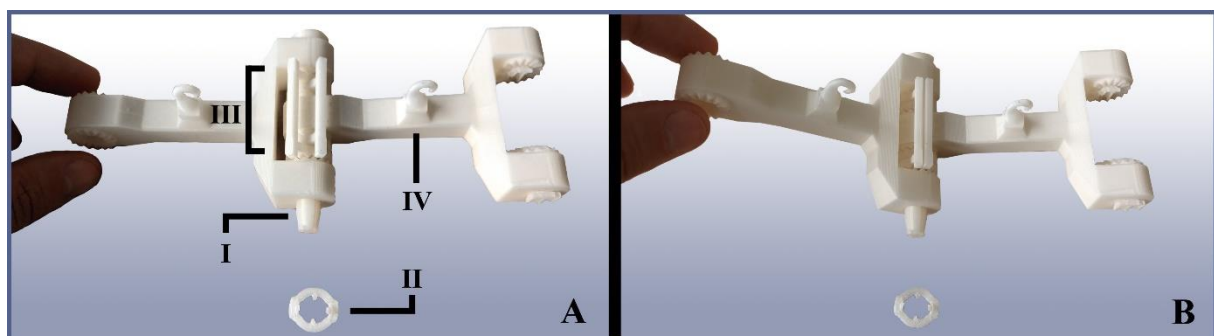


**Figure 5.** Example of the TriTrap gripper's link–link joints. (A) Two isolated links connected by their joint, resting on its axle (I). The axle is held in place by a stopper piece (II), which, in this case, was detached for clarity. Any joint's angular movement is limited by the angle adjusters (III), which can be modified to allow for different folding angles. Each link possesses a tendon guide (IV), which ensures the tendon's relative position with respect to the joints. (B) The same joint in the folded state, illustrating the angle adjusters' function.

Each of the three arms is actuated into flexion by a single tendon that extends from the force-distribution disc through the base plate all the way to the arm tip, where it is attached. On its way, it runs through several specifically designed tendon guides attached to each link in order to ensure the relative position of the tendon with respect to the corresponding

joint regardless of flexion state (Figure 6A). This is necessary to retain the mechanical relationships shown in Figure 2 and to keep it out of the actual gripping space.

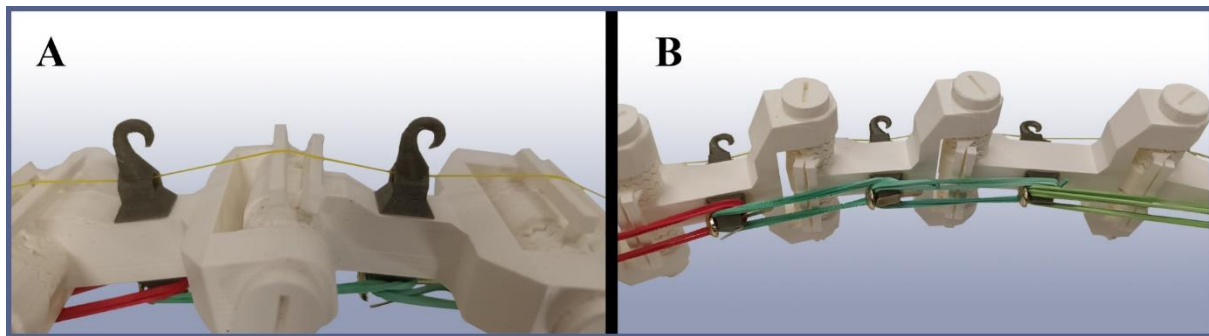


**Figure 6.** Close-up views of the arms. (A) Inner side of the arms, showing the tendon (yellow) and its guides that are necessary to keep it in its correct relative position with respect to the joints. (B) Outer side of the arms, showing the elastic relaxation (unfolding) mechanism made of standard rubber bands.

In the prototype, a specialist fiber fishing gear was used as the tendon. This was necessary after the mechanical demands placed upon the tendon during operation had shown themselves to exceed the properties of other, more conventional fiber types. The reversal movement, i.e., relaxation or opening, does not possess an active actuation but instead is facilitated by elastic bands on the outer side of each arm (Figure 6B). When flexing, those bands get elongated and then pull the arm back into its open state as soon as the actuation force is no longer applied. Additionally, the relative strength of the bands between different link pairs has been chosen such that the flexion movement occurs from bottom to top, as opposed to the top-to-bottom movement that would occur without elastic resistance.

#### 4.3. Actuation Cage

Below the base plate, a cage-like structure is attached, which, on the one hand, houses the force-distribution disc and, on the other hand, serves as an anchor point for the actuation handle. The force-distribution disc is a basic 3D-printed disc with four holes—one in the center and the other three at equidistant points from it—forming an equilateral triangle (Figure 7A). The three outer holes serve as attachment points for the arm tendon ends, while in the middle one, the handle cord is attached. When the handle is pulled, the handle cord exerts a pulling force at the center of the disc, which then starts to move away from the base plate. Since the arm tendons are attached to it as well, they also retract and actuate the arms they are attached to. The purpose of the disc here is twofold. First, it distributes the handle force equally among the arms, letting them flex together and in the same way as long as each of them encounters the same closing resistance. Second, in case the arms do not encounter equal closing resistance, e.g., because the object to grip possesses a strongly asymmetrical shape, it tilts to let the unjammed arms close irrespective of the jammed one (Figure 7B). This way, a single linear actuation can be used without impairing the gripper's flexibility when it comes to adapting to the gripping object shapes.

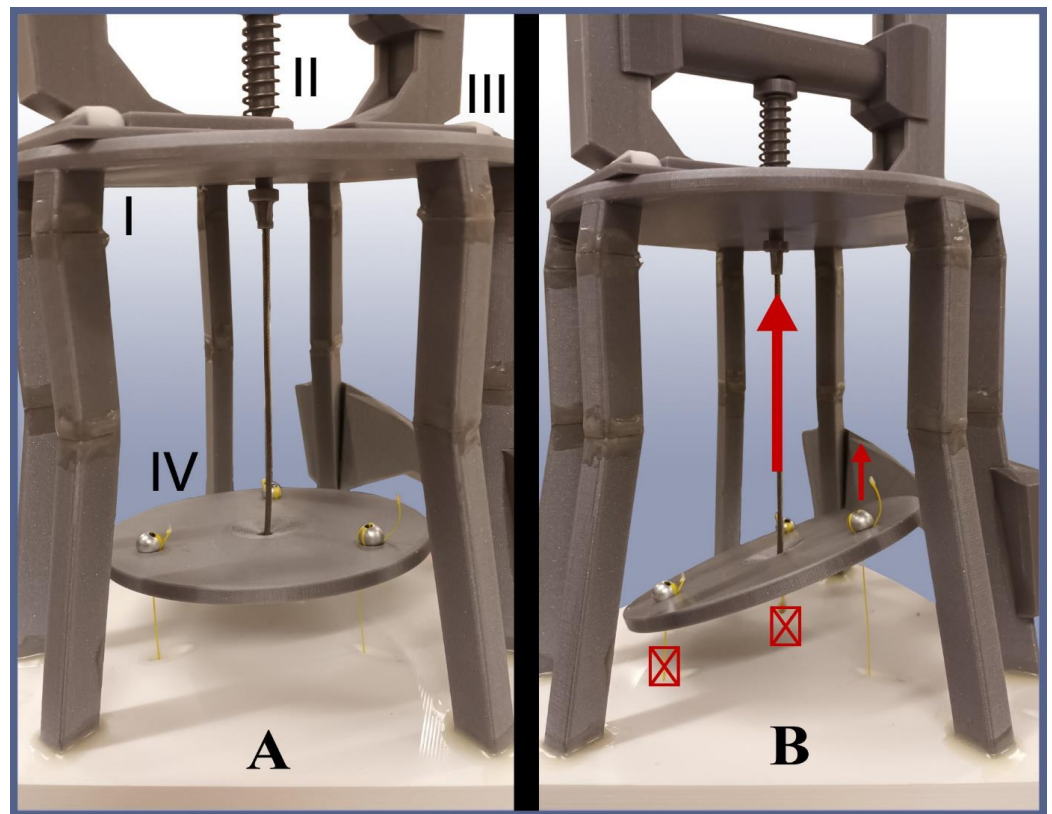


**Figure 7.** The TriTrap gripper’s actuation cage (I) and its components: tendon and preload spring (II), handle assembly (III), and force-distribution disc (IV). (A) Disc in equilibrium; all arms either currently require the same force to be folded or they are resting. (B) Tilted disc, the main actuation cord is pulled (big arrow). Two of the three arms require a stronger force to fold (crossed boxes) or might even be jammed due to the specific object’s shape. The remaining one is free to fold further (small arrow).

The handle consists of two bars: the fixed and the mobile one, the latter of which can be gripped and pulled at to actuate the gripper. The periphery of the handlebars, as well as the bars themselves, have been fitted with a quick disassembly mechanism that enables rapid adjustments to the travel path of the handle, if necessary, for example, in the case of different operators, different maximum closing states, or during the replacement of broken parts (Figure 8).



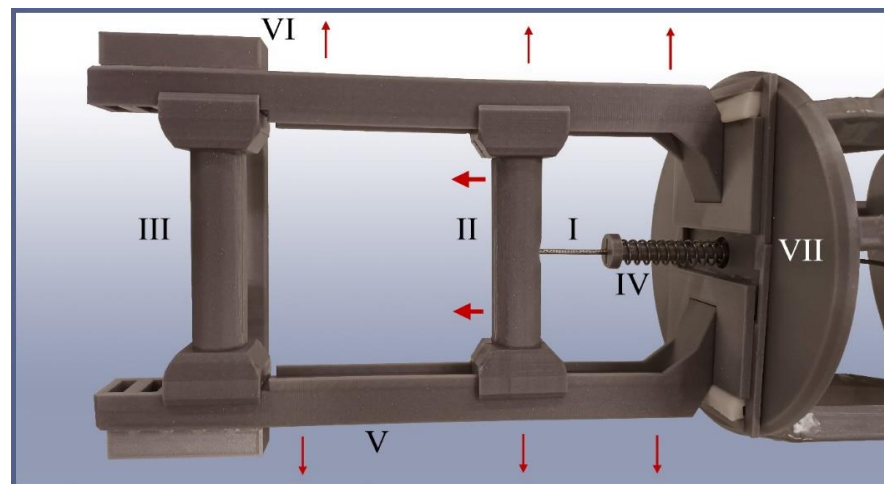


**Figure 8.** TriTrap gripper's handle assembly. I: main actuation cord, running from the lower handle to the force-distribution disc (off to the right). II: lower handle, mounted on sliding rails to enable its movement (big arrows). III: upper handle, mounted in a fixed way as a counter grip. IV: preloader spring, used to keep a minimum strain on the system under idle conditions for handling reasons. V: sliding rails for the lower handle and overall framework for the handle assembly. VI: upper clipping lock, which keeps the sliding rails from detaching to the sides. VII: lower clipping lock, which keeps the sliding rails from detaching in the same way. If disassembly is required, the upper and lower clipping locks can be removed, and the sliding rails slide out to the sides (small arrows), granting access to the handles.

#### 4.4. Initial Gripping Tests and Evaluation

After the gripper prototype had been assembled in its current working state, a range of everyday objects was used to roughly test its capabilities before moving on to optimize it (Figure 3). For each object, multiple attempts were made to pick it up, carry it, and release it again. Most objects offered more than one unique standing and/or lying state due to the absence of symmetry. Because initial tests showed that final results depended strongly on the above states chosen for the attempt, several of them were randomly picked for those objects for each gripping attempt. These results are meant to prove the concept and to highlight the direction inevitable optimization would have to go in. That being said, the gripper was able to lift all objects off the ground except for the water boiler (no success in any orientation) and managed to transport them around before dropping them off (Figure 9 and Supplementary Videos S1–S6). A common pattern observed in all gripping attempts was that success was strongly tied to the object's surface features (i.e., rough, smooth, etc.), which was unsurprising and hinted at the necessity of a compliant and friction-increasing interface between the arms and the object. Because of this, in the TriTrap's current state, most of the time, the wedges at the top of the arms are the elements that are actually gripping the objects instead of the arms themselves, whose passive conformability acts in a supporting fashion for the wedges.

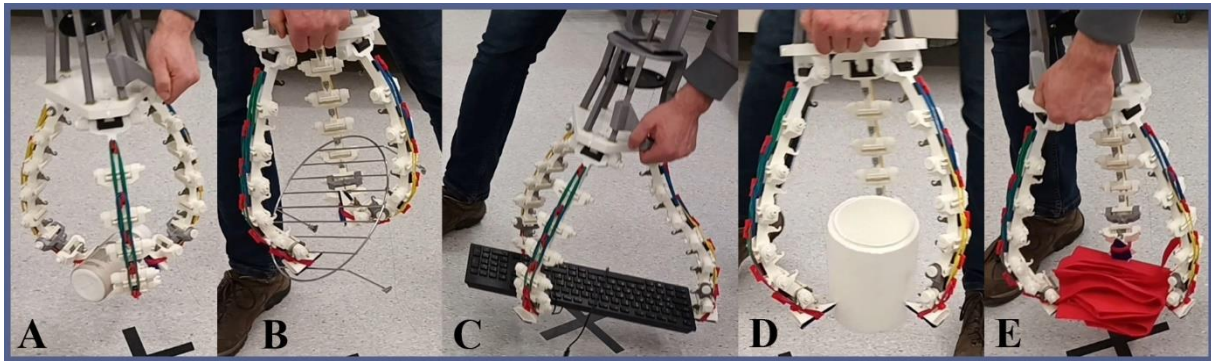


**Figure 9.** Snapshots of the TriTrap gripper gripping and transporting objects: (A) plastic bottle, (B) grill attachment, (C) keyboard, (D) polystyrene vase, and (E) textile bag.

Additionally, because the gripper was mainly constructed of 3D-printed polymers, the maximum actuation force with which the gripper could still safely be used was too low for heavier workloads, as was the case with the water boiler.

## 5. Discussion

The TriTrap gripper presented herein has been shown to work, confirming the biomimetic concepts inspired by the insect tarsus. Even though its core principle is derived from insect tarsal chains, the gripper's arms that are actually employing it deviate slightly in their exact construction in comparison to the biological prototype. One example would be the number of folding elements/segments corresponding to the biological tarsomeres found in the arms, which differs from the number found in most species in nature [33]. This is mainly because of geometric constraints during design and construction: a higher number (seven) was needed to fulfill some design goals, such as the arms' ability to precisely fit each other and close in the center of the gripper (when all arms are folded), or to achieve a certain arm trajectory that was deemed advantageous for performance.

Another deviation is the number of passive degrees of freedom: In the biological system, in addition to active flexion in the direction of the ground, the tarsal chain is able to bend along several unactuated axes at every tarsomere–tarsomere joint [11]. As mentioned in the introduction, we decided against this potentially large amount of added complexity in order to gradually approximate the working principle in a controlled fashion. Therefore, the TriTrap gripper's link elements are monoaxial, with active actuation towards the closing direction and passive relaxation in the opposite direction. Additionally, the allowed angles between the elements were deliberately chosen for this use case, and therefore, they are not connected to those found in the biological prototype.

In spite of all the deviations from the biological prototype and lack of optimization, the TriTrap gripper was able to prove the basic concept very well. Utilizing the tarsal chain principle found in nature, it was able to grip, hold, and move different objects without further modifications, even though there clearly is room for improvement. Firstly, the gripper's interfaces with the objects to grip, i.e., the inner faces of the arms, are bare, hard 3D-printed PLA surfaces in the prototype. This also means that both their conformability with the gripping object, as well as the friction generation, are suboptimal. On the contrary, in the biological prototype, the tarsomeres are equipped with different interfacing structures, such as adhesive/frictional pads, spines or hairy structures, or their combinations, depending on the species [2], which alleviate this problem. In future developments of the gripper, it would clearly make sense to approximate these designs using the general design of the gripper as the platform to test various supplementary adhesive, frictional, and interlocking devices on the inner surfaces of the gripper arms. There are multiple possible ways to approach this, such as soft foam pads (corresponding to friction-generating pads found on insect legs), brushes, or other hair-type structures (corresponding to hairy structures likewise found on insect legs to improve friction and adhesion) that would be attached to the individual

links. Friction- or interlocking-generating surface coatings/coverages or systems enlarging the interface area would also be possible, or a combination of these principles [2]. This is especially promising since, in some form, these types of structures are also found on the biological tarsi. Since these supplementary interfaces evolved multiple times in animal evolution [36], we can assume that they significantly contribute to gripping performance and should be replicated or approximated in the development of future technical grippers.

Secondly, a disadvantage that made itself apparent during testing was TriTrap's relatively unfavorable relationship between input force and output force. The tendons run through a series of channels and come into contact with different parts of the arms over their length, which generates a significant amount of friction that needs to be overcome with every actuation cycle. Additionally, the transmission ratio between tendon pull and arm flexion results in relatively high force requirements for flexion in the first place. Furthermore, for every actuation cycle, the elastic bands' resistance needs to be overcome as well. Overall, this leads to considerable force requirements to operate the gripper, even with no target object present. Some of this is intrinsic to tarsal chains as a concept, but all of it could be significantly alleviated by further engineering and optimization. The prototype was actuated by a human hand for project simplicity, but because the required mechanical input is a simple linear pull on its tendon, a tarsal-chain-based gripper could be actuated using any other suitable means, such as a stepper motor. This also means that larger required input forces are not necessarily a problem, depending on the task and the kind of operational platform to which the gripper, as an end effector, is mounted.

It bears mentioning that for the aforementioned reasons of force transmission and tendon friction, the gripper's requirements with respect to mechanical material properties are relatively high. Sufficient closing forces need to be generated over the length of three multi-segmented arms. Additionally, a finalized gripper using the tarsal chain concept would need to be able to securely hold multiples of its own weight in workload, which consequently requires very durable tendon material. On the same note, the arm material itself needs to be as durable and as lightweight as possible. None of these requirements are hard to meet, but within the constraints of 3D PLA printing, which was used to produce the TriTrap gripper, there is a very distinct limit to the mechanical stability of the design. While this manufacturing method is supremely suited for rapid prototyping, in the case of industrial design, the parts should be recreated using other techniques/materials in order to reach the full potential of the gripper.

Since the proof of concept of the insect tarsal gripper is provided here, other applications of the tarsal chain principle beyond gripping are also conceivable. Examples include but are not limited to, clamping, walking, climbing, or, with some effort, even complex manipulation. Additionally, the original gripper could be modified to tailor the gripping movement to specific applications—by increasing/decreasing the number of links on the arms and adjusting their angles, angle orders, lengths, and length orders. The potential movement variety, which could be provided by the combination of the above variables, is very large and likely contains many useful configurations. To the knowledge of the authors, not much research has yet been conducted on this topic; however, the TriTrap gripper proves to be a very promising avenue for future investigation.

## 6. Conclusions

In this study, the biological tarsal chain principle was investigated as to its viability in gripping applications. For this, a prototype biomimetic gripping device inspired by an insect tarsal chain was designed, constructed, and qualitatively tested. The device, called the TriTrap gripper, features three tarsal-chain-based arms working in concert to secure a hold of target objects. The insect tarsal chain in nature is mainly used for locomotion, featuring a relatively simple general structure and only requiring very little actuation and control to function while still being able to perform a wide range of tasks. This work tried to capitalize on these features by creating a device actuated by a single linear pulling move that nonetheless is able to adapt to varying circumstances and object shapes passively.

After construction, qualitative gripping testing on a variety of objects with different shapes and sizes was carried out, which successfully proved the concept. Additionally, further avenues of optimization were determined so that the TriTrap gripper may be enhanced in the future and reach its full potential. In the end, however, the TriTrap gripper is only one of many possible examples to showcase the insect tarsal chain's ability to passively conform to objects and features of unknown nature, which makes any gripper using the concept well suited for applications where that condition applies, such as domestic environments or different kinds of outdoor-related work, to name a few. Additionally, requiring only very basic actuation and not having to rely on advanced controls, sensors, and computation would be beneficial for many cases, as well as cheaper.

**Supplementary Materials:** The following supporting information can be downloaded at: <https://www.mdpi.com/article/10.3390/biomimetics9030142/s1>, Video S1: Boiler; Video S2: Bottle; Video S3: Grill Attachment; Video S4: Keyboard; Video S5: Styro; Video S6: Textile Bag.

**Author Contributions:** Conceptualization, J.W. and S.N.G.; methodology, J.W.; software, J.W.; validation, J.W., T.H.B. and S.N.G.; formal analysis, J.W.; investigation, J.W.; resources, J.W. and S.N.G.; data curation, J.W.; writing—original draft preparation, J.W.; writing—review and editing, J.W., T.H.B. and S.N.G.; visualization, J.W.; supervision, S.N.G.; project administration, S.N.G.; funding acquisition, S.N.G. All authors have read and agreed to the published version of the manuscript.

**Funding:** This research was funded by the German Science Foundation (DFG) grant number GO 995/34–1.

**Data Availability Statement:** The data presented in this study are available in this article and its Supplementary Materials.

**Acknowledgments:** This work was supported by the grant GO 995/34–1 from the German Science Foundation (DFG) within the Special Priority Programme SPP 2100 ‘Soft Material Robotic Systems’ awarded to S.N.G.

**Conflicts of Interest:** The authors declare no conflicts of interest.

## References

- Langowski, J.K.A.; Sharma, P.; Shoushtari, A.L. In the soft grip of nature. *Sci. Robot.* **2020**, *5*, eabd9120. [CrossRef]
- Gorb, S. *Attachment Devices of Insect Cuticle*; Springer: Hingham, The Netherlands, 2007.
- Winand, J.; Buscher, T.H.; Gorb, S.N. Learning from Nature: A review on biological gripping principles and their application to robotics. In *Soft Robotics*; Monkman, G., Ed.; Bentham Science Publishers: Sharjah, United Arab Emirates, 2022; pp. 21–59.
- Resh, V.H.; Cardé, R.T. *Encyclopedia of Insects*; Elsevier BV: Amsterdam, The Netherlands, 2009; ISBN 9780123741448.
- Gorb, S.N. The jumping mechanism of cicada *Cercopis vulnerata* (Auchenorrhyncha, Cercopidae): Skeleton-muscle organisation, frictional surfaces, and inverse-kinematic model of leg movements, *Arthropod Structure and Development*. *Arthropod Struct. Dev.* **2004**, *33*, 201–220. [CrossRef]
- Martins, A.C.; Melo, G.A.; Renner, S.S. The corbiculate bees arose from New World oil-collecting bees: Implications for the origin of pollen baskets. *Mol. Phylogenetics Evol.* **2014**, *80*, 88–94. [CrossRef]
- Büsse, S.; Büscher, T.H.; Kelly, E.T.; Heepe, L.; Edgerly, J.S.; Gorb, S.N. Pressure-induced silk spinning mechanism in webspinners (Insecta: Embioptera). *Soft Matter* **2019**, *15*, 9742–9750. [CrossRef] [PubMed]
- Zhang, Z.; Zhang, Y.; Zhang, J.; Zhu, Y. Structure, mechanics and material properties of claw cuticle from mole cricket *Grylloblatta orientalis*. *PLoS ONE* **2019**, *14*, e0222116.
- Bell, G. *Selection: The Mechanism of Evolution*; Oxford University Press: New York, NY, USA, 2008.
- Gorb, S.N. Design of insect unguitractor apparatus. *J. Morphol.* **1996**, *230*, 219–230. [CrossRef]
- Frantsevich, L.; Gorb, S. Structure and mechanics of the tarsal chain in the hornet, *Vespa crabro* (Hymenoptera: Vespidae): Implications on the attachment mechanism. *Arthropod Struct. Dev.* **2004**, *33*, 77–89. [CrossRef] [PubMed]
- Radnikow, G.; Bässler, U. Function of a Muscle Whose Apodeme Travels through a Joint Moved by Other Muscles: Why the Retractor Unguis Muscle in Stick Insects is Tripartite and Has No Antagonist. *J. Exp. Biol.* **1991**, *157*, 87–99. [CrossRef]
- Matsumura, Y.; Lima, S.P.; Rafael, J.A.; Câmara, J.T.; Beutel, R.G.; Gorb, S.N. Distal leg structures of Zoraptera—Did the loss of adhesive devices curb the chance of diversification? *Arthropod Struct. Dev.* **2022**, *68*, 101164. [CrossRef] [PubMed]
- Gladun, D.; Gorb, S.N. Insect walking techniques on thin stems. *Arthropod-Plant Interact.* **2007**, *1*, 77–91. [CrossRef]
- Bücher, T.H.; Becker, M.; Gorb, S.N. Attachment performance of stick insects (Phasmatodea) on convex substrates. *J. Exp. Biol.* **2020**, *223 Pt 17*, jeb226514. [CrossRef] [PubMed]

16. Dürr, V.; Theunissen, L.M.; Dallmann, C.J.; Hoinville, T.; Schmitz, J. Motor flexibility in insects: Adaptive coordination of limbs in locomotion and near-range exploration. *Behav. Ecol. Sociobiol.* **2018**, *72*, 15. [CrossRef]
17. Tai, K.; El-Sayed, A.-R.; Shahriari, M.; Biglarbegian, M.; Mahmud, S. State of the Art Robotic Grippers and Applications. *Robotics* **2016**, *5*, 11. [CrossRef]
18. Shintake, J.; Cacucciolo, V.; Floreano, D.; Shea, H. Soft Robotic Grippers. *Adv. Mater.* **2018**, *30*, e1707035. [CrossRef] [PubMed]
19. Di Canio, G.; Stoyanov, S.; Larsen, J.C.; Hallam, J.; Kovalev, A.; Kleinteich, T.; Gorb, S.N.; Manoonpong, P. A robot leg with compliant tarsus and its neural control for efficient and adaptive locomotion on complex terrains. *Artif. Life Robot.* **2016**, *21*, 274–281. [CrossRef]
20. Zi, P.; Xu, K.; Tian, Y.; Ding, X. A mechanical adhesive gripper inspired by beetle claw for a rock climbing robot. *Mech. Mach. Theory* **2023**, *181*, 105168. [CrossRef]
21. Gorb, S.N.; Pullwitt, T.; Kleinteich, T.; Busshardt, P. The insect unguitractor plate in action: Force transmission and the micro CT visualizations of inner structures. *J. Insect Physiol.* **2019**, *117*, 103908. [CrossRef]
22. Goldsmith, C.; Szczecinski, N.; Quinn, R. Drosophibot: A Fruit Fly Inspired Bio-Robot. In *Biomimetic and Biohybrid Systems; Living Machines Lecture Notes in Computer Science*; Springer: Cham, Switzerland, 2019; pp. 146–157.
23. Liu, G.; Liu, Y.; Wang, X.; Wu, X.; Mei, T. Design and experiment of a bioinspired wall-climbing robot using spiny grippers. In Proceedings of the 2016 IEEE International Conference on Mechatronics and Automation, Harbin, China, 7–10 August 2016; pp. 665–670.
24. Xie, H.; Kong, D.; Wang, Q. Optimization and experimental study on structural parameters of bio-inspired tarsus compliant end-effector to reduce the risk of fruit sliding out from end-effector for cherry tomato harvesting. *Proc. Inst. Mech. Eng. Part C J. Mech. Eng. Sci.* **2022**, *236*, 6440–6450. [CrossRef]
25. Iii, L.R.P.; Diller, E.; Quinn, R.D. Toward Gravity-Independent Climbing Using a Biologically Inspired Distributed Inward Gripping Strategy. *IEEE/ASME Trans. Mechatron.* **2015**, *20*, 631–640. [CrossRef]
26. Kim, H.; You, J.M.; Hwang, M.; Kyung, K.U.; Kwon, D.S. Sigmoidal auxiliary tendon-driven mechanism reinforcing structural stiffness of hyper-redundant manipulator for endoscopic surgery. *Soft Robot.* **2022**, *10*, 234–245. [CrossRef]
27. Tran-Ngoc, P.T.; Lim, L.Z.; Gan, J.H.; Wang, H.; Vo-Doan, T.T.; Sato, H. A robotic leg inspired from an insect leg. *Bioinspiration Biomim.* **2022**, *17*, 056008. [CrossRef] [PubMed]
28. Ishibashi, K.; Ishii, H. Insect-Tarsus-Inspired Legs: Toward Improvement of Gripping Ability of Small Tree-Climbing Robots. In Proceedings of the 2022 9th IEEE RAS/EMBS International Conference for Biomedical Robotics and Biomechatronics (BioRob), Seoul, Republic of Korea, 21–24 August 2022; IEEE: New York, NY, USA, 2022; pp. 1–6.
29. Shi, Y.; Hou, X.; Na, Z.; Zhou, J.; Yu, N.; Liu, S.; Xin, L.; Gao, G.; Liu, Y. Bio-inspired Attachment Mechanism of Dynastes Hercules: Vertical Climbing for On-Orbit Assembly Legged Robots. *J. Bionic Eng.* **2023**, *21*, 137–148. [CrossRef]
30. Palmer, L.R.; Diller, E.D.; Quinn, R.D. Toward a rapid and robust attachment strategy for vertical climbing. In Proceedings of the 2010 IEEE International Conference on Robotics and Automation, Seoul, Republic of Korea, 21–24 August 2022; IEEE: New York, NY, USA, 2022; pp. 2810–2815.
31. Wang, H.; Liu, P.; Chen, H.; Ngoc, P.T.T.; Li, B.; Li, Y.; Sato, H. Toward the Smooth Mesh Climbing of a Miniature Robot Using Bioinspired Soft and Expandable Claws. *IEEE Trans. Med Robot. Bionics* **2023**, *6*, 351–361. [CrossRef]
32. Liu, Y.; Wang, L.; Niu, F.; Li, P.; Li, Y.; Mei, T. A track-type inverted climbing robot with bio-inspired spiny grippers. *J. Bionic Eng.* **2020**, *17*, 920–931. [CrossRef]
33. Betz, O. Structure of the tarsi in somestenus species (Coleoptera, Staphylinidae): External morphology, ultrastructure, and tarsal secretion. *J. Morphol.* **2003**, *255*, 24–43. [CrossRef]
34. Gorb, S.N. Insect-Inspired Technologies: Insects as a Source for Biomimetics. In *Insect Biotechnology*; Vilcinskas, A., Ed.; Springer: Dordrecht, The Netherlands, 2011; pp. 241–264.
35. Michels, J.; Appel, E.; Gorb, S.N. Functional diversity of resilin in Arthropoda. *Beilstein J. Nanotechnol.* **2016**, *7*, 1241–1259. [CrossRef]
36. Büscher, T.H.; Gorb, S.N. Physical constraints lead to parallel evolution of micro- and nanostructures of animal adhesive pads: A review. *Beilstein J. Nanotechnol.* **2021**, *12*, 725–743. [CrossRef]

**Disclaimer/Publisher’s Note:** The statements, opinions and data contained in all publications are solely those of the individual author(s) and contributor(s) and not of MDPI and/or the editor(s). MDPI and/or the editor(s) disclaim responsibility for any injury to people or property resulting from any ideas, methods, instructions or products referred to in the content.



## Article

# Capillary Wicking on *Heliamphora minor*-Mimicking Mesoscopic Trichomes Array

Fenglin Chen <sup>1,2</sup>, Ziyang Cheng <sup>1,2</sup>, Lei Jiang <sup>1,2</sup> and Zhichao Dong <sup>1,2,\*</sup> <sup>1</sup> CAS Key Laboratory of Bio-Inspired Materials and Interfacial Science, Technical Institute of Physics and Chemistry, Chinese Academy of Sciences, Beijing 100190, China<sup>2</sup> School of Future Technology, University of Chinese Academy of Sciences, Beijing 100049, China

\* Correspondence: dongzhichao@mail.ipc.ac.cn

**Abstract:** Liquid spontaneously spreads on rough lyophilic surfaces, and this is driven by capillarity and defined as capillary wicking. Extensive studies on microtextured surfaces have been applied to microfluidics and their corresponding manufacturing. However, the imbibition at mesoscale roughness has seldom been studied due to lacking fabrication techniques. Inspired by the South American pitcher plant *Heliamphora minor*, which wicks water on its pubescent inside wall for lubrication and drainage, we implemented 3D printing to fabricate a mimetic mesoscopic trichomes array and investigated the high-flux capillary wicking process. Unlike a uniformly thick climbing film on a microtextured surface, the interval filling of millimeter-long and submillimeter-pitched trichomes creates a film of non-uniform thickness. Different from the viscous dissipation that dominated the spreading on microtextured surfaces, we unveiled an inertia-dominated transition regime with mesoscopic wicking dynamics and constructed a scaling law such that the height grows to  $2/3$  the power of time for various conditions. Finally, we examined the mass transportation inside the non-uniformly thick film, mimicking a plant nutrition supply method, and realized an open system siphon in the film, with the flux saturation condition experimentally determined. This work explores capillary wicking in mesoscopic structures and has potential applications in the design of low-cost high-flux open fluidics.



**Citation:** Chen, F.; Cheng, Z.; Jiang, L.; Dong, Z. Capillary Wicking on *Heliamphora minor*-Mimicking Mesoscopic Trichomes Array. *Biomimetics* **2024**, *9*, 102. <https://doi.org/10.3390/biomimetics9020102>

Academic Editors: Stanislav N. Gorb, Giuseppe Carbone, Thomas Speck and Peter Fratzl

Received: 4 January 2024

Revised: 31 January 2024

Accepted: 6 February 2024

Published: 9 February 2024



**Copyright:** © 2024 by the authors. Licensee MDPI, Basel, Switzerland. This article is an open access article distributed under the terms and conditions of the Creative Commons Attribution (CC BY) license (<https://creativecommons.org/licenses/by/4.0/>).

**Keywords:** capillary wicking; *Heliamphora minor*; 3D printing; mesoscopic trichomes

## 1. Introduction

Liquid touching superlyophilic rough surfaces spontaneously spreads into the texture, driven by capillarity; this is called capillary wicking [1–7] and is of significant interest in a broad range of applications such as microfluidics [8–11], the design of self-cleaning surfaces [12], and lab-on-a-chip technology [13–15]. Extensive research on the wetting of microtextured surfaces [1–6,10,16–23] demonstrates that liquid behavior on surfaces with microscopic structures is influenced by the combined effects of the surface wetting properties, structure shapes, and liquid properties. In detail, surface energy serves as primary driving force, while viscous dissipation hinders the spreading or imbibition of liquid [24,25], and the surface roughness, defined as the ratio between the actual and projected surface areas, enhances the release of surface energy [1,2,26]. The scaling law known as the Lucas–Washburn equation [27] states that the macroscopic wicking distance increases to  $1/2$  the power of time due to the balance between surface tension and viscosity. The initial stage is dominated by inertia [28], which follows a power law of 1. Furthermore, a microscopic view of a fringe film extending into the roughness interval was addressed recently, in which the meniscus grew to  $1/3$  the power when the front was far from the microscale structure [4,29]. However, microtextured surfaces cannot achieve high-flux wicking due to the limitation posed by their structure size and film thickness. To utilize spontaneous capillary wicking in practical applications, it is essential to explore and understand the dynamics of wetting the modified surfaces of large-scale structures.



Inspired by the plant strategy of modifying the surface with millimeter-long trichomes to manipulate their interaction with water for survival, we systematically investigated the capillary wicking on *Heliamphora minor*, a representative species of South American pitcher plants, and revealed that a lubrication layer spontaneously forms on the pubescent wall to capture insects as well as assist in draining excess water from the pitcher [30,31]. With the speed and resolution improvement of additive manufacturing, the rapid preparation of mesoscale structures is convenient, allowing for the fabrication of a mimetic millimeter-long trichomes array for further study of the wicking dynamics under various experimental conditions. We discovered that the wicking on mesoscopic trichomes forms a non-uniformly thick film which enables high flux flow and explained the profile of this film with respect to the concept of the catenary line. Moreover, we demonstrated that the wicking dynamics on mesoscopic structures differs from that on microscopic structures, with the distance growing to  $2/3$  the power of time. Additionally, we used the mimetic trichomes array to construct an open siphon and examined the change of flux with height. Through a simulation using salt and sugar, we demonstrated the mass transportation in a thick wicking film, displaying an active method utilized by plants for nutrient supply. Overall, this work provides innovative insight into the design of mesoscopic structures that achieve spontaneous capillary wicking, and advances our understanding of this phenomenon for practical applications requiring high flux.

## 2. Materials and Methods

### 2.1. Biological Characterization and the Fabrication of Biomimetic Samples

*Heliamphora minor*, whose lid is smaller than the pitcher (Figure 1a, images taken by Nikon D750, Toyko, Japan), was cultivated in a greenhouse with the environment maintained at a temperature of 23–28 °C, and a humidity of 90–95%. The sectional view from the middle (Figure 1b) presents the pitcher's inside wall morphology, with a constriction that splits the wall into two zones; the upper is covered with millimeter-long trichomes and called the pubescent zone, and the lower is the smooth zone. A stereomicroscope (Figure 1c, DSX 1000, Olympus, Toyko, Japan) and scanning electron microscopy at 10 kV (Figure 1d, SEM, SU8020, Hitachi, Toyko, Japan) were utilized for detailed characterization of trichomes on the inside wall (Figure 1e for statistical analysis by Origin 2024). The trichomes are downward-pointing and densely arranged, with a base diameter,  $d$ , of  $49.3 \pm 18.1 \mu\text{m}$ , and a mutual pitch,  $p = 176.1 \pm 36.9 \mu\text{m}$ . The trichomes' length,  $L$ , ranges from  $153.4 \mu\text{m}$  to  $922.2 \mu\text{m}$ , with an average of  $547.1 \mu\text{m}$ . In general, the trichomes' distribution is in mesoscale, which is ubiquitous in nature [32].

Contact angle measurements of the pubescent zone (Figure 1f–h, DCAT 21, Data-Physics, Filderstadt, Germany) indicate that the wettability is superhydrophilic and water spontaneously wicks into the trichomes as soon as it touches the surface. The lightning-fast wicking process was observed and recorded using a high-speed camera at 1000 fps (Figure 1i,j, FASTCAM Mini UX100, Photron, Toyko, Japan); water injected by a syringe from a distribution pump (TS-1A, Longer Pump, Baoding, China) at a rate of  $200 \mu\text{L s}^{-1}$  spread radially on the pubescent wall and filled the interval at the same time. Therefore, the film thickness increases as the height becomes higher. Finally, the film covers the trichomes and serves as the lubrication layer. Mimicking the pubescent zone, a polymerization-based 3D printer (Mini 8K, Phrozen Tech., Taiwan, China) using an ultraviolet liquid crystal display to initiate the photo reaction of the monomer methyl methacrylate— $\text{TiO}_2$ — $\text{SiO}_2$  mixture was used (Figure 1k), and the layer resolution and pixel resolution were  $20 \mu\text{m}$  and  $18 \mu\text{m}$ , respectively. After preparation, the mimetic samples were ultrasonically washed in commercial cleaning solutions (Go Print Co., Ningbo, China) for 5 min, dried by  $\text{N}_2$  flow and post-cured under UV light for 3 min. Oxygen plasma treatment (DT-03, OPS Plasma Technology Co., Shenzhen, China) at an RF power of 300 W for 10 min was performed to adjust surface superhydrophilicity. SEM images of the printed mimetic samples sputtered with a thin layer of platinum (EM ACE, Leica, Wetzlar, Germany) at 10 kV were obtained

(Figure 1l). The particles of  $\text{TiO}_2$  and  $\text{SiO}_2$  increase surface roughness and enable chemical modification (Figure 1m for energy-dispersive spectrometer).

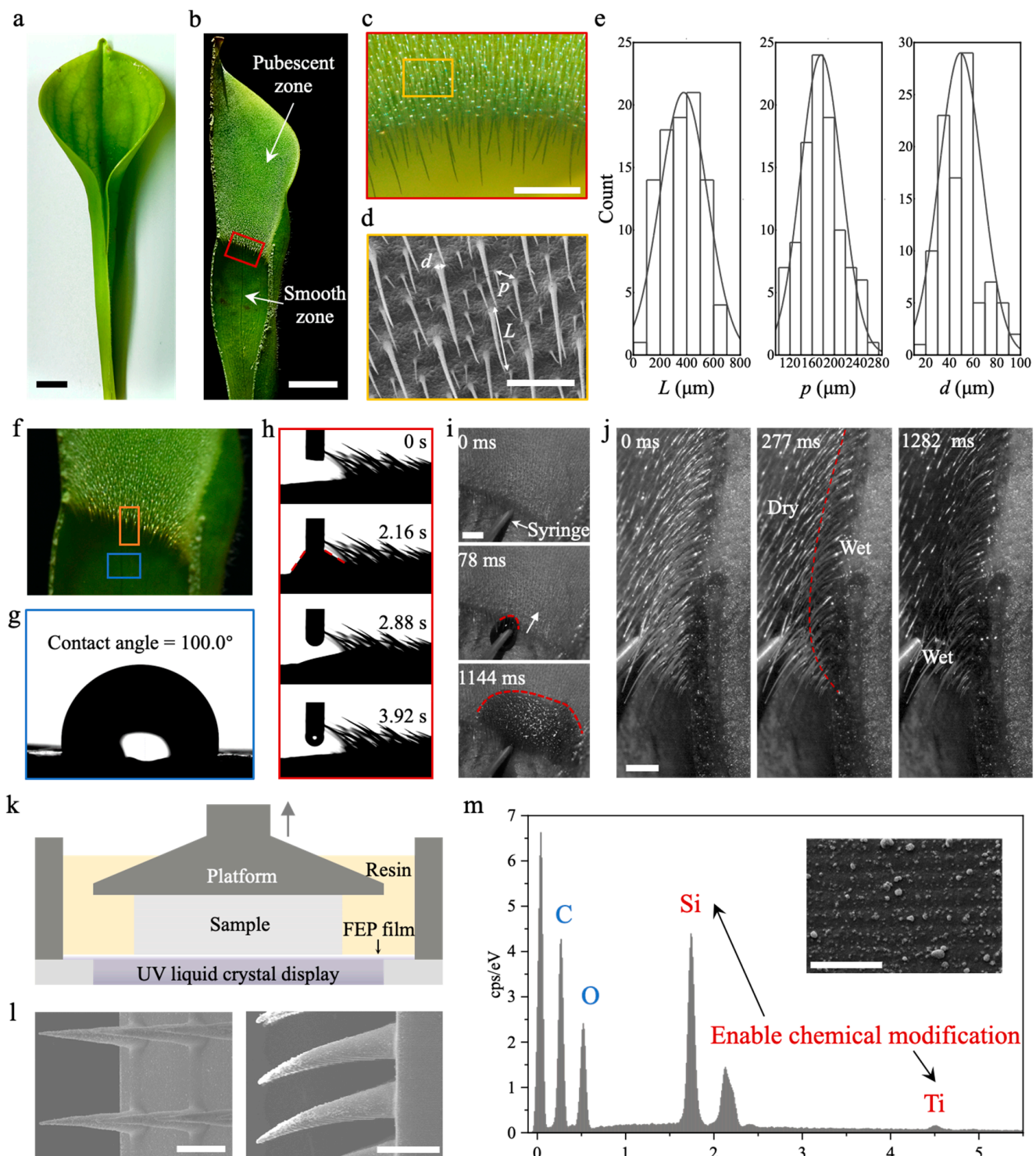


**Figure 1.** Characterization of *Heliamphora minor* and fabrication of biomimetic trichomes. (a) Optical images of *H. minor*; (b) sectional view of pitcher inside wall, above is a pubescent zone and below is a smooth zone; (c) stereomicroscope of the red-box-indicated region in (b); (d) SEM image of the yellow-box-indicated region in (c), trichomes of length  $L$  and base diameter  $d$  are arranged with a mutual pitch,  $p$ ; (e) statistical analysis of  $L$ ,  $p$ ,  $d$  with normal distribution fitting; (f) illustration of

sample resources from pitcher inside wall. The orange and blue boxes indicate the sample from the pubescent zone and smooth zone, respectively; (g) water contact angle on surface of smooth zone; (h) water contact angle changing on surface of pubescent zone, which gradually decreases to  $\sim 0^\circ$ ; (i) high-speed front view of water injected from syringe wicking on pubescent zone, the red dotted line indicates the fringe front; (j) high-speed side view of water wicking and filling the trichomes' intervals, the red dotted line indicates the border of dry and wet regions; (k) schematic of bottom-up 3D printer based on photo-initiated polymerization of resin using liquid crystal display as UV source; (l) SEM images of 3D-printing fabricated biomimetic trichomes array, the left is top view and the right is side view; (m) energy-dispersive spectrometry of printed surface, Si and Ti elements are from  $\text{SiO}_2$  and  $\text{TiO}_2$  nanoparticles, which turn the surface superhydrophilic. The inset is a zoomed-in view of the surface. Scale bars: 1 cm in (a,b); 1 mm in (c,d,i,j); 500  $\mu\text{m}$  in (l); 50  $\mu\text{m}$  in (m).

## 2.2. Capillary Wicking, High-Flux Siphon Application, and Mass Transportation

The fabricated biomimetic trichomes array was inserted into a dish filled with blue-dyed water (Figure 2a as a schematic), and the dish diameter was 10 cm, which was large enough to avoid the wicking process disturbing the surface. A colored 4K resolution high-speed camera at 1000 fps (Wave, Freefly, WA, USA) was used to observe and record the wicking dynamics from the side, front, and oblique view. The water fringe front extending on substrates of various trichome geometries was tracked by Tracker software (6.0.10 version), starting from the moment of contact with the water level. Additionally, we utilized micro-computed tomography (Micro-CT, Skyscan 1272, Bruker, German) to reconstruct the wicking film profile and investigate the formed curvature gradient. Furthermore, mimicking the biological function of assisting drainage from pitcher, we modified an n-shaped arc surface of mesoscale trichomes, which was also prepared by 3D printing, and put the higher side of the model in contact with water tank, measuring the mass of water flowing out using an analytical balance (104E, Mettler Toledo, Switzerland). The flux was reported in the form of the measured mass divided by time. Finally, we dissolved  $\text{CuSO}_4$ ,  $\text{FeCl}_3$ , and glucose, respectively, into water and repeated the wicking process. After long enough time for evaporation, the solute crystallization from the solution process was recorded using a Nikon D750, which reveals the mass transportation inside the wicking film.

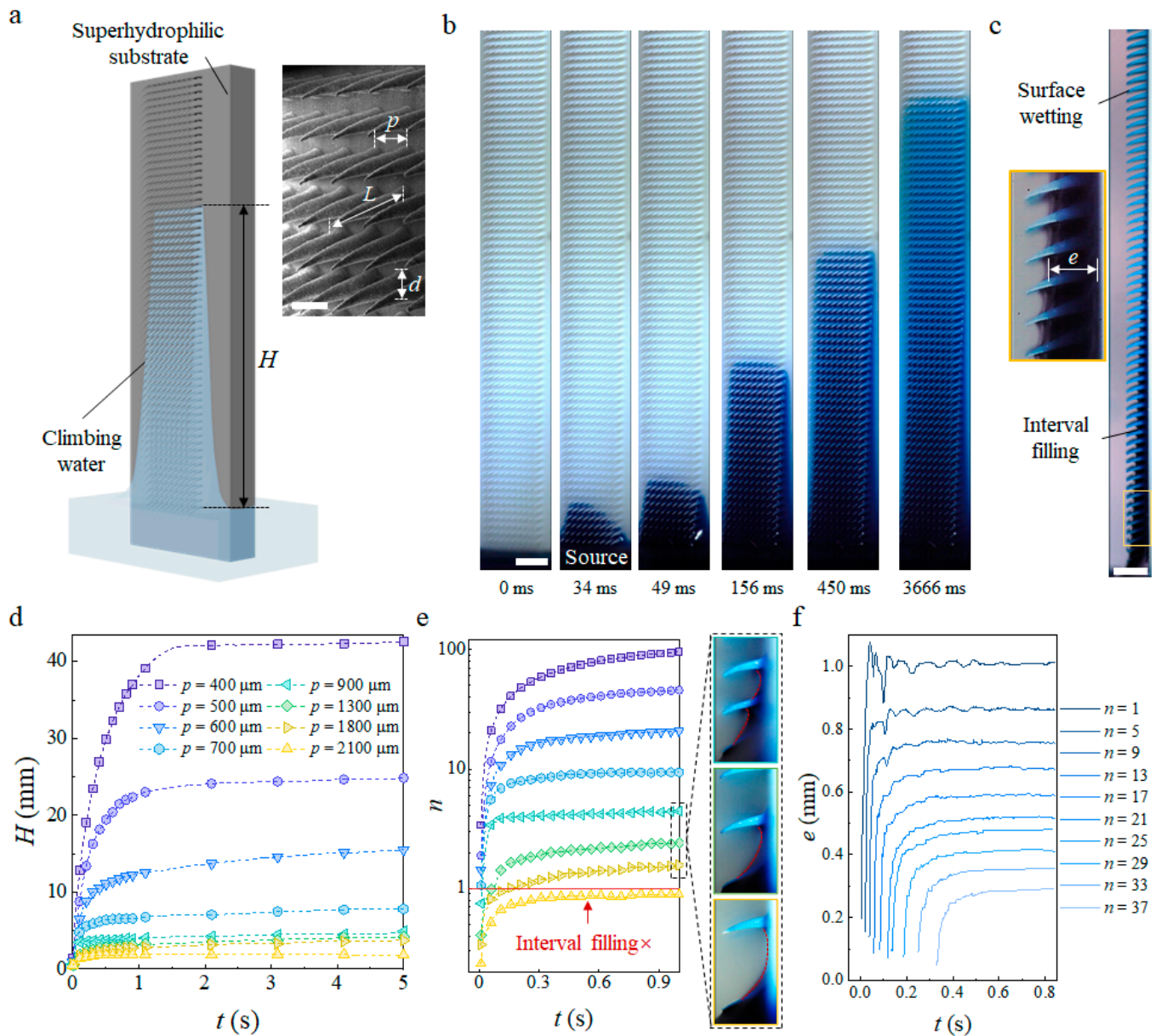


**Figure 2.** Capillary wicking on biomimetic trichomes array. (a) Schematic of capillary wicking on modified surface of superhydrophilic trichomes as the climbing water reaches a height of  $H$ . The SEM image shows the biomimetic trichomes array; (b) Oblique view of the wicking process on  $L = 2$  mm,  $p = 500$   $\mu\text{m}$ ,  $d = 200$   $\mu\text{m}$  trichomes array; (c) Side view of final wicking state. The film thickness,  $e$ , decreases with increasing  $H$ ; (d) Climbing height,  $H$ , changes with time,  $t$ , on trichomes arrays of different pitches with fixed  $L = 2$  mm and  $d = 200$   $\mu\text{m}$ ; (e) Number of climbed intervals ( $n$ ) changing with  $t$ . To the right are side views of  $p = 900$   $\mu\text{m}$ ,  $1300$   $\mu\text{m}$ , and  $1800$   $\mu\text{m}$  from top to bottom; (f) Thickness of different intervals changing with  $t$  as the water climbs. Scale bars:  $500$   $\mu\text{m}$  in (a),  $2$  mm in (b,c).

### 3. Results and Discussion

#### 3.1. Capillary Wicking Height and Film Thickness

Once water touched the mesoscopic trichomes array, wicking between the trichomes was observed on the hydrophilic and superhydrophilic substrates (Figure S1) whose contact angles were smaller than the hydrophilic–hydrophobic boundary of  $65^\circ$  [33]. Conversely, water did not climb on the hydrophobic substrate. The front of the advancing meniscus exhibits a parabolic shape (Figure 2b) until it is fully developed at approximately 50 ms.

Then, water climbing on the substrate and filling the intervals of the trichomes occur at the same time, which results in a film of non-uniform thickness and only wets the surface of the trichomes at higher heights (Figure 2c).

Similar to the capillary rise in a tube with a small radius (Figure S2), where the equilibrium rising height decreases as the diameter increases, known as Jurin's law [34], the equilibrium wicking height,  $H$ , decreases as the pitch increases (Figure 2d). Notably, the mesoscopic structures of the discontinuous periodical biomimetic trichomes differ from the continuous tube wall. On the former substrate, the meniscus must extend from the first row to reach the second row (Figure 2e, inset) to ensure a continued wicking process. The pitch limitation,  $p_m$ , of our fabricated material was determined to be 2200  $\mu\text{m}$ , above which no obvious capillary wicking and interval filling were observed. This limitation is attributed to an insufficient driven pressure in the first interval, while the maximum pitch of two closet trichomes satisfies the condition where the pressure at the advancing meniscus in the first interval,  $P_M$ , is balanced by the hydrostatic pressure,  $P_h$ , such that

$$P_M = P_{\text{air}} - \sigma L / p_m^2 = P_h = P_{\text{air}} - \rho g p_m \quad (1)$$

where  $\sigma$  is liquid–air surface tension,  $\rho$  is the density of the liquid, and  $g$  is the acceleration of gravity. The maximum pitch obtained from Equation (1) is  $p_m = (L l_c)^{1/3}$ , where  $l_c$  is  $(\sigma / \rho g)^{1/2}$  and called the capillary length. For the  $L = 2 \text{ mm}$  used in our experiments, Equation (1) predicted a pitch limitation of 2.4 mm which is consistent with our results.

In addition, the film thickness in single interval changes with time, not monotonically increasing but oscillating around the final thickness. This oscillation starts after the water imbibes into the interval and lasts for  $O(0.1 \text{ s})$ , which is particularly evident in intervals at lower heights, indicating that previously filled intervals act as a source to supply the meniscus extending to the next row and repeating the filling process.

### 3.2. Microscopic Capillary Wicking Dynamics

An enlarged observation of the capillary wicking process (Figure 3a) shows that the advancing meniscus front (red dotted line) extends over the substrate at the same velocity, but water first wets only the bottom of trichomes. Driven by capillary forces,  $F_c$ , along the perimeter of trichomes (Figure 3b), water gradually fills the interval and eventually covers almost the whole surface. The competition between the extension of the advancing meniscus on the substrate and the water spreading on the surface of trichomes contributes to the oscillation of film thickness in single interval that delays the spreading process.

Racing to the  $n$ th interval from the bottom to the top, the capillary forces,  $F_c = \sigma \pi d_n$ , where  $\pi$  is the circular constant and  $d_n$  is the contact diameter of the trichomes in the  $n$ th row, decrease as the water spreads towards the tip of the trichomes due to their smaller  $d_n$ . Additionally, the film thickness in the  $n$ th interval,  $e_n$ , is non-uniform and decreases as the row number,  $n$ , increases (Figure 2c). Consequently, the capillary force along the perimeter of the trichomes varies with  $n$  and deforms the liquid–air interface in each interval to different extent during the filling process. Because  $e_n$  is obviously influenced by the trichome length,  $L$ , as longer trichomes support a thicker film, the ratio between  $e_n$  and  $L$ , denoted as  $\alpha_n$ , is utilized as a dimensionless quantity to describe the profile of the film. In the case of trichome lengths of 1 mm, 2 mm, and 3 mm, the variation of  $\alpha_n$  with  $n$  shows a similar tendency, suggesting a self-similarity of the film profile.



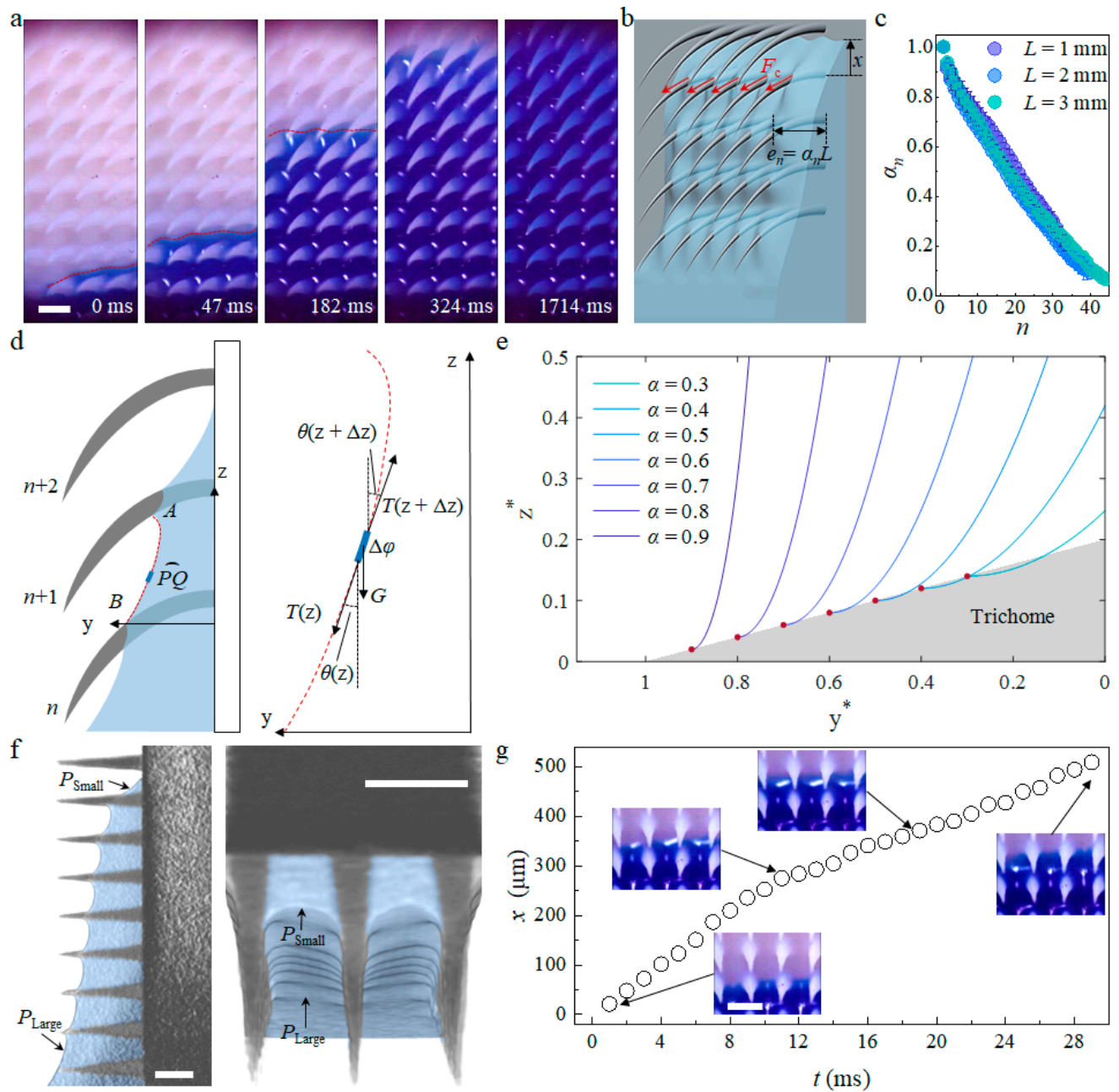


**Figure 3.** Microscopic capillary wicking dynamics and meniscus profile. (a) Microscopic view of capillary wicking on biomimetic trichomes array. The red dotted line indicates the meniscus front; (b) Schematic of capillary force on the perimeter of the trichomes and the film thickness in the  $n$ th interval.  $e_n = \alpha_n L$ , where  $\alpha_n$  is the ratio between trichome thickness and length, and the meniscus front extends on the substrate to a distance of  $x$  from the  $(n + 1)$ th row; (c) Self-similarity of film profiles for trichomes arrays of different lengths. The ratio,  $\alpha_n$ , changing with  $n$ , collapses into a narrow region, implying a similar tendency across the arrays; (d) Catenary line schematic of meniscus  $AB$  in the  $n$ th interval (left), and force analysis of a small arc  $PQ$  in the meniscus of length  $\Delta\varphi$  (right). The tension force,  $T$ , and gravity,  $G$ , are two major forces acting on two end points, and the tangential deflection angle is  $\theta$ ; (e) Meniscus profile of different trichome thickness to length ratios,  $\alpha$ . Normalized  $z^* = z/p$  and  $y^* = y/p$  are used; (f) Film profile reconstructed from Micro-CT scanning. Both cross-sectional views in the  $y$ - $z$  plane and perpendicular to  $z$  axis follow the catenary line, which results in a pressure gradient that is large at the bottom and small at the top. The blue false color indicates the water phase; (f) Meniscus extending with time,  $t$ , in a single interval at  $H \approx 13$  mm. The insets are in situ snapshots corresponding to the arrow-indicated point. Scale bars: 500  $\mu\text{m}$  in (a,f,g).



To investigate the relationship between the thickness and the meniscus profile, we employ the catenary line concept for detailed analysis and description (Figure 3d). As shown in the left schematic, we consider an arbitrary arc of a small length,  $PQ$ , in the  $n$ th interval, and the difference in the  $z$  direction between points  $P$  and  $Q$  is denoted as  $\Delta z$ . The force balances between the surface tension force,  $T(z)$ , and gravity,  $G(z)$ , in the horizontal and vertical directions are

$$T(z) \sin(\theta(z)) = T(z + \Delta z) \sin(\theta(z + \Delta z)), \quad (2)$$

$$T(z + \Delta z) \cos(\theta(z + \Delta z)) - T(z) \cos(\theta(z)) = G(z) = \rho g S_n [\varphi(z + \Delta z) - \varphi(z)] \quad (3)$$

where  $\varphi(z)$  is the path of the profile from point  $B$  to  $P$ ,  $\theta(z)$  is the tangential angle with respect to the  $z$  axis, and  $S_n \sim e_n p$  is the cross-sectional area perpendicular to the  $z$  axis. Considering an infinitely small step as  $\Delta z$  approaches 0, and dividing Equations (2) and (3) by  $\Delta z$ , their differential forms are given as

$$d(T \sin \theta) / dz = 0, \quad (4)$$

$$d(T \cos \theta) / dz = \rho g S_n d\varphi / dz \quad (5)$$

Equation (4) implies that  $T \sin \theta = F$ , where  $F$  is a constant comparable to the surface tension force along the contact perimeter of the trichomes, which scales as  $\sigma d_n$ . Substituting  $T$  into Equation (5) as well as the path,  $\varphi$ , by the profile function,  $f(z)$ , obtains an equation describing the  $f(z)$ :

$$-f'' / (f')^2 = K_n (1 + (f')^2)^{1/2} \quad (6)$$

where  $f'$  and  $f''$  denote the first and second derivatives of the profile,  $f$ , and  $K_n = \rho g S_n / F$  is a constant related to the film thickness,  $e_n$ . The boundary conditions are rigorously adjusted by the curvature at the contact points  $A$  and  $B$  to satisfy the Laplace pressure balance of the hydrostatic pressure.

The general solution of Equation (6) describes the meniscus profile in the  $n$ th interval (see Appendix A for the mathematical derivation). To visualize the profile, we plot normalized  $z$  coordinates,  $z^* = z/p$ , against normalized  $y$  coordinates,  $y^* = y/L$ , for different film thickness ratios  $\alpha$  (Figure 3e). As the film thickness in the interval decreases, the meniscus becomes flatter and the curvature of the meniscus,  $\kappa$ , induced by the deformation of the profile,  $f$ , is

$$\kappa = -K_n / (K_n z + C)^2 \quad (7)$$

where  $C$  is a negative constant determined by the boundary condition of the profile. As indicated by Equation (7), the curvature-determined Laplace pressure increases from the bottom to the top of each interval ( $z$  increases from 0 to  $p$ ). In other words, a pressure gradient forms inside the film at the  $n$ th interval, which propels the meniscus front to extend on substrate to reach the  $(n + 1)$ th row of trichomes. As the meniscus advances, the capillary force along the perimeter of the trichomes drives the liquid spreading along the trichomes to fill the  $(n + 1)$ th interval and finally renews the pressure gradient, with the coefficient  $K_n$  modified to  $K_{n+1}$ .

The repeated behavior of substrate climbing and interval filling results in different meniscus profiles in each interval along the wicking direction (Figure 3f). Cross-sectional views perpendicular to the  $z$  axis and in the  $y$ - $z$  plane prove that this pressure gradient; that the pressure at the bottom is large, and small at the top. In a single interval (Figure 3g), the release of the trichomes' surface energy accelerates the flow, as water reaches the base of the trichomes while viscous dissipation slows down the flow, which is consistent with previous work on the wetting of rough surfaces decorated with sparsely arranged microscopic structures [4]. In general, the capillary force acting on the perimeter of a trichome leads to a catenary line-shaped meniscus profile, which induces a pressure gradient, propelling

the repeated climbing–filling process that eventually forms a non-uniformly thick film of height  $H$ .

### 3.3. Macroscopic Capillary Wicking Dynamics

Different from the capillary rise in a closed tube [34] of a large diameter that enables a higher flux (larger amount of water raised) but results in a slower speed and lower height, capillary wicking in a mesoscopic trichomes array with different lengths but a fixed pitch and diameter exhibits a similar height change over time, as shown in Figure 4a, which implies that the interval filling process and substrate climbing process are independent. In other words, a faster wicking speed, higher wicking height, and thicker wicking film allow for the achievement of a higher flux at the same time.

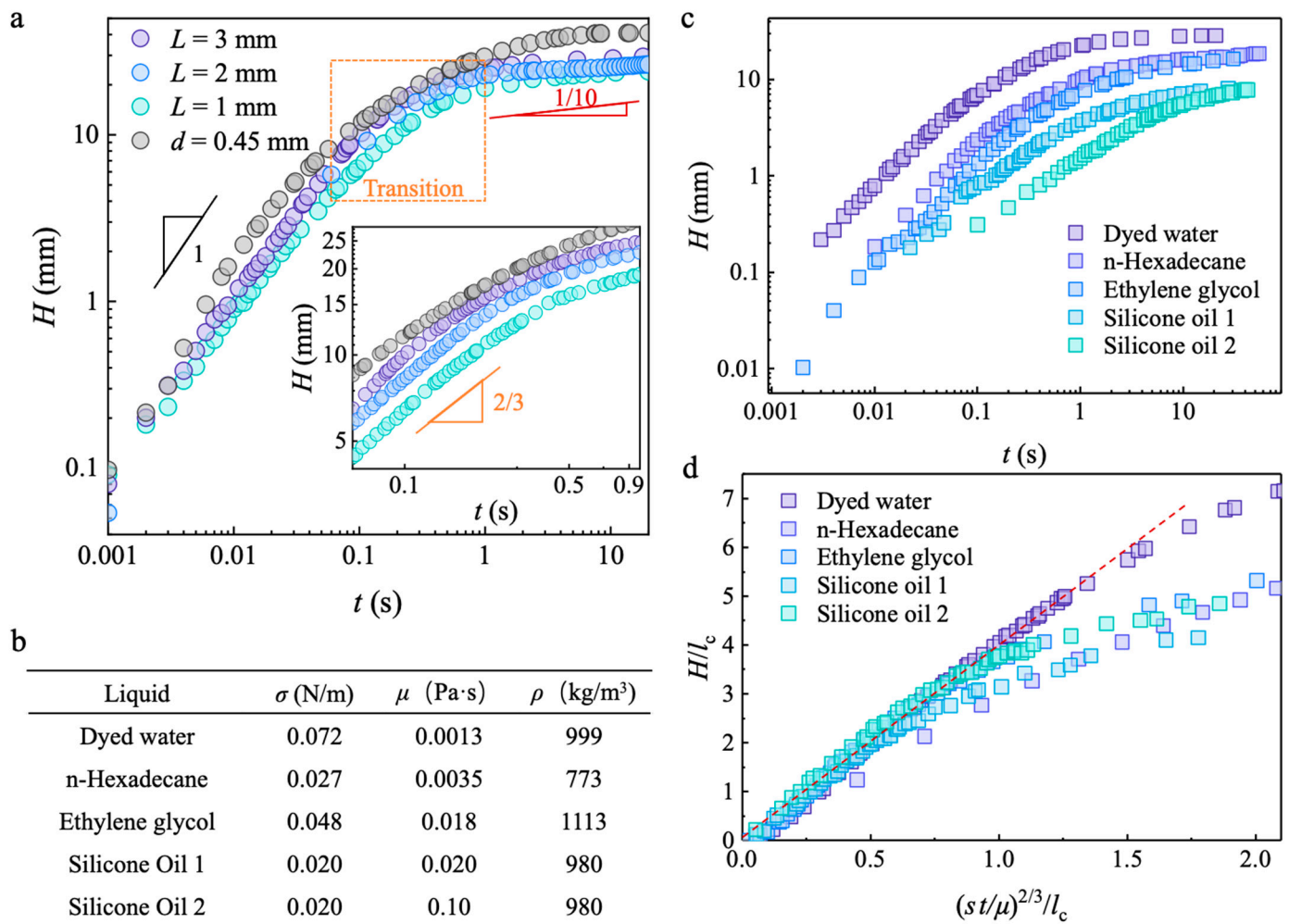


**Figure 4.** Macroscopic capillary wicking dynamics and generality of scaling law for different liquids. (a) Capillary wicking height,  $H$ , changes with time,  $t$ . The dynamics of capillary rise in a closed tube of diameter,  $d = 0.45$  mm, is plotted in gray for comparison, and the logarithm coordinates are used to present the scaling law. The inset enlarges the transition regime between the inertia-dominated regime ( $H \sim t$ ) and the viscosity-dominated thin-film spreading regime ( $H \sim t^{1/10}$ ). The scaling law fits the transition regime of capillary wicking that is  $H \sim t^{2/3}$  when the capillary is  $H \sim t^{1/2}$ ; (b) Properties of different liquids including surface tension, viscosity, and density; (c) Capillary wicking dynamics of different liquids in a trichomes array, with parameters of  $L = 2$  mm,  $p = 500$   $\mu$ m, and  $d = 200$   $\mu$ m; (d) Dimensionless capillary wicking height with respect to normalized time. The trends of viscous liquids deviate from that of dyed water (indicated by the red dotted line) in the late stage due to the thin film and as the slow flow of the Reynolds number decreases, meaning viscous dissipation plays an important role in influencing the dynamics.

In addition, capillary rise is usually classified into three regimes [35,36] (Figure S2): the initial stage is dominated by inertia following a scaling law,  $H \sim t$ ; the final stage of thin-film wetting is influenced by viscosity, which follows Tanner's law [37–39],  $H \sim t^{1/10}$ ; and the regime between the two stages is called the inertia–viscosity transition, which is described by the Lucas–Washburn equation as  $H \sim t^{1/2}$ . However, mesoscopic structures enhance surface energy release and reduce the velocity gradient, which determine the viscous drag. The Reynolds number,  $Re = \rho u e_n / \mu$ , is  $O(10^2)$ , indicating that inertia dominates over viscosity, where  $u$  is the wicking velocity and  $\mu$  is the viscosity of the liquid. The Bond number,  $Bo = \rho g H e_n / \sigma$ , is  $O(10^{-2})$ , implying that the influence of gravity is negligible. Therefore, the governing equation for the mesoscopic wicking dynamics of a single interval column takes the following form:

$$d(mu)/dt = u dm/dt + m du/dt = F = \sigma^* p \quad (8)$$

where  $\sigma^*$  is the equivalent surface tension considering the surface roughness [1,4] and  $m$  is the mass of the wicking liquid, which can be expressed as  $k \rho H p e_n$ , where  $k$  is a geometric factor and  $u = H'$  is the first derivative of  $H$ . Considering that the thickness relates to the wicking height as  $e_n \sim \beta H$  (Figure 3c),  $m$  is expressed as  $k' \rho H^2 p$ , where  $k' = k \beta$  and a different scaling law can be obtained from Equation (8) (see Appendix A for detail):

$$H \sim \left( \frac{3\sigma^*}{2k'\rho} t \right)^{2/3} \quad (9)$$

which describes the transition regime dynamics of mesoscopic wicking and is in accord with the experimental results.

Furthermore, we confirm the general applicability of the new scaling law regarding the transition regime of capillary wicking on a mesoscopic trichomes array. The height change over time for different liquids wetting our fabricated materials is reported in Figure 4c, which reveals a similar trend, but the low surface tension of viscous liquids such as silicone oil exhibits a slower climbing rate compared to high-surface-tension liquids with a low viscosity, such as water. Dimensionless height,  $H/l_c$ , with respect to normalized time,  $\sigma t / \mu$ , was used to assess deviations from the expected tendency of different liquids (Figure 4d). The results indicate that all liquids follow the scaling law at the beginning, but deviate from their expected tendencies in the late stage because the viscosity-negligible condition that  $Re$  is large does not hold for thin films of viscous liquids such as silicone oil and ethylene glycol in our experiments.

### 3.4. High-Flux Open Siphon Applications and Mass Transportation

Subsequently, we curved the straight plate into “n” shape (Figure 5a), so that the film on the trichomes array acts as a water path connecting two levels and facilitating water transfer from the higher level to the lower level, functioning as an open siphon device [40–42]. Compared to the “n” shape device without a trichomes array modification (Figure 5b), water spontaneously wicks between the trichomes once it touches the modified region and follows the trichomes' path, flowing into the other side of the device. As water accumulates in the outlet side, the meniscus rises to touch the modified region, enabling continuous water transfer until the meniscus levels on the inlet side and outlet side are equal. Similar to a traditional siphon in a closed tube, the height difference between the inlet and outlet,  $h_{out} - h_{in}$ , where  $h_{in}$  is the height difference from the inlet tank's bottom to its ridge top and  $h_{out}$  is the height difference from the outlet tank's bottom to its ridge top, influences the siphon flux [43] (Figure 5c).

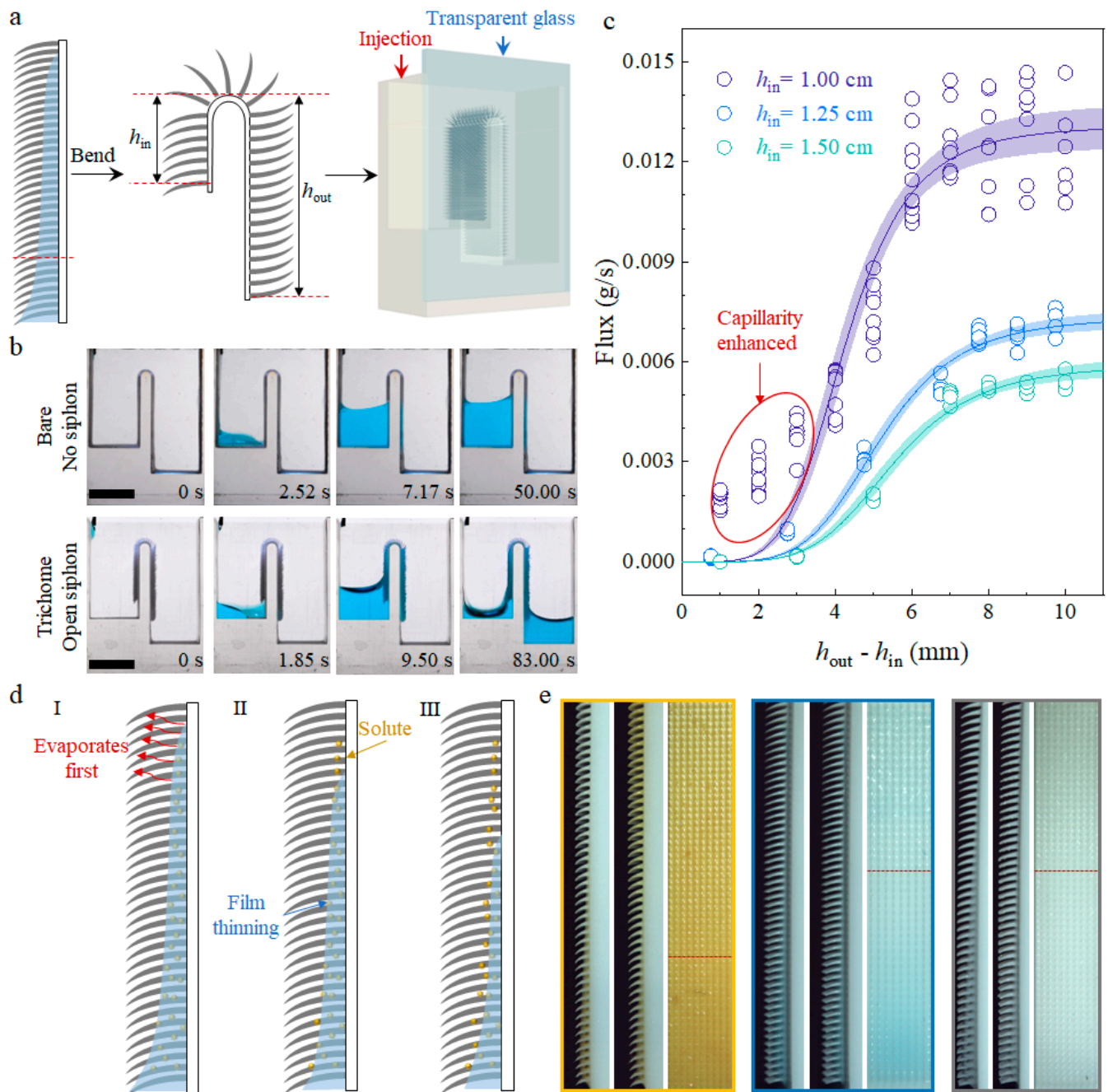


**Figure 5.** High-flux open siphon application and mass transportation through capillary wicking. (a) Schematic of open siphon construction, the straight surface is bent into an “n” shape with the inlet height difference  $h_{in}$  and outlet height difference  $h_{out}$ , transparent glass was used for the observation of the water flow injected from inlet. The red dotted line to the left indicates the bending position; (b) Comparison between bare and trichomes-array-modified devices shows that no siphon forms on the bare side wall, while spontaneous wicking on the trichomes connects the two sides; (c) Flux measurement of different two-sided height differences for different  $h_{in}$ . Meniscus deformation leads to large Laplace pressure, which enhances the flux, deviating from the fitting tendency; (d) Schematic of mass transportation and thin-film evaporation (I) leading to solute crystallization (II), (III) is the final state. (e) Side and front views of film thinning and solute crystallization. From left to right, the solutes are  $FeCl_3$ ,  $CuSO_4$ , and glucose, respectively. Above the red dotted line is crystallized solute, which reflects light. Scale bars: 1 cm in (b).

However, as reported in previous work, the flux of an open siphon exhibits a maximum flat stage [42], such that increases in the two-sided height difference have little influence on the flux. Instead, the maximum flux is influenced by the inlet height difference,  $h_{in}$ , which determines the driving pressure difference across the free surface. The flux of our trichomes array achieved an open siphon, which is also strongly influenced by the  $h_{in}$ , which the maximum flux reduces to half when the  $h_{in}$  increases from 1.00 cm to 1.25 cm. Except for the maximum flux, flux under small two-sided height differences is enhanced by capillarity if the  $h_{in}$  is small, which is attributed to a larger Laplace pressure difference across the meniscus for a small  $h_{in}$ . Siphon applications that require high flux such as irrigation systems and drainage systems can be enhanced by adding a trichomes array with an optimized height difference on their surface.

The application of water wicking on a trichomes array extends beyond liquid transfer, which can be utilized for mass transportation as well. Various solutions carrying mineral salts or nutrients, such as glucose, wick on the biomimetic trichomes array and form a non-uniformly thick film (Figure 5d). The thinner film at higher levels evaporates first, causing solute crystallization to cover the surface. Over time, as the film gets thinner, solutes from the resources are transported to the surface at high levels (Figure 5e). In this way, a pitcher plant like *H. minor* can carry nutrients such as sugar and digestive liquid from the glandular organ at the bottom of pitcher to the upper pubescent zone, which attracts insects after crystallization. This process requires further investigation of the biological subject [31].

#### 4. Conclusions

Inspired by the capillary wicking on the pubescent inside wall of *Heliamphora minor*, we fabricated a biomimetic array of millimeter-long and sub-millimeter-pitched trichomes through LCD-based 3D printing, with a high resolution of up to 18  $\mu\text{m}$ , to investigate mesoscopic wicking dynamics. Our results demonstrate that the water wicking on a trichomes array consists of two independent processes: the filling intervals of the trichomes and the meniscus advancing on the substrate. The filling of the trichomes' intervals is driven by capillary forces along the perimeter of the trichomes, resulting in the formation of a film with non-uniform thickness, and the film profile at each interval is described by a catenary line. Additionally, we unveiled that the transition regime of wicking on a mesoscopic-trichomes-modified surface is dominated by inertia. The dynamics follows a scaling law of  $H \sim t^{2/3}$ , which is distinct from the  $H \sim t^{1/2}$  observed in traditional capillary rising or wicking on surfaces modified with microscopic structures. Because the thickness and wicking dynamics are independent, high flux and fast speed can be achieved at the same time, which can improve the flow efficiency and has potential in applications such as high-flux siphons. Finally, we examined the mass transportation inside the film and observed thin-film evaporation, resulting in solute crystallization at higher levels first, which indicates a method utilized by the plant to transport nutrients in the digestive fluid from the pitcher to the upper pubescent zone, assisting in the attraction of insects. This work, exploring the capillary wicking phenomena on mesoscopic structures, advances our understanding of high-flux wetting behaviors and improves the design of efficient liquid transfer devices.

**Supplementary Materials:** The following supporting information can be downloaded at <https://www.mdpi.com/article/10.3390/biomimetics9020102/s1>, Figure S1: wettability of pitcher pubescent zone and smooth zone; Figure S2: scanning electron microscopy and energy-dispersive spectrometry of the 3D-printed material.

**Author Contributions:** Conceptualization and methodology, F.C., L.J., Z.C. and Z.D.; software, F.C.; investigation, F.C. and Z.C.; writing—original draft preparation, F.C.; writing—review and editing, F.C. and Z.D.; visualization, F.C.; supervision, L.J. and Z.D.; funding acquisition, L.J. and Z.D. All authors have read and agreed to the published version of the manuscript.

**Funding:** This research was funded by the National Natural Science Foundation (52173293, 22122508), the National Key Research and Development Program of China (2021YFA070008), the Young Elite Scientists Sponsorship Program of the China Association for Science and Technology, and the Key Research Program of the Chinese Academy of Sciences (KJZD-EW-M01).

**Institutional Review Board Statement:** Not applicable.

**Data Availability Statement:** Data are contained within the article and Supplementary Materials.

**Conflicts of Interest:** The authors declare no conflicts of interest.

## Appendix A

The Solution to Equation (6) can be obtained by changing the variable and direct integral, as below:

1. Let  $w(z) = f'(z)$ , and the equation transforms into

$$-\frac{dw}{w^2\sqrt{1+w^2}} = K_n dz \quad (A1)$$

The direct integration of Equation (A1) gives

$$\frac{1+w^2}{w} = K_n z + C \quad (A2)$$

where C is an integral constant determined by the boundary condition. And  $w$  can be expressed by  $v = K_n z + c$  as

$$|w| = 1/\sqrt{v^2 - 1} \quad (A3)$$

2. The solution of  $w$  from Equation (A3) can be obtained by substituting  $w(z) = f'(z) = K_n f'(v)$ :

$$|w| = |K_n f'(v)| = 1/\sqrt{v^2 - 1} \quad (A4)$$

and  $f$  expressed by  $v$  is

$$f(v) = C' + \begin{cases} \frac{\ln|v + \sqrt{v^2 - 1}|}{K_n} & v > 1 \\ \frac{\ln|v - \sqrt{v^2 - 1}|}{K_n} & v < -1 \end{cases} \quad (A5)$$

and  $C'$  is determined by the boundary conditions. The expressing of  $v$  in terms of  $z$  can generate a profile  $f$  represented by  $z$ .

3. From Equation (A5), the curvature of meniscus  $\kappa$ , which is defined as

$$\kappa = \frac{|f''|}{(1+f'^2)^{\frac{3}{2}}} \quad (A6)$$

can be obtained as  $\kappa = -K_n/(K_n z + C)^2$ .

Equation (8), can be treated as a Bernoulli differential equation to solve to obtain the scaling law of transition dynamics. The right-hand side is constant such that  $\sigma^*$  is the equivalent surface energy considering the roughness, which enhances energy releasing by enlarging the contact area, and  $p$  is the mutual pitch of the trichomes. Therefore, only the left-hand side needs further processing, as below:

1. Take  $m = k'\rho H^2 p$  and  $u = H'$  into consideration; eliminating  $p$  obtains

$$H^2 H'' + 2H(H')^2 = \sigma^*/pk' \quad (A7)$$



2. Let  $\Phi(H) = H'$ ; Equation (A7) can be transformed into

$$H_2\Phi\Phi' + 2H\Phi^2 = \sigma^*/pk' \quad (\text{A8})$$

which can be solved directly as

$$\Phi^2 = 2\sigma^*/3pHk' + C_1/H^4 \quad (\text{A9})$$

where  $C_1$  is an integral constant.

3. Replace  $\Phi$  with  $H'$ , and the solution to Equation (A9) can be acquired as

$$2H^3\sigma^*/3pk' + C_1 = (t\sigma^*/pk' + C_2)^2 \quad (\text{A10})$$

and the boundary condition of the initial stage is that  $H = 0$  for  $t = 0$  s, which implies  $C_1 = C_2^2$ . If the initial velocity is considered infinitely small or zero, the simplest form of the scaling law is Equation (9), that is  $C_1 = C_2 = 0$ .

## Appendix B

A summary of the symbols used is provided in Table A1 for reference.

**Table A1.** Definitions of symbols used in the mathematical calculations.

Symbols	Definition	Unit
$\sigma$	Surface tension	N/m
$\rho$	Density of liquids	kg/m <sup>3</sup>
$\mu$	Viscosity of liquids	Pa·s
$g$	Gravitational acceleration constant	kg·m/s <sup>2</sup>
$l_c$	Capillary length	m
$L$	Length of trichomes	m
$p$	Center-to-center pitch of trichome's base	m
$d$	Diameter of trichome's base	m
$H$	Capillary wicking height	m
$u$	Capillary wicking velocity	m/s
$T$	Tension force on meniscus profile	N
$\theta$	Deflection angle of profile tangent with respect to the z direction	°
$F$	Constant lateral force representing $T\sin\theta$	N
$f$	Function describing the meniscus profile	\
$\varphi$	Path length from point B to P	m
$e_n$	Thickness in the $n$ th interval	m
$\alpha_n$	Ratio of thickness to trichome length	\
$S_n$	Area of cross-section perpendicular to z axis	m <sup>2</sup>
$K_n$	Coefficient equals $\rho g S_n / F$	m <sup>-1</sup>
$\kappa$	Curvature of meniscus	m <sup>-1</sup>

## References

1. Bico, J.; Tordeux, C.; Quéré, D. Rough wetting. *Europhys. Lett.* **2001**, *55*, 214–220. [CrossRef]
2. Bico, J.; Thiele, U.; Quéré, D. Wetting of textured surfaces. *Colloids Surf. A Physicochem. Eng. Asp.* **2002**, *206*, 41–46. [CrossRef]
3. Ishino, C.; Reyssat, M.; Reyssat, E.; Okumura, K.; Quéré, D. Wicking within forests of micropillars. *Europhys. Lett.* **2007**, *79*, 56005. [CrossRef]
4. Kim, J.; Moon, M.-W.; Kim, H.-Y. Dynamics of hemiwicking. *J. Fluid Mech.* **2016**, *800*, 57–71. [CrossRef]
5. Chen, X.; Chen, J.; Ouyang, X.; Song, Y.; Xu, R.; Jiang, P. Water Droplet Spreading and Wicking on Nanostructured Surfaces. *Langmuir* **2017**, *33*, 6701–6707. [CrossRef] [PubMed]
6. Lee, J.; Suh, Y.; Dubey, P.P.; Barako, M.T.; Won, Y. Capillary Wicking in Hierarchically Textured Copper Nanowire Arrays. *ACS Appl. Mater. Interfaces* **2019**, *11*, 1546–1554. [CrossRef] [PubMed]
7. Lee, J.H.; Jung, B.; Park, G.-S.; Kim, H.-Y. Condensation and wicking of water on solid nanopatterns. *Phys. Rev. Fluid* **2022**, *7*, 024202. [CrossRef]
8. Courbin, L.; Denieul, E.; Dressaire, E.; Roper, M.; Ajdari, A.; Stone, H.A. Imbibition by polygonal spreading on microdecorated surfaces. *Nat. Mater.* **2007**, *6*, 661–664. [CrossRef] [PubMed]

9. McHale, G. Surface wetting: Liquids shape up nicely. *Nat. Mater.* **2007**, *6*, 627–628. [CrossRef] [PubMed]
10. Li, J.; Song, Y.; Zheng, H.; Feng, S.; Xu, W.; Wang, Z. Designing biomimetic liquid diodes. *Soft Matter* **2019**, *15*, 1902–1915. [CrossRef]
11. Gelebart, A.H.; Mc Bride, M.; Schenning, A.P.H.J.; Bowman, C.N.; Broer, D.J. Photoresponsive Fiber Array: Toward Mimicking the Collective Motion of Cilia for Transport Applications. *Adv. Funct. Mater.* **2016**, *26*, 5322–5327. [CrossRef]
12. Zhang, S.; Huang, J.; Chen, Z.; Yang, S.; Lai, Y. Liquid mobility on superwetable surfaces for applications in energy and the environment. *J. Mater. Chem. A* **2019**, *7*, 38–63. [CrossRef]
13. Dittrich, P.S.; Manz, A. Lab-on-a-chip: Microfluidics in drug discovery. *Nat. Rev. Drug Discov.* **2006**, *5*, 210–218. [CrossRef] [PubMed]
14. Si, Y.; Wang, T.; Li, C.; Yu, C.; Li, N.; Gao, C.; Dong, Z.; Jiang, L. Liquids Unidirectional Transport on Dual-Scale Arrays. *ACS Nano* **2018**, *12*, 9214–9222. [CrossRef] [PubMed]
15. van Erp, R.; Soleimanzadeh, R.; Nela, L.; Kampitsis, G.; Matioli, E. Co-designing electronics with microfluidics for more sustainable cooling. *Nature* **2020**, *585*, 211–216. [CrossRef] [PubMed]
16. Quéré, D. Wetting and Roughness. *Annu. Rev. Mater. Res.* **2008**, *38*, 71–99. [CrossRef]
17. Kim, S.J.; Moon, M.-W.; Lee, K.-R.; Lee, D.-Y.; Chang, Y.S.; Kim, H.-Y. Liquid spreading on superhydrophilic micropillar arrays. *J. Fluid Mech.* **2011**, *680*, 477–487. [CrossRef]
18. Hancock, M.J.; Sekeroglu, K.; Demirel, M.C. Bioinspired Directional Surfaces for Adhesion, Wetting and Transport. *Adv. Funct. Mater.* **2012**, *22*, 2223–2234. [CrossRef]
19. Chen, H.; Zhang, P.; Zhang, L.; Liu, H.; Jiang, Y.; Zhang, D.; Han, Z.; Jiang, L. Continuous directional water transport on the peristome surface of *Nepenthes alata*. *Nature* **2016**, *532*, 85–89. [CrossRef]
20. Krishnan, S.R.; Bal, J.; Putnam, S.A. A simple analytic model for predicting the wicking velocity in micropillar arrays. *Sci. Rep.* **2019**, *9*, 20074. [CrossRef]
21. Feng, S.; Zhu, P.; Zheng, H.; Zhan, H.; Chen, C.; Li, J.; Wang, L.; Yao, X.; Liu, Y.; Wang, Z. Three-dimensional capillary ratchet-induced liquid directional steering. *Science* **2021**, *373*, 1344–1348. [CrossRef]
22. Lecointre, P.; Laney, S.; Michalska, M.; Li, T.; Tanguy, A.; Papakonstantinou, I.; Quéré, D. Unique and universal dew-repellency of nanocones. *Nat. Commun.* **2021**, *12*, 3458. [CrossRef] [PubMed]
23. Zhu, Q.; Li, B.; Li, S.; Luo, G.; Zheng, B.; Zhang, J. Superamphiphobic Cu/CuO Micropillar Arrays with High Repellency towards Liquids of Extremely High Viscosity and Low Surface Tension. *Sci. Rep.* **2019**, *9*, 702. [CrossRef] [PubMed]
24. de Gennes, P.-G.; Brochard-Wyart, F.; Quéré, D.; Reisinger, A.; Widom, B. *Capillarity and Wetting Phenomena: Drops, Bubbles, Pearls, Waves*; Springer: New York, NY, USA, 2004.
25. Delannoy, J.; Lafon, S.; Koga, Y.; Reyssat, É.; Quéré, D. The dual role of viscosity in capillary rise. *Soft Matter* **2019**, *15*, 2757–2761. [CrossRef] [PubMed]
26. Yuan, Q.; Zhao, Y.-P. Multiscale dynamic wetting of a droplet on a lyophilic pillar-arrayed surface. *J. Fluid Mech.* **2013**, *716*, 171–188. [CrossRef]
27. Washburn, E.W. The Dynamics of Capillary Flow. *Phys. Rev.* **1921**, *17*, 273–283. [CrossRef]
28. Quéré, D. Inertial capillarity. *Europhys. Lett.* **1997**, *39*, 533. [CrossRef]
29. Kim, J.; Moon, M.-W.; Kim, H.-Y. Capillary rise in superhydrophilic rough channels. *Phys. Fluids* **2020**, *32*, 032105. [CrossRef]
30. Jaffe, K.; Michelangeli, F.; Gonzalez, J.M.; Miras, B.; Christine Ruiz, M. Carnivory in pitcher plants of the genus *Heliamphora* (Sarraceniaceae). *New Phytol.* **1992**, *122*, 733–744. [CrossRef]
31. Bauer, U.; Scharmann, M.; Skepper, J.; Federle, W. ‘Insect aquaplaning’ on a superhydrophilic hairy surface: How *Heliamphora nutans* Benth. pitcher plants capture prey. *Proc. R. Soc. Lond. B Biol. Sci.* **2013**, *280*, 20122569. [CrossRef]
32. Wang, X.; Shen, C.; Meng, P.; Tan, G.; Lv, L. Analysis and review of trichomes in plants. *BMC Plant Biol.* **2021**, *21*, 70. [CrossRef]
33. Vogler, E.A. Structure and reactivity of water at biomaterial surfaces. *Adv. Colloid Interface Sci.* **1998**, *74*, 69–117. [CrossRef]
34. Jurin, J., II. An account of some experiments shown before the Royal Society; with an enquiry into the cause of the ascent and suspension of water in capillary tubes. *Philos. Trans. R. Soc. Lond.* **1718**, *30*, 739–747. [CrossRef]
35. Weislogel, M.M. Compound capillary rise. *J. Fluid Mech.* **2012**, *709*, 622–647. [CrossRef]
36. Das, S.; Mitra, S.K. Different regimes in vertical capillary filling. *Phys. Rev. E* **2013**, *87*, 063005. [CrossRef]
37. Tanner, L.H. The spreading of silicone oil drops on horizontal surfaces. *J. Phys. D Appl. Phys.* **1979**, *12*, 1473. [CrossRef]
38. de Gennes, P.G. Wetting: Statics and dynamics. *Rev. Mod. Phys.* **1985**, *57*, 827–863. [CrossRef]
39. Delgadino, M.G.; Mellet, A. On the Relationship between the Thin Film Equation and Tanner’s Law. *Commun. Pure Appl. Math.* **2021**, *74*, 507–543. [CrossRef]
40. Ganci, S.; Yegorenkov, V. Historical and pedagogical aspects of a humble instrument. *Eur. J. Phys.* **2008**, *29*, 421–430. [CrossRef]
41. Boatwright, A.; Hughes, S.; Barry, J. The height limit of a siphon. *Sci. Rep.* **2015**, *5*, 16790. [CrossRef]
42. Wang, K.; Sanaei, P.; Zhang, J.; Ristroph, L. Open capillary siphons. *J. Fluid Mech.* **2022**, *932*, R1. [CrossRef]
43. Yu, K.; Cheng, Y.-G.; Zhang, X.-X. Hydraulic characteristics of a siphon-shaped overflow tower in a long water conveyance system: CFD simulation and analysis. *J. Hydrodyn. Ser. B* **2016**, *28*, 564–575. [CrossRef]

**Disclaimer/Publisher’s Note:** The statements, opinions and data contained in all publications are solely those of the individual author(s) and contributor(s) and not of MDPI and/or the editor(s). MDPI and/or the editor(s) disclaim responsibility for any injury to people or property resulting from any ideas, methods, instructions or products referred to in the content.



## Article

# Bioinspire-Explore: Taxonomy-Driven Exploration of Biodiversity Data for Bioinspired Innovation

Adrien Saint-Sardos <sup>1,\*†</sup>, Annabelle Aish <sup>2,†</sup>, Nikolay Tchakarov <sup>1,†</sup>, Thierry Bourgoïn <sup>3</sup> , Luce-Marie Petit <sup>1</sup>, Jian-Sheng Sun <sup>2</sup> and Régine Vignes-Lebbe <sup>3</sup>

<sup>1</sup> Centre d'Études et d'Expertises en Biomimétisme de Senlis (CEEBIOS), 62 Rue du Faubourg Saint-Martin, 60300 Senlis, France

<sup>2</sup> Bioinspire-Museum, Museum National d'Histoire Naturelle, 57 rue Cuvier, 75005 Paris, France; annabelle.aish@mnhn.fr (A.A.)

<sup>3</sup> Sorbonne Université, Muséum National d'Histoire Naturelle, CNRS, EPHE, Université des Antilles, Institut de Systématique Évolution Biodiversité, ISYEB, CP 48, 57 Rue Cuvier, 75005 Paris, France

\* Correspondence: adrien.saint-sardos@ceebios.com

† These authors contributed equally to this work.

**Abstract:** Successful bioinspired design depends on practitioners' access to biological data in a relevant form. Although multiple open-access biodiversity databases exist, their presentation is often adapted to life scientists, rather than bioinspired designers. In this paper, we present a new tool, "Bioinspire-Explore", for navigating biodiversity data in order to uncover biological systems of interest for a range of sectors. Bioinspire-Explore allows users to search for inspiring biological models via taxa (species, genera, etc.) as an entry point. It provides information on a taxon's position in the "tree of life", its distribution and climatic niche, as well as its appearance. Bioinspire-Explore also shows users connections in the bioinspiration literature between their taxon of interest and associated biological processes, habitats, and physical measurements by way of their semantic proximity. We believe Bioinspire-Explore has the potential to become an indispensable resource for both biologists and bioinspired designers in different fields.

**Keywords:** biodiversity; bioinspiration; data science; computer-aided biomimetics; taxonomy; open-access; NLP; biology push



**Citation:** Saint-Sardos, A.; Aish, A.; Tchakarov, N.; Bourgoïn, T.; Petit, L.-M.; Sun, J.-S.; Vignes-Lebbe, R. Bioinspire-Explore: Taxonomy-Driven Exploration of Biodiversity Data for Bioinspired Innovation. *Biomimetics* **2024**, *9*, 63. <https://doi.org/10.3390/biomimetics9020063>

Academic Editors: Stanislav N. Gorb, Giuseppe Carbone, Thomas Speck and Peter Fratzl

Received: 20 December 2023

Revised: 16 January 2024

Accepted: 17 January 2024

Published: 23 January 2024



**Copyright:** © 2024 by the authors. Licensee MDPI, Basel, Switzerland. This article is an open access article distributed under the terms and conditions of the Creative Commons Attribution (CC BY) license (<https://creativecommons.org/licenses/by/4.0/>).

## 1. Introduction

Bioinspiration is a creative approach based on the observation of living systems [1]. Over the past twenty years, bioinspiration has helped solve engineering problems [2–4], inspire architectural programs [5], improve water management [6], support cybersafety [7,8], and even resolve in-orbit servicing challenges [9–11]. As impressive as these case studies are, they are based on a few dozen, perhaps a few hundred, biological models [12,13], despite more than 2 million species having been identified [14]. To reach its full potential, the field needs a greater range of "biological muses" from molecular [15] to ecosystem scales [16,17]. Advances in the fields of biology and ecology are able to provide this inspiration: we know more about living systems today than ever before. Moreover, technological developments allow us to mimic and/or incorporate nature into design in ways that were impossible even a decade ago. How can this potential be unlocked to support the ambitions of a growing number of bioinspiration organisations, startups, laboratories etc. [13,18]? Moreover, how can we draw attention to the lesser known taxonomic groups, whose diversity of form and function has much to teach us [19–21]? Several initiatives have been set up over the last decade(s) to support bioinspired designers' access to biological information. Through the AskNature platform, living systems can be explored with a focus on functions, using the Biomimicry 3.8 "Taxonomy" to translate these into biological "strategies" that have or could inspire innovation [22]. Other initiatives have combined this functional

approach with advanced algorithms, processing large datasets (texts, images, etc.) that support online biomimicry tools, such as Mimicus (<https://www.lib.mimic.us/ap/> accessed on 1 January 2024), developed by Sun-Young Kim and colleagues, or PeTal from NASA [23]. Finally, one of the most promising ways to explore scientific literature is the “trade-off” approach, focused on the balance between different functions necessary for a species’ survival [24,25]. Such an approach, combined with biomimetic ontologies and engineering-to-biology thesauri developed during the 2000s [26–28], led to the development of the E2BMO tool. This computer-aided user interface allows the exploration of scientific literature using the concepts of functions and trade-offs [29]. All these tools help to generate ideas for bioinspired products, processes, and systems. However, at present, these (and other available resources) orientate the user towards a limited set of taxa. In this article, we present a new tool, Bioinspire-Explore (<https://Bioinspire-Explore.mnhn.fr/> accessed on 1 January 2024), developed to simplify access to biodiversity data in order to facilitate “biology push” approaches to bioinspiration without inherent taxonomic bias. Bioinspire-Explore offers the bioinspired designer the phylogenetic “tree of life” as a starting point, allowing the exploration of (known) extant biodiversity in its entirety. It is structured around taxa (i.e., names of species, genus, families, etc.) entered by users based on their curiosity or existing knowledge. While the immensity of taxonomic data may seem overwhelming to a non-biologist [30], Bioinspire-Explore aims to support the user in their discovery of the living world and present connections between taxa and associated information (ecological, climatic, visual) of relevance. Above all, its value lies in its ability to display the semantic proximity between taxa, biological processes, habitats, and physical measurements within the scientific literature on bioinspiration. Bioinspire-Explore does not replace interaction with biologists: transdisciplinary collaboration is essential to understanding the principles that govern the living world [31] and for effective bioinspiration [32,33]. However, Bioinspire-Explore provides a means to begin biological exploration, individually or as a team, and to stimulate bioinspiration in all its forms (i.e., biomimicry, bioassistance, bioproduction, Nature Based Solutions, etc. . . ) [34].

## 2. Materials and Methods

### 2.1. Data Sources

Table 1 presents the data sources behind Bioinspire-Explore. Taxonomic data are provided via the application programming interface (API) of the Global Biodiversity Information Facility GBIF (<https://gbif.org/> accessed on 1 January 2023), with names of taxa (vernacular and scientific), their occurrences, (spatial coordinates), taxonomic rank, and images. The GBIF taxon identification number is used to query Wikidata. If the Wikidata node of the taxon in question is found, the first paragraph and image of its Wikipedia page is displayed on the Bioinspire-Explore interface via the Wikipedia representational state transfer (REST) API. Going through the Wikidata graph prevents “false friend-associated” pages (e.g., avoiding a query using the word “Vespa” displaying information on motorcycles). Images are imported through the GBIF API and originate from the iNaturalist database.

**Table 1.** Data sources and their providers.

Data Type	Sourced From
Taxonomic backbone	GBIF
Occurrence data	GBIF
Taxon-related photographs	iNaturalist
General information on given taxon	Wikipedia
Geo-climatic data	WorldClim
List of biological process	Wikidata
Related entities, e.g., co-cited species	Biomig corpus

Climatic data for each taxon are provided by the WordClim (<https://www.worldclim.org/> accessed on 1 January 2024) initiative. Plotting a taxon's climatic conditions involves several steps: (i) Nine monthly climatic variables (elevation, average precipitation, max. precipitation, min. precipitation, solar irradiance, average temp, min. temp, max. temp, and wind speed) are downloaded. (ii) Taxon occurrence maps are downloaded from GBIF, containing a list of hexagonal geographical zones where the taxon has been recorded. (iii) The climatic variables maps are overlaid with the occurrences maps. (iv) The final metric, as displayed in the Climate Tab, represents a spatial mean over the distribution range, averaged over 12 months of the year. To provide the range, maximums and the minimums are calculated over the monthly distributions.

## 2.2. Architecture

Bioinspire-Explore is an open-source tool developed as a full-stack application; in other words, it comprises an entire set of software/technologies with both front end (user-side) and back end (server-side) elements. The back-end aspects are based on Python scripts and Fast APIs, whereas the front end is written using the JavaScript React application. The full repository of the Bioinspire-Explore project can be found here: GitHub <https://github.com/ceebios/Bioinspire-Explore-app> (accessed on 1 January 2024).

## 2.3. Word Vectorization and Expansion

Bioinspire-Explore allows the user to evaluate the semantic proximity of entities ("Taxon", "Biological Process", "Habitat", and "Physical Measurement") within a body of scientific literature pertaining to bioinspiration. This supports bioinspiration by offering potential links between a taxon and its associated biological functions, environment, or physical characteristics. Bioinspire-Explore's functionality is based on a Word2Vec model [35] that was trained on tokenized sentences from the BIOMIG Corpus. The BIOMIG corpus is a dataset developed by Tchakarov et al. 2023 [36] containing scientific papers evaluated as relevant for bioinspiration.

In the Word2Vec model, entities were defined as follows:

- "Taxon" entities were taken from the GBIF taxonomic backbone [37].
- "Biological Process" entities were derived from a Wikidata list of biological processes <https://www.wikidata.org/wiki/Property:P682> (accessed on 1 January 2023), filtered manually by the authors to remove irrelevant content.
- "Habitat" entities are those listed under "biome" in the ontology ENVO [38].
- "Measurement" entities are listed as the "quantities" in Ontology of units of Measure (OM) <https://www.ebi.ac.uk/ols/ontologies/om> (accessed on 1 January 2023).

The compatibility score between entities is calculated as follows: for a given word entered by the user (e.g., "vespa"), the model looks for the N possible entries in the model that contain this word (e.g., "vespa mandarina", "vespa ducalis"). The cosine similarities between the vectors of these entries and the vectors of all the entities stored in the model (e.g., the words "resistance" or "venom") are calculated. The compatibility of each entity is defined as the minimum of these N similarity values. For each input word, N similarity values are provided, with 100% indicating "perfect compatibility" between the term chosen (in this case, "vespa") and the associated entity. Bioinspire-Explore's objective is to suggest entities that are the most compatible with all entries containing the word "vespa". The final top 20 suggestions shown on the user interface represent those entities with the highest compatibility score.

## 3. Results

### 3.1. Dynamic Taxon Search Capability

Bioinspire-Explore's first key feature is to support users in their search for a taxon of interest. As text is entered, the search bar automatically suggests up to 20 scientific names associated with a query at different taxonomic levels (i.e., species, genus, family, order, etc.). Each taxonomic rank is colour-coded, from red for species to blue for kingdom.

As seen in Figure 1A, a query beginning with the text “hymenopt” yields ten taxa suggestions at different levels. (Note that an identical request on Google may yield many more results, but these are focused solely on the order Hymenoptera, and not its taxonomic “children”.) Users can search for species using either their Latin (scientific) or common (vernacular) names. For example, the user request “mockingbird” provides eight species names identified as mockingbird taxa, as seen in Figure 1B. Table 2 shows the taxonomic results of sample user queries (e.g., “blue whale”, “mockingbird”, “nikolay”, and “escherichia”), and their explanation.

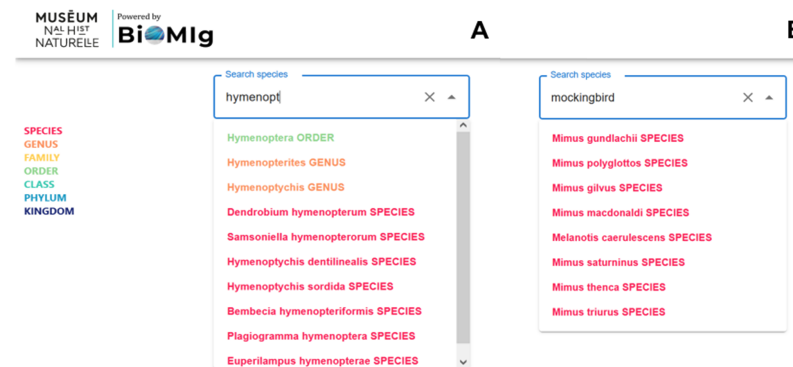


**Figure 1.** Search bar automatically suggests taxonomic terms associated with a query, covering both (A) scientific names and (B) vernacular names.

**Table 2.** Illustration of how the search bar helps the user navigate taxonomic data, depending on the type of request.

User Request	Propositions of the Research Bar	Explanation of the Result
“blue whale”	<i>Balaenoptera musculus</i> , <i>Prionace glauca</i>	two taxa associated with the vernacular name “blue whale”
“mockingbird”	<i>Mimus gundlachi</i> , <i>Mimus polyglottos</i> , <i>Mimus macdonaldi</i> , <i>Mimus gilvus</i> , <i>Melanotis caerulescens</i> , <i>Mimus saturninus</i> , <i>Mimus triurus</i> , <i>Mimus thenca</i>	eight species associated with the vernacular “mockingbird”
“nikolay”	<i>Bolinichthys nikolayi</i> , <i>Chersodromia nikolayi</i> , <i>Melamphaes nikolayi</i> , <i>Stauroneis nikolayi</i> , <i>Conterinia nikolayi</i> , <i>Prodalmanitina nikolayevi</i> , <i>Pseudepipona nikolayi</i>	seven taxa whose specific epithet contain “nikolay”
“escherichia”	<i>Escherichia</i> (Genus), <i>Escherichia hermannii</i> , <i>Escherichia vulneris</i> , <i>Escherichia fergusonii</i> , <i>Escherichia albertii</i> , <i>Escherichia marmotae</i> , <i>Escherichia ruysiae</i> , <i>Escherichia coli</i>	exact match with genus and generic names

For a given query or set of queries, an accompanying diagram is created that allows the user to locate their taxa in the “tree of life”. This dynamic taxonomic representation is based on the GBIF taxonomic backbone. For example, let us say a user is interested in exploring the taxonomy of insect species that could inspire the management of heat and light, in this case bees and ants [39,40]. Following the user’s query for the bee *Megachile kalina*, a linear taxonomic diagram is created, presenting its taxonomic “location” in Figure 2A. Subsequently, five other species of the genus *Megachile* were searched for (Figure 2B) with Bioinspire-Explore showing the taxonomic connections between these “new” species and the “original” species *Megachile kalina*. The user then enters a new query, this time for the species of desert ant *Cataglyphis bombycina*. Bioinspire-Explore “remembers” the previous searches (unless the clear button is used in between queries) and adds this species’ taxonomy, leading to a bifurcation in the diagram seen in Figure 2C. These taxonomic diagrams are exportable as a PNG files that the user can then download.



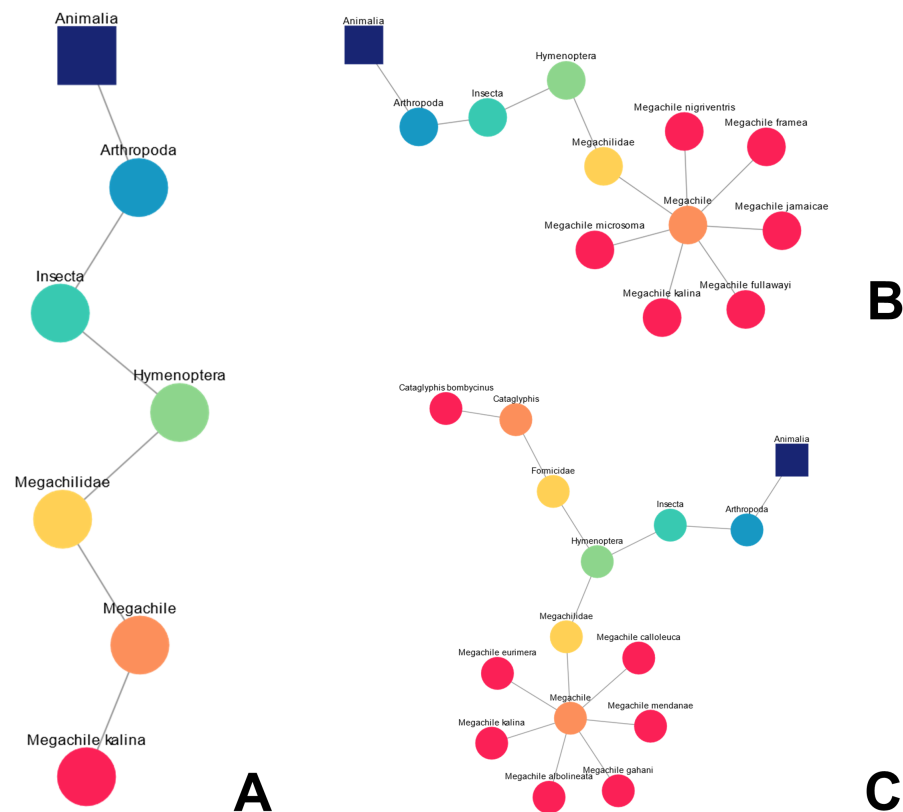


**Figure 2.** Examples of dynamic taxonomic diagrams following multiple queries associated with bees. (A) Linear diagram created after single search for the bee species *Megachile kalina*; (B) expansion of the “taxonomic children” of the genus *Megachile*; (C) subsequent search for the desert ant species *Cataglyphis bombycinus*.

### 3.2. Biological and Environmental Data

A great deal of biological and environmental data are freely available online. However, at present, exploring this information involves going back and forth between different websites, which can be time consuming and distracting. Bioinspire-Explore has been designed as a “one stop shop” connecting multiple external open-access data sources via a taxon’s name.

Figure 3 shows the results of a query for *Arnica montana*, a flowering plant species found in western Europe. The first window displays the first paragraph and first image of the Wikipedia page associated with Wikidata node for the species Q207848 (<https://www.wikidata.org/wiki/Q207848> (accessed on 1 January 2023)). If the Wikidata graph is missing a node for the taxon in question, this window will be empty. An external link will then automatically search for the taxon name in Wikipedia to provide associated data for this window. The second window, seen in Figure 3B, shows occurrence data for *Arnica montana*, plotted on a world map (with an option to zoom in and out, depending on the scale of interest). Figure 3C displays iNaturalist images tagged with *Arnica montana*. By clicking on an image, the user will be led to the iNaturalist website. Figure 3D shows the average climatic conditions, as well as minimums and maximums, for *Arnica montana*, as found under the fourth window. Windows 3 and 4 aim to provide information on a taxon’s environmental context, highlighting the abiotic conditions to which it is adapted (temperature, rainfall, sun exposure, wind speed, etc.).

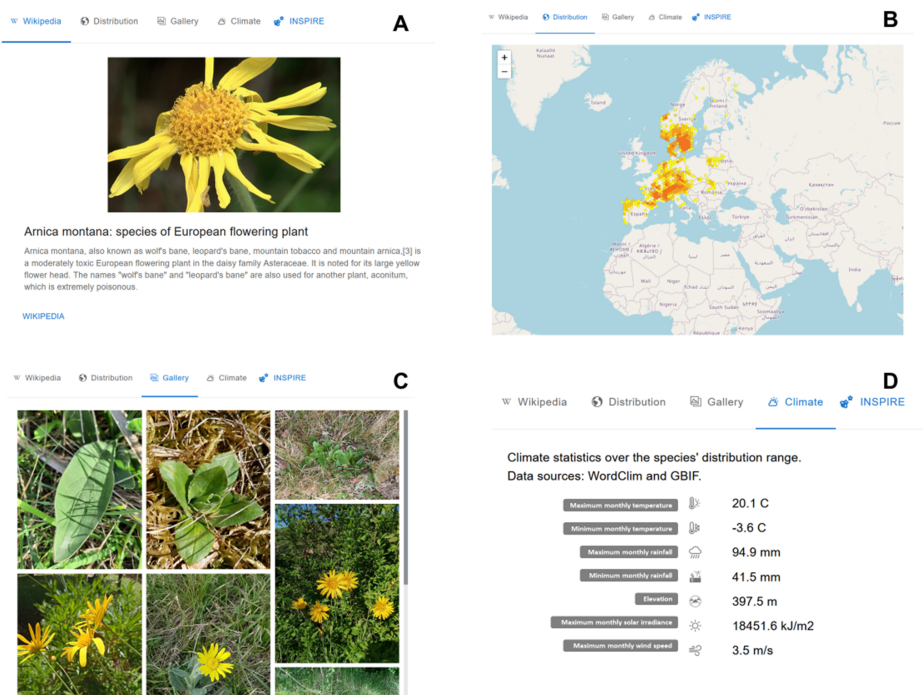


**Figure 3.** Four main types of information are provided through Bioinspire-Explore for a selected taxon *Arnica montana*. (A) Its Wikipedia page, (B) spatial distribution, (C) images, and (D) climate characteristics.

3.3. Semantic Proximity between Biological Entities

As outlined, Tchakarov et al. 2023 [36] developed a neural network model Word2Vec [35] based on a corpus of scientific articles judged relevant for bioinspiration (the “BIOMIG Corpus”). Using this model, Bioinspire-Explore is able to assess the semantic proximity of text entities (taxon, biological process, habitat, physical measurements) stored as word “embeddings” within this scientific corpus. These entities were chosen as being the most relevant in the context of a “biology push” approach to bioinspiration, providing users with ideas in terms biological processes, functions, structures, and systems of potential interest for innovation (see examples in Table 3).

**Table 3.** Examples of entities related to two taxa queries *Vespa soror* and *Morpho menelaus*.

User Request	Taxon	Process	Habitat	Measure
<i>Vespa soror</i>	<i>Platygastridae</i> , <i>Argidae</i> , <i>Theroa zethus</i>	hunting, swarm, autothysis	plant, tropical, meadow	heat, frequency, length
<i>Morpho menelaus</i>	<i>Greta oto</i> , <i>Papilio ulysses</i> , <i>Callophrys rubi</i>	polyphenism, colouration, flying	feather, desert, meadow	angle, heat, hydrophobicity

Figure 4A presents a more detailed example of how these text embeddings, and the evaluation of their semantic proximity with the scientific corpus, work in practice. Here, seven text entities are represented as vectors in a fictive 3D-space: three taxon names (“*Pica pica*”, “*Corvus corone*”, and “*Vespa soror*”); two biological processes (“diving” and “swarming”); and two habitat characteristics (“forest” and “tropical”).

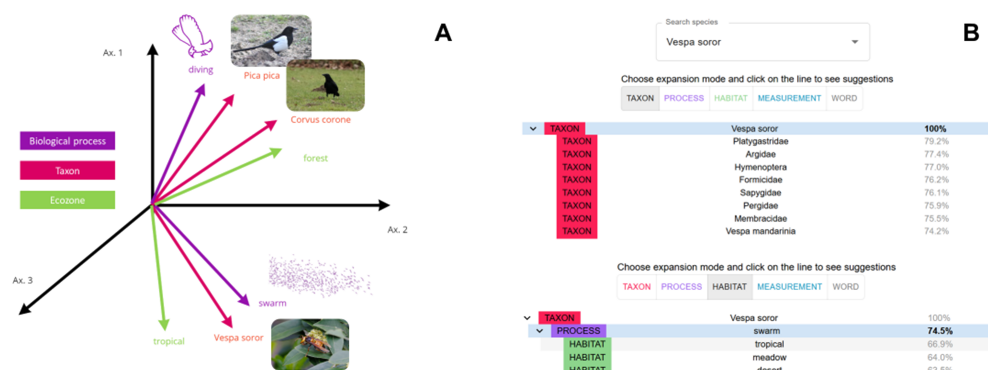


**Figure 4.** (A) Schematic illustration of semantic proximity of various types of entities “taxon”, “ecozone/habitat”, “biological process”; (B) screenshot of the semantic expansion module in Bioinspire-Explore. Here, the taxon entity *Vespa soror* appears semantically related to other taxa such as Hymenoptera.

The taxon entities *Pica pica* and *Corvus corone* are represented as close vectors, because both these taxa belonging to the Corvidae family. The Asian wasp *Vespa soror* is represented as a vector with more distant coordinates from the two Corvidae, as their phylogenetic relationship is further apart. The biological process “swarm” is shown to be semantically closer to the *Vespa soror* than to the two Corvidae. This is because swarming is a behaviour typically associated with this wasp (rather than Corvidae), and the scientific literature reflects this. Conversely, “diving” is more likely to be found in Corvidae than *Vespa soror*, and therefore appears closer to the two birds. In terms of habitat characteristics, the entity “tropical” is directionally closer to the text embedding of *Vespa soror* than to the Corvidae, as the latter live in temperate climates of western Europe.

How are the results of this neural network model presented within Bioinspire-Explore? In Figure 4B, we show two screenshots of the “Biodiversity” page within Bioinspire-Explore, where the concept of semantic proximity between taxa, biological processes, habitats, or measurements is explored. In the first screenshot, we explore entities related to our wasp *Vespa soror*. We start with the “taxon” tab to understand how this wasp is connected to other taxa within the scientific literature. As to be expected, the model indicates greatest semantic proximity with other insect families of the order Hymenoptera, such as Platygasteridae, Sapygidae, Pergidae, or Argidae. By clicking on the “Process” tab, we find the biological process “swarm” with a 74.5% semantic proximity to *Vespa soror*. Selecting this process, we are interested in understanding the proximity of the “Habitat” entities connected to both *Vespa soror* and swarming behaviour. This is shown in the second screenshot of Figure 4B. Having been asked for habitats semantically close to both *Vespa soror* and swarm, Bioinspire-Explore cites “tropical”, “meadow”, and “desert” as related entities. The compatibility scores between this trio of habitat entities are 67%, 64%, and 63.5%, respectively. This means that, in the scientific literature (BIOMIG Corpus) used by the Bioinspire-Explore model, connections between swarming (process) of *Vespa soror* (taxon) in tropical areas (habitat) appear to be the most significant, with a combined score of 67%.

### 3.4. An Example “User Journey” in Bioinspire-Explore

Figure 5 presents how a user might explore the Bioinspire-Explore tool. If they are new to the concept of bioinspiration, they may start by visiting the “Bioinspirations” page (Figure 5A) that presents a handful of existing initiatives in the field of bioinspired design (using images, videos, text, and references). Via this page, they might read about the navigational abilities of the desert ant *Cataglyphis fortis*. They decide they would like to learn more about this species via the “Biodiversity” page (being redirected automatically via the species name, or by typing its name directly into the search box). Figure 5B shows the information that is provided at this stage (as already described in Figure 2): the species taxonomic position, its appearance, its geographical distribution, and climatic niche.

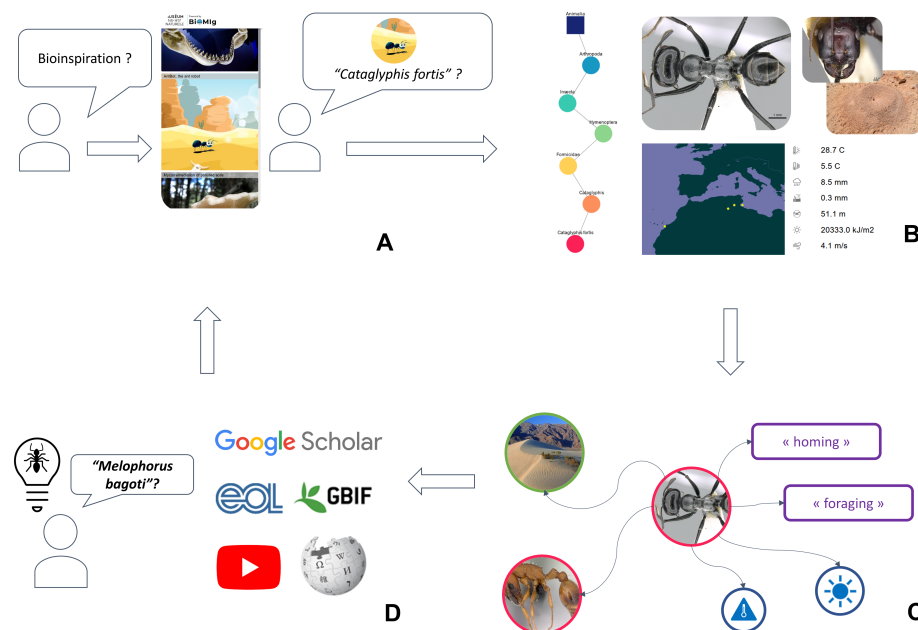


**Figure 5.** User journey within Bioinspire-Explore, illustrating the functionalities of different tabs within the tool: (A) visit of the “Bioinspirations” page presenting bioinspiration examples; (B) then moving to the “Biodiversity” page to learn more on a given taxon; (C) the “Go Further” page gives an overview of closely-related entities within the scientific literature; and (D) end of the user journey by either doing another research or using the pre-filled external links.

Finally, the user may wish to dive deeper via the “Go further” page in Bioinspire-Explore (Figure 5C), getting an overview of closely related entities within the scientific literature associated with *Cataglyphis fortis*. These insights usually lead the user either (i) to further research on the taxon in question (using other platforms (EOL, GBIF...)) or via the scientific articles presented in the Biomig Corpus) or (ii) to a new request about another taxon presenting a similar interest (for example, the user might identify the desert ant *Melophorus bagoti* as an alternative additional biological model for navigation).

## 4. Discussion

### 4.1. Bioinspire-Explore’s Audience

Bioinspire-Explore is an innovative new tool, providing a unique way to explore biodiversity data and visualise relationships between taxa as well as between entities of relevance to bioinspiration. Bioinspire-Explore’s focus is on a “biology-push” approach to bioinspiration, that is to say, the identification of biological systems of potential interest, the abstraction of their associated functions, followed by their transposition to a technical domain. However, Bioinspire-Explore could also be used to support of a “technology-pull” approach, as described by Fayemi et al. [41], i.e., once a team has transposed technological needs into biological functions, and is searching for biological models that fulfill those functions (See Figure 6).

The authors did not carry out a formalized process to generate scientifically robust user feedback for the first iteration of the Bioinspire-Explore tool. Bioinspire-Explore was, however, thoroughly tested with users from different institutions and communities on five separate occasions (three Masters courses and two scientific workshops) and received constructive feedback that fed into the project, either into the tool itself or this article. Future feedback will be collected via a dedicated email address.

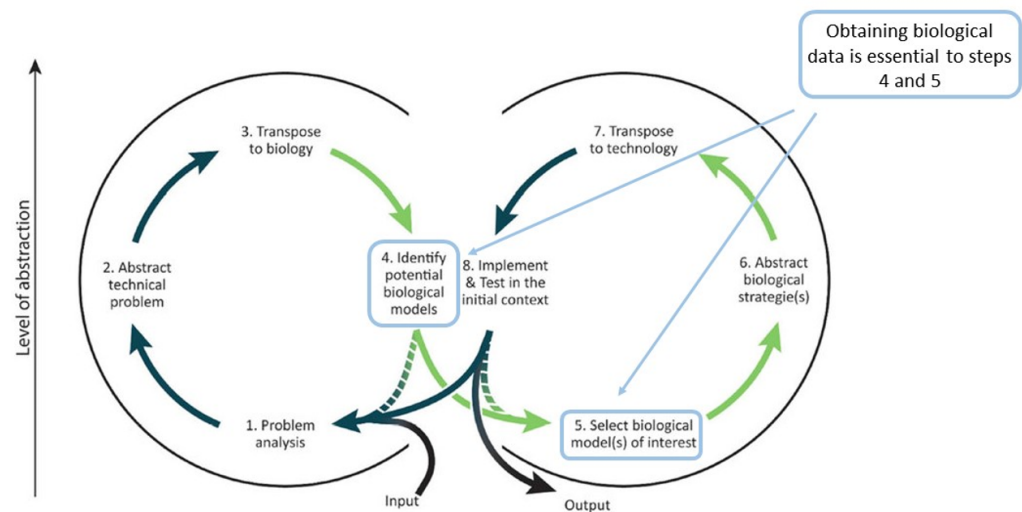


**Figure 6.** Possible uses Bioinspire-Explore within a biomimetic methodological framework. After Fayemi et al. (2017) [41].

Moreover, although designed to help bioinspiration practitioners, Bioinspire-Explore could also serve as an educational tool in many different settings. Not only does the tool facilitate access to biological data, it offers an interactive interface to “play” with taxonomic information and phylogenetic relationships. Over and above finding relevant data for a bioinspired project, Bioinspire-Explore helps users understand how life on earth is organised scientifically, putting bioinspiration into its biological context. Thus, Bioinspire-Explore could be used as a way to tackle both difficulties in understanding biology as well challenges associated with the transfer of knowledge from biology to technology, as identified by Wanieck et al. [42]: both obstacles within the bioinspiration field.

#### 4.2. Challenges and Next Steps

Bioinspire-Explore represents a first iteration in the development of an online “biology push” bioinspiration tool. As a prototype, it still faces challenges in terms of data sources and functionality. With regard to data sources, Bioinspire-Explore provides access to international biodiversity data via the most well recognised open access source: the Global Biodiversity Information Facility (GBIF). Despite the significant advantages associated with facilitating access to this vast dataset, Bioinspire-Explore’s connections with GBIF mean that its limitations are interwoven as well. In other words, Bioinspire-Explore’s data contain the same biases as GBIF’s, and the same challenges in terms of staying up to date with constant phylogenetic and taxonomic developments [43–46]. For example, if a species’ scientific name has recently changed, Bioinspire-Explore will present only those data relating to the new species’ name and not its previous name. This means that all data associated with its previous name are no longer available to users. The reverse also holds true, if taxonomic updates have not yet been made in GBIF, Bioinspire-Explore will relay nomenclature inconsistencies. Nevertheless, efforts are underway to improve the quality of GBIF data [47,48], and this will directly benefit the Bioinspire-Explore tool and its taxonomic accuracy.

Moreover, not all geographical areas covered by GBIF have the same density of data points [49,50]; nor do all taxonomic groups have equivalent amounts of data on their geographical distribution [20]. This affects the accuracy of climatic ranges of certain taxa calculated within Bioinspire-Explore, for example.

In terms of the bioinspiration literature that informs the analyses of semantic proximity metrics, the “BIOMIG corpus” is updated every three months with new literature relevant to bioinspiration. Although the BIOMIG corpus has been developed to include all pertinent scientific articles (even when they do not mention bioinspiration or biomimetics explicitly), this corpus cannot claim to be exhaustive: there will inevitably be published scientific literature useful to bioinspiration that is not automatically identified as such. Despite the regular updating of the BIOMIG corpus (every three months), the Word2Vec model, trained from this corpus, is static (and does not change). This is a deliberate choice of the development team. Indeed, the point of Word2Vec is to unravel the semantic meaning of entities (words), and the relationship between these entities, using a large number of sentences. Considering the extent of the BIOMIG corpus (several decades worth of scientific papers), a regular re-training of Word2Vec on an updated corpus would not provide significant changes in these semantic relationships between words. For example, the entity “*Morpho menelaus*” is currently related to “reflection” or to other butterfly taxa; in a year, the small amount of papers related to *Morpho* will not be a sufficient “signal” to modify this semantic proximity. That being said, we should indeed retrain the Word2Vec model every few years, or could even replace this semantic expansion tool with more costly Large Language models in the future.

Our intention is to continue to improve Bioinspire-Explore’s functionality and scope in the future, based on feedback following its use in educational and professional settings. Several possible avenues for its improvement already exist. From a functionality perspective, building the tool’s capacity for non-taxa entry points is one priority. Presently, Bioinspire-Explore’s capability lies chiefly in the assessment of semantic proximity between a taxon (as the starting point) and other entities (biological processes, physical measures, and habitats) in the scientific literature. For now, starting a search with one of these other entities provides less obvious results in terms of connections in the scientific literature. For example, if one were to begin a search with “energy” as a physical measurement, and then “photo-protection” as a biological process, the results in terms of semantic proximity linking these entities to specific taxa are weak. This currently limits the ability of a bioinspired designer to pursue “property-led” rather than “taxon-led” research.

In terms of climate data, Bioinspire-Explore uses the last available “snapshot” of the WorldClim database, issued in 2020, and covering the 1970 to 2000 period of time. We are aware of the limitations of this database’s scope and the importance of having up-to-date relationships between taxa and their precise climatic conditions. This aspect could be improved in future iterations of the tool.

In terms of the potential integration of new datasets into Bioinspire-Explore, two types of information stand out: morphological and palaeontological. Morphological descriptions are those used to identify living organisms, presenting their specific structures and characteristics. These properties are closely linked to an organism’s function, and therefore of potential interest to bioinspiration practitioners. Bioinspire-Explore could be expanded to include morphological (and anatomical) knowledge extracted from relevant scientific literature via AI text analysis methods. This information could be presented in the form of graphs or RDF triplets, for example, as proposed by Sahraoui et al. [51].

Finally, palaeo-bioinspiration is a growing field [52], and one that requires access to information about species from previous geological epochs. The biodiversity data available through Bioinspire-Explore are currently based on a classification system that does not fully take into account the fossil record. Although international, open-access palaeobiodiversity databases exist [53], their utilisation would require the harmonious integration of the classification of fossils with that of current species. Presently, integrating the multiple branches of fossil lineages at higher taxonomic levels pose both theoretical and technical challenges; these difficulties would need to be evaluated and resolved before a unified catalogue of past and present biodiversity could be made available through Bioinspire-Explore. The tool is currently being tested by Masters and PhD students as part of their bioinspired design curricula, as well as professionals within the bioinspiration domain.



Their user feedback will provide insight on the functional, visual, and ergonomic choices made by Bioinspire-Explore's development team. Particular attention will be given to improving the semantic expansion tool to assess whether it is understood, intuitive, and useful in the application of bioinspiration.

## 5. Conclusions

In a context of growing environmental challenges, professionals are increasingly looking to the living world to provide inspiration for more sustainable alternatives to today's systems. Bioinspire-Explore's principle audience is this new generation of designers, engineers, chemists, architects, urban planners, and more. It can be operated by a single user, but can also facilitate interaction between different disciplines in a group setting. Crucially, Bioinspire-Explore is intended to act as a guide, not as a replacement for the active involvement of biologists in bioinspiration projects [31,54]. Rather, it orientates the user towards promising information regarding living systems of interest and presents those systems in their scientific context. It offers relevant scientific literature to bioinspiration practitioners seeking stimulus for many different variants of bioinspiration [34]: for example, exploring properties of biological materials to support biofabrication/bioprocess engineering initiatives; or identifying ecological characteristics of taxa that could be integrated into nature based solutions. Bioinspire-Explore is a powerful tool for browsing and visualizing biological data, using taxonomy as an entry point. The platform's user-friendly interface and comprehensive databases make it an accessible way to explore biological data, particularly as part of a "biology push" approach to bioinspiration, and provide meaningful insights into the diversity and evolution of life on earth. Its unique value lies in its ability to combine, within a single tool (i) taxonomic data; (ii) ecological information; and (iii) indications of the semantic proximity of terms ("entities") cited in bioinspiration-related literature. In the future, we anticipate that Bioinspire-Explore will continue to evolve and improve, with the addition of new features, functionality, and datasets in order to respond to the growing ambitions of the bioinspiration community.

**Author Contributions:** Conceptualization, A.S.-S., A.A., R.V.-L., J.-S.S., T.B., L.-M.P. and N.T.; methodology, L.-M.P., A.S.-S. and A.A.; software, N.T.; validation, A.A., A.S.-S., J.-S.S., T.B. and R.V.-L.; formal analysis, N.T. and A.S.-S.; investigation, all authors; resources, T.B. and R.V.-L.; data curation, N.T.; writing—original draft preparation, A.S.-S., A.A. and R.V.-L.; writing—review and editing, A.S.-S. and A.A.; visualization, A.S.-S., A.A. and N.T.; supervision, J.-S.S., A.S.-S. and A.A.; project administration, A.A.; funding acquisition, A.S.-S., A.A., R.V.-L., J.-S.S. and T.B. All authors have read and agreed to the published version of the manuscript.

**Funding:** We hereby acknowledge the financial support of the French Government's "France Relance" programme, which financed the creation of Bioinspire-Explore via the ITN5 "12-363-DNUM-CENS-0030" project coordinated by the French Inter-ministerial Directorate for Digital Technology. This project is co-financed by the European Union as part of the NEXT GEN EU plan.

**Data Availability Statement:** The data presented in this study are openly available in GitHub at <https://github.com/ceebios/Bioinspire-Explore-app> (accessed on 1 January 2024).

**Acknowledgments:** We sincerely thank Chrystelle Roger from Myceco for her vision, time, and invaluable advice on setting up and running the ITN5 project. Our thanks also go to Théo Alves DaCosta and the "Data for Good" Association for their contribution to Bioinspire-Explore's first iteration. The BIOMIG corpus of scientific literature was kindly provided by the BIOMIG Consortium and CEEBIOS. We would also like to thank those who tested Bioinspire-Explore during its development, including the "Nature Inspired Design" Masters students from ENSCI-Les Ateliers, Paris. The Bioinspire-Explore project won an innovation purchasing award from the French State's Purchasing Division in 2023. We thank our colleagues at the MNHN for supporting our submission for this award and are grateful for the national recognition it confers.

**Conflicts of Interest:** The authors declare no conflicts of interest.

## References

1. ISO 18458:2015; Biomimetics: Terminology, Concepts and Methodology. ISO: Geneve, Switzerland, 2015.
2. Shao, H.; Bachus, K.N.; Stewart, R.J. A Water-Borne Adhesive Modeled after the Sandcastle Glue of *P. californica*. *Macromol. Biosci.* **2009**, *9*, 464–471. [CrossRef] [PubMed]
3. Jones, J.; Adamatzky, A. Computation of the travelling salesman problem by a shrinking blob. *Nat. Comput.* **2014**, *13*, 1–16. [CrossRef]
4. Dupeyroux, J.; Serres, J.R.; Viollet, S. AntBot: A six-legged walking robot able to home like desert ants in outdoor environments. *Sci. Robot.* **2019**, *4*, eaau0307. [CrossRef] [PubMed]
5. Cruz, E. Biomimétisme: Le vivant, une bibliothèque pour l'innovation. *Technica* **2018**, *1*, 15–22.
6. Boucle, S.P.; Boutin, C. Compte-Rendu Commenté de la Visite de la ZRV de St Just (34) (Zone Libellule). HAL. 2015. Available online: <https://agris.fao.org/search/en/providers/122439/records/64747234425ec3c088f288ee> (accessed on 1 January 2024).
7. Mthunzi, S.N.; Benkhelifa, E.; Bosakowski, T.; Hariri, S. A Bio-inspired Approach to Cyber Security. In *Machine Learning for Computer and Cyber Security*, 1st ed.; A Science Publishers Book; Gupta, B.B., Sheng, M., Eds.; CRC Press: Boca Raton, FL, USA; Taylor & Francis Group: Abingdon, UK, 2019; pp. 75–104. [CrossRef]
8. Lechner, M.; Hasani, R.; Amini, A.; Henzinger, T.A.; Rus, D.; Grosu, R. Neural circuit policies enabling auditable autonomy. *Nat. Mach. Intell.* **2020**, *2*, 642–652. [CrossRef]
9. Vasileiou, T.; Summerer, L. A biomimetic approach to shielding from ionizing radiation: The case of melanized fungi. *PLoS ONE* **2020**, *15*, e0229921. [CrossRef]
10. Ellery, A. Tutorial Review of Bio-Inspired Approaches to Robotic Manipulation for Space Debris Salvage. *Biomimetics* **2020**, *5*, 19. [CrossRef]
11. Xu, B.; Yang, Y.; Zhang, B. Bionics design and dynamics analysis of space webs based on spider predation. *Acta Astronaut.* **2019**, *159*, 294–307. [CrossRef]
12. Müller, R.; Abaid, N.; Boreyko, J.B.; Fowlkes, C.; Goel, A.K.; Grimm, C.; Jung, S.; Kennedy, B.; Murphy, C.; Cushing, N.D.; et al. Biodiversifying bioinspiration. *Bioinspir. Biomimetics* **2018**, *13*, 053001. [CrossRef]
13. Hayes, S.; Desha, C.; Baumeister, D. Learning from nature—Biomimicry innovation to support infrastructure sustainability and resilience. *Technol. Forecast. Soc. Chang.* **2020**, *161*, 120287. [CrossRef]
14. Bánki, O.; Roskov, Y.; Döring, M.; Ower, G.; Hernández Robles, D.R.; Plata Corredor, C.A.; Stjernegaard Jeppesen, T.; Örn, A.; Vandepitte, L.; Hobern, D.; et al. *Catalogue of Life Checklist*; Leiden, The Netherlands, 2023. Available online: <https://biss.pensoft.net/article/111684/> (accessed on 1 January 2024).
15. Mitov, M. Cholesteric liquid crystals in living matter. *Soft Matter* **2017**, *13*, 4176–4209. [CrossRef] [PubMed]
16. Sivasankaran, P.N.; Ward, T.A.; Viyapuri, R.; Johan, M.R. Static strength analysis of dragonfly inspired wings for biomimetic micro aerial vehicles. *Chin. J. Aeronaut.* **2016**, *29*, 411–423. [CrossRef]
17. Audibert, C.; Chaves-Jacob, J.; Linares, J.M.; Lopez, Q.A. Bio-inspired method based on bone architecture to optimize the structure of mechanical workpieces. *Mater. Des.* **2018**, *160*, 708–717. [CrossRef]
18. Graeff, E.; Maranzana, N.; Aoussat, A. Biological practices and fields, the missing pieces of the biomimetics' methodological puzzle. *Biomimetics* **2020**, *5*, 62. [CrossRef] [PubMed]
19. Kim, S.J.; Lee, J.H. A study on metadata structure and recommenders of biological systems to support bio-inspired design. *Eng. Appl. Artif. Intell.* **2017**, *57*, 16–41. [CrossRef]
20. Troudet, J.; Grandcolas, P.; Blin, A.; Vignes-Lebbe, R.; Legendre, F. Taxonomic bias in biodiversity data and societal preferences. *Sci. Rep.* **2017**, *7*, 9132. [CrossRef] [PubMed]
21. Cruz, E.; Hubert, T.; Chancoco, G.; Naim, O.; Chayaamor-Heil, N.; Cornette, F.; Menezo, C.; Badarnah, L.; Raskin, K. Design processes and multi-regulation of biomimetic building skins: A comparative analysis. *Energy Build.* **2021**, *246*, 111034. [CrossRef]
22. Deldin, J.; Schuknecht, M. The AskNature Database: Enabling Solutions in Biomimetic Design. In *Biologically Inspired Design*; Springer: Berlin/Heidelberg, Germany, 2014; pp. 17–27.
23. Shyam, V.; Friend, L.; Whiteaker, B.; Bense, N.; Dowdall, J.; Boktor, B.; Johnny, M.; Reyes, I.; Naser, A.; Sakhamuri, N.; et al. PeTaL (Periodic Table of Life) and Physiometrics. *Designs* **2019**, *3*, 43. [CrossRef]
24. Vincent, J.F. The trade-off: A central concept for biomimetics. *Bioinspired Biomim. Nanobiomater.* **2017**, *6*, 67–76. [CrossRef]
25. Kruiper, R. Trade-offs in Computer-aided Biomimetics. In *Engineering Conferences International Proceedings*; 2019. Available online: [https://dc.engconfintl.org/nature\\_inspired/10/](https://dc.engconfintl.org/nature_inspired/10/) (accessed on 1 January 2024).
26. Chiu, I.; Shu, L.H. Bridging Cross-Domain Terminology for Biomimetic Design. In *Proceedings of the Volume 5a: 17th International Conference on Design Theory and Methodology*, Long Beach, CA, USA, 24–28 September 2005; Volume 2005, pp. 93–101. [CrossRef]
27. Chakrabarti, A.; Sarkar, P.; Leelavathamma, B.; Nataraju, B. A functional representation for aiding biomimetic and artificial inspiration of new ideas. *AI EDAM* **2005**, *19*, 113–132. [CrossRef]
28. Nagel, J.K.S.; Stone, R.B.; McAdams, D.A. An Engineering-to-Biology Thesaurus for Engineering Design. In *Proceedings of the Volume 5: 22nd International Conference on Design Theory and Methodology*, Special Conference on Mechanical Vibration and Noise, Montreal, QC, Canada, 15–18 August 2010; pp. 117–128. [CrossRef]

29. McNerney, S.; Khakipoor, B.; Garner, A.; Houette, T.; Unsworth, C.; Rupp, A.; Weiner, N.; Vincent, J.; Nagel, J.; Niewiarowski, P. E2BMO: Facilitating User Interaction with a BioMimetic Ontology via Semantic Translation and Interface Design. *Designs* **2018**, *2*, 53. [CrossRef]
30. Troudet, J.; Vignes-Lebbe, R.; Grandcolas, P.; Legendre, F. The Increasing Disconnection of Primary Biodiversity Data from Specimens: How Does It Happen and How to Handle It? *Syst. Biol.* **2018**, *67*, 1110–1119. [CrossRef] [PubMed]
31. Lecointre, G.; Aish, A.; Améziane, N.; Chekchak, T.; Goupil, C.; Grandcolas, P.; Vincent, J.F.V.; Sun, J.S. Revisiting Nature's "Unifying Patterns": A Biological Appraisal. *Biomimetics* **2023**, *8*, 362. [CrossRef] [PubMed]
32. Graeff, E. Biomimetics from practical feedback to an interdisciplinary process. *Res. Eng. Des.* **2021**, *32*, 349–375. [CrossRef]
33. Letard, A.; Maranzana, N.; Brun, J.; Raskin, K.; Aoussat, A. Biomimetics practice in industrial context: Methodological parameters to promote interdisciplinary collaboration and knowledge transfer. *Creat. Innov. Manag.* **2024**, *unpublished, under revision*.
34. Aish, A.; Sun, J.S. Bioinspire-Museum: Scoping Paper. Muséum National d'Histoire Naturelle, Paris, 24 Pages. 2020. Available online: [https://www.mnhn.fr/sites/mnhn.fr/files/atoms/files/bioinspire\\_museum\\_scoping\\_paper.pdf](https://www.mnhn.fr/sites/mnhn.fr/files/atoms/files/bioinspire_museum_scoping_paper.pdf) (accessed on 1 January 2023).
35. Mikolov, T.; Yih, W.t.; Zweig, G. Linguistic Regularities in Continuous Space Word Representations. In Proceedings of the NAACL, Atlanta, GA, USA, 9–14 June 2013.
36. Tchakarov, N.; Racca, L.; Peybernes, T.; Saint-Sardos, A. A Scientific Corpus and Search Engine for Biomimetics. *SSRN Electron. J.* **2023**. [CrossRef]
37. Secretariat, G. GBIF Backbone Taxonomy. Checklist Dataset. 2022. Available online: <https://www.gbif.org/dataset/d7dddbf4-2cf0-4f39-9b2a-bb099caae36c> (accessed on 1 January 2023).
38. Buttigieg, P.; Morrison, N.; Smith, B.; Mungall, C.J.; Lewis, S.E.; The ENVO Consortium. The environment ontology: Contextualising biological and biomedical entities. *J. Biomed. Semant.* **2013**, *4*, 43. [CrossRef]
39. Willot, Q.; Simonis, P.; Vigneron, J.P.; Aron, S. Total Internal Reflection Accounts for the Bright Color of the Saharan Silver Ant. *PLoS ONE* **2016**, *11*, e0152325. [CrossRef]
40. Wang, Y.; Shang, S.; Chiu, K.I.; Jiang, S. Mimicking Saharan silver ant's hair: A bionic solar heat shielding architextile with hexagonal ZnO microrods coating. *Mater. Lett.* **2020**, *261*, 127013. [CrossRef]
41. Fayemi, P.E.; Wanieck, K.; Zollfrank, C.; Maranzana, N.; Aoussat, A. Biomimetics: Process, tools and practice. *Bioinspir. Biomimetics* **2017**, *12*, 011002. [CrossRef]
42. Wanieck, K.; Ritzinger, D.; Zollfrank, C.; Jacobs, S. Biomimetics: Teaching the tools of the trade. *FEBS Open Bio.* **2020**, *10*, 2250–2267. [CrossRef] [PubMed]
43. Meyer, C.; Weigelt, P.; Kreft, H. Multidimensional biases, gaps and uncertainties in global plant occurrence information. *Ecol. Lett.* **2016**, *19*, 992–1006. [CrossRef] [PubMed]
44. Waller, J. Finding Data Gaps in the GBIF Backbone Taxonomy. *Biodivers. Inf. Sci. Stand.* **2022**, *6*, e91312. [CrossRef]
45. Smith, B.E.; Johnston, M.K.; Lücking, R. From GenBank to GBIF: Phylogeny-Based Predictive Niche Modeling Tests Accuracy of Taxonomic Identifications in Large Occurrence Data Repositories. *PLoS ONE* **2016**, *11*, e0151232. [CrossRef] [PubMed]
46. Bourgoin, T.; Bailly, N.; Zaragueta, R.; Vignes-Lebbe, R. Complete formalization of taxa with their names, contents and descriptions improves taxonomic databases and access to the taxonomic knowledge they support. *Syst. Biodivers.* **2021**, *19*, 738–746. [CrossRef]
47. Zizka, A.; Antunes Carvalho, F.; Calvente, A.; Rocio Baez-Lizarazo, M.; Cabral, A.; Coelho, J.F.R.; Colli-Silva, M.; Fantinati, M.R.; Fernandes, M.F.; Ferreira-Araújo, T.; et al. No one-size-fits-all solution to clean GBIF. *PeerJ* **2020**, *8*, e9916. [CrossRef]
48. Secretariat, G. GBIF to Serve as Administrative Host for Species 2000 Secretariat. 2024. Available online: <https://www.gbif.org/news/5LO3xYHTbo53rB8UwcSpG/gbif-to-serve-as-administrative-host-for-species-2000-secretariat> (accessed on 16 January 2024).
49. Beck, J.; Böller, M.; Erhardt, A.; Schwanghart, W. Spatial bias in the GBIF database and its effect on modeling species' geographic distributions. *Ecol. Inform.* **2014**, *19*, 10–15. [CrossRef]
50. García-Roselló, E.; González-Dacosta, J.; Lobo, J.M. The biased distribution of existing information on biodiversity hinders its use in conservation, and we need an integrative approach to act urgently. *Biol. Conserv.* **2023**, *283*, 110118. [CrossRef]
51. Sahraoui, M.; Pignal, M.; Vignes Lebbe, R.; Guigue, V. NEARSIDE: Structured kNoWledge Extraction frAmework from SpecIes DEscriptions. *Biodivers. Inf. Sci. Stand.* **2022**, *6*, e94297. [CrossRef]
52. Aish, A. Palaeo-Bioinspiration: Drawing on the Fossil Record to Advance Innovation. 2024, *in press*. Available online: <https://palaeo-bioinsp.sciencesconf.org/> (accessed on 1 January 2024).
53. Alroy, J. The Paleobiology Database. 2021. Available online: <https://paleobiodb.org/#/> (accessed on 1 January 2024).
54. Graeff, E.; Maranzana, N.; Aoussat, A. Engineers' and Biologists' Roles during Biomimetic Design Processes, towards a Methodological Symbiosis. *Proc. Des. Soc. Int. Conf. Eng. Des.* **2019**, *1*, 319–328. [CrossRef]

**Disclaimer/Publisher's Note:** The statements, opinions and data contained in all publications are solely those of the individual author(s) and contributor(s) and not of MDPI and/or the editor(s). MDPI and/or the editor(s) disclaim responsibility for any injury to people or property resulting from any ideas, methods, instructions or products referred to in the content.



## Article

# Target-Following Control of a Biomimetic Autonomous System Based on Predictive Reinforcement Learning

Yu Wang <sup>1</sup>, Jian Wang <sup>2,3</sup> , Song Kang <sup>2,3</sup> and Junzhi Yu <sup>2,4,\*</sup>

- <sup>1</sup> Department of Automation, Tsinghua University, Beijing 100084, China; yu\_wang@tsinghua.edu.cn  
<sup>2</sup> The Laboratory of Cognitive and Decision Intelligence for Complex System, Institute of Automation, Chinese Academy of Sciences, Beijing 100190, China; jianwang@ia.ac.cn (J.W.)  
<sup>3</sup> The School of Artificial Intelligence, University of Chinese Academy of Sciences, Beijing 100049, China  
<sup>4</sup> The State Key Laboratory for Turbulence and Complex Systems, Department of Advanced Manufacturing and Robotics, College of Engineering, Peking University, Beijing 100871, China  
\* Correspondence: junzhi.yu@ia.ac.cn

**Abstract:** Biological fish often swim in a schooling manner, the mechanism of which comes from the fact that these schooling movements can improve the fishes' hydrodynamic efficiency. Inspired by this phenomenon, a target-following control framework for a biomimetic autonomous system is proposed in this paper. Firstly, a following motion model is established based on the mechanism of fish schooling swimming, in which the follower robotic fish keeps a certain distance and orientation from the leader robotic fish. Second, by incorporating a predictive concept into reinforcement learning, a predictive deep deterministic policy gradient-following controller is provided with the normalized state space, action space, reward, and prediction design. It can avoid overshoot to a certain extent. A nonlinear model predictive controller is designed and can be selected for the follower robotic fish, together with the predictive reinforcement learning. Finally, extensive simulations are conducted, including the fix point and dynamic target following for single robotic fish, as well as cooperative following with the leader robotic fish. The obtained results indicate the effectiveness of the proposed methods, providing a valuable sight for the cooperative control of underwater robots to explore the ocean.



**Citation:** Wang, Y.; Wang, J.; Kang, S.; Yu, J. Target-Following Control of a Biomimetic Autonomous System Based on Predictive Reinforcement Learning. *Biomimetics* **2024**, *9*, 33. <https://doi.org/10.3390/biomimetics9010033>

Academic Editor: Jinyou Shao

Received: 13 November 2023

Revised: 16 December 2023

Accepted: 2 January 2024

Published: 4 January 2024



**Copyright:** © 2024 by the authors. Licensee MDPI, Basel, Switzerland. This article is an open access article distributed under the terms and conditions of the Creative Commons Attribution (CC BY) license (<https://creativecommons.org/licenses/by/4.0/>).

**Keywords:** biomimetic motion; biomimetic autonomous system; target following; deep reinforcement learning; predictive control

## 1. Introduction

With the rapid development of science and technology, the field of biomimetics has witnessed substantial advance in recent years, garnering widespread attention from researchers globally. With a long history of natural evolution, biological fish have acquired remarkable motion capabilities. They demonstrate proficiency in executing various acrobatic maneuvers, including rapid start and stop, inter-media leaping, and other sophisticated actions. Additionally, natural fish can achieve hydrodynamic drag reduction and energy efficiency through the utilization of diverse biological mechanisms.

Inspired by nature, the biomimetic robotic fish has attracted the attention of many scientists and engineers [1–6]. Katzschmann et al. designed a new kind of soft robotic fish named Sofi, which can interact with remote control personnel through ultrasonic communication module and realize the close observation of underwater organisms with a maximum diving depth of 18 m [1]. By mimicking yellowfin tuna, White et al. developed a series of high-speed biomimetic robotic tuna [7,8], and achieved tail-fin flapping frequencies of up to 15 Hz. To quantify the role of body flexibility in high-speed swimming, they further presented Tunabot Flex, which could achieve a high swimming speed of 4.6 BL/s (body length per second, BL/s) at a swing frequency of 8 Hz. Yu et al. designed a robotic dolphin. Based on the motion control strategies, a high swimming speed of 2.05 m/s (2.85 BL/s)

was achieved, and the action of repetitive leaping similar to that of biological dolphins was completed [9]. Compared with the traditional autonomous underwater vehicles (AUVs), the biomimetic robotic fish has the advantages of high maneuverability, strong concealment, and better biocompatibility. These attributes underscore their considerable potential for application across diverse domains.

More importantly, by learning the motion mechanism of biological fish, the movement performance of the robotic fish can be further improved, e.g., by using fish schooling movement to save energy. It is hypothesized that fish schooling movements can improve the hydrodynamic efficiency via a certain swimming mode [10]. In a school of fish, the leader fish tend to consume more energy than the follower fish. The eddy current generated by the tail of leader fish can provide a certain amount of water power to the follower, thus achieving the effect of energy saving. This movement has a similar phenomenon in birds. As a result, biological fish tend to travel in flocks for long-distance voyages. Many researchers have investigated the fish schooling mechanism. Li et al. focused on how the fish plan their movement to save energy and achieve larger thrust from the vortices generated by others [11,12]. They designed some bionic robotic fish to measure the energy consumption when the robotic fish swim in the pool. Further, a vortex phase-matching strategy was obtained, indicating that the schooling fish exhibited a tailbeat phase difference that varied linearly with front-back distance. They also found that when the fish swim side by side, an individual could improve its efficiency if they changed the tailbeat phase to a certain angle, such as  $0.25\pi$ . By measuring the actual movement of 15 fish, Marras et al. found that compared with the individual swimming, the schooling fish in any position can save energy, and the fish swimming behind the neighbours showed the best performance [13]. Thandiackal et al. conducted an interesting experiment to observe the movement of natural trout when it interacted with the thrust wakes via a robotic mechanism. The results illustrated that the trout exhibited reduced pressure drag, further proving the energy saving [14]. Li et al. investigated the pressure and vorticity fields between a single fish and a pair of fish, and offered some results. However, there are insufficient conclusions about motion benefits of fish schooling [15]. Dai et al. investigated a variety of stable formations with the schooling of two, three and four self-propelled fish-like swimmers, and examined the energy efficiency of each formation [16]. Verma et al. explained the energy-saving mechanism in the schooling behavior of fish. By combining deep reinforcement learning and fluid simulation, an energy-saving strategy was proposed, which enabled followers to save energy by using vortices in the leader's wake [17]. More studies can be found in [18].

With regard to the target following control, there are many related results. Dai et al. [19] designed a robust tube model predictive controller (MPC) with an extended Kalman filter target observer for an underwater vehicle-manipulator system, specifically tailored to address the challenge of capturing moving targets. Cui et al. [20] proposed an optimal trajectory tracking method for AUVs, applying reinforcement learning techniques with critic and action neural networks. He et al. [21] formulated asynchronous multithreading proximal policy optimization-based algorithms to tackle issues related to path planning and trajectory tracking in unmanned underwater vehicles. Jiang et al. [22] introduced a model-free attention-based, model-agnostic meta-learning algorithm for AUVs, demonstrating efficacy in achieving high-precision tracking tasks. Zou et al. [23] designed an image-guided motion controller which consists of a genetic algorithm-based linear quadratic regulator velocity controller and direction controller to realize mobile target following for micro-robotic swarms. Yan et al. [24] designed a reinforcement learning and orthogonal fractional factorial design-based tracking controller for AUVs to enhance the scalability of uncertainty evaluation. Shi et al. [25] applied a hybrid actors-critics architecture to improve following control accuracy of AUVs. Gao et al. [26] introduced a fixed-time resilient cooperative edge-triggered estimation and control framework designed to facilitate cooperative target tracking for unmanned surface vehicles (USVs). Wai et al. [27] constructed an adaptive following control scheme with a dynamic recurrent fuzzy neural network that allowed

the vision-based mobile robot to track the moving target. Huang et al. [28] designed a homography-based visual servo controller that allowed the unmanned aerial vehicle to track the moving ship trajectory. Lin et al. [29] designed an image-based visual servoing geometric controller for quadrotors for tracking the desired trajectory.

Our work is motivated by the collective motion observed in fish schooling, where a phenomenon is known to enhance motion efficiency and reduce energy consumption. The studies on fish schooling movement can be theoretically categorized into kinematic and behavioral levels. At the kinematic level, the studies primarily focus on the macroscopic distances and swimming postures among fish. By closely observing the swimming patterns within fish schools, optimal distances and directions can be discerned. Further, at the behavioral level, greater emphasis may be placed on the individual body swimming postures of fish. For instance, in the context of tail-wagging fish swimming, it becomes imperative to synthesize parameters such as tail-wagging frequency, amplitude, and phase differences within the fish school. In this paper, we focus on the kinematic level, wherein we translate the complexities of fish schooling swimming into the pursuit of target position and attitude, thereby providing foundational support for biomimetic research at the behavioral level. The primary contributions of this paper can be concluded in three aspects.

- Inspired by fish schooling movement, we focus on the kinematic level and propose a target following control framework, including a predictive deep deterministic policy gradient controller (PDDPG) and nonlinear model predictive controller (NMPC).
- Aiming to address the hysteresis characteristics of following control for the robotic fish, we introduce the predictive concept into the deep deterministic policy gradient method. By predicting the future state and adding it to the buffer pool, we effectively mitigate the overshooting phenomenon during the tracking process. Furthermore, the state space is intentionally designed in a normalized manner, concurrently featuring a multi-objective optimization reward function.
- Taking the kinematic and dynamic models as the predictive model, we derive the nonlinear model predictive control law with full consideration of the stage cost and terminal cost. Extensive simulations are carried out to verify the effectiveness of the proposed PDDPG and NMPC methods.

The subsequent sections of this paper are structured as follows. Section 2 provides an exposition of the problem statement and the control framework. Section 3 delves into the target-following control methodologies, encompassing the predictive deep deterministic policy gradient controller and the nonlinear model predictive controller. Furthermore, Section 4 presents simulation results, followed by a comprehensive analysis. Finally, Section 5 offers concluding remarks to summarize the paper.

## 2. Problem Statement and Control Framework

In this section, we commence by introducing the target-following task and succinctly present the kinematic and dynamic models pertaining to the underwater robot. Subsequently, aligned with the specified task, we formulate a target-following framework for the robotic fish. Additionally, an alternative movement strategy is proposed, which integrates both the predictive deep deterministic policy gradient controller and the nonlinear model predictive controller.

In view of the observations that fish schooling movement in nature can save energy consumption and improve movement efficiency, this paper aims to design a target-following control method for the robotic fish. As shown in Figure 1, by selecting a robotic fish as the leader, a path cruise task that involves setting target points can be executed.  $P_l = (x_l, y_l)$  denotes the real-time position of the leader robotic fish while  $\varphi_l$  is its yaw angle.  $d_g$  and  $\varphi_g$  indicate the Euclidean distance and relative direction between the leader robotic fish and the target points, respectively.  $\varphi_{lg} = \varphi_l - \varphi_g$  illustrates the attitude direction difference between the leader robotic fish and the target points.



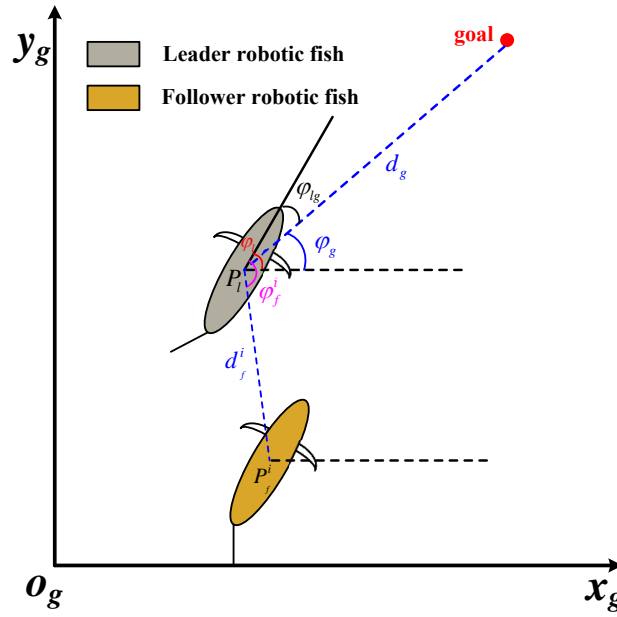


**Figure 1.** The illustration of the target-following task and coordinate system definition.

Furthermore, we set some robotic fish as followers.  $P_f^i = (x_f^i, y_f^i)$  denotes the real-time position of the follower robotic fish, where  $i = 1, 2, \dots, n$ . The purpose of the following task is to maintain the set target distance  $d_f^i$  and direction  $\varphi_f^i$  between the follower and leader robotic fish. Given the aforementioned variables, the target position point for the follower can be obtained as follows:

$$\begin{aligned} x_f^i &= x_l + d_f^i \cos(\varphi_f^i - \varphi_l) \\ y_f^i &= y_l + d_f^i \sin(\varphi_f^i - \varphi_l) \end{aligned} \quad (1)$$

It should be noted that the target point undergoes real-time variations with the movements of the leader. Consequently, for the follower, this task is characterized as a dynamic following mission. One of the principal improvements of this study lies in the approach based on a deep reinforcement learning framework. During training, static target-following scenarios are employed, yet the method is endowed with the capability to dynamically follow targets. Besides, for each single robotic fish, we offer the kinematic model for the following control, which can be formulated by

$$\dot{x} = u \cos \varphi - v \sin \varphi, \quad (2)$$

$$\dot{y} = u \sin \varphi + v \cos \varphi, \quad (3)$$

$$\dot{\varphi} = r, \quad (4)$$

where  $p(t) = (x(t), y(t), \varphi(t))$  represent the position and yaw angle with respect to inertia frame, respectively.  $(u, v, r)$  denote the linear and angular velocities with respect to body frame, respectively. Thereafter, the dynamic model can be derived as follows:

$$\dot{u} = \frac{1}{m_{11}}(\tau_u + m_{22}vr - d_{11}u), \quad (5)$$

$$\dot{v} = \frac{1}{m_{22}}(-m_{11}ur - d_{22}v), \quad (6)$$

$$\dot{r} = \frac{1}{m_{33}}(\tau_r + (m_{11} - m_{22})uv - d_{33}r), \quad (7)$$

where  $(m_{11}, m_{22}, m_{33})$  and  $(d_{11}, d_{22}, d_{33})$  are the mass and damping parameters larger than zero.  $\tau_u$  and  $\tau_r$  indicate the thrust force and yaw moment, respectively.

Therefore, based on the aforementioned problem statement, this paper proposes a target-following control framework, as illustrated in Figure 2. The framework comprises a biomimetic autonomous system consisting of one leader robotic fish (referred to as Agent\_0) and multiple follower robotic fish. Initially, a cruising target point is set for the leader robotic fish. Utilizing the proposed PDDPG controller, real-time control force and moment can be generated to achieve cruising control. It is noteworthy that although these target points are discrete, if they are relatively close, an effect similar to continuous path following can be achieved. Subsequently, through a task allocation module based on the principles of natural fish, real-time target following positions can be determined for each follower robotic fish. Furthermore, for each follower robotic fish, a controller selector is designed, corresponding to the proposed PDDPG controller and NMPC, to output real-time control force and moment for target following. It is essential to emphasize the dual purposes of designing the selector. On one hand, the PDDPG controller exhibits strong environmental adaptability and scalability, suggesting that it has an advantage over NMPC when introducing random obstacle avoidance tasks in this mission. However, NMPC features stable solution finding and smooth motion output, contributing to improved control stability. On the other hand, in this paper, the two controllers are independent and are switched through a toggle switch. In practice, they can be organically integrated based on certain principles, such as event-triggered mechanisms, according to different task scenarios.

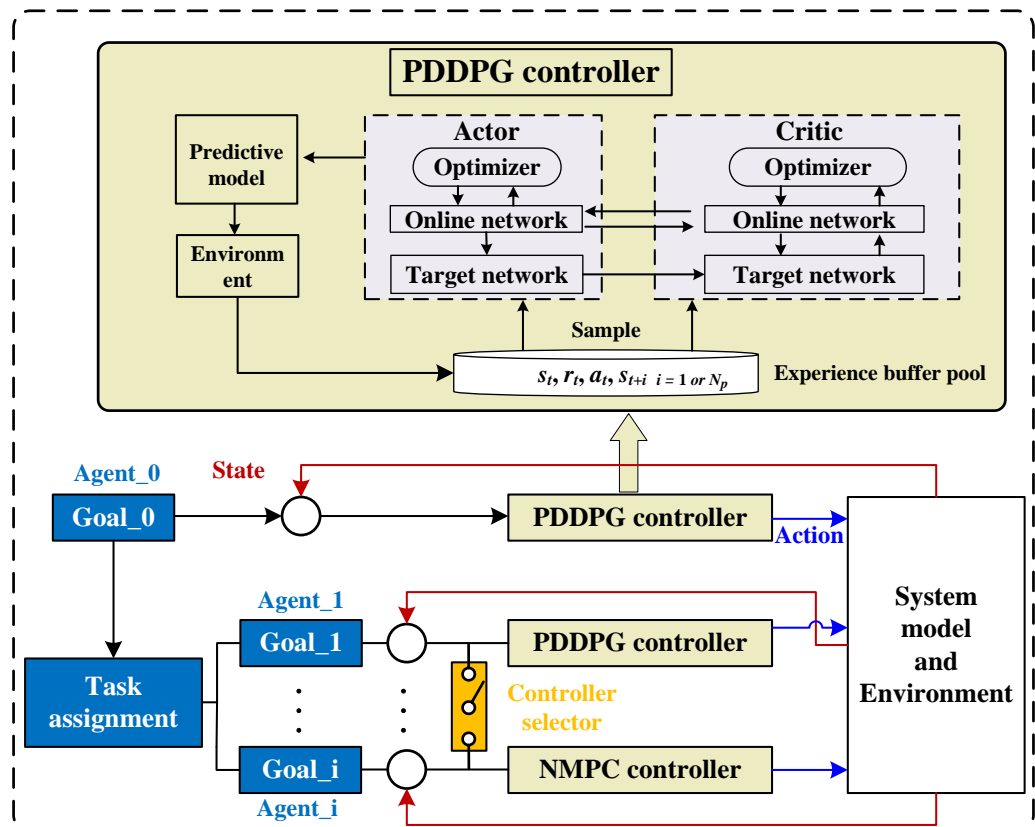


Figure 2. The target following control framework.

### 3. The Methodology of Target Following Control

#### 3.1. The Predictive Deep Deterministic Policy Gradient Controller

In consideration of the dynamic characteristics and strong interference in underwater environments, this section introduces a following controller based on a predictive deep

deterministic policy gradient. Firstly, the target-following problem is formulated as a multi-objective optimization issue through the design of network architecture, state space, action space, and reward function. Secondly, to enhance the training performance, normalization scaling is applied to the designed state variables, and reward values are standardized. More importantly, due to the highly nonlinear nature exhibited by biomimetic robotic fish, traditional control methods often result in following overshooting. To address this issue, the predictive approach is incorporated into the conventional deep deterministic policy gradient (DDPG) method. Specifically, when certain conditions are met, state variables and reward values after  $N_p$  steps are calculated and stored in a buffer pool. During the testing stage, actions can be output from the network based on the state variables after  $N_p$  steps. This technique can expand the training space to some extent, effectively avoiding overshooting without increasing the state space, thereby reducing network complexity.

First, the target-following task can be regarded as a Markov decision process. The tuple data comprises the state variable  $s \in \mathcal{S}$ , the action variable  $a \in \mathcal{A}$ , the reward function  $\mathcal{R}(s)$ , the state transition function  $\mathcal{F} : (s, a) \rightarrow s'$ , and the discount factor  $\gamma$ . By inputting the current state into a neural network, the action variable can be outputted, leading to the transition to the next state. The optimization objective is to maximize the reward function, driving parameter updates in the neural network. In recent years, DDPG has come to stand out as a reinforcement learning algorithm that has garnered substantial interest in recent years due to its efficacy in addressing challenges associated with continuous action space problems. Its applications span diverse domains, including robotics, control, and various other fields. DDPG amalgamates concepts from both value-based and policy-based reinforcement learning, utilizing a dual-neural network architecture comprising the Critic and the Actor. In this paper, we introduce certain enhancements to the conventional DDPG framework to accomplish the target-following task.

For deep reinforcement learning algorithms, the selection of appropriate state and action spaces, along with the design of a suitable reward function, stands as a pivotal determinant of network performance. In the subsequent section, specific design methodologies will be elucidated.

### 3.1.1. State Space

In pursuit of reducing the complexity of deep neural networks, we exclusively focus on the design of two state variables as follows:

- $d_{sg}$ : The state variable considered in this context pertains to the distance between the current position of the robot and the target point. This variable primarily ensures that the robot consistently approaches the target point at a predetermined velocity.
- $\varphi_{sg}$ : The state variable involves the angular separation between the robot's current position and the target point. This variable is crucial for ensuring the robot's sustained alignment towards the target, serving the dual purpose of minimizing travel distance and maintaining a stable motion posture.

To enhance training performance and expedite convergence, we propose a normalization and scaling technique for a specific set of state variables. Firstly, we determine the maximum values for two state variables. In this study, the Euclidean distance between the robot's starting point  $(x_o, y_o)$  and the target point  $(x_g, y_g)$  is designated as the maximum value for  $d_{sg}$ , as follows:

$$d_{\max} = \sqrt{(x_o - x_g)^2 + (y_o - y_g)^2}. \quad (8)$$

As for  $\varphi_{\max}$ , we set it to  $2\pi$ . Additionally, after normalization, we introduce a scale-up factor for two primary purposes. Firstly, post-normalization, the values fall within the  $[0, 1]$  range, which might be unsuitable for network convergence. Hence, amplification is applied. Secondly, considering the difference in the physical interpretations of  $d_{sg}$  and  $\varphi_{sg}$ , it is necessary to balance their magnitudes for faster convergence when inputting into the network. It is noteworthy that the selection of  $d_{\max}$  is not a fixed value due to the real-time

variability of the follower robot's target. Hence, by dynamically updating the target point  $(x_g, y_g)$  for the follower robot, more effective action values can be obtained. Considering these aspects, the formulated state variables are expressed as follows:

$$\begin{aligned}\tilde{d}_{sg} &= k_1 \frac{d_{sg}}{d_{\max}} \\ \tilde{\varphi}_{sg} &= k_2 \frac{\varphi_{sg}}{\varphi_{\max}}\end{aligned}\quad (9)$$

### 3.1.2. Action Space

Based on the kinematic and dynamic models of biomimetic robotic fish, we define forward thrust and yaw moment as action variables. In contrast to conventional kinematic navigation approaches, we directly employ control quantities as actions, implying that it is necessary to traverse two layers of non-linear models, namely kinematics and dynamics, which increases the learning complexity. Additionally, building upon our previous work, we set the action ranges for forward thrust and yaw torque to  $[0, 6 \text{ N}]$  and  $[-6 \text{ Nm}, 6 \text{ Nm}]$ , respectively. Moreover, since this study does not involve information exchange among robot swarms, the leader robotic fish does not decelerate when the distance between the leader and follower robotic fish is substantial. Hence, it is essential to ensure that the follower robotic fish possesses the ability to catch up with the leader, leading to the specification of the maximum forward thrust range for the follower robotic fish as  $[0, 8 \text{ N}]$ .

Furthermore, the forward thrust of the robotic fish is constrained to be consistently greater than zero, while the yaw torque exhibits bilateral symmetry. Therefore, a bilateral correction is applied to the forward thrust. Specifically, during both the network output and replay buffer storage phases, the range of forward thrust is adjusted to  $[-3 \text{ N}, 3 \text{ N}]$ . When inputted into the training environment, the forward thrust outputted by the network is increased by 3 N, rendering it unilaterally positive, and subsequently fed into the motion model to update the environmental information.

### 3.1.3. Reward Function

The reward function constitutes a pivotal element in deep reinforcement learning. With full consideration of path smoothness and length factors, a multi-objective optimization reward function is proposed as follows:

$$R = \sum_{i=1}^3 c_i r_i, \quad (10)$$

where  $c_i$  denotes the weight coefficients and  $r_i$  represents the different reward forms. There are three principles.

- The principle of minimum distance: it is expressed as  $r_1 = -|\tilde{d}_{sg}|$ , primarily employed to minimize the length of the motion path.
- The principle of directional convergence: it is expressed as  $r_2 = -|\tilde{\varphi}_{sg}|$ , with the aim of guiding the robot to orient itself towards the target point during motion. This principle not only contributes to the reduction in path length but also serves to ensure a certain degree of stability in the output yaw moment.
- The path-smoothing principle: it is characterized by  $r_3 = -|\tilde{\varphi}_{sg} - \tilde{\varphi}'_{sg}|$ , where  $\tilde{\varphi}'_{sg}$  represents the previous time step's  $\tilde{\varphi}_{sg}$ . This principle primarily aims to enhance control stability by minimizing the yaw angle difference between consecutive time steps, thereby smoothing the motion path.

### 3.1.4. Predictive Concept-Based Improvement

In light of the aforementioned state space, action space, and reward function, it is evident that the learning objective of the proposed method is to achieve rapid and smooth target following. However, in practical tracking scenarios, due to the highly nonlinear

characteristic of the system, the steering of robotic fish exhibits a certain degree of lag, leading to the occurrence of overshooting phenomena. To address this issue, the most direct solution is to introduce angular velocity as an additional state variable and incorporate it into the learning network. Nevertheless, this approach encounters two primary challenges. Firstly, the introduction of angular velocity increases the complexity of the state space, thereby escalating the training difficulty. Secondly, in real-world applications, angular velocity information is typically obtained from inertial measurement unit (IMU) sensor modules, making it susceptible to external environmental factors and noise, manifesting notable information instability such as abrupt fluctuations. Therefore, angular velocity is deemed unsuitable as a state variable. With these considerations, this paper integrates a predictive approach into the traditional DDPG framework, presenting a novel training architecture. This structure effectively mitigates overshooting phenomena without introducing additional state variables.

In the conventional DDPG algorithm, the replay buffer stores a series of experience tuples  $(s_t, a_t, s_{t+1}, r_t)$ , including the representation of the state at the next time step  $s_{t+1}$ , i.e.,  $s_{t+1} = f(s_t, a_t)$ . Here,  $f$  denotes a composite motion model of kinematics and dynamics. The key improvement in the proposed method lies in the replacement of the current state with the state quantity obtained after  $N_p$  steps when the steering angular velocity exceeds a predefined threshold. Both the state after  $N_p$  steps and the current state are then stored in the replay buffer, i.e.,  $(s_t, a_t, s_{t+N_p}, r_t)$ . This process generates a sequence of states as

$$S = \left( s_{t+N_p}, s_{t+N_p-1}, \dots, s_{t+1}, s_t \right) . \quad (11)$$

$$s_{t+i} = f(s_{t+i-1}, a_t)$$

Based on the above illustration, the calculation process of PDDPG is presented in Algorithm 1.

---

**Algorithm 1** Algorithm for PDDPG

---

- 1: Initialize the parameters of Actor network and Critic network.
  - 2: Initialize the experience replay buffer pool.
  - 3: **for** episode = 1 to  $N$  **do**
  - 4:     Reset the control system, and obtain the initial states  $s_0$ .
  - 5:     **for** step = 1 to  $M$  **do**
  - 6:         According to the trained strategy, select the output action with the added noise information.
  - 7:         Perform actions in the model environment.
  - 8:         **if**  $\dot{\phi} > 20^\circ/s$  **then**
  - 9:             Apply the predictive model, and calculate  $s_{t+N_p}$ .
  - 10:            Put  $(s_t, a_t, s_{t+N_p}, r_t)$  into buffer pool.
  - 11:         **else**
  - 12:             Based on the motion model, calculate  $s_{t+1}$ .
  - 13:             Put  $(s_t, a_t, s_{t+1}, r_t)$  into buffer pool.
  - 14:         **end if**
  - 15:         Sample a subset of data from the experience replay buffer for network updating.
  - 16:         Update the Critic network according to the loss.
  - 17:         Update the Actor network based on deterministic policy gradient followed by the target Actor network.
  - 18:     **end for**
  - 19: **end for**
- 

### 3.2. The Nonlinear Model Predictive Controller

In recent years, the utilization of MPC has become increasingly prevalent within the domain of robotics. MPC proves valuable not only in tackling the intricacies of systems with multiple inputs and outputs, but also in addressing and managing control constraints

effectively. The control approach employed in this paper can be considered as a means of achieving setpoint stabilization to a certain extent. This is achieved by designing a controller that effectively stabilizes a predefined stationary setpoint.

Although the approach proposed in this paper also allows for dynamic target points to be followed, the switching of these dynamic targets is governed by specific triggering rules. On one hand, for the leader robotic fish, the target point switching criterion is based on the condition that the robotic fish is within a certain threshold distance from the target. As a result, this type of target point switching can be considered as setpoint stabilization on a time scale. On the other hand, for the follower robotic fish, the target points change in real time with the position of the leader robotic fish. However, due to the time-independence characteristic of target point locations during the controller design process, these changes can be simplified as setpoint stabilization. Furthermore, in order to achieve the following control, we need to stabilize the key variables, including the planar position and the yaw attitude. Hence, based on the kinematic and dynamic models of the robotic fish, the state variables can be selected as  $P_f = (x, y, \varphi)$ . Correspondingly, we consider the forward thrust and yaw moment as control variables, i.e.,  $u_f = (\tau_u, \tau_r)$ .

This design implies the incorporation of both the kinematic and dynamic models as components of the predictive model, which simplifies the controller design process. However, the combination of two nonlinear models may introduce a degree of computational complexity and elevate optimization challenges. Iterative solution-seeking is necessary, and parameter adjustments are implemented to address these complexities. Therefore, by defining the reference  $\Lambda_f = (x_d, y_d, \varphi_d)$  and error item  $e$ , we can consider the cost function as follows:

$$J(e(t_k), u_f) = \int_{t_k}^{t_k+T} L(e(\tau), u_f) d\tau + g(e(t_k + T)), \quad (12)$$

where  $L$  indicates the stage cost while  $g$  is the terminal penalty.  $T$  is the prediction horizon. Furthermore, the optimal control problem addressed at each sampling instant can be structured as follows:

$$\min_{u_f} J(e(t_k), u_f), \quad (13)$$

Subject to

$$e(t_k) = \zeta(x(t_k), y(t_k), \varphi(t_k), R_f), \quad (14)$$

$$L = e(\tau|t_k)^T Q e(\tau|t_k) + u_f(\tau|t_k)^T R u_f(\tau|t_k), \quad (15)$$

$$g = e(t_k + T|t_k)^T K e(t_k + T|t_k), \quad (16)$$

$$u_f \in [u_{f \min}, u_{f \max}], \quad (17)$$

where  $\zeta$  can be calculated by the motion model of the robotic fish.  $Q$ ,  $R$ , and  $K$  represent the coefficient matrix. Through the resolution of the optimization problem outlined above, the optimal control sequence can be derived. Subsequently, solely the control sequence up to the next sampling instant is considered, and the optimization process is reiterated in a receding horizon way.

#### 4. Simulation and Analysis

In this section, extensive simulation tests were conducted to validate the effectiveness of the proposed target following method. Firstly, we constructed a simulated pool environment and performed network training using Pytorch 1.12.1. In pursuit of real-time performance, a four-layer fully connected structure was chosen for the architecture of the Actor and Critic networks. The neuron counts in the intermediate two hidden layers are set to 400 and 300, respectively. For key training parameters, the discount factor was set to 0.9, the learning rate to  $1 \times 10^{-5}$ , the target smoothing coefficient to 0.005, the minimum batch size to 256, the maximum training episodes to 3000, and the maximum training steps per



episode to 300. The control period is 0.1 s. The other key parameters of the motion model and control system can be seen in more detail in Table 1.

**Table 1.** Parameters of the following control system.

Item	Value	Item	Value	Item	Value
$m_{11}$	9.9 kg	$m_{22}$	14.5 kg	$m_{33}$	1.8 kg
$d_{11}$	17.2 kg/s	$d_{22}$	19.3 kg/s	$d_{33}$	1.1 kg·m/s <sup>2</sup>
$Q$	$\text{diag}\{50, 50, 0.2\}$	$R$	$\text{diag}\{0.005\}$	$K$	$\text{diag}\{0.5\}$
$c_1$	0.4	$c_2$	0.4	$c_3$	0.2
$k_1$	10	$k_2$	20	$T$	10
$u_{f \min}$	$\tau_u = 0, \tau_r = -6$	$u_{f \max}$	$\tau_u = 8, \tau_r = 6$		

#### 4.1. Training Results and Analysis

In this section, the neural network constructed based on the proposed reinforcement learning method was trained. When the prediction step size was set to five, Figure 3 presented the results of six training sessions, including rewards, Actor loss, and Critic loss. The shaded area in the figure represents the range of the maximum and minimum values for each round in the six training sessions. The obtained results indicate that the proposed method exhibits a relatively rapid convergence rate in the initial stages, achieving preliminary convergence at around 500 steps. By the time the training steps reach 3000, complete convergence is achieved, resulting in satisfactory training outcomes.

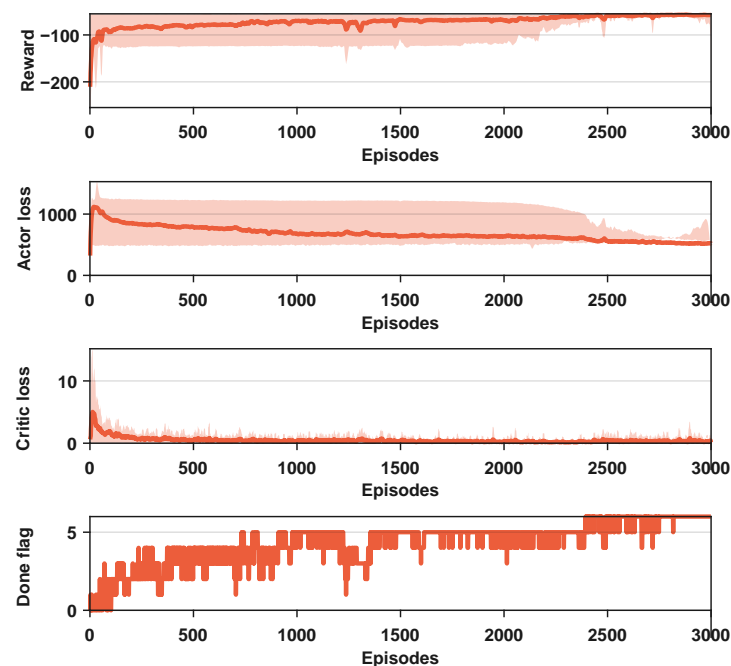


**Figure 3.** The training results of PDDPG when  $N_p = 5$ .

It should be noted that in Figure 3, the Done flag is used to indicate whether the target point is reached in each training round. In each training session, if the target point was reached within the current round, the variable was set to 1; otherwise, it was set to 0. The Done flag represents the cumulative sum of these binary values in the six training sessions, with a minimum value of zero and a maximum value of six. Therefore, the results suggest that with an increase in the number of training steps, the Done flag exhibited an overall upward trend, indicating that convergence was ultimately achieved in each training session. As a whole, from the reward and loss results, it can be seen that the values reached a satisfactory level after 3000 iterations, and the curves appeared relatively smooth. In terms

of completion, the Done flag was essentially at the maximum value around 3000 steps, indicating successful attainment of the target point in each training instance.

To investigate the impact of different prediction steps on training outcomes, we conducted relevant simulation experiments. Initially, we set the parameter  $N_p$  to values of 0, 3, 5, 8, and 10, employing identical training parameters. The training results are illustrated in Figure 4a. The findings indicate optimal training performance when  $N_p$  is set to 5, followed by  $N_p = 3$ . Notably, with  $N_p = 5$ , not only did rapid convergence occur, but a certain degree of training stability was also observed. Subsequently, we performed an extension of training for the case where  $N_p$  was set to 5, reaching 5000 steps. The results demonstrate that the reward has stabilized without significant fluctuations.

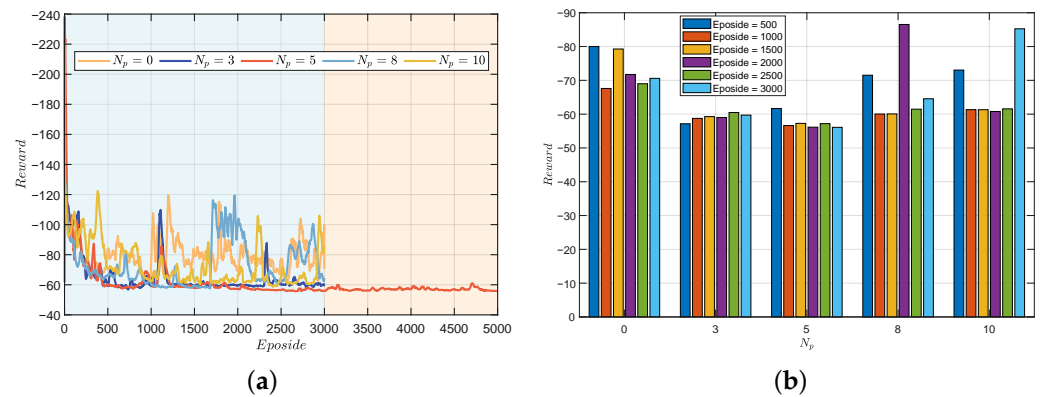


**Figure 4.** The reward comparison of testing results. (a) Under different  $N_p$ . (b) Under different episodes.

Further analysis is presented in Figure 4b, depicting comparative results of training with fixed steps under different  $N_p$ . Overall, PDDPG exhibits superior training performance compared to traditional DDPG, with  $N_p = 3$  and  $N_p = 5$  showcasing particularly outstanding results. However, it is noteworthy that temporary divergence phenomena were observed during the training processes with  $N_p = 8$  and  $N_p = 10$ . This suggests that when the prediction step size is too small or too large, the training outcomes are unsatisfactory. This phenomenon can be attributed to two main factors. Firstly, a too small prediction interval implies an ineffective restriction on overshooting, leading to frequent changes in system attitude and triggering substantial penalties. Secondly, influenced by the inaccuracy of the motion model, longer prediction intervals may render the system more sensitive to model uncertainty, since model predictions over extended periods may accumulate errors. This could result in a decrease in the robustness of control performance, particularly in the presence of uncertainty or environmental changes.

Hence, the selection of an appropriate prediction interval is crucial for enhancing model training effectiveness, as both excessively small and large prediction intervals may impact the stability and performance of training results. The obtained results support the selection of  $N_p$  as 5 during the training process, as it exhibits superior performance in terms of rapid convergence and training stability. These findings provide valuable insights into the optimization of prediction step parameters for effective model training.

## 4.2. Testing Results and Analysis

### 4.2.1. Fix-Point Target Following under Single Robotic Fish

To further validate the effectiveness of the proposed method, simulation tests were conducted in this section. Firstly, fix-point target following tests under single robotic fish were performed by setting the initial position, initial attitude, and target point. The trained network results were evaluated based on different prediction horizons. Figure 5a illustrates the motion trajectories of the robotic fish under different prediction horizons. Figure 5b depicts the motion trajectories of the robotic fish at different episodes when  $N_p = 5$ . Motion

data results, including distance to the target point, the yaw angle difference, forward thrust, and yaw moment, are presented in Figure 6.

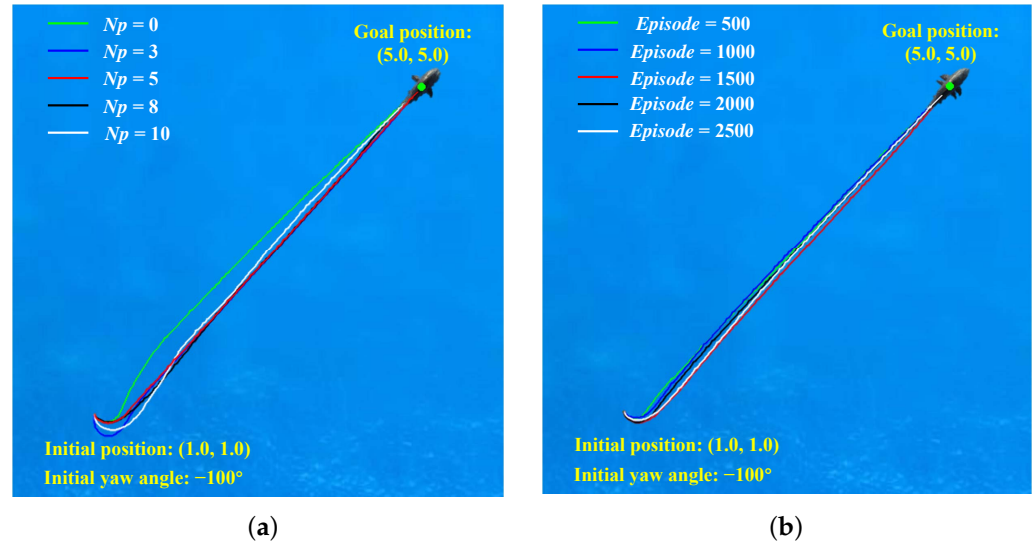


**Figure 5.** The trajectories comparison of testing results. (a) Under different prediction horizons. (b) Under different episodes.

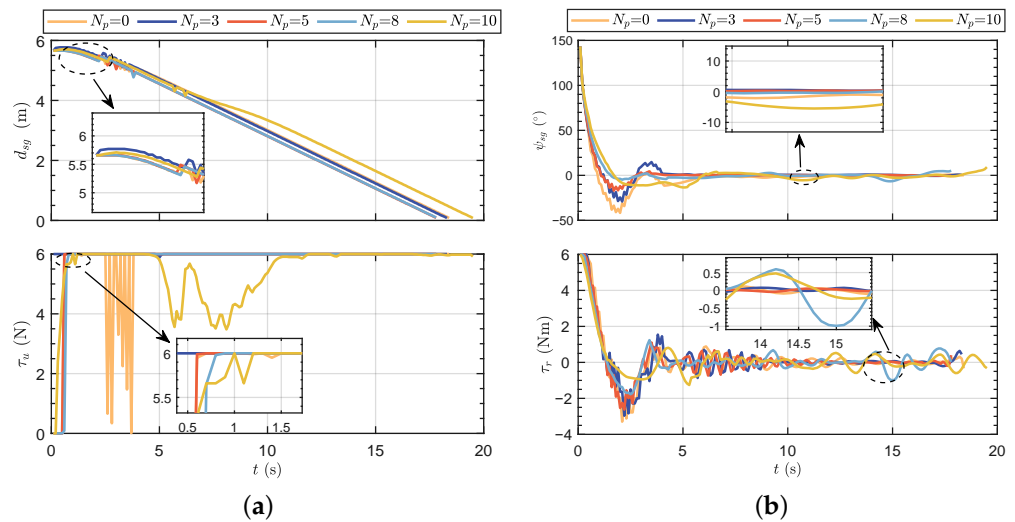


**Figure 6.** The motion data results of testing results. (a) Distance to the target point and forward thrust. (b) Yaw angle difference and yaw moment.

It can be seen that the trajectories reveal noticeable overshoot phenomenon in the early stages, when the initial pose set at  $-100^\circ$ . Without a prediction horizon, the control performance exhibits poor performance. As the prediction horizon increases, the overshoot is effectively suppressed. However, when the prediction horizon reaches 8, some motion instability phenomena begin to emerge. Particularly in the case of  $N_p = 10$ , the yaw angle curve is unsmooth; the reason for this may be that the increased prediction horizon can lead to a chaotic learning process. Specially, although the performance of  $N_p = 3$  is superior to  $N_p = 8$  from a training perspective, the motion trajectories suggest that the performance of  $N_p = 8$  seems more favorable. The reasons for this phenomenon may be identified in Figure 6b. It can be observed that the test results for  $N_p = 8$  show small oscillations in the yaw moment even after entering the steady-state following process, indicating an instability in its swimming posture. The obtained results indicate that there are interactions between the prediction horizon and control performance, and it also influences overshoot suppression and post-steady-state stability in following motion.

#### 4.2.2. Dynamic Target Following under Single Robotic Fish

To assess the effectiveness of the proposed methods in dynamic target following, a standard circle was employed for testing, establishing a foundation for collaborative following. Initially, the circle's center was positioned at (4, 4) with a set radius of 2. The circle was then partitioned into 200 points and followed sequentially. The robotic fish transitioned to the next target point when its distance to the target point fell below 0.3 m.

Figure 7 presents the following path, while Figure 8a,b provide insights into the following data. The results demonstrate the successful implementation of the proposed method for standard circle following, yielding some conclusions. Initially, during the stable following process, the distance between the robotic fish and the dynamic target point is maintained at 0.32 m. According to the switch criterion for dynamic target following, the proposed method can be validated to accomplish following promptly and effectively. Subsequently, the yaw attitude during the following process exhibits relative stability but with subtle oscillations. The forward thrust remains at its maximum value for the majority of the time, which is primarily attributed to the consistent distance between the robotic fish and the dynamic target point. In the context of turning motion, a certain degree of lateral movement is induced, resulting in a lateral velocity. Finally, consistent with the performance of yaw attitude, both the yaw moment and turning angular velocity display slight oscillations characterized by small amplitudes, without significantly affecting the system stability.

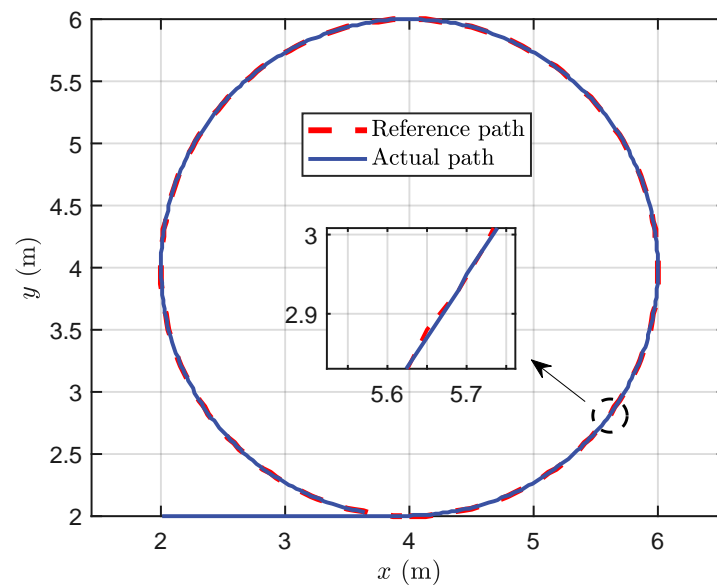


**Figure 7.** The simulation results of circle following trajectory.

#### 4.2.3. Cooperative Following Control under Multiple Robotic Fish

In this section, inspiration from the efficient mechanisms of fish schooling motion is applied to multi-robot cooperative motion. Studies indicate that maintaining a certain distance and direction between multiple fish swimming together can enhance hydrodynamic performance. For instance, swimming in a side-by-side following manner can reduce energy consumption. Therefore, we emulate the principles of fish swarm motion at the locomotion level, laying the foundation for research on robotic fish swarms. It should be noted that the proposed methods in this paper can be directly applied to any agent in the cluster, and are not limited to the number of agents. To better demonstrate simulation results, this section takes the example of a following task with two biomimetic robotic fish to validate the effectiveness of the proposed methods.

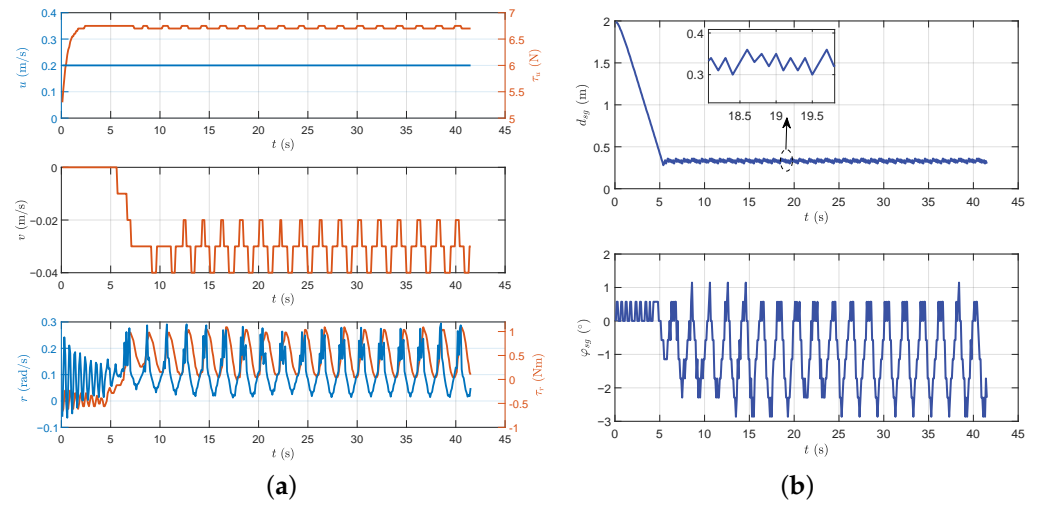


**Figure 8.** The motion data results of dynamic target following control. (a) The velocity illustration and control force/moment. (b) The following distance and yaw attitude.

Throughout the cooperative following involving multiple robotic fish, the dynamic repositioning of the leader robotic fish prompts a corresponding adjustment in the target-following coordinates  $P_f^i$  for the follower robotic fish. Hence, if the initial position of the follower robotic fish remains fixed,  $d_{\text{max}}$  is a variable which will introduce a notable drawback. In the scenario where the leader robotic fish is engaged in a single-point following task, the ongoing following motion results in a progressive increase in the distance  $P_f^i$  from the initial point, leading to an augmentation of the follower robotic fish's  $d_{\text{max}}$ , as indicated in Equation (9). Despite the continuous pursuit of the leader by the follower robotic fish, it is indicated that there is potential for a decreasing  $d_{\text{max}}$ , ultimately causing a gradual reduction in pursuit speed until it becomes insufficient for successful following. To mitigate this challenge, both  $d_{\text{max}}$  for the leader and follower robotic fish are intentionally maintained as constants, specifically set at 6 during the testing phase in this section.

Furthermore, we outline a task for a biomimetic autonomous system. The task involves a leader robotic fish guiding a collective of follower robotic fish in the exploration of a predefined area. The exploration process is facilitated by establishing search target points for the leader robotic fish, with the other follower robotic fish collaboratively tailing the leader in the exploration endeavor. Besides, the distances and orientations during the following process can be determined based on biological mechanisms observed in natural fish. Consequently, this section presents the simulation testing of leader–follower cooperative following control. First, the corner points of a square are defined as search target points for the leader robotic fish, specifically at (6, 2), (6, 6), (2, 6), and (2, 2). The leader robotic fish aligns its movement towards these target points, switching to the next target point when the distance from the current target falls below 0.3 m. Further, the follower robotic fish dynamically follows the movement of the leader robotic fish in real time.

In alignment with the biological mechanisms of collaborative motion [16], we stipulate a distance of  $d_f^i = 0.5$  m and a target orientation of  $\varphi_f^i = 135^\circ$  concerning the leader robotic fish. Thus, based on Equation (1), we can derive the real-time target position for the follower robotic fish. Figure 9 provides snapshot sequences of the cooperative following control, encompassing leader trajectory generated by PDDPG, and the follower trajectories generated by PDDPG and NMPC. The obtained results demonstrate that the leader robotic fish successfully completes the standard square path search task with minimal overshooting. Notably, the follower robotic fish, under the control of both PDDPG and NMPC methods, successfully accomplishes the following task.

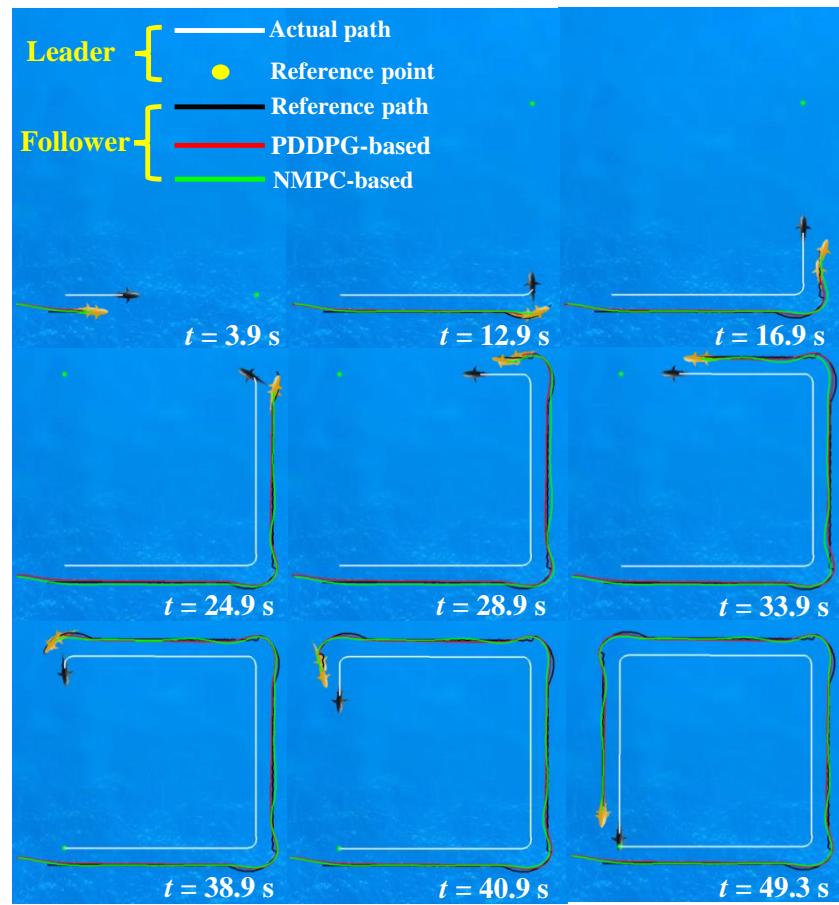


**Figure 9.** The snapshot sequences of cooperative following control.

Figure 10 depicts the motion data results for cooperative following. Based on  $d_{sg}$ , it can be seen that NMPC displays a marginally superior performance in following distance compared to PDDPG, indicating a capacity for faster target following. However, concerning  $\varphi_{sg}$ , PDDPG significantly outperforms NMPC, especially when the leader robotic fish switches target points for a right-angle turn. The distinct weak overshooting characteristic of PDDPG is conspicuously manifested, while NMPC exhibits a noticeable degree of overshooting, resulting in unstable yaw attitude. To further verify the superiority of the proposed method, some quantitative comparison results are offered. On one hand, the total lengths of the following path generated by PDDPG and NMPC are 18.34 m and 18.36 m, respectively, which indicates the slim margin for PDDPG. On the other hand, when the robotic fish turns at a right angle, the overshoot phenomenon is obvious. Taking the time interval of  $t = [10 \text{ s}, 20 \text{ s}]$  as an example, the root-mean-square error (RMSE) of  $\varphi_{sg}$  for PDDPG and NMPC are  $8.3^\circ$  and  $45.6^\circ$ , respectively. Additionally, the mean absolute error (MAE) of  $\varphi_{sg}$  for PDDPG and NMPC are  $7^\circ$  and  $25.5^\circ$ , respectively. Therefore, the obtained results illustrate that the proposed PDDPG shows more satisfactory performance.

Moreover, Figure 11 provides insight into the control quantities of forward thrust and yaw moment. In terms of forward thrust, PDDPG seldom reaches its maximum value, whereas NMPC consistently maintains a near-maximum swimming speed throughout the pursuit process. This may be attributed to PDDPG learning, which revealed that that overshooting is prone to occur during high-speed turns, prompting the model to avoid utilizing maximum thrust to prevent this phenomenon. Regarding yaw moments, consistent with yaw attitudes during turning, NMPC outputs a more substantial moment amplitude during turning phases. Nevertheless, it can be observed that in the steady-state tracking phase, NMPC's yaw moment is more stable, while PDDPG exhibits slight oscillations, resembling the swimming behavior of real tail-flapping fish.



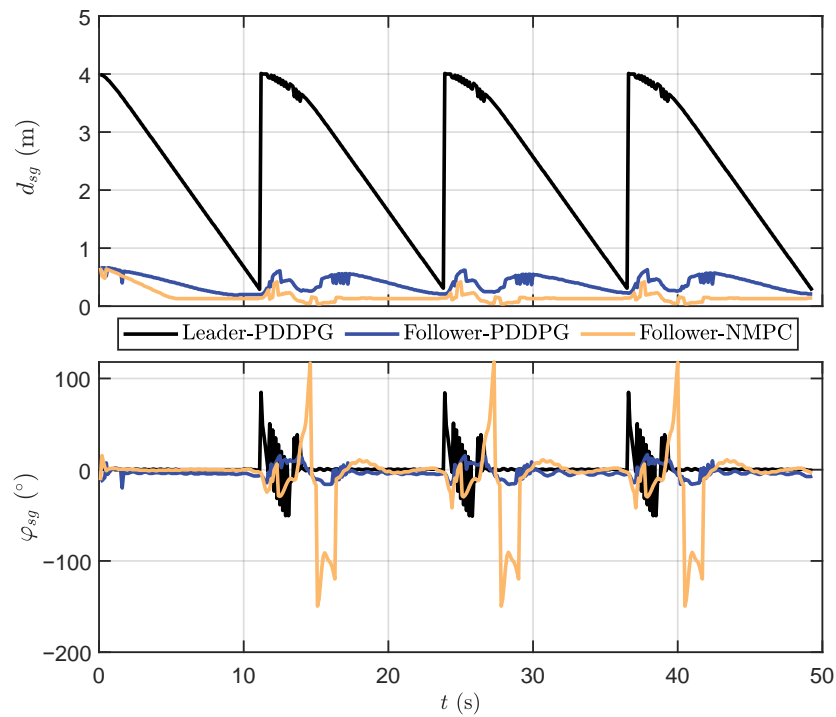


**Figure 10.** The motion data results of cooperative following distance and yaw difference.

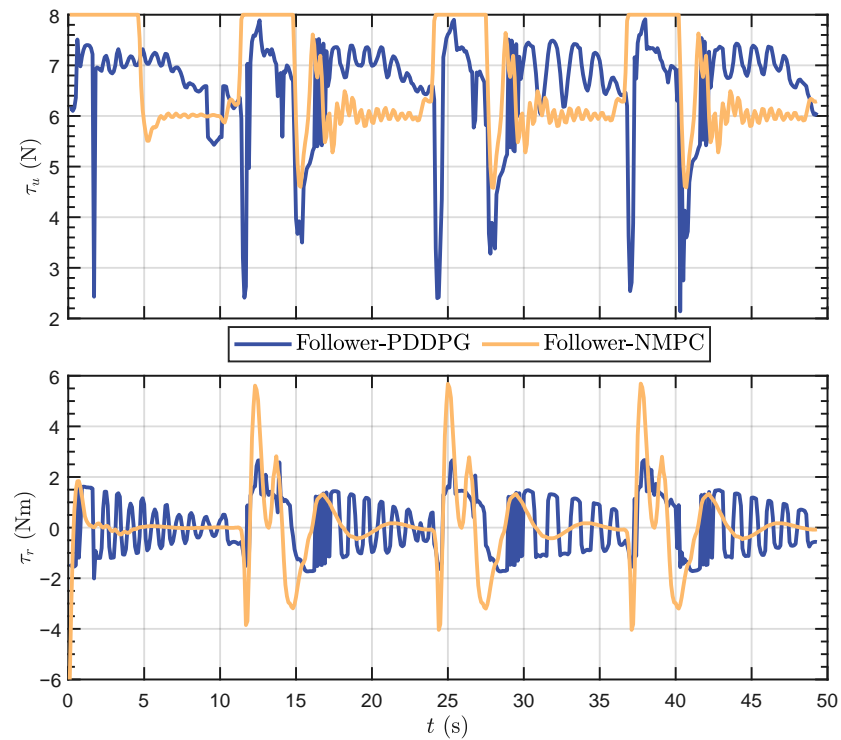


**Figure 11.** The motion data results of control quantities.

#### 4.3. Discussion

Drawing inspiration from the schooling movement of biological fish, a target-following method based on deep reinforcement learning is proposed, leading to successful implementation of cooperative following control. On one hand, by incorporating predictive thinking into the traditional DDPG algorithm, the system overshooting is effectively reduced. Notably, the method utilizes static target-following scenarios during training but

demonstrates the ability to follow dynamic targets. On the other hand, as an auxiliary control, a target-following controller based on NMPC is designed.

When adjusting the parameters of neural networks and hyperparameters of deep reinforcement learning, we adhere rigorously to the principle of cross-validation to identify the most suitable parameter combinations for a specific task while mitigating issues such as overfitting or underfitting. With the consideration of model complexity, we explore multiple combinations of neurons, conduct cross-validation, and ultimately select appropriate parameters. With regard to the discount factor, learning rate, smoothing coefficient, and batch size, we conduct preliminary tests based on conventional DDPG parameters and further engage in simulation testing to finalize the parameters. Concerning certain parameter settings in the reward function of deep reinforcement learning, we adjust the parameters from the aspects of objectives significance and simulation test results. Regarding generalization performance, we employed several strategies to enhance generalization, including the normalization and scaling technique for the state variables, adding the noise for action generation, and adjusting the target network update frequency. Further, in dynamic target following and cooperative following control simulations, even with real-time changes to the target point, the proposed method consistently demonstrated effective following capabilities, providing further evidence of its robust generalization performance.

Furthermore, extensive simulations are conducted. First, the training results reveal optimal performance with a prediction step of  $N_p = 5$ . Excessively large or small prediction periods yield unsatisfactory performance. This conclusion is further validated through stationary target-following tests. Second, to assess dynamic target-following performance, the proposed PDDPG algorithm successfully follows a circular trajectory. Finally, by setting up a cooperative following task, the proposed method accomplishes cooperative exploration in a quadrilateral environment, concluding with a performance comparison between PDDPG and NMPC, confirming the effectiveness and superiority of the proposed method.

Despite the successful implementation of cooperative following control, there are still some limitations. On one hand, this paper places particular emphasis on the motion of individual robotic fish, with the goal of directly transferring learned target-following capabilities to swarm control. Consequently, considerations such as inter-swarm motion constraints or obstacle avoidance are omitted. By incorporating neighboring robotic fish states into the state space and devising appropriate reward functions, this issue may be addressed. On the other hand, we focus on the kinematic level of biological fish schooling movement, without delving into behavioral level [30]. To this end, it is required that the joint dynamic models and biomimetic motion control algorithms should be introduced, which is our ongoing endeavor.

## 5. Conclusions and Future Work

In this paper, we have developed a target-following control framework, including a predictive deep deterministic policy gradient controller and a nonlinear model predictive controller. Inspired by the mechanism of hydrodynamic efficiency improvement observed in fish schooling movement, we aim to investigate a target following method that can be applied to achieve a cooperative following task. In view of the nonlinear characteristics in the motion model of the robotic fish, the predictive modeling concept is incorporated into the conventional DDPG algorithm. On this basis, the training framework is developed, including the normalization of the state space, action space, and the standardization of the reward function. Additionally, we introduce an auxiliary controller based on a nonlinear predictive model, offering an alternative for cooperative following control of the follower robotic fish. Finally, extensive simulations are conducted, demonstrating the effectiveness of the proposed method.

In future work, we plan to further investigate the mechanistic aspects of the behavioral level in the biological fish schooling movement. By incorporating inter-cluster motion constraints, more intelligent cooperative following can be achieved. Furthermore, how

to realize three-dimensional cooperative following control is another issue worthy of in-depth study.

**Author Contributions:** Conceptualization, Y.W. and J.Y.; methodology, Y.W. and J.W.; software, Y.W. and S.K.; validation, Y.W., J.W. and J.Y.; formal analysis, Y.W. and S.K.; investigation, Y.W. and S.K.; resources, Y.W. and J.Y.; data curation, Y.W. and J.Y.; writing—original draft preparation, Y.W. and J.Y.; writing—review and editing, Y.W., J.W., S.K. and J.Y.; visualization, S.K.; supervision, J.Y.; project administration, Y.W. and J.Y.; funding acquisition, Y.W., J.W. and J.Y. All authors have read and agreed to the published version of the manuscript.

**Funding:** This work was supported in part by the National Natural Science Foundation of China under Grant 62303260, Grant 62203436, Grant 62233001.

**Institutional Review Board Statement:** Not applicable.

**Informed Consent Statement:** Not applicable.

**Data Availability Statement:** The data generated during the current study are available from the corresponding author on reasonable request.

**Conflicts of Interest:** The authors declare no conflicts of interest.

## References

- Katzschmann, R.K.; DelPreto, J.; MacCurdy, R.; Rus, D. Exploration of underwater life with an acoustically controlled soft robotic fish. *Sci. Robot.* **2018**, *3*, eaar3449. [CrossRef]
- Yu, J.; Wang, T.; Chen, D.; Meng, Y. Quantifying the leaping motion using a self-propelled bionic robotic dolphin platform. *Biomimetics* **2023**, *8*, 21. [CrossRef] [PubMed]
- Shao, H.; Dong, B.; Zheng, C.; Li, T.; Zuo, Q.; Xu, Y.; Fang, H.; He, K.; Xie, F. Thrust improvement of a biomimetic robotic fish by using a deformable caudal fin. *Biomimetics* **2022**, *7*, 113. [CrossRef]
- Wang, J.; Wu, Z.; Dong, H.; Tan, M.; Yu, J. Development and control of underwater gliding robots: A review. *IEEE/CAA J. Autom. Sin.* **2022**, *9*, 1543–1560. [CrossRef]
- Cao, Q.; Wang, R.; Zhang, T.; Wang, Y.; Wang, S. Hydrodynamic modeling and parameter identification of a bionic underwater vehicle: Robdact. *Cyborg Bion. Syst.* **2022**, *2022*, 9806328. [CrossRef] [PubMed]
- Zhang, C.; Zhang, Y.; Wang, W.; Xi, N.; Liu, L. A manta ray-inspired biosyncretic robot with stable controllability by dynamic electric stimulation. *Cyborg Bion. Syst.* **2022**, *2022*, 9891380. [CrossRef]
- Zhu, J.; White, C.; Wainwright, D.K.; Di Santo, V.; Lauder, G.V.; Bart-Smith, H. Tuna robotics: A high-frequency experimental platform exploring the performance space of swimming fishes. *Sci. Robot.* **2019**, *4*, eaax4615. [CrossRef]
- White, C.; Lauder, G.V.; Bart-Smith, H. Tunabot Flex: A tuna-inspired robot with body flexibility improves high-performance swimming. *Bioinspir. Biomim.* **2020**, *16*, 026019. [CrossRef]
- Yu, J.; Wu, Z.; Su, Z.; Wang, T.; Qi, S. Motion control strategies for a repetitive leaping robotic dolphin. *IEEE/ASME Trans. Mechatron.* **2019**, *24*, 913–923. [CrossRef]
- Weih, D. Hydromechanics of fish schooling. *Nature* **1973**, *241*, 290–291. [CrossRef]
- Li, L.; Nagy, M.; Graving, J.M.; Bak-Coleman, J.; Xie, G.; Couzin, I.D. Vortex phase matching as a strategy for schooling in robots and in fish. *Nat. Commun.* **2020**, *11*, 5408. [CrossRef]
- Li, L.; Ravi, S.; Xie, G.; Couzin, I.D. Using a robotic platform to study the influence of relative tailbeat phase on the energetic costs of side-by-side swimming in fish. *Proc. R. Soc. A* **2021**, *477*, 20200810. [CrossRef] [PubMed]
- Marras, S.; Killen, S.S.; Lindström, J.; McKenzie, D.J.; Steffensen, J.F.; Domenici, P. Fish swimming in schools save energy regardless of their spatial position. *Behav. Ecol. Sociobiol.* **2015**, *69*, 219–226. [CrossRef] [PubMed]
- Thandiackal, R.; Lauder, G. In-line swimming dynamics revealed by fish interacting with a robotic mechanism. *eLife* **2023**, *12*, e81392. [CrossRef] [PubMed]
- Li, G.; Kolomenskiy, D.; Liu, H.; Thiria, B.; Godoy-Diana, R. On the interference of vorticity and pressure fields of a minimal fish school. *J. Aero Aqua-Bio* **2019**, *8*, 27–33. [CrossRef]
- Dai, L.; He, G.; Zhang, X.; Zhang, X. Stable formations of self-propelled fishlike swimmers induced by hydrodynamic interactions. *J. R. Soc. Interface* **2018**, *15*, 20180490. [CrossRef] [PubMed]
- Verma, S.; Novati, G.; Koumoutsakos, P. Efficient collective swimming by harnessing vortices through deep reinforcement learning. *Proc. Natl. Acad. Sci. USA* **2018**, *115*, 5849–5854. [CrossRef]
- Liu, Y.; Jiang, H. Research development on fish swimming. *Chin. J. Mech. Eng.* **2022**, *35*, 114. [CrossRef]
- Dai, Y.; Yu, S.; Yan, Y.; Yu, X. An EKF-based fast tube MPC scheme for moving target tracking of a redundant underwater vehicle-manipulator system. *IEEE/ASME Trans. Mechatron.* **2019**, *24*, 2803–2814. [CrossRef]
- Cui, R.; Yang, C.; Li, Y.; Sharma, S. Adaptive neural network control of AUVs with control input nonlinearities using reinforcement learning. *IEEE Trans. Syst. Man Cybern. Syst.* **2017**, *47*, 1019–1029. [CrossRef]

21. He, Z.; Dong, L.; Sun, C.; Wang, J. Asynchronous multithreading reinforcement-learning-based path planning and tracking for unmanned underwater vehicle. *IEEE Trans. Syst. Man Cybern. Syst.* **2022**, *52*, 2757–2769. [CrossRef]
22. Jiang, P.; Song, S.; Huang, G. Attention-based meta-reinforcement learning for tracking control of AUV with time-varying dynamics. *IEEE Trans. Neural Netw. Learn. Syst.* **2022**, *33*, 6388–6401. [CrossRef]
23. Zou, Q.; Du, X.; Liu, Y.; Chen, H.; Wang, Y.; Yu, J. Dynamic path planning and motion control of microrobotic swarms for mobile target tracking. *IEEE Trans. Autom. Sci. Eng.* **2023**, *20*, 2454–2468. [CrossRef]
24. Yan, J.; Li, X.; Yang, X.; Luo, X.; Hua, C.; Guan, X. Integrated localization and tracking for AUV with model uncertainties via scalable sampling-based reinforcement learning approach. *IEEE Trans. Syst. Man Cybern. Syst.* **2022**, *52*, 6952–6967. [CrossRef]
25. Shi, W.; Song, S.; Wu, C.; Chen, C.P. Multi pseudo Q-learning-based deterministic policy gradient for tracking control of autonomous underwater vehicles. *IEEE Trans. Neural Netw. Learn. Syst.* **2019**, *30*, 3534–3546. [CrossRef] [PubMed]
26. Gao, S.; Peng, Z.; Liu, L.; Wang, D.; Han, Q.L. Fixed-time resilient edge-triggered estimation and control of surface vehicles for cooperative target tracking under attacks. *IEEE Trans. Intell. Veh.* **2023**, *8*, 547–556. [CrossRef]
27. Wai, R.J.; Lin, Y.W. Adaptive moving-target tracking control of a vision-based mobile robot via a dynamic petri recurrent fuzzy neural network. *IEEE Trans. Fuzzy Syst.* **2013**, *21*, 688–701. [CrossRef]
28. Huang, Y.; Zhu, M.; Zheng, Z.; Low, K.H. Homography-based visual servoing for underactuated VTOL UAVs tracking a 6-DOF moving ship. *IEEE Trans. Veh. Technol.* **2022**, *71*, 2385–2398. [CrossRef]
29. Lin, J.; Wang, Y.; Miao, Z.; Fan, S.; Wang, H. Robust observer-based visual servo control for quadrotors tracking unknown moving targets. *IEEE/ASME Trans. Mechatron.* **2023**, *28*, 1268–1279. [CrossRef]
30. Godoy-Diana, R.; Vacher, J.; Raspa, V.; Thiria, B. On the fluid dynamical effects of synchronization in side-by-side swimmers. *Biomimetics* **2019**, *4*, 77. [CrossRef]

**Disclaimer/Publisher’s Note:** The statements, opinions and data contained in all publications are solely those of the individual author(s) and contributor(s) and not of MDPI and/or the editor(s). MDPI and/or the editor(s) disclaim responsibility for any injury to people or property resulting from any ideas, methods, instructions or products referred to in the content.



## Article

# Locomotory Behavior of Water Striders with Amputated Legs

Javad Meshkani <sup>1,\*</sup>, Hamed Rajabi <sup>2</sup> , Alexander Kovalev <sup>1</sup> and Stanislav N. Gorb <sup>1</sup> <sup>1</sup> Functional Morphology and Biomechanics, Institute of Zoology, Kiel University, 24118 Kiel, Germany<sup>2</sup> Division of Mechanical Engineering and Design, School of Engineering, London South Bank University, London SE1 0AA, UK

\* Correspondence: meshkani.javad@gmail.com

**Abstract:** The stability of the body during locomotion is a fundamental requirement for walking animals. The mechanisms that coordinate leg movement patterns are even more complex at water–air interfaces. Water striders are agile creatures on the water surface, but they can be vulnerable to leg damage, which can impair their movement. One can assume the presence of certain compensatory biomechanical factors that are involved in the maintenance of postural balance lost after an amputation. Here, we studied changes in load distribution among the legs and assessed the effects of amputation on the locomotory behavior and postural defects that may increase the risk of locomotion failure. Apparently, amputees recover a stable posture by applying leg position modifications (e.g., widening the stance) and by load redistribution to the remaining legs. Water striders showed steering failure after amputation in all cases. Amputations affected locomotion by (1) altering motion features (e.g., shorter swing duration of midlegs), (2) functional constraints on legs, (3) shorter travelled distances, and (4) stronger deviations in the locomotion path. The legs functionally interact with each other, and removal of one leg has detrimental effects on the others. This research may assist the bioinspired design of aquatic robots.

**Keywords:** locomotion; aquatic bugs; robotics; morphology; insects



**Citation:** Meshkani, J.; Rajabi, H.; Kovalev, A.; Gorb, S.N. Locomotory Behavior of Water Striders with Amputated Legs. *Biomimetics* **2023**, *8*, 524. <https://doi.org/10.3390/biomimetics8070524>

Academic Editor: Jinyou Shao

Received: 3 October 2023

Revised: 22 October 2023

Accepted: 26 October 2023

Published: 4 November 2023



**Copyright:** © 2023 by the authors. Licensee MDPI, Basel, Switzerland. This article is an open access article distributed under the terms and conditions of the Creative Commons Attribution (CC BY) license (<https://creativecommons.org/licenses/by/4.0/>).

## 1. Introduction

The legs serve as supports for the body of insects in standing posture and during locomotion [1]. Stability of the body is an imperative requirement that must be maintained by all six legs [2,3]. Even though many studies have documented how the mechanical characteristics of legs influence the locomotion in terrestrial insects [4–7], the biomechanics of locomotion and the requirements for stability in semi-aquatic insects have only been studied to a very limited extent.

Water striders are carnivorous insects that dwell on the calm surface of diverse waterbodies [8–11] (Figure 1A). Their body weight is supported by the water surface owing to the cohesive property of water molecules [12–15]. They perform striding, leaping and jumping to move around on the water surface for finding nutrients, chasing each other to mate or fight, and for predation avoidance [16–21]. It is common for water striders to be attacked by predators, such as birds, fishes and aquatic beetles [22–24], which may lead to physical injury with leg loss, as we frequently observed in the studied population of water striders (Figure 1B).

The effect of amputation on terrestrial locomotion has been studied extensively in insects with tripod gaits [25–28]. In view of their sculling abilities and sliding on the water surface, water striders are particularly suitable semi-aquatic insects to study the compensatory behavior during aquatic locomotion in amputated animals. It has been shown that water striders can modify their motion by regulating leg movements [29–32], but it is unclear, which compensatory leg movements facilitate their ability to cope with the new conditions associated with missing supporting legs. In addition, the efficiency of striding changes following leg amputations is unknown. Non-synchronized leg movements can

reduce the efficiency of locomotion in insects due to the unbalanced body [33]. Earlier studies indicated that amputation in crickets leads to impairments of locomotory behavior [34], but this effect in a similar situation has not been documented in water walking insects. Water striders with their various body alignments are, therefore, suitable models to study the potential impairments of aquatic locomotion.

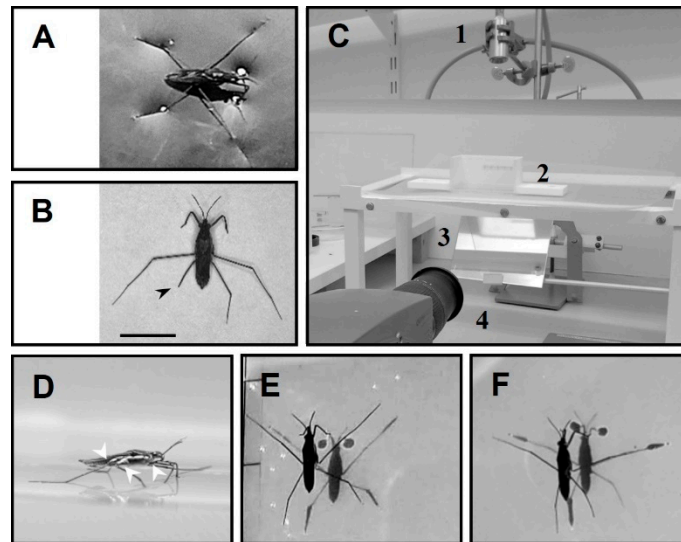


**Figure 1.** The experimental setup. (A) Water strider in its natural resting position. (B) Wild captured water strider missing part of hind leg (arrowhead). (C) The experimental setup including aquarium (2), light source on the top (1), high speed camera (4) and mirror (3) below the aquarium. (D) Side view of a water strider in standing position, the white arrowheads indicate joints that were disabled by gluing. (E) Water strider during standing position while all legs are in contact with water surface. (F) Water strider with an amputation in the right hindleg. Scale bar = 5 mm.

It has been not previously documented how water striders enact adaptive striding patterns when they become deprived of their natural leg number. In the present paper, we manipulated the legs by immobilizing them in order to investigate the effects of mechanical dysfunction on the insect's mobility. Therefore, the severity of amputations was categorized in three grades based on their stable balance during standing and motion. Striding is more likely to be performed by amputees with one unilaterally or maximum two contralaterally amputated legs. But for individuals with bilaterally and ipsilaterally amputated legs, it was difficult or impossible to traverse the water surface.

Additionally, we conducted tests to investigate how the reduced number of supporting sites could affect the distribution of the bodyweight. As a means of understanding motion modifications after amputation, we assessed the alterations in body posture, as well as the sequential order of leg movements involved in performing a sculling stroke. This modelling approach may be useful in determining the biomechanical requirements for maintaining floating bodies on the water surface under a variety of conditions. In general, this research not only helps understand aquatic locomotion control in water striders but may potentially assist the bioinspired design of aquatic robots.

## 2. Material and Methods

### 2.1. Animals

Water striders, *Gerris argentatus*, were collected from a pond located in the botanical garden of Kiel University, Kiel, Germany. Several groups of amputees were established in the laboratory to simulate physical injuries. We immobilized their legs rather than cut them during the experiments to avoid wounds and causing misbalance by asymmetrical removal of weight. A bead volume of glue was applied to the joint between the coxa and



femur while the femur was flexed upward to keep the tip of the target leg away from the water surface (Figure 1D,F).

## 2.2. Protocol of Measurement of Load Changes

Load change on the legs were estimated by the shadow tracking method, which has been used in previous studies [31,35–37]. As water striders float on the top of water, the surface below the legs is deformed in significant relationship with the load on each leg [38] (Figure 1A). As light beams pass through water, dimples cause them to be distorted, which leads to the appearance of a shadow area with a bright perimeter on the bottom of the aquarium. After proper calibration, the loads on individual legs can be estimated by measuring the size of these shadows [36,37]. According to the shadow method, vertical forces on the water surface have a significant correlation with the shadow area of the corresponding leg at the bottom of the vessel, and the bodyweight of water striders can be estimated by the total shadow areas of the legs [37].

Based on the measurements of leg shadows, the load applied by each leg can be expressed as a fraction of the total in percentage. In the present paper, based on the size of leg shadows, the load applied by each leg was calculated, and the measurements were converted into percentages to visualize the patterns of load changes for the amputated water striders.

## 2.3. Experimental Setup

Individuals were tested in a vessel with dimensions 10 cm × 5 cm × 5 cm (L × W × H) and filled with distilled water (ca. 5 mm in height), (Figure 1C). The tested groups performed striding freely, unassisted with external stimuli, to start or finish the motion. A source of illumination (*Storz Techno Light 270 Cold Light Projector*, KARL STORZ SE & Co., Tuttlingen, Germany) was installed on the top. The bottom of the vessel was lined with a 125-micron white semi-transparent polymer sheet (GBC) to make the shadows visible. An inclined mirror (45°) was placed below the vessel, to guide the shadow images to the camera. The animals were video-recorded over a period of 255 ms using a high-speed camera at 2000 frames per second (Olympus I-Speed 3 Series High-Speed Cameras, Olympus, Tokyo, Japan). The experiments were conducted at room temperature (25 °C).

## 2.4. Analysis Procedure

The frames of the captured videos were analysed using ImageJ to measure the shadow areas caused by the legs [39]. From the shadows, we tracked the positions of the body center and legs using the Manual Tracking plugin in ImageJ. We assumed the body center corresponded to the likely position of the center of body mass. Statistical analyses were performed by using SigmaPlot 12.0 (Systat Software Inc., San José, CA, USA).

## 2.5. Labeling of Legs and Their Amputations

The dark spots on the bottom of the aquarium are the shadows of the legs (Figure 1E). The shadows correspond to the dimples in the water surface tension film under the legs. The shadows of forelegs, midlegs, and hindlegs on the left and right sides are indicated by (LF, LM and LH) and (RF, RM and RH), respectively [40] (Figure 2A). FL, ML, and HL indicate the pairs of forelegs, midlegs, and hindlegs, respectively.

We amputated animals by immobilizing the target legs to assess different effects depending on the disability of particular legs or their combinations. “−” indicates the body side with the amputated leg, “+” represents the normal side of body, and “&” indicates the combination of two amputations. This study addresses the impact of unilateral (−/+ or +/−), bilateral (−/−), ipsilateral (−/+ & −/+ or +/−) and contralateral (−/+ & +/−) amputations. Accordingly, the amputation possibilities are listed in Table 1.

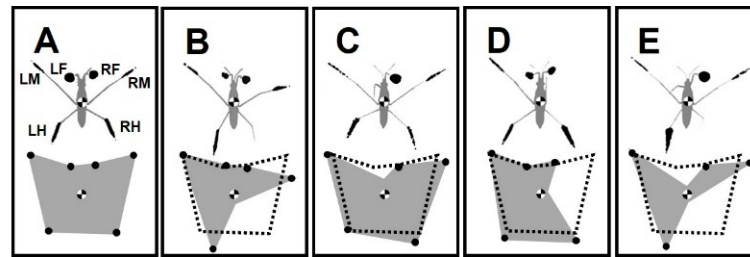


**Figure 2.** Illustration of shadow areas of legs and BOS for intact water striders and those with amputations. (A–E) The scheme of corresponding shadow area for the forelegs, midlegs and hindlegs which are labeled as LF, LM and LH, and as RF, RM and RH, on left and right sides, respectively. The black dots denote the contact points of legs. The scheme of BOS for the amputees. The normal BOS (shown with the dotted-line) is repeated in (B–E). (A) Intact water strider. (B) Right-hindleg amputation  $+/-$  RH. (C) Left-foreleg amputation  $-/+$  LF. (D) Right-hindleg and left-foreleg amputation  $+/-$  RH &  $-/+$  LF. (E) Right-midleg amputation  $+/-$  RM.

**Table 1.** The amputation possibilities.

Symbols	Amputated Leg(s)
$+/-$ RH	Right-hindleg
$-/+$ LF	Left-foreleg
$-/-$ HL	Hindlegs pair
$-/-$ ML	Midlegs pair
$-/-$ FL	Forelegs pair
$+/-$ RH & $+/-$ RM	Right-hindleg and Right-midleg
$+/-$ RF & $+/-$ RM	Right-foreleg and Right-midleg

### 3. Results

#### 3.1. Severity Grades of Amputations

A common trait among all amputees was the inability to perform straightforward striding. Striding occurs through the symmetrical process of sculling, which is carried out by the midlegs (scull-legs) while the body slides on the water by the forelegs and hindlegs (ski-legs) [31,35] (Figure 3A). A sculling stroke is generated by the midlegs during the driving phase as the tips of legs move backward from the catch position to the finish position. Following this, the midlegs swing forward through the air to the recovery position, while the body continues to slide without effort during the passive sliding. On the basis of the experimental data, we classified the severity effect of amputations into three grades based on their ability to execute sculling (Table 2).

**Table 2.** Severity grades of amputations.

Grade I	Grade II	Grade III
$+/-$ RH	$+/-$ RH & $-/+$ LF	$-/-$ HL
$-/+$ LF	$-/-$ FL	$-/-$ ML
$+/-$ RM		$+/-$ RH & $+/-$ RM
		$+/-$ RF & $+/-$ RM

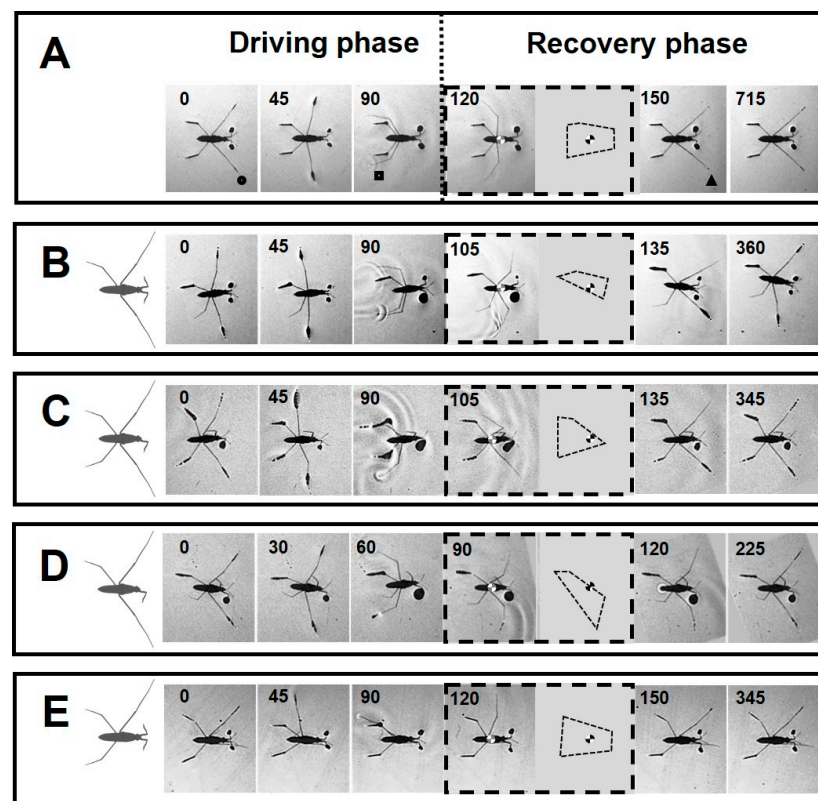


**Figure 3.** Sequences of leg kinematics during striding cycles. (A–E) The body position within a striding sequence for intact and individuals with  $+/-RH$ ,  $-/+LF$ ,  $+/-RH$  &  $-/+LF$  and  $+/-RM$  amputations, respectively. The insets indicate the BOS and the position of the center of the body during swinging the midlegs. The number in each frame indicates the time in millisecond. (A) Dotted line separates the driving phase (left) and the recovery phase (right). The circle, square and triangle indicate three key positions of the midlegs at the catch, finish and recovery positions, respectively. During the driving phase, the midlegs travel backward from the catch position to the finish position and touch-off from the water surface. The recovery phase starts with swing of the midlegs while the body passively continues sliding. During passive sliding, the body slides across the surface of the water without effort of the midlegs. The midlegs after swing touch-down to the water surface at the recovery position.

Grade I: Amputees, with ability to maintain standing position, can execute sculling ( $+/-RH$ ,  $-/+LF$ , and  $+/-RM$ ) (Figures 2B,C,E and 3B–E).

Grade II: Amputees can stand on water, while unable to perform a typical striding ( $+/-RH$  &  $-/+LF$  and  $-/-FL$ ) (Figures 2D, 3D and 4A). In  $-/-FL$ , the ventral side of the thorax serves as a bearing point for a short period of time during swinging of midlegs (Figure 4A). In  $+/-RH$  &  $-/+LF$ , the right midleg never swings through the air and stays attached to the water surface.

Grade III: This grade of amputation leads to the inability to stand and move over water ( $-/-ML$ ,  $-/-HL$ ,  $+/-RH$  &  $+/-RM$  and  $+/-RF$  &  $+/-RM$ ). In this case, the water striders are trapped in the water and sink shortly after being above the water surface (Figure 4B,C; Figure 5A,B). Similar outcomes are expected for more severe amputations. Individuals without both midlegs can remain over the water surface and perform a staggering motion (Figure 4B). The motion is accomplished by rotation of the body to one side and pulling forward the hindleg on the other side, then repeating the motion to the other side. These amputees can only travel over a very short distance of a few millimeters. Although the grooming behavior is normal behavior for intact individuals, with of rubbing midlegs against forelegs or hindlegs on the same side, in our observations,  $+/-RH$  &  $+/-RM$  and

+/-RF & +/- RM amputations were trapped by the water as soon as they were put on the water surface (Figure 5A,B).

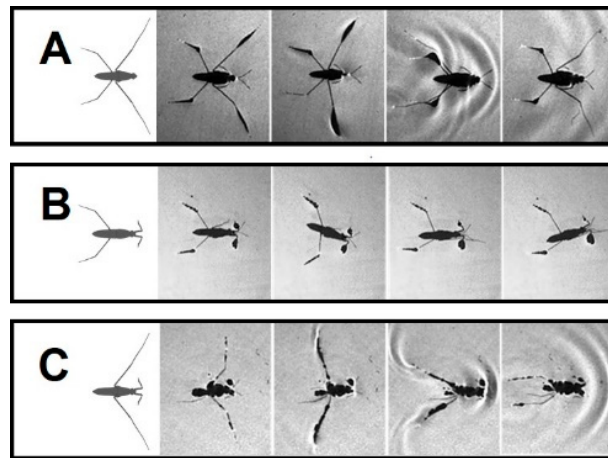


**Figure 4.** The body positions for water striders with bilateral amputation. (A) Forelegs amputation -/- FL. (B) Midlegs amputation -/- ML. (C) Hindlegs amputation -/- HL.



**Figure 5.** +/- HL & +/- ML (A) and +/- FL & +/- ML (B) amputations were trapped in water immediately after they were put on the water surface.

Amputees of all types demonstrate non-symmetrical leg movement in comparison with intact individuals. In this study, we report on measurements mainly performed for amputees in Grades I and II.

### 3.2. Changes in Standing Posture

Generally, water striders stand with six points of contact, while the body center is located over the middle of the base of support (BOS) (Figure 2A). BOS refers to the imaginary area beneath the body and within the points where the legs contact the surface. BOS is associated with maintaining the equilibrium of body posture [41]. An amputation leads to an asymmetry in the BOS, while the area of BOS varies by the number of legs circumscribing the area. On the same scale, the BOS for the studied insects showed a variety of shapes and sizes (Figure 2B–E). BOS measurements for the intact, +/- RH, -/+ LF, +/- RH & -/+ LF, and +/- RM amputated individuals were 274, 177, 288, 144, and 220 mm<sup>2</sup>, respectively.

### 3.3. Load Change on the Legs during Locomotion

The kinematics of leg sequences for amputees differed from those of intact individuals (Figure 3A–E). We plotted the load changes on the legs for amputees during a given time (Figure 6A–D). The load change graphs for amputees showed different load patterns for all legs, compared with intact individuals (Supplementary Figure S1).

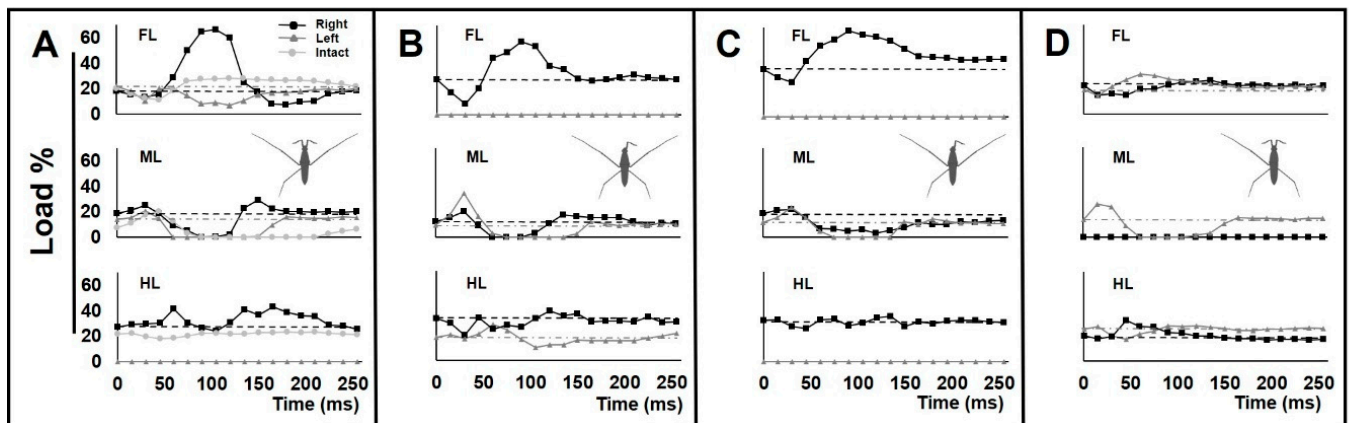


**Figure 6.** Load changes on the legs during striding. (A–D) The graphs of load changes on the legs in percentage for individuals with  $+/-RH$ ,  $-/+LF$ ,  $+/-RH$  &  $-/+LF$  and  $+/-RM$  amputations, respectively. Each graph shows the mean value of load, with the legs of each pair presented in one plot. Black lines with squared joints represent right-legs, and gray lines with triangled joints represent left-legs. The dashed lines are the baselines that represent the average load value applied on right-legs in the static state, and the dash-dotted gray lines are the baselines that represent the average load value applied on left-legs in the static state. (A) Faint gray lines with circled joints represent normal mean values of load for intact individuals for reference (Supplementary Figure S1).  $N = 3$ .

For  $+/-RH$ , an abnormal increase in the load on the right foreleg was observed. This was accompanied by a decrease in the load on the left foreleg (Figure 6A). For  $-/+LF$ , the initial load reduction on the only foreleg was followed by a massive load increase to a peak value (Figure 6B). The increasing load acting on the forelegs could be due to anterior leaning of the body. In both types of  $+/-RH$  and  $-/+LF$  amputations, the swing duration of the midlegs was shorter than in intact animals, particularly on the affected side of body.

In the case of the  $+/-RH$  &  $-/+LF$  amputation, the range of load disruption for the legs was more extensive than in all other amputees (Figure 6C). Also, the right midleg acted as a support during the passive sliding phase and was constantly in contact with the water surface (Figure 3D). Following the driving phase, the load increased on the remaining foreleg.

In the case of  $+/-RM$  amputation, with a shortened swing period, the load on the only midleg was higher than normal (Figure 6D). There was an unusually high level of pressure on the left foreleg and hindleg during the sculling stroke.

### 3.4. Positioning of Bodies during Striding Cycle

In amputees, the striding cycle was associated with heading error, while the bodies rotated around the vertical axis of the body center (Figure 7). Based on the body center tracking, the heading error angles for  $+/-RH$ ,  $-/+LF$ ,  $+/-RH$  &  $-/+LF$  and  $+/-RM$  were  $\alpha = 8^\circ$ ,  $\beta = 21^\circ$ ,  $\gamma = 10^\circ$  and  $\varepsilon = 47^\circ$ , respectively, and the body yaw angles were  $\tau = 19^\circ$ ,  $\phi = 29^\circ$ ,  $\omega = 20^\circ$  and  $\varphi = 35^\circ$  and  $9^\circ$ , respectively. For  $\varphi$ , we presented two values as the animals initially showed a sharp yaw angle, but the body continued sliding with a low change in the yaw angle. Contralateral amputation of one foreleg and one hindleg resulted in the rotation of the body in zigzagged patterns, but the striding cycle ended with a deviation, as well as rotation toward the direction of the amputated hindleg (Figure 7D). The amputees travelled shorter distances than intact animals during a given time (255 ms), with distances of 28, 23, 21, 14, and 18 mm for the intact,  $+/-RH$ ,  $-/+LF$ ,  $+/-RH$  &  $-/+LF$ , and  $+/-RM$  individuals, respectively (Figure 8A).

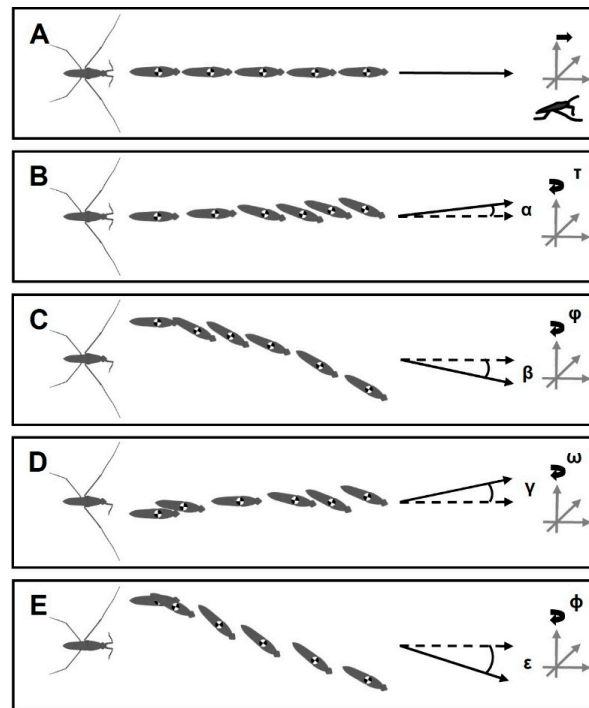


**Figure 7.** Illustration of the body trajectory. (A–E) The body positions during a striding cycle. The black arrow lines indicate the real direction of body sliding. (B–E)  $\alpha = 8^\circ$ ,  $\beta = 21^\circ$ ,  $\gamma = 10^\circ$  and  $\varepsilon = 47^\circ$  show the angle of deviation between the direction of body sliding and the reference pose of the body (Dashed arrow lines).  $\tau = 19^\circ$ ,  $\phi = 29^\circ$ ,  $\omega = 20^\circ$  and  $\phi = 35^\circ$  and  $9^\circ$  indicate the spinning angles of heads relative to the vertical axis of the body center. (A) Intact water strider. (B) Right-hindleg amputation +/- HL. (C) Left-foreleg amputation +/- FL. (D) Right-hindleg and left-foreleg amputation +/- FL & +/- HL. (E) Right-midleg amputation +/- ML.

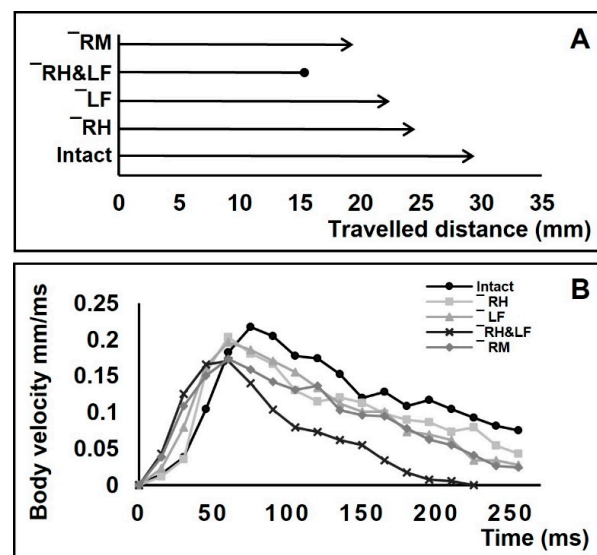


**Figure 8.** Comparison of travelling distance and the body velocity before and after amputations. (A,B) Travelling distances within a given time (255 ms) for intact, right-hindleg amputation +/- HL, left-foreleg amputation +/- FL, right-hindleg and left-foreleg amputation +/- FL & +/- HL, and right-midleg amputation +/- ML. The lines with arrowhead denote the bodies still moving, the line with a dot at the end denotes a body that stopped within the given time. (B) Velocity of bodies over time for intact, right-hindleg amputation +/- HL, left-foreleg amputation +/- FL, right-hindleg and left-foreleg amputation +/- FL & +/- HL, and right-midleg amputation +/- ML.



The loss of one foreleg and one hindleg, or contralateral limb loss, causes the velocity of the body to rapidly reach peaks that are lower than normal for intact individuals and then drop to zero in a short period of time (Figure 8B).

### 3.5. Jumping Ability

Although only striding has been characterised, the ability of the amputees to jump was also noted in this study. According to previous studies, synchronized movements of the midlegs and the hindlegs are required to perform jumping [30,32]. The amputee water striders with one missing foreleg, one hindleg, one midleg, both forelegs, a combination of one foreleg and one hindleg, and a combination of one midleg and one foreleg were able to jump, whereas individuals missing both midlegs, both hindlegs or a combination of one midleg and one hindleg were unable to jump. Consequently, water striders must possess a minimum of three middle and hind legs (both midlegs with one hindleg, or one midleg with both hindlegs) to be able to jump.

## 4. Discussion

### 4.1. Postural Change after Amputation

A highly sprawled position of the legs can provide insects with a stable posture [42]. However, insects can stand on fewer than six legs in contact with the water surface during the grooming behavior [43,44]. The absence of support from a single leg leads to immediate body postural changes [45]. Nevertheless, amputated insects adjust the legs to widen their stance in order to increase the size of the BOS [26]. As we observed for the examined amputee groups of water striders, the BOS changed in different ways due to different sets of weight-supporting legs (Table 2). With a larger area BOS, there is more chance for the center of the body to be positioned within the BOS and to increase body stability [28]. Based on the size and shape of the BOS, we anticipate that individuals are in unstable position in the following order with the first one as the most unstable:  $+/-RH \& -/+LF$ ,  $+/-RM$ ,  $+/-RH$  and  $-/+LF$  (Figure 2B–E). Although the individuals without forelegs can perform a kind of sculling, those with an absence of support from the hindlegs are even unable to stay on the water surface (Figure 4A,C). Our previous study indicated that the midlegs play a compensatory role during absence of support from the forelegs [31]. Also, amputation of each hindleg alone or in combination with other legs has a more substantial impact on falling risk due to the strong shrinkage of the BOS. Based on the natural configuration of the legs, the removal of both hindlegs causes the center of the body mass to be located outside the BOS (Figures 2A and 4C).

Compared with the pattern of weight distribution in intact individuals, the shadows below the legs of amputees resized, whereas the shadows on the left and right sides were not equal (Figure 2A–E). The leg sensory equipment assists with the control of load distribution among the legs [46,47]. Amputated insects can benefit from this mechanism to coordinate the rest of their legs with a gentle load shift among them. Quantifying changes in the shadow sizes of the legs provides a precise measurement that indicates the extra weight from removed legs was unevenly shifted to different remaining legs (Table 3). Based on the particular set of missing legs, the body shows some degree of leaning toward a side. In the absence of support from one leg, the adjacent leg, and the rest of legs on the same side of amputation primarily take the load bearing, and also those on the opposite side play a compensatory role to support the body.

The water striders are extremely efficient and agile water surface walkers, which makes them ideal for inspiring the design of robots that need to operate on water surfaces [48,49]. This knowledge can assist with understanding how multi-legged aquatic robots could coordinate support on the water surface to maintain a stable stance.

**Table 3.** Static measurements.

Animal Model	Load Value on Legs (%)						BOS (mm <sup>2</sup> )
	R1	R2	R3	L1	L2	L3	
Intact *	19	10	21	19	10	21	274
+ / − RH	21	18	0	20	13	28	177
− / + LF	30	10	22	0	11	27	288
+ / − RH & − / + LF	34	22	0	0	15	29	144
+ / − RM	21	0	27	20	13	19	220

\* Typical pattern of bodyweight distribution in intact water striders [31].

#### 4.2. The Presence of All Legs Is Essential for Straightforward Striding

A major challenge for walking animals is maintaining body balance, particularly during the transition between two gaits, when the stability of the body is low [28]. A larger BOS that is obtained by widening the angle of the legs improves stability of the body during stepping [25–27]. In terrestrial insects, the BOS is small in size during the tripod gait when only three legs are in contact with the surface [3,28,42]. In addition to the shrinkage of the BOS, an amputation-induced condition moves the center of the body to the edge of the BOS, resulting in an unstable state, which is further exacerbated, when it is situated outside of the BOS [50–54] (Figure 2B–E). However, insects can slightly improve their mechanical efficiency by adjusting locomotory behavior after amputation [27].

Prior to performing motion, semi-aquatic insects can adjust the position of their legs, to achieve a six-legged starting posture with appropriate weight distribution [31,35,55]. In the case of severe types of amputation, falling of the body occurs in the standing position or immediately at the beginning of sculling (Figure 5). Despite this, some types of amputees can adjust their legs to execute striding. However, synchronization of midlegs movement, which is imperative for straightforward striding [56,57], is not commonly achieved for all amputees (Figure 3A–E).

Hence, the most important consequence of leg amputation was the change in the body locomotion trajectory (Figure 7). The body of disabled water striders rotated toward the affected side due to a lack of any support from the hindleg and midleg, or toward the opposite side after removal of the foreleg. This rotation causes the body to pull to the same side and results in the heading error.

A substantial risk of steering control loss can occur after the removal of a hindleg and particularly in combination with the amputation of a foreleg when the amputees were unable to keep the body in the initial posture (Figure 7B–D). On the other hand, following a sharp rotation about the vertical axis of body at the beginning of locomotion, the striding path was improved for the individuals with − / + LF and + / − RM characteristics (Figure 7C,E). It seems that the hindlegs enable the insects to reverse the body rotation and direct it on a nearly straight path; however, a little heading error remains as the body continues sliding. The heading error is opposite or toward the side on which only the midleg or foreleg are in contact with the water surface in the cases of − / + LF and + / − RM amputations, respectively. This shows that the hindlegs are functionally essential, but not sufficient, for steering.

In terrestrial insects, the legs work together to provide an optimal locomotion process [58]. Similarly, in water striders, all the legs are seen to play an essential role in efficient striding. Previous studies reported a rudder role for the hindlegs during striding [16,59,60]. However, the rudder function of hindlegs to direct and improve the locomotion trajectory is not independent of the natural movements of other legs. In other words, the hindlegs are unable to perform their steering function when other legs are not functioning properly. However, further studies are needed to uncover how the kinematic chain of each leg, which is dependent on the degrees of freedom of their joints, is important in motion trajectory control.

#### 4.3. Asymmetrical Load Changes on the Legs during Locomotion

Sculling performance is well known to fluctuate with changes in body posture and the distribution of load on the legs [56,57,61]. During sculling, loading and unloading of the legs must occur symmetrically to ensure straightforward sliding [31,35]. Load shifting among the legs is an important factor strongly affecting the insect walking [50,62]. Insects are unable to execute stepping without the compensatory weight support by the other legs [45]. By switching from the more stable six-legged posture [1] to a stance with fewer legs, the body posture of the water strider becomes asymmetrical (Figure 2). In response, during striding, an irregular pattern is observed with increases and decreases in the load carried by the remaining legs that is different from the symmetrical pattern in an intact water strider (Figures 3 and 6) (Supplementary Figure S1). This is important because the power generation for walking is influenced by the pattern of load distribution among the legs [63]. During passive sliding, the loads on the legs gradually return to the levels at the starting position. With dysfunction of the legs, the amputees are unable to avoid the irregularity of body sliding, and lean back to the normal posture, which causes a load perturbation on the legs (Figure 6). With an increasing number of amputated legs, the range of the load perturbation for the remaining legs was more extensive (Figure 6C). Thus, with the complete set of legs in intact animals which allows load balancing, the disturbance of locomotion performance remains minimal.

Amputation of any leg interferes with the load-bearing task of the other legs (Figure 2). Subsequently, disproportionate load distribution influences the sequential order of locomotion features, which leads to abnormality in the striding performance (Figures 3 and 6–8). Earlier studies have shown that irregular loading of legs directly influences kinematics of insects [64,65]. However, during terrestrial locomotion, insects can coordinate the movements of their legs during stepping and modify their motion in response to load changes [66,67]. With a fair striding performance, individuals with  $+/-$  RH or  $-/+$  LF can roughly re-establish their postural control. This shows that there is a degree of coordination between the legs which allows water striders to optimize their ability to float in water.

As a result of amputations, terrestrial insects change their stepping pattern due to alterations in their balance. In turn, this leads to an increasing energy cost of locomotion [34,68]. Water striders with amputations must put their legs in unusual positions to fulfil the supportive function, which can restrict their normal leg movements. Consequently, it becomes increasingly difficult for amputees to maintain their floating on the water surface. In addition, they are unable to achieve a smooth load shifting among the legs that is required for a gentle striding performance (Supplementary Figure S1).

#### 4.4. Changes in Locomotory Behavior after Amputations

The horizontal thrust of body is exclusively provided through the sculling stroke, by using the midlegs [14,56,69,70]. In the present paper, this was also confirmed by observing the inability of the amputees without midlegs to execute striding (Figure 4B). Absence of support from one leg interferes with the kinematics of the other legs since the latter change their usual function, which in turn affects the efficiency of locomotion [45,71]. Quantification of velocity and travelling distance associated with the locomotion of intact water striders provided us with an indicator to assess the interaction between sculling and striding. Shorter traveling distances by amputees with only one midleg is attributed to impaired sculling stroke (Figure 8A). The travelling distances indicating the efficiency of sculling stroke were negatively affected by all types of amputation, even if both midlegs remained intact. It seems that missing any other supporting leg also leads to impaired locomotory behavior. Impaired locomotion also leads to reduced walking speed in terrestrial insects, such as cockroaches [72], mole crickets [73], and stick insects [58,74]. In water striders, the results are similar, showing that amputations affect both floating of the body and the generation of propulsion.

Despite having both midlegs,  $+/-$  RH &  $-/+$  LF,  $+/-$  RH and  $-/+$  LF amputees were found to be unable to execute symmetrical sculling. This exacerbates the lack of

steering control that affects the locomotion parameters. For instance, the velocity of the body drops faster than normal (Figure 8B). The initial surge in body velocity that is followed by a gradual deceleration occurs during steady sliding [31]. The common feature of the amputees is a rapid drop in velocity from the peak that is gained during the sculling stroke (Figure 8B). It is unclear whether the presence of all legs is essential for a gradual reduction in the body velocity or if animals behaviorally reduce it in response to weak steering control. The striding cycle ended during the given time for the  $+/-RH$  &  $-/+LF$  amputees, but the remaining amputees were able to maintain velocity to cover further distances. Affected by a lack of stabilizing function provided by the hindlegs and forelegs, amputees may have greater loss of control over their stability and thus reduce their speed to avoid toppling (Figure 8B). Thus, it can be deduced that instability of the body negatively affects striding during both driving and passive sliding phases. It shows the efficient striding of water striders requires synergic function of all legs, especially the midlegs. If missing any leg, water striders are unable to sustain a proper balance, and a considerable amount of propelling power may be wasted in attempting to maintain body floating and steering. This is manifested as a reduction in travelling distances during a given period of time (Figure 8A). Even so, the exact mechanism of how water striders control their speed during passive sliding is unknown, which can be explored in future studies. We predict the presence of certain mechanical constraints on the degrees of freedom in leg joints leading to unbalanced posture of the body that in turn increases the expenditure of energy.

#### 4.5. Characterizations of Striding after Amputation

Utilizing their sensory system, insects govern their normal leg kinematics and adapt to various walking surfaces [45,75]. Adaptive spatiotemporal coordination patterns after leg amputation are known in cockroaches [45,68], stick insects [53,58], desert ants [76,77], and fruit flies [78,79]. Even after amputation, insects can execute a coordinated approach to adaptation of leg movement patterns to improve their mechanical efficiency [27]. In water striders, the leg pairs on two sides of the body normally move in synchrony with each other during both phases of driving and passive sliding. The supportive role of the legs extensively changes after amputation, mainly with asymmetrical alterations in leg movement timings (Figure 3). Amputations induce dramatic changes in patterns of the midleg movements, particularly in the timing of key events including sculling stroke, touch-off from and touch-down to the water surface, swing and so on (Figure 3). Water striders use asymmetrical sculling in some cases, such as when carrying prey. They support their bodies with one midleg and propel themselves forward with the other [80]. In the amputated water striders, the midlegs never detach from the water surface, or swing quickly in a shorter period of time (Figure 3). This illustrates that the midlegs are required to take more weight-bearing responsibilities as the body is in an instable state. It is a sign of coordination of the legs, which ensures a proportionate load distribution between the remaining legs. The assessment of the leg loading patterns of water striders indicates their partial dependency on each other. Although it seems that the sculling movements of midlegs are largely independent of each other, their kinematics are loosely coupled with the function of other legs (Figure 3).

An amputation impedes the natural leg placement and reduces the leg's ability to govern movements. In fact, the dysfunction of each leg adversely affects the overall functioning of the locomotion system. Although their mobility continues, the amputees show difficulties in maintaining a stable locomotion trajectory, velocity and travelling distance (Figures 7 and 8). However, amputated water striders can partially adapt the orchestration of leg movements to establish striding. Although the forelegs and hindlegs do not contribute to sculling, they may actively minimize the body instability imperfections to enable smooth locomotion [31]. There seems to be a predominant impact on striding performance associated with the loss of the hindleg (Figures 6 and 7).

Amputations, depending on their severity, lead to behavioral changes in striding. Since the probability of falling becomes more pronounced, as the center of body approaches

the edge of the BOS, animals reduce the time of sculling and sliding, depending on the severity of their amputation (Figures 3 and 8). Hence, the present study represents a useful approach for understanding adaptability of the locomotory system of water striders to challenging situations.

The amputees, in some cases, can perform locomotion in a rather stable manner despite differences from the typical striding. Thus, water striders can be a good model system for the optimisation of walking robots after accidental damage. Our findings can also potentially help to develop aquatic-legged robots for use in environments with high risks of damage.

## 5. Conclusions

Water striders with missing legs achieve posture stability by adapting their BOS using their remaining legs. Despite not being sufficiently coordinated, they modify the position of their legs after amputation to improve weight distribution and avoid falling. Water striders spread their legs further apart from the body to compensate for the shrinkage of the BOS that results from a decreased number of contact points. Only individuals with one or two unpaired missing supports can stand over water, but this does not imply their ability to execute sculling. After amputation, the efficiency of striding becomes lower, the risk of falling higher, the travelling distance shorter and the maximum velocity lower. During locomotion, the amputees control leg movements by a fast recovery that is coupled with a rapid body re-alignment, which minimizes the induced irregularities in locomotion and prevents the body from toppling. There is a certain interdependence between the kinematics of each leg and that of the other legs. In either case, steering control error of the body appears to result from the loss of hindlegs and forelegs at the first and second ranks, respectively. Our results help to elucidate the adaptability of water strider locomotion to the challenging condition of missing extremities. Additionally, this research may facilitate the design of stable water-walking robots with different numbers of supporting limbs.

**Supplementary Materials:** The following supporting information can be downloaded at: <https://www.mdpi.com/article/10.3390/biomimetics8070524/s1>. Figure S1: Load changes on the legs during striding. (A) The gray boxes in the background indicate the driving phase. The dashed lines are the baselines that represent the average load value applied on the legs in the static state. Gray lines are individuals, and the black lines are the mean for each leg. (B) The black lines are the mean for each leg pair. The dashed lines are the baselines that represent the average load value applied on the legs in the static state. Shadows below the forelegs, midlegs and hindlegs are labeled as LF, LM and LH, and as RF, RM and RH, on the left and right sides, respectively. FL ML and HL represent the pairs of forelegs, midlegs, and hindlegs respectively [31].

**Author Contributions:** S.N.G., J.M. and A.K. designed the study; J.M. executed the experiment and carried out the analysis. H.R. and A.K. confirmed the analytical results. J.M. wrote the manuscript with assistance from H.R., A.K. and S.N.G. S.N.G. supervised this project. All authors discussed the results and contributed to the final manuscript. All authors have read and agreed to the published version of the manuscript.

**Funding:** This work was partially funded by the German Science Foundation (Deutsche Forschungsgemeinschaft (DFG) grant GO 995/38-1).

**Institutional Review Board Statement:** This work complies with the ethical guidelines of Kiel University.

**Data Availability Statement:** All supporting data are made available in the article.

**Acknowledgments:** Special thanks to Halvor T. Tramsen for his helpful discussion and insightful comments.

**Conflicts of Interest:** The authors declare there are no conflicts of interest to disclose.

# References

1. Hughes, G.M. The Co-Ordination of Insect Movements: I The Walking Movements of Insects. *J. Exp. Biol.* **1952**, *29*, 267–285. [CrossRef]
2. Cruse, H. The Function of the Legs in the Free Walking Stick Insect, *Carausius morosus*. *J. Comp. Physiol. A* **1976**, *112*, 235–262. [CrossRef]
3. Delcomyn, F. Insect Locomotion on Land. In *Locomotion and Energetics in Arthropods*; Springer US: New York, NY, USA, 1981; pp. 69–91. [CrossRef]
4. Full, R.J.; Tu, M.S. Mechanics of a Rapid Running Insect: Two-, Four-, and Six-Legged Locomotion. *J. Exp. Biol.* **1991**, *156*, 215–231. [CrossRef] [PubMed]
5. Dürr, V.; Theunissen, L.M.; Dallmann, C.J.; Hoinville, T.; Schmitz, J. Motor Flexibility in Insects: Adaptive Coordination of Limbs in Locomotion and Near-range Exploration. *Behav. Ecol. Sociobiol.* **2018**, *72*, 15. [CrossRef]
6. Schmitt, J.; Holmes, P. Mechanical Models for Insect Locomotion: Dynamics and Stability in the Horizontal Plane I. Theory. *Biol. Cybern.* **2000**, *83*, 501–515. [CrossRef] [PubMed]
7. Weihmann, T. The Smooth Transition From Many-Legged to Bipedal Locomotion-Gradual Leg Force Reduction and its Impact on Total Ground Reaction Forces, Body Dynamics and Gait Transitions. *Front. Bioeng. Biotechnol.* **2022**, *9*, 769684. [CrossRef] [PubMed]
8. Andersen, N.M. *The Semiaquatic Bugs*; Scandinavian Science Press Ltd.: Klampenborg, Denmark, 1982; Volume 3.
9. Andersen, N.M. The evolution of marine insects: Phylogenetic, ecological and geographical aspects of species diversity in marine water striders. *Ecography* **1999**, *22*, 98–111. [CrossRef]
10. Crumière, A.J.J.; Santos, M.E.; Sémon, M.; Armisen, D.; Moreira, F.F.F.; Khila, A. Diversity in Morphology and Locomotory Behavior Is Associated with Niche Expansion in the Semi-aquatic Bugs. *Curr. Biol.* **2016**, *26*, 3336–3342. [CrossRef]
11. Ortega-Jimenez, V.M.; von Rabenau, L.; Dudley, R. Escape Jumping by Three Age-Classes of Water Striders from Smooth, Wavy and Bubbling Water Surfaces. *J. Exp. Biol.* **2017**, *220*, 2809–2815. [CrossRef]
12. Bush, J.W.M.; Hu, D.; Prakash, M. The Integument of Water-walking Arthropods: Form and Function. *Adv. Insect Physiol.* **2007**, *34*, 117–192. [CrossRef]
13. Denny, M.W. Paradox Lost: Answers and Questions about Walking on Water. *J. Exp. Biol.* **2004**, *207*, 1601–1606. [CrossRef] [PubMed]
14. Hu, D.L.; Chan, B.; Bush, J.W.M. The Hydrodynamics of Water Strider Locomotion. *Nature* **2003**, *424*, 663–666. [CrossRef]
15. White, H.E. *Modern College Physics*; van Nostrand: New York, NY, USA, 1948; ISBN 978-0-442-29401-4.
16. Andersen, N.M. A comparative study of locomotion on the water surface in semiaquatic bugs (Insects, Hemiptera, Gerromorpha). *Videnskabelige Meddelelser fra Dansk Naturhistorisk Forening* **1976**, *139*, 337–396.
17. Caponigro, M.A.; Eriksen, C.H. Surface Film Locomotion by the Water Strider, *Gerris remigis* Say. *Am. Midl. Nat.* **1976**, *95*, 268–278. [CrossRef]
18. Hu, D.L.; Bush, J.W.M. The Hydrodynamics of Water-Walking Arthropods. *J. Fluid Mech.* **2010**, *644*, 5–33. [CrossRef]
19. Kim, H.; Amauger, J.; Jeong, H.; Lee, D.; Yang, E.; Jablonski, P.G. Mechanics of Jumping on Water. *Phys. Rev. Fluids* **2017**, *2*, 100505. [CrossRef]
20. Kovalev, A.; Filippov, A.E.; Gorb, S.N. Numerical Model of the Spatio-Temporal Dynamics in a Water Strider Group. *Sci. Rep.* **2021**, *11*, 18047. [CrossRef]
21. Waldbauer, G.A. *Walk around the Pond: Insects in and over the Water*; Harvard University Press: Cambridge, MA, USA, 2006; pp. 109–111.
22. Armisen, D.; Nagui Refki, P.; Crumière, A.J.J.; Viala, S.; Toubiana, W.; Khila, A. Predator strike shapes antipredator phenotype through new genetic interactions in water striders. *Nat. Commun.* **2015**, *6*, 8153. [CrossRef]
23. Haskins, K.; Sih, A.; Krupa, J. Predation Risk and Social Interference as Factors Influencing Habitat Selection in Two Species of Stream-Dwelling Waterstriders. *Behav. Ecol.* **1997**, *8*, 351–363. [CrossRef]
24. Krupa, J.J.; Sih, A. Comparison of Antipredator Responses of Two Related Water Striders to a Common Predator. *Ethology* **1999**, *105*, 1019–1033. [CrossRef]
25. Gruhn, M.; Zehl, L.; Buschges, A. Straight Walking and Turning on a Slippery Surface. *J. Exp. Biol.* **2008**, *212*, 194–209. [CrossRef] [PubMed]
26. Merienne, H.; Latil, G.; Moretto, P.; Fourcassié, V. Walking Kinematics in the Polymorphic Seed Harvester Ant *Messor barbarus*: Influence of Body Size and Load Carriage. *J. Exp. Biol.* **2020**, *223*, jeb205690. [CrossRef]
27. Merienne, H.; Latil, G.; Moretto, P.; Fourcassié, V. Dynamics of Locomotion in the Seed Harvesting Ant *Messor barbarus*: Effect of Individual Body Mass and Transported Load Mass. *PeerJ* **2021**, *9*, e10664. [CrossRef] [PubMed]
28. Ting, L.H.; Blickhan, R.; Full, R.J. Dynamic and Static Stability in Hexapedal Runners. *J. Exp. Biol.* **1994**, *197*, 251–269. [CrossRef]
29. Baek, M.; Lawin, K.M.; Codden, C.J.; Lim, H.; Yang, E.; Kim, H.; Lee, S.; Jablonski, P.G. Water strider females use individual experience to adjust jumping behaviour to their weight within physical constraints of water surface tension. *Sci. Rep.* **2020**, *10*, 18657. [CrossRef]
30. Koh, J.S.; Yang, E.; Jung, G.P.; Jung, S.P.; Son, J.H.; Lee, S.I.; Jablonski, P.G.; Wood, R.J.; Kim, H.Y.; Cho, K.J. Jumping on Water: Surface Tension-Dominated Jumping of Water Striders and Robotic Insects. *Science* **2015**, *349*, 517–521. [CrossRef]



31. Meshkani, J.; Rajabi, H.; Kovalev, A.; Gorb, S.N. Patterns of Load Distribution among the Legs in Small Water Striders during Standing and Striding. *J. Zool.* **2023**, *320*, 84–95. [CrossRef]
32. Yang, E.; Son, J.H.; Lee, S.I.; Jablonski, P.G.; Kim, H.Y. Water Striders Adjust Leg Movement Speed to Optimize Takeoff Velocity for Their Morphology. *Nat. Commun.* **2016**, *7*, 13698. [CrossRef]
33. Perez Goodwyn, P.; Maezono, Y.; Takamatsu, H.; Fujisaki, K. Semiaquatic Heteroptera Locomotion: Coral Treaders (*Hermatobates weddi*, Hermatobatidae), Sea Skaters (*Halovelia septentrionalis*, Veliidae), and Water Striders (*Metrocoris histrio*, Gerridae). Usual and Unusual Gaits. *Hydrobiologia* **2009**, *630*, 219–229. [CrossRef]
34. Fleming, P.; Bateman, P. Just Drop It and Run: The Effect of Limb Autotomy on Running Distance and Locomotion Energetics of Field Crickets (*Gryllus bimaculatus*). *J. Exp. Biol.* **2007**, *210*, 1446–1454. [CrossRef]
35. Lu, H.; Zheng, Y.; Yin, W.; Tao, D.; Pesika, N.; Meng, Y.; Tian, Y. Propulsion Principles of Water Striders in Sculling Forward through Shadow Method. *J. Bionic Eng.* **2018**, *15*, 516–525. [CrossRef]
36. Yin, W.; Zheng, Y.L.; Lu, H.Y.; Zhang, X.J.; Tian, Y. Three-Dimensional Topographies of Water Surface Dimples Formed by Superhydrophobic Water Strider Legs. *Appl. Phys. Lett.* **2016**, *109*, 163701. [CrossRef]
37. Zheng, Y.; Lu, H.; Yin, W.; Tao, D.; Shi, L.; Tian, Y. Elegant Shadow Making Tiny Force Visible for Water-Walking Arthropods and Updated Archimedes' Principle. *Langmuir* **2016**, *32*, 10522–10528. [CrossRef] [PubMed]
38. Steinmann, T.; Arutkin, M.; Cochar, P.; Raphaël, E.; Casas, J.; Benzaquen, M. Unsteady Wave Pattern Generation by Water Striders. *J. Fluid Mech.* **2018**, *848*, 370–387. [CrossRef]
39. Schneider, C.; Rasband, W.; Eliceiri, K. NIH Image to ImageJ: 25 Years of Image Analysis. *Nat. Methods* **2012**, *9*, 671–675. [CrossRef]
40. Pearson, K.G.; Franklin, R. Characteristics of Leg Movements and Patterns of Coordination in Locusts Walking on Rough Terrain. *Int. J. Robot. Res.* **1984**, *3*, 101–112. [CrossRef]
41. Binder, M.D.; Hirokawa, N.; Windhorst, U. *Encyclopedia of Neuroscience*; Springer: Berlin/Heidelberg, Germany, 2008. [CrossRef]
42. Alexander, R.M.N. *Size and Shape*; Edward Arnold: London, UK, 1971.
43. Mahadik, G.; Hernández-Sánchez, J.F.; Arunachalam, S.; Gallo Jr, A.; Cheng, L.; Farinha, A.S.; Thoroddsen, S.T.; Mishra, H.; Duarte, C.M. Superhydrophobicity and Size Reduction Enabled Halobates (Insecta: Heteroptera, Gerridae) to Colonize the Open Ocean. *Sci. Rep.* **2020**, *10*, 7785. [CrossRef]
44. Walker, E.D.; Archer, W.E. Sequential Organization of Grooming Behaviors of the Mosquito, *Aedes triseriatus*. *J. Insect Behav.* **1988**, *1*, 97–109. [CrossRef]
45. Hughes, G.M. The Co-Ordination of Insect Movements: II The Effect of Limb Amputation and the Cutting of Commissures in The Cockroach (*Blatta Orientalis*). *J. Exp. Biol.* **1957**, *34*, 306–333. [CrossRef]
46. Noah, A.J.; Quimby, L.; Frazier, S.F.; Zill, S.N. Force Detection in Cockroach Walking Reconsidered: Discharges of Proximal Tibial Campaniform Sensilla When Body Load Is Altered. *J. Neurosci.* **2001**, *187*, 769–784. [CrossRef] [PubMed]
47. Noah, J.A.; Quimby, L.; Frazier, S.F.; Zill, S.N. Sensing the Effect of Body Load in Legs: Responses of Tibial Campaniform Sensilla to Forces Applied to the Thorax in Freely Standing Cockroaches. *J. Comp. Physiol. A Neuroethol. Sens. Neural Behav. Physiol.* **2004**, *190*, 201–215. [CrossRef]
48. Hu, D.L.; Prakash, M.; Chan, B.; Bush, W.M. Water-Walking Devices. *Exp. Fluids* **2007**, *43*, 769–778. [CrossRef]
49. Song, Y.S.; Sitti, M. STRIDE: A Highly Maneuverable and Non-Tethered Water Strider Robot. In Proceedings of the IEEE International Conference on Robotics and Automation, Rome, Italy, 10–14 April 2007; pp. 980–984. [CrossRef]
50. Alexander, R.M.N. *Principles of Animal Locomotion*; Princeton University Press: Princeton, NJ, USA, 2013. [CrossRef]
51. Delcomyn, F. Perturbation of the Motor System in Freely Walking Cockroaches. I. Rear Leg Amputation and the Timing of Motor Activity in Leg Muscles. *J. Exp. Biol.* **1991**, *156*, 483–502. [CrossRef]
52. Delcomyn, F. Perturbation of the Motor System in Freely Walking Cockroaches. II. The Timing of Motor Activity in Leg Muscles after Amputation of a Middle Leg. *J. Exp. Biol.* **1991**, *156*, 503–517. [CrossRef]
53. Graham, D. The Effect of Amputation and Leg Restraint on the Free Walking Coordination of the Stick Insect *Carausius morosus*. *J. Comp. Physiol.* **1977**, *116*, 91–116. [CrossRef]
54. Pearson, K.G.; Iles, J.F. Nervous Mechanisms Underlying Intersegmental Co-ordination of Leg Movements during Walking in the Cockroach. *J. Exp. Biol.* **1973**, *58*, 725–744. [CrossRef]
55. Kong, X.Q.; Liu, J.L.; Zhang, W.J.; Qu, Y.D. Load-Bearing Ability of the Mosquito Tarsus on Water Surfaces Arising from Its Flexibility. *AIP Adv.* **2015**, *5*, 037101. [CrossRef]
56. Bush, J.W.M.; Hu, D.L. Walking on Water: Biocomotion at the Interface. *Annu. Rev. Fluid Mech.* **2006**, *38*, 339–369. [CrossRef]
57. Darnhofer-Demar, B. Zur Fortbewegung des Wasserl~ufers *Gerris lacustris* L. auf der Wasseroberfl~che. *Verh Dtsch. Zool Ges.* **1968**, *28*, 430–439.
58. Grabowska, M.; Godlewska, E.; Schmidt, J.; Daun-Gruhn, S. Quadrupedal Gaits in Hexapod Animals—Inter-Leg Coordination in Free-Walking Adult Stick Insects. *J. Exp. Biol.* **2012**, *215*, 4255–4266. [CrossRef]
59. Pratt, R.Y. Striding Habits in the Gerridae. *Pan-Pac. Entomol.* **1938**, *14*, 157.
60. Tseng, M.; Rowe, L. Sexual Dimorphism and Allometry in the Giant Water Strider *Gigantometra gigas*. *Can. J. Zool.* **1999**, *77*, 923–929. [CrossRef]
61. Gao, P.; Feng, J. A Numerical Investigation of the Propulsion of Water Walkers. *J. Fluid Mech.* **2011**, *668*, 363–383. [CrossRef]
62. Zill, S.N.; Keller, B.R.; Duke, E.R. Sensory Signals of Unloading in One Leg Follow Stance Onset in Another Leg: Transfer of Load and Emergent Coordination in Cockroach Walking. *J. Neurophysiol.* **2008**, *101*, 2297–2304. [CrossRef]

63. Akay, T.; Ludwar, B.C.; Goritz, M.L.; Schmitz, J.; Buschges, A. Segment specificity of load signal processing depends on walking direction in the stick insect leg muscle control system. *J. Neurosci.* **2007**, *27*, 3285–3294. [CrossRef] [PubMed]
64. Bässler, U. Sensory control of leg movement in the stick insect *Carausius morosus*. *Biol. Cybern.* **1977**, *25*, 61–72. [CrossRef] [PubMed]
65. Dean, J. Control of Leg Protraction in the Stick Insect: A Targeted Movement Showing Compensation for Externally Applied Forces. *J. Comp. Physiol. A* **1984**, *155*, 771–781. [CrossRef]
66. Delcomyn, F. Walking Robots and the Central and Peripheral Control of Locomotion in Insects. *J. Comp. Physiol. A Sens. Neural Behav. Physiol.* **1999**, *185*, 259–270. [CrossRef]
67. Schmitz, J. Load-Compensating Reactions in the Proximal Leg Joints of Stick Insects During Standing and Walking. *J. Exp. Biol.* **1993**, *183*, 15–33. [CrossRef]
68. Owaki, D.; Aonuma, H.; Sugimoto, Y.; Ishiguro, A. Leg Amputation Modifies Coordinated Activation of the Middle Leg Muscles in the Cricket *Gryllus bimaculatus*. *Sci. Rep.* **2021**, *11*, 1327. [CrossRef]
69. Feng, X.Q.; Gao, X.F.; Wu, Z.N.; Jiang, L.; Zheng, Q.S. Superior Water Repellency of Water Strider Legs with Hierarchical Structures: Experiments and Analysis. *Langmuir* **2007**, *23*, 4892–4896. [CrossRef] [PubMed]
70. Gao, X.; Jiang, L. Biophysics: Water-Repellent Legs of Water Striders. *Nature* **2004**, *432*, 36. [CrossRef] [PubMed]
71. Full, R.J.; Zuccarello, D.A.; Tullis, A. Effect of Variation in Form on the Cost of Terrestrial Locomotion. *J. Exp. Biol.* **1990**, *150*, 233–246. [CrossRef]
72. Delcomyn, F. The Effect of Limb Amputation on Locomotion in the Cockroach *Periplaneta americana*. *J. Exp. Biol.* **1971**, *54*, 453–469. [CrossRef]
73. Zhang, Y.; Zhang, J.; Ren, L. The Terrestrial Locomotion of a Mole Cricket with Foreleg Amputation. *Sci. China Technol. Sci.* **2015**, *58*, 999–1006. [CrossRef]
74. Bateman, P.W.; Fleming, P.A. Direct and indirect costs of limb autotomy in field crickets, *Gryllus bimaculatus*. *Anim. Behav.* **2005**, *69*, 151–159. [CrossRef]
75. Zill, S.; Schmitz, J.; Büschges, A. Load Sensing and Control of Posture and Locomotion. *Arthropod Struct. Dev.* **2004**, *33*, 273–286. [CrossRef]
76. Wittlinger, M.; Wehner, R.; Wolf, H. The Ant Odometer: Stepping on Stilts and Stumps. *Science* **2006**, *312*, 1965–1967. [CrossRef]
77. Wittlinger, M.; Wehner, R.; Wolf, H. The Desert Ant Odometer: A Stride Integrator That Accounts for Stride Length and Walking Speed. *J. Exp. Biol.* **2007**, *210*, 198–207. [CrossRef]
78. Berendes, V.; Zill, S.N.; Büschges, A.; Bockemühl, T. Speed-dependent interplay between local pattern-generating activity and sensory signals during walking in *Drosophila*. *J. Exp. Biol.* **2016**, *219*, 3781–3793. [CrossRef]
79. Wosnitza, A.; Bockemühl, T.; Dubbert, M.; Scholz, H.; Buschges, A. Inter-Leg Coordination in the Control of Walking Speed in *Drosophila*. *J. Exp. Biol.* **2013**, *216*, 480–491. [CrossRef] [PubMed]
80. Kim, W.; Pham, T.H.; Nguyen, P.D.; Tran, A.D.; Ha, J.; Jablonski, P.G.; Lee, S. Locomotion and Flow Speed Preferences in Natural Habitats by Large Water Striders, *Ptilomera tigrina*, with Micro-Morphological Adaptations for Rowing. *J. Ethol.* **2022**, *40*, 211–221. [CrossRef]

**Disclaimer/Publisher’s Note:** The statements, opinions and data contained in all publications are solely those of the individual author(s) and contributor(s) and not of MDPI and/or the editor(s). MDPI and/or the editor(s) disclaim responsibility for any injury to people or property resulting from any ideas, methods, instructions or products referred to in the content.



MDPI AG  
Grosspeteranlage 5  
4052 Basel  
Switzerland  
Tel.: +41 61 683 77 34

*Biomimetics* Editorial Office  
E-mail: [biomimetics@mdpi.com](mailto:biomimetics@mdpi.com)  
[www.mdpi.com/journal/biomimetics](http://www.mdpi.com/journal/biomimetics)



Disclaimer/Publisher's Note: The title and front matter of this reprint are at the discretion of the Guest Editors. The publisher is not responsible for their content or any associated concerns. The statements, opinions and data contained in all individual articles are solely those of the individual Editors and contributors and not of MDPI. MDPI disclaims responsibility for any injury to people or property resulting from any ideas, methods, instructions or products referred to in the content.





Academic Open  
Access Publishing

[mdpi.com](http://mdpi.com)

ISBN 978-3-7258-3389-4